IBRACON
Instituto Brasileiro do Concreto

REVISTA IBRACON DE ESTRUTURAS E MATERIAIS
IBRACON STRUCTURES AND MATERIALS JOURNAL

Volume 12, Number 1
February, 2019
ISSN 1983-4195

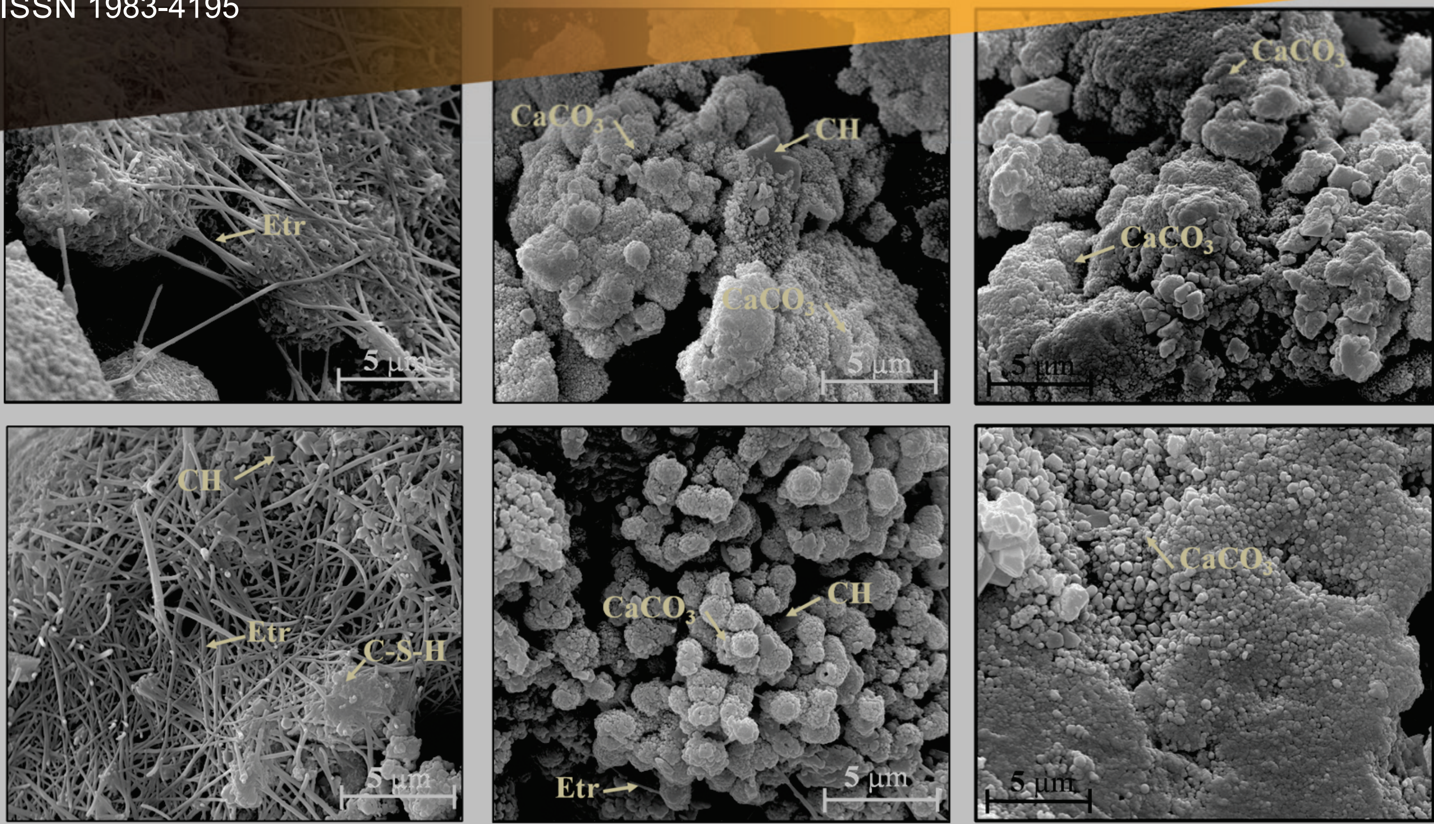

Contents

Analysis of the brazilian federal bridge inventory
C. B. L. OLIVEIRA, M. GRECO and T. N. BITTENCOURT

Analytical study of cylindrical tanks including soil-structure interaction
R. L. C. SILVA, G. B. MARQUES, E. N. LAGES and S. P. C. MARQUES

Geometric optimization associated with the use of high-strength concrete in viaducts
E. V. W. TRENTINI and C. H. MARTINS

Effects of Bacillus subtilis biocementation on the mechanical properties of mortars
N. SCHWANTES-CEZARIO, M. F. PORTO, G. F. B. SANDOVAL, G. F. N. NOGUEIRA, A. F. COUTO and B. M. TORALLES

Numerical study of the behaviour of loop bar splicing in joints of reinforced concrete structures
T. D. L. VASCONCELOS and V. G. HAACH

Experimental analysis of load capacity in beams with steel fiber reinforcement on the compression face
C. C. DEGHENHARD, B. V. SILVA and F. PELISSER

Strut-and-tie models for linear and nonlinear behavior of concrete based on topological evolutionary structure optimization (ESO)
R. M. LANES, M. GRECO and M. B. B. F. GUERRA

Pervious concrete: study of dosage and polypropylene fibers addiction
S. E. PILZ, P. OLIVEIRA, F. REGOSO, V. A. PAULON and M. F. COSTELLA

A numerical analysis of a concrete slab breaching using high explosives
M. L. COSTA NETO and G. N. DOZ

Comparative analysis among standards of the area calculation of transversal reinforcement on reinforced concrete beams of high resistance subjected by shear force
D. H. L. BRAZ, R. BARROS and J. N. DA SILVA FILHO

Behavior of the self-compacting mortar with sugarcane bagasse ash in the fresh and hardened state
V. C. SANTOS, R. D. VANDERLEI, K. K. MORAES, E. T. D. F. ROSINA and G. M. BALBINO

Analysis of strengthening procedures of reinforced concrete highway bridges: a brazilian case study
D. M. CARVALHO and J. M. F. CALIXTO

Editorial

The first issue of 2019 of the IBRACON Structures and Materials Journal (Volume 12 Number 1, February 2019) is now available online. The first article aims at an appropriate support to decision-making for maintenance, rehabilitation and repair strategies under constraint of limited budgets. An analytical study on the design of cylindrical liquid storage tanks resting on deformable foundations is the subject of the second article. The third article discusses the economic aspects of high-strength concrete associated with geometrical optimization of decks of post-tensioned multi-girder overpasses. The fourth article brings an evaluation of the influence of Bacillus subtilis AP91 spores addition on the mechanical properties of mortars. The fifth article presents a study on the loop joint behavior in reinforced concrete structures under tension. The sixth article discusses experimental results related to load capacity of beams with steel fiber reinforcement on the compression face. The seventh article has the objective of presenting the application of the linear and non-linear strut-and-tie models on some typical structural elements, using the Evolutionary Topological Optimization Method. The eighth article presents a study of dosage and addition of polypropylene fibers for pervious concrete. The ninth article presents a numerical study on the explosive breaching of a concrete wall using an optimized contact explosive charge with cylindrical shape. In the tenth article, a comparative analysis is presented among standards of transversal reinforcement computation for high strength reinforced concrete beams subjected to shear action. The eleventh article investigates the behavior of the self-compacting mortars with sugarcane bagasse ash in fresh and hardened state. The goal of the twelfth is the evaluation of the widening and strengthening procedures used in reinforced concrete highway bridges.

We acknowledge the dedication of authors and reviewers to the quality of this issue.

The Editors

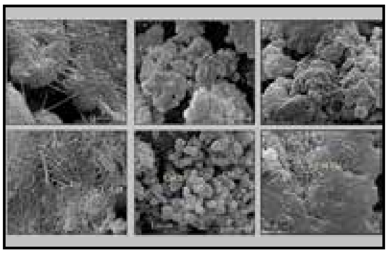

Cover: SEM image of Bacillus subtilis biocementation

Courtesy: N. SCHWANTES-CEZARIO, State University of Londrina, Brazil

IBRACON

Ibracon Structures and Materials Journal is published bimonthly (February, April, June, August, October and December) by IBRACON.

IBRACON
Instituto Brasileiro do Concreto
Founded in 1972

R. Julieta do Espirito Santo Pinheiro, 68
Jardim Olímpia, São Paulo – SP
Brasil – 05542-120
Phone: +55 11 3735-0202
Fax: +55 11 3733-2190
E-mail: arlene@ibracon.org.br
Website: http://www.ibracon.org.br

Volume 12, Number 1
February, 2019
ISSN: 1983-4195

REVISTA IBRACON DE ESTRUTURAS E MATERIAIS

IBRACON STRUCTURES AND MATERIALS JOURNAL

Contents

Analysis of the brazilian federal bridge inventory
C. B. L. OLIVEIRA, M. GRECO and T. N. BITTENCOURT
1

Analytical study of cylindrical tanks including soil-structure interaction
R. L. C. SILVA, G. B. MARQUES, E. N. LAGES and S. P. C. MARQUES
14

Geometric optimization associated with the use of high-strength concrete in viaducts
E. V. W. TRENTINI and C. H. MARTINS
23

Effects of* Bacillus subtilis *biocementation on the mechanical properties of mortars
N. SCHWANTES-CEZARIO, M. F. PORTO, G. F. B. SANDOVAL, G. F. N. NOGUEIRA, A. F. COUTO and B. M. TORALLES
31

Numerical study of the behaviour of loop bar splicing in joints of reinforced concrete structures
T. D. L. VASCONCELOS and V. G. HAACH
39

Experimental analysis of load capacity in beams with steel fiber reinforcement on the compression face
C. C. DEGHENHARD, B. V. SILVA and F. PELISSER
69

Strut-and-tie models for linear and nonlinear behavior of concrete based on topological evolutionary structure optimization (ESO)
R. M. LANES, M. GRECO and M. B. B. F. GUERRA
87

Pervious concrete: study of dosage and polypropylene fibers addiction
S. E. PILZ, P. OLIVEIRA, F. REGOSO, V. A. PAULON and M. F. COSTELLA
101

A numerical analysis of a concrete slab breaching using high explosives
M. L. COSTA NETO and G. N. DOZ
122

Comparative analysis among standards of the area calculation of transversal reinforcement on reinforced concrete beams of high resistance subjected by shear force
D. H. L. BRAZ, R. BARROS and J. N. DA SILVA FILHO
139

Behavior of the self-compacting mortar with sugarcane bagasse ash in the fresh and hardened state
V. C. SANTOS, R. D. VANDERLEI, K. K. MORAES, E. T. D. F. ROSINA and G. M. BALBINO
179

Analysis of strengthening procedures of reinforced concrete highway bridges: a brazilian case study
D. M. CARVALHO and J. M. F. CALIXTO
199

Aims and Scope

The IBRACON Structures and Materials Journal is a technical and scientifical divulgation vehicle of IBRACON (Brazilian Concrete Institute). Each issue of the periodical has 5 to 8 papers and, possibly, a technical note and/or a technical discussion regarding a previously published paper. All contributions are reviewed and approved by reviewers with recognized scientific competence in the area.

Objectives

The IBRACON Structures and Materials Journal´s main objectives are:

- Present current developments and advances in the area of concrete structures and materials;
- Make possible the better understanding of structural concrete behavior, supplying subsidies for a continuous interaction among researchers, producers and users;
- Stimulate the development of scientific and technological research in the areas of concrete structures and materials, through papers peer-reviewed by a qualified Editorial Board;
- Promote the interaction among researchers, constructors and users of concrete structures and materials and the development of Civil Construction;
- Provide a vehicle of communication of high technical level for researchers and designers in the areas of concrete structures and materials.

Submission Procedure

The procedure to submit and revise the contributions, as well as the formats, are detailed on IBRACON's WebSite (www.ibracon.org.br). The papers and the technical notes are revised by at least three reviewers indicated by the editors. The discussions and replies are accepted for publication after a revision by the editors and at least one member of the Editorial Board. In case of disagreement between the reviewer and the authors, the contribution will be sent to a specialist in the area, not necessarily linked to the Editorial Board.

Contribution Types

The periodical will publish original papers, short technical notes and paper discussions. Announcements of conferences and meetings, information about book reviews, events and contributions related to the area will also be available in the periodical's WebSite. All contributions will be revised and only published after the Editorial and Reviewers Boards approve the paper. Restrictions of content and space (size) are imposed to the papers. The contributions will be accepted for review in Portuguese, Spanish or English. The abstracts are presented in Portuguese or Spanish, and in English, independently of the language in which the paper is written. After the review process, papers originally written in Portuguese or Spanish should be translated into English, which is the official language of the IBRACON Structures and Materials Journal. Optionally, papers are also published in Portuguese or Spanish.

Original papers will be accepted as long as they are in accordance with the objectives of the periodical and present quality of information and presentation. The instructions to submit a paper are detailed in the template (available on IBRACON's WebSite).

The length of the papers must not exceed 20 pages.

A technical note is a brief manuscript. It may present a new feature of research, development or technological application in the areas of Concrete Structures and Materials, and Civil Construction. This is an opportunity to be used by industries, companies, universities, institutions of research, researchers and professionals willing to promote their works and products under development. The instructions to submit a technical note are detailed on IBRACON's WebSite.

A discussion is received no later than 3 months after the publication of the paper or technical note. The instructions to submit a discussion are detailed on IBRACON's WebSite. The discussion must be limited to the topic addressed in the published paper and must not be offensive. The right of reply is guaranteed to the Authors. The discussions and the replies are published in the subsequent issues of the periodical.

Internet Access

IBRACON Structural Journal Page in http://www.ibracon.org.br

Subscription rate

All IBRACON members have free access to the periodical contents through the Internet. Non-members have limited access to the published material, but are able to purchase isolated issues through the Internet. The financial resources for the periodical´s support are provided by IBRACON and by research funding agencies. The periodical will not receive any type of private advertisement that can jeopardize the credibility of the publication.

Photocopying

Copyright

IBRACON

Rua Julieta do Espírito Santo Pinheiro, nº 68 ,Jardim Olímpia,
São Paulo, SP – Brasil CEP: 05542-120
Phone: +55 11 3735-0202 Fax: +55 11 3733-2190
E-mail: arlene@ibracon.org.br.

Disclaimer

Papers and other contributions and the statements made or opinions expressed therein are published on the understanding that the authors of the contribution are the only responsible for the opinions expressed in them and that their publication does not necessarily reflect the support of IBRACON or the journal.

Objetivos e Escopo

A Revista IBRACON de Estruturas e Materiais é um veículo de divulgação técnica e científica do IBRACON (Instituto Brasileiro do Concreto). Cada número do periódico tem 5 a 8 artigos e, possivelmente, uma nota técnica e/ou uma discussão técnica sobre um artigo publicado anteriormente. Todas as contribuições são revistas e aprovadas por revisores com competência científica reconhecida na área.

Objetivos

Os objetivos principais da Revista IBRACON de Estruturas e Materiais são:

- Apresentar desenvolvimentos e avanços atuais na área de estruturas e materiais de concreto;
- Possibilitar o melhor entendimento do comportamento do concreto estrutural, fornecendo subsídios para uma interação contribua entre pesquisadores, produtores e usuários;
- Estimular o desenvolvimento de pesquisa científica e tecnológica nas áreas de estruturas de concreto e materiais, através de artigos revisados por um corpo de revisores qualificado;
- Promover a interação entre pesquisadores, construtores e usuários de estruturas e materiais de concreto, e o desenvolvimento da Construção Civil;
- Prover um veículo de comunicação de alto nível técnico para pesquisadores e projetistas nas áreas de estruturas de concreto e materiais.

Submissão de Contribuições

O procedimento para submeter e revisar as contribuições, assim como os formatos, estão detalhados na página Internet do IBRACON (www.ibracon.org.br). Os artigos e as notas técnicas são revisadas por, no mínimo, três revisores indicados pelos editores. As discussões e réplicas são aceitas para publicação após uma revisão pelo editores e no mínimo um membro do Corpo Editorial. No caso de desacordo entre revisor e autores, a contribuição será enviada a um especialista na área, não necessariamente do Corpo Editorial.

Tipos de Contribuição

O periódico publicará artigos originais, notas técnicas curtas e discussões sobre artigos. Anúncios de congressos e reuniões, informação sobre revisão de livros e contribuições relacionadas à área serão também disponibilizadas na página Internet da revista. Todas as contribuições serão revisadas e publicadas apenas após a aprovação dos revisores e do Corpo Editorial. Restrições de conteúdo e espaço (tamanho) são impostas aos artigos. As contribuições serão aceitas para revisão em português, espanhol ou inglês. Os resumos serão apresentados em português ou espanhol, e em inglês, independentemente do idioma em que o artigo for escrito. Após o processo de revisão, artigos originalmente escritos em português ou espanhol deverão ser traduzidos para inglês, que é o idioma oficial da Revista IBRACON de Estruturas e Materiais. Opcionalmente, os artigos são também publicados em português ou espanhol.

Artigos originais serão aceitos desde que estejam de acordo com os objetivos da revista e apresentam qualidade de informação e apresentação. As instruções para submeter um artigo estão detalhadas em um gabarito (disponível no sítio do IBRACON).

A extensão dos artigos não deve exceder 20 páginas.

Um nota técnica é um manuscrito curto. Deve apresentar uma nova linha de pesquisa, desenvolvimento ou aplicação tecnológica nas áreas de Estruturas de Concreto e Materiais, e Construção Civil. Esta é uma oportunidade a ser utilizada por indústrias, empresas, universidades, instituições de pesquisa, pesquisadores e profissionais que desejem promover seus trabalhos e produtos em desenvolvimento. As instruções para submissão estão detalhadas na página de Internet do IBRACON.

Uma discussão é recebida não mais de 3 meses após a publicação do artigo ou nota técnica. As instruções para submeter uma discussão estão detalhadas na página de Internet do IBRACON. A discussão deve se limitar ao tópico abordado no artigo publicado e não pode ser ofensivo. O direito de resposta é garantido aos autores. As discussões e réplicas são publicadas nos números subseqüentes da revista.

Acesso via Internet

Página da Revista IBRACON de Estruturas e Materiais em http://www.ibracon.org.br

Assinatura

Todos os associados do IBRACON têm livre acesso ao conteúdo do periódico através da Internet. Não associados têm acesso limitado ao material publicado, mas podem adquirir números isolados pela Internet. O financiamento para suporte à revista é provido pelo IBRACON e por agências de financiamento à pesquisa. A revista não receberá qualquer tipo de anúncio privado que possa prejudicar a credibilidade da publicação.

Fotocópias

Fotocópias no Brasil, A Lei Brasileira de Direitos Autorais é aplicada a usuários no Brasil. O IBRACON detém os direitos autorais das contribuições na revista a menos que haja informação em contrário no rodapé da primeira página da contribuição. Onde o IBRACON detém os direitos autorais, autorização para fotocopiar itens para uso interno ou pessoal, ou uso interno ou pessoal de clientes específicos, é concedida para bibliotecas e outros usuários registrados no IBRACON.

Direitos autorais

IBRACON

Rua Julieta do Espírito Santo Pinheiro, nº 68 , Jardim Olímpia,
São Paulo, SP –Brasil CEP: 05542-120
Fone: +55 11 3735-0202 Fax: +55 11 3733-2190

E-mail: arlene@ibracon.org.br.

Aviso Legal

Artigos e outras contribuições e declarações feitas ou opiniões expressas aqui são publicadas com o entendimento que os autores da contribuição são os únicos responsáveis pelas opiniões expressas neles e que sua publicação não necessariamente reflete o apoio do IBRACON ou da revista.

Diretoria

Diretoria
Biênio 2017/2019

Diretor Presidente
Julio Timerman

Assessores da Presidência
Augusto Carlos de Vasconcelos
José Tadeu Balbo
Selmo Chapira Kuperman

Assessor da Presidência – Atuação ABCP/ABESC
Hugo da Costa Rodrigues Filho

Assessor da Presidência – Atuação Construtoras
Alexandre Couso – ESSER

Diretor 1º Vice-Presidente
Luiz Prado Vieira Júnior

Diretor 2º Vice-Presidente
Bernardo Tutikian

Diretor 1º Secretário
Antonio Domingues de Figueiredo

Diretor 2º Secretário
Carlos José Massucato

Diretor 1º Tesoureiro
Claudio Sbrighi Neto

Diretor 2º Tesoureiro
Nelson Covas

Diretor de Marketing
Hugo Rodrigues

Diretor de Eventos
César Daher

Assessores da Diretoria de Eventos
Maurice Antoine Traboulsi
Sônia Regina Cottas Freitas

Diretor Técnico
Paulo Helene

Diretor de Relações Institucionais
Túlio Nogueira Bittencourt

Diretor de Publicações e Divulgação Técnica
Íria Lícia Oliva Doniak

Diretor de Pesquisa e Desenvolvimento
Leandro Mouta Trautwein

Diretor de Cursos
Enio José Pazini Figueiredo

Diretor de Certificação de Pessoal
Gilberto Antônio Giuzio

Diretora de Atividades Estudantis
Jéssika Pacheco

Conselho Diretor
Biênio 2017/2019

Sócios Titulares Individuais

Cláudio Sbrighi Neto
Augusto Carlos de Vasconcelos
Júlio Timerman
Luiz Prado Vieira Júnior
Antônio Domingues de Figueiredo
Vladimir Antonio Paulon
Carlos José Massucato
Maurice Antoine Traboulsi
Nélson Covas
César Henrique Sato Daher
Luiz Carlos Pinto da Silva
Inês Laranjeira da Silva Battagin
Antonio Laranjeiras
Enio Pazini Figueiredo
Geraldo Cechella Isaia
Mário Willian Esper

Sócios Titulares Mantenedores e Coletivos

ABCP – Associação Brasileira de Cimento Portland
POLI-USP – Escola Politécnica da Universidade de São Paulo
IPT – Instituto de Pesquisas Tecnológicas de São Paulo
FURNAS Centrais Elétricas S.A.
LAFARGE HOLCIM
CNO – Construtora Noberto Odebrecht
ABCIC – Associação Brasileira da Construção Industrializada de Concreto
L. A. Falcão Bauer Centro Tecnológico de Controle de Qualidade Ltda.
ABESC – Associação Brasileira das Empresas de Serviços de Concretagem
GERDAU

Conselheiros Permanentes

Eduardo Antonio Serrano
José Marques Filho
Paulo Helene
Ronaldo Tartuce
Rubens Machado Bittencourt
Selmo Chapira Kuperman
Simão Priszkulnik
Tulio Nogueira Bittencourt

Volume 12, Number 1 (February 2019) p. 1 – 13 • ISSN 1983-4195
http://dx.doi.org/10.1590/S1983-41952019000100002

REVISTA IBRACON DE ESTRUTURAS E MATERIAIS
IBRACON STRUCTURES AND MATERIALS JOURNAL

Analysis of the brazilian federal bridge inventory

Análise do inventário das pontes federais do Brasil

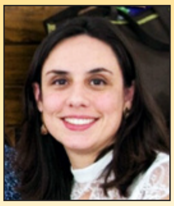

C. B. L. OLIVEIRA [a]
carolineburatto@yahoo.com.br
http://orcid.org/0000-0002-8951-0511

M. GRECO [a]
mgreco@dees.ufmg.br
http://orcid.org/0000-0001-5500-0225

T. N. BITTENCOURT [b]
tbitten@gmail.com
http://orcid.org/0000-0001-6523-2687

Abstract

Bridge Management aims to provide an appropriate support to decision-making for maintenance, rehabilitation and repair strategies under constraint of limited budgets. In this regard, the Federal Brazilian Department of Transportation (DNIT) has developed the SGO - a Brazilian Bridge Management System (B-BMS) - and promoted the most comprehensive road bridge inventory under its direct administration. To improve the management of these bridge assets, the DNIT is working to develop a statistical model to predict the future condition of bridge: the most efficient and effective tool in a BMS to planning when the maintenance actions will be required. The current paper reports on findings of inventory, predominantly composed of reinforced concrete bridges, focusing on potential deterioration agents reported and checking their influence on deterioration conditions. Based on national database, the paper proposes a methodology to forecast Brazilian bridges deterioration rates. An example of application is demonstrated and satisfactory prediction accuracy obtained, even for few inspection cycles and under restricted database information.

Keywords: bridge management systems, bridge inventory, bridge deterioration models, Markov chains.

Resumo

A gestão de pontes promove suporte na tomada de decisões gerenciais, otimizando as intervenções necessárias sob limitações orçamentárias. Nessa perspectiva, o Departamento Federal de Transportes (DNIT) desenvolveu o Sistema Brasileiro de Gerenciamento de Pontes (SGO) e promoveu o mais abrangente inventário de pontes rodoviárias sob sua administração direta. Atualmente, o DNIT promove pesquisa para o desenvolvimento de um modelo estatístico de previsão das futuras condições das pontes: ferramenta basilar e de importância crucial no gerenciamento. O presente artigo apresenta os resultados do inventário, predominantemente composto de pontes em concreto armado, focando no registro dos potenciais agentes de deterioração e da sua possível influência no estado de conservação dessas estruturas. Baseado nas características do inventário, o artigo propõe uma metodologia para a previsão das taxas de deterioração de pontes brasileiras com um exemplo da sua aplicação, obtendo boa previsão do estado futuro mesmo quando utilizada em parques de obras com poucos ciclos de inspeções e restritas informações do banco de dados.

Palavras-chave: sistemas de gestão de pontes, inventário de pontes, modelos de deterioração, cadeias de Markov.

[a] *Federal University of Minas Gerais, Belo Horizonte, MG, Brazil;*
[b] *University of São Paulo, São Paulo, SP, Brazil.*

Received: 14 Jan 2018 • Accepted: 06 Jun 2018 • Available Online: 05 Feb 2019

1. Introduction

Bridges play a crucial role in civil infrastructure by providing crossings at critical locations. They maintain network continuity, traversing natural and human-made features that otherwise would add significant travel time and cost [1]. Concrete bridge structures designed to maintain their service and function over extended periods. However, they are exposed to the environmental conditions and subjected to many deteriorative influences, such as traffic wear and tear, exposure to deteriorative agents such as sulfates, chloride ions, construction or design errors and inadequate maintenance programs [2]. Bridges are crucial elements of any transportation network due to their strategic location and dangerous consequences if they collapse or if their capacity is impaired. An effective bridge-management program is a prerequisite to a successful horizontal transportation system.

Nonetheless, managing thousands of highway bridges has become increasingly critical in the past few decades, which led to the development of tools that help government agencies. Bridge Management Systems (BMS) are being designed to enhance the management strategies of large bridge networks. The primary objective of a BMS is to assist a bridge manager in making optimal decisions regarding allocation of a budgets to the Maintenance, Rehabilitation, and Replacement (MR&R) needs of individual bridges (project level) or a group of bridges (network level) based on their life cycle cost assessment [3]. The BMS enables to a systematic determination of present and future predicted needs, as well as to list and prioritize maintenance, rehabilitation, and replacement actions and also provide guidance in the practical use of specific funds with possible regards to safety and budgetary constraints.

The effectiveness of a BMS relies on quality and accuracy of information contained in bridge inventory and data obtained through field inspections [4]. The database and inventory allow bridge managers to be fully informed about the conditions of the bridges under their control, so that they can make well based decisions about future maintenance and repair activities. In addition to the database, BMS usually have three more modules: deterioration models, cost models, and MR&R decisions or optimization models.

The deterioration module basilar and required to develop plans for MR&R actions. There are several methodologies to forecasting bridge deterioration; mainly Markov chains models, regression-based models, dynamic response sensors and artificial intelligence. All existing methods depend on the inspection data and each application is derived from the specific data available from inspections. Hence, the adoption of the methodology and its applicability rely on the characteristics of the inspections carried out. All the aspects considered, to obtain more accurate outcomes of deterioration rates, the inventory must have its peculiarities well identified to set the most appropriate method.

1.1 Background

Different agencies manage bridges in Brazil at the federal, state and municipal governments (public sector) levels. The Federal Department of Transport Infrastructure (Departamento Nacional de Infraestrutura em Transportes - DNIT) currently supervises the design, construction, operation, maintenance, repair, rehabilitation, and replacement of more than 5,000 bridges across the federal road network. The average age of the bridges in Brazil has been increasing continuously since 1960, which means that the bridges are aging despite the limited maintenance budget, due to Brazil's bottleneck economic development in transportation infrastructures [5].

As funding to meet the growing needs for new infrastructure and Maintenance, Repair, and Rehabilitation (MR&R) of infrastructure becomes more difficult to obtain and maximize the service life of bridges. Tools to assist in optimizing need-based scheduling of MR&R activities, as well as tools to aid with decision-making strategies, are essential to the efforts of DNIT's Structures Department. To support performance-based and data-driven planning, a bridge management system denominated SGO (Sistema de Gestão de Obras-de-arte) stores bridge data, including bridge characteristics, inspection data, and rating information. To improve SGO, DNIT is

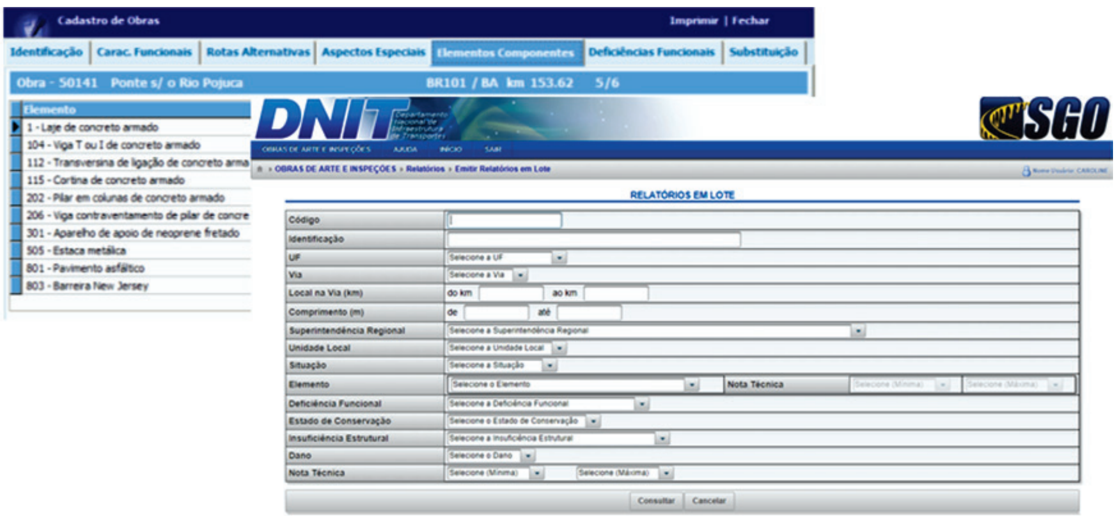

Figure 1
Data entry screen of SGO Mobile inspector version

promoting research to develop deterioration and economic models to predict outcomes and to guide network-level and project-level decisions and optimal preservation policy.

After the latest implemented version of SGO, in 2004, the new software design has improved advanced computer tools for inspection data entry, prepared to gather inspection information, catalogue pictures and drawings of basic schemes as well as short videos. Mobile devices were able to register inspections through SGO Mobile and send the information directly to SGO Web [6]. Figure 1 show the data entry screen of SGO Mobile inspector version and the data query module of SGO Web.

Above all technological improvement, the most important advance has been the introduction to a bridge element-level approach. Bridges are presented in terms of their structural components, and recording their different types include beams, arches, decks and deck slabs; railings and traffic barriers, bearings, deck joints, piers and columns, abutments, approach slabs, among others. The characteristics for each element are assigned, as their geometrical form, material and structural function. The latest inventory was finished in 2017. It was the most comprehensive national inventory, with 4,732 structures performed at element-level inspection, including almost 80% of total road bridge infrastructure.

1.2 Objectives

DNIT inventory data was organized in a logical outline to give a complete overview of inventory contents. The primary focus is to identify required information, which will improve research methods to forecast Brazilian bridges deterioration, so as to enhance SGO. Therefore, possible deterioration agents and damages, its types, frequency and location should be singled out.

Generally supporting significant MR&R strategies, BMS is based on a reliable bridge deterioration model [7]. Similarly to BMS, the deterioration model accuracy depends mainly on registering as much pertinent information on the bridge as possible. The singularities of the national inventory it is also essential to develop a methodology to forecast Brazilian bridges deterioration. These findings will determine the most appropriated method, considering a minimum required accuracy, best suited to national practices of inspection of concrete bridges and, mainly, adjusted to available data characteristics in SGO. The lack of available information about bridges degradation rates in Brazil prevents managers from being able to predict when these structures will need maintenance services. Therefore, it considerably affects strategic planning and schedule of MR&R actions.

Notably, DNIT Transport Programs and Projects costs need to be predicted one year in advance, so that the Brazilian Speaker of the House of Representatives requests the funds. If DNIT does not have any predictive tool to foresee the future of the bridge conditions, the programmed cost may vary from the real cost needed to carry out the MR&R required actions. In addition, private companies would also be able to plan their required actions and associated costs.

2. Condition index

Regarding risk identification, required maintenance, strengthening and replacement of components, bridge assessment data is a crucial input to decision-making. This information together with engineering judgment composes the basis for the development of work programs. Infrastructure maintenance and rehabilitation decision making are based on current and future facility conditions [8]. To this end, inspections are conducted to document noticeable changes from a new-condition. It is a widespread practice to qualitatively evaluate the condition of a bridge and its elements using an ordinal scale. The condition of each element is reported according to a condition state (technical evaluation in SGO) or "Index of Condition" (IC), which is a quantitative measure of deterioration, safety and serviceability. The IC is determined based on the specific degradation or defects apparent at the time of inspection.

The IC can be assigned by element, by set of bridge elements or by general structures and reflects the final result of the inspection. Usually, the IC adds a subjective attribute of the structural condition of the bridge, linked with bridge safety. The Brazilian standards DNIT 010/2004 [9] and NBR-9452/2016 [10] adopted five discrete levels of rating, 1 to 5, from the worst to best state. Frequently, IC=1 and IC=2 are referred to as reaching or having reached an intervention point, which acts as a trigger to perform an action. These IC typically represent the need for measures to be taken soon or immediately. Also, IC=1 could denote reduced structural capacity or serviceability.

Before the SGO latest version, the inspection data evaluated the listed materials, the physical condition of the deck, superstructure, substructure and infrastructure of bridge, including elements. As a result there were five IC, one general and four specific attributes for major regions. The SGO's third version made it possible to assign condition ratings to each bridge element. It also permitted to certify whether or not the component has structural function.

3. Bridge deterioration models

There are several approaches to forecast bridge deterioration. The models of bridge deterioration are categorized in empirical or mechanistic methods. The empirical models are based on experimental data, while the mechanistic models are developed from analytical models associated to degradation mechanisms. Despite the different techniques, these methods could be classified in deterministic, stochastic and artificial intelligence models [11].

The deterministic models of deterioration are the most straightforward approach to predict future condition of bridges. They are obtained through the use of straight or curved lines, and a regression process sets their shapes and parameters. Stochastic models measure the bridge deterioration process as one or more random variables and attributed occurrence probabilities of a specific state within a sample. The third method, artificial intelligence models, exploits computer techniques that aim to automate intelligent behaviors [12].

4. Markov chain method

Stochastic deterioration models aim to associate time with degradation process based on one or more random variables. To researches in the field of bridge deterioration, Markov process is discrete in time and in variables, especially due to the discrete nature of IC observed in inspections. Thus, Markov chains, a particular case of the Markov Process, are suitable and widely used to develop statistical models of deterioration of various types of infrastructure materials, such as pavements, bridges, buildings, among others. In state-based models, the deterioration process is modeled through as a transition from the current state *i* at an initial time to a state *j* at time given by:

$$P_{(\Delta t)ij} = P_r(X_{\Delta t} = jX_{\Delta t} = i) \quad (1)$$

The process is independent of type: for any given condition state, a fixed probability exists for its transition into another condition state. The probabilities of a bridge change IC are represented by a matrix *(n x n)*, where *n* is each IC levels, denominated *Transition Probability Matrix* (TPM):

$$P = \left[p_{ij}\right] = \begin{bmatrix} p_{11} & p_{12} & \cdots & p_{1n} \\ p_{21} & p_{22} & \cdots & p_{2n} \\ \vdots & \vdots & \ddots & \vdots \\ p_{m1} & p_{m2} & \cdots & p_{mn} \end{bmatrix} \quad (2)$$

Markov Chains is applied in cases of bridge deterioration based on cumulative and probabilistic damage approach, in which the IC decreases, after several transition periods, is expected [13].

5. Brazilian bridges characteristics

The recent Brazilian bridge inventory registered 4,725 bridges. It represents more than 80% of the number estimated by various jurisdictions of federal government. 65.53 km of bridge extension were registered by the inventory. The vast majority of the federal highways located in Rio de Janeiro and São Paulo are directly administrated by these states. For this reason they were not inspected in this inventory conducted by the DNIT. The majority of the bridges inspected in the DNIT inventory are reinforced concrete (RC) bridges (99.2%). The most used system, more than 58% is reinforced concrete beam (2,764 bridges), followed by reinforced concrete slab, 777 bridges and the post-tensioned system, 622 bridges. This results in the need of more management attention considering that RC bridges face problems due to fatigue caused by repeated loading which can lead to progressive deterioration of bond and may cause premature failure. Furthermore, corrosion of steel bars can lead to substantial reduction of loading cycles and bond failure.

Due to slip growth, repeated loading leads to the increase of crack width and deflection, which under aggressive environment conditions strongly affect durability of RC structures. For high corrosion level, if the longitudinal bars and the contact stirrups were severely damaged or even ruptured, brittle failure may occur at a very low load. This is quite dangerous in the case of safety-related structures [14].

Most Brazilian federal highways structures were built over rivers, totalizing 3,789 bridges (74%). There were 752 overpasses through roads and 153 through railways. These bridges show evidences of the characteristics of Brazilian infrastructure: predominance of highway traffic as compared to rail traffic and presence of most of the highways in rural areas of relatively low population density [15]. Although the available bridges designs were exhaustively investigated, only 22% (1,032 bridges) had their age recorded. For the sake of practicality, the bridges were into periods by existing standards, as determined in The Manual of Road Bridges of the National Road Research Institute (IPR) [16]. Almost 25,7% (265 bridges) of the total of 1,032 bridges whose age was recorded were constructed before 1960. Most of them (about 531 bridges, 52% of the total) were built between 1960 and 1975. According to The Manual of Road Bridges, these structures followed Brazilian Standards number 1, 2 and 6/1960, with a loading capacity of up to 36T (tons per axle), 10 meters total deck width , and 0.90 meters high obsolete railings.

There were 2,025 registers of bridge live load capacity, 74% of which being overloaded, 256 design loading bridges of up to 24kN (axle load), and 1,260 of up to 36kN. Functionally obsolete due to inadequate design, ever-increasing and changing traffic, and absence of needed strengthening interventions, are common challenges faced by governments, even in developed countries [17].

Most of the bridges (80% of 4,725 bridges) are over flat surfaces, and more than 93% are two-way traffic bridges, 65% of the lanes being equal to or wider than 3.6 meters. However, there are 1,419 (35%) bridges whose lane widths are insufficient - less than 3.6 meters per lane in double lane roads.

Access equipment was not used in the inspections. For this reason, 2,229 bridges (47%) did neither have their bearings checked, neither had their type registered nor their function and damage states registered. The most commonly observed functionality deficiency was obsolete railings, registered in 2,095 bridges. The research also registered 2,849 bridges with no shoulders and 3,271 bridges less than 2.5 meters shoulders. Figure 2 gives an overall idea of the typical cross-section of Brazilian bridges.

Drainage was insufficient in 681 bridges. High levels of heavy vehicle traffic were observed in 2,923 (49%) of the bridges, a fact which is likely to affect the deterioration rates of the structural elements. These results provide evidence to the facts that weight vehicle control and planed regular inspections are fundamental factors to preserve bridge structural integrity. The comparison between the static effects of the actual traffic of heavy vehicles and those generated by the live load model given in the current national

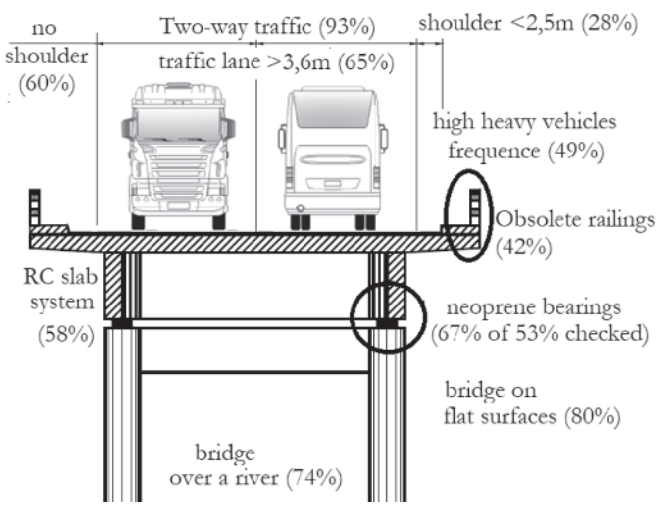

Figure 2
Typical cross-section of Brazilian bridges

code NBR 7188/2013[18] raises another concern. The simulation showed that Brazilian code load models may not adequately reproduce the real traffic of heavy vehicles and may, in many cases, be non-conservative [19].

6. Brazilian bridges inspection results

Inspections were conducted according to the Brazilian Standards NBR-9542/2016 (2016 version) [9] and DNIT010/2004-PRO [10]. The worst general IC=1, suggesting immediate intervention, was found in only 8 bridges. Besides, 196 bridges were classified in IC=2, demanding mid-term interventions, resulting in 4.2% of total bridges inspected requiring MR&R scheduled actions. Approximately 38% of inspected structures were evaluated as IC=3 (1,803 bridges), having minor structural damages, and need of maintenance and regular inspections only, not requiring emergency action.
Finally, 1,987 bridges were evaluated IC=4 and 756 IC=5,

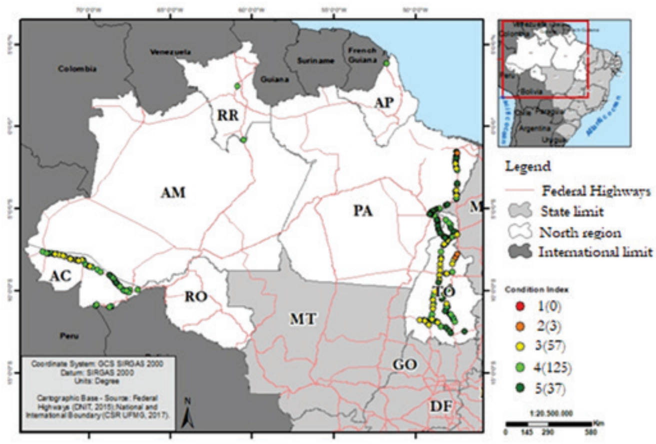

Figure 3
Geographic distribution of bridges inventory and IC registered in North region

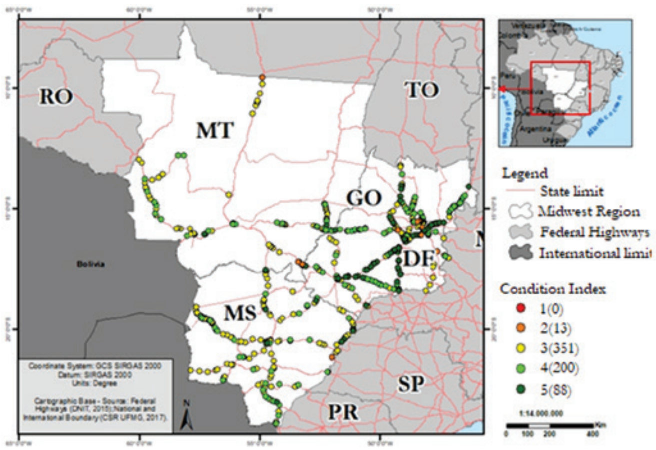

Figure 4
Geographic distribution of bridges inventory and IC registered in Midwest region

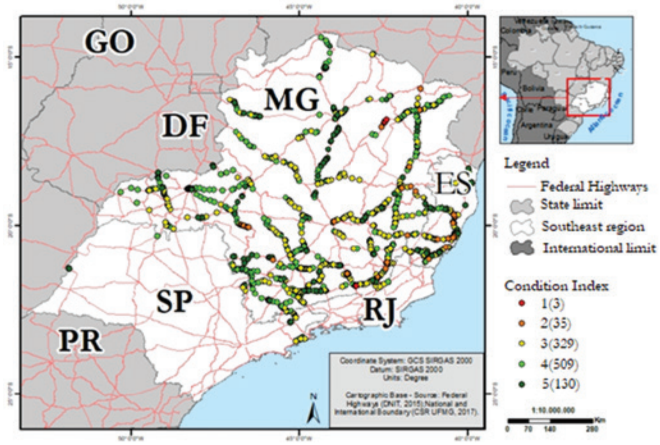

Figure 5
Geographic distribution of bridges inventory and IC registered in Southeast region

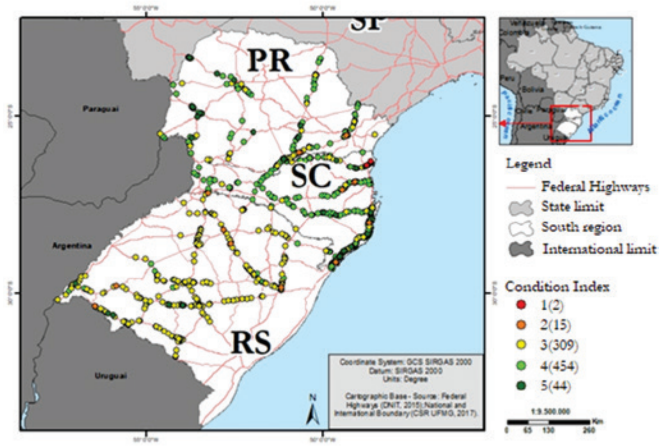

Figure 6
Geographic distribution of bridges inventory and IC registered in South region

totalizing 58% of the total with no structural damages, demanding only maintenance and regular inspection. These records suggest a positive scenario for the conservation conditions of Brazilian structures, considering their 40 year-old age average, their exposure to aggressive agents and the absence of a maintenance program before the inventory.
The SGO recorded information of geographic coordinates of each bridge during the inventory. This information was exported to a free geographic information system application. For the analysis of the data, the IC of each bridge was assigned in according to the results of the inspection. The Brazilian federal roadmap was used, and the bridge coordinates were corrected. Figures 3 to 7 show the distribution of bridges and their condition, considering Brazilian geographic and statistical regions.
Ever since the time of the inspection, DNIT has made several bridge interventions according to the observed condition and the average traffic analysis. However, it is essential to understand the

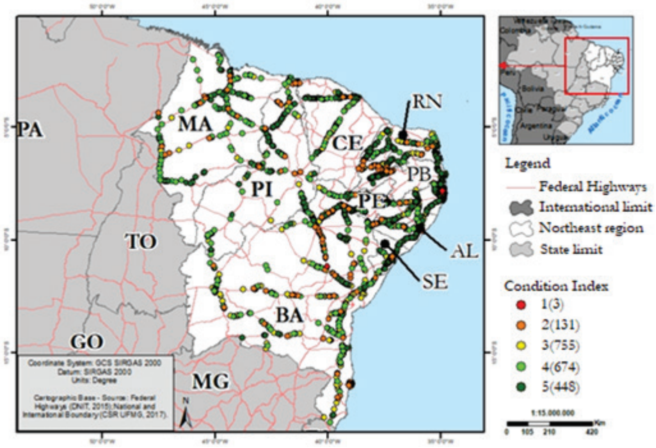

Figure 7
Geographic distribution of bridges inventory and IC registered in Northeast region

deterioration mechanisms of structural materials and components to develop more accurate maintenance and replacement programs to prevent continuous deterioration and to ensure optimal budget spending.

6.1 Damages incidence

Most of the numerous damages identified on inspections are shown in Table 1 and represent 75% of 20,389 defect registers. They were evaluated according to their severity degree, and for each incidence, an IC was marked. It is important to emphasize the importance of damage measure per element in addition to regular inspections. Regular inspections at element-level provide significant data which enable researches to develop a deterioration model of Brazilian bridges, crucial knowledge to life cycle analysis leading to optimal bridge management.
Most of the prevailing damages were associated with reinforcement corrosion and concrete degradation, corresponding to 66% of total registered defects, followed by expansion joints damages with 9.4%. Reinforcement corrosion constitutes the major factor of RC structures degradation. It results from the change of steel mechanical properties, longitudinal cracking of concrete cover, change of bond strength between steel and concrete, loss of serviceability and eventually loss of safety [20]. For instance, the mechanical behavior intended during the design phase may not be observed during the structural life, indeed, and it can change drastically when corrosion effects are accounted [21]. Therefore, its high occurrence requires more detailed MR&R actions plan focused on increasing the durability of these structures and to ensure safety.
Figure 8 show the damages by structural elements. Concrete deck was the structural that showed more damage incidence, corresponding to 4,983 of the registered occurrences (31%). Due mainly to the effects of direct exposure to traffic loads and environmental degradation factors, numeral types of research focus on the deck system, thus considered the weakest system of highway bridges [2]. In the same way, the rate at which bridge decks deteriorates is an important element used to estimate MR&R costs. Efflorescence and leaching of concrete was the most observed deck defect (38%), followed by water leakage trough concrete cracks (31%), spalled concrete and exposed steel rebars (20%) and corroded steel rebars(6%).
The second structural element with high damage occurrence (2,376 times) was longitudinal girders. They are directly connected to the deck to transmit efforts to mesostructure. Spalled concrete and exposed steel rebars totalizing 31%, efflorescence and leaching of concrete, 29% and 16% spalled concrete and steel rebars exposed and already corroded of total longitudinal girders damage registered. Retaining wall was the third element (1,804 occurrences) with 39% of water leakage through concrete cracks, 32% efflorescence and leaching of concrete damage.

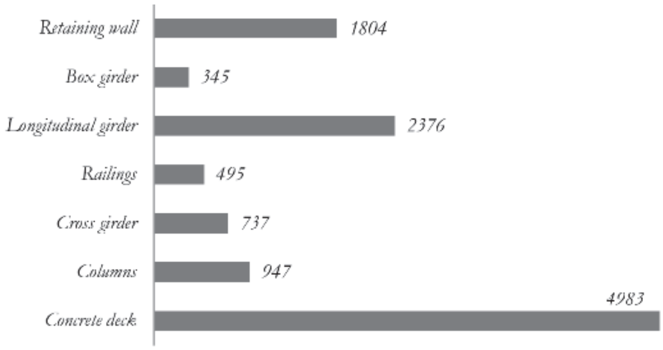

Figure 8
Damage frequency by structural RC element of DNIT bridges inventory

Table 1
Frequence and IC of major damages registered in DNIT bridges inventory

	IC				
Damage	1	2	3	4	5
Efflorescence and leaching of concrete	5	146	1,798	2,480	21
Damage in expansion joints	1	187	514	1,206	12
Spalled concrete and exposed steel rebars	6	177	1,613	1,730	19
Spalled concrete and exposed and corroded steel rebars	4	140	745	860	10
Water leakage through concrete cracks	4	103	1,371	1,346	6
Steel rebars without cover protection	2	54	277	534	5

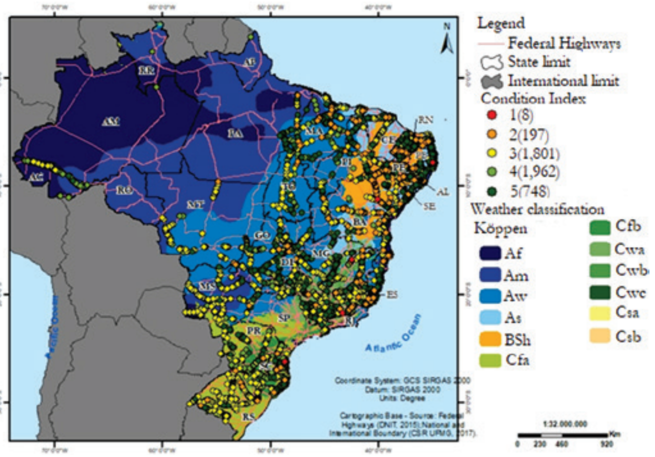

Figure 9
Köppen-Geiger climate classification and IC distribution

7. Reported deterioration agents effects on IC value analysis

Deterioration of bridge elements depend on several parameters related to bridge design, construction, geographical location and environment, and traffic volume. Therefore, it is important to classify bridges based on the values of these parameters, so that homogenous and consistent data can be used to develop deterioration models with required accuracy. For this reason, filtered data records are classified based on the following parameters.

7.1 Climate

To investigate a probable relationship between climate characteristics and current IC, the geographic coordinates of bridges were processed by a geoprocessing system on a Köppen-Geiger climate classification. Figure 9 shows compiled information. Indeed, climatic bridge location is not the exclusive and conclusive deteriorative agent to influence IC. As a result, it is possible to have contrasted IC values in the same climatic classification. However, it is possible to verify that some climatic regions have the largest number of bridges with IC=1 and IC=2 than others. To better analyze that relationship, these bridges are shown apart in Figure 10.

The bridges showing the worst IC concentrate mostly in the Northeast region. Of the 2,011 inspected bridges in this region, 6.5% were classified as IC = 2. It is also possible to verify some road segments with a sequence of bridges with IC=1 and IC=2. These bridges were located mainly in the Northeast region with BSh Köppen-Geiger characteristics. The Bsh classification stands for a semi-arid climate, with low annual precipitation index only in the winter season below potential evapotranspiration, resulting in very dry and hot atmospheric conditions.

In the Southeast region, 35 inspected bridges were evaluated as IC = 2, representing 3.5% of the 1,006 total bridges inspected in Minas Gerais and Espírito Santo states. It is possible to verify that IC=1 and IC=2 scores had meaningful incidence in Aw Köppen-Geiger region climate and bordering regions. The Aw classification shows a tropical environment, often composed of two basics seasons: winter and summer. However, a winter season is less prominent or even inexistent. The temperatures remain relatively hot throughout the year, and there is a heavy annual precipitation concentrated only in summer season, resulting in dry winter season.

The Southern region has the lowest IC incidence, having only 15 IC = 2 bridges out of 824. It represents only 1.8% of the total number of bridges in the region. The location of these bridges does not seem to follow a pattern, but they are mostly related to the Cfa climate classification. This type of climate is classified as humid subtropical climate, with hot and humid summers and mild winters. There are precipitations all over the year.

The results of the inspection show that the bridges in the poorest condition are located mainly in a hot and dry climate. As regions register an incidence of higher precipitation and low temperatures, the condition of concrete bridges is better, and the number of bridges in poor condition decreases. The bridges in the Southern region follow this course. The Cfa climate is alongside the Cfb classification is alongside the Cfa climate in Southern Region and the main difference between these classifications is the variation in summer temperatures. The Cfb climate region has higher temperatures than Cfa region. This influence has already been evaluated by renowned researches and some Brazilian ones as well, such as research conducted by LENCIONI [22]. This conclusion leads to further investigation on the deterioration rates per climatic region, where different deterioration indexes are expected.

7.2 Bridge age

At the inventory shows, only 1,032 bridges are registered with their corresponding age in SGO. This is probably due to the non-existence of the necessary records of the original designs and successive MR&R actions. Nonetheless, this age register has crucial importance and is the most frequently used database to present the deterioration rates and to predict the future condition of bridge assets.

For the group of bridges having their age listed in the inventory, the IC probably decreases when bridge age increases. However,

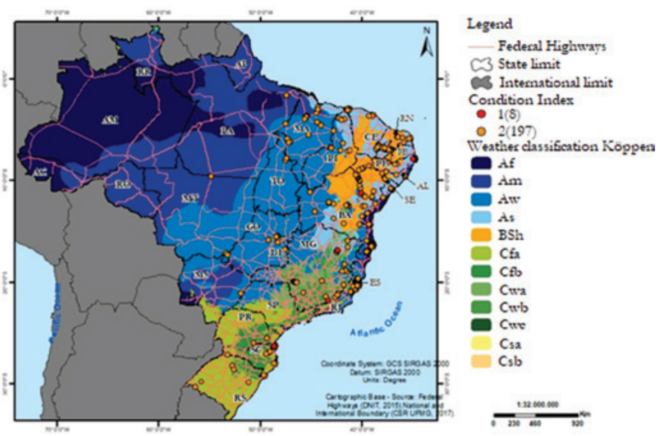

Figure 10
Köppen-Geiger climate classification and IC=1 and IC=2 distribution

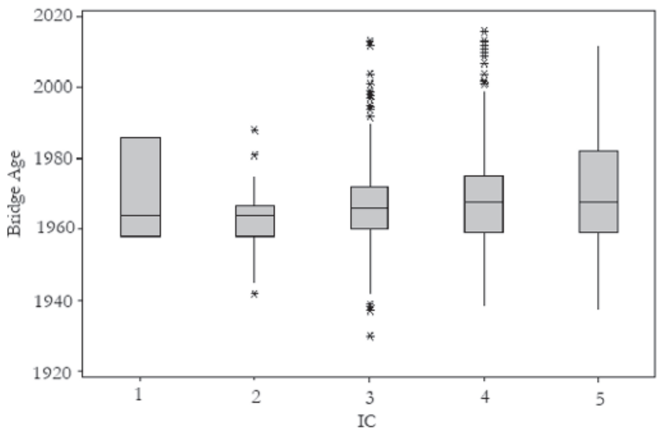

Figure 11
IC *versus* Bridge Age

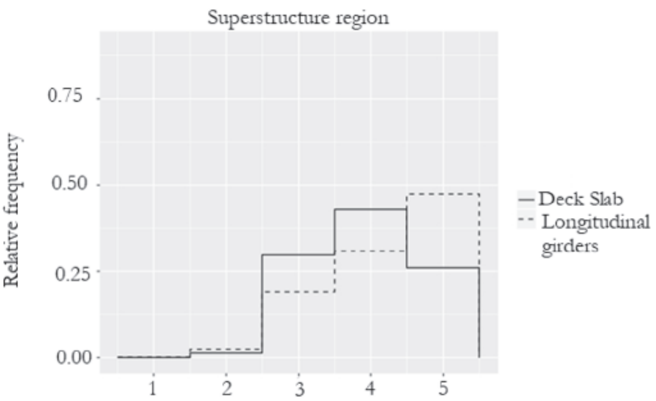

Figure 12
IC distribution of Deck Slab and Longitudinal girders

Figure 11 shows that there is no apparent relationship between these variables. Spearman's correlation coefficient between the variables "Bridge age" and "IC" was 0.13 (p-value = 0.000), suggesting that these variables present very low or non-existent correlation for practical purposes. Spearman's correlation evaluates the monotonic relationship between two continuous, discrete, or ordinal variables. It is a non-parametric method that uses only the stations and makes no assumptions about the distribution of the data. Correlation values of -1 or 1 imply an exact linear relationship. The zero indicates absence of a monotonic relation [23].
MOSCOSO [24] conducted research that proposed deterioration models for Brazilian bridges, using estimate deterioration rates of Nevada bridge assets. To apply these rates to Brazilian bridges, MOSCOSO analyzed registered ages and found bridges with IC = 5, regardless the old age of them had. According to MOSCOSO, this finding possibly has its cause possibly in not registered MR&R actions along this period.
To determine deterioration rates, the age input of a given bridge is usually changed if maintenance actions resulted in significant IC changes. For example, if a singular bridge has changed its condition state from IC=2 to IC=5 after MR&R action, it is possible to infer that its previous conditions in the past have significantly changed. Its future durability conditions will also be substantially affected. In this case, the bridge age variable must be adjusted in order to measure deterioration taxes. In contrast, if the bridge age is not adequate to deterioration measurement rates, it will lead to a significant deviation of IC bridge predictions, with a misleading future condition state output [25]. Seen from this perspective, for deterioration rates the bridge age strongly depends on performed interventions over the years. Such interventions must be registered on BMS with characterized MR&R action. Considering the limited database in SGO and the absence of MR&R actions records, investigations on Brazilian bridge deterioration rates based on bridge age and starting from the current IC can lead to unreliable results.

7.3 Element type

The deterioration process shows the complex phenomena of physical and chemical changes occurring in different bridge

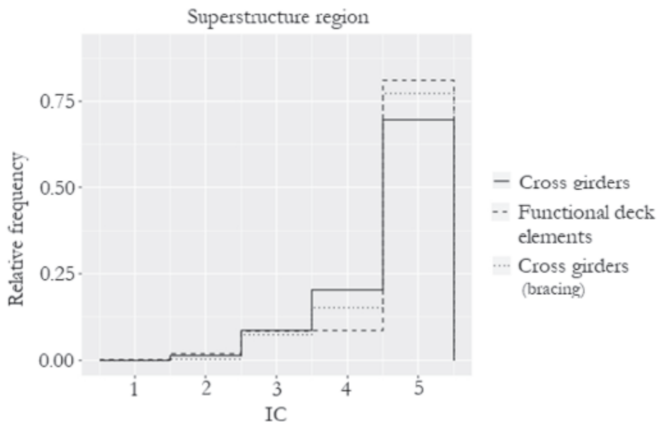

Figure 13
IC distribution of cross girders and functional deck elements

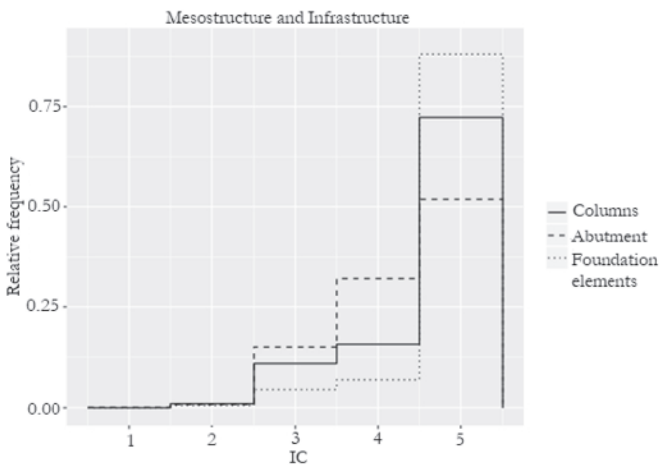

Figure 14
IC distribution of columns, abutment and foundation elements

components. What makes the problem more complex is the fact that each element has its own deterioration rate [26]. To achieve probable differences registered in DNIT inventory, the IC frequency for the three main bridge components, superstructure, mesostructure and infrastructure, was analyzed and is showed in Figures 12 to 14. The results presented the highest amount of characterization in low ICs associated to bridge deck. The low IC incidence tends to decrease as the structural element as more distant from the region receiving direct impact of vehicles. Such results confirm recognized scientific studies and suggest particular deterioration rates to each bridge component.

7.4 Other possible deterioration influences

Traffic load design is another possible deterioration agent in road bridges. DNIT inventory reported related to 2,023 bridges inspected according to NBR 7188/2003 [18]. Figure 15 shows a moderate bias to better condition states assigned to designed T45 truckload bridges. This result could be justified by newer bridges or rehabilitation actions on old ones. Besides, bridges design to modern standards and with improved durability characteristics may perform much better than older bridges, in the same operational environment [27]. Therefore, deterioration rate studies can lead distinct results according to bridges load truck design.

In addition to this analysis, a high incidence of heavy traffic wheel loads was reported for 2,149 bridges (45% of total inspected). Due to these Brazilian highways traffic characteristics, the T45 bridges could be more adjusted to current operational loads. The bridges characterized with heavy wheel load presence follows the IC global distribution: 4.9% with IC=2, 39.6% with IC=3, 36.7% with IC=4 and 18.8% with IC=5. In fact, to provide a more effective analysis, the data of traffic volume and vehicles characteristics should be recorded in data inventory for each bridge.

The analysis of impact of aggressive environment conditions is difficult to perform in view of the scarce number of bridges with this data recorded, only to 69 bridges. In addition, these bridges showed the same IC global distribution. For a better prediction accuracy, future inspections must contain information on traffic characteristics, volume, as well as more detailed aggressive environmental aggressive conditions.

8. Assumptions

In general, stochastic simulations based on bridge age can hardly be processed. Despite the availability of bridge age, insufficient registers of MR&R actions could lead to unsuitable parameters. To predict future IC, artificial intelligence methods can hardly be performed based on available SGO information. These methods rely on more comprehensive data information to link the current performance with the characteristics of the bridge and the external factors to which it is submitted. A bridge having poor durability characteristics may deteriorate much more rapidly than one with good durability characteristics. These data description are not included in the SGO.

The polynomial regression analysis requires sufficient bridge inspections cycles with IC decreases. Bridge condition does not usually change significantly during short-term periods, and it reflects in a very reduced database to established reliable parameters to determinate models [7]. Moreover, Brazilian IC scale has only 5 levels, resulting in a higher probability of bridge remaining in the same condition state or IC, even after MR&R actions or under some deterioration occurrences.

Widely used in BMS, statistical models based on Markov method have merely computational implementation with relative accurate outputs. Despite the fact that DNIT database started the register of bridge inspections only in 2013, after 4 (four) or more inspection future cycles, it will be possible to forecast probable future IC with enough accuracy to provide a more realistic federal budget. Transition Probabilistic Matrices (TPM) for each deterioration influent agent related in item 7 can be elaborated to estimate specific deterioration rates using the same method.

Deterioration models methods frequently use bridge age to assign data future state prediction. However, DNIT data sets do not have this information, and achieving complete data can present a significant challenge. Despite these usual practices, state-based models as Markov methods, and specifically Markov chains, could result in important management results to short-term predictions analysis, while the information is not complete gathered. For the suggested methodology, time interval will be computed from the first inspection with related IC. As a result, when deterioration curves start from the current bridge current state (IC), it may assume initial values different from 5. The method will not indicate a complete model for bridge deterioration, but it is able to show the deterioration rates for short periods of time. The estimated annual bridge MR&R cost estimates of the Federal budget will also have a real-based index for its most accurate evaluation. Above all, this approach could be already implemented in SGO to achieve acceptable results after few inspection cycles. After having the routine implemented, SGO can improve its use up to a more efficient bridge management system.

9. Benchmark example

As benchmark example, a bridge network is selected to demonstrate the advantages of the proposal approach. The information of bridge network is from Brazilian Road BR-381, knowing as "*Rodovia Fernão Dias*", obtained from the Brazilian Agency of Land

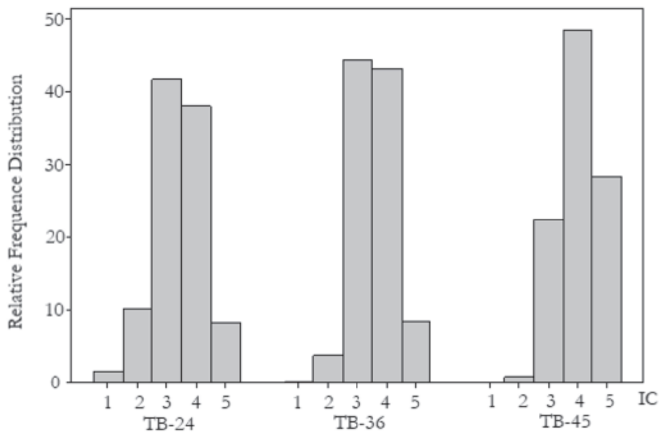

Figure 15
IC distribution *versus* truck-load design bridge

Table 2
IC bridges distribution of *Fernão Dias* road dataset

Year	IC=5	IC=4	IC=3	IC=2	IC=1
2008	2 (1%)	268 (91%)	16 (5%)	7 (2%)	0
2009	3 (1%)	216 (73%)	68 (23%)	6 (2%)	0
2010	0	221 (75%)	68 (23%)	4 (1%)	0
2011	0	220 (75%)	70 (24%)	3 (1%)	0
2013	10 (3%)	245 (84%)	36 (12%)	2 (1%)	0
2014	13 (4%)	240 (82%)	39 (13%)	1 (1%)	0
2015	13 (4%)	240 (82%)	39 (13%)	1 (1%)	0

Transport (ANTT). Bridge inspections were carried out from 2008 to 2015, resulting in 7 cycles, with annual inspections, according to the Brazilian standards NBR-6123 (old version - 2013) and DNIT 010/2004, as well as DNIT inventory. The main bridge regions as superstructure, mesostructure and infrastructure were evaluated with respective IC. The ANTT data was available only in non-editable files reports, and a computational routine was implemented to organize data to enable stochastic simulation.

To select data more representative of the deterioration process, a filtered data was implemented according to AGRAWAL & KAWAGUCHI [28]. Inspections reports with missing or incomplete data were removed. For example, IC during periods between two inspections should be the same as the IC at the previous inspection for bridges without MR&R actions. To better understand rates, all data cycle with IC improvement rejected. Bridge data with unusual IC drops were disregarded because natural deterioration process decreases gradually over time. However, a sudden drop in IC over two consecutive inspections may be caused by occasional situations, for example, natural disasters, traffic accidents, etc. These occurrences do not reflect normal operational deterioration, peculiar to the database showing a one-year inspection interval. Every increased IC to a higher level was not included; this can be considered as a consequence of MR&R actions.

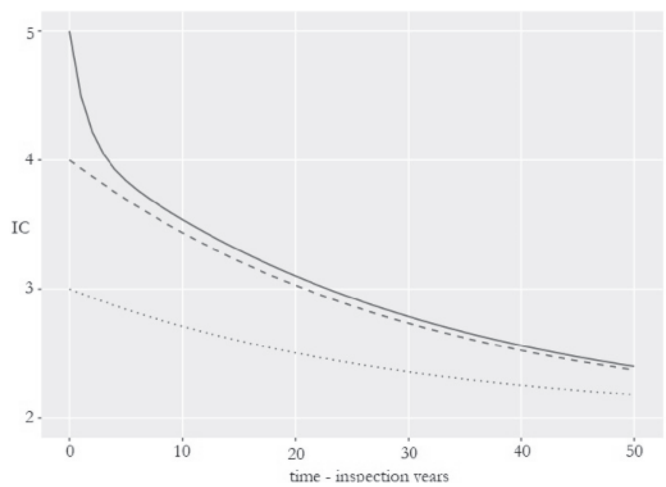

Figure 16
Deterioration model of *Fernão Dias Road* bridges – General IC

The Markov chain use was possible because inspections were performed annually, resulting in the discrete time necessary to apply the method, according to ANTT Road Exploration Program (PER). Unusually, the inspection cycle from year 2012 to 2013 has 17 months, which is above the discrete interval of 1 year. Therefore, this cycle was also removed to estimate Markovian transition probability matrix (TPM). The bridge network has 306 bridges, being 292 located in *Minas Gerais* State and 104 in *São Paulo* State. Only RC bridges whose span is over 10 meters were considered in this approach. After the filtering, 293 bridges were left for stochastic simulation. Thus, there are seven IC for each analyzed bridge, making longitudinal the data nature.

After inspection report review, special filters needed to be developed. Inspectors diverged at components of bridge regions: for some inspectors, abutment was considered as part of mesostructure and for others, as part of the infrastructure. Similarly, some inspectors disagreed over columns regions. To reliable simulation results, these data were adequate to Brazilian standards. Besides, due to small dataset, the TPM was calculated according to the frequency approach method [13, 11, 29]. This method considers all the transition periods at one time, that is, it directly obtains the TPM *pij* ratios using the following expression:

$$p_{ij} = \frac{Nii}{Ni} \quad (3)$$

Where *Nii* is the number of bridges in state *i* before and after any transaction period and N*i* is the total number of bridges started with state *i* at each transition period. Table 2 shows general IC distribution for 293 bridges on *Rodovia Fernão Dias*. The resulting IC distribution differs from DNIT inventory IC distribution, probably due to the current maintenance program carried out by *Rodovia Fernão Dias* administration. Notably, there are more bridges classified in IC=4.

Routines were implemented to estimate TPM, using the statistical programming language "*R*". As explained in this methodological application, variable "age" was substituted by "inspection time", considering 2008 as starting point. Infrastructure data were not sufficient to estimate transition probabilities because there were not enough IC variations, having almost all inspections attributed IC=5 to this region along the period. Moreover, a reduced 4x4 TPM was obtained because there was not IC=1 incidence. The TPM is represented by:

$$\begin{bmatrix} 1 & 0 & 0 & 0 \\ 0{,}0035 & 0{,}9665 & 0 & 0 \\ 0 & 0{,}0648 & 0{,}9352 & 0 \\ 0 & 0 & 0{,}5 & 0{,}5 \end{bmatrix} \quad (4)$$

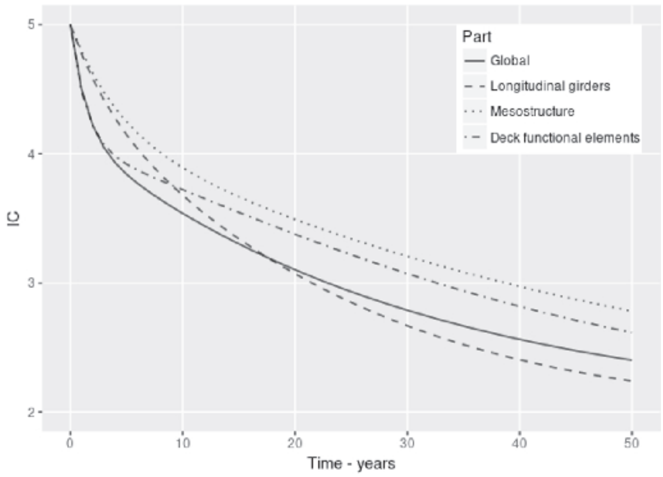

Figure 17
Deterioration model of *Fernão Dias Road* bridges – IC per bridge region

Singular TPM was constructed for each bridge region. Deterioration rates curves are shown in Figures 16 and 17 for a 50 years period. It is possible to verify different rates for each bridge region, following the founded pattern in the Brazilian inventory. To measure methodology accuracy, singular TPM was calculated considering only the data of the first five inspection cycles (2009 to 2014) and predicted IC values for 2015 were obtained through the following expression:

$$E(N_t) = N_0.(TPM)^t \tag{5}$$

Where, N_t is the vector of number of bridges in each IC at interval time t. N_0 is a vector of the number of bridges in each IC in a given year. Equation 5 gives the expected number of bridges in each IC after t years from the initial period. It can be interpreted as expected bridge conditions preview in a specific year, with no MR&R actions in a presumed period. Table 3 shows values of the dataset and predictive IC using the proposed methodology. The results obtained from statistical simulation are satisfactory predictors for the following year's bridge condition states of this set and have a practical use to estimate expected costs.

10. Conclusions

The present paper describes the current state of the bridge management procedures, as well as tools developed and implemented by DNIT. The SGO bridge management system provides a relevant inventory of catalogued road bridge structures. The overall condition of inspected bridges is presented and classified in a comprehensive way. The knowledge and availability of these results are essential for the scientific community. The data provided is vital to support current research projects and encourage others works. The appropriate use and analysis of public and official data may contribute to a more effective asset management in this area.

The inventory of Brazilian bridge conditions was evaluated by comparing IC value distribution with the presence of deterioration agents. Possible correlations were found in available data, mainly related to climate region, localization and design classification. It was demonstrated that the development of a predictive model of the future condition state for Brazilian bridges based on the age of these structures could hardly be implemented, due to the lack of registered information concerning the bridge construction time and MR&R actions in SGO's database. However, future MR&R action planning depends on the knowledge of future bridge condition. For instance, the article proposed a methodology using successful Markov chains for short-term predictions, considering mainly the time of deterioration from the registered condition of the bridges' first inspection. It is relevant to attempt to regular interval inspections required to Markov Chains, but if it were a challenge, the application of methods of backward prediction models could be implemented [7]. To demonstrate its applicability, the methodology was applied using *Fernão Dias* road bridge dataset. Results using five cycles of IC transitions were able to provide a satisfactory prediction of bridge future conditions to a dataset.

The new version of Brazilian inspection standards may cause a favorable scenario to the development of this research area. The possible use of a guided BMS by standardizes procedures on the same basis to catalogue inspection data, both for private and public bridge managers, can promote a more integrated national database, necessary to more effective management. Analyzes such as those performed on bridges of *Fernão Dias* road presented in this paper are difficult to be carried out due to to the lack of data in a suitable system. Furthermore, statistical simulations to forecast deterioration at large bridge network require a meaningful size for sample space. Despite the challenge of compiled disperse existing data, researches sharing this goal are being carried out to record existing inspections and estimate specific bridge deterioration rates.

To forecast more reliable deterioration rates that enable mid-term predictions, potential deterioration agents must be recorded in SGO and must be included in the inspection routine. The current traffic must be verified and updated at each inspection. It is important to precisely classify all aggressive environment aspects to enable more specific studies of diverse deterioration rates. In addition, it is necessary to improve SGO with entries of MR&R actions to be appropriately registered. Above all, inspections procedures must result in organized and standardized information.

With this approach, it is expected in mid-term run to be feasible to determine deteriorating rates according to age, environmental conditions, traffic volume, among other possible incidences of deteriorating agents, and to measure different impacts of each agent on deterioration rates. In long-term run, adopting optimized planning of needed MR&R actions, the Brazilian Federal Government will be able to guaranty economic development, maximizing the cost-benefit of these investments to society.

Table 3
Number of Bridges Predicted by IC using proposal methodology

	IC=2	IC=3	IC=4	IC=5
2014 (real)	0	29	237	13
2015 (real)	1	38	232	8
2015 (predicted)	1	43	228	7

11. Acknowledgments

The authors would like to acknowledge the support and data provided by the Federal Brazilian Department of Transportation (DNIT) and Brazilian Agency of Land Transport (ANTT). The contents discussed herein are solely based on the scientific observations made by the authors, by using publicly available data sources provided by DNIT and ANTT. For financial support, the authors would also like to thank the Brazilian Research Funding Agencies CNPq (Conselho Nacional de Desenvolvimento Científico e Tecnológico) and FAPEMIG (Fundação de Amparo à Pesquisa do Estado de Minas Gerais).

12. Referências bibliográficas

[1] CAVALLINE, T. L.; WHELAN, M. J., TEMPEST, B. Q., GOYAL, R.; RAMSEY, J. D. Determination of Bridge Deterioration Models and Bridge User Costs for the NCDOT Bridge Management System. Department of Civil and Environmental Engineering University of North Carolina at Charlotte, NCDOT Project, 2014-07, FHWA/NC/2014-07, 201, 188 p.

[2] MORCOUS, G. Performance prediction of Bridge Deck Systems Using Markov Chains. Journal of Performance of Constructed Facilities, v. 20 (2), 146-155, 2006.

[3] MORCOUS, G., LOUNIS, Z., MIRZA, M.S. Life-cycle assessment of highway bridges. Institute for Research in construction IRC, National Research Council Canada, 2002, 23 p.

[4] AMERICAN ASSOCIATION OF STATE HIGHWAY AND TRANSPORTATION OFFCIALS - AASHTO. The Manual for Bridge Evaluation. Washington, USA, 2013, 588p.

[5] CRUZ, C.O., MARQUES, R. C.; FRANCO, D. Road-Network Development in Quickly Growing Economies: Brazilian Case Study MG-050 Journal of Infrastructure Systems, v. 21 (4), 254-261, 2015.

[6] FONTES, F.F.; VERLY, R. C.; SANTOS, G. S.; MAGALHÃES, E. P. A Bridge Management System for Brazil. 7th International Conference on Bridge Maintenance, Safety and Management - IABMAS, Shangai, China, 2008, p. 537 – 543.

[7] BU, G.P., SON, J.B., LEE, J.H., GUAN, H. Typical deterministic and stochastic bridge deterioration modeling incorporating backward prediction model. Civil Structures Health Monitoring Journal. Vol. 3, 141-152, 2013.

[8] MISHALANI, R. G., MADANAT, S. M. Computation of Infrastructure Transition Probabilities Using Stochastic Duration Models. Journal of Infrastructure Systems, vol. 8 (4), p. 139 - 148.

[9] ASSOCIAÇÃO BRASILEIRA DE NORMAS TÉCNICAS – ABNT. NBR 9542: Concrete bridge Inspection. Vistoria de Pontes e Viadutos de Concreto. Rio de Janeiro, 2016.

[10] BRAZILIAN FEDERAL DEPARTAMENT OF TRANSPORT INFRASTRUCTURE (Departamento Nacional de Infraestrutura em Transportes – DNIT). Standard DNIT 010/2004 – PRO – Reinforced and prestressed concrete bridges inspections. Brazilian Road Research Institute – (Instituto de Pesquisas Rodoviárias- IPR), Rio de Janeiro, 2004.

[11] SETUNGE, S.; HASAN, M.S. Concrete Bridge Deterioration Prediciton using Markov Chain Approach. RMIT University, Melbourne, Austrália, 2011.

[12] YIANNU, P. C., NEVES, L. C., RAMA, D., ADREWS, J.D, DEAN, R. Incorporating local environmental factors into railway bridge asset management. Engineering Structures Journal, v. 128, p. 362-373, 2016.

[13] JIANG, Y. Application and Comparison of Regression and Markov Chain Methods in Bridge Condition Prediction and System Benefit Optimization. Journal of the Transportation Research Forum, Vol. 49, No. 2, pp. 91-110, 2010.

[14] PELLIZER, G.P.; LEONEL, E.D.; NOGUEIRA, C.G. Influence of reinforcement's corrosion into hyperstatic reinforced concrete beams: a probabilistic failure scenarios analysis. IBRACON Structures and Materials Journal v. 8, 479-490, 2012.

[15] NATIONAL TRANSPORT CONFEDERATION (CNT) – Survey of brazilian highways – Management Report. Brazília, Brasil, 2016.

[16] NATIONAL ROAD RESEARCH INSTITUTE – Instituto de Pesquisas Rodoviárias (IPR). Manual of road bridge inspections. Rio de Janeiro, Brazil, 2004.

[17] MARKOW, M. J.; HYMAN, W. A. Bridge Management Systems for Transportation Agency Decision. National Cooperative Highway Research Program. Transportation Research Board, Washington, USA, 2009, 127p.

[18] ASSOCIAÇÃO BRASILEIRA DE NORMAS TÉCNICAS – ABNT. NBR 7188: Live Load and Pedestrian-Load in bridges, footbridges and other structures. Rio de Janeiro, 2013.

[19] ROSSIGALI, C.E., PFEIL, M. S., BATTISTA, R.C., SAGRILO, L.V. Towards actual brazilian traffic load models for short span highway bridges. IBRACON Structures and materials journal, v. 8, 124-139, 2015.

[20] WANG, H. W, LI, B., GAO, X.H., LIU, X.L. Shear behaviour of RC beams with corrosion damaged partial length. Materials and Structures, v. 45, 351-379, 2012.

[21] LIN, H, ZHAO, Y, OZ˘BOLT, J., HANS-WOLF, R. The bond behavior between concrete and corroded steel bar under repeated loading. Engineering Structures, v. 140, 309-405, 2017.

[22] LENCIONI, J.W. , FERREIRA, J.B. Concrete Bridge deterioration index proposal. 56º Brazilian Concrete Conference, p. 1-11, 2014.

[23] KENDALL, M. G. GIBBONS, J. D. Rank correlation methods. Oxford University Press, New York, NY,1990.

[24] MOSCOSO, Y. F. M. Deterioration models to Bridge Management Systems. Doctoral Thesis. Brazilia University (UNB), 2017.

[25] BOLUKBASIL, M., MOHAMMADI,J. ARDITI, D. Estimating the Future Condition of Highway Bridge Components Using National Bridge Inventory Data. Practice periodical on structural design and construction. American Society of Civil Engineers, v.1, 16-25, 2004.

[26] THOMPSON, P. Decision Support Analysis in Ontario's New Bridge Management System - Proceedings of the 2001 Structural Congress and Exposition. ASCE,Washington, D.C, 2001.

[27] NASRROLLI MASSOUD, M., WASHER, G. Estimating Inspection Intervals for bridges based on statistical analysis of national bridge inventory data. Journal of Bridge Engineering, vol. 20 (9), 2015.

[28] AGRAWAL, AK & KAWAGUCHI, A., Bridge element deterioration rates: final report, project C-01-51. New York State Department of Transportation, New York, NY, USA. p. 15 a 21, 2009.

[29] MUÑOZ, Y. F., PAZ, A, FUENTE-MELLA, H., FARIÑA, J. V., SALES, G. M. Estimating Bridge Deterioration by Using Small Data Sets. University of Nevada, USA, 2016.

Volume 12, Number 1 (February 2019) p. 14 – 22 • ISSN 1983-4195
http://dx.doi.org/10.1590/S1983-41952019000100003

IBRACON

REVISTA IBRACON DE ESTRUTURAS E MATERIAIS
IBRACON STRUCTURES AND MATERIALS JOURNAL

Analytical study of cylindrical tanks including soil-structure interaction

Estudo analítico de tanques cilíndricos incluindo interação solo-estrutura




R. L. C. SILVA [a]
engrafaelleandro@hotmail.com
https://orcid.org/0000-0003-3591-1309

G. B. MARQUES [b]
glauberbatistamarques@gmail.com
https://orcid.org/0000-0001-6170-5926

E. N. LAGES [c]
enl@lccv.ufal.br
https://orcid.org/0000-0001-6704-4057

S. P. C. MARQUES [c]
smarques@lccv.ufal.br
https://orcid.org/0000-0003-3476-0289

Abstract

An analytical study aiming the design of cylindrical liquid storage tanks resting on deformable foundations is developed in this work. The soil under the tanks is modeled as an elastic linear medium. The cylindrical wall is considered rigidly connected to the plate foundation. Here, concrete tanks are emphasized, although the study can be extended to other construction materials. For the analysis of the design forces acting on the tanks, efficient and simplified approximate expressions are derived based on rigorous analytical theories for thin shells and circular plate on elastic foundations. To verify the proposed approximate expressions and investigate the influence of the foundation deformability on displacements and design forces, parametric analyses of concrete tanks with different soil stiffness values are presented. The results illustrate the strong influence of the foundation stiffness on the tank design quantities and a very good performance of the simplified expressions.

Keywords: concrete cylindrical tank, interaction soil-structure, elastic foundation, structural design.

Resumo

Um estudo analítico voltado para o projeto de tanques cilíndricos para armazenagem de líquidos, apoiados sobre fundação deformável, é desenvolvido neste trabalho. O solo sob os tanques é modelado como um meio elástico linear. A parede cilídrica é considerada rigidamente conectada à placa de fundação. Aqui, tanques de concreto são enfatizados, mas o estudo pode ser estendido para outros materiais de construção. Para a análise dos esforços atuantes sobre os tanques, eficientes e simplificadas expressões aproximadas são deduzidas com base em teorias analíticas rigorosas para cascas delgadas e placas circulares sobre fundações elásticas. Para verificar as expressões aproximadas propostas e investigar a influência da deformabilidade das fundações sobre os esforços e deslocamentos, análises paramétricas de tanques de concreto com diferentes valores de rigidez do solo são apresentadas. Os resultados ilustram a forte influência da rigidez da fundação sobre grandezas de projeto dos tanques e um desempenho muito bom das expressões aproximadas.

Palavras-chave: tanques cilíndricos de concreto, interação solo-estrutura, fundação elástica, projeto estrutural.

[a] *Faculdade de Tecnologia de Alagoas (FAT), , Maceió, AL, Brasil;*
[b] *Centro de Tecnologia, Universidade Federal de Alagoas, Maceió, AL, Brasil;*
[c] *Laboratório de Computação Científica e Visualização, Centro de Tecnologia, Universidade Federal de Alagoas, Maceió, AL, Brasil.*

Received: 15 Feb 2018 • Accepted: 09 Apr 2018 • Available Online: 05 Feb 2019

1. Introduction

Cylindrical circular concrete tanks resting on the ground are commonly used in water-supply system and wastewater treatment plants. For reasons of simplification of design and mechanical behavior, it is desirable that at the ground level the soil provides condition of firm foundation. However, this condition may not be available and, then, in most cases the tanks are designed and constructed on deformable soils. Several researchers have shown that the deformability of the soil under the base slab has a strong influence on the forces and moments acting along the tank walls. To evaluate this influence, Kukreti et al. [1] developed an analytical study on the behavior of a cylindrical tank resting on an isotropic elastic soil medium. They assumed an approximate power series expansion for the base slab deflection and applied the principle of minimum potential energy for evaluating the unknown series coefficients. The results of a numerical example were verified using a finite element solution. After, Kukreti and Siddiqi [2] presented a similar analytical study including foundation-superstructure interaction
using the differential quadrature method. El Mezaini [3] studied the effects of soil-structure interaction on the behavior of cylindrical tanks using finite element analysis. This study showed that the soil stiffness, as well as the base geometries, has significant influence on the design forces of the tanks. These finite element results also indicated great discrepancies when compared with the values obtained from design coefficients provided by the Portland Cement Association [4], which is a popular tool for the design of cylindrical tanks. Vichare and Inamdar [5] used an analytical formulation based on the thin shell and plates on elastic foundation theories for the analysis of cylindrical tanks founded on uniform deformable soil with different levels of stiffness. To obtain the design forces of cylindrical tanks with flat base slab, these later researchers combined the complete solution for the circular plate on elastic foundation given by Timoshenko and Woinowsky-Krieger [6] with results due to Kelkar and Sewell [7]. As results, Vichare and Inamdar [5] presented complex analytical expressions in terms of Bessel functions for evaluating displacements, moments and forces in the cylindrical wall and base slab. For a numerical example, the authors used a finite element solution to verify the analytical expressions. Mistrikova and Jendzelovsky [8] analyzed the behavior of cylindrical tanks considering their interactions with different types of subsoil. Dehadrai and Ingle [9] employed a finite element code to analyze cylindrical water tanks resting on an elastic soil medium with varying stiffness. More recently, Das and Deb [10] used the concentric equivalent ring method to study the behavior of a cylindrical storage tank resting on a stone column-improved ground. A recent analytical study about cylindrical tank on deformable foundation was also developed by Silva [11].

All these studies have shown a great influence of the soil stiffness on the forces and moments in the tank wall and base plate. To avoid problems, such as leakage, groundwater pollution and corrosion of the reinforcing steel, the design of the concrete tanks must usually be controlled by rigorous serviceability criteria. Then, an accuracy evaluation of the design forces and moments is very important. For this reason, a realistic value of the soil stiffness and the soil-structure interaction effects must be considered.

This paper presents a practical analytical study on structural behavior of cylindrical liquid storage tanks resting on deformable foundation. The studied tanks have their walls rigidly connected to the plate foundation and the soil is supposed as a linear elastic medium represented by the Winkler model. The study has as focus an investigation about the influence of the soil stiffness on the tank behavior, as well as, the derivation of simple and efficient approximate expressions to obtain the relevant displacements and forces used in the structural design. The idea is to provide to the designers efficient and mathematically simple expressions obtained by elimination of the complex Bessel functions appearing in Vichare and Inamdar [5] formulation. To investigate the influence of the foundation deformability on the important design quantities, a cylindrical tank rested on soils with four different levels of stiffness (soft, medium, stiff and very stiff) is analyzed and the results are presented and discussed. The efficiency of the proposed simplified expressions is also verified from a parametric analysis involving a very large range of soil stiffness levels. The results demonstrate the strong influence of the foundation stiffness on the tank design quantities. The comparative analyses between the closed and approximate solutions show a very good performance of the simplified expressions.

2. Preliminary considerations

Figure 1 shows the typical cylindrical ground-water tanks considered in this study. The tanks have a height H and a diameter 2R and rest on uniform deformable soils. The flat base slab and the wall have constant thicknesses t and h, respectively, and are monolithically connected. The tank material is assumed as homogeneous, isotropic and linear elastic with elasticity modulus E and Poisson's ratio ν. The soil is modeled by continuously distributed vertical elastic springs with stiffness k_s (Winkler's foundation) as shown in Fig. 2.

In the tanks, the considered loadings are hydrostatic pressure and self-weight of the wall and base slab. In addition to the wall self-weight, a symmetrical vertical distributed load on the top of the wall due to a roof, for instance, can be applied. The forces and

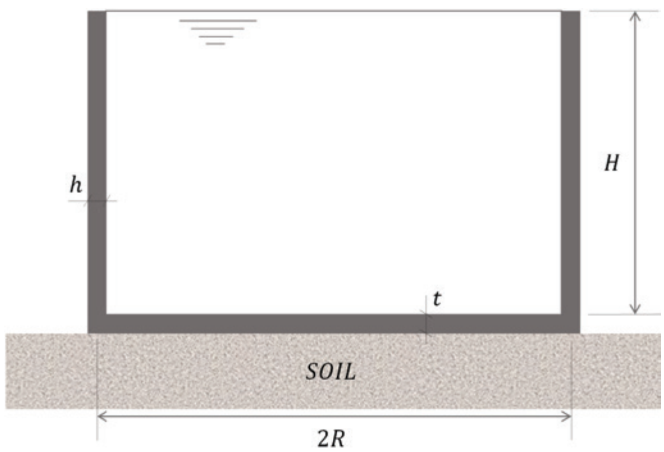

Figure 1
Schematic representation of the cylindrical tank on deformable foundation

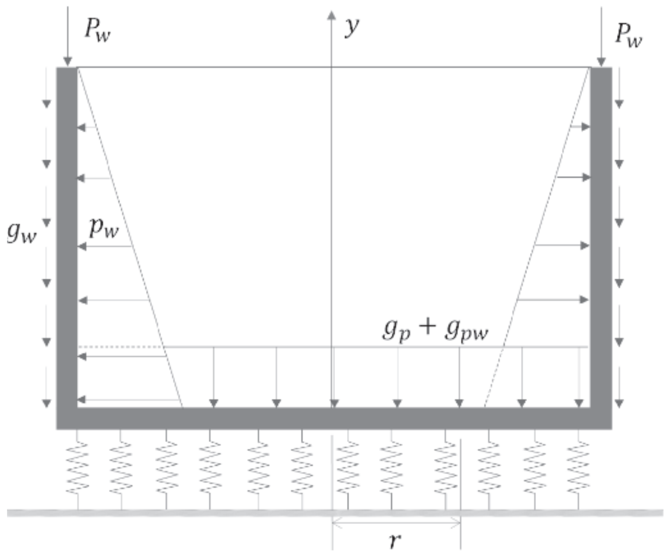

Figure 2
External loadings acting on the tank and elastic springers

moments acting on the wall and base plate are illustrated in Fig. 3. In this figure, M_0, H_0 and Q_0 represent the interaction forces between the tank wall and the plate foundation. Hence, the plate foundation is subjected to the self-weight $g_p = \gamma_m t$, liquid pressure $g_{pw} = \gamma_l H$ and interaction forces and moments (M_0, H_0 and Q_0) distributed along the external perimeter. γ_m and γ_l are the weights per unit volume of the tank material and stored liquid, respectively. The cylindrical wall is subjected to the reactions of those interaction forces and moments at the bottom end, hydrostatic load $p_w = \gamma_l (H-y)$ on the internal side, self-weight $g_w = \gamma_m h$ and an axisymmetric vertical load P_w distributed along the superior end.

The plate foundation subjected to those mentioned loads exhibits greater settlement at its perimeter than at the center. This differential settlement occurs due to the presence of the forces and moments Q_0 and M_0 distributed along the plate boundary. Assuming the soil as a homogeneous medium, the uniform loadings g_p and g_{pw} do not create bending moments, shear or tension forces on the plate. Hence, they only cause uniform settlements along the plate and, consequently, do not influence the design forces and moments. On the other hand, due to the rigid connection between the wall and the plate foundation, the differential settlements can have a great influence on the bending moments, shear and normal forces acting along the tank wall.

The interaction force Q_0 is statically determined in function of the known loads P_w and g_w by the expression:

$$Q_0 = P_w + g_w H = P_w + \gamma_m h H \tag{1}$$

On the contrary, the interaction force H_0 and moment M_0 are not statically determined and their computation can be made imposing compatibility conditions between the horizontal displacements and rotations of the plate foundation and tank wall along their junction (Billington [12]; Vichare and Inamdar [5]). Through this procedure and using flexibility coefficients of thin cylindrical shells and circular plates on elastic base, Vichare and Inamdar [5] derived complex equations for evaluating M_0 and H_0. In the next section, these equations are used as basis for derivation of very simple and efficient equations to evaluate the interaction forces and moments acting along the tank wall-foundation plate junction.

3. Analytical procedures

3.1 Evaluation of interaction forces at the wall-foundation plate joint

For a circular plate rested on an elastic base with stiffness k_s and subjected to a symmetrical external loading q(r), the vertical deflections (settlements) w are given by (Timoshenko and Woinowsky-Krieger [6]):

$$\left(\frac{d^2}{dr^2} + \frac{1}{r}\frac{d}{dr}\right)\left(\frac{d^2 w}{dr^2} + \frac{1}{r}\frac{dw}{dr}\right) = \frac{q(r) - k_s w}{D_p} \tag{2}$$

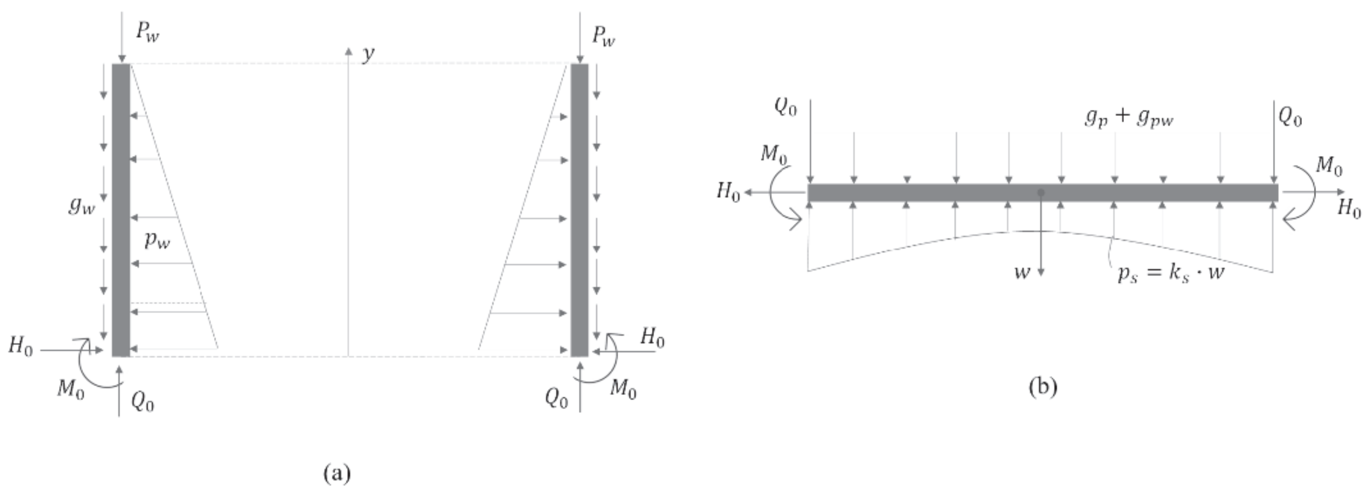

Figure 3
Free body diagrams of the cylindrical wall (a) and base plate (b)

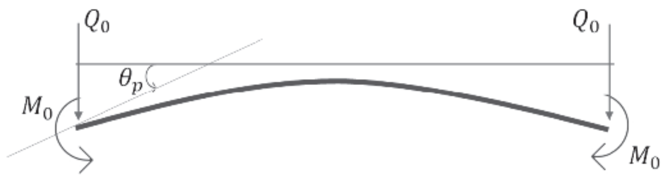

Figure 4
Rotation at the plate edge

where r is the radial coordinate and D_p indicates the flexural rigidity of the plate defined in the form:

$$D_p = \frac{Et^3}{12(1-\nu^2)} \tag{3}$$

As described above, a uniform continuously distributed load q(r) does not influence the design forces and moments and, then, it can be made equal to zero in eq. (2). For this case, the solution for the plate deflection w can be written as (Vichare and Inamdar [5]):

$$w = A_1 ber_0\left(\frac{r}{l}\right) + 4A_2 bei_0\left(\frac{r}{l}\right) \tag{4}$$

where, in general, ber_n (x) and bei_n (x) represent, respectively, the real and imaginary parts of the Bessel function of the first kind of order n, J_n ($i^{3/2}x$), (see Wylie and Barrett [13]). The parameter l appearing in eq. (4) is defined as:

$$l = \sqrt[4]{D_p/k_s} \tag{5}$$

The constants A_1 and A_2 are determined using the following boundary conditions at r = R:

$$\left(\frac{d^2w}{dr^2} + \frac{\nu}{r}\frac{dw}{dr}\right)_{r=R} = \frac{M_0}{D_p} \tag{6}$$

$$\left[\frac{d}{dr}\left(\frac{d^2w}{dr^2} + \frac{1}{r}\frac{dw}{dr}\right)\right]_{r=R} = -\frac{Q_0}{D_p} \tag{7}$$

The expressions of A_1 and A_2 can be found in Vichare and Inamdar [5]. Using eq. (4), the vertical rotation at the plate edge due to both Q_0 and M_0 can be written as (see Fig. 4):

$$\theta_p = \left(\frac{dw}{dr}\right)_{r=R} = \frac{G_1(\alpha)l}{D_p}M_0 + \frac{G_2(\alpha)l^2}{D_p}Q_0 \tag{8}$$

being α = R/l and

$$G_1(\alpha) = \frac{\sqrt{2}\,\alpha C_1}{\alpha[C_2 ber_0(\alpha) + C_3 bei_0(\alpha)] + \sqrt{2}\,(1-\nu)C_1} \tag{9}$$

$$G_2(\alpha) = \frac{C_3 ber_0(\alpha) - \alpha C_2 bei_0(\alpha)}{\alpha[C_2 ber_0(\alpha) + C_3 bei_0(\alpha)] + \sqrt{2}\,(1-\nu)C_1} \tag{10}$$

with $C_1 = ber_1(\alpha)^2 + bei_1(\alpha)^2$, $C_2 = ber_1(\alpha) - bei_1(\alpha)$ and $C_3 = ber_1(\alpha) + ber_1(\alpha)$.

The radial displacement produced by the radially distributed forces H_0 at the edge of the circular plate is given by:

$$\delta_p = -\frac{(1-\nu)R}{Et}H_0 \tag{11}$$

For the cylindrical wall, the horizontal displacement δ_w and rotation θ_w at the bottom can be computed by the following expressions (Billington [12]):

$$\delta_w = 2\beta\frac{R^2}{Eh}H_0 - 2\beta^2\frac{R^2}{Eh}M_0 - \frac{\gamma_l HR^2}{Eh} - \frac{\nu\gamma_m HR}{E} - \frac{\nu P_w R}{Eh} \tag{12}$$

$$\theta_w = -2\beta^2\frac{R^2}{Eh}H_0 + 4\beta^3\frac{R^2}{Eh}M_0 + \frac{\gamma_l R^2}{Eh} + \frac{\nu\gamma_m R}{E} \tag{13}$$

being:

$$\beta^4 = \frac{3(1-\nu^2)}{R^2h^2} \tag{14}$$

Now, applying the displacement compatibility conditions at the base plate – wall junction, $\delta_w = \delta_p$ and $\theta_w = \theta_p$, the values of M_0 and H_0 can be obtained by the expressions:

$$M_0 = \frac{1}{B_1 + B_2G_1(\alpha)}[B_3 + B_4G_2(\alpha)] \tag{15}$$

$$H_0 = \frac{(\nu\gamma_m h + \gamma_l R)H + \nu P_w + 2\beta^2 RM_0}{2\beta R + (1-\nu)\frac{h}{t}} \tag{16}$$

where

$$B_1 = 1 + \frac{\beta^3 t^2 R}{3(1+\nu)} \tag{17}$$

$$B_2 = -(1+B_1)\beta l\left(\frac{h}{t}\right)^3 \tag{18}$$

$$B_3 = \frac{(\nu\gamma_m h + \gamma_l R)(2\beta H - 1 - B_1) + 2\nu\beta P_w}{4\beta^3 R} \tag{19}$$

$$B_4 = -B_2 lHh\gamma_m \tag{20}$$

These equations have been determined from the closed analytical formulation derived by Vichare and Inamdar [5]. They are exact expressions, however, the use of them requires the evaluation of the complex functions G_1 (α) and G_2 (α). For the current practical applications, it is interesting to found simple and accurate expressions that allow obtaining the values of M_0 and H_0. Here, the complicated eq. (15) is replaced by the simplified expression:

$$M_0 = \frac{1}{B_1 + B_2\widetilde{G}_1(\alpha)}\left[B_3 + B_4\widetilde{G}_2(\alpha)\right] \tag{21}$$

where the complex functions G_1 (α) and G_2 (α) are substituted for approximate and very simple functions $\widetilde{G}_1(\alpha)$ and $\widetilde{G}_2(\alpha)$, respectively, being:

$$\widetilde{G}_1(\alpha) = -\frac{0.570 + 1.414\alpha^{0.968}}{0.028 + \alpha^{0.968}} \tag{22}$$

$$\widetilde{G}_2(\alpha) = -\frac{1.720 + 0.999\alpha^{0.912}}{1.375 + \alpha^{0.912}} \tag{23}$$

These later equations have been fitted for α ≥ 4 by using a linear regression method known as MMF model (Morgan et al. [14]). It is worth noticing that, for usual geometrical dimensions of base plates and soil stiffnesses, the values of the parameter α belong to that interval.

Comparisons between those exact and approximate functions for the interval $4 \le \alpha \le 100$ show relative maximum errors of only 0.86% and 0.44% for $\tilde{G}_1(\alpha)$ and $\tilde{G}_2(\alpha)$, respectively, occurring at $\alpha = 4$. The parametric analysis shown in the next section demonstrates the efficiency of the proposed approximate expression (21) for the computation of the design forces and moments of a cylindrical tank with a large range of soil stiffness. The interaction force H_0 can be readily calculated from eq. (16) using the approximate value of M_0.

3.2 Computation of displacements and forces along of the cylindrical wall

For the axisymmetrical forces shown in Fig. 3(a), the middle surface of the cylindrical wall presents vertical and radial displacements u and v, respectively. Using the classical theory of thin shells (Billington [12]), the radial displacement of the wall can be obtained in function of the interaction forces at the junction of the tank wall and plate foundation by:

$$v(y) = -\frac{e^{-\beta y}}{2\beta^3 D_w}[\beta M_0(cos\beta y - sin\beta y) - H_0 cos\beta y] - \frac{\gamma_l R^2}{Eh}(H - y) \quad (24)$$

where D_w is the flexural rigidity of the cylindrical shell given by:

$$D_w = \frac{Eh^3}{12(1-\nu^2)} \quad (25)$$

In eq. (24), the radial displacement v is considered as positive when it is directed to the interior of the cylindrical shell.
The hoop force N_θ and the vertical bending moment M_y acting along the wall can be obtained by:

$$N_\theta = -\frac{Ehv}{R} \quad (26)$$

$$M_y = -D_w \frac{d^2 v}{dy^2} \quad (27)$$

Here, M_y is taken as positive if it produces tension stress in the internal side of the wall whereas tension hoop force N_θ is considered as positive (Fig. 5).

Additionally, the cylindrical wall is also submitted to the circumferential horizontal bending moment M_θ and the transverse shearing force Q_y defined by:

$$M_\theta = \nu M_y \quad (28)$$

$$Q_y = -D_w \frac{d^3 v}{dy^3} \quad (29)$$

3.3 Approximate analysis of the plate foundation

The deflection w of the circular plate foundation is given by eq. (4), where the integration constants A_1 and A_2 are dependent upon the edge conditions related to the moment M_0, eq. (6), and shearing force Q_0, eq. (7). The radial bending moments M_r and shearing forces Q_r acting on the plate can be obtained by the following relations (Fig. 5):

$$M_r = -D_p\left(\frac{d^2 w}{dr^2} + \frac{\nu}{r}\frac{dw}{dr}\right) \quad (30)$$

$$Q_r = D_p\left[\frac{d}{dr}\left(\frac{d^2 w}{dr^2} + \frac{1}{r}\frac{dw}{dr}\right)\right] \quad (31)$$

To simplify the computation of the deflections, bending moments and shearing force of the plate, the Bessel functions appearing in eq. (4) can be approximated by the asymptotic expressions (Timoshenko and Woinowsky-Krieger [6]):

$$ber_0(x) \cong \frac{e^{x/\sqrt{2}}}{\sqrt{2\pi x}} cos\left(\frac{x}{\sqrt{2}} - \frac{\pi}{8}\right) \quad (32)$$

$$bei_0(x) \cong \frac{e^{x/\sqrt{2}}}{\sqrt{2\pi x}} sin\left(\frac{x}{\sqrt{2}} - \frac{\pi}{8}\right) \quad (33)$$

It is worth observing that these two approximate relations are valid for not very small values of the argument x as can be seen in Fig. 6. This figure shows that the approximations (32) and (33) do not work well only for a small region close to the origin of the x-axis. However, for the circular plate region of usual particular interest in

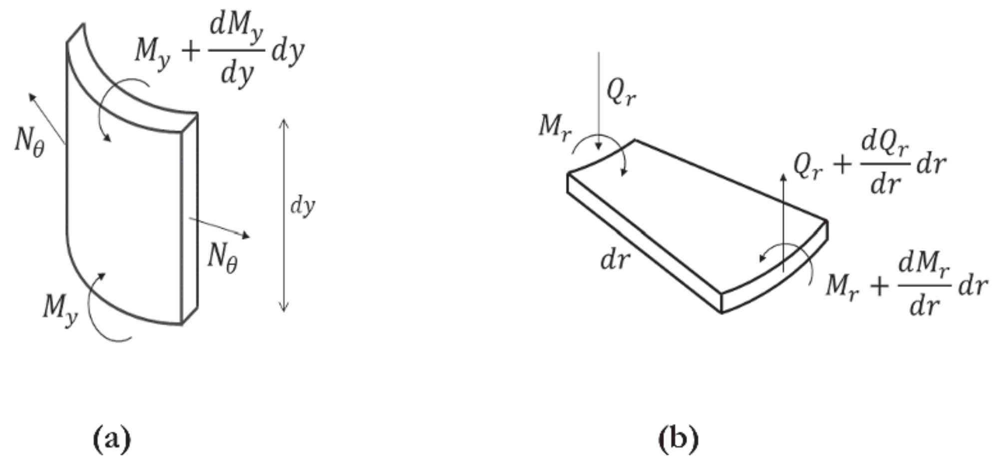

Figure 5
Hoop force and vertical bending moment in the wall (a) and radial bending moment and shear force in the plate (b)

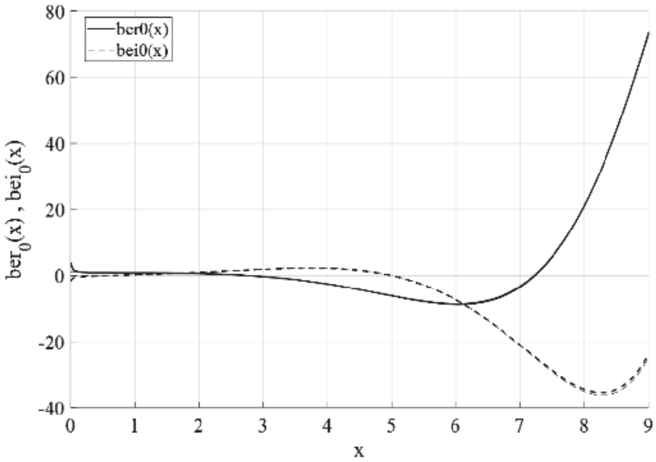

Figure 6
Exact and approximate (thicker lines) functions ber_0 (x) and bei_0 (x)

structural designs such approximations provide accurate predictions as shown in the next section.
Introducing eqs. (32) and (33) into eq. (4) and using the boundary
Introducing eqs. (32) and (33) into eq. (4) and using the boundary
conditions given by the relations (6) and (7), the constants A_1 and A_2 are readily determined and, consequently, the expression of the plate deflection is obtained. With the known plate deflection w, the bending moments and shearing forces can be computed through the expressions (30) and (31).

4. Numerical examples and discussion of results

In order to illustrate the influence of the soil deformability on the design mechanical quantities and verify the approximate expressions presented in this paper, a concrete cylindrical water tank rested on a soil with four different levels of deformability (soft, medium, stiff and very stiff) was analyzed. The following numerical data were considered (see Fig. 1):

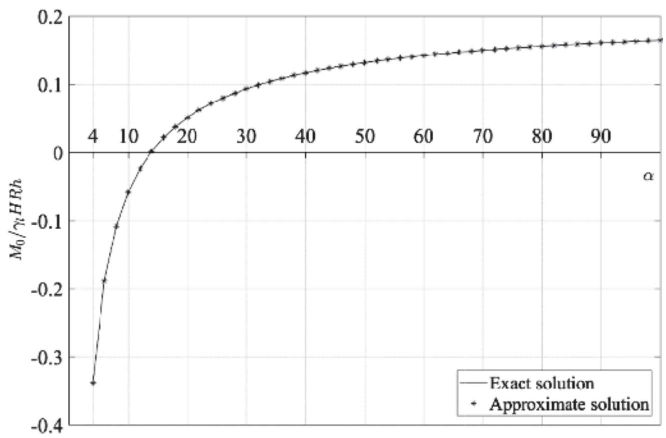

Figure 7
Variation of the moment at the base plate-wall junction in function of α

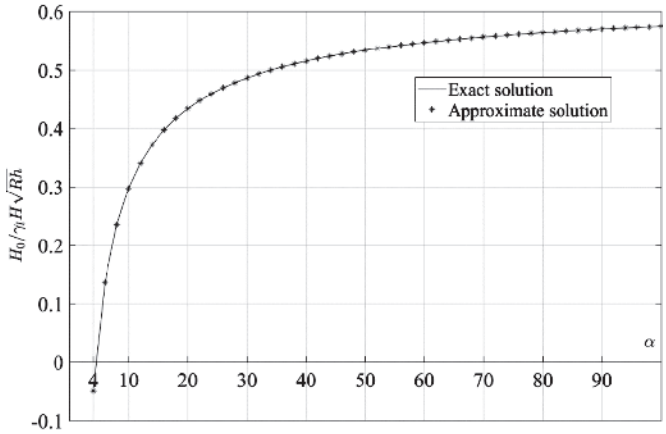

Figure 8
Variation of the shear force at the base plate-wall junction in function of α

Geometrical dimensions: R = 658.75 cm, t = h = 17.50 cm and H = 350 cm.
Concrete properties: E = 20 GPa, ν = 0.2 and γ_m = 25 kN/m³.
Soil stiffness k_s (kN/m³): 25,000, 50,000, 100,000 and 10^{10}.
Weight per unit volume of water: γ_l = 10 kN/m³.
To demonstrate the performance of the proposed approximate functions $\tilde{G}_1(\alpha)$ and $\tilde{G}_2(\alpha)$ in replacement of the complex functions G_1 (α) and G_2 (α), a parametric analysis of M_0 for a large interval of α (4 ≤ α ≤ 100) was made. Figure 7 shows the comparison between the exact and approximate curves of M_0 obtained by eqs. (15) and (21), respectively. Using the exact and approximate values of M_0 into eq. (16), the curves corresponding to the force H_0 as function of the parameter α can be found (Fig. 8). As can be seen, the exact and approximate functions provide practically coincident values for the design forces at the base plate-wall junction. Figure 7 also shows that there is a value of the parameter α for which the moment M_0 is null, i. e., a value corresponding to the transition of

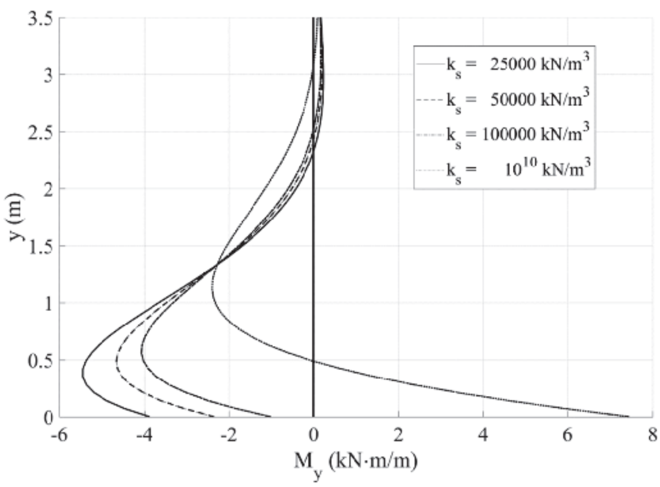

Figure 9
Bending moment M_y along the wall for different soil stiffness

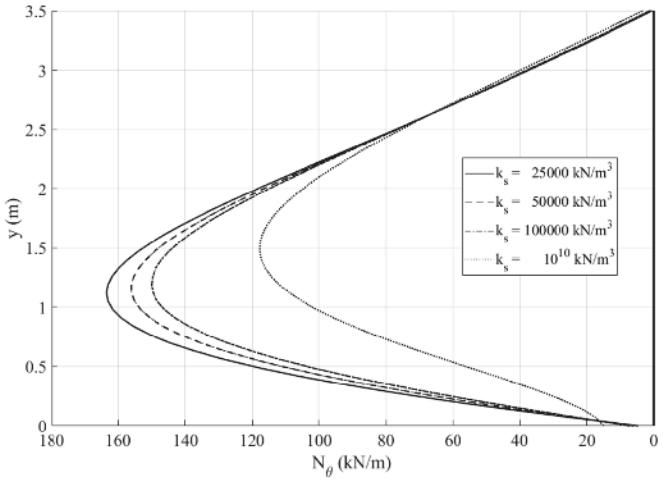

Figure 10
Hoop force N_θ along the wall for different soil stiffness

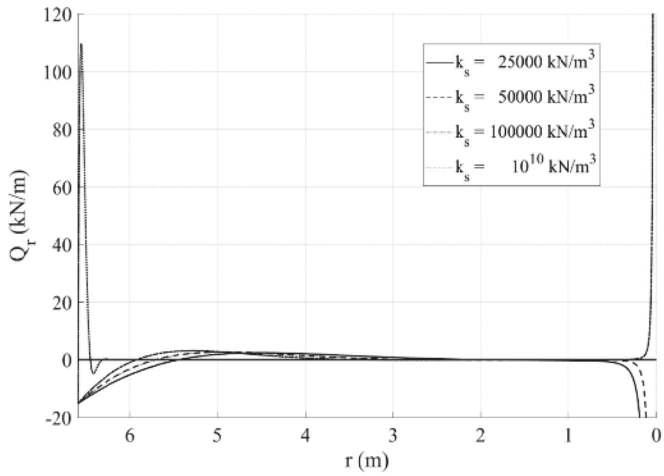

Figure 12
Radial shear force Q_r in the base plate for different soil stiffness

the moment sign. For the present case, this value is equal to 13.86, which corresponds to a ratio $D_p/(k_s = 0.051$ m^4 or a soil stiffness k_s = 182,440.60 kN/m$_3$.

To verify the effects of the soil deformability on the design forces and moments acting along the wall and base plate, the tank was analyzed as rested on four soil types, classified as soft, medium, stiff and very stiff, with stiffness (k_s): 25,000 kN/m^3, 50,000 kN/m^3, 100,000 kN/m^3 and10^{10} kN/m^3, respectively. This later stiffness value was used to simulate the conditions of an infinitely rigid soil. The results of forces, moments and deflections corresponding to the different soil stiffness are represented in Figs. 9 – 13. The exact and approximate curves of M_y and N_θ for the same value of the soil stiffness are practically coincident so that the differences between them cannot be visualized in Figs. 9 and 10. The results show the significant influence of the elastic foundation on the bending moments and hoop forces developed in the tank wall. It is very important to observe that even for soils classified as rigid the actual bending moment distribution along the wall can be completely different from that obtained through the usual design assumptions by which the lower edge of the wall is assumed as built into an absolutely rigid foundation or the plate base is supported by a soil infinitely rigid. The very small bending moments appearing at the top of the wall in Fig. 9 are justified by the used simplification of cylindrical shell enough long so that each edge (top and bottom) can be treated independently. This assumption is commonly employed in design procedures when $\beta H > \pi$.

Figures 11 and 12 show the distributions of the approximate radial bending moments and radial shear forces, respectively, for the circular base plate. As described above and observed in Figs. 11 and 12, the approximate solution provides discrepant results for regions very close to the plate center. However, for the rest of

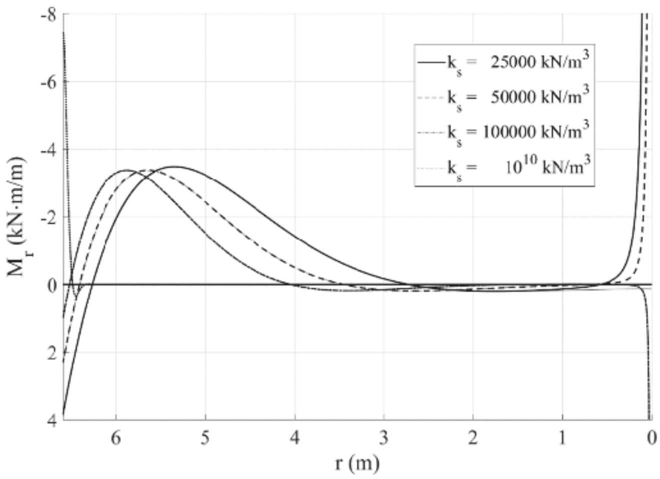

Figure 11
Radial bending moment M_r in the base plate for different soil stiffness

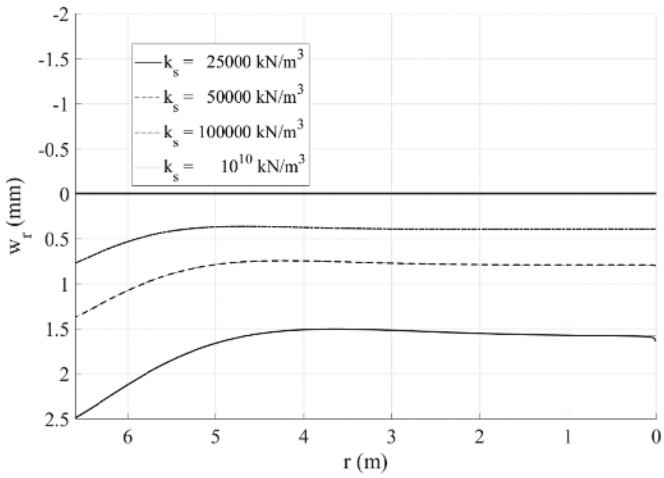

Figure 13
Vertical deflection w_r in the base plate for different soil stiffness

the plate the approximate and exact solutions present a very good agreement for all adopted levels of soil stiffness, so that the differences between corresponding curves are not graphically visible. It is interesting to emphasize that in design of tanks rested on the ground the shear forces and bending moments in the region close to the plate center usually do not have so much significance.
The results of the plate vertical displacements are shown in Fig. 13. In this figure the differences between the curves of the approximate (thicker lines) and exact (thinner lines) deflections are not visible, except in a small region very close to the plate center. It is also observed that the magnitude of such differences decreases with the increase of the soil stiffness. Figures 11 - 13 show that the disturbances of the approximate solution for the bending moments and shear forces are relatively higher than for the deflections. This occurs because these moments and forces depend on derivatives of the approximate functions given by eqs. (32) and (33).
As illustrated in Fig. 13, a central circular region of the plate, whose size depends on the soil stiffness, holds practically flat. For the same geometrical dimensions and loading, the diameter of such region decreases with the increase of the soil deformability.
The numerical values of maximum and minimum displacements and forces in the tank obtained by exact and approximate solutions are presented in Table 1 for the four soil stiffnesses. As can be seen, the approximate values are in very good agreement with those obtained by the exact solution. The major differences between the corresponding exact and approximated values in Table 1 occur for the base plate, where a largest relative error of approximately 3.15% is observed in the maximum radial shear force occurring for the softer soil with k_s = 25,000 kN/m³.

5. Conclusions

An analytical study aiming the design of liquid storage circular tanks resting on deformable foundation has been developed. The procedures accounted for the soil-structure interactions. The soil behavior has been modeled by a continuous set of elastic vertical springers. An exact analytical formulation expressed in terms of complex Bessel functions was used as basis for derivation of simplified and efficient approximate expressions to evaluate mechanical quantities which are important for the structural design of the mentioned tanks. Comparisons of results showed that the simplified approximate expressions allow obtaining the displacements, forces and moments along the tank wall with an excellent accuracy in relation to the exact solution. For the analyzed tank, the largest relative difference between corresponding extreme values of displacements and forces in the wall, computed by using the exact and approximate solutions, was 0.143%.
To evaluate the displacements, shear forces and bending moments along the plate foundation, the study used approximate expressions for the real and complex parts of the Bessel functions. The analyses demonstrated that such approximations provide very good results for the important mechanical quantities for the plate design and their unrealistic values are concentrated in a small region near the plate center. A largest relative difference of approximately 3.15% between

Table 1
Values of the maximum and minimum forces and displacements of the tank

Units [kN; m]			k_s = 25,000	k_s = 50,000	k_s = 100,000	k_s = 10^{10}
M_y	Max	Exact	0.2357	0.2011	0.1759	7.4486
		Approx.	0.2356	0.2010	0.1758	7.4486
	Min	Exact	-5.4531	-4.6539	-4.0692	-2.3899
		Approx.	-5.4506	-4.6519	-4.0680	-2.3899
N_θ	Max	Exact	163.4696	156.1208	150.0996	117.6479
		Approx.	163.4556	156.1093	150.0916	117.6479
	Min	Exact	0.4911	0.8619	1.1849	3.2336
		Approx.	0.4918	0.8625	1.1853	3.2336
v (× 10^{-3})	Max	Exact	-0.000924	-0.001622	-0.002230	-0.006086
		Approx.	-0.000926	-0.001623	-0.002231	-0.006086
	Min	Exact	-0.311593	-0.297691	-0.286313	-0.224773
		Approx.	-0.311566	-0.297668	-0.286298	-0.224773
M_r	Max	Exact	3.8802	2.3485	1.0143	0.3255
		Approx.	3.8283	2.3147	0.9924	0.3255
	Min	Exact	-3.4684	-3.3679	-3.3658	-7.4486
		Approx.	-3.4779	-3.3755	-3.3717	-7.4486
Q_r	Max	Exact	2.2960	2.5926	3.0254	109.5791
		Approx.	2.3683	2.6413	3.0615	109.5816
	Min	Exact	-15.3125	-15.3125	-15.3125	-15.3125
		Approx.	-15.1756	-15.1897	-15.2032	-15.3026
W_r (× 10^{-3})	Max	Exact	2.487558	1.368909	0.769170	0.000848
		Approx.	2.489538	1.369853	0.769621	0.000848
	Min	Exact	1.507159	0.744499	-0.365083	0.000158
		Approx.	1.508066	0.744847	-0.365217	0.000158

the corresponding extreme values of displacements and forces, computed by exact and approximate solutions, was observed for the maximum radial shear force in the plate.

Comparative analyses of a cylindrical tank rested on soils with different levels of stiffness (soft, medium, stiff and very stiff) demonstrated that the effects of soil-structure interaction have crucial importance for the tank design. The results showed that the critical design forces of the tank are very sensitive to differential settlements of the plate foundation and that even for soils usually classified as rigid the actual resultant forces in the wall can be very different from those obtained through the simplified design procedures in which the soil-structure interactions are neglected.

6. Acknowledgements

The authors acknowledge the financial support provided by the Brazilian federal agencies CNPq and CAPES.

7. References

[1] Kukreti, AR, Zaman, MM, and Issa, A. Analysis of fluid storage tanks including foundation-superstructure interaction. Applied Mathematical Modelling, v.17, n.12, 1993; p. 618-631.

[2] Kukreti, AR and Siddiqi, ZA. Analysis of fluid storage tanks including foundation-superstructure interaction using differential quadrature method. Applied Mathematical Modelling, v.21, 1997; p. 193-205.

[3] El Mezaini, N. Effects of soil-structure interaction on the analysis of cylindrical tanks. Practice Periodical on Structural Design and Construction, ASCE, v.11, n.1, 2006; p. 50-57.

[4] Portland Cement Association (PCA). Circular concrete tanks without prestressing, Skokie, IL, USA, 1993.

[5] Vichare, S and Inamdar, MM. An analytical solution for cylindrical concrete tank on deformable soil. International Journal of Advanced Structural Engineering, v.2, n.1, 2010; p. 69-90.

[6] TIMOSHENKO, S.P. and WOINOWSKY-KRIEGER, S. Theory of plates and shells, New York: McGraw-Hill, 2ed, 1959, 580 p.

[7] KELKAR, V.S. and SEWELL, R.T. Fundamentals of the analysis and design of shell structures, Eaglewood Cliffs: Prentice-Hall Inc., 1987, 510 p.

[8] Mistrikova, Z. and Jendzelovsky, N. Static analysis of the cylindrical tank resting on various types of subsoil. Journal of Civil Engineering and Management, v.18, n.5, 2012; p. 744-751.

[9] Dehadrai, VP and Ingle, RK. Cylindrical water tanks resting on soil of varying stiffness. Practice Periodical on Structural Design and Construction, ASCE, v.21, n.3, 2016; 04016006-1.

[10] Das, AK and Deb, K. Response of cylindrical storage tank foundation resting on tensionless stone column-improved soil. International Journal of Geomechanics, ASCE, v.17, n.1, 2017; 04016035.

[11] SILVA, R.L.C. Contribuição ao projeto de reservatórios cilíndricos de concreto armado apoiados em base deformável, Maceió, 2017. Dissertação (Mestrado em Engenharia Civil), Universidade Federal de Alagoas, 209 p.

[12] BILLINGTON, D.P. Thin shell concrete structures, New York: McGraw-Hill, 2ed, 1982, 373 p.

[13] WYLIE, C.R. and BARRETT, L.C. Advanced engineering mathematics, New York: McGraw-Hill Companies, 6ed, 1995, 1103 p.

[14] Morgan, PH, Mercer, LP and Flodin, NW. General model for nutritional responses of higher organisms. Proceedings of the National Academy of Sciences, USA, v.72, n.1, 1975, p. 4327-4331.

Volume 12, Number 1 (February 2019) p. 23 – 30 • ISSN 1983-4195
http://dx.doi.org/10.1590/S1983-41952019000100004

IBRACON

REVISTA IBRACON DE ESTRUTURAS E MATERIAIS
IBRACON STRUCTURES AND MATERIALS JOURNAL

Geometric optimization associated with the use of high-strength concrete in viaducts

Otimização geométrica associada à utilização de concreto de alta resistência em tabuleiros de viadutos de múltiplas longarinas pós-tensionadas


E. V. W. TRENTINI [a]
eduardowtrentini@gmail.com
https://orcid.org/0000-0001-8500-2723

C. H. MARTINS [a]
chmartins2007@gmail.com
http://orcid.org/0000-0001-7342-5665

Abstract

In Brazil, there is a lack of infrastructure investment in roads, given that they facilitate the transportation of more than half the country's cargo volume. One of the main variables in road infrastructure is overpass construction and maintenance. Concrete overpasses with post-tensioned I-section beams have been extensively used in Brazil. This study discusses the economic aspects of the use of high-strength concrete (HSC) associated with the geometrical optimization of decks of post-tensioned multi-girder overpasses. Twelve overpass decks were dimensioned and divided into two groups. In Group A the characteristic concrete strength varied, but not the geometrical characteristics of the deck. In Group B, the characteristic strength and the geometrical characteristics of the deck varied. These were the configurations that presented the best results for each group of characteristic concrete strength. It was determined that the use of HSC significantly decreases the reinforcement ratio–especially shear reinforcement. In addition, although the HSC has a higher cost per m3, it is still considered a viable option owing to the reduction in the reinforcement ratio. Lastly, in addition to providing the benefits that are widely commented on in literature, using HSC can also provide more economical overpass structures compared to conventional concrete.

Keywords: bridges, concrete structures, viaducts, structures and design.

Resumo

O Brasil carece de investimentos em infraestrutura rodoviária, uma vez que este é responsável por mais da metade do volume de cargas transportado no território nacional. Quando se aborda o tema de infraestrutura rodoviária, uma das principais variáveis é, sem dúvida, a construção e a manutenção de viadutos. Viadutos em concreto de longarinas protendidas com seção I tem sido amplamente utilizadas no território nacional. Este trabalho tem como objetivo discutir os aspectos econômicos da utilização de concreto de alta resistência (CAR) associada à otimização geométrica de tabuleiros de viadutos de múltiplas longarinas pós-tensionadas. Para tanto, foram dimensionados doze tabuleiros de viaduto dividindo dois grupos. No Grupo A, a resistência característica do concreto variava e as características geométricas do tabuleiro não. Já no Grupo B a resistência característica variava, assim como as características geométricas do tabuleiro, haja vista que estas eram as configurações que apresentavam os melhores resultados para cada grupo de resistência característica do concreto. Sendo assim foi possível identificar que a utilização CAR diminui significativamente a taxa de armaduras, principalmente as armaduras de cisalhamento. Também observou-se que, apesar do CAR possuir um custo mais elevado por m³, ele ainda é considerado uma opção viável devido a redução da taxa de armaduras proporcionada. E por fim, a sua utilização além de proporcionar os benefícios amplamente comentados na literatura, ainda pode proporcionar estruturas de viadutos com custo de construção mais econômicos que o concreto convencional.

Palavras-chave: viadutos, pontes, CAR, otimização.

[a] *State University of Maringá Department of Civil Enginnering, , Maringá, PR, Brazil.*

Received: 25 Apr 2018 • Accepted: 27 Jun 2018 • Available Online: 05 Feb 2019

1. Introduction

According to Eller [9], in Brazil more than half of the total cargo volume is transported by road.
The unsatisfactory conditions of this system have caused the Brazilian products to have costly shipping and vehicle maintenance, thus reducing their competitiveness. Therefore, owing to the constant need for investments in road conservation, the public resources are not sufficient to maintain the quality of the system [9].
Investments for recovery and duplication are being made, as well as concessions, but they are still not sufficient to satisfy the country's deficiency in road infrastructure. Martins, Soares, and Cammarata [11] estimate that it would be necessary to build 21,000 km of road network to obtain a significant reduction in the transportation time, the number of accidents, and the shipping costs in Brazil.
Overpasses and bridges, commonly named "special construction works," are one of the most important structures with regard to road infrastructure, given that they are costly and demand detailed planning.
Bridges built with multiple prestressed I-sections and precast girders are becoming common in Brazil, given that they are ideal for short-to-medium overpasses (20 to 60 m) owing to their moderate weight, structural efficiency, ease of manufacture, fast construction, and ease of maintenance [1].
With regard to the characteristic strength of concrete, special attention is drawn to the use of high-strength concrete (HSC). Currently, it is known that HSC has a characteristic compressive strength equal to or greater than 55 MPa – according to NBR 8953:2015 [7]. In the last few years, its use has become widespread owing to the technological breakthroughs in the executive processes, and the fact that technological and project control have required the concrete to have increasingly higher structural performance.
In addition to the improvement of mechanical properties, according to Mehta [13], one of the main characteristics of HSC is its durability as compared to conventional concrete – it is stronger when subjected to the action of aggressive agents. This improvement is caused by the low water–cement ratio that leads to a decrease in porosity and consequently the permeability, increasing the service life of the structure and reducing maintenance costs.
According to Aïtcin [2], after 1960, HSC has begun to be used in large quantities in noticeable structures. Until the 1990s, an improvement was made by including superplasticizer additives, followed by the use of silica.
Peinado et al. [14] commented that, in addition to increasing the concrete strength, and therefore, decreasing the use of cement, the use of active silica is recommended due to technical and environmental issues, given that it is a by-product of the production of metal alloys.
Rebmann [15] highlights that cement production is a highly energetic process, and the production of 1,000 kg of concrete is responsible for the emission of approximately 830 kg of CO_2 into the atmosphere, depending on the clinker content used.
According to the annual report by the National Union of the Cement Industry (Sindicato Nacional da Indústria do Cimento – SNIC), in 2013, 71 million tons of cement were produced in Brazil. Considering the average CO_2 emissions presented by Rebmann (830 kg/ton of cement), the cement production accounted for the emission of approximately 59 million tons of CO_2 into the atmosphere this year.
According to studies performed by the Federal Government, in the same year, 460 million tons of CO_2 were emitted in Brazil; therefore, cement production is responsible for approximately 12.8% of the CO_2 emissions in Brazil.
Hence, considering the environmental issues, there is an evident need for research in relation to each class of strength that is more appropriate for the dimensioning of each structure in order to reduce the use of cement in concrete and the use of steel per structure/structural element [14].
According to Dal Morin [8], in the mid-1990s the HSC combined with post-stressing was widely applied to overpasses with medium and long spans with the purpose of limiting the deflection, decreasing its own weight, and reducing the creep.
In bridge decks, cracks have been the subject of studies over the years. However, there are still many questions on how to effectively minimize this problem given that its occurrence leads to the corrosion of the reinforcement [12] and, according to Aïtcin [2], the penetration of chloride ions triggers this process early.
High-performance concrete contains noble materials such as superplasticizer additives and supplementary cementitious materials (active silica, fly ash, blast-furnace slag, etc.) that cause it to be costlier as compared to conventional cement. In turn, the improvements in its mechanical properties have direct benefits, such as the reduction in the reinforcement ratio.
Considering the factors mentioned so far (reduction in the use of cement and therefore, reduced CO_2 emissions, reduction in the

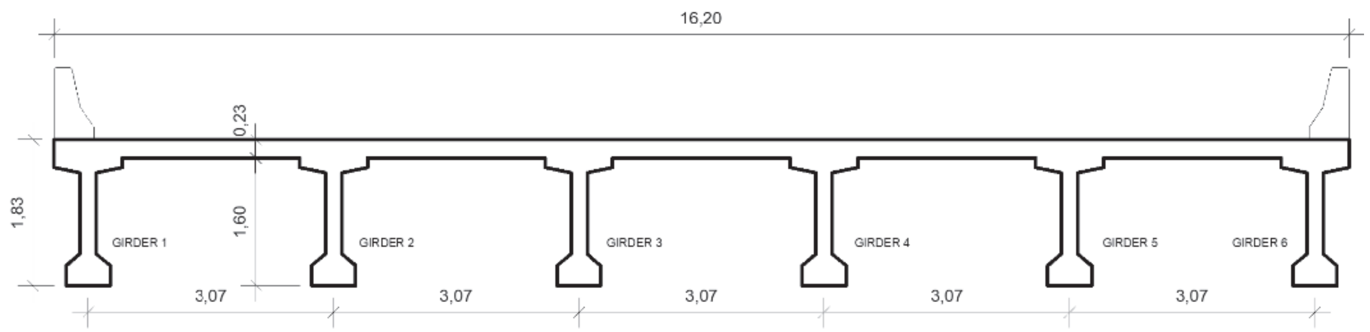

Figure 1
Cross section of the deck of Group A (dimensions in meters)

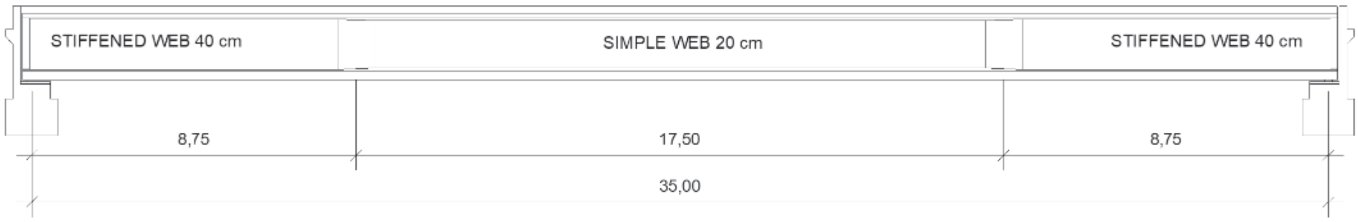

Figure 2
Longitudinal elevation of the deck (dimensions in meters)

deflection, reduction in creep, and the higher durability of the structure), the use of HSC is advantageous. This study aims to discuss the influence of the improvements obtained by using HSC on the cost of overpass decks.

2. Materials and methods

To evaluate the influence of the changes in concrete strength on the total cost of the deck, 12 decks with a 35-m span and 16.2-m width were separated into two groups. Group A consists of six decks with the same geometrical configurations and different characteristic concrete strengths (35, 45, 55, 65, 75, and 90 MPa). In turn, Group B consists of six decks with different geometrical configurations as well as different characteristic concrete strengths (the same as Group A).
Trentini [18] created software that determines the optimal pre-dimensioning in relation to the lowest cost for this type of deck– available at “*http://www.pcv.uem.br/programas/”.* The selected geometrical configurations were obtained from this study, hence, the combination of the independent variables of Group A (Figure [1] and Figure [2]) is the one that provides the lowest cost for the deck with the characteristic concrete strength equal to or greater than 35 MPa, as shown below:
N_{lg} = 6 girders;
H_{lg} = 1.60 m;
H_{lj} = 23 cm;
E_{lg} = 8.75 m.
For Group B, each deck has a single geometrical configuration, i.e., each deck has the combination of independent variables that results in the lowest cost for its concrete strength class based on the study by Trentini [18].

2.1 Premises for the design

During the design the load prescribed in NBR 7188:2013 [5] was applied – moving road load and pedestrians on bridges, overpasses, pedestrian overpasses and other structures – considering the following, “the standard moving road load TB-450 is defined by a 450 kN vehicle type with 6 wheels, P = 75 kN, three cargo axles with 1.5 m spacing and occupation area of 18.0 m², surrounded by a constant load with uniform distribution p = 5 kN/m².”
Because the two-dimensional structure of the deck forms a grid, the variation of the position of the vehicle type according to NBR 7188:2013 [5] in the plane should be considered. Knowing the influence of the load points, it is possible to minimize the hypotheses of the structure calculations, thus evidencing the most unfavorable position for each dimensioning situation. Fauchart [10] elaborated on a method for the calculation of the transverse influence for this type of structure.
Fauchart’s process is applied to multi-girder decks without intermediate cross beams. Furthermore, the girders should be fixed and have a constant inertia. In this process, the longitudinal work of the slabs is not considered [17].
To distinguish which part of the load is oriented to which girder, the cross-section of the deck is loaded, while observing the cross-sectional influence line that results from Fauchart’s process. The vehicle type is positioned at the points of maximum positive and negative influence along the beam, and the load is multiplied by the value of the corresponding influence.
The result of this process is called a “load train”, where each girder has its own graph of influence and, therefore, its train with independent load. The girders are then considered as fixed beams subjected to a load train.
During the construction process of this structure, the precast girders are lifted and placed on the supports. Thus, the weight of the girder is supported only by itself as the slab has not been built yet. Only after applying concrete and curing the slab, the additional loads can be considered to act on the composite section of the girder and the slab. The dimensioning presented in this study considers that any load acts on the section of the composite girder with slab, and therefore, none of the differences provided by these models are significant for what is proposed in this study.
The characteristic forces calculated so far need to be combined using the equations and coefficients proposed by NBR 8681:2003 – Structural actions and safety – Procedure, to become design forces [6].
To comply with the limits of durability demanded by item 13.4 of NBR 6118:2014 – Concrete structure design – Procedure [3], it is important that the parts with limited prestressing obey the limits of crack formation (ELS-F item 3.2.2) for the frequent combination and at the decompression limit state (ELS-D item 3.2.5) for the almost permanent combination, where the prestressing force P_∞ should be enough to obey both limits.
The present study adopts an estimated loss of prestressing force of 25% (10% immediate and 15% progressive) for the purpose of simplification. When dealing with the dimensioning of pro-stressed sections, it is important to consult item 9.6.3, Loss of prestressing force, of NBR 6118:2014 [3].
The dimensioning of the flexural longitudinal reinforcements is performed, considering it to be at the conventional state of rupture by

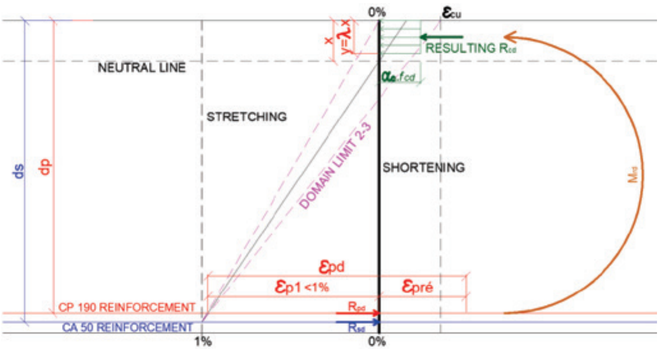

Figure 3
Specific deformation in ELS

excessive plastic stretching, i.e., it is stretched by 1%. Hence, the deformations in the section of the girder at the ultimate limit state (ULS) are distributed as presented in Figure 3 and the internal moment of resistance of the section (M_{rd}) is calculated using Equation [1].

$$M_{rd} = R_{cd} \cdot \left(dp - \frac{\lambda}{2} \cdot x \right) + R_{sd} \cdot (ds - dp) \tag{1}$$

For the calculation of the shear reinforcements, model I of ABNT NBR 6118:2014 [3] provided in item 17.4.2.2 is used. In turn, for the calculation of the torsional reinforcements, item 17.5 of the same standard is used, considering θ = 45°.

It is also necessary to verify if the maximum stress variation in the stirrups during the frequent combination does not exceed 85 MPa, as per item 23.5.5 of NBR 6118:2014 [3]. In this verification, the standard allows the consideration of only half of the contribution of concrete.

The vertical curves of the prestressing cables generate favorable forces for the shear stress that acts on the girders; however, for the purpose of simplicity, this effect will not be considered in this study.

In contrast to the girders, Fauchart's process is not applied to obtain the forces on the slab, as it neglects the longitudinal distribution of the load on the structure.

The uniformly distributed forces, such as the weight of the slab itself, can be analyzed as applied on a fixed beam, because the entire cross-section of the overpass has the same load. Nevertheless, because the non-uniform load distribution occurs in a different way in each direction, it is important to use a theory that best represents this situation. Rüsch [16] developed a set of practical tables for the dimensioning of bridge slabs using the plate theory, which considers the work of the loads in the cross-sectional direction as well as in the longitudinal direction of the deck. Therefore, Rüsch's tables will be used to obtain the forces on the slab.

After calculating the characteristic forces, the equations and coefficients of NBR 8681:2003 [6] are applied to obtain the calculated forces. The dimensioning of the slab is performed using the classical theory of the beam subjected to simple flexure, assuming the unitary width *b* and Equations (2) and (3).

$$x = \frac{1}{\lambda} \cdot d \left(1 - \sqrt{1 - \frac{M_d}{\frac{\alpha_c}{2} \cdot b \cdot d^2 \cdot f_{cd}}} \right) \tag{2}$$

$$A_s = \frac{M_d}{f_{yd} \left(d - \frac{\lambda}{2} \cdot x \right)} \tag{3}$$

It is also necessary to verify that the fatigue in the slab reinforcement is similar to the one performed in the girder. In NBR 6118:2014 [3], item 23.5.5 establishes the limit for the variation of stress during the frequent combination of 190 MPa for longitudinal, straight, flexural reinforcements with a diameter less than 16 mm.

There is the possibility that the reinforced slab can resist the acting force only with the longitudinal reinforcement, and a verification is performed according to item 19.4.1 of ABNT NBR 6118:2014 [3]. If the use of supplementary reinforcement is necessary, it is calculated according to item 17.4.2.2 of NRB 6118:2014 [3].

2.2 Cost function

The total cost of the deck C_T is determined by the sum of the costs of the construction and assembly materials.

Peinado et al. [14] presents, in their study, the cost of the different concrete classes provided by a concrete manufacturer company from the region of Maringá, Paraná and dated April 2014. For all unitary prices used in the calculation of the total cost to have the same date, the value presented by the authors was corrected by the National Construction Cost Index (INCC – Índice Nacional de Custo da Construção), which was 13.15% in the period of April 2014 to November 2015. The values in Table 2 already include 9.28 \$/m³ for workforce and 10.61 \$/m³ for pumping.

The cost of the girder casts $C_{f,lg}$ varies according to the number of repetitions, with 15.74 \$/m² for two, 12.04 \$/m² for two to five, 9.11 \$/m² for five to eight, and 7.51 \$/m² for more than eight repetitions, all of which were obtained from the SINAPI table of june 2015.

Table 1
Geometrical characteristics of the decks of Group B

f_{ck} (MPa)	N_{lg}	H_{lg} (m)	H_{lj} (m)	E_{lg} (m)
35	6	1.6	0.23	8.75
45	6	1.5	0.22	7.00
55	6	1.5	0.22	7.00
65	6	1.5	0.22	7.00
75	6	1.6	0.20	8.75
90	6	1.6	0.20	8.75

Table 2
Cost of concrete in function of the characteristic strength

Concrete strength class	Cost in April/2014 (\$/m³)	Cost in November/2015 (\$/m³)
C35	89.92	101.75
C45	99.47	112.55
C55	108.58	122.86
C65	115.90	131.14
C75	122.15	138.21
C90	130.15	147.27

Table 3
Unit costs

Variable	Unit of measurement	Cost	Source
$C_{c,lg}$	\$/m³	101.75~147.27	Peinado et al (2014, p. 7) + 13.25%
$C_{f,lg}$	\$/m²	16.32~7.81	SINAPI, PR, 06/2015 + 3.95%
$C_{a,lf,lg}$	\$/kg	1.70	SINAPI, PR, 06/2015 + 3.95%
$C_{a,lt,lg}$	\$/kg	1.70	SINAPI, PR, 06/2015 + 3.95%
$C_{a,vct,lg}$	\$/kg	1.70	SINAPI, PR, 06/2015 + 3.95%
$C_{p,lg}$	\$/kg	2.79	Hejos Construções Civis 2015
$C_{cj,p,lg}$	\$/un	100.76	Hejos Construções Civis 2015
$C_{i,lg}$	\$/un	54.39/ton	Hejos Construções Civis 2015
$C_{c,lj}$	\$/m³	101.75~147.27	Peinado et al (2014, p. 7) + 13.25%
$C_{a,lj}$	\$/kg	1.70	SINAPI, PR, 06/2015 + 3.95%

The costs obtained from the SINAPI table, PR, June 2015 were adjusted to the same date of November 2015, considering the correction index of 3.95%.
The cost of the cast to manufacture the pre-slabs is not evaluated in this function, as the comparison of costs is performed between overpasses with the same longitudinal span and the same cross-sectional width. Therefore, it is the same for all solutions and can be disregarded.
Some very specific services, such as prestressing, set of anchorage, and the lifting of girders are not included in conventional quotation tables. Therefore, this cost was provided by a construction company from the region of Maringá, specialized in this type of construction.
The cost of the lifting of precast girders is calculated as a function of the weight of the girders, assuming that the cost increases linearly with the lifted weight.
Additional costs such as corrugated metal sheaths and cement laitance injection were not considered because they are very low as compared to the total cost of the construction.

3. Results and discussions

Initially, the twelve decks were dimensioned, following the premises discussed in section 2.1. After the dimensioning, the costs of each combination were calculated using the unit costs presented in section 2.2.

3.1 Group A

Group A presents the same geometrical configuration and different characteristic concrete strengths. Table [4] presents the cost of each one of the six combinations. Figure [4] shows the variation of the cost as a function of the characteristic concrete strength, f_{ck}. It is possible to observe a small percentage variation in the cost (0.31% is the greatest variation between two combinations). Because all decks in Group A have the same geometrical configuration, i.e., they have the same concrete volume, the same cast area, the same lifting cost, and the same quantity of active reinforcement, the variation in the cost is in the cost of the concrete and the cost of the passive reinforcements.
To better visualize this dependency, Figure [5] shows the cost of the concrete and the cost of the passive reinforcement as a function of the characteristic concrete strength for Group A.
As observed in Figure [5], the cost of the passive reinforcement decreases when higher values are used for the characteristic concrete strength because, as seen in Figure [3], for higher concrete strength values, the height of the compressed concrete y is lower, which increases the lever arm of the flexural reinforcement in the calculation of the internal moment of resistance of the section and,

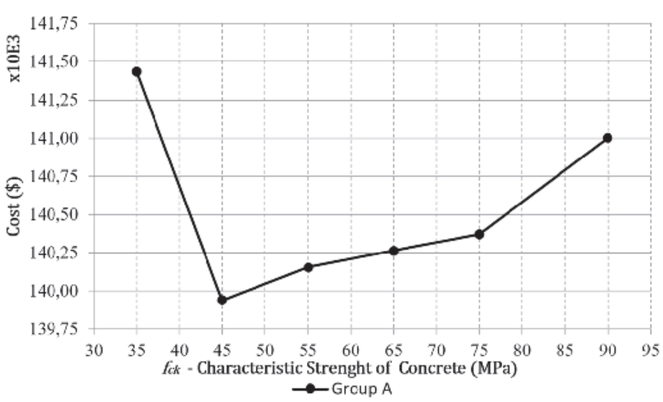

Figure 4
Cost as a funcion of f_{ck}, Group A

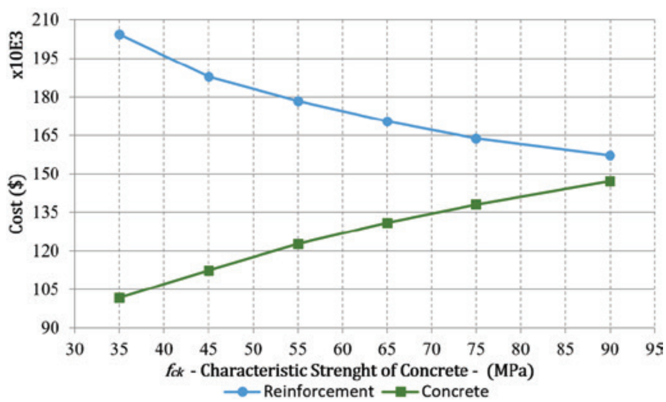

Figure 5
Cost of reinforcement as a funcion of f_{ck}, Group A

Table 4
Cost of the deck in function of the characteristic strength of concrete, Group A

f_{ck} (MPa)	N_{lg}	H_{lg} (m)	H_{lj} (m)	E_{lg} (m)	Cost ($)
35	6	1.6	0.23	8.75	141,436.12
45	6	1.6	0.23	8.75	139,937.98
55	6	1.6	0.23	8.75	140,155.21
65	6	1.6	0.23	8.75	140,264.41
75	6	1.6	0.23	8.75	140,372.06
90	6	1.6	0.23	8.75	141,000.89

Table 5
Cost of the deck in function of the characteristic strength of concrete, Group B

f_{ck} (MPa)	N_{lg}	H_{lg} (m)	H_{lj} (m)	E_{lg} (m)	Cost ($)
35	6	1.6	0.23	8.75	141,436.11
45	6	1.5	0.22	7.00	136,713.18
55	6	1.5	0.22	7.00	137,008.97
65	6	1.5	0.22	7.00	138,724.59
75	6	1.6	0.20	8.75	140,051.89
90	6	1.6	0,20	8.75	140,789.30

consequently, decreases the amount of reinforcement required. For the calculation of the shear reinforcement, the effect of the concrete strength is even greater (model I of NBR 6118:2014 [3] item 17.4.2.), and therefore, could also provide a smaller amount of reinforcement.
To observe this behavior, Figure [6] is presented, where the costs of the flexural and shear reinforcements of the girders from Group A are separated.
Hence, Figure [6] shows higher savings with the shear reinforcement than with the flexural, given that the comparison of the results for 35 MPa and 90 MPa provided a cost difference of 21.96% for the flexural reinforcement and of 36.00% for the shear reinforcement.

3.2 Group B

The cost of each combination of the decks from Group B is presented in Table [5].

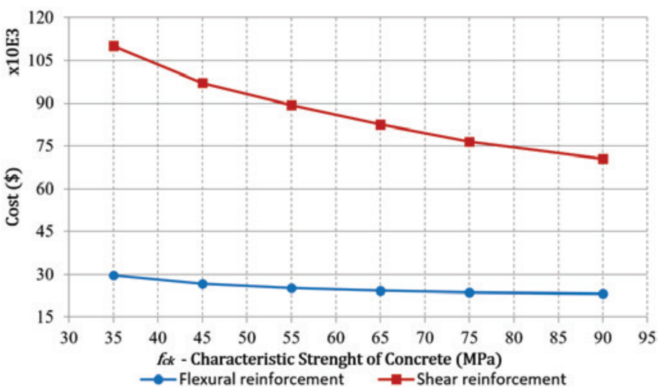

Figure 6
Cost flexural reinforcement and shear of the girder according f_{ck}, Group A

To better interpret the differences between the costs of the Groups A and B, Figure [7] presents the cost of both groups as a function of the characteristic concrete strength.
Hence, Figure [7] shows that, by combining the independent variables of dimensioning, it is possible to find more economical solutions.
On analyzing Table [5], it can be noted that for the higher concrete strengths, the optimal results contain beams with larger cross-sections. This occurs because the shear reinforcements make up a great part of the total cost of the deck and there is still the tendency that, by resisting a greater part of the shearing force with the concrete section, more economical results will be obtained. When lower concrete strength values are used, the increase in the cross-section does not cause a significant increase in the shear strength and, additionally, it increases the weight of the structure. In turn, in combinations that include stronger concretes, the increase in the cross-sectional area causes a more beneficial effect in the shear strength that balances the increase in the weight of the structure itself.

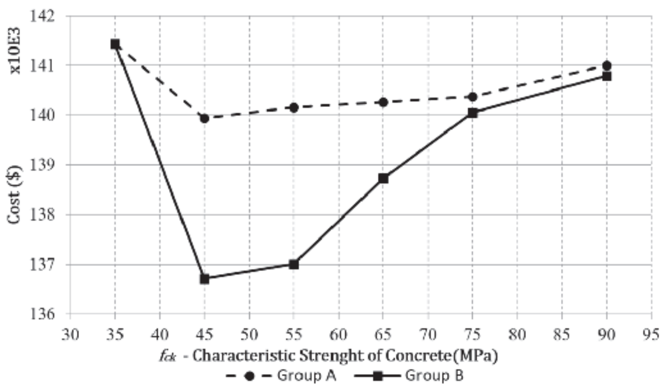

Figure 7
Cost as a funcion of f_{ck}, Group A and B

4. Conclusions

The aim of this study was to evaluate the economic aspects of the use of HSC associated with the geometrical optimization of decks from post-stressed multi-girder overpasses.

The main benefit of the use of HSC is the reduction of reinforcement, where the shear reinforcement is the one associated with the best savings. Special attention is drawn to the fact that by changing the f_{ck} from 35 MPa to 90 MPa, there is a 36% reduction in the shear reinforcement of the girder that also implies a reduction in the time required to build the structure.

This study also showed that not only alterations in the characteristic concrete strength, but also in the geometrical configurations of the deck are able to provide a better use of the variables that, in this case, provided a 3.34% reduction in the cost of the 45-MPa deck as compared to the 35-MPa deck.

Despite all beneficial effects provided by the use of HSC, i.e., the reduction in the use of cement, the reduction in CO_2 emissions, the reduction in deflections, the reduction of creep, and the greater durability of the structure associated with the geometrical optimization, the use of HSC also provides an overall reduction in the costs of the construction of the structure.

5. Acknowledgements

The authors would like to acknowledge the National Council for the Improvement of Higher Education (CAPES) and the State University of Maringá (UEM) which collectively funded this project.

6. References

[1] Ahsan R, Rana S and Ghani SN (2012) *Cost Optimum Design of Posttensioned I-Girder Bridge Using Global Optimization Algorithm.* Journal of Structural Engineering, **ASCE 138**: 273–284.

[2] Aïtcin PC (2000) *Concreto de alto desempenho*. PINI, São Paulo, Brazil. (in Portuguese)

[3] ABNT (Brazilian Association of Technical Standards) (2014) *ABNT NBR 6118:2014 Design of concrete structures – Procedure.* Rio de Janeiro, BR.

[4] ABNT (Brazilian Association of Technical Standards) (2003) *ABNT NBR 7187:2003 Design of reinforced and prestressed concrete bridges - Procedure.* Rio de Janeiro, BR.

[5] ABNT (Brazilian Association of Technical Standards) (2013) *ABNT NBR 7188:2013 Road and pedestrian live load on bridges, viaducts, footbridges and other structures.* Rio de Janeiro, BR.

[6] ABNT (Brazilian Association of Technical Standards) (2003) *ABNT NBR 8681:2003 Actions and safety of structures - Procedure*. Rio de Janeiro, BR.

[7] ABNT (Brazilian Association of Technical Standards) (2015) *ABNT NBR 8953:2015 Concrete for structural use - Density, strength and consistence classification.* Rio de Janeiro, BR.

[8] Dal Molin DC (1995) *Contribuição ao estudo das propriedades mecânicas dos concretos de alta resistência com e sem adição de sílica ativa.* EGD Thesis. São Paulo, University of São Paulo, Brazil.

[9] Eller RAG, Sousa Junior WC and Curi MLC (2011) *Custos do transporte de carga no Brasil: rodoviário versus ferroviário.* Journal of Transport Literature, **5(1):** 50 – 64.

[10] Luchi LAR (2006) *Reavaliação do Trem-tipo à luz das cargas reais nas rodovias brasileiras.* EGD Thesis. São Paulo, University of São Paulo, Brazil.

[11] Martins F, Soares V and Commarata F (2015) *Infraestrutura rodoviária no Brasil: uma proposta para desenvolvê-la.* BAIN & COMPANY, São Paulo, jun. 2013, See http://www.bain.com/offices/saopaulo/en_us/publications/articles/road-infrastructure-in-brazil.aspx (accessed 07/05/2015).

[12] Mcleod HAK (2009) *Development and Construction of Low-Cracking High-Performance Concrete (LC-HPC) Bridge Decks: Construction Methods, Specifications, and Resistance to Chloride Ion Penetration.* EGD Thesis. Kansas, University of Kansas, United States.

[13] Mendes SES (2002) *Estudo experimental de concreto de alto desempenho utilizando agregados graúdos disponíveis na região metropolitana de Curitiba.* MNG Dissertation. Curitiba, Federal University of Paraná, Brazil.

[14] Peinado HS, Vanderlei RD and Nagano MF (2014) *Produção de pilares com concreto de alta resistência: aspectos econômicos e ambientais.* XXXVI JSIE: 1-15, Montevideo, UDELAR, Uruguai.

[15] Rebmann MS (2011) *Durabilidade de concretos estruturais com baixo consumo de cimento Portland e alta resistência.* MNG Dissertation. São Paulo, School of Engeneering of São Carlos of University of São Paulo, Brazil.

[16] Rüsch H (1956) *Berechnungstafeln für rechtwinklige Fahrbahnplatten von Strassenbrücken*, Wilhelm Ernst & Sohn, Berlin, Germany.

[17] Stucchi, FR (2006) *Pontes e Grandes Estruturas – Apostila Meso e infra*. São Paulo, University of São Paulo, Brazil.

[18] Trentini EVW (2016) *Otimização de seções de viadutos e pontes de múltiplas longarinas pré-moldadas e protendidas.* MNG Dissertation. Paraná, State University of Maringá, Brazil.

5. List of notation

N_{lg} is the number of girders;
H_{lg} is the height of the girders;
H_{lj} is the slab height;
E_{lg} is the length of the web stiffening;
f_{ck} is the characteristic strength of concrete;
M_{rd} is the internal bending moment;
R_{cd} is the total reaction of compressed concrete;
d_p is the distance between the upper face of the composite girder with the slab and the center of the protension force;
x is the neutral line height;
R_{sd} is the reaction of passive steel;
d_s is the distance between the upper face of the composite girder with the slab and the center of the passive steel;
λ is the coefficient of approximation of the height of the reaction of compressed concrete during the ULS, 0.8 for $f_{ck} \leq 50$ MPa or 0.8 - $(f_{ck} - 50)/400$ for $f_{ck} > 50$ MPa;
α_c is the coefficient of approximation of the compressive stress of the concrete during the ULS, 0.85 for f_ck≤50 MPa or $0.85 \cdot [1.0 - (f_{ck} - 50)/200]$ for $f_{ck} > 50$ MPa;

- b is the width of the beam;
- d is the depth of the compressed edge to the centroid of reinforcement;
- f_{cd} is the concrete design strength;
- f_{yd} is the steel design strength;
- A_s is the steel area (for b width used);
- $C_{c,lg}$ is the cost of the pumped ready mixed concrete, including the application and densification – girder;
- $C_{f,lg}$ is the cost of the cast for the concrete structures, including the manufacturing, assembly, and disassembly – girder;
- $C_{a,lf,lg}$ is the cost of the reinforcement, CA-50 steel, including the sectioning, 10% loss, bending and placement – longitudinal reinforcement resistant to the flexion of the girder;
- $C_{a,lt,lg}$ is the cost of the reinforcement, CA-50 steel, including the sectioning, 10% loss, bending and placement – longitudinal reinforcement resistant to the torsion of the girder;
- $C_{a,vct,lg}$ is the cost of the reinforcement, CA-50 steel, including the sectioning, 10% loss, bending and placement – cross-sectional reinforcement resistant to the shearing force and torsion of the girder;
- $C_{p,lg}$ is the cost of the prestressing reinforcement, CP-190 RB steel, including the sectioning, placement and prestressing – girder;
- $C_{cj,p,lg}$ is the cost of the set for the anchorage of prestressing reinforcement, including the setup – girder;
- $C_{i,lg}$ is the cost of the lifting of each girder;
- $C_{c,lj}$ is the cost of the pumped ready mixed concrete, including the application and densification – slab;
- $C_{a,lj}$ is the cost of the reinforcing bars, CA-50 steel, including the sectioning, 10% loss, bending and placement – longitudinal reinforcement resistant to the flexion and shearing of the slab.

Volume 12, Number 1 (February 2019) p. 31 – 38 • ISSN 1983-4195
http://dx.doi.org/10.1590/S1983-41952019000100005

REVISTA IBRACON DE ESTRUTURAS E MATERIAIS
IBRACON STRUCTURES AND MATERIALS JOURNAL

Effects of *Bacillus subtilis* biocementation on the mechanical properties of mortars

Efeitos da biocimentação promovida por Bacillus subtilis *nas propriedades mecânicas de argamassas*


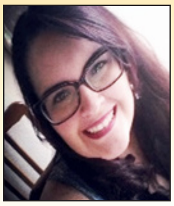



N. SCHWANTES-CEZARIO [a]
nicoleschwantes@hotmail.com
https://orcid.org/0000-0002-3254-6396

M. F. PORTO [a]
mfeernanda.porto@hotmail.com
https://orcid.org/0000-0002-9313-1215

G. F. B. SANDOVAL [a]
gersson.barreto@gmail.com
https://orcid.org/0000-0002-8702-8844

G. F. N. NOGUEIRA [a]
geovanasouzanogueira@gmail.com
https://orcid.org/0000-0002-7059-257X

A. F. COUTO [a]
alissoncouto@ymail.com
https://orcid.org/0000-0002-7998-7973

B. M. TORALLES [a]
betoralles@gmail.com
http://orcid.org/0000-0001-8828-7250

Abstract

This study aims to evaluate the influence of *B. subtilis* AP91 spores addition on the mechanical properties of mortars. *B. subtilis* strain AP91, isolated from rice leaves of the needle variety, which has an early cycle of production, was used at the concentration of 105 spores/mL in mortars with cement-to-sand ratio of 1:3 (by weight) and water-to-cement ratio (w/c) of 0.63. These spores were added in two different ways: in the mixing water and by immersion in a solution containing bacterial spores. Scanning Electron Microscope (SEM) analysis showed crystals with calcium peaks on the EDS, which possibly indicates the presence of bioprecipitated calcium carbonate. The results obtained in the mechanical analysis showed that the bioprecipitation of $CaCO_3$ by *B. subtilis* strain AP91 was satisfactory, particularly when the spores were added in the mixing water, increasing the compressive strength up to 31%. Thus, it was concluded that the addition of *B. subtilis* AP91 spores in the mixing water of cement mortars induced biocementation, which increased the compressive strength. This bioprecipitation of calcium carbonate may very well have other advantageous consequences, such as the closure of pores and cracks in cementitious materials that could improve durability properties, although more research is still needed on this matter.

Keywords: calcium carbonate, biocementation, *B. subtilis*, mechanical properties, SEM.

Resumo

Este estudo tem como objetivo avaliar a influência da adição de esporos de *B. subtilis* AP91 nas propriedades mecânicas de argamassas. Para tanto, a bactéria *B. subtilis* AP91 isolada de folhas de arroz da variedade agulha precoce foi utilizada na concentração de 105 esporos/mL em argamassas com traço de 1:3 (em massa) e relação água/cimento (a/c) de 0,63. Os esporos bacterianos foram adicionados de duas diferentes formas: na água de amassamento e por imersão em solução contendo os esporos. A análise por Microscopia Eletrônica de Varredura (MEV) com Sistema de Energia Dispersiva (EDS) mostrou cristais com picos de cálcio, o que possivelmente indica a presença de carbonato de cálcio bioprecipitado. Os resultados obtidos a partir da análise mecânica mostraram que a bioprecipitação de $CaCO_3$ pela bactéria *B. subtilis* AP91 foi satisfatória, particularmente quando os esporos foram adicionados à água de amassamento, aumentando a resistência à compressão em até 31%. Portanto, conclui-se que a adição de esporos de *B. subtilis* AP91 na água de amassamento das argamassas induziu a biocimentação, que aumentou a resistência à compressão. A bioprecipitação de carbonato de cálcio pode ter outras consequências benéficas, como o fechamento de poros e fissuras em materiais cimentícios, que poderiam melhorar a durabilidade, embora mais pesquisas neste aspecto ainda sejam necessárias.

Palavras-chave: carbonato de cálcio, biocimentação, *B. subtilis*, propriedades mecânicas, MEV.

[a] *State University of Londrina, Department of Building Construction, Londrina, PR, Brazil.*

Received: 04 Aug 2017 • Accepted: 07 May 2018 • Available Online: 05 Feb 2019

1. Introduction

Except for water, the cementitious materials are the most consumed substances on Earth [1]. Because of that, they should be studied to present satisfactory performance and, for that matter, several works are being performed nowadays to improve the mechanical properties of such materials.

In view of the growing concern about improving the characteristics and durability of cementitious materials, additions of bacteria, mainly of the genus *Bacillus*, are being studied for crack filling and increasing of the compressive strength through calcium carbonate ($CaCO_3$) precipitation [2]. Because of that, the bioprecipitation of $CaCO_3$ by bacteria in cementitious materials is also called biocementation [4].

It should be noted that bacteria already exist for billions of years, however many of their biotechnological applications are not yet widespread [5]. Although many researchers are interested in the bioprecipitation of $CaCO_3$, the whole process is not yet clear and defined. Once the bacteria can precipitate calcium carbonate through several mechanisms, the physiology and genetic involved are complex and difficult to understand [6], [7], [8].

Some bacteria that have the ability of producing minerals were used to repair limestone monuments [9], [10], [11], [12], [13], [14] and to fill pores and cracks in concrete and other cementitious materials [5], [8], [15], [16], [17], [18], which can improve their mechanical properties and durability.

Among the bacteria used in researches about biocementation, the bacteria *B. subtilis* stand out. These bacteria can produce calcite, a crystalline form of $CaCO_3$, which is precipitated when they're exposed to a medium with a calcium source [25], [26], [27].

The biocementation can be induced by two ways of addition of bacteria: in the mixing water of mortars [1] [3], [15], [19], [22], [28], [29] or by immersion of the specimens in a solution containing bacteria [18], [30]. However, the studies that confront these two ways of bacteria addition are rare, so that researches comparing both are important.

The aim of this study was to evaluate the influence of biocementation, induced by two different ways of spores addition, on the mechanical properties of mortars. Thus, the spores of bacteria *B. subtilis* strain AP91 were used.

2. Materials and methods

2.1 Bacteria and growth conditions

B. subtilis AP91, isolated in Brazil from rice leaves of the early cycle needle variety, was used [31]. To achieve the required concentration, the bacterium was incubated in a Luria-Bertani (LB) medium under agitation of 170 rpm at 37°C for 48 hours. The medium was poured into 15mL polystyrene tubes, which were centrifuged at 4,000 rpm and 23°C for 3 minutes, in order to separate the bacterial cells from the growing medium. The supernatant was discarded and the pellet containing the bacterial cells was re-suspended in a phosphate buffer solution, homogenized and centrifuged again. This procedure was performed four times.

The obtained concentration was quantified in a spectrophotometer with a reading of 600nm, from the Equation 1 described by [15]:

$$X = 8.59 \,.\, 10^7 \,.\, Y^{1.3627} \quad (1)$$

Where X is the concentration in cells/mL and Y is the reading of the spectrophotometer at 600nm.

From the found concentration, the dilution calculations were made in order to achieve a concentration of 10^5 cells/mL. The dilution was made in a phosphate buffer solution, then stored at 8°C for 48 hours for the spores formation.

2.2 Mortars

The mortars were produced using:

- Portland cement (CP-II E-32, Brazilian denomination);
- Quartz fine sand: fineness modulus of 1.51, maximum size of 1.18mm and specific gravity of 2.604 g/cm³;
- Potable water;
- Phosphate buffer solution: 1.05 g/L dibasic-anhydrous sodium phosphate (0.07% of the cement bulk), 0.36 g/L monobasic sodium phosphate (0.02% of the cement bulk) and 8.17 g/L sodium chloride (0.51% of the cement bulk);
- *B. subtilis* AP91.

The spores of bacteria, in a concentration of 10^5 spores/mL, were added to the mixture in two different ways: in the mixing water and by immersion in a phosphate buffer solution containing the spores. For that, four variations of mortars were produced in this study; the nomenclature and composition of those are presented in Table 1.

The cement-to-sand ratio used was 1:3, by weight, and the bacterial culture or water-to-cement ratio (w/c) was kept at 0.63. The mixture proportions are shown in Table 2.

2.3 Experimental methods

The microstructure of the mortars was evaluated by Scanning Electron Microscopy (SEM) and Energy Dispersive System (EDS). In these analysis it was found crystals of calcium carbonate ($CaCO_3$) in the mortars with addition of spores. In order to evaluate the influence of $CaCO_3$ crystals on the mechanical properties of mortars, all of them were tested by compressive strength, indirect tensile strength (Brazilian test) and dynamic modulus of elasticity.

Table 1
Nomenclature of the mortars

Mortars	Composition of mortars
REF_WT	Reference mortar produced with water: cement, sand and water.
SP_IM*	Mortar with addition of spores by immersion: cement, sand and water.
REF_PB	Reference mortar produced with phosphate buffer: cement, sand and phosphate buffer.
SP_MW	Mortar with addition of spores in the mixing water: cement, sand and phosphate buffer with 105 spores/mL.

* Spores were added during the curing time, when this mortar was submerged in a tank with phosphate buffer with a concentration of 105 spores/mL.

Table 2
Mixture proportions

Mortars	Cement (g)	Sand (g)	Water (mL)	Phosphate buffer (mL)	Spores of *B. subtilis*/mL
REF_WT	2362.5	7087.5	1488	–	–
SP_IM	2362.5	7087.5	1488	–	10^5 *
REF_PB	2362.5	7087.5	–	1488	–
SP_MW	2362.5	7087.5	–	1488	10^5 *

* The concentration of 10^5 spores/mL was dispersed in the phosphate buffer solution.

2.3.1 SEM analysis

SEM was used to observe the mortar microstructure and the precipitation of calcium carbonate ($CaCO_3$). The microanalysis was performed using an FEI-Quanta 200 Scanning Electron Microscope with an accelerating voltage of 25 kV for determination of the chemical elements. The mortars specimens of 10x10x10mm had their surface covered with gold and were tested after 7 and 28 days of curing.

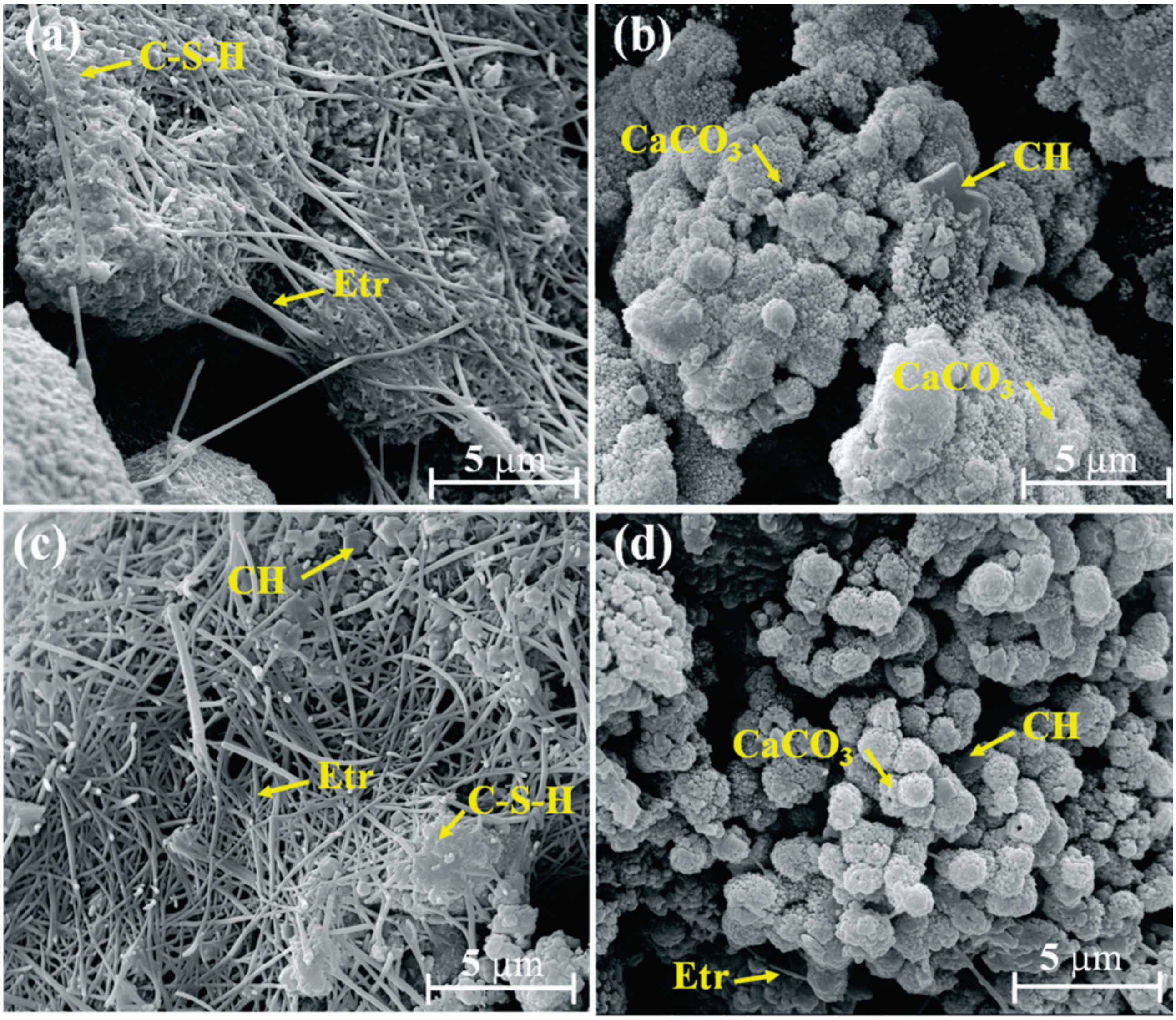

Figure 1
SEM of mortars after 7 days of curing at magnification of 12.000x. (a) REF_WT. (b) SP_IM. (c) REF_PB and (d) SP_MW

2.3.2 Mechanical properties of the mortars

To study the compressive strength [32], indirect tensile strength [33] and dynamic modulus of elasticity, cylindrical specimens of 50mm diameter and 100mm height were molded according to [32]. All specimens were cured by immersion at room temperature until testing after 7 and 28 days of curing. The mortars REF_WT, REF_PB and SP_MW were cured in a tank of lime-saturated water and the mortar SP_IM was cured in a tank containing a phosphate buffer solution with 10^5 spores/mL of *B. subtilis* AP91, also saturated with lime.

3. Results and discussions

3.1 Microscopic investigation

To search for evidence of microbial calcium carbonate precipitation, the mortar specimens were examined under a Scanning Electron Microscope (SEM). Fig. 1 shows a scanning electron micrograph of the mortars after 7 days of curing, in which Fig. 1(a) shows the reference mortar (REF_WT) highlighting the cement hydration products, such as calcium silicate hydrate (C-S-H) and ettringite (etr). Fig. 1(b) shows the mortar with the addition of spores of *B. subtilis* strain AP91 by immersion (SP_IM), in which were highlighted the bioprecipitation of calcium carbonate ($CaCO_3$) can be observed. Finally, Fig. 1 (c) shows the mortar with phosphate buffer replacing water (REF_PB), where can be noted the presence of calcium hydroxide (CH), calcium silicate hydrate (C-S-H) and an intensive amount of ettringite. At last, Fig. 1(d) shows the addition of spores of *B. subtilis* in the mixing water, in which was highlighted the bioprecipitated calcium carbonate ($CaCO_3$).
Analyzing the SEM in Fig. 1 it can be observed that the mortars have shown the formation of cement hydration products, like

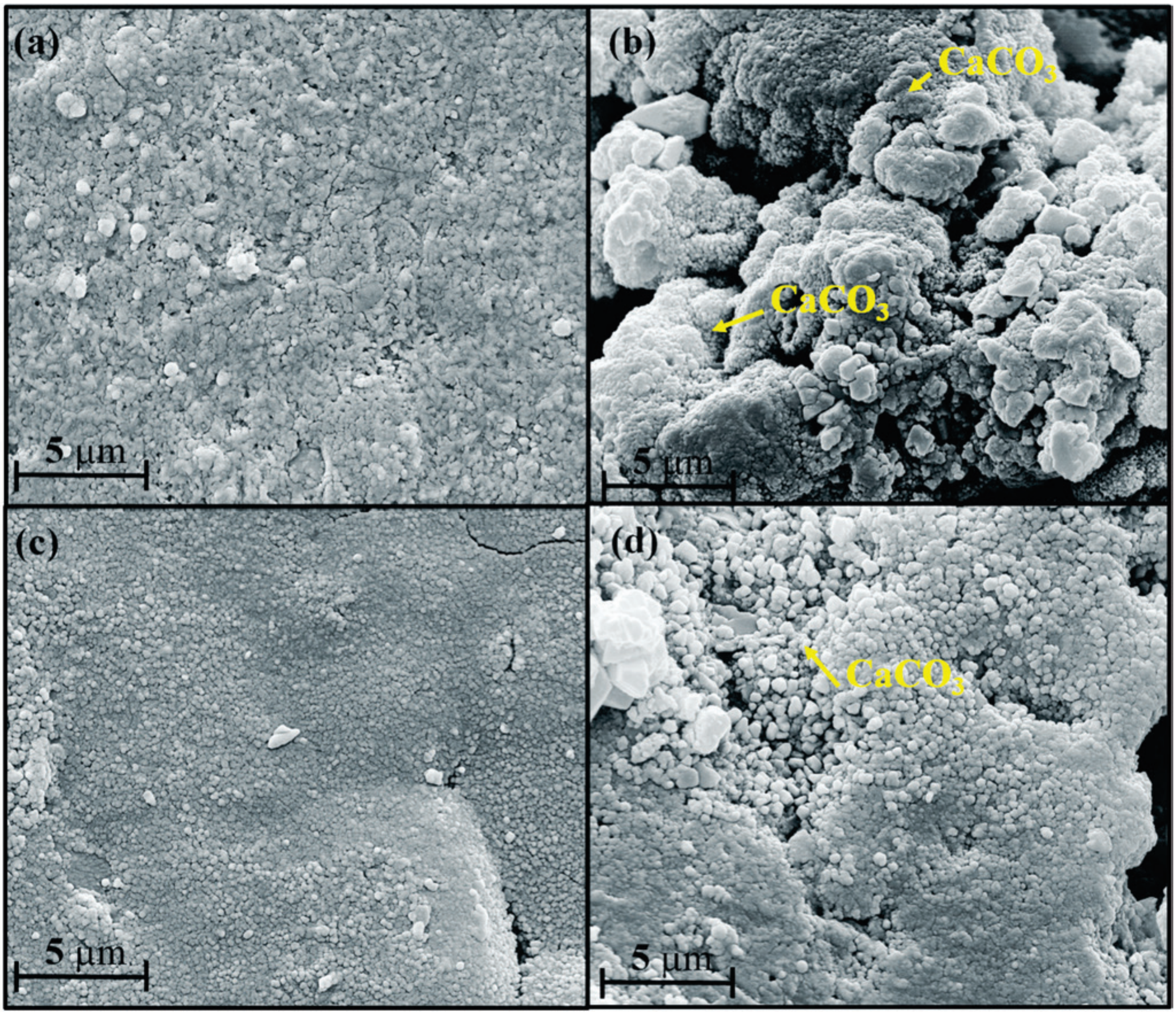

Figure 2
SEM of mortars after 28 days of curing at magnification of 12.000x. (a) REF_WT. (b) SP_IM. (c) REF_PB and (d) SP_MW

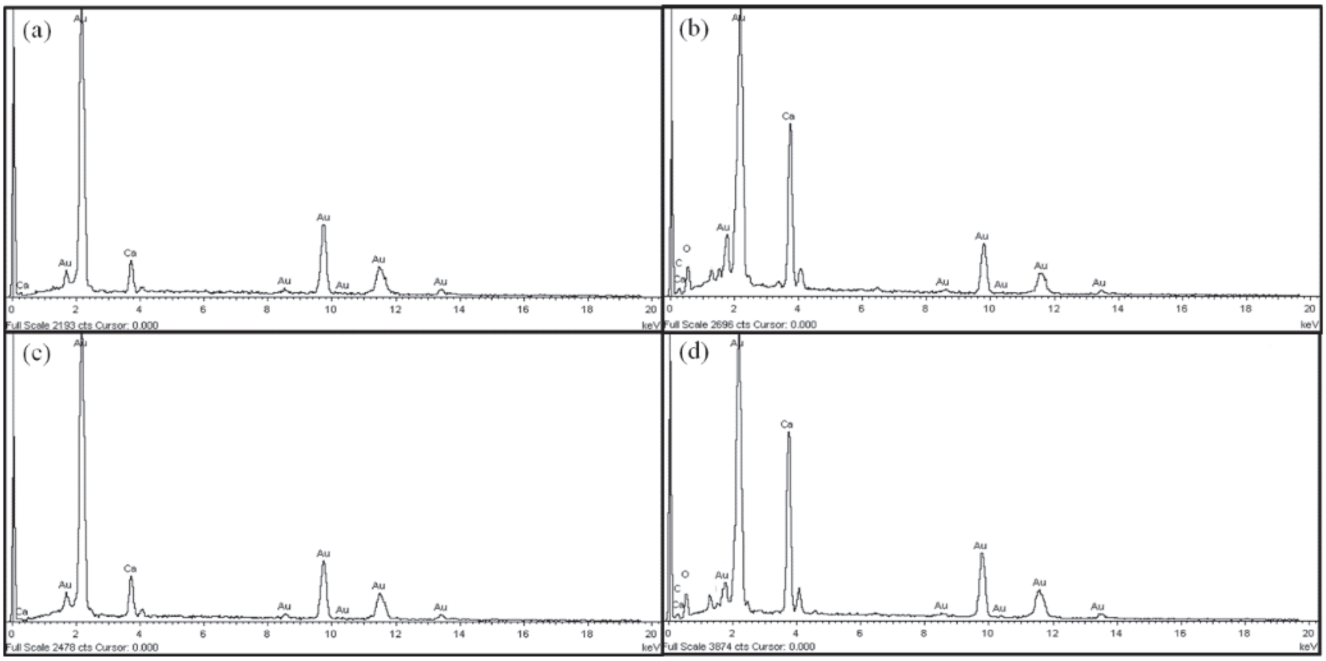

Figure 3
EDS of mortars after 28 days of curing. (a) REF_WT. (b) SP_IM. (c) REF_PB. (d) SP_MW

C-S-H, ettringite (etr) and CH. The presence of $CaCO_3$ was observed only in mortars with addition of *B. subtilis* spores (Fig. 1 b and d), both by immersion and in the mixing water.
After 28 days of curing, other SEM images were taken to verify if the calcium carbonate was still present in the samples with addition of *B. subtilis* spores. Fig. 2 shows all mortars after 28 days of curing.
Considering the images in Fig. 2, it was found the precipitation of calcium carbonate crystals only in the mortars with addition of *B. subtilis* spores (Fig. 2 b and d). After 28 days of curing, about 95% of cement is hydrated, so in these images, no hydration products can be seen. Similar crystals of $CaCO_3$, with rounded structures, were found by Park et al. [2] , Hammes et al. [6] , Braissant et al. [35], Dupraz et al. [36] and Daskalakis et al. [37].
To complete this analysis, the specimens were submitted to an Energy Dispersive System (EDS), to verify the peaks of the chemical elements present in the sample. From the EDS shown in Fig. 3, it was observed that all mortars present peaks of calcium, but the peaks are higher when the *B. subtilis* spores have been added (Fig. 3 b and d). It is known that the cement has calcium, but in the mortars analyzed there was a greater presence of calcium when the spores were added, probably because the spores might have used the calcium present in cement hydration products and in the lime of the curing water to precipitate $CaCO_3$. The greater presence of calcium indicates that the calcium carbonate crystals deposit themselves in the cement matrix (Fig. 2 b and d). Besides that, it should be noticed that the gold peaks present in all the samples are due to the coating, so that high-resolution images could be obtained.

3.2 Compressive strength

The medium compressive strength of different mortars (n = 5) after 7 and 28 days of curing are summarized in Fig. 4. The compressive strength statistically increased in the mortar specimens that contained *B. subtilis* AP91 spores added to the mixing water (SP_MW), both after 7 and 28 days of curing. When the mortar specimens were immerged (SP_IM) there were no significant

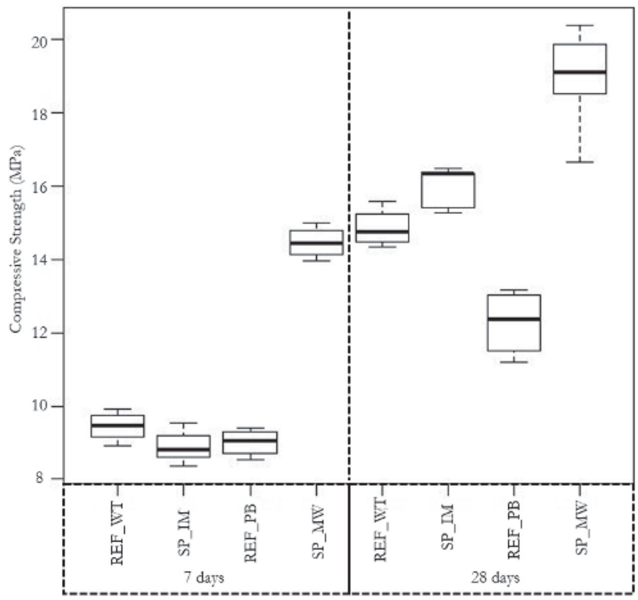

Figure 4
Effect of *B. subtilis* strain AP91 on the compressive strength of cement mortars after 7 and 28 days of curing

differences on the compressive strength in both studied ages, compared to the control mortar (REF). That may be explained by the fact that the spores would have to penetrate the specimens to have access to the hydration products in order to react and precipitate $CaCO_3$; moreover, the spores could find it difficult to penetrate in the specimens because of the use of release agent to mold them. Perhaps, given the sufficient amount of time and the absence of the release agent, this procedure of spores' addition could have been more efficient.
The same was found in the mortar with phosphate buffer (PB) at 7 days of curing, but at 28 days it was verified a significant decrease on the compressive strength presented by these samples. Ramachandran et al. [15] found that the addition of phosphate buffer in mortars caused better mechanical performance when compared to saline solution. However, these authors do not analyze the influence of phosphate buffer compared to a reference mortar.
It should be noticed that the results of addition of bacteria in the mixing water corroborate with what was presented in other works by Ghosh et al. [38], Reddy et al. [39], Chahal et al. [40] e Chahal and Siddique [41], who added different types of bacteria in the concentration of 10^5 cells/mL and found an increase on compressive strength.
The improvement in compressive strength by *B. subtilis* strain AP91 is induced by the deposition of calcium carbonate on the cell surfaces, which may have the ability of closing pores and cracks of cementitious materials [15, 42, 43, 44].

3.3 Indirect tensile strength (Brazilian test)

Fig. 5 shows the effect of addition of *B. subtilis* strain AP91 on the indirect tensile strength of mortars. In this test, the same tendency of the compressive strength test was verified, in which the highest indirect tensile strength, both at 7 and 28 days of curing, was found in the mortar with addition of *B. subtilis* AP91 in the mixing water. It can be pointed out that the improvement on tensile strength is consequence of the improvement of the compressive strength, since the former is usually around 10% of the latter.

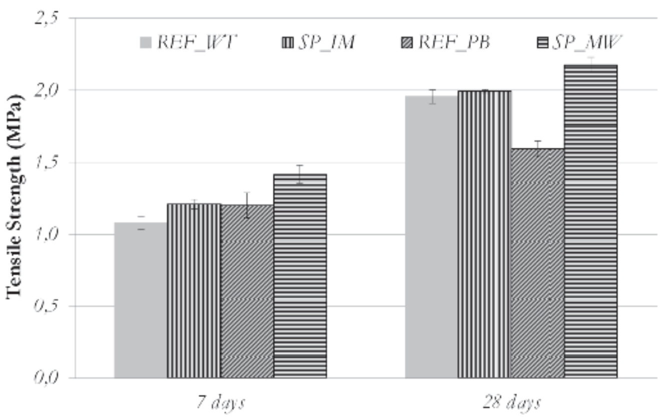

Figure 5
Effect of *B. subtilis* strain AP91 on the indirect tensile strength of mortars after 7 and 28 days of curing. Values are mean ± Sd (n = 3)

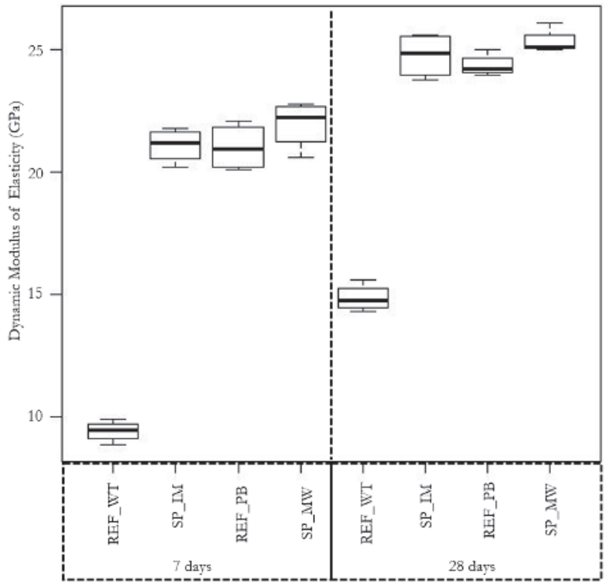

Figure 6
Dynamic modulus of elasticity of the mortars. Values are mean ± SD (n = 5)

3.4 Dynamic modulus of elasticity

The modulus of elasticity was calculated from the velocity of propagation of the ultrasonic waves, by direct transmission, through the Equation 2 described in the Brasilian standard 15630/2008 [34]. The results obtained are shown in Fig. 6.

$$Ec = \frac{V^2 \, x \, (1+\vartheta) \, x \, (1-2\vartheta)}{(1-\vartheta)} \, x10^{-3} \quad (2)$$

It was verified that there was a small gradual increase in the modulus of elasticity of the mortars when were added the buffer solution and also the bacteria spores, both by immersion (SP_IM) and in the mixing water (SP_MW). It should be noticed that the mortars with the highest modulus of elasticity also corresponded to the higher strengths, for both tensile and compression. It was expected that the modulus of elasticity of the mortar containing phosphate buffer would present a lower value when compared to the reference mortar, once it also presented lower compressive strength. However, this test was performed with air-dried specimens that could still have water inside the pores, which can affect the propagation of ultrasonic waves. This could also be related to presence of salts in the buffer solution, which could have filled smaller pores in the matrix, also affecting the velocity of the ultrasonic waves.
Furthermore, the pore filling by biocementation could cause an increase in the velocity of propagation of the ultrasonic waves and, consequently, promote a higher modulus of elasticity of the specimens containing bacteria when compared to the reference.

4. Conclusion

- The SEM and EDS analysis verified that the addition of

B. subtilis AP91 spores in mortars induced biocementation through the bioprecipitation of calcium carbonate crystals;

- When the spores of *B. subtilis* AP91 were added in the mixing water, they presented better mechanical performance in all tests when compared to the addition by immersion;
- *B. subtilis* AP91 added into mixing water has shown to be a microrganism with great potential for application in cementitious materials, since the precipitation of $CaCO_3$ can increase both compressive and tensile strength.
- Because of the precipitation of $CaCO_3$, the application of this microorganism for the closure of pores and fissures in cementitious materials should continue to be studied, in order to prevent early deterioration.

5. Acknowledgments

The authors are grateful to the State University of Londrina and to CNPq for all financial support. We also thank the Laboratory of Electron Microscopy and Microanalysis - LMEM of the State University of Londrina for the help in the analysis of SEM and EDS.

6. References

[1] KRISHNAPRIYA, S.; VENKATESH BABU, D. L.; PRINCE ARULRAJ G. Isolation and identification of bacteria to improve the strength of concrete. Microbiological research, v. 174, 2015; p. 48-55.

[2] PARK, S. J.; PARK, J. M.; KIM, W. J.; GHIM, S. Y. Application of Bacillus subtilis 168 as a multifunctional agent for improvement of the durability of cement mortar. Journal of Microbiology and Biotechnology, v. 22, 2012; p. 1568-1574.

[3] ABO-EL-ENEIN, S. A.; ALI, A. H.; TALKHAN, F. N.; ABDEL-GAWWAD, H. A. Application of microbial biocementation to improve the physico-mechanical properties of cement mortar. HBRC Journal, v. 9, 2013; p. 36-40.

[4] ACHAL, V.; MUKHERJEE, A.; KUMARI, D.; ZHANG, Q. Biomineralization for sustainable construction–A review of processes and applications. Earth-Science Reviews, v. 148, 2015; p. 1-17.

[5] BANG, S. S.; GALINAT, J.K.; RAMAKRISHNAN, V. Calcite precipitation induced by polyurethane-immobilized *Bacillus pasteurii*. Enzyme and Microbial Technology, v. 28, 2001; p. 404-409.

[6] HAMMES, F.; BOON, N.; DE VILLIERS, J.; VERSTRAETE, W.; SICILIANO, S. D. Strain-Specific Ureolytic Microbial Calcium Carbonate Precipitation. Applied And Environmental Microbiology, v.69, n.8, 2003; p. 4901-4909.

[7] PERITO, B.; MARVASI, M.; BARABESI, C.; MASTROMEI, G.; BRACCI, S.; VENDRELL, M.; TIANO, P. A Bacillus subtilis cell fraction (BCF) inducing calcium carbonate precipitation: biotechnological perspectives for monumental stone reinforcement. Journal of Cultural Heritage, v. 15, n. 4, 2014; p. 345-351.

[8] VAN TITTELBOOM, K.; GRUYAERT, E.; RAHIER, H.; DE BELIE, N. Influence of mix composition on the extent of autogenous crack healing by continued hydration or calcium carbonate formation. Construction and Building Materials, v. 37, 2012; p. 349–359.

[9] GOLLAPUDI, U.K.; KNUTSON, C.L.; BANG, S.S.; ISLAM, M.R. A new method for controlling leaching through permeable channels. Chemosphere, v. 30, 1995; p. 695–705.

[10] STOCKS-FISCHER, S.; GALINAT, J.K.; BANG, S.S. Microbiological precipitation of CaCO3. Soil Biology and Biochemistry, v. 31, 1999; p. 1563–1571.

[11] TIANO, P.; BIAGIOTTI, L.; MASTROMEI, G. Bacterial biomediated calcite precipitation for monumental stones conservation: methods of evaluation. Journal of microbiological methods, v. 36, n. 1, 1999; p. 139-145.

[12] BACHMEIER, K.L.; WILLIAMS, A.E.; WARMINGTON, J.R.; BANG, S.S. Urease activity in microbiologically-induced calcite precipitation. Journal of Biotechnology, v. 93, 2002; p. 171–181.

[13] DICK, J.; DE WINDT, W.; DE GRAEF, B.; SAVEYN, H.; VANDER MEEREN, P.; DE BELIE, N.; VERSTRAETE, W. Bio-deposition of a calcium carbonate layer on degraded limestone by Bacillus species. Biodegradation, v. 17, 2006; p. 357–367.

[14] RODRIGUEZ-NAVARRO, C.; RODRIGUEZ-GALLEGO, M.; BENCHEKROUN, K.; GONZALEZ-MUNOZ, M.T. Conservation of ornamental stone by Myxococcus xanthus-induced carbonate biomineralization. Applied and Environmental Microbiology, v. 69, 2003; p. 2182–2193.

[15] RAMACHANDRAN, S.K.; RAMAKRISHNAN, V.; BANG, S.S. Remediation of concrete using micro-organisms. ACI Materials Journal, v. 98, 2001; p. 3–9.

[16] DE MUYNCK (1), W.; COX, K.; DE BELIE, N.; VERSTRAETE, W. Bacterial carbonate precipitation as an alternative surface treatment for concrete. Construction and Building Materials, v. 22, n. 5, 2008; p. 875-885.

[17] RAMAKRISHNAN, V. Performance characteristics of bacterial concrete—a smart biomaterial. Proceedings of the First International Conference on Recent Advances in Concrete Technology, Washington, DC, 2007; p. 67–78.

[18] VAN TITTELBOOM, K.; DE BELIE, N.; DE MUYNCK, W.; VERSTRAETE, W. Use of bacteria to repair cracks in concrete. Cement and Concrete Research, v. 40, 2010 p. 157-166.

[19] WIKTOR, V.; JONKERS, H. M. Quantification of crack-healing in novel bacteria-based self-healing concrete. Cement e Concrete Composites, v. 33, 2011; p. 763–770.

[20] JONKERS, H. M.; THIJSSEN, A.; MUYZER, G.; COPUROGLU, O.; SCHLANGEN, E. Application of bacteria as self-healing agent for the development of sustainable concrete. Ecological Engineering, v. 36, 2010; p. 230-235.

[21] ACHAL, V.; MUKERJEE, A.; REDDY, M. S. Biogenic treatment improves the durability and remediates the cracks of concrete structures. Construction and Building Materials, v. 48, 2013; p. 1-5.

[22] XU, J.; YAO, W. Multiscale mechanical quantification of self-healing concrete incorporating non-ureolytic bacteria-based healing agent. Cement and Concrete Research, v. 64, 2014; p. 1-10.

[23] DE KOSTER, S. A. L.; MORS, R. M., NUGTEREN, H. W.; JONKERS, H. M.; MEESTERS, G. M. H.; VAN OMMEN, J. R. Geopolymer Coating of Bacteria-containing Granules for

Use in Self-healing Concrete. Procedia Engineering, v. 102, 2015; p. 475-484.

[24] LUO, M.; QIAN, C.; LI, R. Factors affecting crack repairing capacity of bacteria-based self-healing concrete. Construction and Building Materials, v. 87, 2015; p. 1-7.

[25] MONTOYA, C.; MARQUEZ, M. A.; LOPEZ, J. M.; CUERVO, C. Characterization of calcite bioprecipitaded by a native Bacillus subtilis isolate. Revista Colombiana de Biotecnologia, v.7, n.2, 2005; p.1-19.

[26] BARABESI, C.; GALIZZI, A.; MASTROMEI, G.; ROSSI, M.; TAMBURINI, E.; PERITO, B. Bacillus subtilis gene cluster involved in calcium carbonate biomineralization. Journal of bacteriology, v. 189, 2007; p. 228-235.

[27] MARVASI, M.; DAVILA-VARQUEZ, Y. C.; MARTINEZ, L. C. Supplemental Materials for Laboratory Activivy to Effectively Teach Introductory Geomicrobiology Concepts to Non-Geology Majors. Journal of Microbiology e Biology Education, v. 14, n. 2, 2013; p. 206-212.

[28] PEI, R., LIU, J.; WANG, S.; YANG, M. Use of bacterial cell walls to improve the mechanical performance of concrete. Cement e Concrete Composites, v. 39, 2013; p. 122–130.

[29] AL-SALLOUM, Y.; ABBAS, H.; SHEIKH, Q. I.; HADI, S.; AL-SAYED, S.; ALMUSALLAM, T. Effect of some biotic factors on microbially-induced calcite precipitation in cement mortar. Saudi Journal of Biological Sciences, v. 24, n. 2, 2016; p. 286-294.

[30] DE MUYNCK (2), W.; DEBROUWER, D.; DE BELIE, N., VERSTRAETE, W. Bacterial carbonate precipitation improves the durability of cementitious materials. Cement and Concrete Research, v. 38, 2008; p. 1005–1014.

[31] SCHWANTES-CEZARIO, N.; MEIDEIROS, L. P.; DE OLIVEIRA JR, A. G.; NAKAZATO, G. KOBAYASHI, R. K. T; TORALLES, B. M. Bioprecipitation of calcium carbonate induced by Bacillus subtilis isolated in Brazil. International Biodeterioration & Biodegradation, v. 123, 2017; p. 200-2005.

[32] ASSOCIAÇÃO BRASILEIRA DE NORMAS TÉCNICAS. Portland Cement - Determination of compressive strength. -NBR 7215, Rio de Janeiro, 1997.

[33] ASSOCIAÇÃO BRASILEIRA DE NORMAS TÉCNICAS. Mortar and concrete - Determination of the tension stregth of cylindrical specimens submitted to diametrical compression. - NBR 7222, Rio de Janeiro, 2011.

[34] ASSOCIAÇÃO BRASILEIRA DE NORMAS TÉCNICAS. Mortars applied on walls and cellings – Determination of elasticity modulus by the ultrasonic wave propagation. -NBR 15630, Rio de Janeiro, 2008.

[35] BRAISSANT, O.; CAILLEAU, G.; DUPRAZ, C.; VERRECCHIA, E. P. Bacterially induced mineralization of calcium carbonate in terrestrial environments: the role of exopolysaccharides and amino acids. Journal of Sedimentary Research, v. 73, n. 3, 2003; p. 485-490.

[36] DUPRAZ, C.; REID, R. P.; BRAISSANT, O.; DECHO, A. W.; NORMAN, R. S.; VISSCHER, P. T. Processes of carbonate precipitation in modern microbial mats. Earth-Science Reviews, v. 96, n. 3, 2009; p. 141-162.

[37] DASKALAKIS, M. I., RIGAS, F., BAKOLAS, A., MAGOULAS, A., KOTOULAS, G., KATSIKIS, I., MAVRIDOU, A. Vaterite bio-precipitation induced by Bacillus pumilus isolated from a solutional cave in Paiania, Athens, Greece. International Biodeterioration & Biodegradation, v. 99, 2015; p. 73-84.

[38] GHOSH, S.; BISWAS, M.; CHATTOPADHYAY, B. D.; MANDAL, S. Microbial activity on the microstructure of bacteria modified mortar. Cement and Concrete Composites, v. 31, n. 2, 2009; p. 93-98.

[39] REDDY, S.; RAO, M.; APARNA, P.; SASIKALA, C. Performance of standard grade bacterial (Bacillus subtilis) concrete. Asian J Civ Eng (Build Housing), v. 11, 2010; p. 43-55.

[40] CHAHAL, N.; SIDDIQUE, R.; RAJOR, A. Influence of bacteria on the compressive strength, water absorption and rapid chloride permeability of fly ash concrete. Construction and Building Materials, v. 28, n. 1, p. 351-356, 2012.

[41] CHAHAL, N.; SIDDIQUE, R. Permeation properties of concrete made with fly ash and silica fume: influence of Ureolytic bacteria.Construction and Building Materials, v. 49, 2013; p. 161-174.

[42] RAMAKRISHNAN, V.; BANG, S. S.; DEO, K. S. (1998, August). A novel technique for repairing cracks in high performance concrete using bacteria. In Proc. of the Int. Conf. on HPHSC, 1998; p. 597-618.

[43] GHOSH, P.; MANDAL, S.; CHATTOPADHYAY, B. D.; PAL, S. Use of microorganism to improve the strength of cement mortar. Cement and Concrete Research, v. 35, n. 10, 2005; p. 1980-1983.

[44] ACHAL, V.; MUKHERJEE, A.; BASU, P. C.; AND REDDY, M. S. “Lactose mother liquor as an alternative nutrient source for microbial concrete production by Sporosarcina pasteurii.” J. Ind. Microbiol. Biotechnol., v. 36, n. 3, 2009; p.433–438.

Volume 12, Number 1 (February 2019) p. 39 – 68 • ISSN 1983-4195
http://dx.doi.org/10.1590/S1983-41952019000100006

IBRACON

REVISTA IBRACON DE ESTRUTURAS E MATERIAIS
IBRACON STRUCTURES AND MATERIALS JOURNAL

Numerical study of the behaviour of loop bar splicing in joints of reinforced concrete structures

Estudo numérico do comportamento de emendas de barras por meio de laço em juntas de estruturas de concreto armado


T. D. L.VASCONCELOS [a]
thiagodelfino@usp.br
https://orcid.org/0000-0003-1212-6893

V. G. HAACH [a]
vghaach@sc.usp.br
https://orcid.org/0000-0002-9501-4450

Abstract

Sometimes straight bar splicing takes up too much space in a reinforced concrete structure due to the required overlapping length. Therefore, in limited space situations, loop joints may be a good solution, which has been spread in civil construction, although there are very few studies about it. The aim of the present work is to study the loop joint behavior in reinforced concrete structures under tension. Three dimensional numerical simulations are made using the software DIANA®. Firstly, the calibration of the numerical model based on experimental tests of the literature is performed, followed by parametric analyses varying geometric parameters of the concrete elements and reinforcement. The results indicate that arranging the bars as close as possible to a maximum spacing of 60 mm between axes and considering a minimum splice length equal to the bend diameter of the loops may be an ideal situation for the behavior of this type of connection.

Keywords: loop joint, splicing, reinforced concrete, numerical simulation.

Resumo

Emendas com barras retas ocupam muito espaço devido ao comprimento de traspasse necessário. Dessa forma, em situações em que há uma limitação de espaço para a emenda, uma armação que constitui uma solução interessante é a emenda por meio de laço, que, apesar de ter poucos estudos relacionados, vem sendo bastante difundida na construção civil. O objetivo desse trabalho é estudar o comportamento de emendas em laço em juntas de estruturas de concreto armado submetidas à tração. Para isso, realizam-se simulações numéricas no software DIANA® em modelos numéricos 3D. Inicialmente se faz a calibração do modelo numérico com base em ensaios experimentais da literatura, depois é realizada uma análise paramétrica variando parâmetros geométricos das peças e da armação em laço. Os resultados indicam que dispor as barras o mais próximo possível até um espaçamento máximo de 60 mm entre eixos e considerar um traspasse mínimo igual ao diâmetro de dobra dos laços pode ser uma situação ideal para o comportamento deste tipo de ligação.

Palavras-chave: junta, emenda, laço, concreto armado, simulação numérica.

[a] *Universidade de São Paulo, Escola de Engenharia de São Carlos, Departamento de Engenharia de Estruturas, São Carlos, SP, Brasil.*

Received: 30 Jan 2018 • Accepted: 07 Jun 2018 • Available Online: 05 Feb 2019

1. 'Introduction

In constructions, when it is necessary to provide continuity to structure, it is usual the appearance of joints, indispensable for linking the structural elements of reinforced concrete, which can be precast or cast-in-place. Therefore, the structure performance as a monolithic element depends on the joints efficiency. So, it is necessary to provide an appropriate adhesion between the concrete interfaces and an overlapping between the elements that ensures the efforts transmission between them, ensuring a monolithic element.
For the overlappings, straight bars or bended bars are used. Between these last ones, there are the loop bars, which has spread in civil construction, mainly in precast constructions and bridges. The loop joint consists of bars bended in 180˚, forming a U, spaced to ensure the efforts transmission between the loops (see Figure 1). Bruggeling e Huyge [6] recommended the maximum value of 4 times the bar diameter for the spacing between loops.
This kind of overlapping is appropriate for situations where the available space is insufficient for the overlapping length of straight bars, also when it is necessary to reduce the space occupied by the bars of the overlapping and this way, the interference in the construction process. In straight bars overlapping, the efforts transmission is made by the adhesion between the bar and concrete. On the other hand, in loop joints, in addition to transmission the efforts by adhesion, along the straight part of the bar, also arise radial efforts to the loop (Figure 2), transmitting stress for the concrete by radial compression [2].
Futhermore, the loop joint can have transversal bars to the loop plane, in order to reduce the tendency of separation from the concrete by splitting, ensuring that the failure occurs by bar yielding.
Most studies about loop joint is experimental, limited to the evaluation of few test parameters when compared with numerical studies. These studies are divided into two main groups according to the effort studied: bending and tension. In the bending part, Dragosavić et al. [11] propose a formulation to estimate the load capacity of the joints. In this context, Rosenthal and Shimoni [19] analyzed splices with the addition of an auxiliary stirrup, promoting the transfer between the loops. Therefore, these authors concluded that for a better performance of the structure, the overlapping on the auxiliary stirrup bar must be made in the compressed region of the element, as well as an epoxy compound should be applied on the interface of the joint before concreting it, in order to reduce cracking in that region. Hao [13] studied splicings with the loops positioned horizontally and vertically, besides being one of the few works in which the author implements a numerical model in order to estimate the cracking and loading capacity of the tested joints. These authors also carried out tests varying the method of application of roughness on the joint interface, concluding that the best method is sandblasting; same result obtained by Júlio et al. [16]. According to Hao [13], the smaller the distance between loops and the larger the transverse and longitudinal overlappings, the greater the resistance of the structure. In addition, the larger the bending diameter of the loop, the smaller the cracking moment and the higher the resistance of the joint, with this last property being also increased with the use of a higher rate of transverse reinforcement. Villalba et al. [25] performed tests with repeated loads to simulate traffic conditions on bridges, analyzing fatigue. With the results obtained, the authors proposed a formulation for the anchorage length of the loop and recommended to use transverse reinforcements to the loops.
The first researchers to study loop joints under tension were Leonhardt et al. [17], which performed tests on splicing without transverse bar, nonetheless, they emphasized the importance of using transverse bars in the control of cracking due to the tendency of separation between the loop and the concrete. Joergensen and Hoang [15] carried out experiments whose joint rupture is governed by the failure of the concrete present between the loops, concluding that the tensile strength of the splicing grows with the increase of transverse reinforcement rate, with the increase of longitudinal overlapping and with the decrease of the spacing between these bars. Araújo et al. [2] performed the same tests of the previous authors, differentiating only the model used, analyzing the use of steel fibers in the concrete of the joint. In this way, the addition of fibers increases the joint strength and helps to control its cracking. Joergensen and Hoang [15] and Araújo et al. [2] also proposed analytical models to estimate the load capacity of loop joints based on experimental test results. The difference between both models is that the first one is based on the principle of minimum energy and the second one is based on the strut and tie model, which also served as basis to the formulation proposed by Hao [13] for loop joints under tension. Based on a database created through tests, this author proposes analytical models to estimate the loading of cracks opening in the joint and the load capacity of it. Besides these

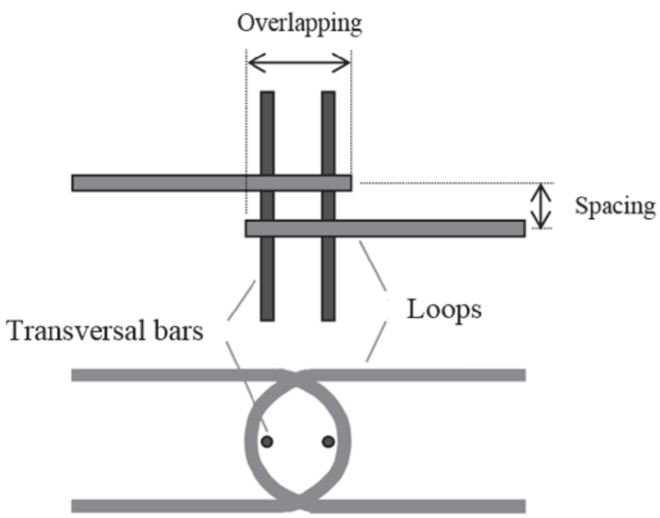

Figure 1
Constructive details of the loop: top view (top) and lateral view (bottom)

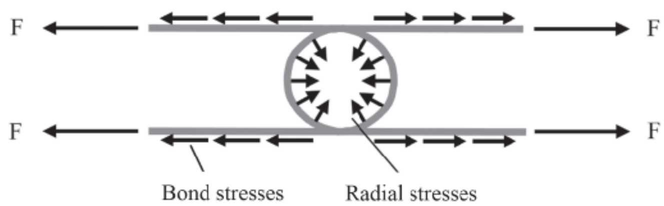

Figure 2
Compression radial stresses

researches, there is the work of Vasconcelos [22], which performs parametric analyzes on numerical models varying the spacing and the overlapping between loops and based on the results obtained, makes suggestions of design values for both parameters. Mattock [18] also studies bars anchoring by means of loop and develops formulations to estimate its resistance, concluding that the larger the loop bars diameter, the greater the resistance of the splicing.
Normative codes, such as Eurocode 2: 1992 [12], CEB-FIP 1990 [7], CEB-FIP2010 [8], BS 8110: 1997 [5], ABNT NBR 9062: 2006 [4] and ABNT NBR 6118 : 2014 [3], while contemplating the use of loop joints as a means of transmitting stresses between precast elements, do not present enough information, such as formulations for predicting the load capacity of the element. These codes only present recommendations for the minimum loop bending diameter and a formulation to obtain the bond stress on the bar.
The aim of the present work is to study the loop joint behavior in reinforced concrete structures under tension, by means of numerical simulations.

2. Methodology

In a first instant, some data were collected from experimental results obtained in the literature studied with the objective of creating a database to evaluate analytical models. Thus, numerical models were developed using DIANA® software. The calibration of the numerical model was performed by varying concrete parameters not present in the work of Joergensen and Hoang [15], work of reference, as the modulus of elasticity, tensile strength, tensile and compressive fracture energy, cracking bandwidth, the compressive strength reduction due to the cracking and the average diameter of the aggregates. To obtain these parameters, CEB 2010 [8] and 1990 [7] and the work of Hilsdorf and Brameshuber [14] were used. With the calibrated models, parametric studies were performed in the DIANA® software, varying the following parameters of the splicing geometry: overlapping length and spacing between loops. After that, the results of the parametric analysis were compared to the values obtained through the analytical models of the literature.

3. Development

The numerical models developed in this paper were calibrated based on the tensile tests performed by Joergensen and Hoang [15], see Figure 3. These authors carried out tensile tests on elements constituted by 3 blocks of reinforced concrete: the end blocks served only to provide stiffness to the structure to facilitate the test, since the central block contained the loop joint. The bars of the loops extended beyond the end blocks, where the authors imposed progressive displacements on the bars of one side and crimping on the others. The parameters varied by Joergensen and Hoang [15] were: the thickness of the concreting joint, the length of the joint, the distance between the loops, the loops overlapping length, the transverse bars diameter, the loop bars diameter, the yield stress of the transverse reinforcement and the yield stress of the loop bars.
In this work, the authors presented only the compressive strength of the concrete, 38.4 MPa, and the maximum diameter of the aggregates, 8 mm, so it was necessary to calculate the other parameters of the concrete only based on this information. In this way, the results obtained with the parameters calculated by CEB 2010 [8] will be presented and when explicit, for some of the parameters used, the calculations were also made by CEB 1990 [7] and based on the work of Hilsdorf and Brameshuber [14].

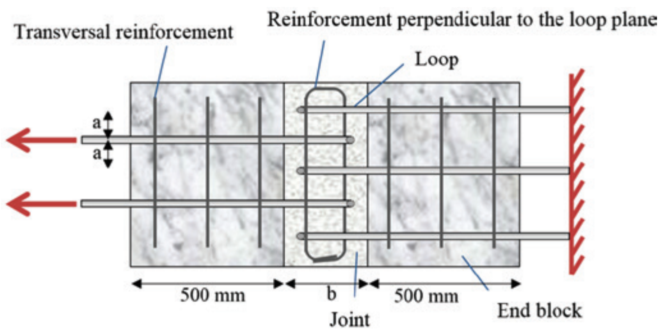

Figure 3
Tensile test studied

3.1 Mesh

For the concrete modelling, solid elements of the type CHX60, of twenty nodes and quadratic approximation, were used. For the reinforcement, beam elements of type L13BE with two nodes were used. Both elements are in the DIANA® 9.5 program library [10]. The average processing time of one model was 3.5 days.
For the modelling of the block, solid elements with equal sides and length of 10 mm were used. From the concrete mesh, the beam elements were divided in order to match all their nodes with the solid element nodes of the concrete. Thus, the curved portions of the reinforcement, such as the loop curve, were represented by several straight beam elements.

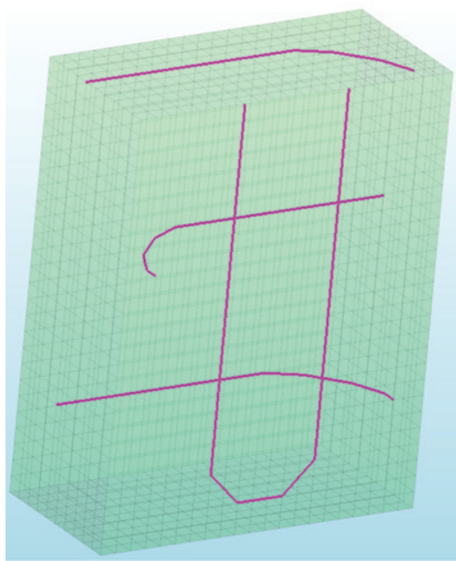

Figure 4
Mesh with reinforcement

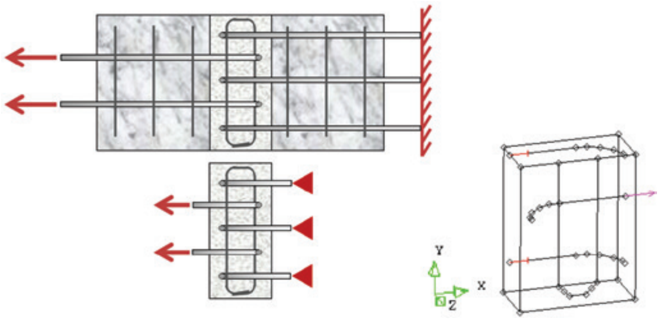

Figure 5
Representation of the boundary conditions in the experiment (left/top) and in numerical model (left/bottom and right)

In order to reduce even more the time of the simulations, it was taken advantage of the double symmetry of the problem, as well as modelling only the concrete joint of the element tested by Joergensen and Hoang [15] (see Figure 4).

3.2 Loading and boundary conditions

In the experimental tensile test carried out by Joergensen and Hoang [15], a displacement was applied on the bars of the side containing the least amount of loops, while the bars of the opposite side were crimped. In the proposed model of the present work, a displacement on X-axis was applied on the end of the single loop and it was restricted the displacement of the ends of the opposite loops on the same direction.

The elements used in the experiments of the aforementioned authors are composed of 3 concrete blocks: the joint block and the other two end blocks. Between the blocks, the interfaces were treated in such a way that there was minimal adherence, in this context, it could be disregarded the restriction to the joint translation on the plane of the blocks interface due to the contact between them. Thus, the degrees of freedom of translation on this plane are only restricted by the pin effect of the loops bars.

Finally, due to the consideration of the double symmetry in the model, constraints of Z translation of the symmetry surface of the XY plane and constraints of translation in Y of the symmetry surface of the XZ plane were also imposed. The Figure 5 illustrates the boundary and loading conditions of the problem. In order to solve the nonlinear equations system, the linear stiffness method was used, besides using the criterion of convergence in energy with a tolerance of 10^{-13}.

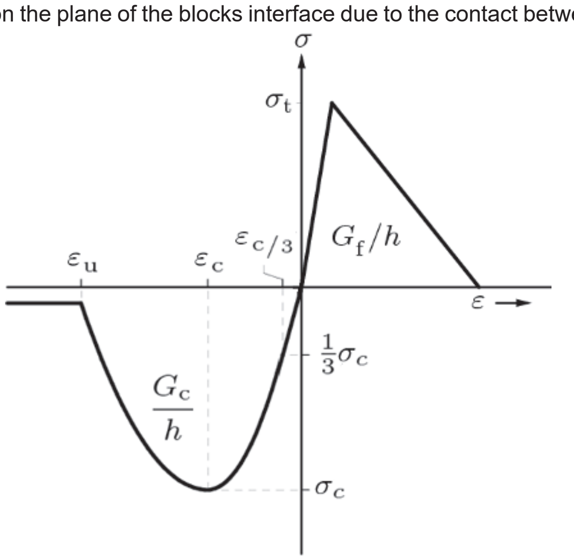

Figure 6
Concrete behavior

3.3 Concrete parameters

The concrete was modelled with the Total Strain Fixed Crack Model, available in DIANA® 9.5 software [9]. In the Fixed Crack Model, the directions of the cracks are fixed and defined from the opening of the first cracks in each node of the elements, which are the directions of the principal stresses. In this way, when the failure criterion is reached, the directions and positions of the cracks are stored and used in subsequent load increments. This model of cracking was developed based on Compression Modified Field Theory, proposed by Vecchio and Collins [23].

For all analyses, the Poisson coefficient was considered constant and equal to 0.2, even after cracking of the concrete.

The reduction of the tensile stress normal to the plane of the crack does not take place at once, it is progressive with the increase of the deformations, in this way, the concrete behavior in tensile in uniaxial state was adopted with linear reduction. In addition, the modulus of elasticity adopted in tensile was the same as in compression, as shown in Figure 6.

The fracture energy in tensile is defined as the energy required to propagate the tensile crack to an unit of area [14], which can be estimated as follows:

According to CEB 2010 [8], there is the Equation 1:

$$G_f = 73 f_c^{0,18}\ (Nm/m^2) \quad (1)$$

According to CEB 1990 [7], there is the Equation 2:

$$G_f = G_{f0}\left(\frac{f_c}{10}\right)^{0,7}\ (Nm/m^2) \quad (2)$$

According to Hilsdorf e Brameshuber [14], there is the Equation 3:

$$G_f = a_d f_c^{0,7}\ (Nm/m^2) \quad (3)$$

Where G_{fo} is the base value of the fracture energy and a_d is an adjustment coefficient of the function, which depends on the maximum diameter of the aggregates, whose values are given in Table 1. The cracking bandwidth can be calculated according to Equation 4 below:

$$h = \frac{2G_f}{\varepsilon_{cu} f_t}. \quad (4)$$

Table 1
Values of G_{fo} and a_d

d_{max} (mm)	G_{fo} (N_m/m^2)	a_d
8	25	4
16	30	6
32	58	10

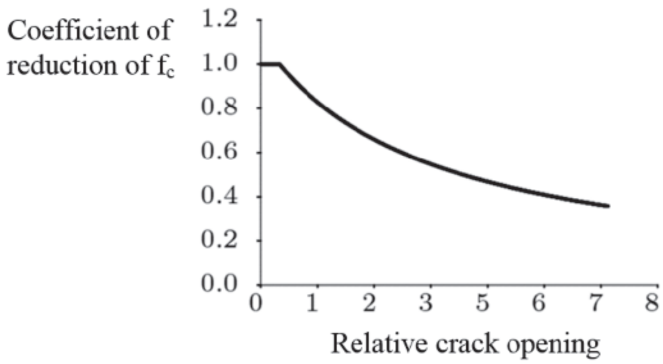

Figure 7
Model of lateral reduction proposed by Vecchio and Collins (1993)

Where ε_{cu} is the ultimate concrete deformation in tensile and f_t is the concrete tensile strength. Considering ε_{cu} as the deformation on the yielding of a CA-50 steel, it was adopted ε_{cu} = 0,24%.
The behavior of the stress-strain diagram of the concrete in the uniaxial compression was considered as parabolic, as shown in Figure 6. This behavior depends on the compression fracture energy G_c and the cracking bandwidth h. Therefore, the compression fracture energy is given by Equation 5:

$$G_c = hf_c\frac{2}{3}(\varepsilon_u - \varepsilon_c) \quad (5)$$

Where G_c is given in Nmm/mm², h is considered in mm, f_c is the concrete compression strength in MPa, ε_c is the peak deformation and ε_u is the final deformation of the concrete under uniaxial compression.
The biaxial behavior of the concrete was also considered in this model, considering the lateral confinement implemented in DIANA® 9.5 [10], based on the model proposed by Selby and Vecchio [21]. In addition, another important factor is the consideration of the compression strength behavior of concrete after the crack formation, as there is a reduction of the concrete resistance parallel to the cracks, as well as the compression stiffness. This phenomenon is better known as softening, which was based on the model implemented in DIANA® 9.5 [10], based on the Vecchio and Collins [24] model, shown in Figure 7. In this figure, the unit of cracks relative opening is strain/strain, since it is the relation between the crack opening deformation and a reference deformation that the authors, Vecchio and Collins [24], considered.
The concrete compression strength of a nodal region formed by the compression strut and the loop can be calculated through Equation 6, from item 6.5.4 of Eurocode 2: 2004.

$$f_c = 0{,}85v'f_{cd} \quad (6)$$

Where v' is a coefficient given by Equation 7:

$$v' = 1 - \frac{f_c}{250}. \quad (7)$$

The Eurocode 2: 2004, in item 6.5.2, presents a formulation to estimate the compression strength of cracked concrete, with cracks in the direction parallel to the compression application, given by Equation 8:

$$f_{cf} = 0{,}6v'f_{cd}. \quad (8)$$

Therefore, the reduction of concrete compression strength due to cracking is given by Equation 9:

$$Red = \frac{f_{cf}}{f_c}. \quad (9)$$

After cracking, the concrete shear stiffness reduces, however, it still has the capacity to transmit shear stresses due to the aggregates interlock and the pin effect of reinforcement. The DIANA®-9.5 [10] models this reduction by applying a reducing coefficient on shear stiffness, according to Equation 10:

$$G^{cr} = \beta G. \quad (10)$$

Where G^{cr} is the shear stiffness of the cracked concrete, G is the shear stiffness of concrete without crack and β is a shear retention coefficient, which varies from 0 to 1. In the present work, the coefficient β was taken as variable and proportional to the cracks opening. Assuming that all contact is lost once the crack length becomes greater than half the average diameter of aggregates, the shear retention can be calculated by Equation 11:

$$\beta = 1 - \frac{2}{d_{agg}}\varepsilon_n h. \quad (11)$$

Where d^{agg} is the average diameter of the aggregates, ε_n is the strain normal to crack and h is the cracking bandwidth. Since the maximum diameter of the aggregates d_{max} is 8 mm, it was adopted, in the present work, a mean diameter of the aggregates of 5 mm.

3.4 Steel behavior

The steel was considered with elastoplastic behavior, presenting the same behavior in tensile and in compression following the Von Mises criterion. The uniaxial behavior of the steel is shown in Figure 8.

3.5 Numerical models validation

The calibration was performed based on the curves that relate the

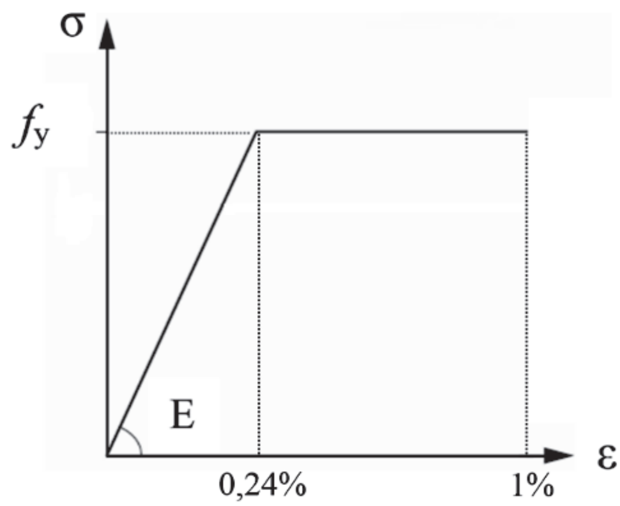

Figure 8
Steel behavior

Table 2
Geometry, properties and results of the tested elements

Element	b (mm)	L (mm)	a (mm)	H (mm)	ϕ_T (mm)	f_{yT} (MPa)	$N_{u.exp}$ (A/B) (kN)
10A/B	210	460	80	170	10	632.1	387.1/391.4
11A/B	*	380	60	*	*	*	459.6/419.6
12A/B	*	300	40	*	*	*	509.4/595.3
13A/B	265	540	100	225	*	*	479.5/470.5
14A/B	340	*	*	300	*	*	571.6/550.7
15A/B	490	*	*	450	*	*	597.5/648.4

* Same value as the previous one.

force applied to the joint with the relative displacement between the joint interface and the precast concrete interface. It is noteworthy that the bars diameter is 20 mm and the yielding stress of the bars is 560.9 MPa.
The models whose parameters were calculated by the expressions of technical standards, as shown in the previous sections, were used as reference for the calibration. Six curves were used to validate the numerical models of the present work, which are related to the elements whose characteristics are shown in Table 2.
The letters A and B, after the elements numbers, indicate that for each set of fixed parameters, two elements were made. In addition, b is the joint thickness in mm, L is the joint length in mm, a is the distance between loops in mm, H is the overlapping length in mm, ϕ_T is the diameter of the transverse bars in mm, f_{yT} is the yielding stress of the transverse bars in MPa and $N_{u,exp}$ is the final tensile load of the elements in kN. Thus, the calibration results are shown in Figure 9 and Table 3.
In the elements 10A, 11A and 12A, in which there was variation of the distance between loops, as this parameter decreases, the disparity between the curves increases. It occurs because this reduction of spacing is not accompanied by a mesh refinement, which reduces the amount of elements between the loops. It could be solved with a better refinement of this region, but the time of the simulations would impair the amount of analyses necessary in the study. Nevertheless, the maximum difference between the resistances of these models and those of the experimental ones is 16%, which shows a good approximation. As for the models 13A, 14A and 15A, in which there is a variation of the longitudinal overlapping length, it is observed that as this parameter increases, there is a greater divergence between the stiffness of the numerical and experimental models, with a tendency to be smaller in these last ones. This is because in the numerical models it was considered perfect bond, that is, there is no slip between the straight part of the loop reinforcement and the surrounding concrete, which leads to a greater stiffness, increasing the disparity of behavior the greater the overlapping. For element 13A, although the resistances diverge, the behavior of the models is quite similar for the most part of the loading. In contrast, the models 14A and 15A present resistances very close to the yielding strength of the reinforcement, showing up as limits for design, as it will be explained later. Therefore, for values of overlapping lower than the one used in these last two models, the behavior of the numerical models approaches the behavior of the experimental models.
The values of the calibrated parameters are shown in Table 4. It is worth noting that most of the parameters were calibrated based on the values calculated by CEB 2010 [8].
Thus, the normative code CEB 2010 [8] and 1990 [7] can be considered for the calculation of concrete parameters when analyzing other types of concrete, since the values obtained by these standards are very close to the calibrated values, as can be seen in Table 4. In addition, the work of Hilsdorf and Brameshuber [14] can be used for the variables related to fracture energy.

Table 3
Models ultimate loads

Element	Ultimate load (kN)		Num/Exp
	Numerical (Num)	Experimental (Exp)	
10A	399.6	389.3	1.03
11A	412.0	439.6	0.94
12A	464.0	552.4	0.84
13A	572.0	475.0	1.20
14A	708.0	561.2	1.26
15A	712.0	623.0	1.14

3.6 Parametric analysis

With the calibrated models, a parametric analysis was performed. For this, the analyzed parameters were the spacing and the overlapping between loops, since the calibration was able to capture their variations reasonably well.

Table 4
Values of concrete parameters calibrated and calculated with CEB 2010

Parameter	Calculated values	Calibrated values	Unit
E_{ci}	43,032	40,000	MPa
Poisson	0.2	0.2	–
f_{ct}	3.41	4.00	MPa
G_f	0.051 (1)	0.050	Nmm/mm²
h	15.78 (2)	15.00	mm
f_c	38.4	38.4	MPa
G_c	1.38	1.00	Nmm/mm²
$f_{c,min}$	0.71 f_c	0.70 f_c	MPa
d_{agg}	5 (3)	5	mm

(1) Value calculated by Hilsdorf e Brameshuber (1991);
(2) Value calculated by CEB 1990;
(3) Value initially estimated.

The idea of the loops is to promote a splicing between bars so that a loop can transmit tensile stresses to the loop on the opposite side, as by the bond stress between steel and concrete, by the appearance of small struts between the straight parts of the loops, as by the radial stresses to the loop, forming, in this last case, a single and larger compression strut between the reinforcements. Therefore, to optimize the stresses transmission by struts, the loops should be arranged as close as possible.

ABNT NBR 6118: 2014 [3], in the item 9.5.2.2, provides a formulation for calculating the overlapping length of straight bars in tensile whose free distance does not exceed 4 times the bar diameter, otherwise, it is necessary to increase the overlapping; in addition,

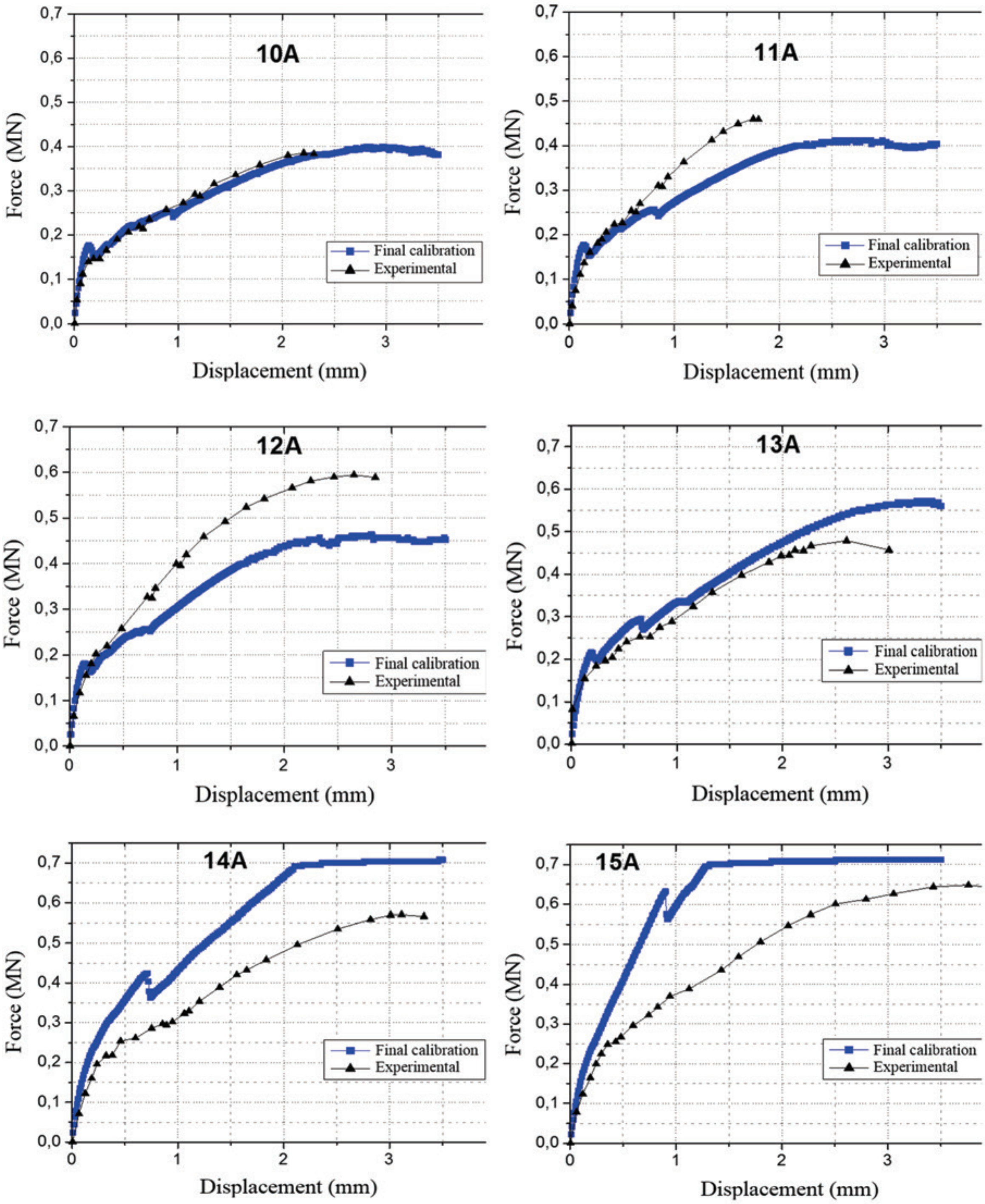

Figure 9
Final calibration of elements

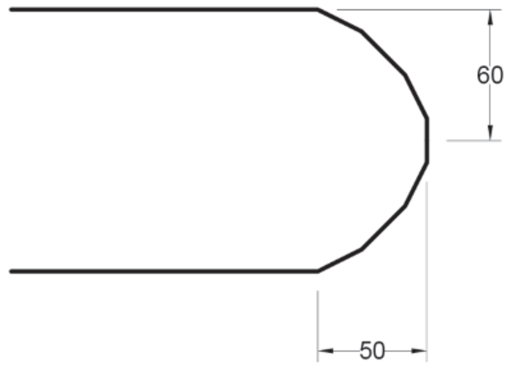

Figure 10
Loop bend dimensions in mm

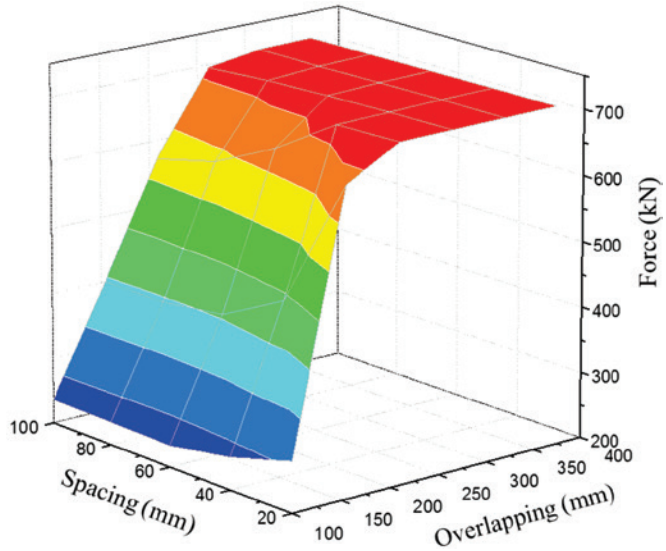

Figure 11
Representation of the parametric analysis results

Bruggeling and Huyge [6] also recommend this value as the upper limit for loop joint. In this way, the ideal situation for the transmission of stress between overlapped straight bars is when the distance between them is less than or equal to 4 times their diameters. Therefore, considering only the transmission mechanism of straight bars, it is necessary to arrange the loops with a maximum free distance of 80 mm, corresponding to a spacing of 100 mm between axes, considering the bar of 20 mm used in the models.
Regarding the second mode of stress transmission, by the appearance of radial stresses to the loop and consequent formation of compression struts, the best arrangement of the overlapped bars is when they are in contact, that is, free distance 0 and spacing of 20 mm. In this case, it is given a minimum inclination for the compression strut between the loops, being more requested by the joint, optimizing the transmission mechanism. Thus, the greater the spacing between the loops, the more they will behave as isolated loops, with no interaction between them. Therefore, for the parametric analysis, the spacing between loops was varied from 20 mm to 100 mm, with intermediate values of 40, 60 and 80 mm.
The loops must be overlapped in such a way that struts between them have the highest height as possible. For this occurrence, the loops must be overlapped at least in the value of their bend diameter, as recommended by Dragosavić et al. [11], who also recommend respecting the minimum value of 13 times the bars diameter, which in this case is 260 mm. The models were calibrated based on the joints tested by Joergensen and Hoang [15], whose bend diameter of the loops is 110 mm. In order to optimize the loop design by means of straight parts of beam members, which should have their nodes coincident with the nodes of the solid elements of the concrete, the loops of the models had to be different diameters in the directions of overlapping and perpendicular to it, of 100 and 120 mm, respectively, as shown in Figure 10. Therefore, for the aforementioned verifications, a diameter of 100 mm was considered, constant during the analyses.
Analyzing the results of the calibration, it is noticed that failure occurred by yielding of the loops in the elements 14A and 15A, therefore, these elements were used as reference of upper limit for overlapping, because the failure load by yielding is known and can not be exceeded. In these elements, the overlappings are 300 and 450 mm, respectively. Thus, considering a value around the mean of these, for the analysis in question, it was considered as a maximum overlapping 370 mm. Therefore, the overlapping values used in the analysis were: 100, 170, 225, 250, 300 and 370 mm.
The results of the simulations are shown in Figure 11. It is noted that as the overlapping increases, the joint strength also increases. In addition, the surface has a well defined landing for overlapping values from 250 mm. In this way, from this overlapping value, the failure of the joint tends to occur by yielding of the loops bars. It is also observed that there is a slight tendency to increase the load capacity of the joint the smaller the spacing between the loops.
In pull-out tests of straight steel bars in concrete, there are four ways of failure [1] (apud [20]):
- Pull-out: consists of sliding of the bar;
- Splitting: referring to the rupture of the concrete adjacent to the steel bar;
- Tensile: consists of the formation of cracks perpendicular to the direction of force application;
- Steel failure: relative to bar yielding.

The first three phenomena above lead to the rupture of only straight bars embedded in concrete, therefore, do not lead to the rupture of loop joints, because even if they occur, there will still be the contribution of the loop part in the resistance of the joint by the formation of compression struts. Thus, in loop joints, there are only two main modes of rupture: compression strut failure and loop yielding.
In Table 5, the values of the ultimate force for each geometry of the joint are shown, according to their overlapping and spacing between loops.
In this table, the combinations whose failure occurred by loop bars yielding are highlighted in red, with the remaining combinations relating to concrete failure of the compression struts. It is noteworthy that, in this case, the stress of 560.9 MPa was considered as reference for the yielding, which corresponds to ultimate force of 704.85 kN.
Thus, for overlappings of 100 and 170 mm, there is a tendency to occur rupture in the concrete for any spacing between loops; in

Table 5
Ultimate force of the elements, in kN

Overlapping (mm)	Spacing (mm)				
	20	40	60	80	100
100	278.1	249.6	232.9	234.6	235.9
170	666.0	464.0	412.0	399.6	400.0
225	711.6	708.8	645.2	596.4	572.0
250	712.4	710.4	707.2	703.2	695.6
300	713.2	712.4	710.8	708.4	708.0
370	713.6	713.2	712.0	710.8	709.6

contrast, for overlappings above 300 mm, there is a tendency to occur rupture by bars yielding for any spacing between loops.
Figure 12 shows the graphs Applied force on the bar x Displacement between interfaces, relative to the joints with variation of spacing and constant overlapping. In the graphics legend, the first value refers to the overlapping, and the second value refers to the spacing between loops.
In this figure, it is noticed that for the overlapping of 100 mm, there is practically no change in the joint behavior, in addition, the load capacity of these joints is much lower than the others. In this way, this overlapping is insufficient for the transmission of stress by the compression struts formed between the loops. For the 170 mm overlapping, there is a significant increase in the ultimate force, especially for the spacing of 20 mm, which increases about 140% in relation to the 100 mm overlapping, reaching a value close to that corresponding to the bar yielding stress. From the overlapping of 225 mm, it begins to occur rupture by the bars yielding. It is also observed that from the 300 mm overlapping, the only difference in the behavior of the joints is related to the joint stiffness, which is larger the smaller the spacing, with the rupture by bars yielding for any spacing between loops. Furthermore, from this overlapping, the curved portion of the loops becomes less and less requested, with a tendency of the bars to work only as straight bars embedded in the concrete. Finally, it is noticed that there is not much

Table 6
Ultimate force of the elements, in kN

Analytical model	Type of joint	Principle	Formulation of the joint load capacity
Hao [13]	2 to 1	Strut and tie model	$N_u = \dfrac{270hHf_c^{\;0,21}}{\sqrt{H^2+a^2}}$
Araújo et al. [2]	1 to 1	Strut and tie model	$N_u = (D+2\phi)w_t f_{cn}\dfrac{H}{\sqrt{s^2+H^2}}$ $w_t = \dfrac{(0.6894-0.0022D)s}{\lambda}$ $\lambda = 0.014s + 0.553 \geq 0.86$ $f_{cn} = 0{,}85f_c$
Joergensen and Hoang [15]	3 to 2	Principle of minimum energy	$\dfrac{N_c}{\nu f_c A_c} = 2\begin{cases} \left(\sqrt{\dfrac{4\Phi}{\nu}\left(1-\dfrac{\Phi}{\nu}\right)+\left(\dfrac{a}{H}\right)^2}-\dfrac{a}{H}\right); & se\ \alpha \geq \varphi\ e\ \alpha \geq \beta\ (a) \\ \dfrac{2\left(\dfrac{\Phi}{\nu}\left(3-4\dfrac{a}{H}\right)+\left(\dfrac{a}{H}\right)^2+1\right)}{4+3\dfrac{a}{H}}; & se\ \alpha < \varphi\ e\ \dfrac{a}{H} < \dfrac{3}{4}\ (b) \\ \sqrt{\left(\dfrac{a}{H}\right)^2+1}-\dfrac{a}{H}; & se\ \alpha < \beta\ e\ \dfrac{a}{H} \geq \dfrac{3}{4}\ (c) \end{cases}$ $\Phi = \left(\dfrac{A_{sT}f_{yT}}{A_c f_c}\right)$ $\nu = \dfrac{0{,}88}{\sqrt{f_c}}\left(1+\dfrac{1}{\sqrt{H}}\right)$ $\alpha = \beta + \sin^{-1}\left(\dfrac{1-\dfrac{2\Phi}{\nu}}{\sqrt{\left(\dfrac{a}{H}\right)^2+1}}\right)$ $\beta = Arctan(a/H)$ $N_u = mín\begin{cases} N_c & (failure\ in\ concrete) \\ N_y = 2A_{sL}f_{yL} & (yielding\ of\ loop\ reinforcement) \end{cases}$

difference in the behavior of the joints with spacing of 80 and 100 mm, therefore, from these spacings, there is a greater tendency of the loops to work separately, that is, it reduces the tendency of compression struts formation between the loops. In Figure 13, the force x displacement graphs of the joints with variation of overlapping and constant spacing are shown. For

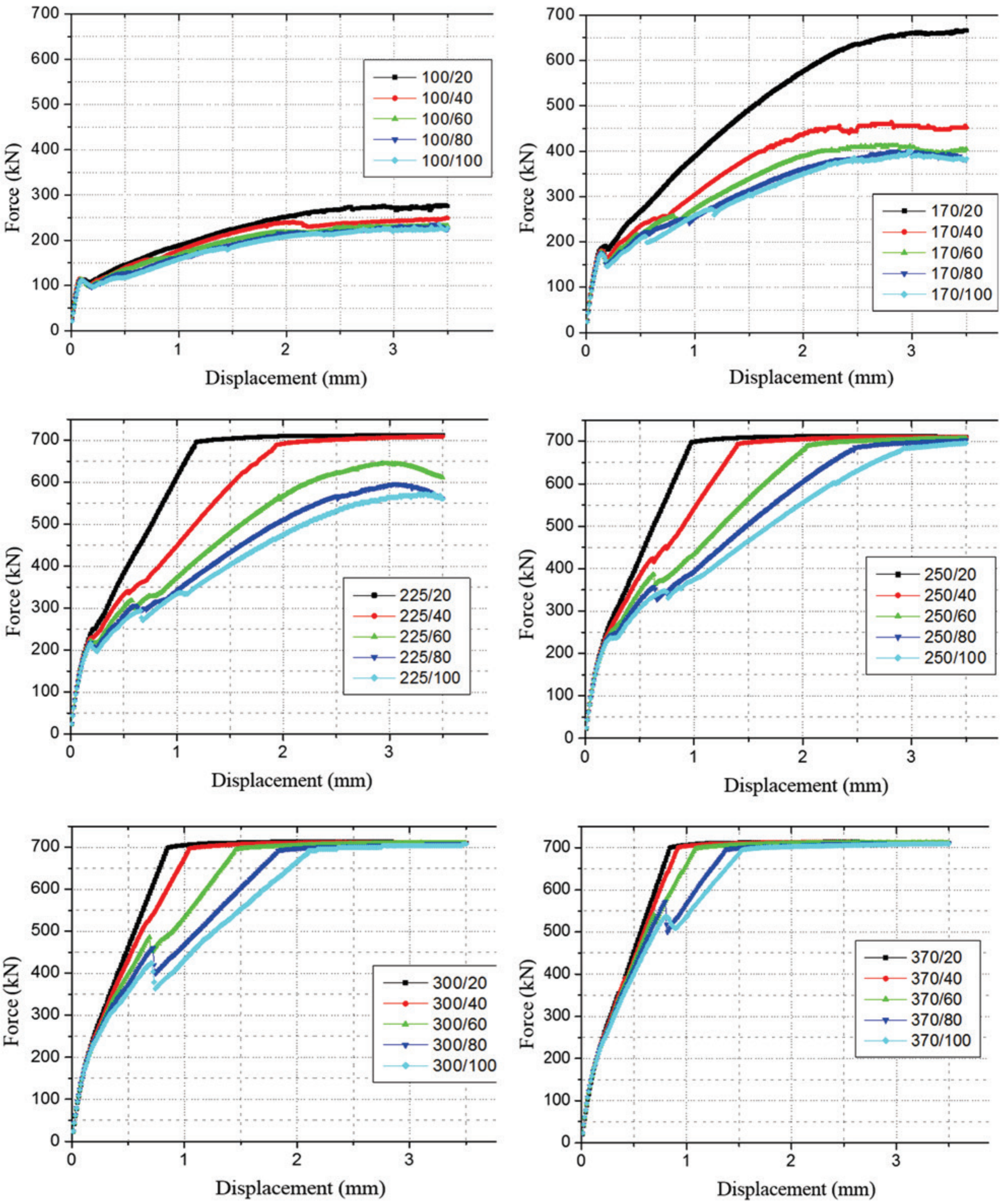

Figure 12
Graphics of the joints with constant overlapping

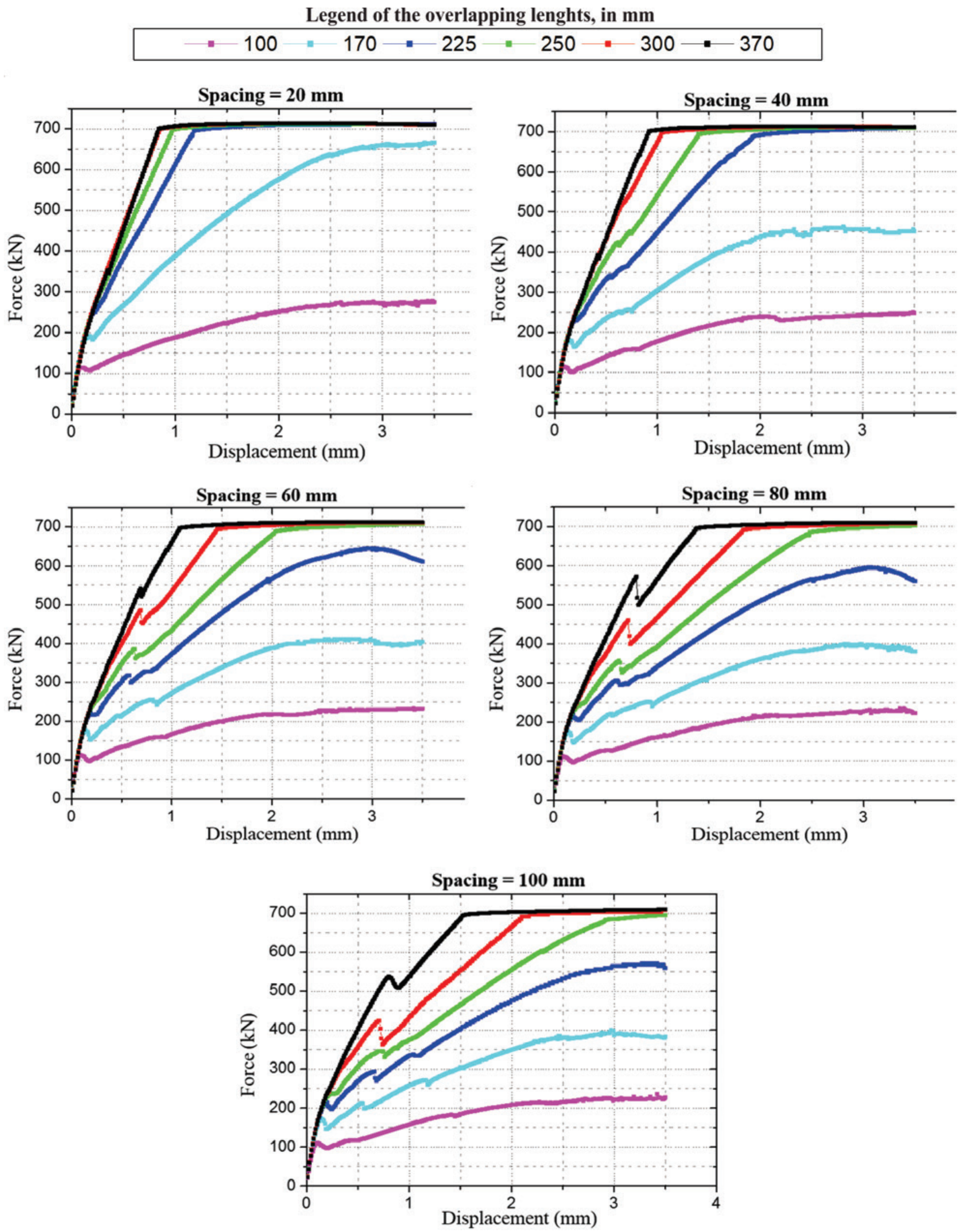

Figure 13
Graphics of the joints with constant spacing

the spacing between loops of 20 mm, that is to say, when the overlapped bars are in contact, with overlapping over or equal to 300 mm, the joints behavior under tensile is quite similar to each other. This fact can be observed in the graphics corresponding to the overlappings of 300 and 370 mm, whose curves are superimposed in most points. Thus, as the overlapping length increases, the joints tend to have the same behavior, represented by the curve corresponding to the joint with spacing of 20 mm and overlapping of 300 mm. This shows that this overlapping is already sufficient to overlap straight bars, because for values from this, the rupture tends to occur by bars yielding. It is also noticed that as the spacing increases, the load capacity and stiffness of the joint decrease.

Finally, the smaller the spacing between loops and the greater the overlapping between them, the greater the load capacity of the joint studied. It is also noteworthy that the loop can cause concrete splitting if there is not enough concrete covering around it, capable of promoting an appropriate confinement of the reinforcement. However, this type of rupture was not evaluated in this study.

3.7 Analytical models of loop joints under tensile

For loop joint under tensile, the analytical models obtained from the literature are described in Table 6, where there are the models of Hao [13], Araújo et al. [2] and Joergensen and Hoang [15].

In the formulation of Hao [13], N_u is the ultimate force in the joint, h is the height of the concrete element, H is the overlapping length of the loops, f_c is the compression concrete strength and a is the spacing between loops.

In the formulations of Araújo et al. [2], N_u is the ultimate force in the joint, D is the internal diameter of the loop, φ is the bar diameter, w_t is the effective thickness of the inclined strut, f_{cn} is the compressive strength of the strut, H is the loop overlapping length, s is the internal spacing between loops, λ is a coefficient related to the softening effect of concrete and f_c is the compression concrete strength.

In the formulations of Joergensen and Hoang [15], N_c is the joint strength considering only the failure of the compression strut between loops, v is a correction factor that takes into account the fact that concrete is not a perfectly plastic material, f_c is the compression concrete strength, A_c is the concrete area between loops

Table 7
Comparison of the results with the analytical models

Spacing	Overlapping	Model	Hao	Araújo	Joergensen	M/H	M/A	M/J
20	100	278.1	227.8	199.8	398.7	1.2	1.4	0.70
	170	666.0	230.8	202.4	590.5	2.9	3.3	1.13
	225	704.8	231.4	203.0	704.8	3.0	3.5	1.00
	250	704.8	231.6	203.1	704.8	3.0	3.5	1.00
	300	704.8	231.8	203.3	704.8	3.0	3.5	1.00
	370	704.8	232.0	203.5	704.8	3.0	3.5	1.00
40	100	249.6	215.7	292.4	312.9	1.2	0.9	0.80
	170	464.0	226.2	306.5	517.4	2.1	1.5	0.90
	225	704.8	228.8	310.0	632.8	3.1	2.3	1.11
	250	704.8	229.4	310.9	677.9	3.1	2.3	1.04
	300	704.8	230.3	312.1	704.8	3.1	2.3	1.00
	370	704.8	231.0	313.1	704.8	3.1	2.3	1.00
60	100	232.9	199.2	323.6	257.5	1.2	0.7	0.90
	170	412.0	219.1	355.9	455.4	1.9	1.2	0.90
	225	645.2	224.5	364.7	568.8	2.9	1.8	1.13
	250	704.8	225.9	367.0	613.6	3.1	1.9	1.15
	300	704.8	227.8	370.1	694.2	3.1	1.9	1.02
	370	704.8	229.3	372.5	704.8	3.1	1.9	1.00
80	100	234.6	181.4	327.2	218.4	1.3	0.7	1.07
	170	399.6	210.2	379.1	403.2	1.9	1.1	0.99
	225	596.4	218.9	394.8	513.1	2.7	1.5	1.16
	250	703.2	221.3	399.0	557.0	3.2	1.8	1.26
	300	704.8	224.5	404.8	636.6	3.1	1.7	1.11
	370	704.8	227.1	409.5	704.8	3.1	1.7	1.00
100	100	235.9	164.3	317.2	188.1	1.4	0.7	1.25
	170	400.0	200.3	386.7	359.4	2.0	1.0	1.11
	225	572.0	212.3	410.0	464.8	2.7	1.4	1.23
	250	695.6	215.7	416.5	507.4	3.2	1.7	1.37
	300	708.0	220.4	425.6	585.3	3.2	1.7	1.21
	370	704.8	224.3	433.1	681.6	3.1	1.6	1.03

Table 8
Average, standard deviation and coefficient of variation of the relations

	M/H	M/A	M/J
Average	2,60	1,87	1,05
Standard deviation	0,73	0,84	0,14
Coefficient of variation	0,28	0,45	0,13

projected on the loop plane, Φ is the mechanical rate of transversal reinforcement, a is the spacing between loops, H is the overlapping between loops, α is the inclination of the relative displacement on the plane of rupture with respect to this plane, ϕ is the concrete friction angle, considered equal to Arctan (3/4) for concrete of normal resistance, β is the inclination of the rupture plane with respect to the loop plane, A_{sT} is the steel area transverse to the loop plane, f_{yT} is the yielding stress of the transversal bars, N_y is the joint resistance considering only the loop yielding, A_{sL} is the total steel area of one loop and f_{yL} is the yielding stress of the loop bar.
The formulations proposed by Hao [13] and Araújo et al. [2] are quite similar, this is due to the fact that both are based on the strut and tie model. The difference between the models is in consideration of the cross sectional area of the compression struts. With respect to the height of the compression strut, Hao [13] considers equal to the joint height, while Araújo et al. [2] consider equal to the loop height, that is, D + 2φ. As for the strut thickness w_t, which is the parameter of greatest divergence between the authors, Hao [13] establishes the calculation based only on the concrete compressive strength, while Araújo et al. [2] define equations based on the loop diameter and the spacing between them.
Although the models proposed by the previous authors have presented satisfactory results in relation to the respective experimental results, they do not take into account some of the parameters that define the joint, such as the transversal reinforcement ratio and its yielding stress. In contrast, the model proposed by Joergensen and Hoang [15] is based on the principle of minimum energy, considering all parameters of influence of joint. Thus, the model proposed by Joergensen and Hoang [15] is presented as the most complete to represent the behavior of loop joint.

3.8 Comparison of the numerical results with the analytical models

The results obtained in the parametric analysis were compared with the joint strengths calculated by the analytical models proposed by Hao [13], Araújo et al. [2] and Joergensen and Hoang [15].
The models developed by Hao [13] and Araújo et al. [2] refer to loop joint 2 to 1 and 1 to 1, respectively. Thus, it was made an extrapolation of the formulations to calculate the resistance of loop joint 3 to 2, used in the present work.
The loading capacities of the joints calculated by the above formulations are shown in Table 7. As also, they are shown the relationships between the values of the Model and Hao (M / H), the Model and Araújo (M / A) and the Model and Joergensen (M / J). In addition, Table 8 shows the averages of these relationships, their respective standard deviations and coefficients of variation.
It is noteworthy that for the calculation of these three parameters, the values of resistance above the force corresponding to the bars yielding were replaced by the value of this force, that is, 704.85 kN, since this value corresponds to the maximum value of the joint rupture, as explained in item 3.6.
As described in item 3.7, the models proposed by Hao [13] and Araújo et al. [2] are similar to each other, which consider the strut and tie model. The only difference between the models is the consideration of the cross sectional area of the compression struts. To calculate the strut thickness, the first author presents a formulation dependent only on the concrete strength and the other authors have a formulation dependent only on the loops bend diameter and the spacing between them. It is noticed a large divergence between the values obtained by means of the numerical model and the values calculated using the formulations of these authors, whose averages of the ratios between them is 2.6 for the Hao model [13] and 1.87 for the model of Araújo et al. [2], besides standard deviations of 0.73 and 0.84 and coefficients of variation of 0.28 and 0.45, respectively.
In the Hao model [13], the overlapping variation between loops practically does not change the joint resistance, presenting a slight increase with the increase of this parameter, and the increase of the spacing between loops reduces the joint resistance, although it is not a significant reduction.
In the model of Araújo et al. [2], the increase in the overlapping also changes little the joint capacity, increasing it. In contrast, increasing the spacing between loops leads to an increase in the joint strength.
In relation to the spacing, the two models diverge from each other, because in the Hao model [13], the spacing is inversely proportional to the joint capacity, in contrast, in the model of Araújo et al. [2], the increase of this variable leads to a greater thickness of the compression strut, increasing, in turn, the joint resistance. On the other hand, with respect to the variation of the overlapping between loops, the formulations show agreement between them.
The aforementioned models consider that the stress transfer between loops occurs only by the formation of compression struts between them, disregarding the bond stress along the straight part of the bars. Therefore, there is a great disparity between the results with the numerical models and with the formulations proposed by Hao [13] and Araújo et al. [2].
The results with the numerical models present excellent agreement with the formulation developed by Joergensen and Hoang [15], with the mean value of the values ration of 1.05, standard deviation of 0.14 and coefficient of variation of 0.13.
Therefore, the models proposed by Hao [13] and Araújo et al. [2] were not appropriate to estimate the load capacity of the joints studied in the present work, being specific to their respective works. On the other hand, the model developed by Joergensen and Hoang [15] is the best one to calculate the loading capacity of 3 to 2 loop joints submitted to tensile.

4. Conclusions

The present work presented a study about loop bar splicing in reinforced concrete joints under tensile. For this, the software DIANA® was used, with which, initially, a calibration of numerical models was performed based on the work of Joergensen and Hoang [15], varying the parameters whose values were unknown. With the calibrated models, a parametric analysis was performed, varying the overlapping and spacing between loops.

4.1 Overlapping

The overlapping values studied ranged from 100 mm to 370 mm. When observing the results of the models, it is noticed that from an overlapping of 300 mm, all the joints had rupture by yielding of the loops bars for any value of spacing between them, in addition, the overlapping of 100 mm, value of the loop bend diameter, proved to be insufficient for the formation of significant compression struts.
Most of the investigated authors recommend as the minimum value for overlapping the value of the loop bend diameter, besides this value, Dragosavić et al. [11] also recommend respecting the minimum value of 13 times the bars diameter, which for the case under study is 260 mm. Thus, in order to optimize the joint strength and ensure that the rupture occurs by yielding of the loop bars, it is recommended to use overlapping values between 11 and 15 times the loop bars diameter, depending on the spacing between them. In addition, it is necessary to consider as minimum overlapping the loop bend diameter.

4.2 Spacing

The spacing values studied varied from 20 mm to 100 mm, with the first value corresponding to the contact between the loops bars, since in the present work, bars with a diameter of 20 mm are used. The results showed that the highest strengths were achieved when 20 mm spacing was used, because, with this value, the compression strut has the lowest possible inclination, thus maximizing the stress on it. It is also noticed that the models with spacing of 80 mm and 100 mm showed very similar behaviors, indicating a tendency that, from these values, the loops work separately, which reduces the joint efficiency. In this way, it is recommended to overlap the loops bars so that they stay in contact and when it is not possible, the limit of 3 times the diameter of these bars must be respected.

4.3 Analytical models

When it was used the analytical models proposed by Hao [13] and Araújo et al. [2] modified for 3 to 2 joints, the results presented very large disparities with respect to the numerical results of the parametric analysis, presenting divergent behaviors in many cases. Therefore, these models should not be extrapolated to joints with other geometries different from those studied by the respective authors, being specific to the joints of each work. On the other hand, in relation to the results obtained with the Joergensen and Hoang model [15], there was excellent agreement with the numerical models results, with the mean value of the joints resistances ratio of 1.05, standard deviation of 0.14 and coefficient of variation of 13%. Therefore, this formulation can be used to estimate the load capacity of 3 to 2 loop joints, subjected to tensile and having any overlapping length and spacing between loops.

5. Acknowledgments

To the School of Engineering of São Carlos for giving me the opportunity to contribute a little more with the Master Program in Structures and for providing me this excellent formation. To the National Council of Scientific and Technological Development (CNPq) for the master scholarship.

6. References

[1] AL-JAHDALI, F. A.; WAFA, F. F.; SHIHATA, S. A. Development length for straight deformed bars in high-strength concrete. ACI Special Publication, v.149, outubro 1994.
[2] (Júlio, Branco e Silva, 2004)ARAÚJO, D. D. L.; CURADO, M. C.; RODRIGUES, P. F. Loop connection with fibre-reinforced precast concrete components in tension. Engineering Structures, v. 72, n. 0, p. 140-151, maio 2014.
[3] ASSOCIAÇÃO BRASILEIRA DE NORMAS TÉCNICAS. NBR 6118: Projeto de estruturas de concreto - Procedimento. Rio de Janeiro, 2014.
[4] ASSOCIAÇÃO BRASILEIRA DE NORMAS TÉCNICAS. NBR 9062: Projeto e execução de estruturas de concreto pré-moldado. Rio de Janeiro, 2006.
[5] BRITISH STANDARDS INSTITUTION. BS 8110: Structural use of concrete. Part 1: Code of practice for design and construction. BSI, Londres, 1997.
[6] BRUGGELING, A. S. G. ; HUYGE, G. F. Prefabrication with concrete. Rotterdam: A.A. Balkema; 1991.
[7] CEB-FIP MODEL CODE 1990 – final draft. Bulletin D'Information, n. 203-205. Thomas Telford, Londres, 1991.
[8] CEB-FIP MODEL CODE 2010 – first complete draft. Bulletin 55, v. 1, Alemanha 2010.
[9] DIANA. DIANA Finite Element Analysis. User's manual release 9.5. Material Library. TNO DIANA, Delft, Netherland, 2014.
[10] DIANA. DIANA Finite Element Analysis. User's manual release 9.5. Element Library. TNO DIANA, Delft, Netherland, 2014.
[11] DRAGOSAVIĆ, M.; VAN DEN BEUKEL, A.; GIJSBERS, F. B. J. Loop connections between precast concrete components loaded in bending. Heron, v. 20, n. 3, 1975.
[12] EUROPEAN STANDARD EN. Eurocode 2: Design of concrete structures – Part 1: General rules and rules for buildings. Comité Européen de Normalisation, Brussels, 225 p., 2004.
[13] HAO, J. Structural behaviour of precast component joints with loop connection. 2004. 395 p. Tese (Doutorado em Engenharia Civil) - Departamento de Engenharia Civil, Universidade Nacional de Singapura, Singapura, 2004.
[14] HILSDORF, H. K.; BRAMESHUBER, W. Code-type formulation of fracture mechanics concepts for concrete. International Journal of Fracture, v. 51, n. 1, p. 61-72, 1991.
[15] JOERGENSEN, H. B.; HOANG, L. C. Tests and limit analysis of loop connections between precast concrete elements loaded in tension. Engineering Structures, v. 52, n. 0, p. 558-569, abr. 2013.
[16] JÚLIO, E. N. B. S.; BRANCO, F. A. B.; SILVA, V. D. Concrete-to-concrete bond strength. Influence of the roughness of the substrate surface. Construction and Building Materials, v. 18, n. 9, p. 675-681, jun. 2004.

[17] LEONHARDT, F.; WALTER, R.; DIETERLE, H. Versuche zur Ermittlung der Tragfähigkeit von Zugschlaufenstößen (Em inglês: Tests for evaluating the tensile strength of loop joints). Deutscher Ausschuss für Stahlbeton, Bulletin nº 226, p. 1-22, 1973.
[18] MATTOCK, A. H. Effectiveness of loop anchorages for reinforcement in precast concrete members. PCI journal, v. 39, n. 6, p. 54-68, 1994.
[19] ROSENTHAL, I.; SHIMONI, J. Bending behavior of a double-loop connection between precast concrete slabs. Concrete International, v. 6, n. 11, p. 30-34, 1984.
[20] SANTANA, I. V. Estudo da influência das fibras metálicas no comportamento da aderência entre barras de aço e concretos de diferentes classes de resistência. 2014. 246 p. Dissertação (Mestrado em Engenharia Civil) - Escola de Engenharia de São Carlos, Universidade de São Paulo, São Carlos, 2014.
[21] SELBY, R. G.; VECCHIO, F. J. Three-dimensional Constitutive Relations for Reinforced Concrete. Universidade de Toronto, Departemento de Engenharia Civil, Toronto, Canada, 1993.
[22] VASCONCELOS, T. D. L. Estudo numérico do comportamento de emendas de barras por meio de laço em juntas de estruturas de concreto armado. 2017. 123 p. Dissertação (Mestrado em Engenharia Civil, Estruturas) – Escola de Engenharia de São Carlos, Universidade de São Paulo, São Carlos, 2017.
[23] VECCHIO, F. J., COLLINS, M. P. The modified compression field theory for reinforced concrete elements subjected to shear. ACI Journal, v. 83, n. 22, p. 219-231, março-abril de 1986.
[24] VECCHIO, F. J., COLLINS, M. P. Compression response of cracked reinforced concrete. Journal of Structural Engineering, v. 119, n. 12, p. 3590-3610, dezembro de 1993.
[25] VILLALBA, S. et al. New structural joint by rebar looping applied to segmental bridge construction: Fatigue strength tests. Journal of Bridge Engineering, v. 18, n. 11, p. 1174-1188, 2013.

Volume 12, Number 1 (February 2019) p. 39 – 68 • ISSN 1983-4195
http://dx.doi.org/10.1590/S1983-41952019000100006

REVISTA IBRACON DE ESTRUTURAS E MATERIAIS
IBRACON STRUCTURES AND MATERIALS JOURNAL

Numerical study of the behaviour of loop bar splicing in joints of reinforced concrete structures

Estudo numérico do comportamento de emendas de barras por meio de laço em juntas de estruturas de concreto armado


T. D. L.VASCONCELOS [a]
thiagodelfino@usp.br
https://orcid.org/0000-0003-1212-6893

V. G. HAACH [a]
vghaach@sc.usp.br
https://orcid.org/0000-0002-9501-4450

Abstract

Sometimes straight bar splicing takes up too much space in a reinforced concrete structure due to the required overlapping length. Therefore, in limited space situations, loop joints may be a good solution, which has been spread in civil construction, although there are very few studies about it. The aim of the present work is to study the loop joint behavior in reinforced concrete structures under tension. Three dimensional numerical simulations are made using the software DIANA®. Firstly, the calibration of the numerical model based on experimental tests of the literature is performed, followed by parametric analyses varying geometric parameters of the concrete elements and reinforcement. The results indicate that arranging the bars as close as possible to a maximum spacing of 60 mm between axes and considering a minimum splice length equal to the bend diameter of the loops may be an ideal situation for the behavior of this type of connection.

Keywords: loop joint, splicing, reinforced concrete, numerical simulation.

Resumo

Emendas com barras retas ocupam muito espaço devido ao comprimento de traspasse necessário. Dessa forma, em situações em que há uma limitação de espaço para a emenda, uma armação que constitui uma solução interessante é a emenda por meio de laço, que, apesar de ter poucos estudos relacionados, vem sendo bastante difundida na construção civil. O objetivo desse trabalho é estudar o comportamento de emendas em laço em juntas de estruturas de concreto armado submetidas à tração. Para isso, realizam-se simulações numéricas no software DIANA® em modelos numéricos 3D. Inicialmente se faz a calibração do modelo numérico com base em ensaios experimentais da literatura, depois é realizada uma análise paramétrica variando parâmetros geométricos das peças e da armação em laço. Os resultados indicam que dispor as barras o mais próximo possível até um espaçamento máximo de 60 mm entre eixos e considerar um traspasse mínimo igual ao diâmetro de dobra dos laços pode ser uma situação ideal para o comportamento deste tipo de ligação.

Palavras-chave: junta, emenda, laço, concreto armado, simulação numérica.

[a] *Universidade de São Paulo, Escola de Engenharia de São Carlos, Departamento de Engenharia de Estruturas, São Carlos, SP, Brasil.*

Received: 30 Jan 2018 • Accepted: 07 Jun 2018 • Available Online: 05 Feb 2019

1. Introdução

Nas construções, quando se deseja proporcionar continuidade à estrutura, é comum o aparecimento de juntas, necessárias para conectar os elementos estruturais de concreto armado, podendo ser pré-moldados ou moldados no local. Dessa forma, o desempenho da estrutura como um todo depende muito da eficiência das juntas. Assim, deve-se proporcionar uma aderência adequada entre as interfaces de concreto e uma emenda entre elementos que garanta a transmissão de esforços entre as partes, a fim de garantir um elemento monolítico.

Para a execução das emendas, podem ser utilizadas barras retas ou dobradas. Entre estas, estão as barras em forma de laço, que apesar de haver poucos estudos sobre esse tipo de emenda, ela vem tendo ampla difusão na construção civil, principalmente em obras com pré-moldados e de pontes. A emenda em laço é constituída por barras dobradas a 180˚, em forma de U, espaçadas entre si de forma a garantir a transferência de esforços entre os laços (ver **Erro! A origem da referência não foi encontrada.**), sendo recomendado por Bruggeling e Huyge [6] o valor máximo de 4 vezes o diâmetro da barra para o espaçamento entre laços.

Esse tipo de emenda é apropriado para situações onde o espaço disponível é insuficiente para o comprimento de transpasse de barras retas, como também quando se deseja reduzir o espaço ocupado pelas barras da emenda e assim, sua interferência no processo construtivo. Em emendas com barras retas, a transferência de esforços se dá apenas pela aderência entre a barra e o concreto. Já em emendas por meio de laço, além de a transmissão de esforços se dar por aderência, na parte reta da barra, também surgem esforços radiais ao laço (**Erro! A origem da referência não foi encontrada.**), transmitindo as tensões para o concreto através de compressão radial [2].

Essa emenda ainda pode conter barras transversais ao plano do laço, a fim de reduzir a tendência à separação do concreto por meio do fendilhamento, garantindo que a falha na junta se dê por escoamento das barras.

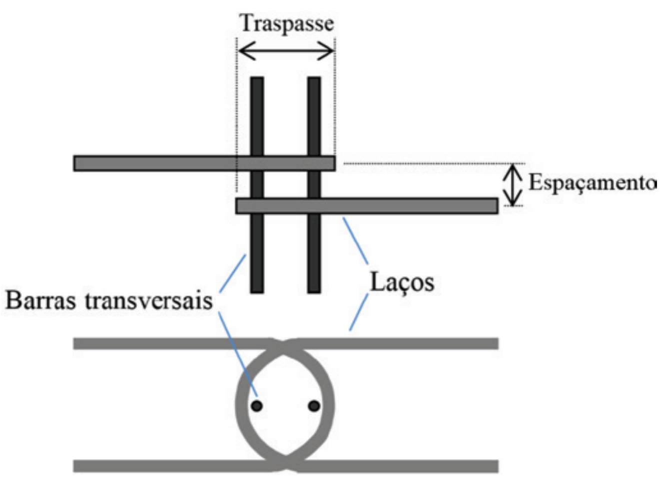

Figura 1
Detalhes construtivos do laço: vista superior (em cima) e vista lateral (embaixo)

A maioria dos estudos sobre emendas em laço é experimental, limitados à avaliação de poucos parâmetros de ensaio quando comparados com estudos numéricos. Esses estudos podem ser divididos em dois grupos principais de acordo com a solicitação estudada: flexão e tração. Na flexão, está o trabalho de Dragosavić et al. [11], os quais também propõem uma formulação para estimar a capacidade de carga das peças. Nesse contexto, Rosenthal e Shimoni [19] analisaram emendas com a adição de um estribo auxiliar, promovendo o traspasse entre os laços. Portanto, estes autores concluíram que para um maior desempenho da estrutura, o traspasse na barra do estribo auxiliar deve ser realizado na região comprimida do elemento, como também se deve aplicar um composto de epóxi na interface da junta antes de concretá-la, com o objetivo de reduzir a fissuração na região. Hao [13] estudou emendas com laços na horizontal e na vertical, além de ser um dos poucos trabalhos no qual o autor implementa um modelo numérico a fim de estimar a fissuração e a capacidade de carga das emendas ensaiadas. Esses autores também realizaram ensaios variando o método de aplicação de rugosidade na interface da junta, chegando à conclusão de que o melhor método é o jateamento de areia; mesmo resultado obtido por Júlio et al.[16]. Ainda segundo Hao [13], quanto menor a distância entre laços e maiores os traspasses transversal e longitudinal, maior é a resistência da estrutura, como também quanto maior o diâmetro de dobra do laço, menor é o momento de fissuração e maior é a resistência da peça, sendo esta última propriedade também aumentada com a utilização de uma maior taxa de armadura transversal. Villalba et al. [25] realizaram ensaios com cargas repetidas a fim de simular as condições de tráfego em pontes, analisando a fadiga. Com os resultados obtidos, os autores propuseram uma formulação para o cálculo do comprimento de ancoragem do laço e recomendaram utilizar armaduras transversais aos laços.

Os primeiros pesquisadores a estudar emendas em laço submetidas à tração foram Leonhardt et al. [17], os quais realizaram ensaios em emendas sem armaduras transversais, apesar disso, ressaltaram a importância do uso de barras transversais no controle da fissuração devido à tendência de separação entre o laço e o concreto. Joergensen e Hoang [15] realizaram experimentos cuja ruptura da junta é governada pela falha no concreto presente entre os laços, concluindo que a resistência à tração da emenda cresce com o aumento da quantidade de armaduras transversais, com o aumento do traspasse longitudinal e com a redução do espaçamento entre estas barras. Araújo et al. [2] realizaram os mesmos ensaios dos autores anteriores, diferenciando apenas o modelo utilizado, analisando o uso de fibras de aço no concreto da emenda. Dessa forma, a adição de fibras aumenta a resistência

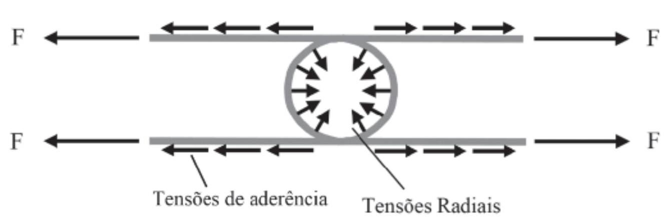

Figura 2
Esforços radiais de compressão

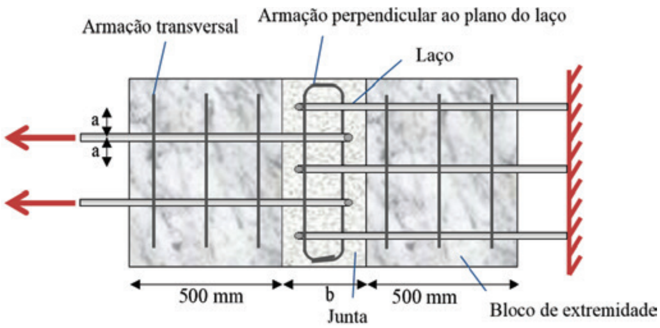

Figura 3
Ensaio de tração estudado

da peça e ajuda a controlar sua fissuração. Joergensen e Hoang [15] e Araújo et al. [2] também propuseram modelos analíticos para estimar a capacidade de carga das emendas a partir dos resultados de ensaios experimentais. A diferença entre ambos os modelos é que o primeiro trabalho se baseia no princípio da mínima energia e o segundo tem como base o modelo de bielas e tirantes, o qual também serviu como premissa para a formulação proposta por Hao [13] para emendas em laço sob tração. Com base em um banco de dados criado por meio de ensaios, este autor propõe modelos analíticos para estimar o carregamento de abertura de fissuras na junta e a capacidade de carga dessas emendas. Além dessas pesquisas, há o trabalho de Vasconcelos [22], o qual realiza análises paramétricas em modelos numéricos variando o espaçamento e o traspasse entre laços e com base nos resultados obtidos, faz sugestões de valores de projeto para ambos os parâmetros; e Mattock [18], o qual estuda ancoragens de barras por meio de laço e desenvolve formulações para estimar suas resistências, constatando que quanto maior o diâmetro das barras do laço, maior a resistência da emenda.

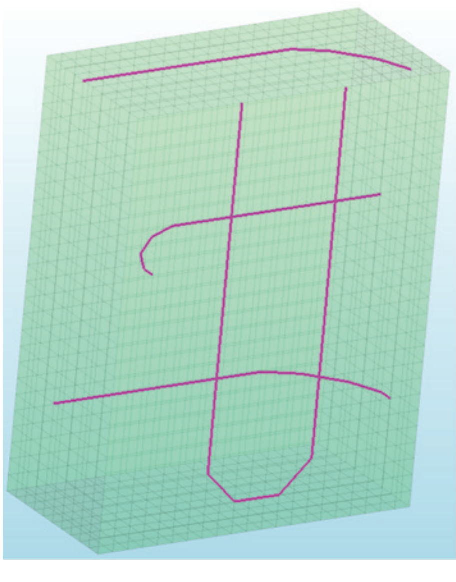

Figura 4
Malha do modelo com as armaduras

Os códigos normativos, tais como o Eurocode 2:1992 [12], CEB-FIP 1990 [7], CEB-FIP2010 [8], BS 8110:1997 [5], ABNT NBR 9062:2006 [4] e ABNT NBR 6118:2014 [3], apesar de contemplarem a utilização de emendas em laço como meio de transmissão de esforços entre elementos pré-moldados, não apresentam informações suficientes, como formulações que auxiliem na previsão da capacidade de carga do elemento. Estas normas apresentam apenas recomendações para o diâmetro mínimo de dobra do laço e a formulação para se obter a tensão de aderência na barra.
O presente trabalho tem como objetivo principal estudar o comportamento de emendas de armaduras em laço em juntas de estruturas de concreto armado submetidas à tração, por meio de simulações numéricas.

2. Metodologia

Em um primeiro instante, foram coletados dados de resultados experimentais obtidos na literatura estudada com o objetivo de criar um banco de dados para alimentar modelos analíticos. Com isso, modelos numéricos foram desenvolvidos utilizando o software DIANA® para, posteriormente, serem calibrados. A calibração foi realizada variando parâmetros do concreto não explicitados no trabalho de Joergensen e Hoang [15], tomado como base, como o módulo de elasticidade, resistência à tração, energia de fratura à tração e à compressão, largura de banda de fissuração, redução da resistência à compressão do concreto fissurado e diâmetro médio dos agregados. Para a obtenção desses parâmetros, foram utilizadas as normas CEB 2010 [8] e 1990 [7] e o trabalho de Hilsdorf e Brameshuber [14].
Com os modelos calibrados, foram realizados estudos paramétricos no software DIANA®, variando os seguintes parâmetros da geometria da emenda: comprimento de traspasse e espaçamento entre laços. Após isso, os resultados da análise paramétrica foram comparados com os valores obtidos através dos modelos analíticos da literatura.

3. Desenvolvimento

Os modelos numéricos desenvolvidos neste artigo foram calibrados com base nos ensaios de tração realizados por Joergensen e Hoang [15], ver Figura 3. Estes autores realizaram ensaios de tração em peças constituídas por 3 blocos de concreto armado, sendo que os blocos de extremidade serviam apenas para proporcionar rigidez à estrutura para facilitar o ensaio, já o bloco central continha a emenda em laço. As barras dos laços se estendiam além dos blocos de extremidade, onde os autores impuseram deslocamentos progressivos nas barras de um lado e engaste nas outras. Os parâmetros variados por Joergensen e Hoang [15] foram: a espessura da junta de concretagem, o comprimento da junta, a distância entre os laços, o comprimento de traspasse dos laços, o diâmetro das barras transversais, o diâmetro da barra do laço, a tensão de escoamento da armadura transversal e a tensão de escoamento da barra do laço.
Nesse trabalho, os autores forneceram apenas a resistência à compressão do concreto, de 38,4 MPa, e o diâmetro máximo dos agregados, de 8 mm, por isso, fez-se necessário o cálculo dos outros parâmetros do concreto apenas com base nessas

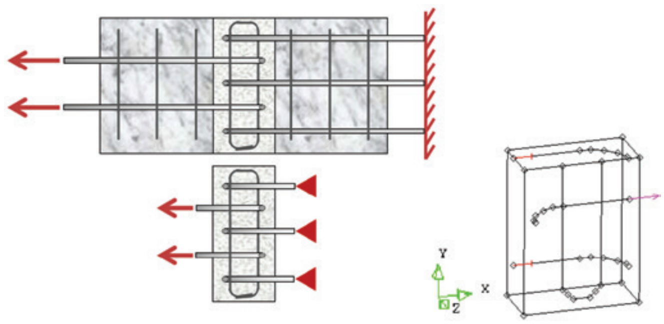

Figura 5
Representação das condições de contorno no experimento (esquerda/em cima) e no modelo numérico (esquerda/embaixo e direita)

informações. Dessa forma, serão apresentados os resultados obtidos com os parâmetros calculados pela norma CEB 2010 [8] e quando explicitado, para alguns dos parâmetros utilizados, os cálculos foram também realizados pela norma CEB 1990 [7] e com base no trabalho de Hilsdorf e Brameshuber [14].

3.1 Malha

Para a modelagem do concreto, foram utilizados elementos sólidos do tipo CHX60, de vinte nós e aproximação quadrática. Para as armaduras, foram utilizados elementos de viga do tipo L13BE com dois nós. Ambos os elementos estão contidos na biblioteca do programa DIANA® 9.5 [10]. O tempo de processamento médio de um modelo foi de 3,5 dias.
Para a modelagem do bloco, utilizaram-se elementos sólidos de lados iguais e comprimento de 10 mm. A partir da malha do concreto, fez-se a divisão dos elementos de viga, a fim de coincidir todos os seus nós com os nós dos elementos sólidos do concreto.

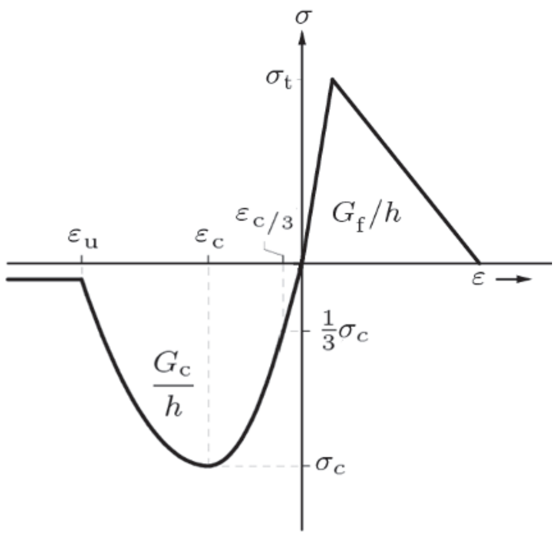

Figura 6
Comportamento do concreto

Logo, as partes curvas da armadura, como a curva do laço, são representadas por vários elementos de viga retos.
Com o objetivo de reduzir ainda mais o tempo das simulações, tomou-se vantagem da dupla simetria do problema, além de modelar apenas a junta de concretagem do elemento ensaiado por Joergensen e Hoang [15] (ver Figura 4).

3.2 Carregamento e condições de contorno

No ensaio experimental de tração realizado por Joergensen e Hoang [15], foi aplicado deslocamento nas barras do lado que contém a menor quantidade de laços, enquanto as barras do lado oposto foram engastadas, assim, no modelo proposto do presente trabalho, aplicou-se deslocamento em X na extremidade do laço único e restringiu-se na mesma direção os deslocamentos das extremidades dos laços opostos.
Os elementos utilizados nos experimentos dos autores supracitados são constituídos por 3 blocos de concreto: o bloco da junta e os outros dois blocos de extremidade. Entre os blocos, as interfaces foram tratadas de forma que houvesse o mínimo de aderência, nesse contexto, pode-se desconsiderar a restrição à translação da junta no plano da interface dos blocos devido ao contato entre eles. Assim, os graus de liberdade de translação nesse plano ficam apenas restritos pelo efeito pino das barras dos laços.
Por fim, devido à consideração da dupla simetria no modelo, também foram impostas restrições de translação em Z da superfície de simetria do plano XY e restrições de translação em Y da superfície de simetria do plano XZ. A Figura 5 ilustra as condições de contorno e de carregamento do problema. Para a resolução do sistema de equações não linear do problema, utiliza-se o método da rigidez linear, além de utilizar o critério de convergência em energia com uma tolerância de 10^{-3}.

3.3 Parâmetros do concreto

Para as simulações, o concreto foi modelado com o modelo de fissuração fixa baseado na deformação total (Total Strain Fixed Crack Model), disponível no software DIANA® 9.5 [9]. No modelo de fissuração fixa, as direções das fissuras ficam fixas e definidas a partir da abertura das primeiras fissuras em cada nó dos elementos, as quais são as direções das tensões principais. Dessa forma, quando se atinge o critério de ruptura, as direções e posições das fissuras são guardadas e utilizadas nos incrementos de carga posteriores. Esse modelo de fissuração foi desenvolvido com base na Teoria do Campo Modificado de Compressão, proposta por Vecchio e Collins [23].
Para todas as análises, o coeficiente de Poisson foi considerado constante e igual a 0,2, mesmo após a fissuração do concreto.
A redução da tensão de tração normal ao plano da fissura não

Tabela 1
Valores de G_{fo} e a_d

$d_{máx}$ (mm)	G_{fo} (N_m/m^2)	a_d
8	25	4
16	30	6
32	58	10

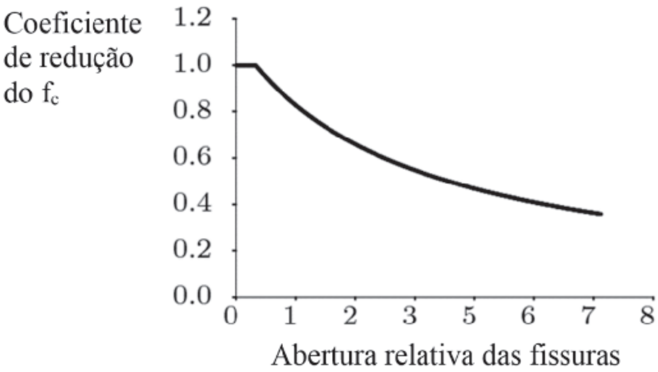

Figura 7
Modelo de redução lateral proposto por Vecchio e Collins (1993)

se dá de forma total, ela é progressiva com o aumento das deformações, dessa forma, o comportamento do concreto à tração em um estado uniaxial foi adotado com redução linear. Além disso, o módulo de elasticidade adotado na tração foi o mesmo da compressão, como mostrado na Figura 6.

A energia de fratura à tração é definida como a energia necessária para propagar a fissura de tração de uma unidade de área [14], podendo ser estimada da seguinte maneira:

De acordo com o CEB 2010 [8], tem-se a Equação 1:

$$G_f = 73 f_c^{0,18}\ (Nm/m^2) \tag{1}$$

De acordo com o CEB 1990 [7], tem-se a Equação 2:

$$G_f = G_{f0}\left(\frac{f_c}{10}\right)^{0,7}\ (Nm/m^2) \tag{2}$$

De acordo com Hilsdorf e Brameshuber [14], tem-se a Equação 3:

$$G_f = a_d f_c^{0,7}\ (Nm/m^2) \tag{3}$$

Onde G_{fo} é o valor de base da energia de fratura e a_d é um coeficiente de ajuste da função, os quais dependem do diâmetro máximo dos agregados $d_{máx}$ cujos valores são dados na Tabela 1. Pode-se calcular a largura de banda de fissuração de acordo com a Equação 4 a seguir:

$$h = \frac{2G_f}{\varepsilon_{cu} f_t}. \tag{4}$$

Onde ε_{cu} é a deformação última do concreto na tração e f_t é a resistência do concreto à tração. Considerando ε_{cu} como a deformação no momento do escoamento de um aço CA-50, como é o caso, foi adotado ε_{cu} = 0,24%.

O comportamento do diagrama tensão-deformação do concreto na compressão uniaxial foi tomado como parabólico, como mostrado na Figura 6. Esse comportamento depende da energia de fratura à compressão G_c e da largura de banda de fissuração h. Portanto, a energia de fratura à compressão é dada pela Equação 5:

$$G_c = h f_c \frac{2}{3}(\varepsilon_u - \varepsilon_c) \tag{5}$$

Onde G_c é dado em Nmm/mm², h é considerado em mm, f_c é a resistência à compressão do concreto em MPa, ε_c é a deformação de pico e ε_u é a deformação última do concreto sob compressão uniaxial. Também foi considerado nesse modelo o comportamento biaxial do concreto, considerando assim o confinamento lateral implementado no DIANA® 9.5 [10], baseado no modelo proposto por Selby e Vecchio [21]. Além disso, outro fator importante é a consideração do comportamento da resistência à compressão do concreto após a formação de fissuras, pois há uma redução da resistência do concreto paralelo às fissuras, bem como da rigidez à compressão. Esse fenômeno é mais conhecido como amolecimento, o qual foi tomado como base o modelo implementado no DIANA® 9.5 [10], baseado no modelo de Vecchio e Collins [24], mostrado na Figura 7. Nesta figura, a unidade da abertura relativa das fissuras é deformação/deformação, pois é a relação da deformação de abertura das fissuras e uma deformação de referência que os autores, Vecchio e Collins [24], consideraram.

A resistência à compressão do concreto da região nodal formada pela biela de compressão e o laço pode ser calculada através da Equação 6, do item 6.5.4 do Eurocódigo 2:2004.

$$f_c = 0{,}85\nu' f_{cd} \tag{6}$$

Onde é um coeficiente dado pela Equação 7:

$$\nu' = 1 - \frac{f_c}{250}. \tag{7}$$

O Eurocódigo 2:2004, no item 6.5.2, apresenta uma formulação para estimar a resistência à compressão do concreto fissurado, com fissuras na direção paralela à aplicação da compressão, dada pela Equação 8:

$$f_{cf} = 0{,}6\nu' f_{cd}. \tag{8}$$

Logo, a redução da resistência à compressão do concreto devido à fissuração é dada pela Equação 9:

$$Red = \frac{f_{cf}}{f_c}. \tag{9}$$

Após a fissuração, a rigidez ao cisalhamento do concreto reduz, no entanto, o mesmo ainda possui capacidade de transmitir tensões de cisalhamento devido ao engrenamento dos agregados e

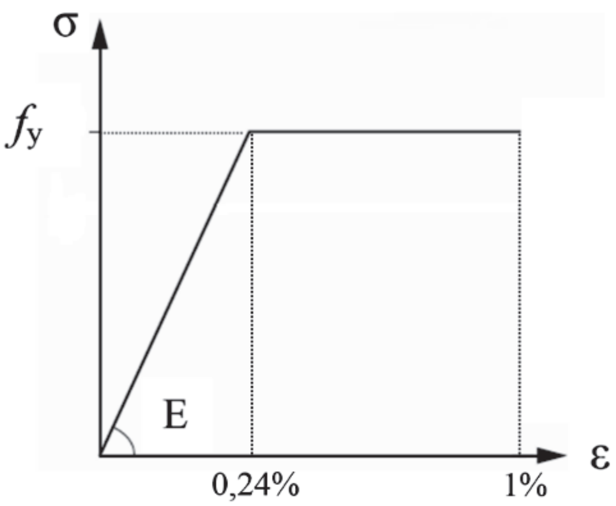

Figura 8
Comportamento do aço

Tabela 2
Geometria, propriedades e resultados dos elementos ensaiados

Elemento	b (mm)	L (mm)	a (mm)	H (mm)	ϕ_T (mm)	f_{yT} (MPa)	$N_{u,exp}$ (A/B) (kN)
10A/B	210	460	80	170	10	632,1	387,1/391,4
11A/B	*	380	60	*	*	*	459,6/419,6
12A/B	*	300	40	*	*	*	509,4/595,3
13A/B	265	540	100	225	*	*	479,5/470,5
14A/B	340	*	*	300	*	*	571,6/550,7
15A/B	490	*	*	450	*	*	597,5/648,4

* Mesmo valor que o anterior,

ao efeito pino das armaduras. O DIANA® 9.5 [10] modela essa redução por meio da aplicação de um coeficiente redutor na rigidez ao cisalhamento, de acordo com a Equação 10:

$$G^{cr} = \beta G. \quad (10)$$

Onde G^{cr} é a rigidez ao cisalhamento do concreto fissurado, G é a rigidez ao cisalhamento do concreto íntegro e β é um coeficiente de retenção do cisalhamento, o qual varia de 0 a 1. No presente trabalho, o coeficiente β é tomado como variável e proporcional à abertura das fissuras. Assumindo que todo o contato é perdido uma vez que o comprimento da fissura torna-se maior que a metade do diâmetro médio dos agregados, a retenção do cisalhamento pode ser calculada pela Equação 11:

$$\beta = 1 - \frac{2}{d_{agg}} \varepsilon_n h. \quad (11)$$

Onde d_{agg} é o diâmetro médio dos agregados, ε_n é a deformação normal à fissura e h é a largura de banda de fissuração. Como foi dado que o diâmetro máximo dos agregados $d_{máx}$ é de 8 mm, adotou-se, no presente trabalho, um diâmetro médio dos agregados de 5 mm.

3.4 Comportamento do aço

O aço foi tomado como tendo comportamento elastoplástico perfeito, apresentando o mesmo comportamento na tração e na compressão e critério de plastificação de Von Mises. O comportamento uniaxial do aço está representado na Figura 8.

3.5 Validação dos modelos numéricos

A calibração foi realizada com base nas curvas que relacionam a força aplicada na emenda com o deslocamento relativo entre as interfaces da junta e do concreto pré-moldado. Vale ressaltar que o diâmetro das barras é de 20 mm e a tensão de escoamento das barras é de 560,9 MPa.

Os modelos cujos parâmetros foram calculados pelas expressões de normas, como mostrado nas seções anteriores, foram utilizados como referência para a calibração. Utilizaram-se 6 curvas para validar os modelos numéricos do presente trabalho, as quais são relativas aos elementos cujas características são mostradas na Tabela 2.

As letras A e B, depois do número dos elementos, indicam que, para cada conjunto de parâmetros fixos, foram moldados dois elementos. Além disso, b é a espessura da junta em mm, L é o comprimento da junta em mm, a é a distância entre laços em mm, H é o comprimento de traspasse em mm, ϕ_t é o diâmetro das barras transversais em mm, f_{yT} é a tensão de escoamento das barras transversais em MPa e $N_{u,exp}$ é a carga última de tração dos elementos em kN. Com isso, os resultados da calibração estão mostrados na Figura 9 e na Tabela 3.

Nos elementos 10A, 11A e 12A, nos quais ocorre variação da distância entre laços, percebe-se que à medida que esse parâmetro diminui, a disparidade entre as curvas aumenta. Isso ocorre, pois essa redução do espaçamento não é acompanhada por um refinamento da malha, o que reduz a quantidade de elementos entre os laços. Isso poderia ser resolvido com uma melhor discretização dessa região, porém o tempo das simulações inviabilizaria a quantidade de análises necessária no estudo. Apesar disso, a diferença

Tabela 3
Carga última dos modelos

Elemento	Carga última (kN)		Num/Exp
	Numérico (Num)	Experimental (Exp)	
10A	399,6	389,3	1,03
11A	412,0	439,6	0,94
12A	464,0	552,4	0,84
13A	572,0	475,0	1,20
14A	708,0	561,2	1,26
15A	712,0	623,0	1,14

Tabela 4
Valores dos parâmetros do concreto calculados com o CEB 2010 e calibrados

Parâmetro	Valores calculados	Valores calibrados	Unidade
E_{ci}	43.032	40.000	MPa
Poisson	0,2	0,2	–
f_{ct}	3,41	4,00	MPa
G_f	0,051 (1)	0,050	Nmm/mm²
h	15,78 (2)	15,00	mm
f_c	38,4	38,4	MPa
G_c	1,38	1,00	Nmm/mm²
$f_{c,mín}$	0,71 f_c	0,70 f_c	MPa
d_{agg}	5 (3)	5	mm

(1) Valor calculado por Hilsdorf e Brameshuber (1991);
(2) Valor calculado pelo CEB 1990;
(3) Valor inicialmente estimado.

máxima entre as resistências desses modelos e as dos experimentais é de 16%, o que demonstra uma boa aproximação. Quanto aos modelos 13A, 14A e 15A, nos quais há variação do comprimento de traspasse longitudinal, observa-se que à medida que esse parâmetro aumenta, há uma maior divergência entre as rigidezes dos modelos numéricos e experimentais, com uma tendência de ser menor nestes últimos. Isso ocorre, pois nos modelos numéricos se considerou aderência perfeita, ou seja, não há escorregamento entre a parte reta da armadura em laço e o concreto envolvente, o que leva a uma maior rigidez, aumentando a disparidade de comportamento quanto maior for o traspasse. Para o elemento 13A, apesar de as resistências divergirem, o comportamento dos modelos é bastante

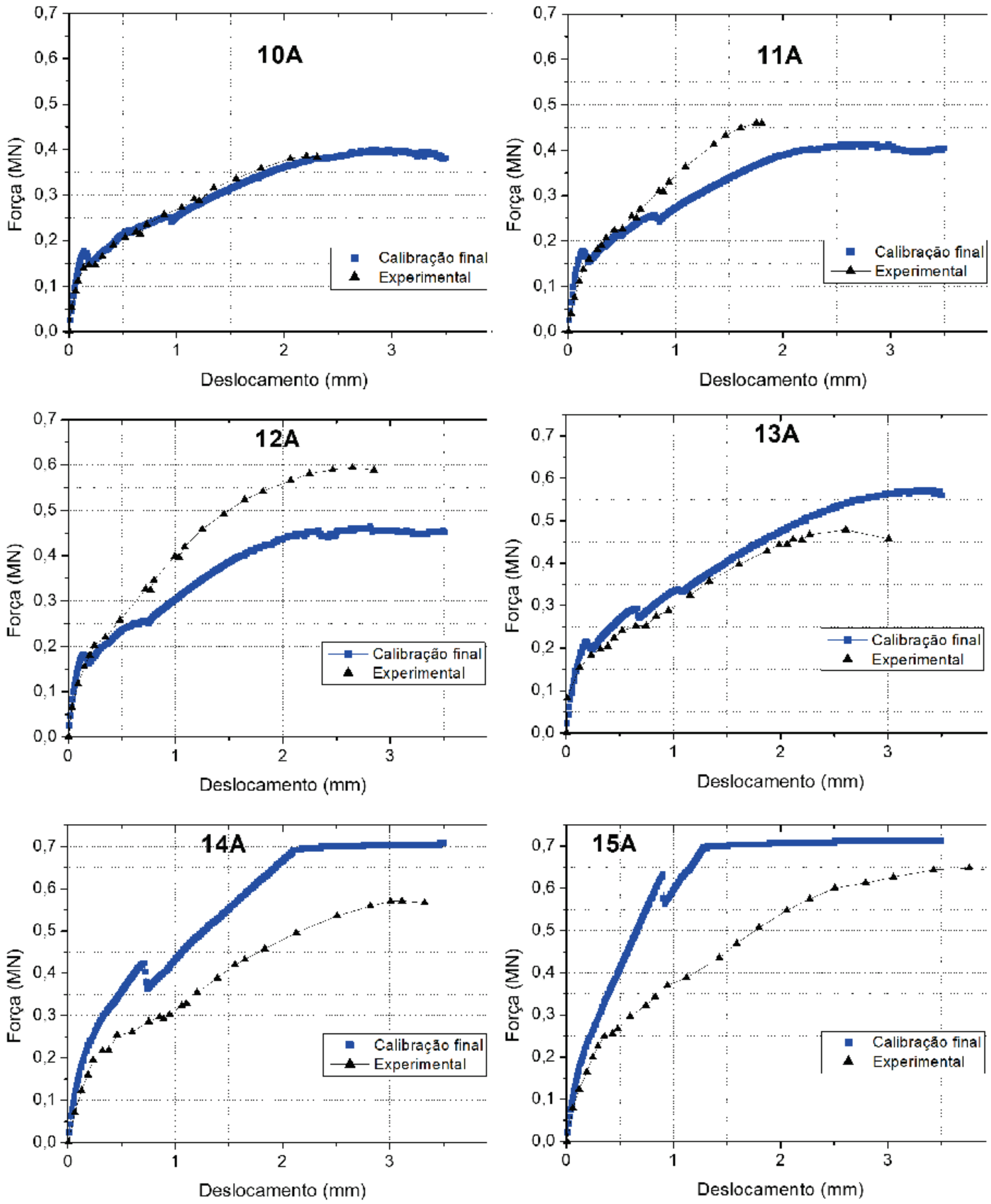

Figura 9
Calibração final dos elementos

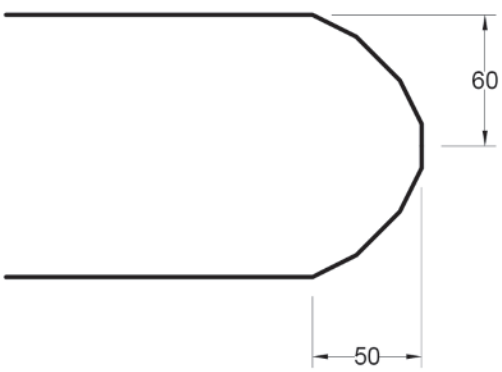

Figura 10
Dimensões da dobra do laço em mm

similar na maior parte do carregamento. Já os modelos 14A e 15A apresentam resistências muito próximas da resistência ao escoamento da armadura, mostrando-se como limites para projeto, como será explicado adiante. Portanto, para valores de traspasse menores que o utilizado nesses dois últimos modelos, o comportamento dos modelos numéricos se aproxima do comportamento dos modelos experimentais.

Os valores dos parâmetros calibrados estão mostrados na Tabela 4. Vale ressaltar que a maioria dos parâmetros foi calibrada com base nos valores calculados com o CEB 2010 [8].

Dessa forma, pode-se considerar o código normativo CEB 2010 [8] e 1990 [7] para o cálculo dos parâmetros do concreto quando da análise de outros tipos de concreto, pois os valores obtidos com estas normas estão muito próximos dos valores calibrados, como pode ser visto na Tabela 4. Além disso, o trabalho de Hilsdorf e Brameshuber [14] pode ser utilizado para as variáveis relativas à energia de fratura.

3.6 Análise paramétrica

Com os modelos calibrados, fez-se uma análise paramétrica. Para tal, os parâmetros analisados foram o espaçamento e o traspasse entre laços, já que a calibração conseguiu capturar razoavelmente bem suas variações.

A ideia dos laços é promover uma emenda entre barras de modo que um laço possa transmitir tensões de tração para o laço do lado oposto, tanto através da tensão de aderência entre aço e concreto, através do surgimento de pequenas bielas entre as partes retas dos laços, quanto através das tensões radiais ao laço, formando, neste último caso, uma biela única e maior de compressão entre as armaduras. Por isso, para otimizar a transmissão de esforços através das bielas, deve-se dispor os laços o mais próximo possível.

A ABNT NBR 6118:2014 [3], no item 9.5.2.2, fornece uma fórmula para o cálculo do comprimento de traspasse de barras retas tracionadas cuja distância livre não exceda 4 vezes o diâmetro da barra, caso contrário, deve-se majorar o traspasse, além disso, Bruggeling e Huyge [6] também recomendam esse valor como limite superior para emendas em laço. Dessa forma, a situação ideal para a transmissão de tensão entre barras retas traspassadas é quando a distância entre elas é menor ou igual a 4 vezes seu diâmetro. Portanto, considerando apenas o mecanismo de transmissão de barras retas, devemos dispor os laços com uma distância livre de no máximo 80 mm, correspondente a um espaçamento de 100 mm entre eixos, considerando a barra de 20 mm utilizada nos modelos.

Em relação ao segundo modo de transmissão de tensões, através do surgimento de tensões radiais ao laço e consequente formação de bielas de compressão, a melhor disposição das barras emendadas é quando estão em contato, ou seja, distância livre 0 e espaçamento de 20 mm, pois, neste caso, dá-se uma inclinação mínima à biela de compressão entre os laços, sendo mais solicitada pela emenda, otimizando o mecanismo de transmissão. Logo, à medida que o espaçamento entre os laços aumenta, mais eles se comportarão como laços isolados, sem interação entre eles. Portanto, para a análise paramétrica, variou-se o espaçamento entre laços de 20 mm até 100 mm, com valores intermediários de 40, 60 e 80 mm.

Os laços devem ser traspassados de forma que surjam bielas entre eles com a maior altura possível, ou seja, para que isso ocorra, os laços devem ser traspassados, no mínimo, no valor do diâmetro de dobra deles, como recomendado por Dragosavić et al.[11], os quais também recomendam respeitar o valor mínimo de 13 vezes o diâmetro das barras, que para o caso em estudo é de 260 mm. Os modelos foram calibrados com base nas amostras de emendas ensaiadas por Joergensen e Hoang[15], cujo diâmetro de dobra dos laços é de 110 mm, porém, a fim de otimizar o desenho do laço por meio de trechos retos de elementos de viga, os quais deveriam ter seus nós coincidentes com os nós dos elementos sólidos do concreto, os laços dos modelos ficaram com diâmetros diferentes nas direções do traspasse e perpendicular a este, de 100 e 120 mm, respectivamente, como mostrado na Figura 10. Por isso, para as verificações supracitadas, considerou-se um diâmetro de 100 mm, constante ao longo das análises.

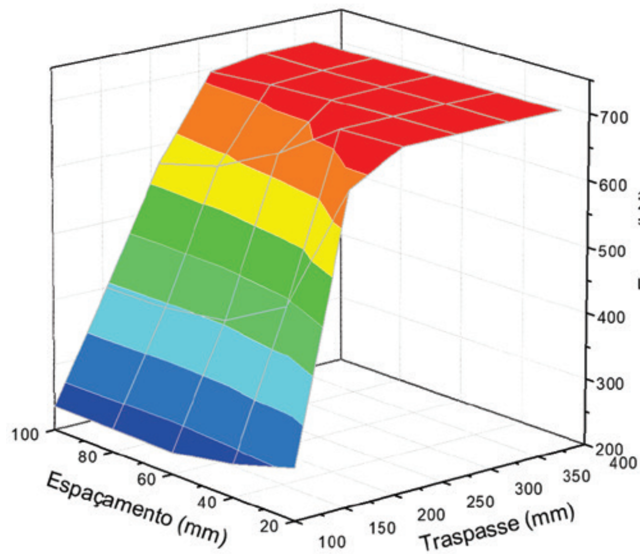

Figura 11
Representação dos resultados da análise paramétrica

Tabela 5
Força última dos elementos, em kN

Traspasse (mm)	Espaçamento (mm)				
	20	40	60	80	100
100	278,1	249,6	232,9	234,6	235,9
170	666,0	464,0	412,0	399,6	400,0
225	711,6	708,8	645,2	596,4	572,0
250	712,4	710,4	707,2	703,2	695,6
300	713,2	712,4	710,8	708,4	708,0
370	713,6	713,2	712,0	710,8	709,6

Ao analisar os resultados da calibração, percebe-se que ocorreu falha por escoamento dos laços nos elementos 14A e 15A, portanto, esses elementos foram utilizados como referência de limite superior para o traspasse, pois a carga de ruptura por escoamento é conhecida e não pode ser ultrapassada. Nesses elementos, os traspasses são de 300 e 450 mm, respectivamente. Com isso, considerando um valor em torno da média destes, para a análise em questão, tomou-se como traspasse máximo 370 mm. Logo, os valores de traspasse utilizados na análise foram: 100, 170, 225, 250, 300 e 370 mm.
Os resultados das simulações estão representados na Figura 11. Nota-se que à medida que o traspasse aumenta, a resistência da emenda também aumenta, além disso, a superfície possui um patamar bem definido para valores de traspasse a partir de 250 mm. Dessa forma, percebe-se que a partir desse valor de traspasse, a falha da emenda tende a ocorrer por escoamento das barras dos laços. Observa-se também que há uma leve tendência de aumento da capacidade de carga da emenda quanto menor o espaçamento entre os laços.
Em ensaios de arrancamento de barras retas de aço em concreto simples, há quatro formas de falha [1] (*apud* [20]):

- Arrancamento: consiste no escorregamento da barra;
- Fendilhamento: referente à ruptura do concreto adjacente à barra de aço;

Tabela 6
Modelos analíticos de emendas em laço submetidas à tração

Modelo analítico	Tipo de emenda	Princípio	Formulação da capacidade de carga da emenda
Hao [13]	2 to 1	Modelo de bielas e tirantes	$N_u = \dfrac{270hHf_c^{\,0,21}}{\sqrt{H^2+a^2}}$
Araújo et al. [2]	1 to 1	Modelo de bielas e tirantes	$N_u = (D+2\phi)w_t f_{cn}\dfrac{H}{\sqrt{s^2+H^2}}$ $w_t = \dfrac{(0.6894-0.0022D)s}{\lambda}$ $\lambda = 0.014s + 0.553 \geq 0.86$ $f_{cn} = 0{,}85 f_c$
Joergensen e Hoang [15]	3 to 2	Princípio da mínima energia	$\dfrac{N_c}{\nu f_c A_c} = 2\begin{cases} \left(\sqrt{\dfrac{4\Phi}{\nu}\left(1-\dfrac{\Phi}{\nu}\right)+\left(\dfrac{a}{H}\right)^2}-\dfrac{a}{H}\right); & se\ \alpha \geq \varphi\ e\ \alpha \geq \beta\ (a) \\ \dfrac{2\left(\dfrac{\Phi}{\nu}\left(3-4\dfrac{a}{H}\right)+\left(\dfrac{a}{H}\right)^2+1\right)}{4+3\dfrac{a}{H}}; & se\ \alpha < \varphi\ e\ \dfrac{a}{H} < \dfrac{3}{4}\ (b) \\ \sqrt{\left(\dfrac{a}{H}\right)^2+1}-\dfrac{a}{H}; & se\ \alpha < \beta\ e\ \dfrac{a}{H} \geq \dfrac{3}{4}\ (c) \end{cases}$ $\Phi = \left(\dfrac{A_{sT}f_{yT}}{A_c f_c}\right)$ $\nu = \dfrac{0{,}88}{\sqrt{f_c}}\left(1+\dfrac{1}{\sqrt{H}}\right)$ $\alpha = \beta + \sin^{-1}\left(\dfrac{1-\dfrac{2\Phi}{\nu}}{\sqrt{\left(\dfrac{a}{H}\right)^2+1}}\right)$ $\beta = Arctan(a/H)$ $N_u = mín\begin{cases} N_c & (falha\ no\ concreto) \\ N_y = 2A_{sL}f_{yL} & (escoamento\ da\ armadura\ do\ laço) \end{cases}$

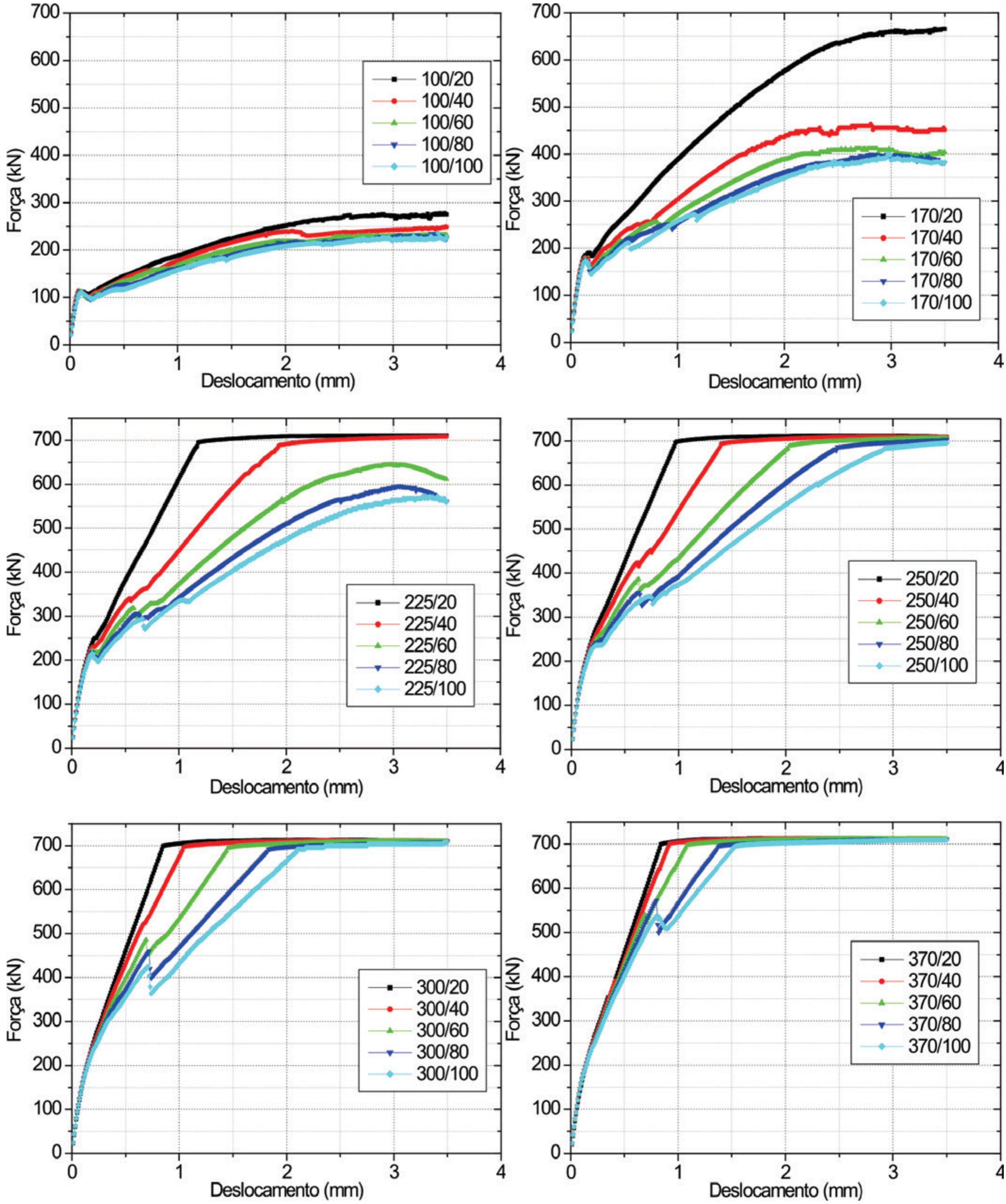

Figura 12
Gráficos das emendas com traspasse constante

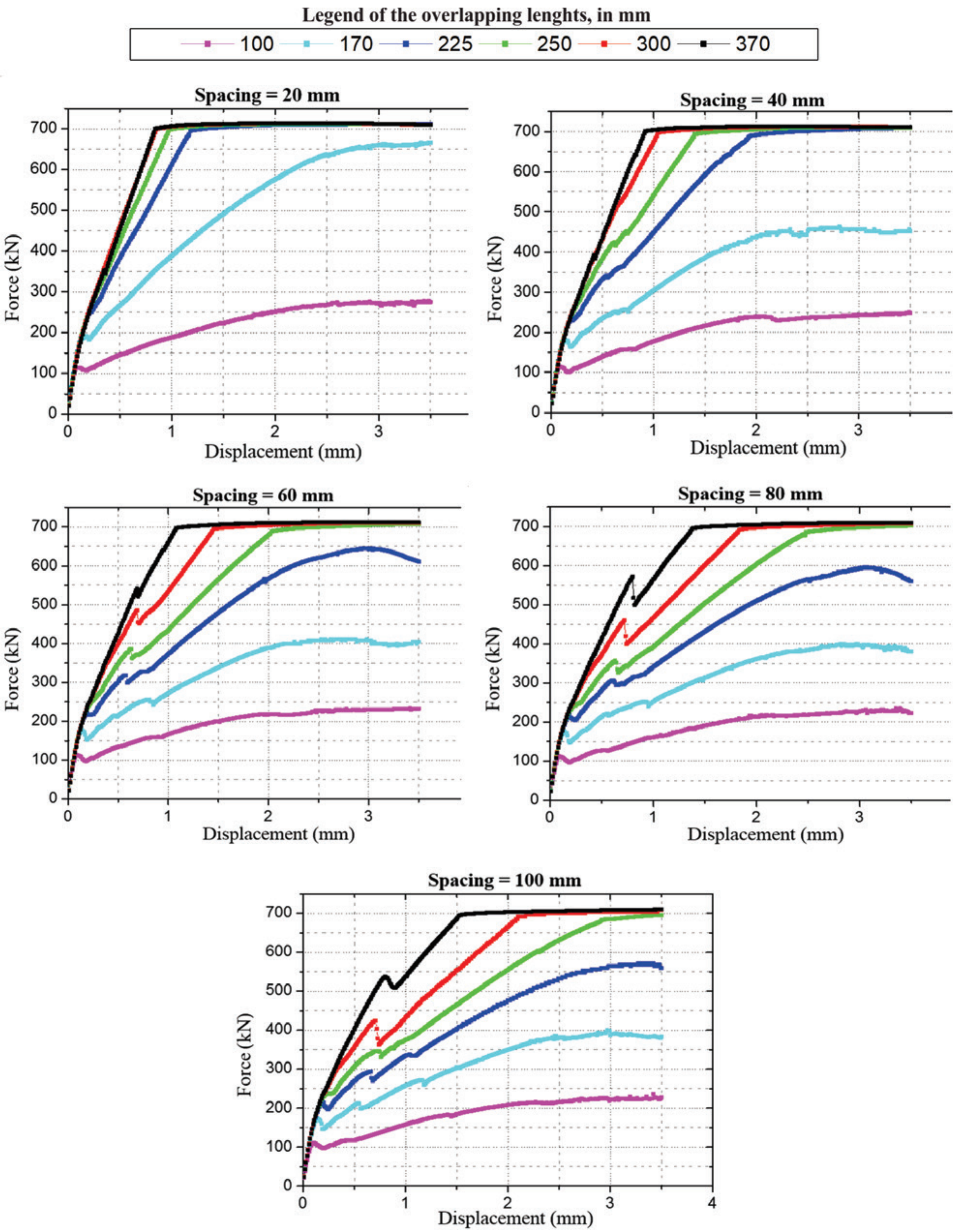

Figura 13
Gráficos das emendas com espaçamento constante

- Tração: consiste na formação de fissuras perpendiculares à direção da aplicação da força; e
- Ruptura do aço: relativa ao escoamento da barra.

Os três primeiros fenômenos acima levam à ruptura apenas de barras retas embebidas no concreto, portanto, não levam à ruptura de emendas do tipo laço, pois, mesmo que ocorram, ainda haverá a contribuição da parte curva do laço na resistência da emenda através da formação de bielas de compressão. Logo, em emendas do tipo laço, há apenas dois modos principais de ruptura: falha na biela de compressão e escoamento do laço.

Na Tabela 5, estão mostrados os valores da força última para cada geometria da emenda, de acordo com seu traspasse e espaçamento entre laços.

Nessa tabela, as combinações cuja falha ocorreu por escoamento da armadura do laço estão realçadas em vermelho, sendo as combinações restantes relativas à ruptura do concreto da biela de compressão. Vale ressaltar que, neste caso, considerou-se a tensão de 560,9 MPa como referência para o escoamento, a qual corresponde a uma força última de 704,85 kN.

Dessa forma, para os traspasses de 100 e 170 mm, há uma tendência de ocorrer ruptura no concreto para qualquer espaçamento entre laços; já para os traspasses acima de 300 mm, há uma tendência de ocorrer ruptura por escoamento das barras para qualquer espaçamento entre laços.

Na Figura 12, estão mostrados os gráficos Força aplicada na barra x Deslocamento entre interfaces, relativos às emendas com variação do espaçamento e traspasse constante. Na legenda dos gráficos, o primeiro valor refere-se ao traspasse e o segundo, ao espaçamento entre laços.

Nessa figura, percebe-se que para o traspasse de 100 mm, praticamente não há modificação no comportamento da emenda, além disso, a capacidade de carga destas emendas é muito inferior às demais. Dessa forma, esse traspasse se mostra insuficiente para a transmissão de esforços através das bielas de compressão formada entre os laços. Já para o traspasse de 170 mm, há um crescimento significativo na força última, principalmente para o espaçamento de 20 mm, o qual aumenta em cerca de 140 % com relação ao traspasse de 100 mm, alcançando um valor próximo ao correspondente à tensão de escoamento das barras. Já a partir do traspasse de 225 mm, começa a ocorrer ruptura por escoamento das barras.

Tabela 7
Comparação dos resultados com modelos analíticos

Espaçamento	Traspasse	Modelo	Hao	Araújo	Joergensen	M/H	M/A	M/J
20	100	278,1	227,8	199,8	398,7	1,2	1,4	0,70
	170	666,0	230,8	202,4	590,5	2,9	3,3	1,13
	225	704,8	231,4	203,0	704,8	3,0	3,5	1,00
	250	704,8	231,6	203,1	704,8	3,0	3,5	1,00
	300	704,8	231,8	203,3	704,8	3,0	3,5	1,00
	370	704,8	232,0	203,5	704,8	3,0	3,5	1,00
40	100	249,6	215,7	292,4	312,9	1,2	0,9	0,80
	170	464,0	226,2	306,5	517,4	2,1	1,5	0,90
	225	704,8	228,8	310,0	632,8	3,1	2,3	1,11
	250	704,8	229,4	310,9	677,9	3,1	2,3	1,04
	300	704,8	230,3	312,1	704,8	3,1	2,3	1,00
	370	704,8	231,0	313,1	704,8	3,1	2,3	1,00
60	100	232,9	199,2	323,6	257,5	1,2	0,7	0,90
	170	412,0	219,1	355,9	455,4	1,9	1,2	0,90
	225	645,2	224,5	364,7	568,8	2,9	1,8	1,13
	250	704,8	225,9	367,0	613,6	3,1	1,9	1,15
	300	704,8	227,8	370,1	694,2	3,1	1,9	1,02
	370	704,8	229,3	372,5	704,8	3,1	1,9	1,00
80	100	234,6	181,4	327,2	218,4	1,3	0,7	1,07
	170	399,6	210,2	379,1	403,2	1,9	1,1	0,99
	225	596,4	218,9	394,8	513,1	2,7	1,5	1,16
	250	703,2	221,3	399,0	557,0	3,2	1,8	1,26
	300	704,8	224,5	404,8	636,6	3,1	1,7	1,11
	370	704,8	227,1	409,5	704,8	3,1	1,7	1,00
100	100	235,9	164,3	317,2	188,1	1,4	0,7	1,25
	170	400,0	200,3	386,7	359,4	2,0	1,0	1,11
	225	572,0	212,3	410,0	464,8	2,7	1,4	1,23
	250	695,6	215,7	416,5	507,4	3,2	1,7	1,37
	300	708,0	220,4	425,6	585,3	3,2	1,7	1,21
	370	704,8	224,3	433,1	681,6	3,1	1,6	1,03

Tabela 8
Média, desvio padrão e coeficiente de variação das relações

	M/H	M/A	M/J
Média	2,60	1,87	1,05
Desvio padrão	0,73	0,84	0,14
Coeficiente de variação	0,28	0,45	0,13

Percebe-se também que a partir do traspasse de 300 mm, a única diferença no comportamento das emendas está relacionada com a rigidez da ligação, sendo maior quanto menor o espaçamento, apresentando ruptura por escoamento das barras para qualquer espaçamento entre laços. Além disso, a partir desse traspasse, a parte curva dos laços passa a ser cada vez menos solicitada, fazendo com que as barras trabalhem apenas como barras retas embebidas no concreto. Por fim, nota-se também que não há muita diferença no comportamento das emendas com espaçamento de 80 e 100 mm, portanto, a partir desses espaçamentos, há uma maior tendência de os laços trabalharem isoladamente, ou seja, reduz a tendência de formação de bielas de compressão entre os laços.
Na Figura 13, estão mostrados os gráficos Força x Deslocamento das emendas com variação do traspasse e espaçamento constante. Para o espaçamento entre laços de 20 mm, ou seja, quando as barras emendadas estão em contato, com traspasse maior ou igual a 300 mm, o comportamento das emendas sob tração é bastante similar entre si, como pode ser observado nos gráficos correspondentes aos traspasses de 300 e 370 mm, cujas curvas estão sobrepostas na maior parte dos pontos. Dessa forma, à medida que o comprimento de traspasse aumenta, as emendas tendem a um mesmo comportamento, representado pela curva correspondente à emenda com espaçamento de 20 mm e traspasse de 300 mm. Isso mostra que esse traspasse já é o suficiente para emendar barras retas, pois para valores a partir deste, a ruptura tende a ocorrer por escoamento das barras. Percebe-se também que à medida que o espaçamento aumenta, a capacidade de carga e a rigidez da emenda diminuem.
Por fim, quanto menor o espaçamento entre laços e maior o traspasse entre eles, maior será a capacidade de carga da emenda estudada. Vale destacar também, que o laço pode causar o fendilhamento do concreto caso não haja cobrimento de concreto suficiente ao redor dele, capaz de promover um adequado confinamento da armadura. No entanto, este tipo de ruptura não foi avaliado neste estudo.

3.7 Modelos analíticos de emendas em laço submetidas à tração

Para emendas em laço submetidas à tração, os modelos analíticos obtidos da literatura estão descritos na Tabela 6, onde estão presentes os modelos de Hao [13], Araújo et al. [2] e Joergensen e Hoang [15].
Na formulação de Hao [13], N_u é a força última na emenda, h é a altura do elemento de concreto, H é o comprimento de traspasse dos laços, f_c é a resistência do concreto à compressão e a é o espaçamento entre laços.
Nas formulações de Araújo et al. [2], N_u é a força última na emenda, D é o diâmetro interno do laço, ϕ é o diâmetro da barra, w_t é a espessura efetiva da biela inclinada, f_{cn} é a resistência à compressão da biela, H é o comprimento de traspasse dos laços, S é o espaçamento interno entre laços, λ é um coeficiente relacionado com o efeito de amolecimento do concreto e f_c é a resistência do concreto à compressão.
Nas formulações de Joergensen e Hoang [15], N_c é a resistência da emenda considerando apenas a falha na biela de compressão entre laços, V é um fator de correção que leva em conta o fato de que o concreto não é um material perfeitamente plástico, f_c é a resistência à compressão do concreto, A_c é a área de concreto entre laços projetada no plano do laço, Φ Φ é a taxa mecânica de armadura transversal, a é o espaçamento entre laços, H é o traspasse entre laços, α é a inclinação do deslocamento relativo no plano de ruptura em relação a esse plano, φ é o ângulo de atrito do concreto, considerado igual a Arctan(3/4) para concretos de resistência normal, β é a inclinação do plano de ruptura em relação ao plano do laço, A_{sT} é a área de aço transversal ao plano do laço, é a tensão de escoamento das barras transversais, N_y é a resistência da emenda considerando apenas o escoamento do laço, A_{sL} é a área total de aço de um laço e f_{yL} é a tensão de escoamento da barra do laço.
As formulações propostas por Hao [13] e Araújo et al. [2] são bastante similares, isso se deve ao fato de ambas se basearem no modelo de bielas e tirantes. A diferença entre os modelos está na consideração da seção transversal das bielas de compressão. Com relação à altura da biela de compressão, Hao [13] considera igual à altura da junta, enquanto Araújo et al. [2] consideram igual à altura do laço, ou seja, . Já em relação à espessura da biela w_t, a qual é o parâmetro de maior divergência entre os autores, Hao [13] estabelece o cálculo baseado apenas na resistência à compressão do concreto, enquanto Araújo et al. [2] definem equações baseadas no diâmetro do laço e no espaçamento entre eles.
Apesar de os modelos propostos pelos autores anteriores terem apresentado resultados satisfatórios em relação aos respectivos resultados experimentais, eles não levam em consideração alguns dos parâmetros que definem a junta, tais como a taxa de armadura transversal e a tensão de escoamento desta. Já o modelo proposto por Joergensen e Hoang [15] baseia-se no princípio da mínima energia, considerando todos os parâmetros de influência da emenda. Dessa forma, o modelo proposto por Joergensen e Hoang [15] apresenta-se como o mais completo para representar o comportamento da emenda em laço.

3.8 Comparação dos resultados numéricos com os modelos analíticos

De posse dos resultados obtidos na análise paramétrica, estes são comparados com as resistências das emendas calculadas pelos modelos analíticos propostos por Hao [13], Araújo et al. [2] e Joergensen e Hoang [15].
Os modelos desenvolvidos por Hao [13] e Araújo et al. [2] referem-se a emendas em laço 2 para 1 e 1 para 1, respectivamente. Dessa forma, fez-se uma extrapolação das formulações para calcular a resistência de emendas em laço 3 para 2, utilizadas no presente trabalho.

As capacidades de carga das emendas calculadas pelas formulações supracitadas estão mostradas na Tabela 7. Como também, são mostradas as relações entre os valores do Modelo e Hao (M/H), do Modelo e Araújo (M/A) e do Modelo e Joergensen (M/J). Além disso, na Tabela 8, são mostrados as médias dessas relações, seus respectivos desvios padrão e coeficientes de variação. Vale ressaltar que para o cálculo destes três parâmetros, os valores de resistência acima da força correspondente ao escoamento das barras foram substituídos pelo valor desta força, ou seja, 704,85 kN, já que esse valor corresponde ao máximo valor de ruptura da emenda, como explicado no item 3.6.
Como descrito no item 3.7, os modelos propostos por Hao [13], Araújo et al. [2] são similares entre si, os quais consideram o modelo de bielas e tirantes. A única diferença entre os modelos é a consideração da seção transversal das bielas comprimidas, em que, para cálculo da espessura da biela, o primeiro autor apresenta uma formulação dependente apenas da resistência do concreto e os outros autores apresentam uma formulação dependente apenas do diâmetro de dobra do laço e do espaçamento entre eles. Percebe-se uma grande divergência entre os valores obtidos por meio do modelo numérico e os valores calculados por meio das formulações desses autores, cujas médias das razões entre estes é de 2,6 para o modelo de Hao [13] e 1,87 para o modelo de Araújo et al. [2], além de desvios padrão de 0,73 e 0,84 e coeficientes de variação de 0,28 e 0,45, respectivamente.
No modelo de Hao [13], a variação do traspasse entre laços praticamente não altera a capacidade da emenda, apresentando uma ligeira elevação com o aumento desse parâmetro, e o aumento do espaçamento entre laços reduz a resistência da emenda, apesar de não ser uma redução significante.
No modelo de Araújo et al. [2], o aumento do traspasse também altera pouco a capacidade da emenda, aumentando-a. Em contrapartida, o aumento do espaçamento entre laços leva a um aumento na resistência da emenda.
Com relação ao espaçamento, os dois modelos divergem entre si, pois no modelo de Hao [13], o espaçamento é inversamente proporcional à capacidade da emenda, já no modelo de Araújo et al. [2], o aumento dessa variável leva a uma maior espessura da biela de compressão, elevando, portanto, a capacidade da emenda. Por outro lado, com relação à variação do traspasse entre laços, as formulações apresentam concordância entre si.
Os modelos supracitados consideram que a transferência de esforços entre laços se dá apenas pela formação de bielas de compressão entre eles, desprezando, dessa forma, a tensão de aderência ao longo da parte reta das barras. Por isso, há uma grande disparidade entre os resultados com os modelos numéricos e com as formulações propostas por Hao [13] e Araújo et al. [2].
Os resultados com os modelos numéricos apresentam excelente concordância com a formulação desenvolvida por Joergensen e Hoang [15], com o valor médio da razão entre os valores de 1,05, desvio padrão de 0,14 e coeficiente de variação de 0,13.
Portanto, os modelos propostos por Hao [13] e Araújo et al. [2] não se mostraram adequados para estimar a capacidade de carga das emendas estudadas no presente trabalho, sendo específicos para seus respectivos trabalhos. Já o modelo desenvolvido por Joergensen e Hoang [15] apresenta-se como o melhor para calcular a capacidade de carga de emendas em laço 3 para 2 submetidas à tração.

4. Conclusões

O presente trabalho apresentou um estudo sobre emendas em laço em juntas de concreto armado submetidas à tração. Para isso, utilizou-se o software DIANA®, com o qual, inicialmente, foi realizada uma calibração de modelos numéricos com base no trabalho de Joergensen e Hoang[15], variando os parâmetros cujos valores eram desconhecidos. Com os modelos calibrados, foi realizada uma análise paramétrica, variando o traspasse e o espaçamento entre laços.

4.1 Traspasse

Os valores de traspasse estudados variaram de 100 mm até 370 mm. Ao observar os resultados dos modelos, nota-se que a partir de um traspasse de 300 mm, todas as emendas tiveram ruptura por escoamento das barras dos laços para qualquer valor de espaçamento entre eles, além disso, o traspasse de 100 mm, valor do diâmetro de dobra do laço, se mostrou insuficiente para a formação de bielas de compressão significativas.
A maioria dos autores pesquisados recomenda como valor mínimo de traspasse o valor do diâmetro de dobra do laço, além desse valor, Dragosavić et al. [11] também recomendam respeitar o valor mínimo de 13 vezes o diâmetro das barras, que para o caso em estudo é de 260 mm. Portanto, a fim de otimizar a resistência da emenda e garantir que a ruptura ocorra por escoamento das barras do laço, recomenda-se utilizar como referência de traspasse valores entre 11 e 15 vezes o diâmetro das barras dos laços, dependendo do espaçamento entre eles, ou seja, valores em torno do valor apresentado pelos autores acima, de 13 vezes o diâmetro das barras dos laços, ao invés de utilizá-lo como valor mínimo. Além disso, deve-se respeitar o traspasse mínimo correspondente ao diâmetro de dobra do laço.

4.2 Espaçamento

Os valores de espaçamento estudados variaram de 20 mm até 100 mm, com o primeiro valor correspondente ao contato entre as barras dos laços, já que no presente trabalho, se utilizam barras com diâmetro de 20 mm. Os resultados mostraram que as maiores resistências foram atingidas quando se utilizou espaçamento entre laços de 20 mm, pois, com este valor, a biela de compressão fica com a menor inclinação possível, maximizando, portanto, a solicitação na mesma. Percebe-se também que os modelos com espaçamentos de 80 mm e 100 mm apresentaram comportamentos bastante similares, indicando uma tendência de que, a partir desses valores, os laços trabalhem isoladamente, o que reduz a eficiência da emenda. Dessa forma, recomenda-se emendar as barras dos laços de forma que elas fiquem em contato e quando não for possível, deve-se respeitar o limite de 3 vezes o diâmetro destas barras.

4.3 Modelos analíticos

Quando utilizados os modelos analíticos propostos por Hao [13] e Araújo et al. [2] modificados para emendas 3 para 2, os resultados apresentaram disparidades muito grandes em relação aos resultados numéricos da análise paramétrica, apresentando comportamentos muitas vezes divergentes. Portanto, esses modelos não devem ser extrapolados para emendas com outras geometrias diferentes daquelas ensaiadas pelos respectivos autores, sendo específicas para as emendas de cada trabalho. Já em relação aos resultados obtidos com o modelo de Joergensen e Hoang [15], houve excelente concordância com os resultados dos modelos numéricos, com o valor médio da razão entre as resistências das emendas de 1,05, desvio padrão de 0,14 e coeficiente de variação de 13%. Portanto, essa formulação pode ser utilizada para estimar a capacidade de carga de emendas em laço 3 para 2, submetidas à tração e possuindo qualquer comprimento de traspasse e espaçamento entre laços.

5. Agradecimentos

À Escola de Engenharia de São Carlos por me conceder a oportunidade de contribuir um pouco mais com o Programa de Mestrado em Estruturas e por me porporcionar essa excelente formação. Ao Conselho Nacional de Desenvolvimento Científico e Tecnológico (CNPq) pela concessão da bolsa de mestrado.

6. Referências bibliográficas

[1] AL-JAHDALI, F. A.; WAFA, F. F.; SHIHATA, S. A. Development length for straight deformed bars in high-strength concrete. ACI Special Publication, v.149, outubro 1994.

[2] (Júlio, Branco e Silva, 2004)ARAÚJO, D. D. L.; CURADO, M. C.; RODRIGUES, P. F. Loop connection with fibre-reinforced precast concrete components in tension. Engineering Structures, v. 72, n. 0, p. 140-151, maio 2014.

[3] ASSOCIAÇÃO BRASILEIRA DE NORMAS TÉCNICAS. NBR 6118: Projeto de estruturas de concreto - Procedimento. Rio de Janeiro, 2014.

[4] ASSOCIAÇÃO BRASILEIRA DE NORMAS TÉCNICAS. NBR 9062: Projeto e execução de estruturas de concreto pré-moldado. Rio de Janeiro, 2006.

[5] BRITISH STANDARDS INSTITUTION. BS 8110: Structural use of concrete. Part 1: Code of practice for design and construction. BSI, Londres, 1997.

[6] BRUGGELING, A. S. G. ; HUYGE, G. F. Prefabrication with concrete. Rotterdam: A.A. Balkema; 1991.

[7] CEB-FIP MODEL CODE 1990 – final draft. Bulletin D'Information, n. 203-205. Thomas Telford, Londres, 1991.

[8] CEB-FIP MODEL CODE 2010 – first complete draft. Bulletin 55, v. 1, Alemanha 2010.

[9] DIANA. DIANA Finite Element Analysis. User's manual release 9.5. Material Library. TNO DIANA, Delft, Netherland, 2014.

[10] DIANA. DIANA Finite Element Analysis. User's manual release 9.5. Element Library. TNO DIANA, Delft, Netherland, 2014.

[11] DRAGOSAVIĆ, M.; VAN DEN BEUKEL, A.; GIJSBERS, F. B. J. Loop connections between precast concrete components loaded in bending. Heron, v. 20, n. 3, 1975.

[12] EUROPEAN STANDARD EN. Eurocode 2: Design of concrete structures – Part 1: General rules and rules for buildings. Comité Européen de Normalisation, Brussels, 225 p., 2004.

[13] HAO, J. Structural behaviour of precast component joints with loop connection. 2004. 395 p. Tese (Doutorado em Engenharia Civil) - Departamento de Engenharia Civil, Universidade Nacional de Singapura, Singapura, 2004.

[14] HILSDORF, H. K.; BRAMESHUBER, W. Code-type formulation of fracture mechanics concepts for concrete. International Journal of Fracture, v. 51, n. 1, p. 61-72, 1991.

[15] JOERGENSEN, H. B.; HOANG, L. C. Tests and limit analysis of loop connections between precast concrete elements loaded in tension. Engineering Structures, v. 52, n. 0, p. 558-569, abr. 2013.

[16] JÚLIO, E. N. B. S.; BRANCO, F. A. B.; SILVA, V. D. Concrete-to-concrete bond strength. Influence of the roughness of the substrate surface. Construction and Building Materials, v. 18, n. 9, p. 675-681, jun. 2004.

[17] LEONHARDT, F.; WALTER, R.; DIETERLE, H. Versuche zur Ermittlung der Tragfähigkeit von Zugschlaufenstößen (Em inglês: Tests for evaluating the tensile strength of loop joints). Deutscher Ausschuss für Stahlbeton, Bulletin nº 226, p. 1-22, 1973.

[18] MATTOCK, A. H. Effectiveness of loop anchorages for reinforcement in precast concrete members. PCI journal, v. 39, n. 6, p. 54-68, 1994.

[19] ROSENTHAL, I.; SHIMONI, J. Bending behavior of a double-loop connection between precast concrete slabs. Concrete International, v. 6, n. 11, p. 30-34, 1984.

[20] SANTANA, I. V. Estudo da influência das fibras metálicas no comportamento da aderência entre barras de aço e concretos de diferentes classes de resistência. 2014. 246 p. Dissertação (Mestrado em Engenharia Civil) - Escola de Engenharia de São Carlos, Universidade de São Paulo, São Carlos, 2014.

[21] SELBY, R. G.; VECCHIO, F. J. Three-dimensional Constitutive Relations for Reinforced Concrete. Universidade de Toronto, Departemento de Engenharia Civil, Toronto, Canada, 1993.

[22] VASCONCELOS, T. D. L. Estudo numérico do comportamento de emendas de barras por meio de laço em juntas de estruturas de concreto armado. 2017. 123 p. Dissertação (Mestrado em Engenharia Civil, Estruturas) – Escola de Engenharia de São Carlos, Universidade de São Paulo, São Carlos, 2017.

[23] VECCHIO, F. J., COLLINS, M. P. The modified compression field theory for reinforced concrete elements subjected to shear. ACI Journal, v. 83, n. 22, p. 219-231, março-abril de 1986.

[24] VECCHIO, F. J., COLLINS, M. P. Compression response of cracked reinforced concrete. Journal of Structural Engineering, v. 119, n. 12, p. 3590-3610, dezembro de 1993.

[25] VILLALBA, S. et al. New structural joint by rebar looping applied to segmental bridge construction: Fatigue strength tests. Journal of Bridge Engineering, v. 18, n. 11, p. 1174-1188, 2013.

Volume 12, Number 1 (February 2019) p. 69 – 86 • ISSN 1983-4195
http://dx.doi.org/10.1590/S1983-41952019000100007

REVISTA IBRACON DE ESTRUTURAS E MATERIAIS
IBRACON STRUCTURES AND MATERIALS JOURNAL

Experimental analysis of load capacity in beams with steel fiber reinforcement on the compression face

Análise experimental da capacidade portante em vigas com reforço de fibras de aço na face tracionada



C. C. DEGHENHARD [a]
caroline.crozeta@gmail.com
https://orcid.org/0000-0003-3718-5718

B. V. SILVA [b]
dovalesilva@hotmail.com
https://orcid.org/0000-0001-5363-5657

F. PELISSER [c]
pelisser@hotmail.com
https://orcid.org/0000-0002-6113-5473

Abstract

The use of steel fibers in the concrete is mainly aimed at increasing the post-peak toughness, due to the adhesion of the fibers to the cementitious matrix. However, there are several typologies of steel fibers, and the main differences are in the form (relation between length and diameter), fiber geometry, and the characterization between macrofibers and microfibers, which generally serve to reduce macrocracking and microcracking, respectively. In this context, this work evaluated the use of microfibers (20 kg/m³ or volume equal to 0.26% (V_f) of concrete volume), macrofibers (20 kg/m³ or V_f = 0.26%) and hybridization (10 kg/m³) + macrofibers (10 kg/m³) inserted in a high strength concrete (f_c = 80 MPa). Two types of steel fibers were used: macrofibers with a diameter of 0.75 mm and a length of 60 mm (a form factor of 80); and microfibers with a diameter of 200 μm and a length of 13 mm (a form factor of 65). The fibers were used in concrete to act as a reinforcement on the compression face of reinforced beams (12×20×160cm), and the mechanical characteristics of the concretes were analyzed: (i) flexural strength in prismatic specimens (10×10×35 cm), (ii) compressive strength in cylindrical specimens (20×Ø10 cm) and (iii) modulus of elasticity in cylindrical specimens (20×Ø10 cm). Analysis of the results showed that compressive strength increased by approximately 8% for all the compositions with fibers compared with concrete without fibers. Similar behavior was verified for the modulus of elasticity. In the prismatic specimens (10×10×35 cm) an increase in toughness was observed, with the macrofibers performing better. In beams measuring 12×20×160 cm, an increase in bearing capacity was verified regarding cracking time and plastic rotation, with the best result also obtained using macrofibers. Overall, it can be concluded that the application of reinforcement with steel fibers in the compression face of beams was efficient, even though it did not present a significant increase in compressive strength, a fact that could be correlated with the reduced volume of fibers used.

Keywords: reinforcement, high-performance concrete, steel fibers, microfibers, macrofibers.

Resumo

A utilização de fibras de aço no concreto visa aumentar principalmente a tenacidade, em função da aderência das fibras à matriz cimentícia. Entretanto como existem diversas tipologias de fibras de aço, as principais diferenças estão no fator de forma (relação entre comprimento e diâmetro), na geometria das fibras, e, na caracterização entre macrofibras e microfibras, que de modo geral servem para reduzir a macrofissuração e microfissuração, respectivamente. Dentro deste contexto, este trabalho avaliou a utilização de microfibras (20 kg/m³ ou volume igual a 0,26% (V_f) do volume de concreto), macrofibras (20 kg/m³ ou V_f = 0,26%) e a hibridização entre os dois tipos (microfibras (10 kg/m³) + macrofibras (10 kg/m³)) inseridas em um concreto de alta resistência (f_c = 80 MPa). Foram utilizados dois tipos de fibras de aço: as macrofibras com diâmetro de 0,75 mm e comprimento de 60 mm (fator de forma igual a 80, com gancho na extremidade); e microfibras com diâmetro de 200 μm e comprimento de 13 mm (fator de forma igual a 65). As fibras foram utilizadas no concreto para atuar como reforço na face tracionada de vigas armadas (12×20×160cm), e foram analisadas as características mecânicas dos concretos: (i) resistência à flexão em corpos de prova prismáticos (10×10×35 cm), (ii) resistência à compressão em corpos de prova cilíndricos (20×Ø10 cm) e (iii) módulo de elasticidade em corpos de prova cilíndricos (20×Ø10 cm). Análise dos resultados mostraram que na resistência à compressão houve um acréscimo de aproximadamente 8% para todas as composições com fibras em relação ao concreto sem fibras. Quanto ao módulo de elasticidade foi verificado comportamento semelhante. Nos corpos de prova prismáticos (10×10×35 cm) ocorreu aumento na tenacidade, sendo que as macrofibras tiveram melhor desempenho. Nas vigas de 12×20×160cm, ocorreu aumento da capacidade portante, quanto ao momento de fissuração e rotação plástica, sendo que o melhor resultado também foi obtido com as macrofibras. De modo geral, pode-se concluir que a aplicação do reforço com fibras de aço na face tracionada das vigas foi eficiente, embora não apresentou aumento significativo na resistência à compressão, fato que pode estar correlacionado ao reduzido volume de fibras utilizado.

Palavras-chave: reforço, concreto de alto desempenho, fibras de aço, microfibra, macrofibras.

[a] *Santa Catarina Extreme South University, Criciúma, SC, Brazil;*
[b] *Adamantinenses University, Civil Engineering Department, Adamantina, SP, Brazil;*
[c] *Federal University of Santa Catarina, Civil Engineering Department, Florianópolis, SC, Brazil.*

Received: 25 May 2017 • Accepted: 11 Jun 2018 • Available Online: 05 Feb 2019

1. Introduction

When they are well designed and executed, reinforced concrete structures show great durability, yet they require preventive and corrective maintenance to ensure their functionality. In the construction industry, reinforcements are solutions used to avoid problems and to increase the carrying capacity of structural elements, which for numerous reasons no longer meet the requirements for which they were designed [1].

One of the ways to reinforce and improve the performance of concrete structures is the addition of fibers, which generally promote a gain in toughness, an increase in static tensile strength, dynamic fatigue and impact, traction, a reduction in demand deformations, and control of the number and speed of propagation of cracks. Together these effects contribute to the increased durability of the structure, since the presence of the fibers assists in reducing crack apertures, while also controlling and delaying their propagation, allowing for the stabilized occurrence of cracks.

Over time and through technological advances, different types of fibers have been investigated and developed, imbued with characteristics that made them more suitable for incorporation into concrete, which has allowed the development of a generation of composites with increasingly better properties, and with greatly-improved performance compared with traditional concrete, in certain respects. In the most recent literature, for example, we find references to such terms as macrofibers and microfibers, used to differentiate larger and more resistant fibers, which act initially in post-cracking of the matrix, from smaller, more disseminated fibers, which act primarily in cracking delay [2]. An example of the contribution of the fibers in the flexural dimensioning of a reinforced concrete beam [3] showed a reduction in the area of steel area of 11, 17 and 21%, using fiber consumption of 20, 30 and 45 kg/m^3, when using Dramix RC 80/60 steel fibers.

This topic isboth relevant and current, since many structures have been built with increased demand for strength and durability, or subject to the most varied demands arising from exceptional support or loading conditions. This study proposed evaluating the performance of steel microfibers, together with macrofibers, used in reinforced concrete as structural reinforcement.

2. Fundamental aspects of fiber reinforced cement matrix composites

The purpose of reestablishing a reinforced concrete structure is to return it to its original strength or increase its load capacity. Reinforcement is the act of correcting a structural or functional deficiency that often focuses solely on reducing the rate of deterioration. Finally, it is expected that a renovated and/or reinforced structure should perform better than it did before the intervention [4].

Steel fibers were chosen, as in work developed by Quinino [5], because they are the most widely used cement matrix reinforcement, due to the numerous benefits and economic importance of this material. Fibers act as a mechanism of tension transfer across cracks, allowing the concrete to present greater deformations under peak load and greater post-cracking load capacity, i.e. the ductility and residual resistance to traction of the material is increased [6]. According to Figueiredo [7], the random distribution of fibers in the material reinforces the structural element overall, in contrast to that which occurs with conventional reinforcements in reinforced concrete. It is important to emphasize that the use of the fibers as reinforcement is generally not considered to be sufficiently efficient to replace conventional reinforcement. In addition, it is imperative that aspects like matrix-fiber compatibility and adhesion are considered, to obtain the desired result.

For Martineau and Agopyan [8], fiber placement modifies the cracking process, acting as a transfer mechanism of forces across cracks, and ensuring minimal change in the load resistance capacity when these occur. Mehta and Monteiro [9] observed that even when fiber-reinforced concretes sustain deformations far superior to conventional concrete fracture deformation, they continue to withstand considerable loads, and the ultimate strength of the first crack depends heavily on matrix parameters and is influenced by the characteristics of the fiber. Doubts remain concerning the efficacy of fiber addition for improving ultimate strength; however, the consensus is that fibers improve the ductility of cementitious composites.

3. Experimental methodology

To begin, four groups were defined: i) reference concrete, without fibers (A); ii) concrete with macrofibers (B); iii) concrete with microfibers (C); and iv) concrete with micro and macrofibers (D). The following test specimens were produced for each group: two 12×20×160 cm reinforced concrete beams for 4-point bending tests; two cylindrical specimens (20×Ø10 cm) for resistance to axial compression and modulus of elasticity; and two 10×10×35 cm prismatic specimens to determine the flexural strength of the concrete.

Flexural reinforcement was dimensioned according to the criteria of NBR 6118 [10], considering a compressive strength for concrete of 80 MPa and CA-50 steel, adopting two 12.5 mm diameter bars for main reinforcement to resist flexural deformation. Stirrup spacing was 10.0 cm and 12.5 cm and the diameter was 5.0 mm. In addition , 2.5 cm spacers were used to ensure reinforcement cover.

Macrofibers measuring 600×0.75 mm (form factor of 80, trade name RC 80/60 BN, manufacturer ArcelorMittal/Dramix®) were used in groups B and D, and microfibers measuring 13 mm×200 µm (form factor of 65, trade name OL 13/.20, manufacturer ArcelorMittal/Dramix®) were used in groups C and D.

Concreting was done in two phases. In the first phase, only some of the beams (12×20×160 cm) from groups B, C, and D were concreted. The beams of group A (reference) were concreted in their entirety because they had no fiber reinforcement. The prismatic (10×10×35 cm) and the cylindrical specimens (20 × Ø10 cm) without fibers also were concreted together with this first phase. The concrete mix proportions were 1:2.3:2.7 cement:sand:gravel, with a water/cement (w/c) ratio of 0.4. The cement used was type CP-IV. The concrete was mixed in a 400 L concrete mixer. The consistency of the concrete was verified by the abatement test and was 11 cm. All the beams were concreted simultaneously with concrete made in the laboratory and densified with immersion vibrators and a vibrating table. The beams were concreted up to a height of 13.75 cm. This limit was controlled during the first concreting phase, by an internal mark inside the form, such that reinforcement used to resist flexural deformation in groups B, C and D was exposed. The reinforcement dimensions in groups B, C and D were determined to be twice that of the reinforcement cover plus the diameter of the reinforcement bar (2.5+2.5+1.25=6.25 cm). This dimension was maintained during the second phase of concreting (groups B, C, and D), and only the type of fiber addition varied.

The second phase of concreting of the beams (12×20×160 cm) was done 24 h after the end of the first phase. The reconstitution of the tensioned face of the beams of groups B, C and D included the presence of fibers in 6.25 cm thickness defined above. The surface was not previously prepared since the stirrups served as the point of bonding for the new concrete. In the groups that received fiber reinforcement, the amount added was 20 kg/m^3 or V_f = 0.26% in relation to the concrete volume. The prismatic (10×10×35 cm) and cylindrical specimens (20×Ø10 cm) with fiber additions were concreted together with this second phase.

Twenty-four hours after concreting, the cylindrical specimens were demolded and placed in submerged curing until 28 days of age, to test axial compressive strength [11] and modulus of elasticity [12]. The prismatic specimens and reinforced concrete beams were demolded 14 days after the final phase of concreting. They were painted to improve crack analysis. The age of rupture for all beams was 28 days after the second phase of concreting. The beams (12×20×160 cm) were identified as follows: group A, beams A1 and A2; group B, beams B1 and B2; group C, beams C1 and C2; and group D, beams D1 and D2. Beams A1, B1, C1 and D1 refer to beams instrumented with strain gauges connected to the steel and concrete, while beams A2, B2, C2 and D2 had no sensors. The prismatic specimens (10×10×35 cm) were identified as Ap, Bp, Cp, and Dp, according to each group.

All the beams were submitted to the 4-point bending test. The loads were applied from top to bottom over a metal profile (Profile I - 10×25.5 cm) which transferred the load to the beams at two point loads precisely dividing the theoretical span of the beam into thirds. The beams were positioned under a metal reaction portal and the load was applied by an electrical hydraulic cylinder, with 500 kN capacity. The load values were recorded by a load cell arranged between the hydraulic cylinder and the distribution beam (Profile I - 10×25.5 cm). The vertical displacements at 3 points (LVDT 1, LVDT 2 (center), LVDT 3) along the length of the beam were evaluated using linear variable differential transformers (LVDT). Deformations were monitored using strain gauges bonded to materials at strategic deformation points: concrete and flexural reinforcement (Figure 1). The equipment was connected to a QuantumX® data acquisition system interface with HBM® catman®Easy software.

Verifications were made to analyze the behavior of each group at different time-points during load application: when the maximum displacement allowed (L/250) was reached, according to the norms, and at rupture. First, the load required to reach the maximum displacement allowed (L/250) was verified, considering L=150 cm as the theoretical span of the beams, which resulted in a displacement of 6.0 mm. Lastly, the load and displacement that led the beam rupturing were verified. The experimental elastic line of the beam was determined using the bending test results - load curves *vs* vertical displacements - obtained with the LVDTs positioned along the beam length. Deformation values provide a better understanding of the limits of the deformation stages regarding bending moment of cracking and bending moment of plastification. A model was developed that characterized the phenomenon of change in deformation stages of a fiber-reinforced beam by observing the relationship between the bending moment and the curvature formed in the cross-section of the beam. Finally, the development of cracks and the form of rupture were mapped.

4. Results and discussion

4.1 Reinforced concrete beams (12 × 20 × 160cm)

4.1.1 Loading and displacement at rupture

The loads and the displacements verified at the rupture of the

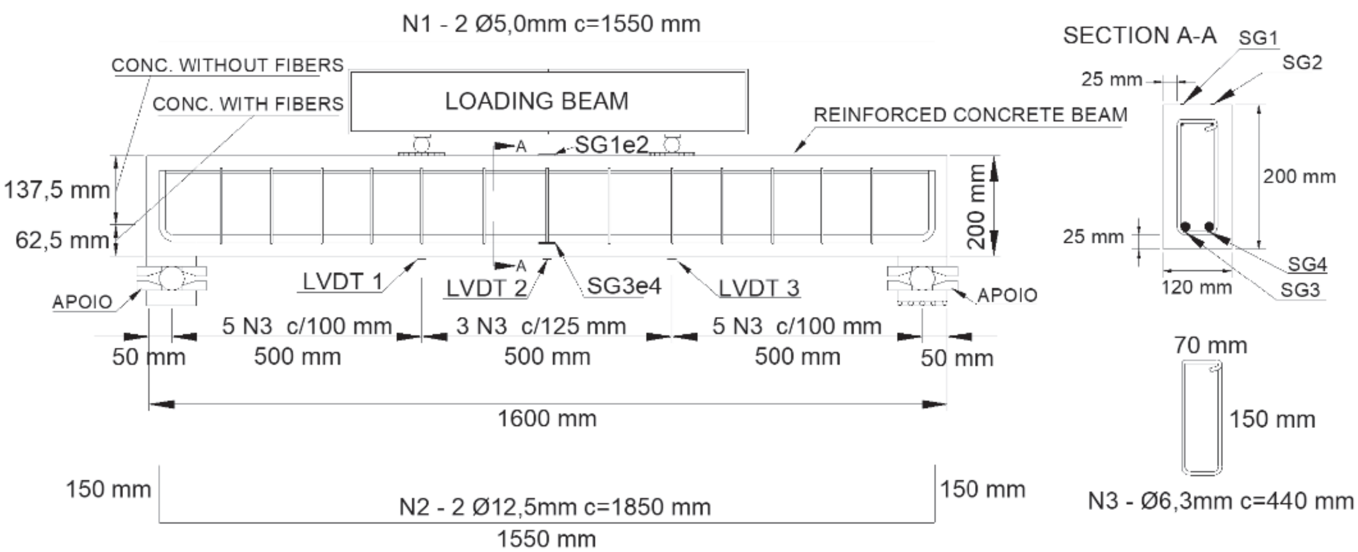

Figure 1
Positions of the LVDTs and SGs along the beam

Table 1
Results of loading and displacement of the beams at rupture (12 × 20 × 160 cm)

GROUP A – No fibers					
Beams	**Load (kN)**	**Displacement left (mm)**	**Displacement middle (mm)**	**Displacement right (mm)**	**Ductility factors**
A1	84.22	13.77	16.91	15.48	1.98
A2	85.60	13.62	15.77	12.61	1.92
Mean (D.P)	84.91 (0.98)	13.69 (0.11)	16.34 (0.81)	14.05 (2.03)	1.95 (0.04)
GROUP B – Macrofibers					
Beams	**Load (kN)**	**Displacement left (mm)**	**Displacement middle (mm)**	**Displacement right (mm)**	**Ductility factors**
B1	89.09	14.33	18.30	16.07	2.00
B2	86.67	9.62	12.72	10.68	1.55
Mean (D.P)	87.88 (1.71)	11.98 (3.34)	15.51 (3.95)	13.38 (3.81)	1.78 (0.32)
GROUP C – Microfibers					
Beams	**Load (kN)**	**Displacement left (mm)**	**Displacement middle (mm)**	**Displacement right (mm)**	**Ductility factors**
C1	88.88	11.20	14.39	11.67	1.77
C2	87.70	14.64	12.24	12.07	1.65
Mean (D.P)	88.29 (0.83)	12.92 (2.43)	13.31 (1.52)	11.87 (0.28)	1.71 (0.08)
GROUP D – Macrofibers + Microfibers					
Beams	**Load (kN)**	**Displacement left (mm)**	**Displacement middle (mm)**	**Displacement right (mm)**	**Ductility factors**
D1	86.99	13.90	18.71	13.91	2.11
D2	85.16	11.37	14.21	11.74	1.85
Mean (D.P)	86.07 (1.29)	12.63 (1.79)	16.46 (3.18)	12.83 (1.54)	1.98 (0.18)

beams and the ductility factors are shown in Table 1. The behavior of the percentages that justify the increase in bearing capacity between the groups was different in displacement up to rupture. To achieve rupture in the beams from group B, the load required was 3.5% higher than for group A, while group C required 4.0% higher loads, and group D required 1.4% higher loads. Regarding displacements, these were very similar between all the groups. When analyzing the average values of loads at rupture (Figure 2), an increase was observed for beams B and C with macrofiber and microfiber additions, respectively. Despite the lower form factor, microfibers showed a tendency to increase, which could be associated with larger amounts of fiber, and their efficiency at reinforcing concrete during microcracking provoked before rupture. When using macrofibers + microfibers (group D), a reduction in rupture load of the beam was observed, but it remained better than the reference beams (group A). Comparison between this result and beams with either macro

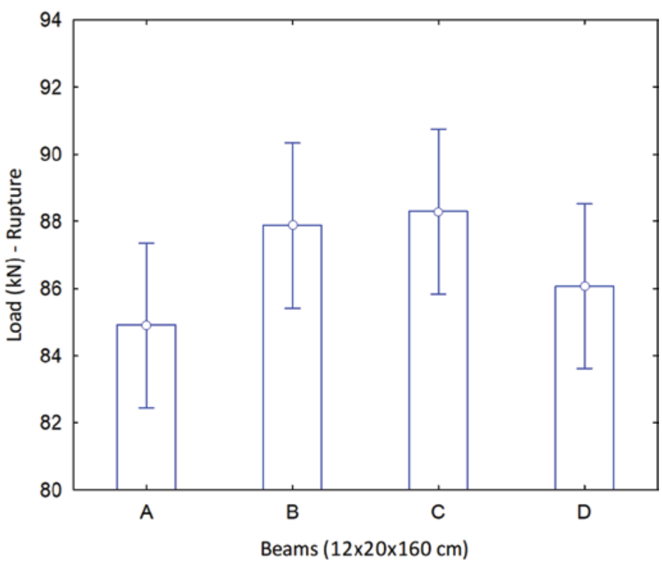

Figure 2
Analysis of load results at rupture – beams (12 × 20 × 160 cm)

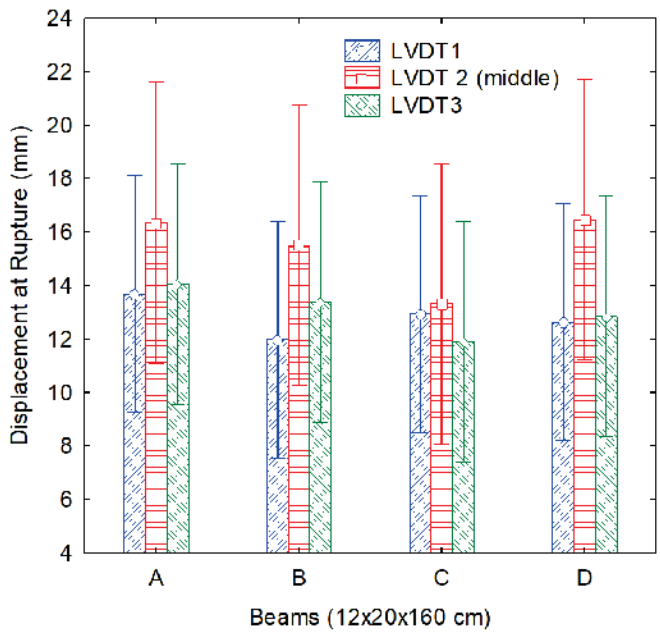

Figure 3
Analysis of the results of displacement at rupture in beams (12 × 20 × 160 cm)

or microfibers suggests the most plausible explanation is a loss of strength due to the lower compactness of the composite cementitious matrix with both fibers. Regarding displacement in the beams at rupture, group C showed that microfibers did not contribute to an increase in the final displacement before rupture. The ductility factor, obtained between the ratio of displacement at rupture and displacement at the moment of plastification, determined that group D showed better behavior than reference group A.

4.1.2 Load behavior *versus* displacement

Figure 4 presents the load versus displacement of all beams (12×20×160 cm). The behaviors between the groups were similar for the ultimate loads and the service loads (L/250). The beams of all groups exceeded the maximum displacement allowed according to current norms (L/250 = 6.0 mm) before coallapsing. All the beams broke by crushing concrete on the compressed face.
The sequence of images in Figure 5 illustrates the particularities of the form of rupture and cracks in the four groups of beams (12×20×160 cm). The reference group A (no fibers in the traction face) presented the largest number of visible cracks, which surpassed the middle third region. Groups B, C, and D were similar regarding the appearance of cracks concentrated in the middle third of the theoretical span of the beam, and the appearance of some shear cracks.

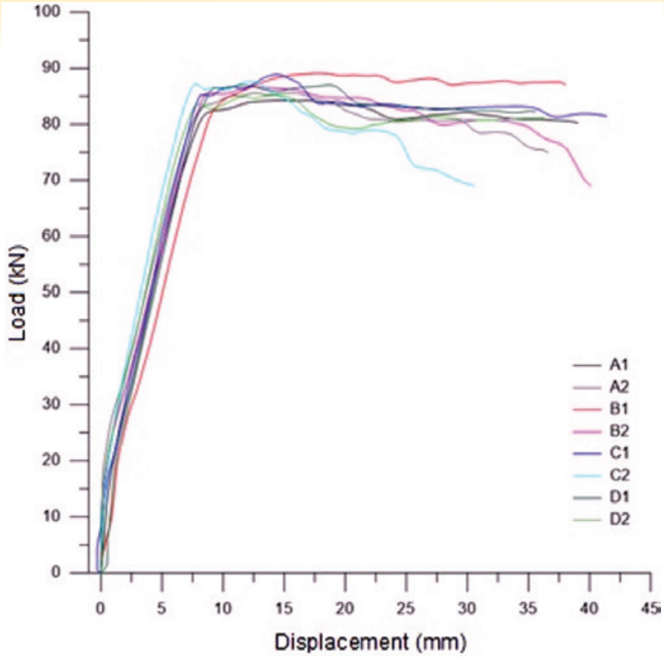

Figure 4
Load *versus* displacement behavior in beams (12 × 20 × 160 cm)

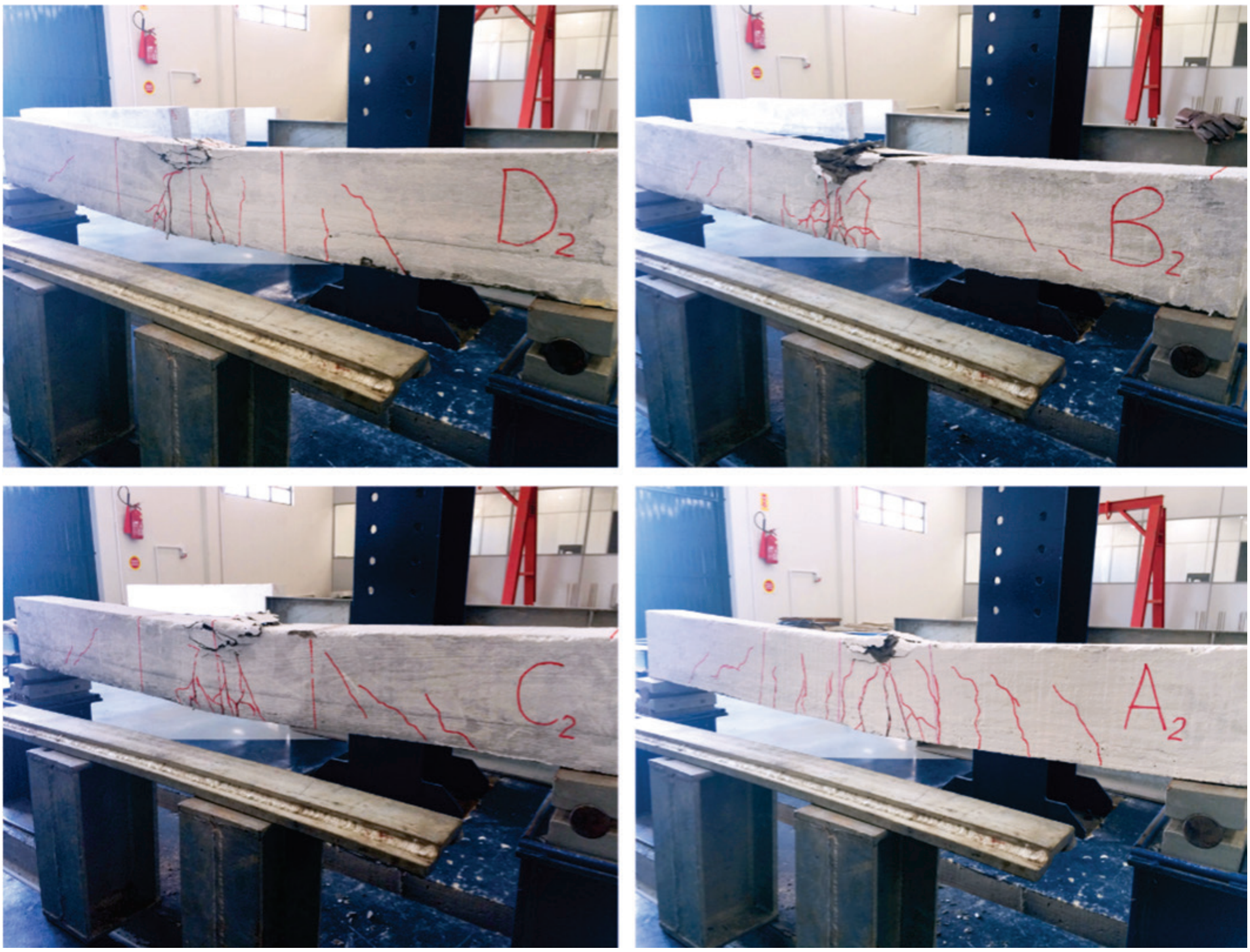

Figure 5
Form of rupture and cracks in beams (12 × 20 × 160 cm)

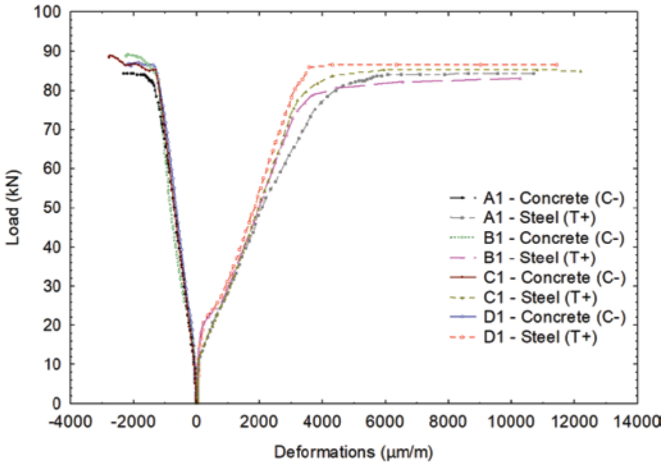

Figure 6
Specific deformations of steel and concrete in beams (12 × 20 × 160 cm)

4.1.3 Analysis of specific deformations

Figure 6 shows specific deformations in the concrete in the uppermost compressed face and that of the steel in the lower, most tensioned face (steel bar, Ø12.5 mm), both located in the central cross section (Figure 1). Note that the final deformations in concrete and steel were similar between the groups, approximately 2200 μm/m for concretes and 11000 μm/m for steels. However, groups B and D presented a smaller steel deformation between loads of 10 kN and 20 kN, which contributed to increasing the period of cracking. When a loading value was set between 10 and 20 kN, the smallest deformation (steel) occurred in the beams with the micro and macrofibers, followed by beams only with microfibers, only with macrofibers and finally, the reference concrete. These results show the potential of using microfibers in conjunction with macrofibers to improve the structural behavior of the reinforcement, before and after the occurrence of cracks. Recent research has shown the beneficial effect of using hybrid fibers - macro and microfibers – to improve the resistance to deformation in multiple cracking states [13].

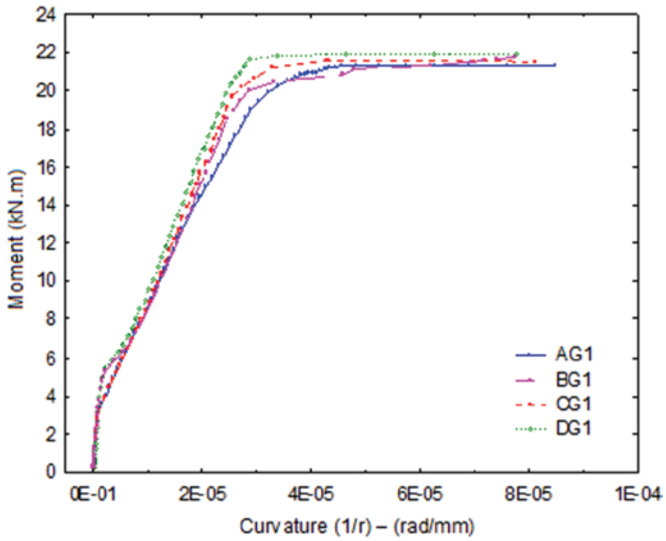

Figure 7
Bending moment-curvature diagram for beams (12 × 20 × 160 cm)

4.1.4 Analysis of the bending moment-curvature diagram

Table 2 presents the results of moments and curvatures and the differences in percentages regarding the reference beam, while Figure 7 shows the bending moment-curvature diagrams for beams A1, B1, C1 and D1. Group B (+ macrofibers) presented 6.5 times greater cracking time than group A (reference), followed by groups D and C. Regarding rotation, the results for cracking time-points (Mr) in group B were 19.6 times higher than group A (reference), followed by groups D and C. This behavior shows that fibers increased the time of cracking and plastic rotation, but the isolated addition of microfibers contributed the least. The geometry

Table 2
Results of the bending moments and curvatures of the beams (12 × 20 × 160 cm)

Moments						
Beams	Moment of cracking M_r (kN.m)	Difference	Moment of plastification M_y (kN.m)	Difference	Moment of rupture M_u (kN.m)	Difference
A	0.7	Ref.	20.6	Ref.	21.3	Ref.
B	5.4	+655.7%	20.5	-0.7%	22.6	+5.7%
C	2.8	+291.8%	19.1	-7.1%	22.5	+5.5%
D	4.5	+529.6%	21.7	+5.3%	22.0	+3.2%

Curvature in moments						
Beams	$1/r$ (M_r)	Difference	$1/r$ (M_y)	Difference	$1/r$ (M_u)	Difference
A	1.15E-07	Ref.	3.57E-05	Ref.	7.65E-05	Ref.
B	2.37E-06	+1960.9%	3.32E-05	-7.1%	8.16E-05	+6.6%
C	7.95E-07	+592.2%	2.47E-05	-30.8%	8.85E-05	+15.7%
D	1.45E-06	+1161.2%	2.90E-05	-18.8%	7.95E-05	+3.9%

Table 3
Results of compressive strength and modulus of elasticity (20 × Ø10 cm)

Samples	f_c (MPa)	Difference	E_c (GPa)	Difference	Compositions
A1	81.8	–	54.2	Ref.	Concrete
A2	80.6	–	–	–	Concrete
Mean (D.P.)	81.2 (0.85)	Ref.	–	–	Concrete
Samples	**f_c (MPa)**	**Difference**	**E_c (GPa)**	**Difference**	**Compositions**
B1	86.3	–	57.3	+5.7%	Concrete + Macrofibers
B2	89.3	–	–	–	Concrete + Macrofibers
Mean (D.P.)	87.8 (2.12)	+8.1%	–	–	Concrete + Macrofibers
Samples	**f_c (MPa)**	**Difference**	**E_c (GPa)**	**Difference**	**Compositions**
C1	86.8	–	57.2	+5.5%	Concrete + Microfibers
C2	89.6	–	–	–	Concrete + Microfibers
Mean (D.P.)	88.2 (1.98)	+8.6%	–	–	Concrete + Microfibers
Samples	**f_c (MPa)**	**Difference**	**E_c (GPa)**	**Difference**	**Compositions**
D1	88.4	–	55.4	+2.2%	Concrete + Macrofibers + Microfibers
D2	88.3	–	–	–	Concrete + Macrofibers + Microfibers
Mean (D.P.)	88.4 (0.07)	+8.8%	–	–	Concrete + Macrofibers + Microfibers

of macrofibers, with their hooks and non-smooth surfaces, unlike microfibers, contribute to this property [13].

4.2 Mechanical properties of the concretes

4.2.1 Compressive strength (f_c) and modulus of elasticity (E_c)

To mechanically characterize the concrete, tests to determine compressive strength and modulus of elasticity were performed. For compressive strength, the maximum difference between the groups was 8.8%, and the concretes with fiber addition showed very similar results to each other, and were approximately 8% better than the reference concrete, without fibers (Table 3). According to Mehta and Monteiro [9], increasing the amount of steel fibers in concrete using contents less than 2% of volume exerts minimal influence on the compressive strength. However, for high strength concretes, an increase in compressive strength was verified for a concentration of 0.5% microfibers [14]. A study by Su et al. [14] used a maximum of 2.5% of two types of steel microfibers, with form factors of 50 (6×0.12 mm) and 125 (15×0.12 mm), and achieved compressive strengths of 114 MPa and 145 MPa, respectively. In this work, the form factor of the microfibers was 65 (13×0.2 mm), and a lower concentration of fibers was used. The increase resistance obtained was satisfactory, and was associated with greater resistance to the propagation of microcracks during loading.
Concerning the modulus of elasticity, the maximum difference between the groups was smaller, approximately 6% (Table 3), between the concrete with macrofibers and microfibers (groups B and C), than for the concrete without fibers. This difference may have been caused by the higher density of the concrete with fibers.

4.2.2 Flexural test – prismatic test bodies (10 × 10 × 35 cm)

Regarding load and displacement at rupture (Figures 8 and 9, respectively), groups C and D achieved higher loads for displacement at rupture; load was 13% higher in group C than in group A, with mean displacement of 0.27 mm, while group D showed a load increase of 8%, with mean displacement of 0.30 mm. Group B showed no increase in resistance in relation to group A. Again, a tendency for increased resistance to cracking, when using microfibers or microfibers plus macrofibers, was verified compared with the reference concrete. When using prismatic specimens, rather than reinforced concrete beams, this improvement was more evidently promoted by microfibers. Although the differences were small, fiber volume was also low (Vf = 0.26%). This low amount was used because the

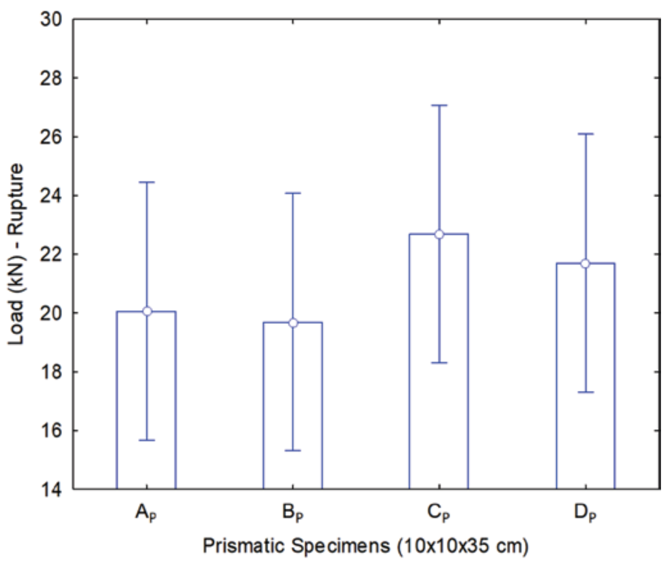

Figure 8
Analysis of the load results on the rupture in prismatic specimens (10 × 10 × 35 cm)

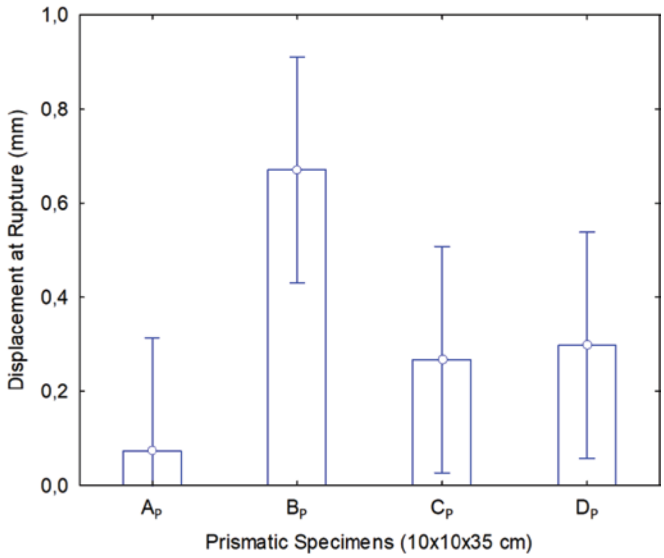

Figure 9
Analysis of the results of displacement at rupture in prismatic specimens (10 × 10 × 35 cm)

concrete being tested had reinforcement, thus maintaining the ease of application. Similar behavior was observed in displacement up to rupture among prismatic specimens with fibers, wherein specimens with microfibers presented the best results.

The results for toughness are presented in Figures 10 and 11 and show a higher index for group B (+ macrofibers). Groups C and D presented lower values than group B and higher than the group A. The higher toughness caused by macrofibers can be explained by its higher form factor and the consequently larger fiber-matrix contact area. In addition , macrofibers have hooks which improve the post-cracking resistance of the concrete when compared with smooth fibers [13].

5. Final considerations

Regarding the results obtained, the following conclusions can be drawn:

- Regarding the loading and displacement results (according to the L/250 norm and at rupture) obtained for reinforced concrete beams (12×20×160 cm) and concrete beams (10×10×35 cm), the results improved for all the groups containing steel fibers on the tensioned face;
- In the bending moment-curvature diagram, both fibers increased cracking time and plastic rotation;
- Cracks in the 10×10×35 cm beams indicate that group A presented fragile behavior, leading to abrupt rupture;
- Compressive strength results were higher (8%) for concretes with fiber additions;
- Macrofibers presented the best results compared with the remaining groups, for 12×20×160 cm and 10×10×35 cm beams;
- Comparing microfiber addition with macrofiber addition, microfibers improved the flexural strength and displacements of reinforced beams and improved compressive strength despite the low volume used. Macrofibers were better for increasing toughness or behavior after rupture;
- Use of a hybrid fiber addition - macrofibers + microfibers - did not present significantly differentiated behavior than when the fibers were used alone, but this combination did contribute to improvements in the region of microcracking and post-cracking, though to a less significant extent.

Finally, the method of applying reinforcement with steel fibers on the tensioned face of the beams proved to be effective, though it did not present increments of high resistance. The fibers contributed numerous results and were particularly efficient at combating cracking.

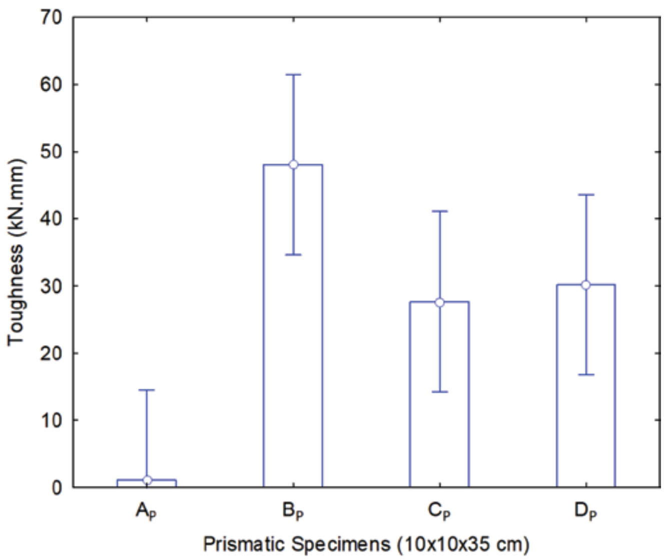

Figure 10
Analysis of toughness results in prismatic specimens (10 × 10 × 35 cm)

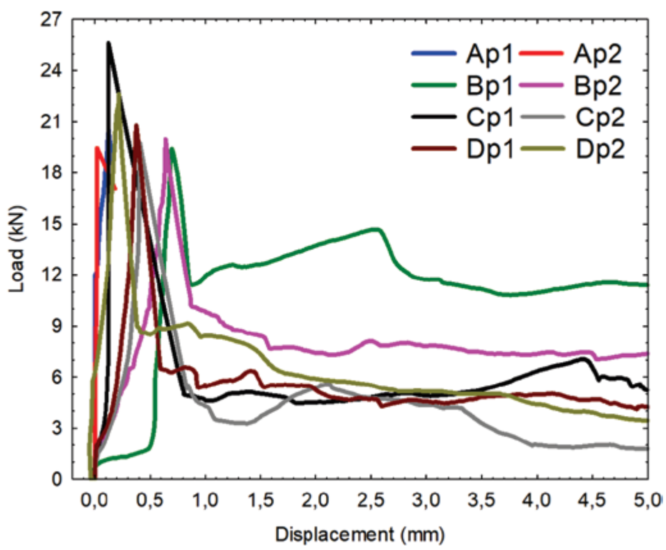

Figure 11
Load *versus* displacement behavior in prismatic specimens (10 × 10 × 35 cm)

6. Acknowledgements

The authors are grateful for the financial support of the National Council for Scientific and Technological Development (CNPq) and to Belgo Bekaert for donating the fibers used herein.

7. References

[1] DEGHENHARD, C. C., TEIXEIRA, T., VARGAS, A., VITO, M., PICCININI, Â. C., DO VALE SILVA, B. Experimental analysis of various configurations of metal sheets in the reinforcement of flexion of reinforced concrete beams. ALCONPAT Journal, v. 6, p. 105-199, 2016.

[2] BERNARDI, S. T. Avaliação do comportamento de materiais compósitos de matrizes cimentícias reforçadas com fibra aramida Kevlar, 2003. Dissertação (Mestrado) – Escola de Engenharia da Universidade Federal do Rio Grande do Sul. Porto Alegre, 2003.

[3] REAL, L.V., NOGUEIRA, A.B., SIMÃO, L., FIGUEIREDO, A.D. Contribuição das fibras de aço para o dimensionamento à flexão de viga armada. Revista Concreto & Construções, n 87, 2017.

[4] FERRARI, V.J., HANAI, J.B. Flexural strengthening of reinforced concrete beams with carbon fibers reinforced polymer (CFRP) sheet bonded to a transition layer of high performance cement-based composite. IBRACON Structures and Materials Journal. v.5, n.5, p. 596-626, 2012.

[5] QUININO, U. C. M. Investigação experimental das propriedades mecânicas de compósitos de concreto com adições híbridas de fibras. Tese (Doutorado em Engenharia Civil) – Programa de Pós Graduação em Engenharia Civil (UFRGS) Universidade Federal do Rio Grande do Sul (UFRGS), Porto Alegre/RS, 2015.

[6] FIGUEIREDO, A.D. Concreto reforçado com fibras, Tese de Livre-Docência, Escola Politécnica, Universidade de São Paulo, São Paulo, 2011.

[7] FIGUEIREDO, A.D. Concreto com fibras. Concreto, Ensino, Pesquisa e Realizações, São Paulo, Ed. Geraldo Cechella Isaia, IBRACON, p.1194-1225, 2005.

[8] MARTINEAU, P., AGOPYAN, V. Conferência Magma I – Compósitos: material inovador. In: Arquimacom'2002. São Paulo, 2002.

[9] MEHTA, P. K. & MONTEIRO, P. J. M. Concreto: Microestrutura, propriedades e materiais. 2º Edição (português). São Paulo, IBRACON, 2014.

[10] ASSOCIAÇÃO BRASILEIRA DE NORMAS TÉCNICAS. NBR 6118: Projeto de estruturas de concreto. Rio de Janeiro, 2014.

[11] ASSOCIAÇÃO BRASILEIRA DE NORMAS TÉCNICAS. NBR 5739: Concreto – Ensaio de compressão de corpos de prova cilíndricos. Rio de Janeiro, 2014.

[12] ASSOCIAÇÃO BRASILEIRA DE NORMAS TÉCNICAS. NBR 8522: Concreto - Determinação do módulo estático de elasticidade à compressão. Rio de Janeiro, 2014.

[13] PARK, S. H., KIM, D.J., RYU, G. S., KOH K. T. Tensile behavior of Ultra High Performance Hybrid Fiber Reinforced Concrete. Cement & Concrete Composites 34, 172–184, 2012.

[14] SU, Y., LI, J., WU, C. WU, P. LI, Z-X. Effects of steel fibres on dynamic strength of UHPC. Construction and Building Materials 114, 708–718, 2016.

Volume 12, Number 1 (February 2019) p. 69 – 86 • ISSN 1983-4195
http://dx.doi.org/10.1590/S1983-41952019000100007

IBRACON

REVISTA IBRACON DE ESTRUTURAS E MATERIAIS
IBRACON STRUCTURES AND MATERIALS JOURNAL

Experimental analysis of load capacity in beams with steel fiber reinforcement on the compression face

Análise experimental da capacidade portante em vigas com reforço de fibras de aço na face tracionada



C. C. DEGHENHARD [a]
caroline.crozeta@gmail.com
https://orcid.org/0000-0003-3718-5718

B. V. SILVA [b]
dovalesilva@hotmail.com
https://orcid.org/0000-0001-5363-5657

F. PELISSER [c]
pelisser@hotmail.com
https://orcid.org/0000-0002-6113-5473

Abstract

The use of steel fibers in the concrete is mainly aimed at increasing the post-peak toughness, due to the adhesion of the fibers to the cementitious matrix. However, there are several typologies of steel fibers, and the main differences are in the form (relation between length and diameter), fiber geometry, and the characterization between macrofibers and microfibers, which generally serve to reduce macrocracking and microcracking, respectively. In this context, this work evaluated the use of microfibers (20 kg/m³ or volume equal to 0.26% (V_f) of concrete volume), macrofibers (20 kg/m³ or V_f = 0.26%) and hybridization (10 kg/m³) + macrofibers (10 kg/m³) inserted in a high strength concrete (f_c = 80 MPa). Two types of steel fibers were used: macrofibers with a diameter of 0.75 mm and a length of 60 mm (a form factor of 80); and microfibers with a diameter of 200 µm and a length of 13 mm (a form factor of 65). The fibers were used in concrete to act as a reinforcement on the compression face of reinforced beams (12×20×160cm), and the mechanical characteristics of the concretes were analyzed: (i) flexural strength in prismatic specimens (10×10×35 cm), (ii) compressive strength in cylindrical specimens (20×Ø10 cm) and (iii) modulus of elasticity in cylindrical specimens (20×Ø10 cm). Analysis of the results showed that compressive strength increased by approximately 8% for all the compositions with fibers compared with concrete without fibers. Similar behavior was verified for the modulus of elasticity. In the prismatic specimens (10×10×35 cm) an increase in toughness was observed, with the macrofibers performing better. In beams measuring 12×20×160 cm, an increase in bearing capacity was verified regarding cracking time and plastic rotation, with the best result also obtained using macrofibers. Overall, it can be concluded that the application of reinforcement with steel fibers in the compression face of beams was efficient, even though it did not present a significant increase in compressive strength, a fact that could be correlated with the reduced volume of fibers used.

Keywords: reinforcement, high-performance concrete, steel fibers, microfibers, macrofibers.

Resumo

A utilização de fibras de aço no concreto visa aumentar principalmente a tenacidade, em função da aderência das fibras à matriz cimentícia. Entretanto como existem diversas tipologias de fibras de aço, as principais diferenças estão no fator de forma (relação entre comprimento e diâmetro), na geometria das fibras, e, na caracterização entre macrofibras e microfibras, que de modo geral servem para reduzir a macrofissuração e microfissuração, respectivamente. Dentro deste contexto, este trabalho avaliou a utilização de microfibras (20 kg/m³ ou volume igual a 0,26% (V_f) do volume de concreto), macrofibras (20 kg/m³ ou V_f = 0,26%) e a hibridização entre os dois tipos (microfibras (10 kg/m³) + macrofibras (10 kg/m³)) inseridas em um concreto de alta resistência (f_c = 80 MPa). Foram utilizados dois tipos de fibras de aço: as macrofibras com diâmetro de 0,75 mm e comprimento de 60 mm (fator de forma igual a 80, com gancho na extremidade); e microfibras com diâmetro de 200 µm e comprimento de 13 mm (fator de forma igual a 65). As fibras foram utilizadas no concreto para atuar como reforço na face tracionada de vigas armadas (12×20×160cm), e foram analisadas as características mecânicas dos concretos: (i) resistência à flexão em corpos de prova prismáticos (10×10×35 cm), (ii) resistência à compressão em corpos de prova cilíndricos (20×Ø10 cm) e (iii) módulo de elasticidade em corpos de prova cilíndricos (20×Ø10 cm). Análise dos resultados mostraram que na resistência à compressão houve um acréscimo de aproximadamente 8% para todas as composições com fibras em relação ao concreto sem fibras. Quanto ao módulo de elasticidade foi verificado comportamento semelhante. Nos corpos de prova prismáticos (10×10×35 cm) ocorreu aumento na tenacidade, sendo que as macrofibras tiveram melhor desempenho. Nas vigas de 12×20×160cm, ocorreu aumento da capacidade portante, quanto ao momento de fissuração e rotação plástica, sendo que o melhor resultado também foi obtido com as macrofibras. De modo geral, pode-se concluir que a aplicação do reforço com fibras de aço na face tracionada das vigas foi eficiente, embora não apresentou aumento significativo na resistência à compressão, fato que pode estar correlacionado ao reduzido volume de fibras utilizado.

Palavras-chave: reforço, concreto de alto desempenho, fibras de aço, microfibra, macrofibras.

[a] *Santa Catarina Extreme South University, Criciúma, SC, Brazil;*
[b] *Adamantinenses University, Civil Engineering Department, Adamantina, SP, Brazil;*
[c] *Federal University of Santa Catarina, Civil Engineering Department,. Florianópolis, SC, Brazil.*

Received: 25 May 2017 • Accepted: 11 Jun 2018 • Available Online: 05 Feb 2019

1. Introdução

As estruturas de concreto armado, quando bem projetadas e executadas, possuem uma grande durabilidade, contudo necessitam de manutenções preventivas e corretivas para garantir a sua funcionalidade. Os reforços são soluções para evitar problemas na construção civil e ainda aumentar a capacidade portante dos elementos estruturais, que por diversos motivos não atendem mais os requisitos para os quais foram projetados [1].
Uma das formas de reforçar e melhorar o desempenho das estruturas de concreto é a adição de fibras, que de uma maneira geral, causa um ganho de tenacidade, um aumento da resistência à ruptura estática, à fadiga dinâmica e ao impacto, melhoramento do comportamento à tração, redução das deformações de solicitação, e o controle de fissuras, considerando seu número e à velocidade de propagação. Esses efeitos contribuem, conjuntamente, com o aumento da durabilidade da estrutura, pois a presença das fibras colabora com a diminuição das aberturas das fissuras, bem como ajuda a controlar e retardar sua propagação, permitindo que ocorra de forma estável.
Com o tempo e os avanços tecnológicos, foram sendo investigados e desenvolvidos diferentes tipos de fibras, com características que as tornavam mais adequadas para a incorporação ao concreto, o que vem permitindo o desenvolvimento de uma geração de compósitos com propriedades cada vez melhores, e com desempenho muito superior ao tradicional, em alguns aspectos. É possível, por exemplo, encontrar na literatura mais recente referências feitas a termos como macrofibras e microfibras, usados para tentar diferenciar as fibras maiores e mais resistentes, que atuam primeiramente na pós-fissuração da matriz, das fibras menores e mais disseminadas, que atuam principalmente no retardo da fissuração [2]. Um exemplo da contribuição das fibras no dimensionamento à flexão de uma viga de concreto armado [3] mostram uma redução da área de aço iguais a 11, 17 e 21%, utilizando consumos de fibras de 20, 30 e 45 kg/m^3 (utilizando fibra de aço Dramix RC 80/60).
Esse é um tema considerado relevante e atual, visto que muitas estruturas têm sido construídas com demanda crescentes de resistência e durabilidade, ou sujeitas às mais variadas solicitações oriundas de condições de suporte ou carregamento excepcionais. O presente estudo pretende avaliar o desempenho das microfibras de aço – em conjunto com as macrofibras - utilizadas em concreto armado como reforço estrutural.

2. Aspectos fundamentais dos compósitos de matriz cimentícia reforçados com fibras

Reestabelecer uma estrutura de concreto armado tem por objetivo retornar ao nível original a sua resistência ou aumentar a capacidade de carga da estrutura. O reforço é o ato de corrigir uma deficiência estrutural ou funcional que muitas vezes focaliza em apenas extinguir a taxa de deterioração. Por fim, espera-se que uma estrutura recuperada e/ou reforçada deva apresentar desempenho superior ao que ela apresentava antes da realização da intervenção. [4]
As fibras de aço foram escolhidas, assim como no trabalho desenvolvido por Quinino [5], por serem as mais difundidas na área de reforço de matrizes cimentícias, em virtude dos inúmeros benefícios e a importância econômica deste material. Fibras agem como ponte de transferência de tensão através das fissuras, possibilitando que o concreto apresente maiores deformações na carga de pico, bem como tenha maior capacidade de carga pós-fissuração, ou seja, há aumento da ductilidade e da resistência residual à tração do material [6]. Para Figueiredo [7], a distribuição aleatória das fibras no material reforça a peça de modo global, diferentemente do que ocorre, por exemplo, com armaduras convencionais no concreto armado. É necessário destacar que, de modo geral, a utilização das fibras como elemento de reforço não é considerada como sendo suficientemente eficiente para substituir as armaduras convencionais. Além disto, é imprescindível atentar para aspectos como a compatibilidade matriz-fibra e a aderência, para que se obtenha o resultado esperado.
Para Martineau e Agopyan [8], a colocação das fibras contribuem no processo de fissuração, atuando como ponte de transferência dos esforços através de trincas, assegurando uma capacidade resistente após a abertura da mesma. Mehta e Monteiro [9] observam que mesmo portando deformações muito superiores a deformação da fratura do concreto convencional, os concretos reforçados com fibras, continuam a resistir a cargas consideráveis, sendo que a resistência última da primeira fissura, depende, intensamente de parâmetros da matriz, como também da influência das características das fibras. Existem ainda dúvidas quanto à eficácia da adição de fibras na melhoria da resistência última. Todavia, é consensual a aceitação do fato de que as fibras melhoram a ductilidade dos compósitos de base cimentícia.

3. Metodologia experimental

Primeiramente foram definidos 4 grupos: i) concreto sem fibras (A); ii) concreto com macrofibras (B); iii) concreto com microfibras (C); iv) concreto com micro e macrofibras (D). Para cada grupo foram produzidos 2 (dois) protótipos de vigas de concreto armado com dimensões de 12×20×160 cm, para ensaios à flexão instrumentado em 4 pontos, 2 corpos de prova cilíndricos (20×Ø10 cm), para ensaios de resistência à compressão axial e módulo de elasticidade, e, 2 corpos de prova prismáticos com dimensões de 10×10×35 cm, para determinação da resistência à flexão do concreto.
Para o dimensionamento dos protótipos, as vigas foram produzidas com seções transversais de 12×20 cm e 160 cm de comprimento. As armaduras de flexão foram dimensionadas segundo os critérios da NBR 6118 [10], considerando a resistência à compressão do concreto de 80 MPa e aço CA-50, adotando-se duas barras de 12,5 mm de diâmetro para armadura principal de combate ao esforço de flexão. Os estribos tiveram espaçamento de 10,0 cm e 12,5 cm e diâmetro de 5,0 mm. Além disso, foram utilizados espaçadores de 2,5 cm, para garantir o cobrimento da armadura.
Foram utilizadas macrofibras (presentes nos grupos B e D), com dimensões de 600 mm×0,75 mm (fator de forma igual a 80, denominação comercial RC 80/60 BN, fabricante ArcelorMittal/Dramix®), e microfibras (presentes nos grupos C e D), com dimensões de 13 mm×200 µm (fator de forma igual a 65, denominação comercial OL 13/.20, fabricante ArcelorMittal/ Dramix®).
A concretagem foi realizada em duas fases: Na primeira fase foram realizadas somente as concretagens de uma parcela das

vigas (12×20×160 cm) dos grupos B, C e D, entretanto as vigas do grupo A (referência) foram concretadas na sua totalidade por não possuir reforço com fibras. Os corpos de prova prismáticos (10×10×35 cm) e os corpos de prova cilíndricos (20×Ø10 cm) sem adição de fibras foram concretados simultaneamente a esta primeira fase. Foi definida uma composição de concreto, utilizando o traço unitário de 1:2,3:2,7:0,4 (cimento:areia:brita:a/c). O cimento utilizado foi tipo CP-IV. A mistura foi realizada em betoneira com capacidade para 400 litros. A consistência do concreto foi medida pelo ensaio de abatimento e foi igual a 11 cm. Todas as vigas foram concretadas simultaneamente com concreto dosado em laboratório e adensadas com auxílio de vibradores de imersão e mesa vibratória. As vigas foram concretadas até uma altura de 13,75 cm. Essa limitação foi controlada no momento da primeira fase da concretagem, através de uma marcação interna na forma, ficando exposta a armadura de combate a flexão dos grupos B, C e D. A dimensão do reforço dos grupos B, C e D foi estabelecida como sendo duas vezes a dimensão do cobrimento das armaduras somado a uma vez o diâmetro da barra de combate a flexão (2,5+2,5+1,25=6,25 cm), esta dimensão foi mantida na concretagem da segunda fase (grupos B, C e D), variando-se apenas os tipos das fibras.

A segunda fase da concretagem das vigas (12×20×160 cm) ocorreu após 24 horas do final da primeira fase, porém a reconstituição do banzo tracionado das vigas dos grupos B, C e D, tiveram a presença de fibras nos 6,25 cm de espessura definidos. Não houve preparo da superfície, pois havia os estribos que serviriam de ponte de ligação (aderência) para o concreto novo. A quantidade de fibras inseridas nos grupos que receberam reforço foi de 20 kg/m³ ou V_f=0,26% em relação ao volume de concreto. Vale ressaltar, que os corpos de prova prismáticos (10×10×35 cm) e os corpos de prova cilíndricos (20×Ø10 cm) com adição de fibras foram concretados simultaneamente a esta segunda fase.

Após 24 horas de concretagem os corpos de prova cilíndricos foram desmoldados e colocados em cura submersa até idade de 28 dias para os ensaios de resistência à compressão axial [11] e módulo de elasticidade [12]. Os corpos de prova prismáticos e as vigas de concreto armado foram desmoldadas 14 dias após a última concretagem, posteriormente foram pintados para melhor análise de fissuras e identificados conforme as sequências dos grupos correspondentes, sendo que a idade de ruptura para todas vigas ocorreu após 28 dias de concretagem da 2ª fase. As vigas (12×20×160 cm) foram identificadas por: grupo A (Vigas A1 e A2), grupo B (Vigas B1 e B2), grupo C (Vigas C1 e C2), grupo D (Vigas D1 e D2). Sendo que as Vigas A1, B1, C1 e D1 se referem a vigas instrumentadas com *Strain Gages,* totalizando 4 vigas, já as identificadas como Vigas A2, B2, C2 e D2 tratam-se das vigas sem a presença de sensores ligados ao aço e ao concreto. Os corpos de prova prismáticos (10×10×35 cm) também receberam as nomenclaturas Ap, Bp, Cp e Dp, respectivamente para cada grupo.

Todas as vigas foram submetidas ao ensaio de flexão em 4 pontos. As cargas foram aplicadas de cima para baixo sobre um perfil metálico (Perfil I – 10×25,5 cm) que transferiu o carregamento para as vigas em duas cargas pontuais divididas exatamente nos terços do vão teórico da viga. As vigas foram posicionas sob um pórtico metálico de reação e a carga foi aplicada mediante um cilíndrico hidráulico de controle elétrico com capacidade de 500 kN. Os valores de carga foram registrados por meio de uma célula de carga disposta entre o cilíndrico hidráulico e a viga de distribuição (Perfil I – 10×25,5 cm). Foram avaliados os deslocamentos verticais em 3 pontos (LVDT 1, LVDT 2(centro), LVDT 3) ao longo do comprimento da viga com a utilização de transdutores indutivos de deslocamentos (LVDT - *Linear Variable Differential Transformes*). As deformações foram monitoradas por meio de extensômetros elétricos (*strain gages*) colados nos materiais em pontos estratégicos de deformação: no concreto e na armadura de flexão, como mostra o croqui da Figura 1. Os equipamentos foram conectados ao sistema de aquisição de dados QuantumX® com interface com o *software* Catman Easy®, ambos da HBM®.

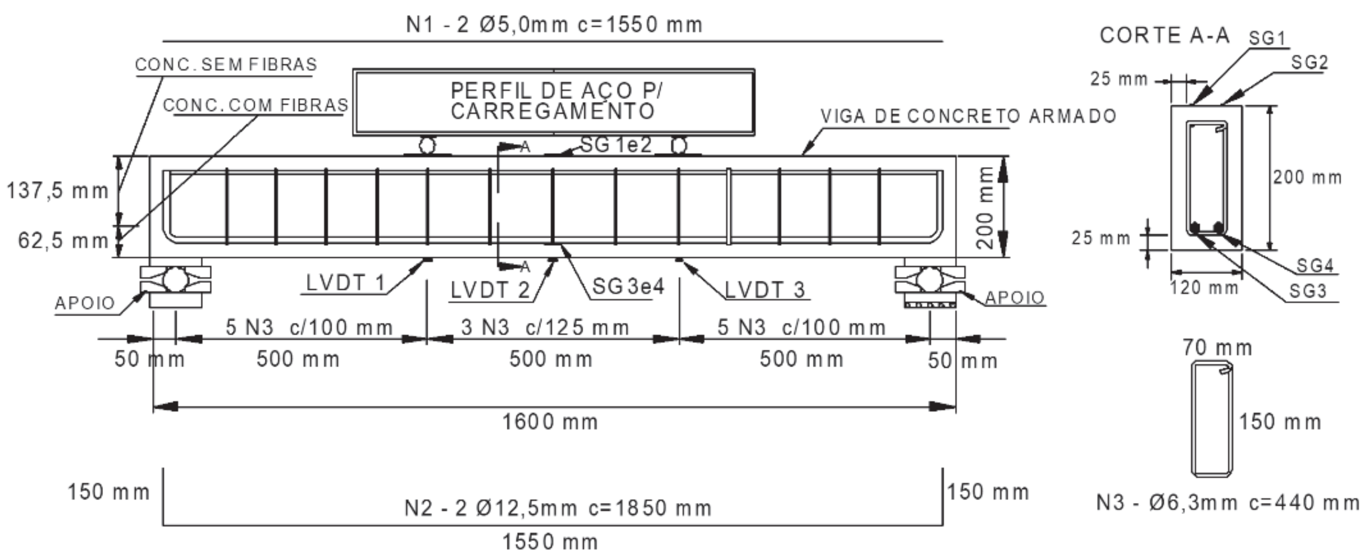

Figura 1
Posicionamentos dos LVDT's e SG's ao longo da viga

Tabela 1
Resultados do carregamento e deslocamento de ruptura das vigas (12 × 20 × 160 cm)

GRUPO A – Sem fibras					
Vigas	**Carga (kN)**	**Desloc, Esq, (mm)**	**Desloc, Meio (mm)**	**Desloc, Dir, (mm)**	**Fator de ductilidade**
A1	84,22	13,77	16,91	15,48	1,98
A2	85,60	13,62	15,77	12,61	1,92
Média (D,P)	84,91 (0,98)	13,69 (0,11)	16,34 (0,81)	14,05 (2,03)	1,95 (0,04)
GRUPO B – Macrofibras					
Vigas	**Carga (kN)**	**Desloc, Esq, (mm)**	**Desloc, Meio (mm)**	**Desloc, Dir, (mm)**	**Fator de ductilidade**
B1	89,09	14,33	18,30	16,07	2,00
B2	86,67	9,62	12,72	10,68	1,55
Média (D,P)	87,88 (1,71)	11,98 (3,34)	15,51 (3,95)	13,38 (3,81)	1,78 (0,32)
GRUPO C – Microfibras					
Vigas	**Carga (kN)**	**Desloc, Esq, (mm)**	**Desloc, Meio (mm)**	**Desloc, Dir, (mm)**	**Fator de ductilidade**
C1	88,88	11,20	14,39	11,67	1,77
C2	87,70	14,64	12,24	12,07	1,65
Média (D,P)	88,29 (0,83)	12,92 (2,43)	13,31 (1,52)	11,87 (0,28)	1,71 (0,08)
GRUPO D – Macrofibras + Microfibras					
Vigas	**Carga (kN)**	**Desloc, Esq, (mm)**	**Desloc, Meio (mm)**	**Desloc, Dir, (mm)**	**Fator de ductilidade**
D1	86,99	13,90	18,71	13,91	2,11
D2	85,16	11,37	14,21	11,74	1,85
Média (D,P)	86,07 (1,29)	12,63 (1,79)	16,46 (3,18)	12,83 (1,54)	1,98 (0,18)

As verificações foram feitas de modo a analisar o comportamento de cada grupo em diferentes instantes de aplicação de carga: i) quando atingido o deslocamento máximo permitido por norma (L/250); ii) na ruptura. No primeiro instante foi verificado o carregamento necessário para que as vigas atingissem o deslocamento máximo estabelecido por norma (L/250), foi considerado (L=150 cm) sendo o vão teórico das vigas, no qual foi encontrado um valor para o deslocamento de 6,0 mm. No segundo e último instante do ensaio, foi verificado o valor do carregamento e deslocamento que levaram a viga à ruptura. Com os resultados do ensaio de flexão, por meio das curvas de carga *versus* deslocamentos verticais, obtida com os LVDT's, posicionados ao longo do comprimento, pode-se traçar a linha elástica experimental da viga. Com os valores de deformação pode-se ter uma melhor compreensão dos limites dos Estádios em valores de momento fletor de fissuração e momento fletor de plastificação. Foi possível caracterizar um modelo para o fenômeno de mudança de Estádios de deformação de uma viga reforçada com fibras através da observação da relação entre o momento fletor e a curvatura formada na seção transversal da viga. Por fim mapeou-se o desenvolvimento das fissuras e a forma ruptura.

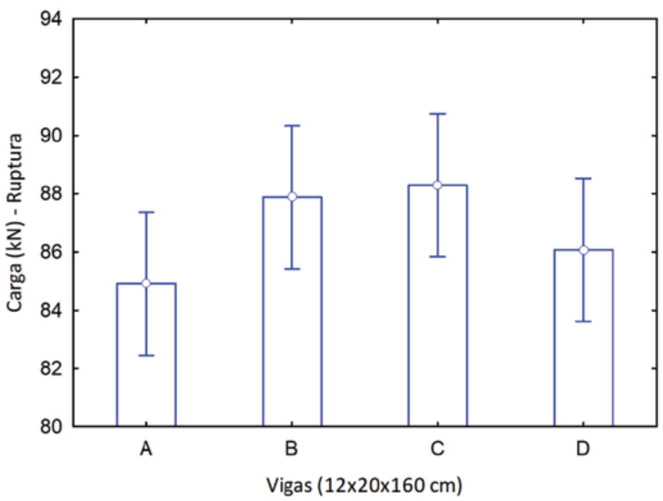

Figura 2
Análise dos resultados de carga na ruptura – vigas (12 × 20 × 160 cm)

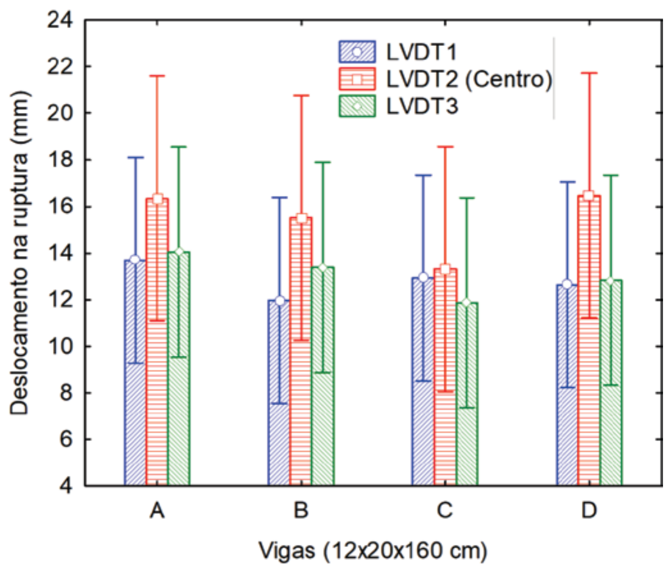

Figura 3
Análise dos resultados do deslocamento na ruptura – vigas (12 × 20 × 160 cm)

4. Resultados e discussões

4.1 vigas de concreto armado (12 × 20 × 160cm)

4.1.1 Carregamento e deslocamento na ruptura

O carregamento, os deslocamentos atingidos na ruptura das vigas e os fatores de ductilidade podem ser observados na Tabela 1. O comportamento dos percentuais que justificam o aumento da capacidade portante entre os grupos, foram diferentes no deslocamento até a ruptura. Para levar as vigas do grupo B à ruptura, teve um incremento de carga de 3,5% superior ao grupo A. O grupo C foi 4,0% mais elevado em comparação ao grupo A, assim como o grupo D, que foi de 1,4%. Com relação aos deslocamentos, estes foram semelhantes e próximos entre todos os grupos. Ao analisar os valores médios de cargas na ruptura, apresentados na Figura 2, observa-se um aumento para as vigas B e C com uso das macrofibras e microfibras, respectivamente. Apesar do fator de forma menor, as microfibras mostram uma tendência de aumento, que pode ser associada a maior quantidade de fibras, e, devido a sua eficiência para reforçar a microfissuração, provocada antes da ruptura. Ao utilizar as macrofibras+microfibras (Grupo D), é observado uma redução de carga de ruptura da viga, mantendo o resultado superior às vigas de referência (Grupo A). Comparando este resultado com as fibras utilizadas isoladamente, a explicação

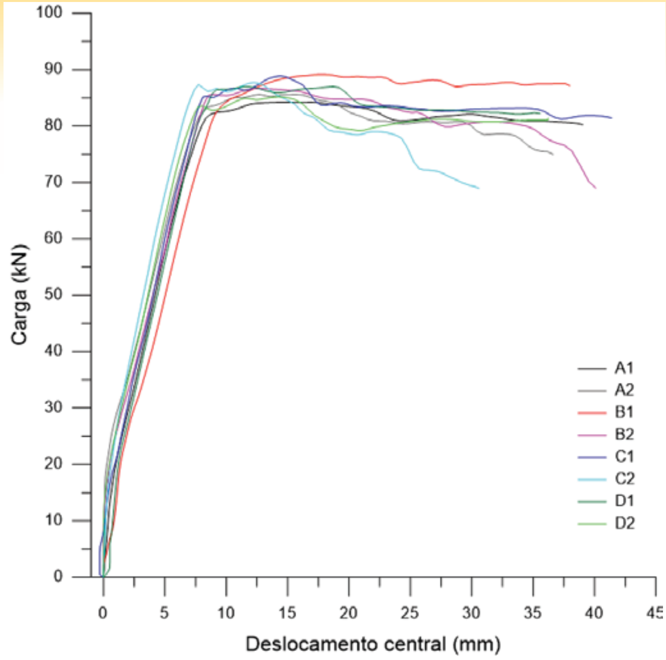

Figura 4
Comportamento carga *versus* deslocamento – vigas (12 × 20 × 160 cm)

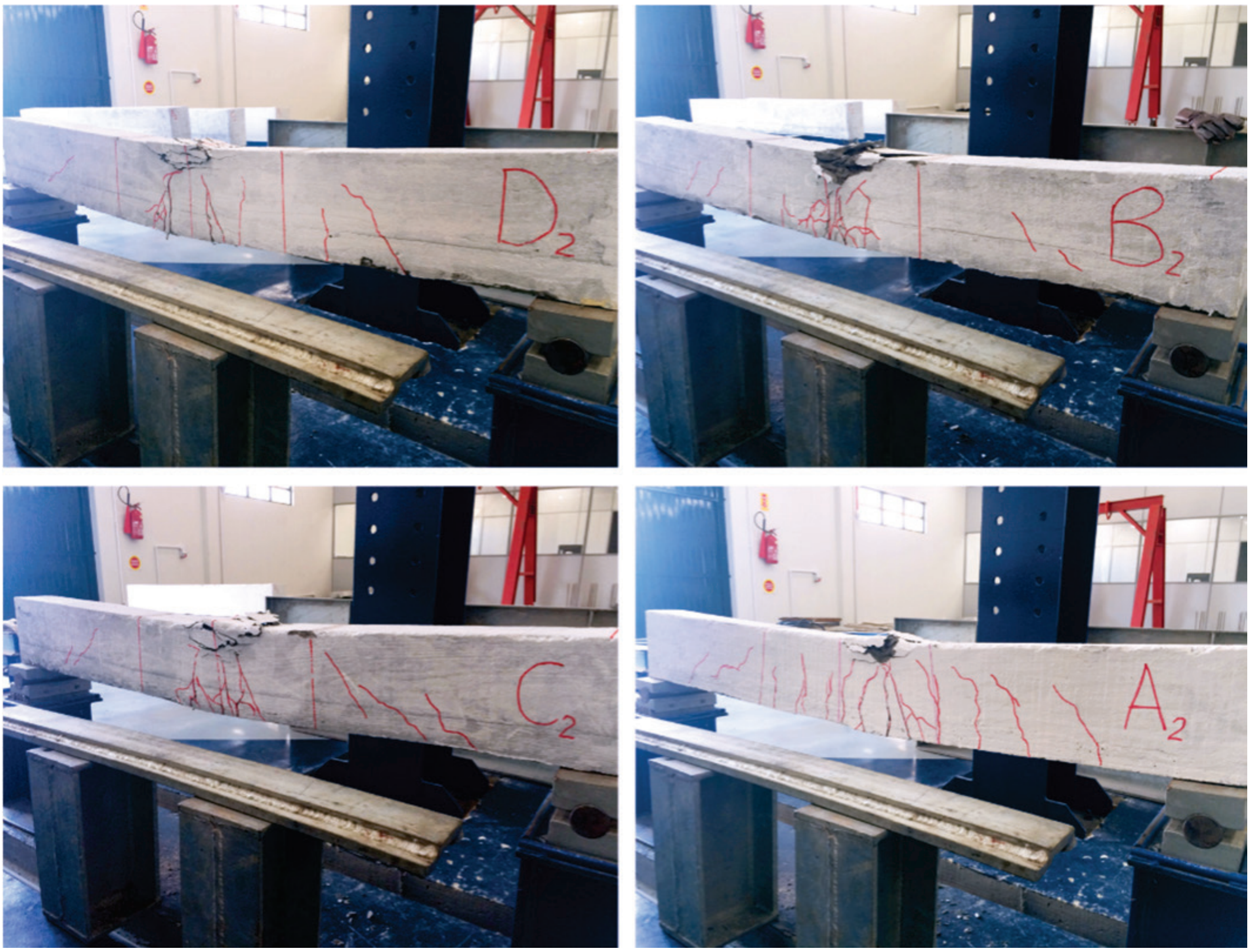

Figura 5
Forma de ruptura e fissuras dos grupos das vigas (12 × 20 × 160 cm)

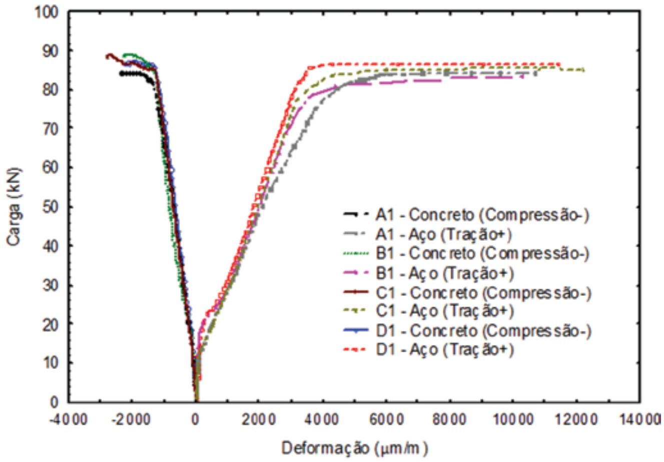

Figura 6
Deformações específicas do aço e concreto – vigas (12 × 20 × 160 cm)

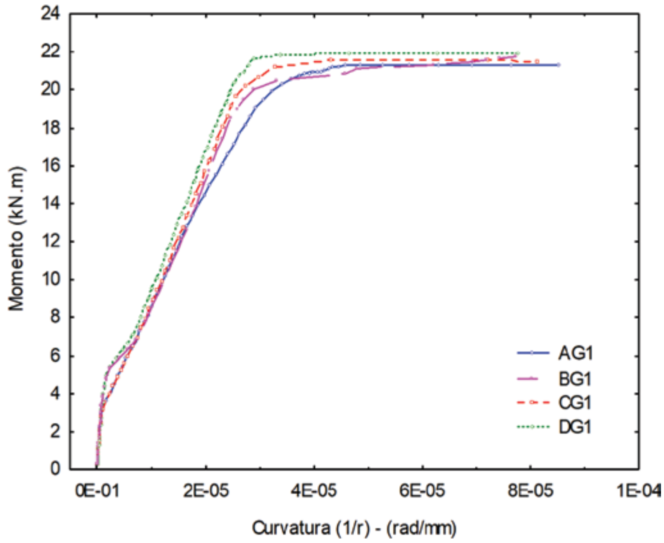

Figura 7
Diagrama momento – curvatura – vigas (12 × 20 × 160 cm)

mais plausível, seria uma perda de resistência devido à menor compacidade da matriz cimentícia composta com as duas fibras. Considerando o deslocamento na ruptura das vigas, o grupo C mostrou que as microfibras não contribuem para o aumento do deslocamento final antes da ruptura. O fator de ductilidade obtido entre a relação do deslocamento na ruptura e o deslocamento no momento de plastificação, mostrou que o grupo D apresentou melhor comportamento em relação ao grupo A de referência.

4.1.2 Comportamento carga *versus* deslocamento

Na Figura 4, estão apresentados os gráficos de carga *versus* deslocamento de todas as vigas (12×20×160 cm). Observa-se que os comportamentos entre os grupos foram similares quanto às cargas últimas e nas cargas de serviço (L/250). Nota-se também, que as vigas de todos os grupos ultrapassaram o deslocamento máximo admitido por norma (L/250 = 6,0 mm) antes do colapso. Todas as vigas romperam por esmagamento do concreto da face comprimida.

Para compreender a forma de ruptura e fissuras entre os grupos de vigas (12×20×160 cm), as imagens na sequência da Figura 5, ilustram estas particularidades. O grupo A, de referência e sem fibras na face tracionada, foi que apresentou maior número de fissuras visuais, ultrapassando até a região do terço médio. Os grupos B, C e D foram semelhantes em relação ao aparecimento de fissuras concentradas no terço médio do vão teórico da viga, e, também para o surgimento de algumas fissuras por cisalhamento.

4.1.3 Análise das deformações específicas

O gráfico da Figura 6 apresenta as deformações específicas do concreto na face superior mais comprimida e a do aço na face inferior (barra de aço - Ø12,5 mm) mais tracionada, ambas localizadas na seção transversal central (Figura 1). Nota-se que as

Tabela 2
Resultados dos momentos e curvaturas das vigas (12 × 20 × 160 cm)

Momentos						
Vigas	Momento de fissuração M_r (kN.m)	Diferença	Momento de plastificação M_y (kN.m)	Diferença	Momento último M_u (kN.m)	Diferença
A	0,7	Ref,	20,6	Ref,	21,3	Ref,
B	5,4	+655,7%	20,5	-0,7%	22,6	+5,7%
C	2,8	+291,8%	19,1	-7,1%	22,5	+5,5%
D	4,5	+529,6%	21,7	+5,3%	22,0	+3,2%

Curvaturas nos respectivos momentos						
Vigas	1/r (M_r)	Diferença	1/r (M_y)	Diferença	1/r (M_u)	Diferença
A	1,15E-07	Ref,	3,57E-05	Ref,	7,65E-05	Ref,
B	2,37E-06	+1960,9%	3,32E-05	-7,1%	8,16E-05	+6,6%
C	7,95E-07	+592,2%	2,47E-05	-30,8%	8,85E-05	+15,7%
D	1,45E-06	+1161,2%	2,90E-05	-18,8%	7,95E-05	+3,9%

Tabela 3
Resultados de resistência à compressão e módulo de elasticidade - CPs (20 × Ø10 cm)

CPs	f_c (MPa)	Diferença	E_c (GPa)	Diferença	Material
A1	81,8	–	54,2	Ref,	Concreto
A2	80,6	–	–	–	Concreto
Média (D.P.)	81,2 (0,85)	Ref,	–	–	Concreto
CPs	**f_c (MPa)**	**Diferença**	**E_c (GPa)**	**Diferença**	**Material**
B1	86,3	–	57,3	+5,7%	Concreto + Macrofibras
B2	89,3	–	–	–	Concreto + Macrofibras
Média (D.P.)	87,8 (2,12)	+8,1%	–	–	Concreto + Macrofibras
CPs	**f_c (MPa)**	**Diferença**	**E_c (GPa)**	**Diferença**	**Material**
C1	86,8	–	57,2	+5,5%	Concreto + Microfibras
C2	89,6	–	–	–	Concreto + Microfibras
Média (D.P.)	88,2 (1,98)	+8,6%	–	–	Concreto + Microfibras
CPs	**f_c (MPa)**	**Diferença**	**E_c (GPa)**	**Diferença**	**Material**
D1	88,4	–	55,4	+2,2%	Concreto + Macrofibras + Microfibras
D2	88,3	–	–	–	Concreto + Macrofibras + Microfibras
Média (D.P.)	88,4 (0,07)	+8,8%	–	–	Concreto + Macrofibras + Microfibras

deformações finais no concreto e no aço foram similares entre os grupos, ficando aproximadamente 2200 µm/m para os concretos e 11000 µm/m para os aços. Entretanto, observa-se que os grupos B e D apresentaram uma deformação menor no aço entre as cargas de 10 kN e 20 kN, o que contribuiu para aumentar o momento de fissuração. Se for fixado um valor de carregamento (entre as cargas de 10 kN e 20 kN), pode ser observado que a menor deformação (aço) ocorre nas vigas com as microfibras e macrofibras, seguido das microfibras, após as macrofibras e por último e mais deformável o concreto de referência. Estes resultados mostram o potencial das microfibras em conjunto com as macrofibras, para a melhoria do comportamento estrutural de um reforço, atuando de forma conjunta, antes e após a ocorrência de fissuras. Pesquisas recentes mostram o efeito benéfico da utilização de fibras híbridas – macro e microfibras – melhorando a resistência a deformação em estados múltiplos de fissuração [13].

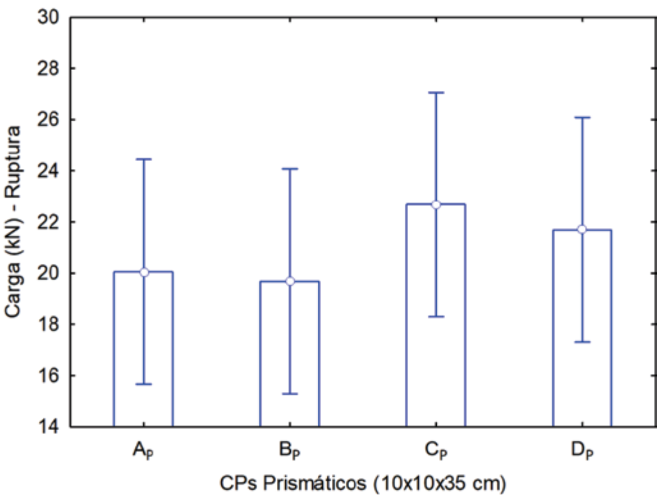

Figura 8
Análise dos resultados de carga na ruptura – CPs prismáticos (10 × 10 × 35 cm)

4.1.4 Análise do diagrama momento – curvatura

A Tabela 2 apresenta os resultados de momentos e curvaturas e as diferenças em porcentagens com relação a viga referência e a Figura 7 observa-se os diagramas momento-curvatura para viga A1, B1, C1 e D1. O grupo B com a presença de macrofibras apresentou 6,5 vezes maior momento de fissuração superior ao grupo A (referência), seguidos dos grupos D e C. Quanto à rotação o grupo B foi 19,6 vezes superior ao grupo A (referência), seguidos dos grupos D e C referente ao momento de fissuração (Mr). Este comportamento mostra que as fibras aumentaram o momento de fissuração e rotação plástica, porém a adição isolada de microfibras foram as que menos contribuíram. A geometria das macrofibras, com ganchos e não lisas como as microfibras, contribuem para esta propriedade [13].

4.2 Propriedades mecânicas dos concretos

4.2.1 Resistência à compressão (f_c) e Módulo de elasticidade (E_c)

Para caracterizar mecanicamente o concreto foram realizados ensaios de resistência à compressão e módulo de elasticidade à compressão. Para resistência à compressão a diferença máxima entre os grupos foi de 8,8%, sendo que os concretos com adições de fibras apresentaram resultados similares e superiores em aproximadamente 8% ao concreto sem fibras (Tabela 3). Segundo Mehta e Monteiro [9] o acréscimo de fibras de aço no concreto em teores inferiores a 2% em volume, exerce pouca influência na resistência à compressão. No entanto para concretos de alta resistência, é verificado aumento na resistência à

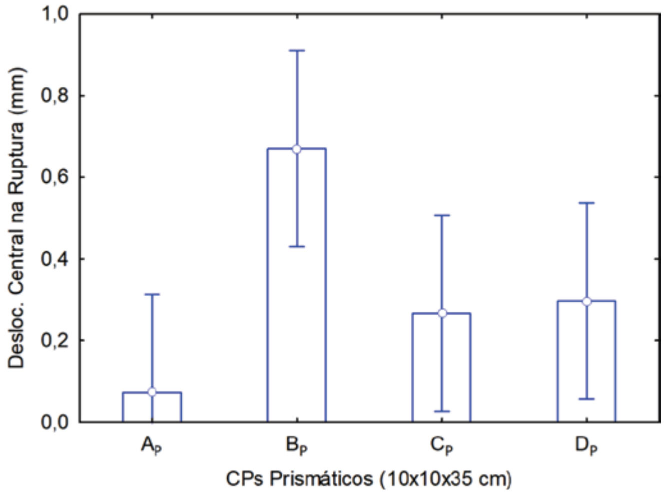

Figura 9
Análise dos resultados do deslocamento na ruptura – CPs prismáticos (10 × 10 × 35 cm)

compressão para concentração de 0,5% de microfibras [14]. Para Su et al. [14] ao utilizarem o teor máximo de 2,5% de microfibras de aço, de dois tipos, com fator de forma de 50 (6 mm×0,12 mm) e 125 (15 mm×0,12 mm), atingiram uma resistência à compressão de 114 MPa e 145 MPa, respectivamente. Neste trabalho, o fator de forma das microfibras foi de 65 (13 mm×0,2 mm), e uma concentração menor de fibras, podendo-se considerar os resultados de aumento da resistência satisfatórios, e, associado a maior resistência a propagação de microfissuras durante o carregamento.

Considerando o módulo de elasticidade, observa-se que a diferença máxima entre os grupos foi menor, de aproximadamente 6% (Tabela 3), entre o concreto com macrofibras e microfibras (Grupo B e C) para o concreto sem fibras. Esta diferença pode ter sido causada pela maior densidade do concreto com fibras.

4.2.2 Ensaio de flexão – corpos de prova prismáticos (10 × 10 × 35 cm)

Com relação a carga e deslocamento na ruptura (Figuras 8 e 9, respectivamente), os grupos C e D atingiram cargas maiores para o deslocamento na ruptura, sendo 13% superior do grupo C em relação ao grupo A com deslocamento médio de 0,27 mm, de mesmo modo, o grupo D apresentou um acréscimo de 8% para o deslocamento determinado de 0,30 mm. O grupo B não obteve aumento da resistência, em relação ao grupo A. Novamente é verificada esta tendência de aumento da resistência à fissuração, utilizando as microfibras ou as microfibras+macrofibras, em relação ao concreto sem fibras. Ao utilizar os corpos de prova prismáticos – ao invés de vigas de concreto armado – ficou mais evidente esta melhoria provocada pelas microfibras. Apesar das diferenças serem pequenas, o volume de fibras também é baixo (V_f=0,26%). Esta quantidade reduzida, foi utilizada por se tratar de um concreto a ser aplicado como reforço, mantendo-se assim a facilidade de aplicação. Este mesmo comportamento foi observado no deslocamento até a ruptura, considerando os corpos de prova prismáticos com fibras, nos quais as microfibras apresentam os melhores resultados.

Com relação à tenacidade os resultados estão apresentados nas Figuras 10 e 11, e, mostram índice superior para o grupo B, utilizando macrofibras. Os grupos C e D apresentaram valores inferiores ao grupo B e superiores ao grupo A. A maior tenacidade causada pelas macrofibras, pode ser explicado, devido ao seu maior fator de forma, e consequentemente maior área de contato fibra-matriz. Complementarmente, as macrofibras com ganchos, melhoram a resistência pós-fissuração do concreto, se comparado com as fibras lisas [13].

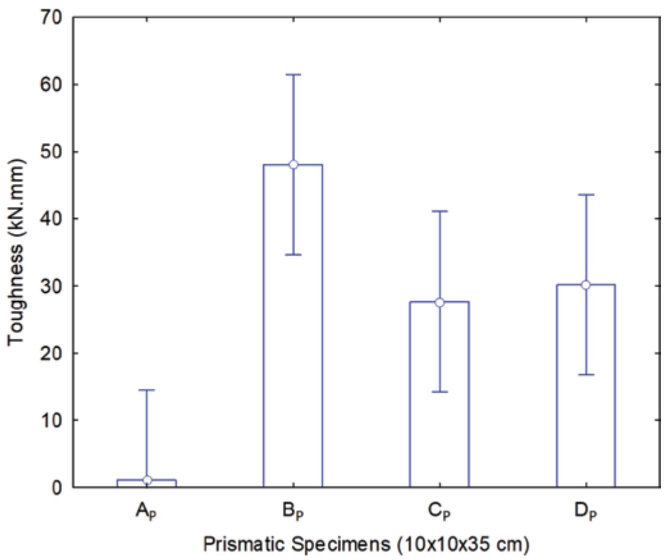

Figura 10
Análise dos resultados de tenacidade – CPs prismáticos (10 × 10 × 35 cm)

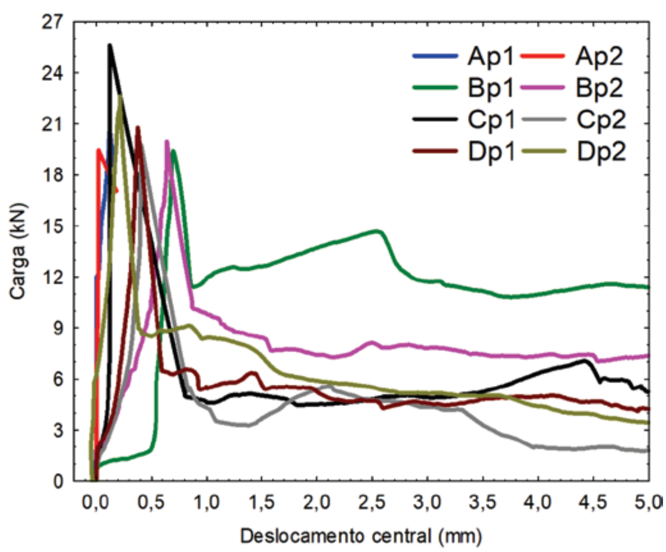

Figura 11
Comportamento carga *versus* deslocamento – CPs prismáticos (10 × 10 × 35 cm)

5. Considerações finais

Referente ao estudo realizado pode-se chegar às seguintes conclusões:

- Com relação aos resultados de carregamento e deslocamento (admitidos por norma L/250 e na ruptura) apresentados para as vigas de concreto armado (12×20×160 cm) e vigas de concreto (10×10×35 cm), conclui-se que para todos os grupos que continham fibras de aço na face tracionada, contribuíram para melhores resultados;
- No diagrama momento – curvatura, todas as fibras aumentaram o momento de fissuração e rotação plástica;
- As fissuras das vigas de 10×10×35 cm mostram que o grupo A teve comportamento frágil, levando a ruptura de forma brusca;
- Os resultados de resistência à compressão foram superiores (8%) para os concretos com adições de fibras;
- As macrofibras apresentaram os melhores resultados diante dos demais grupos, para as vigas de 12×20×160 cm, assim como para as vigas de 10×10×35 cm;
- Comparando as microfibras, com as macrofibras, pode-se concluir que as microfibras melhoraram a resistência a flexão e os deslocamentos das vigas armadas, e, melhoraram a resistência à compressão, apesar do baixo volume utilizado. As macrofibras foram melhores para aumento da tenacidade ou comportamento após a ruptura;
- O uso das fibras híbridas – macrofibras+microfibras – não teve um comportamento diferenciado entre as fibras utilizadas isoladamente, porém contribui para aspectos de melhoria – ainda que de forma menos significativa – na região de microfissuração e pós-fissuração do concreto.

Por fim, o método de aplicação do reforço com fibras de aço na face tracionada das vigas se mostrou eficaz, embora não apresenta incrementos de resistência elevados. As fibras contribuíram para uma série de resultados, atuando de forma eficiente no combate a fissuração.

6. Agradecimentos

Os autores são gratos pelo apoio financeiro do Conselho Nacional de Desenvolvimento Científico e Tecnológico (CNPq) e a empresa Belgo Bekaert pela doação das fibras utilizadas.

7. Referências bibliográficas

[1] DEGHENHARD, C. C., TEIXEIRA, T., VARGAS, A., VITO, M., PICCININI, Â. C., DO VALE SILVA, B. Experimental analysis of various configurations of metal sheets in the reinforcement of flexion of reinforced concrete beams. ALCONPAT Journal, v. 6, p. 105-199, 2016.

[2] BERNARDI, S. T. Avaliação do comportamento de materiais compósitos de matrizes cimentícias reforçadas com fibra aramida Kevlar, 2003. Dissertação (Mestrado) – Escola de Engenharia da Universidade Federal do Rio Grande do Sul. Porto Alegre, 2003.

[3] REAL, L.V., NOGUEIRA, A.B., SIMÃO, L., FIGUEIREDO, A.D. Contribuição das fibras de aço para o dimensionamento à flexão de viga armada. Revista Concreto & Construções, n 87, 2017.

[4] FERRARI, V.J., HANAI, J.B. Flexural strengthening of reinforced concrete beams with carbon fibers reinforced polymer (CFRP) sheet bonded to a transition layer of high performance cement-based composite. IBRACON Structures and Materials Journal. v.5, n.5, p. 596-626, 2012.

[5] QUININO, U. C. M. Investigação experimental das propriedades mecânicas de compósitos de concreto com adições híbridas de fibras. Tese (Doutorado em Engenharia Civil) – Programa de Pós Graduação em Engenharia Civil (UFRGS) Universidade Federal do Rio Grande do Sul (UFRGS), Porto Alegre/RS, 2015.

[6] FIGUEIREDO, A.D. Concreto reforçado com fibras, Tese de Livre-Docência, Escola Politécnica, Universidade de São Paulo, São Paulo, 2011.

[7] FIGUEIREDO, A.D. Concreto com fibras. Concreto, Ensino, Pesquisa e Realizações, São Paulo, Ed. Geraldo Cechella Isaia, IBRACON, p.1194-1225, 2005.

[8] MARTINEAU, P., AGOPYAN, V. Conferência Magma I – Compósitos: material inovador. In: Arquimacom'2002. São Paulo, 2002.

[9] MEHTA, P. K. & MONTEIRO, P. J. M. Concreto: Microestrutura, propriedades e materiais. 2º Edição (português). São Paulo, IBRACON, 2014.

[10] ASSOCIAÇÃO BRASILEIRA DE NORMAS TÉCNICAS. NBR 6118: Projeto de estruturas de concreto. Rio de Janeiro, 2014.

[11] ASSOCIAÇÃO BRASILEIRA DE NORMAS TÉCNICAS. NBR 5739: Concreto – Ensaio de compressão de corpos de prova cilíndricos. Rio de Janeiro, 2014.

[12] ASSOCIAÇÃO BRASILEIRA DE NORMAS TÉCNICAS. NBR 8522: Concreto - Determinação do módulo estático de elasticidade à compressão. Rio de Janeiro, 2014.

[13] PARK, S. H., KIM, D.J., RYU, G. S., KOH K. T. Tensile behavior of Ultra High Performance Hybrid Fiber Reinforced Concrete. Cement & Concrete Composites 34, 172–184, 2012.

[14] SU, Y., LI, J., WU, C. WU, P. LI, Z-X. Effects of steel fibres on dynamic strength of UHPC. Construction and Building Materials 114, 708–718, 2016.

Volume 12, Number 1 (February 2019) p. 87 – 100 • ISSN 1983-4195
http://dx.doi.org/10.1590/S1983-41952019000100008

IBRACON

REVISTA IBRACON DE ESTRUTURAS E MATERIAIS
IBRACON STRUCTURES AND MATERIALS JOURNAL

Strut-and-tie models for linear and nonlinear behavior of concrete based on topological evolutionary structure optimization (ESO)

Modelo de bielas e tirantes para comportamentos linear e não linear do concreto com base na Otimização Estrutural Evolucionária (ESO)



R. M. LANES [a]
rmlanes@yahoo.com.br
https://orcid.org/ 0000-0001-7322-6869

M. GRECO [a]
mgreco@dees.ufmg.br
https://orcid.org/ 0000-0001-5500-0225

M. B. B. F. GUERRA [a]
marcelabbfguerra@gmail.com
https://orcid.org/ 0000-0002-9770-1588

Abstract

The search for representative resistant systems for a concrete structure requires deep knowledge about its mechanical behavior. Strut-and-tie models are classic analysis procedures to the design of reinforced concrete regions where there are stress concentrations, the so-called discontinuous regions of the structure. However, this model is strongly dependent of designer's experience regarding the compatibility between the internal flow of loads, the material's behavior, the geometry and boundary conditions. In this context, the present work has the objective of presenting the application of the strut-and-tie method in linear and non-linear on some typical structural elements, using the Evolutionary Topological Optimization Method (ESO). This optimization method considers the progressive reduction of stiffness with the removal of elements with low values of stresses. The equivalent truss system resulting from the analysis may provide greater safety and reliability.

Keywords: reinforced concrete, strut-and-tie models, Abaqus, FEM, ESO.

Resumo

A busca por sistemas resistentes representativos para estrutura de concreto requer profundo conhecimento sobre seu comportamento mecânico. Os modelos de bielas e tirantes são procedimentos clássicos utilizados no dimensionamento do concreto armado onde existem concentrações de tensão, as chamadas regiões descontínuas da estrutura. No entanto, esse modelo é fortemente dependente da experiência do analista em relação à compatibilidade entre esforços internos, comportamento do material, geometria e condições de contorno. Neste contexto, o presente trabalho tem como objetivo apresentar a aplicação de métodos de bielas e tirantes para análises linear e não-linear em alguns elementos estruturais típicos, utilizando o Método de Otimização Estrutural Evolucionária (ESO). Esse algoritmo de otimização topológica considera a redução progressiva da rigidez com a remoção de elementos com baixos valores de tensões. O sistema de treliça equivalente resultante da análise pode fornecer maior segurança e confiabilidade.

Palavras-chave: concreto armado, modelo de bielas e tirantes, Abaqus, MEF, ESO.

[a] *Universidade Federal de Minas Gerais, Departamento de Engenharia de Estruturas, Programa de Pós-Graduação em Engenharia de Estruturas, Belo Horizonte, MG, Brasil.*

Received: 25 May 2018 • Accepted: 06 Aug 2018 • Available Online: 05 Feb 2019

1. Introduction

In projects' routine, it is necessary to design the components of a structure based on classic theories that describe the mechanical elements' behavior. In general, these theories present an analytical or empirical bias and knowledge about the limit of the application for each of the considered premises is fundamental to ensure the safety and the quality of the project. In the reinforced concrete design, the structure can be divided in two different regions, one governed by Bernoulli-Euler kinematic hypotheses and another governed by the principle of Saint-Venant. It allows the adequate determination of internal forces and the necessary steel for the reinforced concrete. Concrete regions in which the Bernoulli-Euler hypotheses are valid are known in the literature as B-Regions, while D-Regions correspond to regions where the Saint-Venant principle should be applied. This latter region represents a discontinuity area of the structure, distinguished as a static discontinuity (e.g., in support regions), or a geometric discontinuity (e.g., parts with abrupt changes of geometry).

The discontinuous regions of reinforced concrete can be adequately represented by the use of strut-and-tie model. This model consists on the simulation of the parts effectively loaded inside the structure by the idealization of a truss with equivalent mechanical behavior. The methodology is used for the determination of internal forces in the struts (compressed elements of the truss) and in the ties (tensioned elements of the truss).

1.1 Justification

The load supported by the strut-and-tie model must be evaluated by a criterion of ultimate load and, usually, it requires from the designer the experience to choose and placement of elements that defines the equivalent truss. Some normative codes propose standard strut-and-tie models for some specific elements, e.g., CEB-FIP Model Code [10], CSA-A23.3-04 [7], ACI-318 [4] and [5], EUROCODE 2 [9] and ABNT NBR 6118 [6] . However, due to the clear dependence of such models with some parameters related to geometry, their applications become very limited in structural designs routine.

In this context, topological optimization of structures has been frequently used in structural systems assembly in D-Regions of structures in reinforced concrete [12]. The optimized design for structural models is attractive because it allows the design of trusses that tend to exhibit minimal deformation energy, or maximum stiffness, and reduces the empiricism associated with the bar systems assembly.

The Evolutionary Structural Optimization (ESO) method developed by Xie and Steven ([25], [26], [27]) and Chu et al. [8] can been used to optimize continuous structures from the Finite Element Method (FEM) simulation. The ESO formulation was originally developed from an evolutionary algorithm based on a very simple concept that is based on the insertion of voids, that presents fundamentals in the gradual elements' elimination of the model that are less requested (with low level of stresses) of the domain during the process, called a hard-kill procedure. The mathematical representation of the ESO for the problems' solution for topological optimization can presented based on two concepts: stresses or displacements [16].

Since its beginning, the ESO has stood out for being a simple algorithm and for providing an easy insertion in a computational code of the FEM, without additional complex mathematical manipulations. High-performance commercial software enables ESO use in programming platforms, enabling studies for current and future research, as well as favoring the practical application in structural projects.

Therefore, the current article presents some results achieved through a structural topological analysis, via the ESO topological optimization method, implemented by Python programming script in the Abaqus® software for analyzing multiphysical problem.

2. Constitutive model for elastic and plastic damage

The analysis performed in this study consider both material behaviors, the linear elastic and the non-linear. The constitutive model of plastic damage available in Abaqus® software, called CDP (Concrete Damaged Plasticity) has been adopted in the present study, for the nonlinear analysis of the elements in concrete reinforced by FEM. Initially, Lubliner [17] has proposed this model and, later,

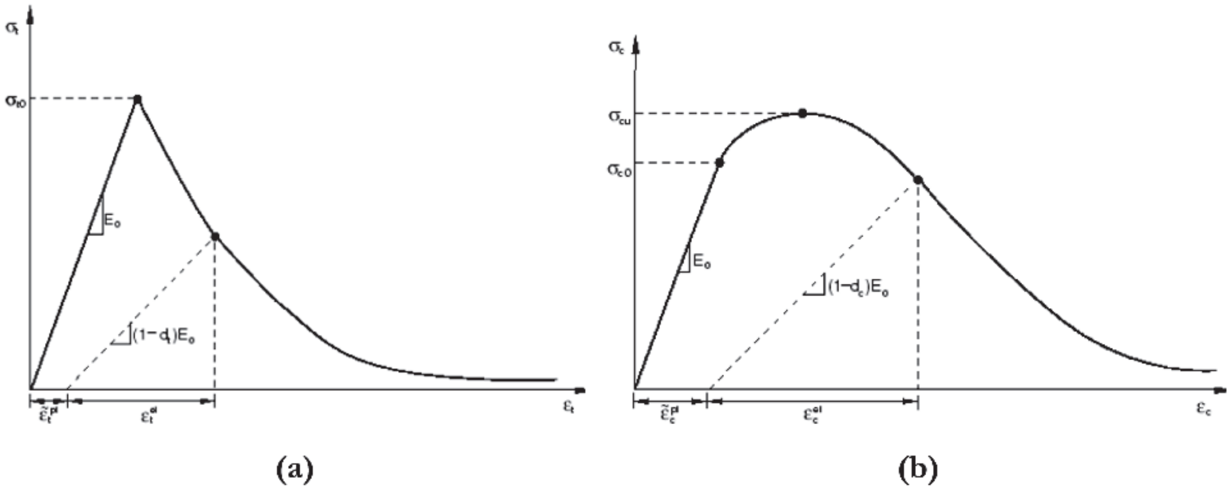

Figure 1
Concrete responses for uniaxial loading (a) in tension (b) in compression [1]

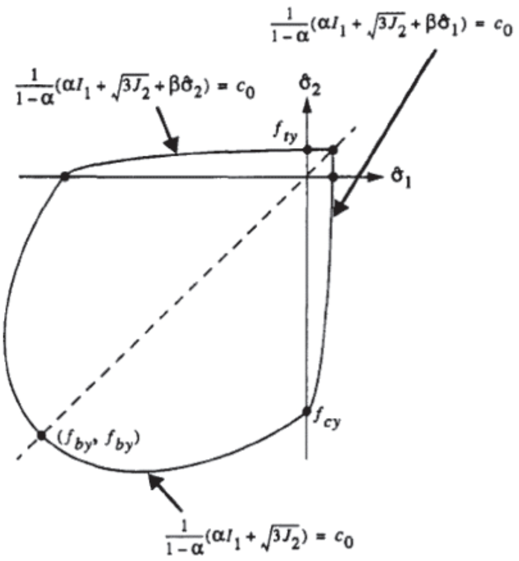

Figure 2
Surface rupture in the plane of stresses [13]

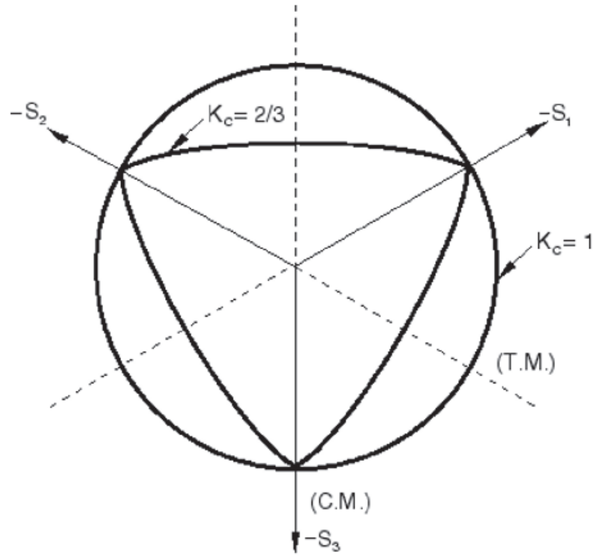

Figure 3
Corresponding values for the parameter [13]

Lee and Fenves [13] suggested the modifications to simulate the multiaxial stress behavior of the concrete.
The material's behavior in linear elastic regime can be represented by Equation 2.1, according to the general Hooke law.

$$\sigma = C.\varepsilon \quad \textbf{(2.1)}$$

Where σ is the stress tensor, ε is the strain tensor and C is the fourth-order constitutive tensor. For nonlinear behavior of plastic damage in the uniaxial case of stresses, stress-strain relationships are governed by scalar elastic damage, as noticed in the Equation 2.2.

$$\sigma = (1 - \mathrm{d}).E_0.(\epsilon^e - \check{\epsilon}^{pl}) \quad \textbf{(2.2)}$$

Being E_0 equal the initial elastic Young's modulus and (1-d) E_0 equal the effective plastic Young's modulus. The d parameter represents the scalar plastic damage variable (ratio of damaged area to total cross-sectional area) for isotropic damage, 0 (zero) for non-damaged material and 1 (one) for completely damaged material ($0 \leq d \leq 1$), while $(\epsilon^e - \check{\epsilon}^{pl})$ means the plastic tensor strain. It is worthy of notice that the evolution of the rupture on surface is controlled by two variables, related to damaging mechanisms due to the loss of tensile strength and compression strength, respectively. Both are characterized, independently, as shown in Figure 1.
The failure surface is represented by the following equation (2.3), due to the stress and the plastic damage variable.

$$f(\sigma, \check{d}_p) = \frac{1}{1-\alpha}\left[\alpha.I_1 + \sqrt{3.J_2} + \beta.(\overline{d}_p).(\sigma_{máx}) - c_c.(\overline{d}_p)\right] \quad \textbf{(2.3)}$$

where α, β are the non-dimensional constants of the material, I_1 is the first stress invariant, J_2 being the second principal invariant of the deviatoric stress, σ_{max} is the maximum algebraic value of the principal stress, c_c is the cohesion variable for compression and, finally, $\overline{d}_p = \begin{vmatrix} d_{pt} \\ d_{pc} \end{vmatrix}$ is the vector plastic damage variable represented by two components, one for tension and other for compression.

The Figure 2 shows the failure surface in the plane stress.
The rule of the plastic yielding allows determining the strains' evolution in the structure from increments of plastic deformation, as the load is applied, and these strains are obtained by means of the derivative of a potential function (G).
The G potential function is a scalar function of stress tensor and the increments of plastic deformation can be determined by partial derivatives with respect to the components of the stress tensor.

$$d\epsilon_{ij}^{pl} = d\gamma.\frac{dG}{d\sigma_{ij}} \quad \textbf{(2.4)}$$

where $d\gamma$ is the constant of proportionality greater than zero, denominated plastic multiplier. The potential plastic function, in the constitutive model adopted, is defined in the space of the effective stresses from the hyperbolic function of Drucker-Prager presented in the following equation (2.5).

$$G = \sqrt{(\sigma_{c0} - e.\sigma_{t0}tan\psi)^2 + \overline{p}^2} - \xi.tan\psi - \sigma \quad \textbf{(2.5)}$$

Being σ_{t0} and σ_{c0} equal the concrete tensile and compressive strength, respectively; ψ is the dilation angle measured in meridional plane at high confining pressures; e is the eccentricity of the plastic potential surface, which doesn't match with the yield surface, in other words, it is non-associative.
Beyond of the definition of scalar plastic damage variable (d) is necessary to define other parameters using the constitutive model in the Abaqus® software. They are presented bellow and the values adopted for the representation of the stresses' multiaxial state effects are detailed too.

- K_c: ratio between the distance of the hydrostatic axis to the meridian of traction and of compression in the diverter plane, varies between 0.5 and 1.0, with K_c = 2/3 being the most adopted. When it assumes the value equal to 1 (one), the cross-section of the failure surface in the anti-spherical plane is in the form of a circle, as in the classical Drucker-Prager criterion, as shown in Figure 3;

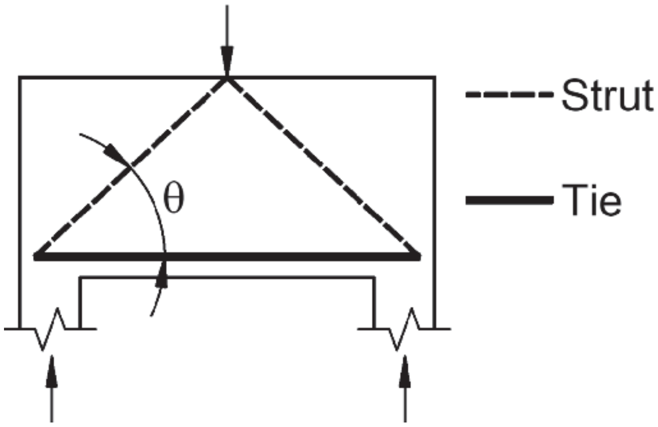

Figure 4
Strut-and-tie models according to Silva and Giongo (adapted from [24])

- Plastic potential eccentricity (e): value comprised between 0≤ and ≤1. When it assumes the value equal to zero, the surface in the meridional plane becomes a straight line, that is, the classic criterion of Drucker-Prager.
- Ratio f_{bc}/f_c: such parameter can be obtained by the relationship of tensile and compressive strengths. The value generally adopted is around 1.16;
- Angle of Dilation (ψ): the angle that will describe the slope of the rupture surface in related to hydrostatic axis. The dilatation angle can be interpreted physically as an angle of internal friction of the concrete, generally adopted being equal to 36° or 40°;
- Viscosity parameter (μ): necessary to regularize the constitutive equations. According to Kmiecik and Kamiński [11], the viscoplastic adjustment consists in the choice of "μ" greater than zero, sometimes being necessary to adjust this value in order to find out the influence of the parameter on the result and what the value least suitable for the problem.

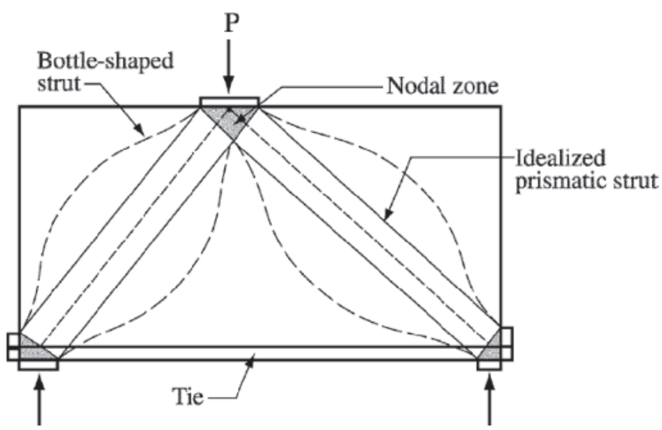

Figure 5
Strut-and-tie Model of a simply supported beam ([5] and [18])

3. Definition of the struts-and-tie model

According to Silva and Giongo [24], the main aspects to be considered for the strut-and-tie model geometry definition are the types of actions that are developed in the element, the angle between the strut and the tie and the boundary conditions which also includes the number of layers of the reinforcement and its cover.
Silva and Giongo [24] also explain that when defining the model it is important to provide a satisfactory space for the struts-and-tie in such a way that the angles θ between these elements do not get too small. Several researchers and some normative codes set limits to the values of these angles. Figure 4 illustrates the model according to Silva and Giongo [24].
MacGregor [18] points out that the struts-and-ties must be arranged in a way that there is a coincidence between the centers of gravity of each element and the lines of action of external forces acting on each node. Figure 5 sketches a beam with its respective arrangement of model elements, struts, ties and nodal zones where the transfer of forces will occur.
Wight and Macgregor [18] claim that a strut-and-tie model must satisfy some criteria, among which the internal stress equilibrium, considering a given set of loads, which must not exceed limits in relation to the actual resistance of the structure. This theory corresponds to the Plasticity Lower Limit Theorem.
Schäfer and Schlaich ([22] and [23]) also indicate such behavior analyzes of the element considering the ultimate limit in the elastic state, to define the strut-and-tie model topology, and the plastic state, to design the structure.
Some commonly adopted criteria for choosing the strut-and-tie model are mentioned in the literature, e.g., those prescribed in normative codes, the criterion adopted by the "Load Path Approach", from elastic analyzes by FEM, from nonlinear analyzes with the considering the concrete cracking, by means of experimental tests and by means of numeric models.

4. ABNT NBR 6118 recommendations

The Brazilian design code ABNT NBR 6118:2014 [6] determines limit values for the struts in the analysis of compression stresses between the nodal regions. The steel reinforcements totally supports the traction in ties.
Both design criteria is summarized in the following items.

4.1 Design of struts

The stresses in the struts should not exceed the values obtained from equations 4.1 to 4.3.

- For nodal regions with only struts (CCC nodes):

$$F_{cd1} = 0{,}85\ \alpha_{v2} f_{cd} \quad (4.1)$$

- For nodal regions with one tie (CCT nodes):

$$F_{cd3} = 0{,}72\ \alpha_{v2} f_{cd} \quad (4.2)$$

- For nodal regions with two or more ties (CTT or TTT nodes):

$$F_{cd2} = 0{,}60\ \alpha_{v2} f_{cd} \quad (4.3)$$

where:
α_{v2} = 1 − f_{ck}/250, with fck being the characteristic compressive strength of the concrete expressed in MPa and;
f_{cd} is the concrete compressive strength, being equal to f_{ck}/γ_c. The parameter γ_c is the concrete reduction factor strength.

4.2 Design of ties

According to Brazilian design code ABNT NBR 6118:2014 [6], the resultant reinforcement area to be applied for each tie is given by Equation 4.4.

$$A_s = \frac{F_{sd}}{f_{yd}} \tag{4.4}$$

where:
F_{sd} is the design tie force and;
f_{yd} is the design reinforcement yield strength.

5. Evolutionary structural optimization (ESO) algorithm

According to Liang et al. [16], the optimization of continuous structures subject to stress constraints may be expressed as follows Equation 5.1.

$$\text{minimize} = \sum_{e=1}^{N} w_e(t_e)$$
$$\text{restriction} = \sigma_{max}^{VM} \le \sigma^* \tag{5.1}$$

Where w_e is the weight of the nth element; t_e is the thickness of the n_{th} element; and σ * is the prescribed limit stress. Thus, the reduction of the mass is carried out from the criterion of maximum stress in the structure, in which the elements with smaller values of stress in the whole structure are selected and disregarded in the mesh (Figure 6).
This removal criterion, initially proposed by Xie and Steven in [25], is described by Inequation (5.2) as follows:

$$\sigma_e^{vM} < RR_i \cdot \sigma_{MAX}^{vM} \tag{5.2}$$

where σ_e^{vM} is the equivalent von Mises stress (scalar value) in the analyzed element; RR_i is the rejection ratio adopted to delay the removal process with the following variation 0 < RR_i < 1,0 and σ_{MAX}^{vM} is the maximum von Mises stress of the iteration.
From that point, it is possible to say that the removal cycle of elements will occur until no more elements can be removed at a given RRi value. However, when reaching this level of equilibrium, without achieving the optimum configuration, the evolutionary process would be redefined by adding RR_i and ER evolution ratio. A new cycle of evolution would begin until there are no more elements to be eliminated with this new rejection ratio. However, (though) once the equilibrium is reached again, the rejection ratio (RR_i) is again updated. Equation (5.3) describes this process.

$$RR_{i+1} = RR_i + ER \quad i = 0,1,2,\ldots \tag{5.3}$$

The initial value of the rejection ratio (RR_i) is defined empirically according to the user experience for each type of problem. The guarantee of the best convergence is given considering small values for the rate of evolution (ER) and rejection ratio (RR_i) around 1%, preventing the removal of a very large region from the domain [20].
The RR will be updated until an optimized configuration is reached or after reaching a required stop criterion. The stopping criterion may be a final volume prescribed for the structure or a final rejection ratio. Thus, the removal ratio of the iteration must always be less than a pre-established maximum removal ratio RR_f.
The equivalent von Mises stress for a plane-stress is getting from the Equation 5.4:

$$\sigma_e^{vM} = \sqrt{\sigma_{11}^2 - \sigma_{11}\sigma_{22} + \sigma_{22}^2 + 3\tau_{12}} \tag{5.4}$$

With σ_{11} and σ_{22} equal the normal components of the tension in the respective x and y directions; τ_{12} equal the shear stress components.
A script was developed from a high-level programming language Phyton with the aim of automating the analysis of topological optimization in structural elements using Abaqus® software. The evolutionary process adopted to implement the computational code is summarized by the following steps:

a) **Step 1:** discretization of the initial domain of the structure, using a fine mesh of finite elements, and application of boundary conditions and prescribed actions;
b) **Step 2:** analyze the structure by finite elements (linear and non-linear behavior);
c) **Step 3:** remove the elements that satisfy the Inequation (5.2);
d) **Step 4:** Increase the rejection ratio according to Equation (5.3) until equilibrium is reached otherwise repeat steps 2 and 3;
e) **Step 5:** Repeat steps 2 through 4 until the optimum design is reached.

In the developed routine, the removal of the elements in the system does not occur with the literal removal of the elements. After the identification of the less requested regions, the mechanical properties of these regions are changed to a section or a material with negligible structural characteristics when compared with its initial mechanical characteristics. Therefore, the routine requires the user to establish physical characteristics (such as low modulus of elasticity and density, among others) for the structural deactivation of the component elements of the domain.
From the topology found, the strut-and-tie models were proposed for the simulation of structural systems of D-Regions of the reinforced concrete.

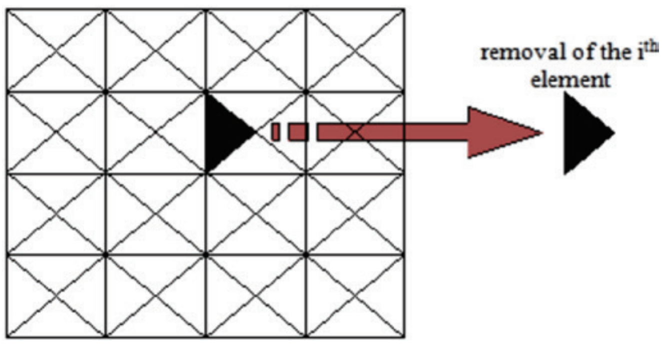

Figure 6
Removal of the element from mesh by the method of optimization [19]

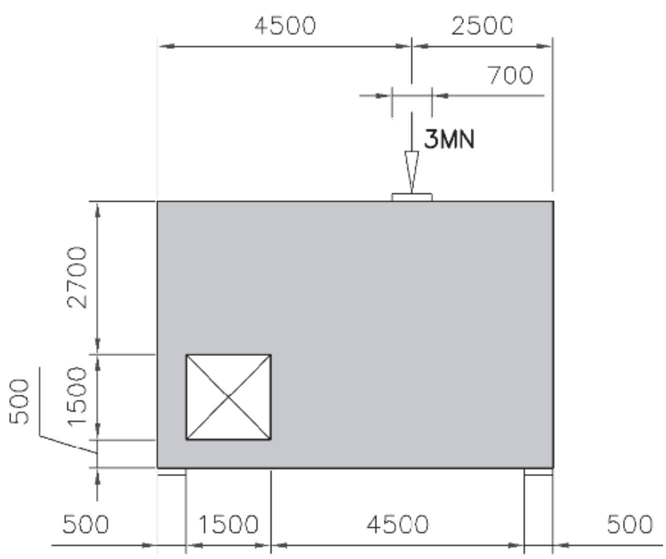

Figure 7
Simply supported deep beam with a hole [21]

6. Numerical examples

With the formulation described in the previous items, a computational system was developed with application of the ESO algorithm in conjunction with the finite element method. ESO was applied to obtain optimum topologies under the hypothesis of material with linear and nonlinear elastic behavior, in order to evaluate the sensitivity of the resulting strut-and-tie models. The completed structural models are considered during analyzes, that is, no symmetry condition was considered.
In the presented parameters on section 2 of this paper were adopted the same for nonlinear concrete behavior in all examples, to know:

- K_c = 2/3 [1];
- Plastic potential eccentricity (e) = 0.1;
- f_{bc}/f_c = 1.16;
- Angle of Dilation (ψ) = 36°;
- Viscosity parameter (μ) = 0.1.

6.1 Example 1: simply supported deep beam with a hole [21]

The structural element is a simply supported deep beam with a hole that is loaded by single force, as detailed in Figure 7 with all geometry presented in millimeters.
The adopted properties for material were adapted from Almeida et al. [2], with beam thickness equal to 800 mm, modulus of elasticity equal to E = 20,820 MPa, characteristic compressive strength of the concrete equal to f_{ck} = 28.0 MPa and γ_c equal to 1.40 and, finally, Poisson coefficient equal to ν = 0.15.
For assembling purposes using Abaqus® software, a simple triangular finite element mesh CPS3 (Continuum/ Plane-Stress/3 Node Element) type was considered. The structure was represented by 6,693 elements and 3,499 nodes. The parameters used for the optimization via ESO were: Removal Factor (RR_0) = 4.0% and the Evolution Factor (ER) = 2.0%. The optimum topologies obtained with the consideration of linear and non-linear behavior of the material to a volume of approximately 50% of the initial volume are presented in Figure 8. The same figure also shows the stress distributions obtained through FEM, with the stress flows in blue color being the compression regions and the red color, the tensile regions.
It is notable that the optimum topologies found by the ESO algorithm for the concrete hypothesis with linear elastic behavior presents results very close to those found in the literature, as shown in Figure 9. This result allows us to validate the implemented optimization code and to admit that the resulting optimum topologies are very close to the expected optimum topologies, regardless the optimization method used.

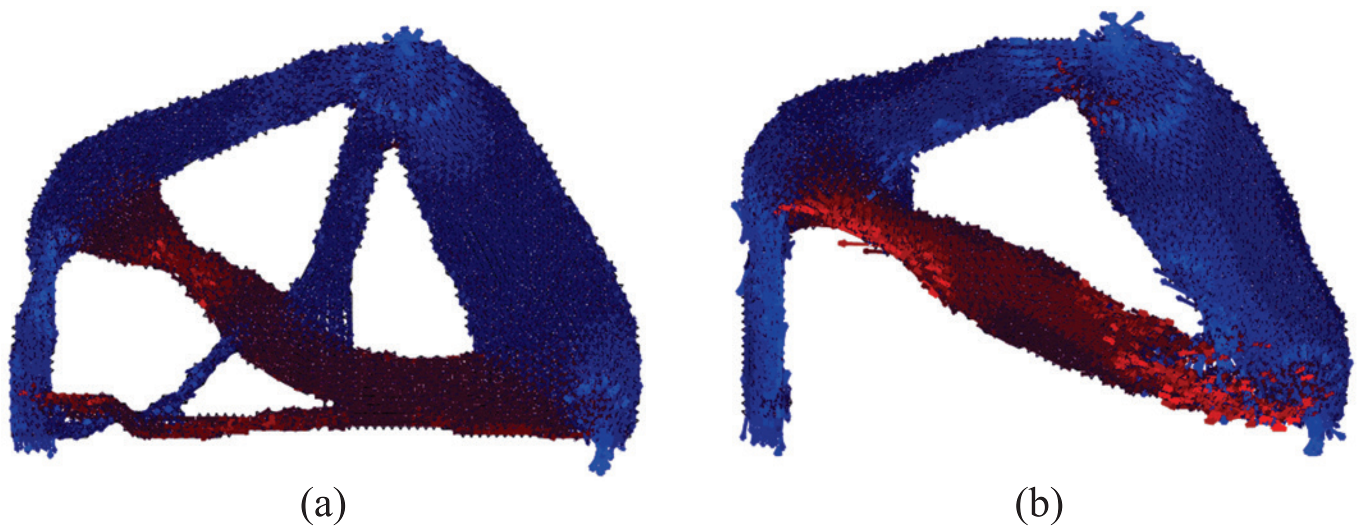

Figure 8
Optimum topologies by ESO and stress distribution obtained for the element, according to FEM (a) considering the linear and (b) non-linear behavior

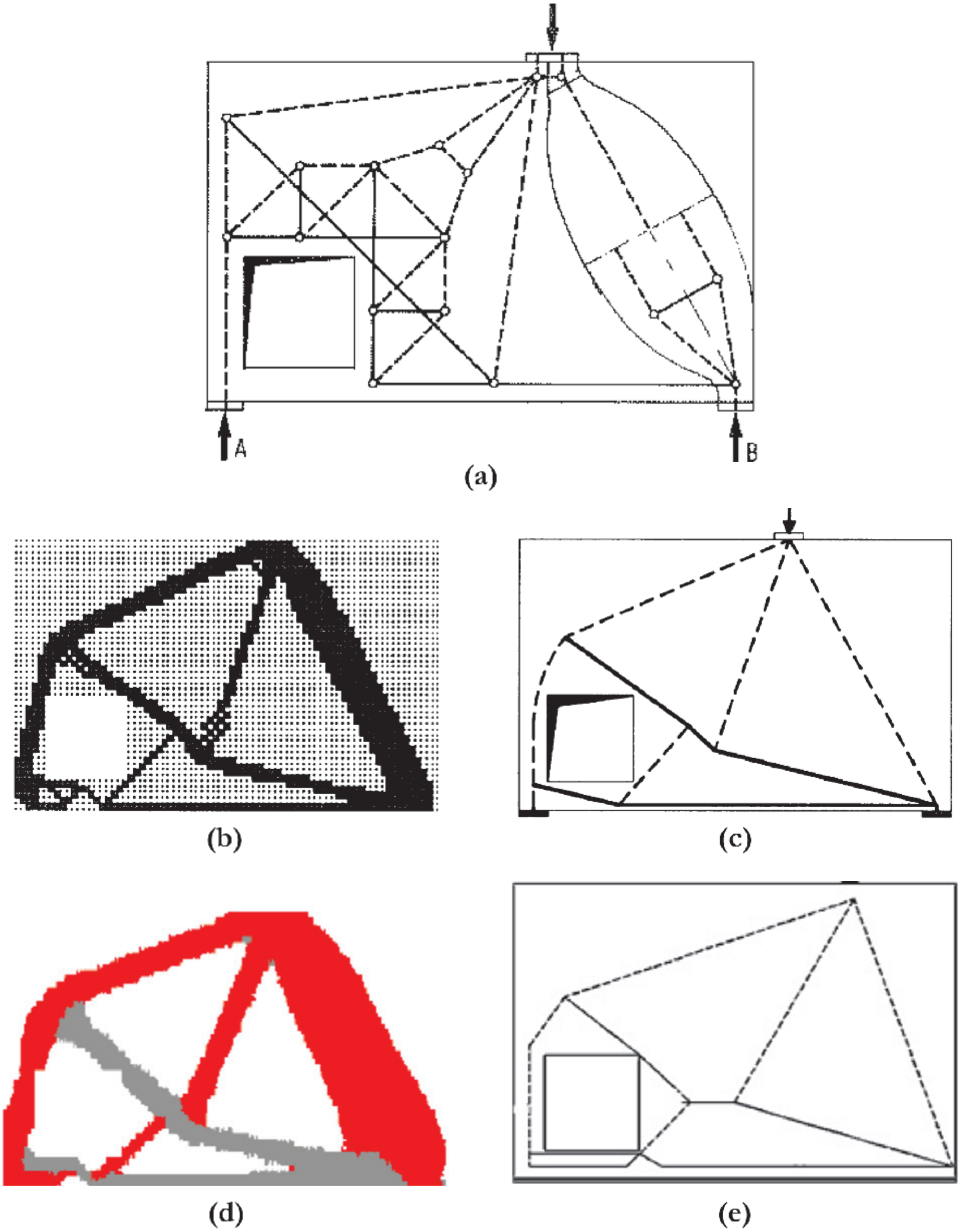

Figure 9
The results are presented in the literature (a) in Schlaich et al. [21] by the process of the load path (b) and (c) in Liang et al. [15] by the method ESO (d) and (e) in Almeida et al. [3] by the SESO method of topological optimization

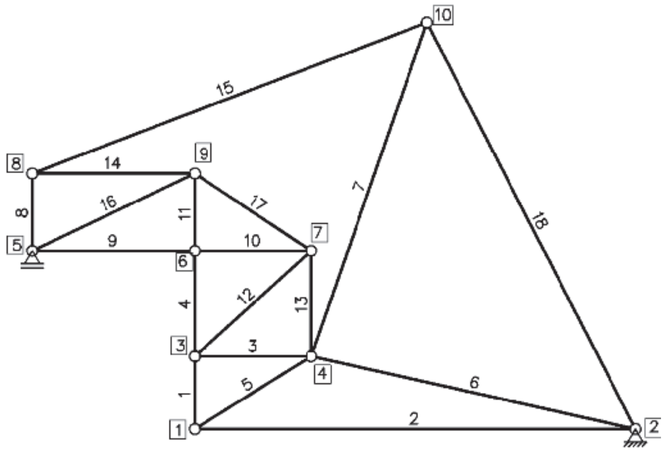

Figure 10
Strut-and-tie model with nodes and member numbers for Example 1

Table 1
Identification of nodes of the Example 1

Node number	X (m)	Y (m)	Type
1	1.730	0.000	CTT
2	6.420	0.000	CTT
3	1.730	0.770	TTT
4	2.970	0.770	TTT
5	0.000	1.890	CCT
6	1.730	1.890	TTT
7	2.970	1.890	CTT
8	0.000	2.710	CCT
9	1.730	2.710	CTT
10	4.200	4.310	CCC

It should be remembered that the stopping criterion corresponds for approximately 50% of the initial volume was applied for the definition of the optimized topology in both Finite Element models and, then, the ESO procedure was used. However, it can be seen that the results obtained to the deep beam structure showed significant differences between the optimum topology of a linear material and the optimum topology of a non-linear material. The optimum model selection, with minimum strain energy, or maximum stiffness, is the model represented by the largest number of bars for a truss system and, therefore, the topology indicated in Figure 8 (a). From this step, the definition of the optimized topology is interpreted to the truss, as indicated in Figure 10. The suggested strut-and-tie model corresponds to an envelope of solutions for concrete behavior, whether in a linear or non-linear regime.

In this context, the coordinates of the nodes and the axial forces

Table 2
Design of the compression bars of the Example 1

Member number	F_{sd} (kN)	A (cm²)	σ_c (MPa)	F_{cd} (MPa)	Criterion	Conclusion
5	-670	3,706	1.81	10.66	TTT	Ok
7	-633	5,288	1.20	10.66	TTT	Ok
8	-328	4,000	0.82	12.79	CCT	Ok
12	-1,160	1,583	7.32	10.66	TTT	Ok
15	-921	2,000	4.60	12.79	CCT	Ok
16	-1,657	1,704	9.72	10.66	CTT	Ok
17	-763	1,294	5.90	10.66	CTT	Ok
18	-2,333	3,560	6.55	10.66	CTT	Ok

Table 3
Characteristics of the footings

Member number	F_{sd} (kN)	Angle between horizontal direction and the member (°)	A_s (cm²)	A_{sx} (cm²)	A_{sy} (cm²)
1	353	90.0	8.1	0.0	8.1
2	569	0.0	13.1	13.1	0.0
3	861	0.0	19.8	19.8	0.0
4	1,131	90.0	26.0	0.0	26.0
6	512	12.6	11.8	12.1	0.0
9	1,497	0.0	34.4	34.4	0.0
10	1,497	0.0	34.4	34.4	0.0
11	1,131	90.0	26.0	0.0	26.0
13	356	90.0	8.2	0.0	8.2
14	861	0.0	19.8	19.8	0.0

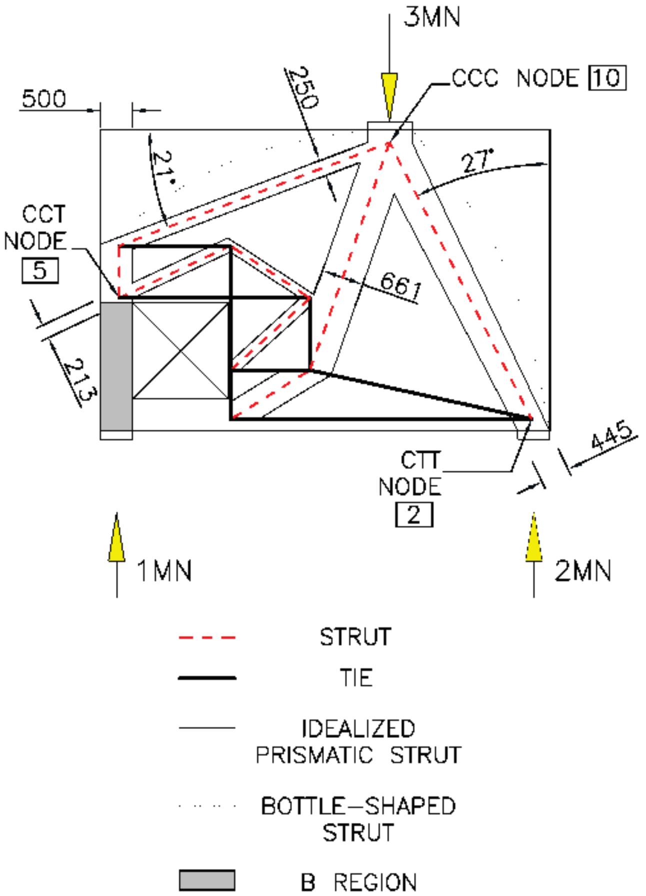

Figure 11
Geometry of strut for Example 1

obtained in the structural analysis of idealized truss are presented in tables 1 to 3 and the Figure 12 presents a project sketch of reinforcement concrete in the proposed model. The rebars' design was based on the Brazilian standard [6] and the steel considered was the CA50, as shown in detail on the next sub items for struts-and-ties design on the example.

6.1.1 Design of struts

To design the compressed bars, the struts, of a simply supported deep beam with a hole shown in Figure 7, it is necessary to identify the truss nodal points, as it is presented on Table 1. As mentioned in Chapter 4.1, these points can be labeled as the CCC, CCT, CTT or TTT node. The Figure 11 shows some dimension of struts in millimeters and the category of the labeled nodes 2, 5 and 10. All of the compression strength resistance verifications for each compressed bar is presented in Table 2 and the strength resistance of the compressed bar must be ensured for both extreme nodes that are connected to the element under analysis.
The A symbol represents the cross section area of compression bars and it is determined by trigonometry or graphical analysis for each strut, as shown for a few in Figure 11. The compressive stress σ_c is obtained by the ratio between F_{sd} and A for all of the bars and, in addition, each compression stress is compared with F_{cd1}, F_{cd2} or F_{cd3} concrete strength in the node region, as presented in Chapter 4.1. In Table 2, the F_{cd} means the F_{cd1}, F_{cd2} or F_{cd3}, which depends of each criterion shown in column number 6 of the same table. Therefore, it can be concluded that all struts for the idealized truss system on Example 1 support the design compressive stresses caused by the concentrated load of 3.0 MN shown in Figure 7.

6.1.2 Design of ties

To design the traction bars, or the ties, of a simply supported deep beam with a hole shown in Figure 7, it is necessary to use the Equation 4.4. This equation provides the steel reinforcement cross

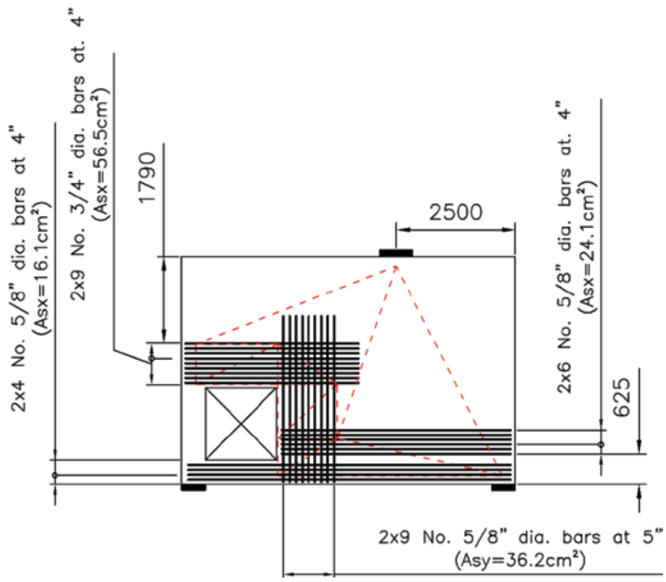

Figure 12
Reinforcement sketch for Example 1

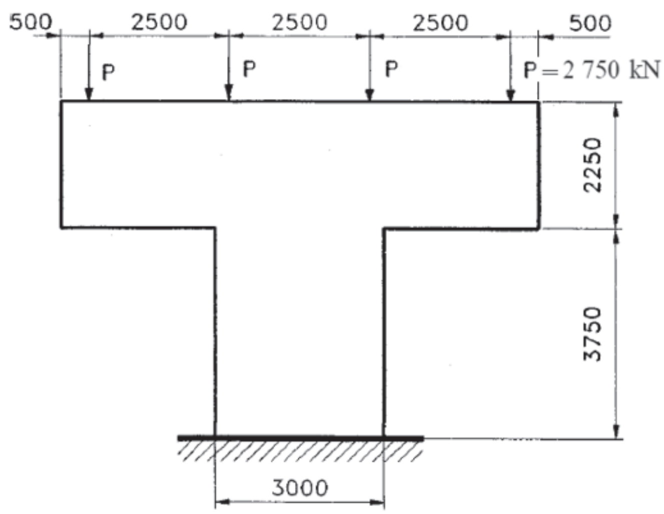

Figure 13
Bridge column [15]

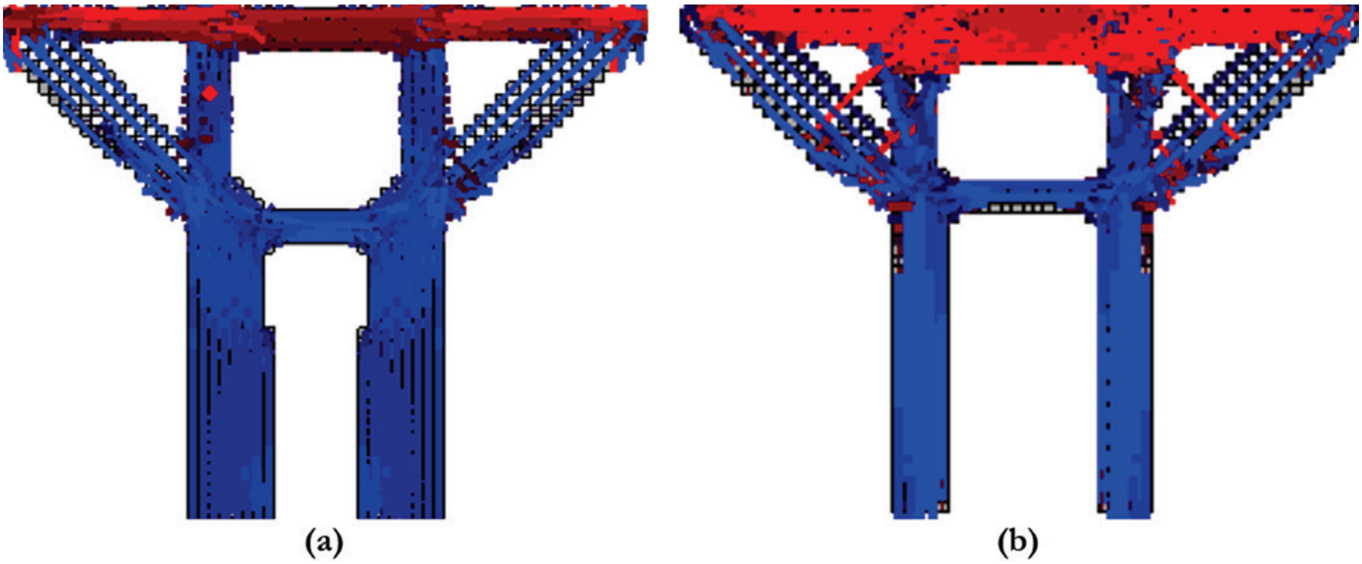

Figure 14
Optimum topologies by ESO and stress distribution required for the element, according to FEM (a) for linear and (b) non-linear behavior

sectional area that is required for equilibrium purposes of idealized truss system. In principle, that reinforcement should be applied at the same position associated to the truss tie. However, for constructive reasons, it is usually interesting that rebars are arranged at horizontal and vertical directions. Independently of the rebar position, reinforcement concrete design needs to respect the required strength at the direction of each traction bar of truss idealized system.

The Table 3 presents the steel reinforcing cross section area determined for all traction bars in parallel direction (A_s), horizontal direction (A_{sx}) and in vertical direction (A_{sy}) for truss idealized

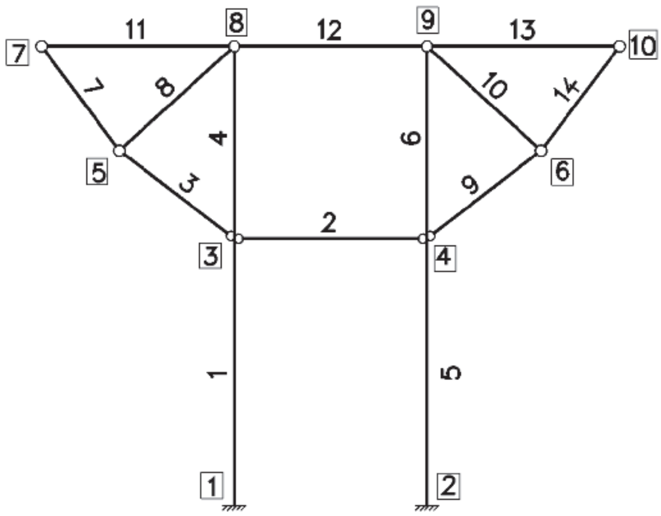

Figure 15
Strut-and-tie model with nodes and member numbers for Example 2

system. Figure 12 presents a sketch of the rebars' design for the structure on Example 1, after knowing all the required steel reinforcing cross section area in horizontal and vertical direction for each traction bar.

6.2 Example 2: bridge column [14]

The structural element is a bridge column that is loaded by four equal forces P, as detailed in Figure 13. The thickness of structure is 1.50m and the properties adopted for the material were the same as those reported in Liang et al. [14], with the modulus of elasticity equal to E = 28,600 MPa, characteristic compressive strength of the concrete equal to f_{ck} = 28.0 MPa and γ_c equal to 1.40, and, finally, the Poisson's coefficient equal to ν = 0.15. The shown dimensions are expressed in millimeters.

To assembly the elements in Abaqus® software, a triangular linear finite element mesh CPS4R (Continuum / Plane-Stress / Shell elements / 4 Node Element) type was considered. The structure was represented by 1,944 elements and 2,061 nodes. For this case, it was considered symmetry in the finite element mesh generation.

The parameters used for ESO optimization were: Removal Factor (RR) = 4.0% and Evolution Factor (ER) = 2.0%. The optimum topology was obtained from a volume of approximately 50% of the initial volume. The solutions, considering the elastic and non-linear behavior of the material, are presented in Figure 14. The same figure also shows the stress distributions obtained through FEM and the stress flows in the blue color being the compression regions and in the red, the tensile regions.

For the studied example, it may be observed that differences between the obtained topology for the linear material and the obtained topology for non-linear material were relatively small. The results interpretation of a structural model with strut-and-tie

Table 4
Identification of nodes of the Example 2

Node number	X (m)	Y (m)	Type
1	10,000	0,000	CCC
2	12,500	0,000	CCC
3	10,000	3,450	CCC
4	12,500	3,450	CCC
5	8,510	4,590	CCT
6	13,980	4,590	CCT
7	7,500	5,940	CCT
8	10,000	5,940	TTT
9	12,500	5,940	TTT
10	15,000	5,940	CCT

presents irrelevant differences in the concept of truss structural system. The result suggests that such response is very close to a global optimum geometry for the structure, either for the linear or nonlinear regime. The optimum model selection, with minimum strain energy, or maximum stiffness, is the model represented by the largest number of bars for the truss and, therefore, the topology indicated in Figure 14(b). From this step, the definition of optimized topology is interpreted for the structure, as shown in Figure 15.

As shown in Liang et al. [14], in order to simplify the solution of truss system, the compressed diagonals can be connected to the compressed horizontal bar in the same node of final topology indicated in Figure 14(b). The procedure subtly adjusts the column length of the bridge until the bottom face of the beam. To not modify in a significantly way, the solution presented in the literature, the procedure was also adopted for this paper. Thus, the nodes' coordinates and the axial forces obtained in the structural analysis of the idealized truss of Example 2 are presented in Table 4.

In this context, the suggested strut-and-tie model corresponds to an envelope of solutions for possible concrete behaviors, either in linear or non-linear regime. Figure 16 presents a project sketch of reinforcement concrete in the proposed model. The design of reinforcement was based on the Brazilian standard [6] and the considered steel was the CA50.

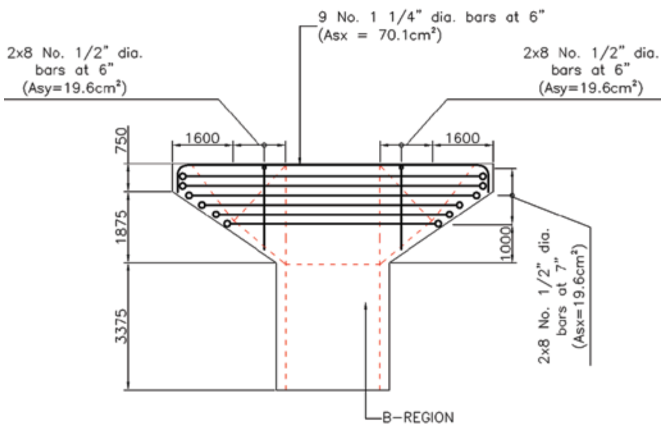

Figure 16
Reinforcement sketch for Example 2

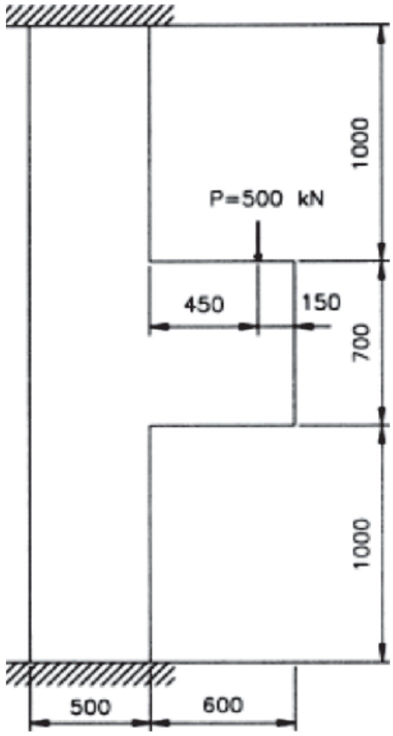

Figure 17
Corbel in a column [15]

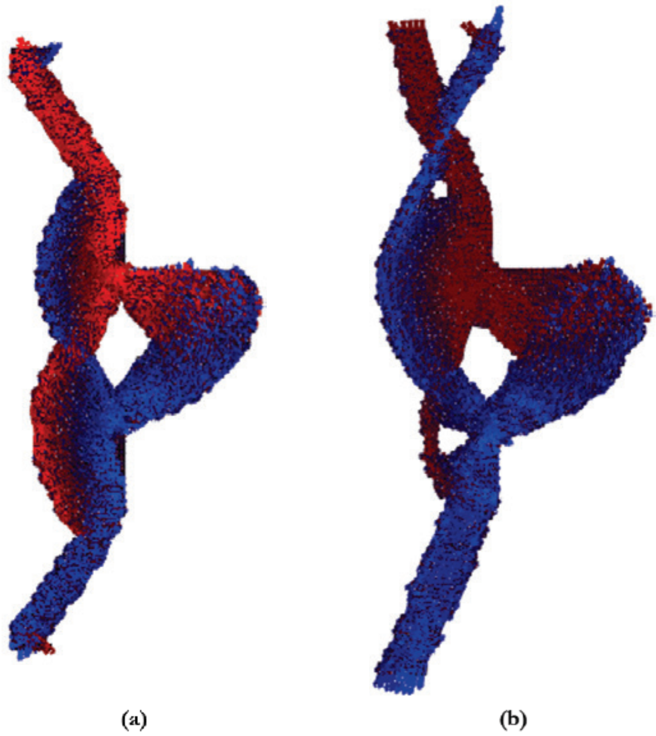

Figure 18
Solution considering the linear behavior of the material and (b) Solution considering the non-linear behavior of the material

6.3 Example 3: corbel in a column [15]

The structural element analyzed is a corbel in a column that is loaded by a single force, as detailed in Figure 17. The properties adopted for the material were the same as those reported in Liang et al. [15], with the modulus of elasticity equal to E = 28,567 MPa , characteristic compressive strength of concrete equal to f_{ck} = 28.0 MPa and γ_c equal to 1.40, and, finally, the and Poisson's coefficient equal to ν = 0.15. The column and corbel width b = 300 mm were assumed.

To assembly the elements in Abaqus® software, a quadrilateral linear finite element CPS4R (Continuum / Plane-Stress / Shell elements/ 4 Node Element) type was considered. The structure was represented by 3,317 elements and 3,470 nodes. The parameters used for ESO optimization were: Removal Factor (RR) = 4.0% and Evolution Factor (ER) = 2.0%. The optimum topology was obtained from a volume of approximately 50% of the initial volume.

The Figure 18 presents responses for compressive stresses distributions (in blue) and traction (in red) for the solutions, considering the linear and non-linear elastic behavior of the material.

The respective strut-and-tie obtained models are presented in detail on Figure 19, when the element removal criterion via ESO admits a smaller volume fraction of remaining material.

For the studied example, it can be noticed that the differences found between linear and nonlinear material topologies were significant. The main observed divergence occurs due to the angle between the axial axis elements. In these circumstances, the selection of optimized model, with minimum strain energy, or maximum rigidity, is the model represented by the largest number of bars for a truss system and, therefore, the topology indicated in Figure 19(a). From this point, the definition of optimized topology is interpreted for the truss structure, shown in Figure 20(a). The nodes coordinates and the axial forces obtained in the structural analysis of idealized truss of Example 3 are presented in Table 6, Table 7 and Table 8. In this context, the suggested strut-and-tie model corresponds to an envelope of solutions for the possible concrete behaviors, either in linear or non-linear regime. The Figure 21 presents a project sketch of reinforcement concrete in

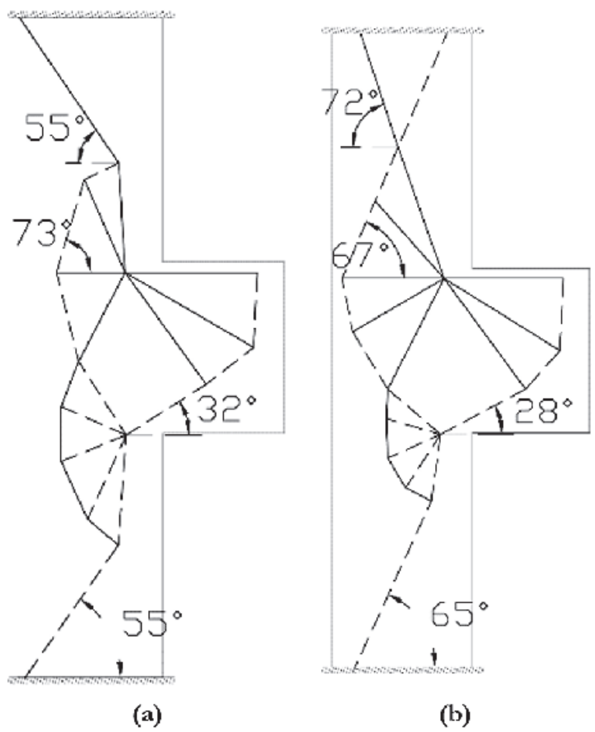

Figure 19
Strut-and-tie model (a) considering the linear behavior and (b) considering the nonlinear behavior. Dotted lines representing struts and continuous lines representing ties

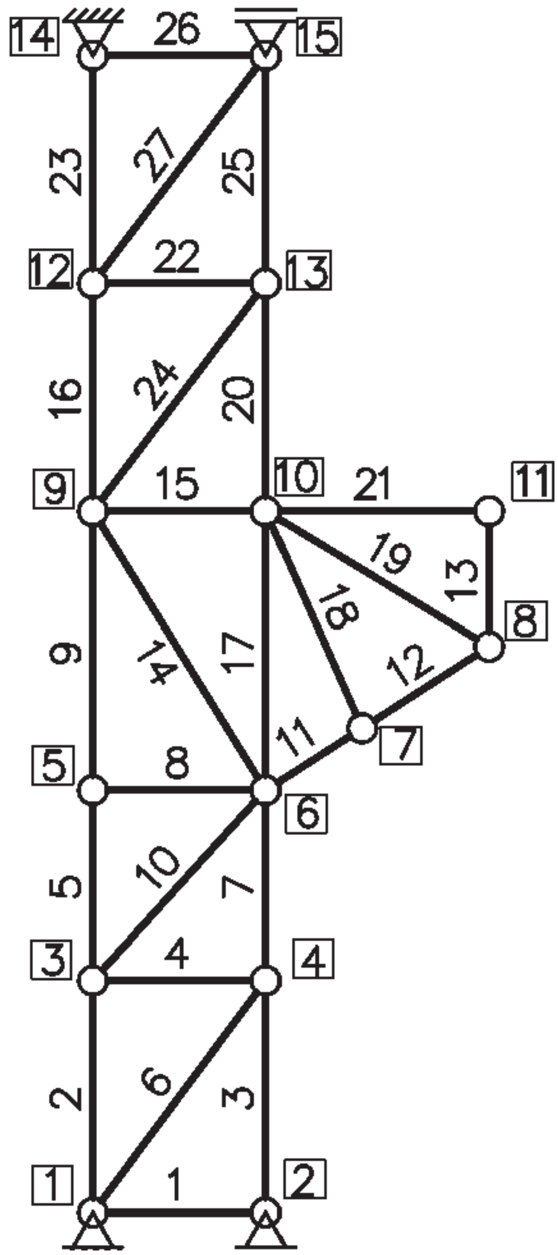

Figure 20
Strut-and-tie model with nodes and member numbers for Example 3

Table 5
Design axial forces in the bars of the Example 2

Member number	Type	F_{sd} (kN)	Member number	Type	F_{sd} (kN)
1	Strut	-5,500	9	Strut	-3,481
2	Strut	-2,753	14	Strut	-3,441
3	Strut	-3,481	8	Tie	937
4	Strut	-3,380	10	Tie	937
5	Strut	-5,500	11	Tie	2,068
6	Strut	-3,380	12	Tie	2,758
7	Strut	-3,441	13	Tie	2,068

Table 6
Identification of nodes of the Example 3

Node number	X (m)	Y (m)	Type
1	0,000	0,000	CCC
2	0,410	0,000	CCC
3	0,000	0,550	CTT
4	0,410	0,550	CCT
5	0,000	1,000	CTT
6	0,410	1,000	CCT
7	0,640	1,150	CCC
8	0,940	1,340	CCT
9	0,000	1,660	CTT
10	0,410	1,660	TTT
11	0,940	1,660	CCC
12	0,000	2,200	CCT
13	0,410	2,200	TTT
14	0,000	2,740	CTT
15	0,410	2,740	CTT

the proposed model. The design of the reinforcement was based on the Brazilian standard [6] and the considered steel was the CA50.

7. Conclusion

In this work, three numerical examples were presented to illustrate the design methodology of strut-and-tie models in concrete structures. In order to evaluate the material's behavior in physical linearity and non-linearity, each structure was optimized, assuming linear behavior and later evaluated with non-linear behavior. Then, the strut-and-tie model was proposed from two topologies under the maximum stiffness criteria

With the studies carried out, it was possible to conclude that optimized model conceptions can be idealized from the linear and nonlinear topological concrete optimization. However, it is recommended that, for design purposes, the optimum topology may be adopted so material intense fissures can be avoided.

Considering the numerical simulations carried out, it can be noticed that obtained solutions for the design of strut-and-tie model are relevant for structural engineering, since they provide a contribution to the proposition of analogous systems for the studied cases and still indicates a simplified methodology in the process of strut-and-tie idealization.

Table 7
Design axial forces in the struts of the Example 3

Member number	Type	F_{sd} (kN)
2	Strut	-126,800
3	Strut	-161,300
6	Strut	-278,800
7	Strut	-384,800
10	Strut	-247,400
11	Strut	-477,000
12	Strut	-477,000
13	Strut	-500,000
14	Strut	-445,200
16	Strut	-102,700
24	Strut	-275,500
27	Strut	-275,500

8. Acknowledgements

The authors acknowledge the financial support granted by CNPq

Table 8
Design axial traction forces in the ties of the Example 3

Member number	Type	F_{sd} (kN)
1	Tie	0,000
4	Tie	166,600
5	Tie	56,000
8	Tie	0,000
9	Tie	56,000
15	Tie	401,500
17	Tie	68,100
18	Tie	0,000
19	Tie	469,000
20	Tie	310,500
21	Tie	0,000
22	Tie	166,600
23	Tie	116,700
25	Tie	91,100
26	Tie	166,600

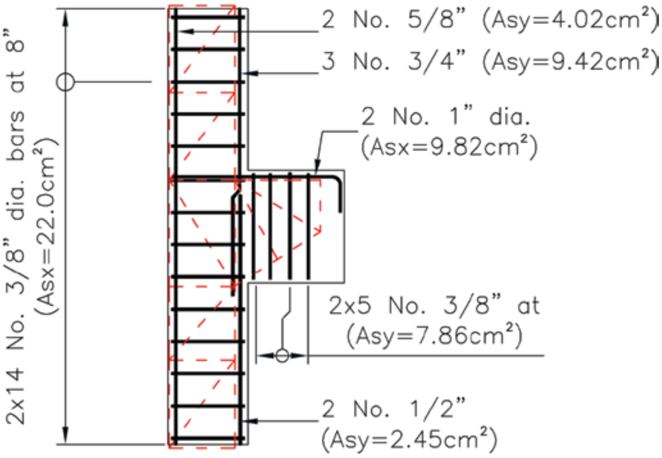

Figure 21
Reinforcement sketch for Example 3

(National Council for Scientific and Technological Development), CAPES (Coordination for the Improvement of Higher Education Personnel), FAPEMIG (Foundation for Research Support of Minas Gerais State) and Federal University of Minas Gerais (UFMG). The authors also thank the revisers for providing such an important work crucial for the paper improvement.

9. References

[1] ABAQUS. Abaqus analysis user's manual, Version 6.10, Dassault Systèmes, 2010.

[2] ALMEIDA, V. S.; SIMONETTI, H. L. AND NETO, L. O. Comparative analysis of strut-and-tie models using Smooth Evolutionary Structural Optimization. Engineering Structures, 56, 1665–1675, 2013.

[3] ALMEIDA, V. S.; SIMONETTI, H. L.; NETO, L. O. Análise de modelos de bielas e tirantes para estruturas de concreto armado via uma técnica numérica. Revista Ibracon de Estruturas e Materiais, Volume 6, 139-157, 2013.

[4] AMERICAN CONCRETE INSTITUTE. ACI 318/95 - Building Code Requeriments for Structural Concrete. Detroit, Michigan, 1995.

[5] AMERICAN CONCRETE INSTITUTE. ACI 318/05 - Building Code Requirements for Structural Concrete and Commentary, APPENDIX A: Strut-And-Tie Models". Detroit, 2005.

[6] ASSOCIAÇÃO BRASILEIRA DE NORMAS TÉCNICAS. NBR 6118. Projeto de Estruturas de Concreto – Procedimentos. Rio de Janeiro, 2014.

[7] CANADIAN STANDARDS ASSOCIATION. CSA Standard-A23.3-04 – Design of Concrete Structures. Ontario: Rexdale, 2004.

[8] CHU, D. N.; XIE, Y. M.; HIRA, A.; STEVEN, G. P. Evolutionaty structural optimization for problems with stiffness constraints. Finite Elements in Analysis and Design, v. 21, p. 239-251, 1996.

[9] EUROCODE 2: Design of Concrete Structures. General Rules and Rules for Buildings, 2002.

[10] FÉDÉRATION INTERNATIONALE DU BÉTON. Fib Model Code 2010 – Final draft. V. 2, Fib nº. 56, p. 53, 2010.

[11] KMIECIK , P.; KAMIŃSKI, M. Modelling of reinforced concrete structures and composite structures with concrete strength degradation taken into consideration. Archives of Civil and Mechanical Engineering. Vol. XI, n°3, p.623-636, 2011.

[12] KUMAR, P.;"Optimal force transmission in reinforced concrete deep beams." Computer and Structure, 8(2), 223–229, 1978.

[13] LEE, J.; FENVES, G. L. Plastic-damage model for cyclic loading of concrete structures, Journal of Engineering Mechanics, Vol. 124, No. 8, p. 892–900, 1998.

[14] LIANG, Q. Q.; STEVEN, G.P. A performance-based optimization method for topology design of continuum structures with mean compliance constraints, Computer Methods in Applied Mechanics and Engineering, 191, 13-14, 1471-1489, 2002.

[15] LIANG, Q. Q.; XIE Y. M.; STEVEN, G.P. Topology optimization of strut-and-tie models in reinforced concrete structures using an evolutionary procedure. ACI Struct. J. 97(2): 322–330, 2000.

[16] LIANG, Q. Q.; XIE Y. M.; STEVEN, G.P.; SCHMIDT L.C. Topology Optimization of Strut-and-Tie Models in Non-Flexural Reinforced Concrete Members. International Conference on Mechanics of Structures, Materials and Systems. p.309-315, February, Wollongong, Australia, 1999.

[17] LUBLINER J.; OLIVER J.; OLLER, S.; OÑATE, E. A plastic-damage model for concrete, International Journal of Solids and Structures, v. 25, p. 299–329, 1989.

[18] MACGREGOR, J.G. Reinforced concrete mechanicas and desing. New Jersey. Prentice Hall, 1997.

[19] FRANÇA, M. B. B.; GRECO, M.; LANES, R. M.; ALMEIDA, V. S.; Topological optimization procedure considering nonlinear material behavior for reinforced concrete designs. Computers and Concrete. Volume 17, Issue 1, pp.141-156, 2016.

[20] QUERIN, O. M. Evolutionary structural optimization stress based formulation and implementation. Ph.D. Thesis. Sydney, Australia: University of Sydney, 1997.

[21] SCHLAICH, J; SCHAFER, K; JENNEWEIN, M. Toward a consistent design of structural concrete. PCI-Journal, vol. 32, nr.3, p. 74–150, May/June, 1987.

[22] SCHÄFER, K.; SCHLAICH, J. Consistent Design of Structural Concrete using Strut and Tie Models. Colóquio sobre comportamento e projeto de Estruturas, Rio de Janeiro, 1988

[23] SCHÄFER, K.; SCHLAICH, J. Design and Detailing of Structural Concrete Using Strut-and-Tie Models. The Structural Engineer, v.69, n.06, p.113-125, 1991

[24] SILVA, R. C.; GIONGO, J.S. Modelo de Bielas e Tirantes Aplicados a Estruturas de Concreto Armado. São Carlos: EESC-USP, 2000.

[25] XIE, Y. M.; STEVEN, G. P. A simple evolutionary procedure for structural optimization. Computers & Structures, v. 49, Issue 5, p. 885-896, 1993.

[26] XIE, Y. M.; STEVEN, G. P. Evolutionary structural optimization for dynamic problems. Computers & Structures, v.58, Issue 6, p.1067-1073, 1996.

[27] XIE, Y. M.; STEVEN, G. P. Evolutionary Structural Optimization. Springer-Verlag, Berlim, 1997.

Volume 12, Number 1 (February 2019) p. 101 – 121 • ISSN 1983-4195
http://dx.doi.org/10.1590/S1983-41952019000100009

IBRACON

REVISTA IBRACON DE ESTRUTURAS E MATERIAIS
IBRACON STRUCTURES AND MATERIALS JOURNAL

Pervious concrete: study of dosage and polypropylene fibers addiction

Concretos drenantes: estudo de dosagem e adição de fibras de polipropileno

S. E. PILZ [a]
silvio@unochapeco.edu.br
https://orcid.org/0000-0003-0361-7658

P. OLIVEIRA [a,b]
poliveira@unochapeco.edu.br
https://orcid.org/0000-0001-8835-6324

F. REGOSO [a]
felipe_regoso@unochapeco.edu.br
https://orcid.org/0000-0002-0270-0495

V. A. PAULON [c]
vpaulon@yahoo.com.br
https://orcid.org/0000-0002-1061-9902

M. F. COSTELLA [b,c]
costella@unochapeco.edu.br
https://orcid.org/0000-0001-6471-9848

Abstract

The use of pervious concrete to minimize the effects caused by the impermeability of the soil as a result of increasing urbanization is an alternative that still requires further studies regarding its design and implementation. From this perspective, this paper presents a study of the characteristics of pervious concrete, including its tensile strength, compressive strength, flexural strength and the permeability coefficient, through the development of various mixtures to adjust the characteristics of the local aggregates. Eight mixtures were studied based on a reference mixture, five of which were related to the pervious concrete with the addition of finer aggregates than the reference mixture without these aggregates. Subsequently, three mixtures were studied with the inclusion of polypropylene fibers in order to analyze the effects of the addition of fibers on the properties of the pervious concrete. It is concluded that the presence of fibers changed the characteristics of the concrete, increasing its strengths while achieving a good permeability in its mixtures. An improvement in the flexural strength of the pervious concrete was observed, which is the main property to be considered for its use in pavements, without harming the permeability, which raises the possibility for its application.

Keywords: pervious concrete, tests, fibers.

Resumo

Utilizar concreto permeável para minimizar os efeitos causados pela impermeabilidade do solo causado pela crescente urbanização é uma alternativa que ainda necessita de estudos quanto à sua concepção e aplicação. Seguindo esta linha, o presente artigo apresenta um estudo das características do concreto drenante, tal como a resistência à tração, resistência à compressão, resistência à tração na flexão e coeficiente de permeabilidade, através do desenvolvimento de varios traços, para ajustar às características dos agregados locais. A partir de um traço referência, foram estudados oito traços, sendo cinco referentes ao concreto drenante com adição de agregados mais finos ao traço referência sem estes agregados. Posteriormente estudou-se três traços com a inclusão de fibras de polipropileno, com o objetivo de analisar os efeitos que a adição de fibras causa nas propriedades do concreto drenante. Concluiu-se então, que a presença das fibras alterou as características do concreto, levando o mesmo a atingir maiores resistências, aliadas a uma boa permeabilidade em seus traços, verificando-se assim a melhoria de capacidade de resistência à tração na flexão do concreto drenante, principal propriedade para uso em pavimentos, sem prejudicar a permeabilidade e avaliando a possibilidade de aplicação do mesmo.

Palavras-chave: concreto permeável, ensaios, fibras.

[a] *Universidade Comunitária da Região de Chapecó, Chapecó, SC, Brasil;*
[b] *Concreoeste, Chapecó, SC, Brasil;*
[c] *Faculdade Meridional, Porto Alegre, RS, Brasil.*

Received: 23 Oct 2015 • Accepted: 23 Jul 2018 • Available Online: 05 Feb 2019

1. Introduction

The growth in urbanization, which leads to the increased impermeabilization of the soil as a result of the paving of streets, sidewalks and buildings, brings with it ever-increasing environmental impacts that are forcing the construction industry to find alternatives to avoid future problems, such as flooding. These covered surfaces may occupy 30% of the area of the drainage basin according to the ABCP [1]. If one considers the runoff coefficient or surface runoff, according to Marchioni et al. [2], very densely constructed areas may have runoff coefficients of 0.70 to 0.95, which means that up to 95% of rainfall creates surface runoff.
According to Merighi et al.[3], pervious concrete is an alternative that can assist in urban drainage and facilitate the direct infiltration of water into the soil. However, in Brazil, its use is still in the early stages. Its application is therefore still restricted, which can be explained by the absence of adequate knowledge in relation to the mechanical and hydraulic behavior and potential applications of this material by the designers and professionals in the field. According to the standard ACI 522R-06 [4], its typical uses include: parking lot pavements, municipal roads, sidewalks, pedestrian areas in zoos, parks and swimming pool decks, among others.
According to the standard ACI 522R-06[4], pervious concrete is typically described as open-graded, zero-slump concrete with no or little fine aggregate, a void content ranging between 18 to 35% and a compression strength between 2.8 to 28 MPa, with permeability of 0.0135 to 0.122 cm/s (*already transformed units*).
For the ABNT [5], a pervious pavement on a site must have a mechanical flexural strength of at least 2.0 MPa and a permeability of 0.100 cm/s, without considering the compression strength requirement.
Rodrigues and Montardo [6] stated that the use of plastic polypropylene fibers as reinforcements in concrete has grown in recent years in Brazil in order to improve the performance of pervious concrete. Several works have used polypropylene fibers, including dams, tunnels, bridges, irrigation channels, water and sewage treatment stations and, especially, concrete pavements and floors. Polypropylene is chemically inert, does not absorb water, does not rust, has low cost and is easy attainable. In this sense, the use of polypropylene fiber is more appropriate than the use of metallic fibers because of corrosion and the need to improve the flexural strength performance, a fundamental requirement for concrete pavements.
Many properties are changed when the cementitious matrix is reinforced with fibers, such as: workability, compressive strength, modulus of rupture (flexural strength), direct tensile strength, impact resistance, resistance to fatigue, increase in tenacity, inhibition of crack propagation. Determining the optimum content is important to increase efficiency and economy, especially regarding the main properties relevant to the intended use. In light of the scarce studies on the behavior of pervious concrete using fibers, studies of concrete mixtures with various levels of fibers have become more important, and this is one of the objectives of this work.
The post-cracking behavior will not be evaluated because the pervious concrete has a high void content, which means it is important to study the behavior of the main mechanical property of a pavement material (flexural strength). It is known, however, that the post-cracking behavior of concrete with fibers is improved with smaller cracks (Rodrigues and Montardo [6]) and the probable increase in flexural strength may explain this behavior. The study of polypropylene fibers in pervious concrete needs behavior evaluations, which is one of the objectives of this work.
In this general context, this paper seeks to observe and analyze the behavior of the mechanical properties (compression strength, split tensile strength and flexural strength) and of the permeability coefficient in different pervious concrete mixtures with and without the addition of polypropylene fibers.

2. Theoretical framework

According to McCain and Dewoolkar [7], the northern states of the United States have been slow in adopting the use of pervious concrete, which is a result of the lack of data on its effects and behavior. Shu et al. [8] highlight that there is a need for laboratory tests to define the appropriate mixtures, studying different types of aggregates, their particle size distribution and various additions. These issues have also been pointed out by Lian and Zhuge [9].
Regarding the permeability, the NCPTC [10] indicates values between 0.0254 and 0.6096 cm/s to consider a concrete as pervious, while the ACI 522R-06 standard [4] establishes values ranging from 0.0135 to 0.122 cm/sec.
Pervious concrete has some disadvantages according to the Environmental Protection Agency [11], namely: the tendency of the pavement to be obstructed by dirt if inadequately installed or maintained; the risk of considerable failure if poorly constructed or in the case of soiling; contamination of the aquifer depending on the soil conditions and the susceptibility of the aquifer; the lack of expertise of the pavement engineers. Teixeira and Fortes [12] conclude that pervious concrete has economically viable costs, but that its compression and tensile strengths are much smaller than conventional concrete. In this sense, Lian and Zhuge [9] highlight that its applications have been almost entirely restricted to pavements.

2.1 Studies conducted on pervious concrete

Ibrahim et al. [13] studied 24 mixtures to check the variation of the properties with the variation of different aggregate fractions, the variation in the water-cement ratio and the content of cement. They concluded that, among other factors, the maximum compression strength for mixtures without fine aggregates is achieved with levels of cement around 250 kg/m^3 and decreases to 75% when the ratio is reduced to 150 kg/m^3.
Lian and Zhuge [9] concluded that the use of fine materials with a particle size between 9.5 and 2.4 mm increased the strength properties of the pervious concrete. However, the use of too fine aggregates, such as active silica, does not significantly alter the strength, because very fine particles tend to segregate due to the porosity of the concrete. Batezini [14] concluded that the addition of fine aggregates in concretes for the improvement of the mechanical properties is a possibility, especially when the permeability coefficient of the mixtures has higher values. In this study, the permeability value was 0.14 cm/s and the split tensile strength and the flexural strength ranged between 57 and 71% for the three mixtures.
Based on the development of concrete mixtures with five different aggregate particle sizes of granitic origin, Merighi et al. [3]

aimed to find a mixture that provided good mechanical strength to be used in the paving of airport runways and roads. The best results regarding strength at 28 days was 31.6 MPa for compression strength and 3.0 MPa for tensile strength for the mixture that used smaller aggregates than the other mixtures, a low w/c ratio, a superplasticizer additive and micro silica. However, Merighi et al. [3] stated that the use of this concrete as draining layer was not recommended because it had a permeability coefficient in the order of 10^{-3} cm/sec.

The discrepancy between permeability and strength, studied by Kajio et al. [15] and Tennis et al. [16], is usually dictated by the quantity of fine aggregate used in the mixtures, with a greater quantity of these aggregates decreasing the void content, increasing strength and reducing permeability. Identifying the optimal ratio between voids, permeability and strength is one of the challenges of researchers regarding the adequate use of aggregates, and this is one of the objectives of this work.

Cosic et al. [17] studied the variation in the properties of pervious concrete as a function of the variation in the type of aggregate and its size. One of their findings was the surprising conclusion that the type of aggregate has a more significant influence on permeability than its size. Lian and Zhuge [9] also found differences in the permeability values as a function of different types of aggregates.

Bonicelli et al. [18] investigated the difference in the properties of pervious concrete when different levels of concrete compaction were used, in addition to the influence of the addition of sand, and their results suggested that the addition of around 5% of the total aggregate mass as sand improved the mechanical properties, highlighting an increase of up to 75% in the tensile strength, but with a decrease in permeability, without compromising the drainage capacity of the concrete, however.

Maguesvari and Narasimha [19] studied the influence of coarse and fine aggregates on pervious concrete and concluded that the increase in fine aggregates reduced permeability, but increased the compression and flexural strength, making it a suitable material for pavements with light traffic.

2.2 Studies of concretes with polypropylene fibers

In a study conducted by Senisse and Dal Molin [20], three concrete mixtures were developed for each of the mixtures evaluated, using a mortar content of 55% and w/c ratios ranging between 0.34 and 0.68. Three types of concrete were prepared: conventional concrete (reference-CC), concrete reinforced with polypropylene macro-fibers (CF) and concrete reinforced with macro-fibers and a superplasticizer additive (CFSP), with a content of 600 g/m³ in fibers and 0.32% of superplasticizer in relation to the cement mass. The results showed that the inclusion of macro-fibers significantly increased the flexural strength (39% for the CF mixture and 27% for the CFSP mixture, even though the compression strength decreased in the CF case). They also concluded that the addition of fibers in the concrete had an insignificant increase in cost (SENISSE; DAL MOLIN [20]).

Perrone et al. [21] commented in a study that the addition of non-metallic fibers can help overcome problems with corrosion and improve the structural performance. Gesoglu et al. [22] studied the properties of pervious concrete with the addition of fibers of different types of rubber tire residues and they concluded that it is possible to obtain pervious concretes with more compression strength or better permeability depending on the characteristics of the waste, but that, on average, the concretes with the residues had worse strength properties and decreased permeability when compared to the reference mixture without residues, but the fracture energy increased with the tire residues and its use was feasible in parking areas.

Hesami et al. [23] studied the use of various materials, including glass fiber, with a content of 0.2 % in pervious concrete, and they observed an increase of up to 30 % in the tensile strength and of up to 64% in the flexural strength, corroborating the tendency of improved mechanical properties with the increase in the percentage of material, with a gradual decrease after the optimal percentage.

Amaral Junior [24] and Lucena [25] observed that the use of polymeric fibers usually means that there is a reduction in the axial compression strength, but the flexural strength increases.

In a study conducted by Guimarães et al. [26], the best performance for flexural strength was found with the fiber content of 1%. Rehder et al. [27] also observed this fact, which may be explained because the pores are connected by fibers, with the contribution of fibers to improve the residual flexural capacity, especially at higher porosities.

In this sense, this paper seeks to investigate the relationship between the use of fibers in different proportions and the behavior of pervious concrete.

3. Methodological procedures

One of the objectives of this work is to study concrete mixtures with the use of regional materials based on a pervious concrete without sand, and based on this verify the behavior of the mechanical and permeability properties when different levels of sand are added. The influence of the addition of non-metallic fibers, in this case polypropylene, on the cited properties, especially on flexural strength and permeability, since these are the parameters indicated by NBR 16416 (ABNT [5]), is also studied.

Based on the mixtures pre-determined by other researchers who showed reasonable results for strength and permeability (Polastre and Santos [28]; Sales [29]; Kajio et al. [15]; Tennis et al. [16]), a reference mixture (mixture A) was established containing only cement and gravel 1. Four other mixtures (B, C, D and E) were then studied to verify the influence of the addition of gravel 0 and sand on the compression strength, the split tensile strength, the flexural strength and the permeability.

Six specimens (CPs) were developed for each mixture for the axial compression tests, 6 CPs for the split tensile strength tests, 6 CPs for the flexural strength test, with the highest value being adopted for each one of them (potential strength, since these were concretes from the same concrete batch) and 6 CPs for the permeability tests, which adopted the means. The molding, curing and execution procedures of the specimens followed the procedures established by the Brazilian standards of the ABNT.

Subsequently, the influence of the addition of polypropylene fibers (1, 2 and 3 kg/m³) to mixture D (which already contained gravel 0 and sand) on the aforementioned properties was studied in three more mixtures. The contents were based on the studies of Guimarães et al. [26] and Reyes and Torres [30].

Table 1
Technical specifications of the Cauê cement

Fineness		Concrete	Cement time		Compression strength (MPa)			
#200 (75 mm)	#300 (45 mm)	3.06	Start (min)	End (min)	1 day	3 days	7 days	28 days
2.7	10.7		190	290	14.4	28.6	32.8	41.0

Table 2
Characteristics of the superplasticizer additive

Parameter	Unit	Specification	Results	Methods
Aspect	–	Liquid	Approved	Visual
Color	–	Light brown	Approved	Visual
pH – 25°C	–	3.00 to 5.00	4.17	NBR 10908:2008
Specific mass – 25°C	g/cm³	1.062 to 1.102	1.082	NBR 10908:2008
Solids	%	38.25 to 42.75	39.92	NBR 10908:2008

When there were significant differences between the expected and obtained values of the properties, the tests were redone to check if it was a trend or a simple error of procedure, and in the case of mixture D, an error in the concrete batch development procedure of the initial study was found.
The mechanical properties studied are the most significant for pervious concrete, but the effect of concrete compaction, the behavior under cyclic actions, abrasion wear and other factors may also deserve specific studies when applying these concretes to light traffic pavements.

3.1 Characterization of materials

The cement used for the tests was CP II-E in bulk. No laboratory tests were performed for the cement, and the technical specifications provided by the manufacturer were used as in Table 1.
For the medium sand coming from the União da Vitória region, characterization assays were performed in the laboratory regarding the bulk density, fineness module and maximum diameter of the fine aggregate.

Figure 1
Polypropylene macro-fibers used

For the gravel 0 and gravel 1, both of basaltic origin and produced in a crusher located in Cordilheira Alta - SC, the bulk density, fineness module and maximum diameter of the aggregate were determined.
The additive used was the Superplasticizer MAXIFLUID 900. Table 2 shows the data of the analysis of the additive as provided by the manufacturer, since no laboratory tests were performed. The quantity of additive used for all traits was 1% in relation to the cement mass, according to the instructions of the manufacturer.
The polypropylene fibers and their specifications were supplied by a company located in São José-SC:

- Alkali resistant;
- Length: 50 mm;
- 27,000 fibers per kg;
- Tensile strength of 350 MPa (per filament);
- Twist – anchoring;
- 50 FF – form factor, characterized as macro-fiber (Figure 1);
- Thickness: 0.9 mm;
- 110%: elongation after fracture;
- Raw material: polypropylene monofilaments.

The water used was from the groundwater located in the town of Chapecó-SC.

3.2 Mixtures

The pervious concrete tests were conducted with five distinct mixtures, all prepared based on the suggestions of Polastre and Santos [28]; Merighi et al. [3] and Teixeira and Fortes [12]. According to these researchers, the pervious concrete must have an aggregate to cement ratio of 4 and 4.5 to 1, a sand to cement ratio between 0 and 1, and w/c ratio between 0.27 and 0.40. The reference mixture was developed based on these studies.
Based on mixture A, 04 other mixtures were studied with the addition of sand and gravel 0, as shown in table 3. Preliminary tests showed the need to increase the w/c ratio in mixtures D and E, this fact is explained by the greater presence of fine aggregates. It is worth noting that it was chosen to limit the additive to 1% of the cement weight.

Table 3
Summary of the mixtures

	Mixture				
Material	**A**	**B**	**C**	**D**	**E**
Cement	1	1	1	1	1
Gravel 1	4	4	4	3	3
Gravel 0	–	–	1	1.3	1.3
Medium sand	–	0.5	0.5	0.5	1
Additive	1% cement weight	1% cement weight	1% cement weight	1% cement weight	1% cement weight
W/c ratio	0.25	0.25	0.25	0.30	0.35

3.3 Addition of fibers

The definition of the mixture of a pervious concrete with the addition of polypropylene fibers was based on studies by Reyes and Torres [30]. Based on mixture (D), which had a good ratio between the strength and permeability properties, three additions with different levels of polypropylene fibers were performed:

- Small addition of fibers (mixture D1): 1 kg/m³ (Figure 2);
- Medium addition of fibers (mixture D2): 2 kg/m³;
- Large addition of fibers (mixture D3): 4 kg/m³.

3.4 Permeability

The permeability test was performed based on the experiment conducted by Neithalath et. al [31]. According to the same authors, the equipment must contain a tube of transparent material (containing the specimen of 15 cm in height) so that it is possible to visualize the flow traveled by the water when it is discharged (Figure 3).
The transparent tube, which is fitted above the location where the concrete is coupled, must have a slightly larger diameter that allows for the fitting, and this fitting should be sealed to prevent water from leaking at this spot. Below the container holding the concrete, there is a horizontal tube of 50 mm in diameter, which in its middle part has a valve to control the water, and it is immediately followed by a vertical tube, which is 10 mm above the concrete specimen.
Still according to Neithalath et al. [31], the test must be performed with the addition of water until the concrete becomes saturated, reaching the maximum level in the vertical tube, which is 1 cm below the specimen. The valve must then be closed and topped off with water until the 290 mm (H0) mark above the horizontal tube. Once it is filled with water, the valve is opened and the time is measured until the 70 mm mark (H1) is reached. This procedure must be repeated 3 times and the arithmetic mean between the obtained values must be taken. The permeability is obtained through Darcy's law, shown below:

$$k = \frac{a.L}{A.\Delta t}.ln\left(\frac{h0}{h1}\right) \quad (1)$$

Where:
k: Permeability coefficient, in cm/s;
a: Inner area of the reservoir, in cm²;
A: Area of the concrete sample, in cm²;
L: Height of the specimen, in cm;
h0: Initial water height, in cm;
h1: Final water height, in cm;
Δt: Percolation time of the water from point h0 to H1, in seconds.
Some changes were made in the test regarding the basic procedure, namely:

- Pervious concrete specimen of 20 cm in height;

Figure 2
Appearance of the pervious concrete in mixture D1

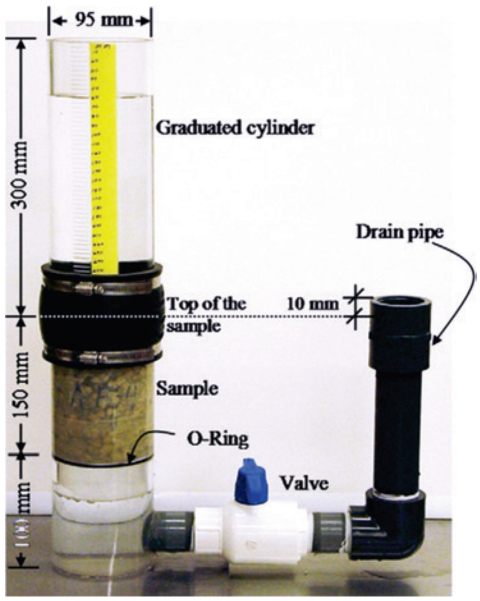

Figure 3
Permeameter model used

Figure 4
Slump test with zero slump

- The specimen is coupled to a PVC pipe of 100 mm in diameter;
- The smaller pipe was made of PVC and was 25 mm in diameter;
- The ball valve used had 25 mm in diameter.

4. Results and discussion

4.1 Results and analysis of aggregates

A fineness modulus of 6.94 and a maximum size of 19 mm was found for the gravel 1. Its bulk density was 1,511.7 kg/m³. A fineness modulus of 5.77 and a maximum size of 9.5 mm was found for the gravel 0. Its bulk density was 1,533.7 kg/m³. A fineness modulus of 2.36 and a maximum size of 4.8 mm was found for the sand. Its bulk density was 1,617.8 kg/m³ and the particle-size distribution ranked it as medium sand - zone 3.

4.2 Properties of the mixtures without fiber

4.2.1 Slump test

In order to examine the consistency of the pervious concrete, a slump test was performed (Figure 4) and all tests found a slump of 0 (zero) cm. The ACI 522R-06 standard[4] classifies pervious concrete as concrete with zero slump.

Given the fact that this concrete has little fineness in its dosage, a low w/c ratio and little paste, it was low workability, requiring greater care in handling and vibration, with the use of powered vibrations being suggested by ACI 522R-06[4]. Considering that the use in pavements is one of the main applications of pervious concrete, the density study with a plate compactor or roller may be viable, improving the mechanical properties, although the permeability should be checked.

Table 4
Axial compression strength

Mixtures	Strength (MPa)		% at 28 days in relation to the reference mixture
	7 days	28 days	
A: (1:4:0:0) (reference)	1.16	2.58	100 %
B: (1: 4: 0: 0.5)	1.47	2.44	94.6 %
C: (1: 4: 1: 0.5)	2.56	4.24	164.3 %
D: (1: 3: 1.3: 0.5)	2.60	4.10	158.9 %
E: (1: 3: 1.3: 1)	4.31	4.66	180.6 %

Table 5
Split tensile strength at 28 days

Mixture	Split tensile strength (MPa)	Split tensile strength (MPa)
A: (1:4:0:0) (reference)	0.54	100 %
B: (1: 4: 0: 0.5)	0.36	66.7 %
C: (1: 4: 1: 0.5)	1.94	359.3 %
D: (1: 3: 1.3: 0.5)	1.92	355.6 %
E: (1: 3: 1.3: 1)	2.59	479.6 %

Figure 5
Flexural strength test

Table 6
Flexural strength at 28 days

Mixture	Flexural strength (MPa)	% in relation to the reference mixture
A: (1:4:0:0) (reference)	1.70	100 %
B: (1: 4: 0: 0.5)	2.45	144.1 %
C: (1: 4: 1: 0.5)	2.52	148.2 %
D: (1: 3: 1.3: 0.5)	2.49	146.5 %
E: (1: 3: 1.3: 1)	6.35	373.5 %

Table 7
Permeability results

Mixture	K (cm/s)
A: (1:4:0:0) (reference)	0.093
B: (1: 4: 0: 0.5)	0.121
C: (1: 4: 1: 0.5)	0.103
D: (1: 3: 1.3: 0.5)	0.110
E: (1: 3: 1.3: 1)	0.078

4.2.2 Axial compression

As can be seen in Table 4, mixture E had the greatest strength at 7 and 28 days. In general, the addition of sand and gravel 0 increases the compression strength, which was already expected, although the water/cement ratio had to be increased in mixtures (D) and (E) from 0.25 to 0.30 and 0.35, respectively. This increase of the w/c ratio was needed to be able to get a more homogeneous mixture because of the finer aggregate, since the preliminary concrete mixtures proved difficult to handle.

4.2.3 Split tensile strength

As can be seen in Table 5, the greatest strength in this test was achieved by mixture E, with a value of 2.59 MPa. The addition of sand and gravel 0 increased the split tensile strength, with relevant gains especially when gravel 0 was added to the mixtures. This fact is due to the tighter packing of the concrete structure with the presence of finer aggregates.

4.2.4 Flexural strength

The trend of the previous test remained, with a considerable gain in mixture E, especially with the observation that the ruptured specimens of mixture E had a greater homogeneity than the other mixtures (Table 6). The flexural strength values (Figure 5) proved to be higher than the split tensile strength, with Batezini [14] also observing this trend with values up to 3 to 4 times higher. From the perspective of the ABNT [5] and with the exception of mixture A, all mixtures had an adequate flexural strength (≥ 2.0 MPa) for light traffic areas, with a minimum thickness of 10 cm.

4.2.5 Permeability

The results in table 7 reveal that mixture E had the lowest permeability as a result of its lower voids content, resulting from the increased presence of sand and gravel 0. On the other hand, it would be expected that mixture A would have one of the best permeabilities for having no sand in its dosage, but this trend was not manifested and the mixture with the best results was mixture B. From the perspective of the ABNT [5] and with the exception of mixtures A and E, all other mixtures reached the recommended minimum permeability values.
Based on the results above, one can conclude that the addition of sand to pervious concretes for pavements molded on site is beneficial, increasing their mechanical strength. The reduction in permeability to values below those recommended by NBR 16416 (ABNT [5]) is only observed when the levels of sand exceed 35%.

Table 8
Axial compression strength after the addition of fibers at 28 days

Mixture	Strength (MPa)	% at 28 days in relation to the reference mixture
D: reference – no fibers	4.10	100 %
D1: with fibers 1 kg/m³	3.46	84.4 %
D2: with fibers 2 kg/m³	3.69	90.0 %
D3: with fibers 4 kg/m³	2.32	56.6 %

4.3 Properties of the mixtures with fiber

4.3.1 Slump test

The slump test was performed, but there was no determination of values for this test because the concrete presented a slump close to zero, suitable for paving with powered mechanical compaction.

Figure 6
Rupture under axial compression of pervious concrete with fibers

Table 9
Split tensile strength after the addition of fibers at 28 days

Mixture	Strength (MPa)	% at 28 days in relation to the reference mixture
D: reference – no fibers	1.92	100 %
D1: with fibers 1 kg/m³	0.82	42.7 %
D2: with fibers 2 kg/m³	1.46	76.1 %
D3: with fibers 4 kg/m³	1.43	74.5 %

4.3.2 Axial compression strength

Table 8 shows the results for the axial compression test carried out at 28 days (Figure 6). As can be seen, there was a decrease in the compression strength with the addition of fibers. This fact can only be explained after the analysis of the ruptured specimens. The fibers hindered the kneading process of the concrete, which by its very nature already had a workability of almost zero. A blistering of fibers could be observed in certain parts of the concrete, generating a weak link where fracture zones were created. This suggests that the fiber-addition process requires very great care, in addition to a kneading process that makes the mixture more homogeneous.

4.3.3 Split tensile strength

The concrete with the highest split tensile strength was mixture D2, with a value of 1.46 MPa at 28 days. The fact that mixture D1 had a smaller amount of fibers in its mixture than mixtures D2 and D3 interfered to provide a small gain in strength, getting close to the strength of the reference mixture D , which did not have fibers in its mixture. The relationship between the values of mixtures D3 and D2 follows the same explicit logic of the axial compression, with D3 having less strength than D2 despite having twice the fibers (Table 9).

4.3.4 Flexural strength

In the case flexural strength, the best result at 28 days was achieved by mixture D3 (2.92 MPa). Based on table 10, one can conclude that the increased strength occurred in conjunction with the increased addition of fibers, and that unlike what occurred with compression, the D3 mixture, which has the largest amount of fibers (4 kg/m³), had the highest flexural strength. With the exception of mixture D1, the mixtures comply with the minimum specified by the ABNT [5] standard.

Table 10
Flexural strength after the addition of fibers at 28 days

Mixture	Strength (MPa)	% at 28 days in relation to the reference mixture
D: reference – no fibers	2.49	100 %
D1: with fibers 1 kg/m³	1.26	50.6 %
D2: with fibers 2 kg/m³	2.74	110.0 %
D3: with fibers 4 kg/m³	2.92	117.3 %

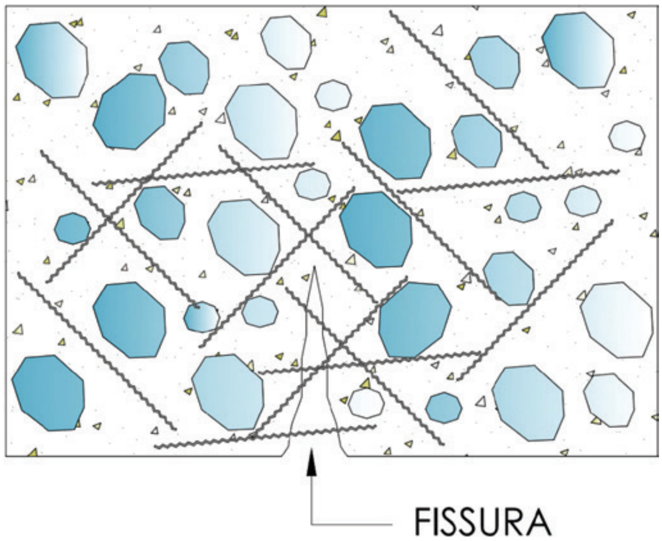

Figure 7
Macro-fibers acting in the crack region in the flexural strength

The improvement in the flexural strength behavior with the addition of fibers can be explained in the post-cracking behavior, when the macro-fibers form a seam in the crack region, acting like a reinforcement, as can be seen in Figure 7.

4.3.5 Permeability

As we can see in Table 11, the permeability coefficient was highest for mixture D1. The mixtures with the addition of 2 kg/m³ and 4 kg/m³ of polypropylene fibers had lower permeability. Mixture D3 had the lowest permeability (k=0.0996cm/s), while mixture D1 had a permeability of 0.1237cm/s, this being the highest value obtained among the mixtures.
According to NCPTC [10], the 3 tested mixtures fall within the permeability standards for pervious concrete. And mixture B, which showed the highest values for permeability (0.121 m/s), can be compared to the mixture by Kajio et al. [15], which obtained values between 0.025 to 0.178 cm/sec. According to the ABNT [5], all the other mixtures have the minimum recommended permeability.

Table 11
Permeability of concretes with fiber

Mixtures	k (cm/s)	% in relation to the reference mixture
D: reference – no fibers	0.110	100 %
D1: with fibers 1 kg/m³	0.124	112.7 %
D2: with fibers 2 kg/m³	0.107	97.3 %
D3: with fibers 4 kg/m³	0.100	90.9 %

Source: developed by the authors

When it comes to pervious concrete pavements molded on site, one can see that the addition of fibers improves the main property to be considered for its use by NBR 16416 (ABNT [5]), which is its flexural strength. The reduction in permeability with the increase in fiber content indicates that the levels should remain below 4 kg/m^3.

5. Concluding remarks

The objective of this work was to study pervious concrete mixtures for use in pervious concrete floors molded on site, checking the compression strength, split tensile strength, flexural strength and permeability properties in mixtures without the addition of fibers, but with the addition of gravel 0 and sand to the reference mixture that contained only gravel 1. Subsequently, the influence of the addition of polypropylene fibers on the properties described above was tested for one of the mixtures that contained gravel 0 and sand. The following can be observed:

1) There were considerable gains in strength when gravel 0 was added in addition to the sand, with the exception of mixture B, which might have had mixing and/or molding problems, and permeability began to decrease in mixture E, when the gravel 0 and sand to gravel 1 ratio reached the range of 43%. In mixtures C and D, this ratio was 27% and 37%, which indicates that the addition of sand is beneficial for the mechanical properties, without affecting permeability up to a certain level, in the order of 35%.
2) All concrete mixtures, with or without fibers, had permeability coefficients within the recommended levels, ranging from 0.124 cm/s to 0.078 cm/s, considered to be whithin the acceptable range according to ACI 522R-06[4] and NCPTC [10]. If the permeability required by NBR 16416 (ABNT [5]) is considered, then only the mixtures A and E failed to reach the minimum value.
3) For the compression strength, the values of the mixtures without fiber remained above the minimum value recommended by ACI 522R-06[4]. It should be noted that this requirement is not the parameter considered by NBR 16.416 (ABNT [5]).
4) The relationship between the split tensile strength and the flexural strength was between 50 and 77%, near the standard studied by Batezini [14] for concrete without fibers, and with the trend holding for the concretes with fibers, therefore.
5) Despite the decrease in compression strength of the mixtures with the addition of fibers, their gains in tensile strength makes the use of fibers attractive, since flexural strength is the criterion that must be met for pervious concrete molded on site according to NBR 16416 (ABNT [5]), and for this criterion, all mixtures have adequate mechanical strength. This increase in flexural strength had already been observed by Hesami et al. [23]. Rehder et al. [27], who also cited the contribution of fibers to the flexing capacity, since long fibers (macro-fibers) with a length equal to or two-times greater than the maximum size of the aggregate, have the ability to "weave" the structure after the beginning of the crack during bending.
6) The values found for mechanical strength and the permeability coefficient for the mixtures C, D and E in the concrete without fibers, and in the mixtures with fiber, already suggest the possibility of their use on the pavement of areas for parking and with light traffic, with no more than the specification of the adequate thickness being required, as suggested by the ABNT [5]. However, in order for the specification of the thicknesses to decrease and become more attractive from an economic point of view (Batezini [14]), studies on the improvement of the mechanical strength, even with a loss in permeability, should be considered. In this sense, continued research is suggested, considering the study of variations in mechanical properties as a function of the variation of the compaction energy.
7) The addition of fibers to pervious concretes, which already brings with it the characteristic of the difficulty in kneading and homogenizing because of the high voids content, is a point that deserves attention to avoid the blistering of the fibers, which can reduce the mechanical strength.
8) The low consistency values indicate that, ideally, mechanical compaction should be used so that the mechanical properties are improved (Bonicelli et al. [18]), suggesting the use of a plate compactor or roller.

6. References

[1] ABCP – Associação Brasileira de Cimento Portland. Projeto Técnico: Pavimento permeável. São Paulo, 2013.

[2] MARCHIONI, M.; SILVA, C. O.;VAQUERO Y MAYOR, A.. Conceitos e requisites para pavimentos de concreto permeável. Associação Brasileira de Cimento Portland, São Paulo, 2011

[3] MERIGHI, João Virgilio; FORTES, Rita Moura; BANDEIRA, Alex. Estudo de propriedades do concreto poroso aplicado a pavimentação. In: IBRACON, 2006, Rio de Janeiro - RJ. Anais do 48° Congresso Brasileiro do Concreto. São Paulo - SP, 2006.

[4] ACI 522R-06 – American Concrete Institute. Pervious Concrete. Michigan, 2006

[5] ABNT – Associação Brasileira de Normas Técnicas. NBR 16.416: Pavimentos permeáveis de concreto- Requisitos e procedimentos. Rio de Janeiro, 2015

[6] RODRIGUES, Públio Penna Firme; MONTARDO, Julio P.. A Influência da Adição de Fibras de Polipropileno nas Propriedades dos Concretos para Pisos e Pavimentos. In: IBRACON, 2002, Belo Horizonte - MG. Instituto Brasileiro do Concreto - 44° Congresso Brasileiro. Belo Horizonte – MG, 2002.

[7] MCCAIN, George N.; DEWOOLKAR, Mandar M. Porous Concrete Pavements: Mechanical and Hidraulic Properties. School of Engineering the University of Vermont. Burlington, USA, 2010.

[8] SHU, X.; HUANG, B.; WU, H,; DONG, Q.; BURDETTE, E.. Performance comparison of laboratory and field produced pervious concrete mixtures. Construction and Building Materials, v. 25, p.3187-3192, 2011.

[9] LYAN, C.; ZHUGE, Y.. Optimum mix design of enhanced permeable concrete – An experimental investigation. Construction and Building Materials, v. 24, p.2664-2671, 2010.

[10] NCPTC - NATIONAL CONCRETE PAVEMENT TECHNOLOGY CENTER. Mix Design Development for Pervious Concrete in Cold Weather Climates. Iowa Department of Transportation. Iowa Concrete Paving Association. 25. fev. 2006.

[11] ENVIROMENTAL PROTECTION AGENCY. Storm Water Technology Fact Sheet, Porous Pavement. EPA 832-F-99-023 Office of Water, Washington, D.C. 1999

[12] TEIXEIRA, B. C. S.; FORTES, R. M. Estudo da Dosagem de Concreto Poroso Aplicado a Pavimentação (Study of Pervious Concrete Dosage For Use In Pavements). In: CONINFRA – Anais do Congresso De Infraestrutura De Transportes, São Paulo. 2009: 12 p.

[13] IBRAHIM, A.; MAHMOUD, E; YAMIN, M; PATIBANDLA, V. C. Experimental study on Portland cement pervious concrete mechanical and hydrological properties. Construction and Building Materials, v. 50, p.524-529, 2014.

[14] BATEZINI, R.. Estudo preliminar de concreto permeáveis como revestimento de pavimento para áreas de veículos leves. 2013. 133 p. Dissertação (Mestrado) - Mestrado de Engenharia Civil, Escola Politécnica da Universidade de São Paulo, São Paulo, 2013.

[15] KAJIO, S.; TANAKA, S.; TOMITA, R.; NODA, E.; HASHIMOTO, S. Properties of Porous Concrete with High Strenght. Proceedings 8th International Symposium on Concrete Roads, Lisboa, p. 171-177, 1988.

[16] TENNIS, P. D.; LEMMING, M. L.; AKERS, D. J. Pervious Concrete Pavements, Skokie, Illinois: Portland Cement Association, 2004

[17] COSIC, K.; KORAT, L; DUCMAN, V.; NETINGER, I.. Influence of aggregate type and size on properties of pervious concrete. Construction and Building Materials, v. 78, p.69-76, 2015.

[18] BONICELLI, A.; GIUSTOZZI, F; CRISPINO, M.. Experimental study on the effects of fine sand addition on differentially compacted pervious concrete. Construction and Building Materials, v. 91, p.102-110, 2015.

[19] MAGUESVARI, M Uma; NARASIMHA, V.L.. Studies on Characterization of Pervious Concrete for Pavement Applications. Procedia - Social and Behavioral Sciences, ed.104, p. 198-207, 2013.

[20] SENISSE, Juliana; DAL MOLIN, D. C. C. A influência de microfibras de polipropileno e de aditivo superplastificante nas propriedades de concretos com níveis de resistência semelhantes. In: IBRACON, 2011, Florianópolis - SC. Anais do 53° Congresso Brasileiro do Concreto. Porto Alegre - RS, 2011.

[21] PERRONE, Vitor Cury et al. Estudo do comportamento à flexão de compósitos cimentícios reforçados com fibras de polipropileno de alta tenacidade. In: IBRACON, 2011, Florianópolis – SC. Anais do 53° Congresso Brasileiro do Concreto. Porto Alegre - RS, 2011.

[22] GESOGLU, M.; GÜNEYISI, E; KHOSHNAW, G.; IPEK, S.. Investigating properties of pervious concretes containing waste tire rubbers. Construction and Building Materials, v. 63, p.206-213, 2014.

[23] HESAMI, Saeid.; AHMADI, Saeed; NEMATZADEH, Mahdi. Effects of rice husk ash and fiber on mechanical properties of pervious concrete pavement. Construction and Building Materials, ed. 53, p. 680-691, 2014.

[24] AMARAL JUNIOR, Josué Coelho. Avaliação da influência da adição de fibras poliméricas nas propriedades térmicas e mecânicas do concreto. Dissertação (Mestrado) – Programa de Pós Graduação em Engenharia de Materiais, Centro Federal de Educação Tecnlógica de Minas Gerais, Belo Horizonte, 2016.

[25] LUCENA, Júlio César Tavares. Concreto reforçado com fibras de polipropileno: estudo de caso para aplicação em painel alveolar de parede fina. Dissertação (Mestrado) - Programa de Pós Graduação em Engenharia Civil. Escola de Engenharia de São Carlos, São Carlos, 2017.

[26] GUIMARÃES, Diego; SILVA FILHO, Luiz C. P. da; PACHECO, Alexandre R. Pisos industriais em concreto armado: determinação de teores ótimos de fibras de aço e polipropileno em ensaios mecânicos. In: IBRACON, 2011, Florianópolis - SC. Anais do 53° Congresso Brasileiro do Concreto. Porto Alegre - RS, 2011.

[27] REHDER, Benjamin.; BANH, Kingsten; NEITHALATH, Narayanan. Fracture behavior of pervious concretes: The effects of pore structure and fibers. Engineering Fracture Mechanics, ed. 118, p. 1-16, 2014.

[28] POLASTRE, B.; SANTOS, L. D. Concreto Permeável. Faculdade de Arquitetura e Urbanismo-USP. São Paulo: 2° Semestre de 2006. Disponível em: <http://www.usp.br> Acesso em: 04 de maio de 2013.

[29] SALES, T. L. Pavimento Permeável com Superfície em Blocos de Concreto de Alta Porosidade. 2008. 188 p. Dissertação (Mestrado) - Mestrado de Engenharia Civil, Departamento de Programa de Pós-graduação em Engenharia, Universidade Federal de Santa Catarina, Florianópolis, 2008.

[30] REYES, Fredy; TORRES, Andrés. Efecto de las fibras plasticas en la flexion de estructuras de pavimentos drenantes. Ingeniería de Construcción, Chile, v. 17, n. 2, p.93-102, 2002.

[31] NEITHALATH, Narayanan.; SUMANASOORIYA, Milani S; DEO, Omkar. Characterizing pore volume, sizes, and connectivity in pervious concretes for permeability prediction. Materials Characterization, ed. 61, p. 802-813, 2010.

Volume 12, Number 1 (February 2019) p. 101 – 121 • ISSN 1983-4195
http://dx.doi.org/10.1590/S1983-41952019000100009

REVISTA IBRACON DE ESTRUTURAS E MATERIAIS
IBRACON STRUCTURES AND MATERIALS JOURNAL

Pervious concrete: study of dosage and polypropylene fibers addiction

Concretos drenantes: estudo de dosagem e adição de fibras de polipropileno

S. E. PILZ [a]
silvio@unochapeco.edu.br
https://orcid.org/0000-0003-0361-7658

P. OLIVEIRA [a,b]
poliveira@unochapeco.edu.br
https://orcid.org/0000-0001-8835-6324

F. REGOSO [a]
felipe_regoso@unochapeco.edu.br
https://orcid.org/0000-0002-0270-0495

V. A. PAULON [c]
vpaulon@yahoo.com.br
https://orcid.org/0000-0002-1061-9902

M. F. COSTELLA [b,c]
costella@unochapeco.edu.br
https://orcid.org/0000-0001-6471-9848

Abstract

The use of pervious concrete to minimize the effects caused by the impermeability of the soil as a result of increasing urbanization is an alternative that still requires further studies regarding its design and implementation. From this perspective, this paper presents a study of the characteristics of pervious concrete, including its tensile strength, compressive strength, flexural strength and the permeability coefficient, through the development of various mixtures to adjust the characteristics of the local aggregates. Eight mixtures were studied based on a reference mixture, five of which were related to the pervious concrete with the addition of finer aggregates than the reference mixture without these aggregates. Subsequently, three mixtures were studied with the inclusion of polypropylene fibers in order to analyze the effects of the addition of fibers on the properties of the pervious concrete. It is concluded that the presence of fibers changed the characteristics of the concrete, increasing its strengths while achieving a good permeability in its mixtures. An improvement in the flexural strength of the pervious concrete was observed, which is the main property to be considered for its use in pavements, without harming the permeability, which raises the possibility for its application.

Keywords: pervious concrete, tests, fibers.

Resumo

Utilizar concreto permeável para minimizar os efeitos causados pela impermeabilidade do solo causado pela crescente urbanização é uma alternativa que ainda necessita de estudos quanto à sua concepção e aplicação. Seguindo esta linha, o presente artigo apresenta um estudo das características do concreto drenante, tal como a resistência à tração, resistência à compressão, resistência à tração na flexão e coeficiente de permeabilidade, através do desenvolvimento de varios traços, para ajustar às características dos agregados locais. A partir de um traço referência, foram estudados oito traços, sendo cinco referentes ao concreto drenante com adição de agregados mais finos ao traço referência sem estes agregados. Posteriormente estudou-se três traços com a inclusão de fibras de polipropileno, com o objetivo de analisar os efeitos que a adição de fibras causa nas propriedades do concreto drenante. Concluiu-se então, que a presença das fibras alterou as características do concreto, levando o mesmo a atingir maiores resistências, aliadas a uma boa permeabilidade em seus traços, verificando-se assim a melhoria de capacidade de resistência à tração na flexão do concreto drenante, principal propriedade para uso em pavimentos, sem prejudicar a permeabilidade e avaliando a possibilidade de aplicação do mesmo.

Palavras-chave: concreto permeável, ensaios, fibras.

[a] *Universidade Comunitária da Região de Chapecó, Chapecó, SC, Brasil;*
[b] *Concreoeste, Chapecó, SC, Brasil;*
[c] *Faculdade Meridional, Porto Alegre, RS, Brasil.*

Received: 23 Oct 2015 • Accepted: 23 Jul 2018 • Available Online: 05 Feb 2019

1. Introdução

O crescimento da urbanização que leva a maior impermeabilização do solo em função do revestimento de ruas, passeios e edificações traz impactos cada vez crescentes ao meio ambiente, exigindo que a construção civil encontre alternativa que evitem futuros problemas como inundações ou enchentes. Estas superfícies revestidas chegam a ocupar 30% da área da bacia de drenagem segundo a ABCP [1]. Se considerar o coeficiente de escoamento ou deflúvio superficial, segundo Marchioni et al. [2], área de edificação muito densa podem ter coeficientes de escoamento de 0,70 a 0,95, o que representa que até 95% da chuva gera escoamento superficial.

De acordo com Merighi et al.[3], o concreto drenante é uma alternativa que auxilia a drenagem urbana e facilita a infiltração da água diretamente para o solo. No entanto, no Brasil a sua utilização está em fase inicial, portanto, sua aplicação ainda é restrita, fato este explicado pela ausência de conhecimento adequado em relação ao comportamento mecânico, hidráulico e da potencialidade de aplicação do material por parte de projetistas e profissionais ligados à área. Segundo a ACI 522R-06 [4], utilizações típicas são: pavimentos para estacionamentos, estradas municipais, calçadas, áreas de pedestres em zoológicos, parques, decks de piscinas entre outras.

Conforme a norma ACI 522R-06[4], concreto drenante é descrito tipicamente como um concreto de slump 0 (zero), de graduação aberta, com nenhum ou pouco agregado fino, teor de vazios variando entre 18 a 35% e resistência à compressão entre 2,8 a 28 MPa, com permeabilidade de 0,0135 a 0,122 cm/s (unidades já transformada).

Para a ABNT [5], o pavimento drenante moldado no local deve ter resistência mecânica de tração na flexão de pelo menos 2,0 MPa e permeabilidade de 0,100 cm/s, não sendo considerado o requisito de resistência à compressão.

Com o intuito de melhorar o desempenho do concreto drenante, Rodrigues e Montardo [6] afirmam que o emprego de fibras plásticas de polipropileno como elementos de reforço no concreto tem crescido nos últimos anos no Brasil. Há diversas obras em que foram utilizadas fibras de polipropileno: barragens, túneis, pontes, canais de irrigação, estações de tratamento de águas e esgoto e, principalmente, em pavimentos e pisos de concreto. O polipropileno é quimicamente inerte, não absorve água, não enferruja, possui baixo custo e é de fácil disponibilidade. Neste sentido a utilização de fibras de polipropileno se torna mais adequada que a de fibras metálicas, em função da corrosão e da necessidade de melhorar o desempenho da tração na flexão, requisito fundamental para concreto de pavimentos.

Quando a matriz cimentícia é reforçada com fibras, muitas das propriedades são alteradas: trabalhabilidade, resistência à compressão, módulo de ruptura (resistência à tração na flexão), resistência à tração direta, resistência ao impacto, resistência à fadiga, aumento da tenacidade, inibição de propagação de fissuras. A determinação do teor ótimo é importante para que se ganhe em eficiência e economia, especialmente nas principais propriedades ao uso ao qual se destina. Em função dos parcos estudos do comportamento de concreto drenante com uso de fibras, estudos de traços com teores diversos de fibras ganham em importância, sendo este um dos objetivos deste trabalho.

O comportamento na pós-fissuração como estudo comportamental, não será avaliado, pois como o concreto drenante tem um teor de vazios elevado, sendo por isto importante estudar o comportamento da principal propriedade mecânica de um material para pisos (tração na flexão), apesar de saber que o comportamento de concretos com fibras na pós-fissuração é melhor e com menor dimensão de fissuras (Rodrigues e Montardo [6]) e o provável aumento de tração na flexão pode explicar este comportamento. O estudo de fibras de polipropileno em concreto drenante merece avaliações do comportamento, sendo este um dos objetivos deste trabalho.

Neste contexto geral, este artigo tem com objetivo observar e analisar o comportamento nas propriedades mecânicas (resistência à compressão, resistência à tração na compressão diametral e resistência à tração na flexão) e do coeficiente de permeabilidade em diferentes traços de concreto drenante com e sem adição de fibras de polipropileno.

2. Referencial teórico

Segundo McCain e Dewoolkar [7], estados do Norte dos Estados Unidos vêm sendo lentos na adoção do uso de concreto drenante, realidade decorrente da falta de dados sobre seus efeitos e comportamento. Shu et al. [8], destacam que há uma necessidade de testes laboratoriais para definir traços adequados, estudando diferentes tipos de agregados, sua graduação e diferentes adições, fatos estes também destacados por Lian e Zhuge [9].

Em relação à permeabilidade, o NCPTC [10] aponta valores entre 0,0254 e 0,6096 cm/s para considerar um concreto como drenante, enquanto a ACI 522R-06[4] tipifica valores entre 0,0135 a 0,122 cm/s.

Segundo o Enviromental Protection Agency [11], o concreto drenante apresenta algumas desvantagens, sendo: a tendência à obstrução do pavimento por sujeiras, caso seja instalado ou mantido de forma inadequada; risco de falha considerável caso seja mal construído ou se houver colmatação; contaminação do aquífero dependendo de como são as condições do solo e a suscetibilidade do aquífero; está sujeito a poucas perícias dos engenheiros nos pavimentos. Teixeira e Fortes [12] concluem ainda que o concreto drenante possui custos economicamente viáveis, porém sua resistência à compressão e à tração é muito menor do que os concretos convencionais. Neste sentido, Lian e Zhuge [9] destacam que em função destas resistências baixas a utilização tem ficado quase que restritamente a pavimentos.

2.1 Estudos realizados em concreto drenante

Ibrahim et al. [13] estudaram 24 traços para verificar a variação da propriedades com a variação das diferentes frações de agregados, da variação da relação água cimento, do teor do cimento e concluíram, entre outros fatores, que as máximas resistências à compressão para traços sem agregados miúdos tem-se com teores de cimento em torno de 250 kg/m^3 e diminuindo 75% quando a relação baixa para 150 kg/m^3.

Lian e Zhuge [9] concluíram que o uso de materiais finos com graduação entre 9,5 e 2,4 mm aumentam as propriedades de resistência do concreto drenante. Porém, o uso de finos muito pequenos, como a sílica ativa não altera significativamente a resistência, pois as partículas muito finas, devido à porosidade do concreto tendem a segregar. Batezini [14] concluiu que a adição de agregados miúdos em concretos para a melhoria das resistências mecânicas é uma possibilidade, especialmente quando o coeficiente de permeabilidade das misturas apresentam valores mais elevados. Nesse estudo os valores de permeabilidade foram de 0,14 cm/s e os de resistência à tração na compressão diametral e resistência à tração na flexão ficaram para as três misturas entre 57 e 71%.

Baseando-se na elaboração de traços de concreto drenante com cinco granulometrias diferentes de agregados de origem granítica, Merighi et al. [3] objetivavam encontrar uma mistura que apresentasse boa resistência mecânica para ser utilizada em camada de revestimento de pistas aeroportuárias e viárias. Os melhores resultados quanto às resistências aos 28 dias foi de 31,6 MPa à compressão e 3,0 MPa à tração no qual se utilizou agregados menores que os demais traços, baixa relação a/c, um aditivo superplastificante e micro sílica. Entretanto, Merighi et al. [3] afirmam não ser recomendável o uso desse concreto como camada drenante, pois apresentou coeficiente de permeabilidade na ordem de 10^{-3} cm/s.

A discrepância entre permeabilidade e resistência, estudada por Kajio et al. [15] e Tennis et al. [16], é normalmente ditada pela quantidade de agregado miúdo utilizado nos traços, sendo que uma maior quantidade deste diminui o índice de vazios, aumentando a resistência e diminuindo a permeabilidade. A identificação da otimização entre vazios, permeabilidade e resistências são os desafios dos pesquisadores, quando dos ajustes aos agregados locais, sendo este um dos objetivos deste trabalho.

Cosic et al. [17] estudaram a variação da propriedades do concreto drenante em função da variação do tipo de agregado e seu tamanho e entre os resultados encontrados, concluíram de forma surpreendente, que o tipo de agregado influencia mais significativamente na permeabilidade do que o seu tamanho. Lian e Zhuge [9] também encontraram diferenças nos valores de permeabilidade em função de diferentes tipos de agregados.

Bonicelli et al. [18] pesquisaram a diferença nas propriedades do concreto drenante quando se utiliza diferentes níveis de compactação do concreto, além da influência da adição de areias, e os resultados sugeriram que o acréscimo de areia em torno de 5% da massa total de agregado melhora as propriedades mecânicas, com destaque de aumento de até 75% na resistência à tração, porém com decréscimo na permeabilidade, porém sem comprometer a capacidade de drenagem do concreto.

Maguesvari e Narasimha [19] estudaram a influência de agregados graúdos e miúdos no concreto drenante e concluíram que o aumento de finos reduz a permeabilidade, porém aumenta a resistência à compressão e a resistência à flexão, tornando um material apropriado para pavimentos de tráfego leve.

2.2 Estudos realizados em concreto com fibras de polipropileno

Em estudo realizado por Senisse e Dal Molin [20], foram moldados três traços de concreto diferentes para cada uma das misturas avaliadas, utilizando um teor de argamassa de 55% e relações a/c variando entre 0,34 e 0,68. Três tipos de concreto foram elaborados: concreto convencional (referência-CC), concreto reforçado com macrofibras de polipropileno (CF) e concreto reforçado com macrofibras e aditivo superplastificante (CFSP), com teor de 600 g/m³ de adição das fibras e de 0,32% de superplastificante em relação à massa de cimento. Os resultados mostraram que a inserção de macrofibras majorou significativamente (39% a resistência à tração na flexão para os CF e 27% para os CFSP, mesmo que a resistência à compressão tenha diminuído, no caso dos CF). Também concluíram que a adição de fibras no concreto teve um aumento insignificante no custo (SENISSE; DAL MOLIN [20]).

Perrone et al. [21] comentam em estudo que a adição de fibras não metálicas pode ajudar a superar os problemas com a corrosão e melhorar o desempenho estrutural. Gesoglu et al. [22] estudaram as propriedades do concreto drenante com a adição de diferentes tipos de resíduos de borrachas de pneus em fibras e concluíram que é possível obter concretos drenantes com maior resistência à compressão ou melhor permeabilidade dependo das características do resíduo, mas que, na média, concretos com resíduos tem menores propriedades de resistência e queda na permeabilidade quando comparados ao traço referência, sem resíduos, porém a energia de fratura aumentou com as aparas de pneus, sendo a utilização do mesmo viável em áreas de estacionamento.

Hesami et al. [23] estudaram o uso de diversos materiais, entre eles a fibra de vidro, com teor de 0,2 % em concreto drenante, e observaram um aumento de até 30 % na resistência à tração e de até 64% na resistência à tração na flexão, corroborando a tendência de aumento das propriedades mecânicas com o aumento da porcentagem do material, com decréscimo gradual após a porcentagem ótima.

Amaral Junior [24] e Lucena [25] observaram que o uso de fibras poliméricas usualmente faz com que haja uma redução da resistência à compressão axial, porém a resistência à tração na flexão aumenta. Em estudo realizado por Guimarães et al. [26] para a resistência à tração na flexão verificou-se que o melhor desempenho se deu para a o teor de fibras de 1%. Rehder et al. [27] também observaram esse fato, pela possibilidade dos poros estarem ligados por fibras, havendo contribuição das fibras para melhorar a capacidade de flexão residual, principalmente em porosidades mais elevadas. Neste sentido, este trabalho busca averiguar a relação do uso de fibras em diversas proporções no comportamento de concretos drenantes.

3. Procedimentos metodológicos

Estudar traços de concreto com a utilização de materiais regionais a partir de um traço de concreto drenante, sem areia, e a partir deste verificar o comportamento das propriedades mecânicas e na permeabilidade, quando se adicionam diferentes teores de areia, é um dos objetivos deste trabalho. Também busca se observar a influência da adição de fibras não metálicas, no caso o polipropileno, nas propriedades citadas, especialmente no comportamento da tração na flexão e permeabilidade, já que estes são os parâmetros indicados pela NBR 16416 (ABNT [5]).

Então, a partir de traços pré-determinados por outros pesquisadores que apresentaram resultados razoáveis entre resistência e permeabilidade (Polastre e Santos [28]; Sales [29]; Kajio et al. [15]; Tennis et al. [16]), foi definido um traço referência (traço A) contendo somente cimento e brita 1. Foram então estudados mais quatro traços (B, C, D e E), para verificar a influência da adição de brita 0 e areia nas propriedades de resistência à compressão, à

Tabela 1
Especificações técnicas do Cimento Cauê

Finura		Massa específica (g/cm³)	Pega		Resistência a compressão (MPa)			
#200 (75 mm)	#300 (45 mm)	3,06	Início (min)	Fim (min)	1 dias	3 dias	7 dias	28 dias
2,7	10,7		190	290	14,4	28,6	32,8	41,0

Tabela 2
Características do aditivo superplastificante

Parâmetro	Unidade	Especificação	Resultados	Métodos
Aspecto	–	Líquido	Aprovado	Visual
Cor	–	Marrom claro	Aprovado	Visual
pH (puro) – 25°C	–	3.00 a 5.00	4.17	NBR 10908:2008
Massa espec. – 25°C	g/cm3	1.062 a 1.102	1.082	NBR 10908:2008
Teor de sólidos	%	38.25 a 42.75	39.92	NBR 10908:2008

tração na compressão diametral e na flexão e na permeabilidade. Para cada traço foram elaborados 6 corpos de prova (CPs) para resistência à compressão axial, 6 CPs para resistência à tração na compressão diametral, 6 CPs para resistência à tração na flexão, sendo que foi adotado para cada um deles o maior valor (resistência potencial, já que se tratava de concretos de mesma betonada) e 6 CPs para estudo da permeabilidade, sendo que neste caso foi adotada a média dos valores. Os procedimentos de moldagem, cura e execução dos ensaios seguiram os procedimentos estabelecidos pelas normas brasileiras da ABNT.
Posteriormente para o traço D (que já continha brita 0 e areia) foi estudada em mais três traços a influência da adição de fibras de polipropileno (1, 2 e 3 kg/m³)nas propriedades referenciadas acima. Os teores foram baseados nos estudos de Guimarães et al. [26] e Reyes e Torres [30].
Quando houve diferenças significativas das propriedades nos valores esperados e valores obtidos, foram refeitos os estudos para verificar se era uma tendência ou simples erro de procedimento, sendo que no caso do traço D, se constatou que no estudo inicial houve erro de procedimento na elaboração da betonada.
As propriedades mecânicas estudadas são as mais significativas para um concreto drenante, porém a influência do efeito de compactação do concreto, comportamento sob ações cíclicas, desgaste à abrasão, entre outros também podem merecer estudos específicos, quando da aplicação do mesmo em pavimentos de tráfegos leves.

Figura 1
Macrofibras de polipropileno utilizadas

3.1 Caracterização dos materiais

O cimento utilizado para os ensaios foi o CP II-E a granel. Não foram efetuados ensaios em laboratório para o cimento, sendo utilizadas especificações técnicas fornecidas pelo fabricante conforme a tabela 1.
Para a areia média proveniente de União da Vitória foram realizados ensaios de caracterização em laboratório referentes à massa unitária, módulo de finura e diâmetro máximo do agregado miúdo. Para a brita 0 e brita 1, ambas de origem basáltica e produzidas em um britador localizado em Cordilheira Alta – SC, foram determinados a massa unitária, módulo de finura e diâmetro máximo do agregado.
O aditivo utilizado foi o superplastificante MAXIFLUID 900. Na tabela 2 estão os dados de análise do aditivo fornecidos pelo fabricante, pois não foram efetuados ensaios em laboratório. A quantidade de aditivo utilizada para todos os traços foi de 1% em relação à massa de cimento, conforme indicações do fabricante.
As fibras de polipropileno e suas especificações foram fornecidas por uma empresa localizada em São José-SC:
- Álcali resistente;
- Comprimento: 50 mm (frisada);
- 27.000 fios por kg;
- 350 MPa de resistência à tração (por filamento);
- Twist – ancoragem;
- 50 FF – fator forma, caracterizada como macro-fibra (Figura 1);
- Espessura: 0,9 mm;
- 110%: alongamento por ruptura;

Tabela 3
Resumo dos traços

	Traços				
Material	**A**	**B**	**C**	**D**	**E**
Cimento	1	1	1	1	1
Brita 1	4	4	4	3	3
Brita 0	–	–	1	1,3	1,3
Areia média	–	0,5	0,5	0,5	1
Aditivo	1% peso cimento	1% peso cimento	1% peso cimento	1% peso cimento	1% peso cimento
Relação a/c	0,25	0,25	0,25	0,30	0,35

- Matéria-prima: monofilamentos de polipropileno.

A água utilizada era proveniente de lençol subterrâneo localizado na cidade de Chapecó-SC.

3.2 Traços

Os ensaios de concreto drenante foram realizados com cinco traços distintos, todos elaborados com embasamento no que sugere Polastre e Santos [28]; Merighi et al. [3] e Teixeira e Fortes [12]. De acordo com estes pesquisadores, o concreto drenante deve ter a relação de agregados graúdos entre 4 e 4,5 para 1 de cimento, a relação da areia entre 0 e 1 para 1 de cimento, e a relação a/c deve estar entre 0,27 e 0,40. A partir destes estudos, foi elaborado o traço referência.

A partir do traço A, foram estudados mais 04 traços acrescentando-se areia e brita 0, conforme se observa na tabela 3. Para os traços D e E, durante os ensaios preliminares observou-se a necessidade de aumentar a relação a/c, fato este explicado pela maior presença de finos. Cabe ressaltar que se optou por limitar o aditivo em 1% do peso de cimento.

3.3 Adição de fibras

Para definir a composição de um concreto drenante com adição de fibras de polipropileno foi baseada em estudos de Reyes e Torres [30]. A partir do traço D, que apresentou boa relação entre as propriedades de resistência e permeabilidade, foram realizadas três adições de diferentes teores de fibras de polipropileno:

- Pouca adição de fibras (traço D1): 1 kg/m³ (Figura 2);
- Média adição de fibras (traço D2): 2 kg/m³;
- Alta adição de fibras (traço D3): 4 kg/m³.

3.4 Permeabilidade

O ensaio de permeabilidade foi realizado baseado no experimento realizado por Neithalath et. al [31]. Segundo os mesmos autores, o equipamento deve conter um tubo de material transparente (contendo o corpo de prova de 15 cm de altura) para que seja possível visualizar o fluxo percorrido pela água quando for despejada (Figura 3).

O tubo transparente que é encaixado acima do local onde está acoplado o concreto deve possuir diâmetro um pouco maior que permita o encaixe, sendo que este deve ser vedado para impedir a saída de água neste local. Abaixo do recipiente que está o concreto há uma tubulação horizontal de 50 mm de diâmetro, possuindo em sua parte intermediária uma válvula para controle da água e, logo após segue um tubo na vertical, que está 10 mm acima do corpo de prova de concreto.

Figura 2
Aspecto do concreto drenante no traço D1

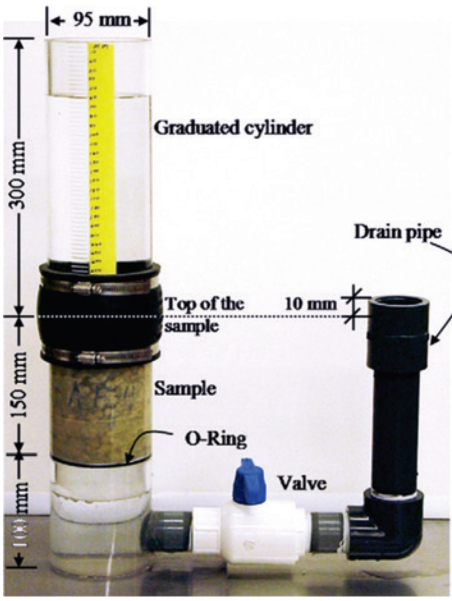

Figura 3
Modelo de permeâmetro utilizado

Figura 4
Ensaio de abatimento com slump zero

Ainda de acordo com Neithalath et al. [31], o ensaio deve ser realizado com adição de água a ponto de que o concreto fique saturado, atingindo o nível máximo na tubulação vertical, que está 1 cm abaixo do corpo de prova. Em seguida deve ser fechada a válvula e deve-se completar com água até a marca de 290 mm (h0) acima do tubo horizontal. Depois de preenchido de água, a válvula é aberta e o tempo é cronometrado até o momento em que seja atingida a marca 70 mm (h1). Este procedimento deve ser repetido por 3 vezes e deve-se efetuar a média aritmética entre os valores obtidos.
A permeabilidade é obtida através da Lei de Darcy, apresentada abaixo:

$$k = \frac{a.L}{A.\Delta t}.ln\left(\frac{h0}{h1}\right) \quad (1)$$

Sendo:
k: Coeficiente de permeabilidade, em cm/s;
a: Área interna do reservatório, em cm²;
A: Área da amostra de concreto, em cm²;
L: Altura do corpo-de-prova, em cm;

Tabela 4
Resistência à compressão axial

Traços	Resistência (MPa)		% aos 28 dias em relação ao traço referência
	7 dias	28 dias	
A: (1:4:0:0) (referência)	1,16	2,58	100 %
B: (1: 4: 0: 0,5)	1,47	2,44	94,6 %
C: (1: 4: 1: 0,5)	2,56	4,24	164,3 %
D: (1: 3: 1,3: 0,5)	2,60	4,10	158,9 %
E: (1: 3: 1,3: 1)	4,31	4,66	180,6 %

Tabela 5
Resistência à tração na compressão axial aos 28 dias

Traço	Resist. à tração na compressão diametral (MPa)	% em relação ao traço referência
A: (1:4:0:0) (referência)	0,54	100 %
B: (1: 4: 0: 0,5)	0,36	66,7 %
C: (1: 4: 1: 0,5)	1,94	359,3 %
D: (1: 3: 1,3: 0,5)	1,92	355,6 %
E: (1: 3: 1,3: 1)	2,59	479,6 %

h0: Altura inicial da água, em cm;
h1: Altura final da água, em cm;
Δt: Tempo de percolação da água do ponto h0 até h1, em segundos.
Foram efetuadas algumas alterações no ensaio em relação ao procedimento base, sendo estas:

- corpo de prova de concreto drenante com 20 cm de altura;
- o corpo de prova era acoplado em um tubo de PVC de 100 mm de diâmetro;
- a tubulação menor era de PVC e possuía 25 mm de diâmetro;
- o registro de esfera utilizado possuía 25 mm de diâmetro.

Figura 5
Ensaio de tração na flexão

Tabela 6
Resistência à tração na flexão aos 28 dias

Traço	Resist. à tração na flexão (MPa)	% em relação ao traço referência
A: (1:4:0:0) (referência)	1,70	100 %
B: (1: 4: 0: 0,5)	2,45	144,1 %
C: (1: 4: 1: 0,5)	2,52	148,2 %
D: (1: 3: 1,3: 0,5)	2,49	146,5 %
E: (1: 3: 1,3: 1)	6,35	373,5 %

Tabela 7
Resultado da permeabilidade

Traço	K (cm/s)
A: (1:4:0:0) (referência)	0,093
B: (1: 4: 0: 0,5)	0,121
C: (1: 4: 1: 0,5)	0,103
D: (1: 3: 1,3: 0,5)	0,110
E: (1: 3: 1,3: 1)	0,078

4. Resultados e discussões

4.1 Resultado e análise dos agregados

Para a brita 1 foi encontrado um módulo de finura de 6,94 e uma dimensão máxima de 19 mm. Sua massa unitária é de 1.511,7 kg/m³. Para a brita 0 foi encontrado um módulo de finura de 5,77 e uma dimensão máxima de 9,5 mm. Sua massa unitária é de 1.533,7 kg/m³. Para a areia foi encontrado um módulo de finura de 2,36 e uma dimensão máxima de 4,8 mm. Sua massa unitária é de 1.617,8 kg/m³ e a curva granulométrica classificou a mesma como sendo areia média – zona 3.

4.2 Resultados das propriedades dos traços sem fibras

4.2.1 Abatimento do tronco de cone (slump test)

A fim de analisar a consistência do concreto drenante foi realizado o ensaio de abatimento do tronco de cone (Figura 4) e para todos os testes realizados encontrou-se slump 0 (zero) cm. A ACI 522R-06[4] classifica o concreto drenante como concreto com slump zero.
Dado ao fato de este concreto possuir baixa finura em sua dosagem, baixa relação a/ c e pouca pasta, o mesmo apresenta baixa trabalhabilidade, exigindo maiores cuidados de manuseio e vibração, sendo sugerida a utilização de vibração energética, conforme sugere a ACI 522R-06[4]. Considerando que uma das principais aplicações do concreto drenante é o uso em pavimentações, o estudo do adensamento através de placa vibratória ou de rolo compactador pode ser viável, melhorando as características das propriedades mecânicas, porém deve ser verificada a permeabilidade.

4.2.2 Compressão axial

Como pode ser visualizado na tabela 4, o traço E foi o que apresentou maior resistência aos 7 e 28 dias. De modo geral a adição de areia e brita 0 faz aumentar a resistência à compressão, o que já era esperado, mesmo nos traços D e E onde a relação água/cimento teve que ser aumentada de 0,25 para 0,30 e 0,35, respectivamente. Este acréscimo da relação a/c foi necessário para poder resultar numa mistura mais homogênea em função do agregado mais fino, já que nas misturas preliminares o concreto apresentava dificuldade de manuseio.

Tabela 8
Resistência à compressão axial após adição de fibras aos 28 dias

Traços	Resistência (MPa)	% aos 28 dias em relação ao traço referência
D: referência – sem fibras	4,10	100 %
D1: com fibras 1 kg/m³	3,46	84,4 %
D2: com fibras 2 kg/m³	3,69	90,0 %
D3: com fibras 4 kg/m³	2,32	56,6 %

4.2.3 Tração na compressão diametral

Para este ensaio, conforme se observa na tabela 5, o traço que obtive melhor resistência foi o E, com valor de 2,59 MPa. A adição de areia e brita 0 faz aumentar a resistência à tração à compressão diametral, com ganhos relevantes especialmente quando se adicionou brita 0 nos traços. Este fato é devido ao maior empacotamento da estrutura do concreto pela presença de agregados mais finos.

4.2.4 Tração na flexão

Da mesma forma que no ensaio anterior, manteve-se a tendência, com um ganho considerável no traço E, especialmente por se ob-

Figura 6
Ruptura à compressão axial de concreto drenante com fibras

Tabela 9
Resistência à tração na compressão axial após adição de fibras aos 28 dias

Traços	Resistência (MPa)	% aos 28 dias em relação ao traço referência
D: referência – sem fibras	1,92	100 %
D1: com fibras 1 kg/m³	0,82	42,7 %
D2: com fibras 2 kg/m³	1,46	76,1 %
D3: com fibras 4 kg/m³	1,43	74,5 %

servar nos corpos de prova rompido que o traço E apresentava uma homogeneidade maior que os demais traços (Tabela 6). Os valores de tração na flexão (Figura 5) apresentaram-se maiores que da tração na compressão diametral, sendo que Batezini [14] também observou esta tendência com valores de 3 a 4 vezes maiores. Sob a ótica da ABNT [5], com exceção do traço A, todos os demais apresentam resistência à tração na flexão adequada (≥ 2,0 MPa) para áreas de trafego leve, com espessura mínima de 10 cm.

4.2.5 Permeabilidade

Pelos resultados da tabela 7, o traço E foi o que apresentou menor permeabilidade, em consequência do menor índice de vazios, resultante da maior presença de areia e brita 0. Já a tendência era que o traço A atingisse uma das melhores permeabilidades por não possuir areia em sua dosagem, porém, a tendência não se concretizou e o traço que atingiu melhores resultados foi o B. Sob a visão da ABNT [5], com exceção dos traços A e E, todos os demais apresentam a permeabilidade mínima recomendada.
Pode-se, a partir dos resultados acima, concluir que a adição de areia em concretos drenantes para pavimentos moldados no local é benéfica, aumentando as resistências mecânicas. A diminuição da permeabilidade com valores abaixo dos recomendados pela NBR 16416 (ABNT [5]), somente se observa quando os teores de areia passam de 35%.

4.3 Resultados das propriedades dos traços com adição de fibras

4.3.1 Consistência pelo abatimento do tronco de cone

Foi realizado o ensaio da consistência pelo abatimento do tronco

Tabela 10
Resistência à tração na flexão após adição de fibras aos 28 dias

Traços	Resistência (MPa)	% aos 28 dias em relação ao traço referência
D: referência – sem fibras	2,49	100 %
D1: com fibras 1 kg/m³	1,26	50,6 %
D2: com fibras 2 kg/m³	2,74	110,0 %
D3: com fibras 4 kg/m³	2,92	117,3 %

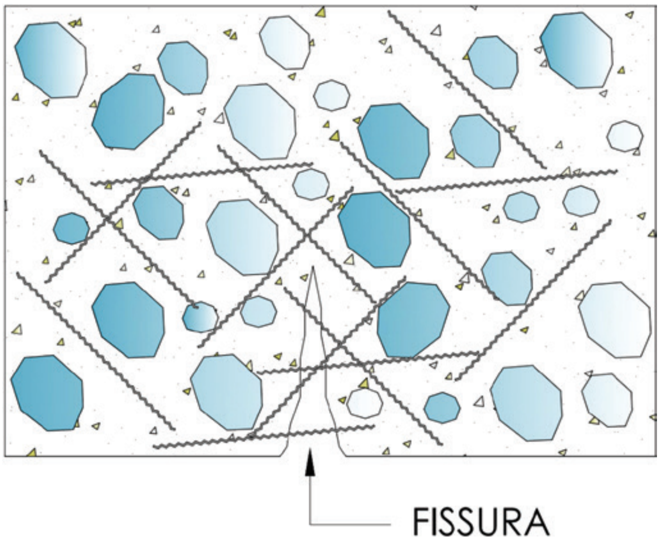

Figura 7
Macrofibras agindo na região da fissura na tração na flexão

de cone, porém não houve determinação de valores para este teste, pois o concreto apresentou abatimentos próximos a zero, adequado para pavimentação com compactação mecânica enérgica.

4.3.2 Resistência à compressão axial

Na tabela 8 são apresentados os resultados de resistência obtidos no ensaio de resistência à compressão axial aos 28 dias (Figura 6). Observa-se que houve um decréscimo da resistência à compressão com a adição de fibras. Este fato pode-se explicar somente quando da análise dos corpos de prova rompidos. As fibras dificultaram o processo de amassamento do concreto, que por natureza já apresenta trabalhabilidade quase nula. Notou-se que houve empolamento das fibras em certas partes do concreto, gerando um elo fraco, onde se gerou as zonas de fratura. Isto sugere que o processo de adição de fibras requer um cuidado muito grande, além de um processo de amassamento que torne a mistura mais homogênea.

4.3.3 Resistência à tração na compressão diametral

O concreto que apresentou maior resistência à tração na compressão diametral foi o traço D2, com um valor de 1,46 MPa aos

Tabela 11
Permeabilidade dos concretos com fibra

Traços	Permeabilidade k (cm/s)	% em relação ao traço referência
D: referência – sem fibras	0,110	100 %
D1: com fibras 1 kg/m³	0,124	112,7 %
D2: com fibras 2 kg/m³	0,107	97,3 %
D3: com fibras 4 kg/m³	0,100	90,9 %

Fonte: desenvolvido pelos autores

28 dias. O fato de o traço D1 possuir uma menor quantidade de fibras em sua composição que os traços D2 e D3 interferiu de maneira a proporcionar um ganho de resistência pequeno, ficando próximo da resistência do traço D referência, que não possui fibras em sua composição. Já a relação entre os valores dos traços D3 e D2 segue a mesma lógica explícita na compressão axial, onde mesmo possuindo o dobro de fibras que D2, D3 apresentou menor resistência (Tabela 9).

4.3.4 Resistência à tração na flexão

No caso de resistência à tração na flexão, o traço D3 foi o que apresentou maior resistência aos 28 dias (2,92 MPa). A partir da tabela 10, concluiu-se que o aumento de resistência deu-se de maneira conjunta ao aumento de adição de fibras, e que diferentemente dos casos de compressão, o traço D3, que possui a maior quantidade de fibras (4 kg/m³) apresentou maior resistência à tração da flexão. Pela ABNT [5], com exceção do traço D1, os demais apresentam a resistência mecânica mínima especificada por esta norma.

A melhora do comportamento da tração na flexão, quando da adição de fibras, pode ser explicada, na pós-fissuração, quando as macrofibras fazem uma costura na região da fissura, agindo à semelhança de uma armadura, conforme a Figura 7.

4.3.5 Permeabilidade

Como se pode perceber na tabela 11, o coeficiente de permeabilidade foi maior para o traço D1. Os traços que possuíam adição de 2 kg/m³ e 4 kg/m³ de fibras de polipropileno apresentaram menor permeabilidade. O traço D3 foi o que apresentou menor permeabilidade (k=0,0996cm/s), enquanto o traço D1 apresentou permeabilidade de 0,1237cm/s, sendo este o maior valor obtido entre os traços.

Conforme NCPTC [10], os 3 traços realizados estão dentro dos padrões de permeabilidade para o concreto drenante. E ainda, o traço B que apresentou o maior dos valores para permeabilidade (0,121 m/s), pode ser comparado ao traço de Kajio et al. [15] que obteve valores entre 0,025 a 0,178 cm/s. Pela ABNT [5], todos os demais apresentam permeabilidade mínima recomendada.

Pode-se então observar que a adição de fibras, quando se fala em pavimento de concreto drenante moldado no local, melhora a principal propriedade a ser considerada para uso pela NBR 16416 (ABNT [5]), que é a resistência à tração na flexão. A redução da permeabilidade com o aumento do teor de fibras indica que os teores devem estar abaixo de 4 kg/m³.

5. Considerações finais

Este trabalho teve como objetivo o estudo de traços de concreto drenante para uso em pisos de concreto drenante moldado no local, verificando as propriedades de resistência à compressão, resistência à tração na compressão axial, resistência à tração na flexão e permeabilidade em traços sem adição de fibras, porém acrescentando-se brita 0 e areia ao traço referência que continha somente brita 1. Posteriormente, para um dos traços que continha brita 0 e areia, estudou-se a influência da adição de fibras de polipropileno nas propriedades acima descritas. Pode-se observar o seguinte:

1) Quando se adicionou além de areia também a brita 0, com exceção do traço B, em que pode ter ocorrido problemas de mistura e/ou moldagem, houve ganhos consideráveis das resistências, sendo que a permeabilidade começou a diminuir no traço E, quando a relação agregado brita 0 e areia com a brita 1 chegou na faixa de 43%. Nos traços C e D esta relação estava em 27% e 37%, o que indica que a adição de areia é benéfica para as propriedades mecânicas, sem afetar, até determinado teor, na ordem de 35%, a permeabilidade.
2) Todos os traços de concreto, com ou sem fibra apresentaram coeficientes de permeabilidade dentro do recomendado, variando de 0,124 cm/s a 0,078 cm/s, considerado na faixa do aceitável conforme a ACI 522R-06[4] e a NCPTC [10]. Se for considerada a permeabilidade exigida pela NBR 16416 (ABNT [5]), somente os traços A e E não atingiram o valor mínimo.
3) Para a resistência à compressão, os valores dos traços sem fibra mantiveram-se acima do valor mínimo indicado pela ACI 522R-06[4]. Deve-se destacar que este requisito não é parâmetro considerado pela NBR 16.416 (ABNT [5]).
4) A relação entre a resistência à tração na compressão diametral e a resistência à tração na flexão ficou entre 50 e 77%, próximos ao padrão estudado por Batezini [14] para concreto sem fibras, sendo que, portanto, a tendência se manteve nos concretos com fibras.
5) Para os traços com adição de fibras, apesar da diminuição da resistência à compressão, o ganho na resistência à tração torna atrativo o uso de fibras, já que o critério de atendimento de concreto drenante moldado no local da NBR 16416 (ABNT [5], é a resistência à tração na flexão e neste critério todos os traços apresentam resistência mecânica adequada. Este aumento da resistência à tração na flexão já havia sido observado por Hesami et al. [23]. Rehder et al. [27] também citaram a contribuição da fibra na capacidade de flexão, pois a mesma, quando fibra longa (macrofibra), com comprimento igual ou maior que duas vezes o tamanho máximo do agregado, tem a capacidade de “costurar” a estrutura, após o início da fissuração na flexão.
6) Os valores encontrados de resistência mecânica e de coeficiente de permeabilidade para os traços C, D e E nos concreto sem fibras, e nos traços com fibra, já sugerem a possibilidade de utilização em pavimentos para áreas de estacionamento e circulação de veículos leves, bastando a definição de dimensionamento de uma espessura adequada, conforme sugere a ABNT [5]. Porém, para que no dimensionamento as espessuras possam diminuir e tornar mais atrativo do ponto de vista econômico (Batezini [14]), estudos da melhoria da resistência mecânica, mesmo que com uma perda da permeabilidade, deve ser considerado. Neste sentido sugere-se a continuidade da pesquisa, considerando o estudo das variações das propriedades mecânicas em função da variação da energia de compactação.
7) A adição de fibras em concretos drenantes, que já tem a característica da dificuldade de amassamento e homogenização em função do alto indice de vazios, é um ponto que merece atenção para evitar empolamento das fibras, o que pode reduzir as resistências mecânicas.
8) Os baixos valores da consistência indicam que o ideal é usar compactação mecânica para que as propriedades mecânicas

sejam melhoradas (Bonicelli et al. [18]), sugerindo-se o uso de placa vibratória ou rolo compactador.

6. Referências

[1] ABCP – Associação Brasileira de Cimento Portland. Projeto Técnico: Pavimento permeável. São Paulo, 2013.

[2] MARCHIONI, M.; SILVA, C. O.;VAQUERO Y MAYOR, A.. Conceitos e requisites para pavimentos de concreto permeável. Associação Brasileira de Cimento Portland, São Paulo, 2011

[3] MERIGHI, João Virgilio; FORTES, Rita Moura; BANDEIRA, Alex. Estudo de propriedades do concreto poroso aplicado a pavimentação. In: IBRACON, 2006, Rio de Janeiro - RJ. Anais do 48° Congresso Brasileiro do Concreto. São Paulo - SP, 2006.

[4] ACI 522R-06 – American Concrete Institute. Pervious Concrete. Michigan, 2006

[5] ABNT – Associação Brasileira de Normas Técnicas. NBR 16.416: Pavimentos permeáveis de concreto- Requisitos e procedimentos. Rio de Janeiro, 2015

[6] RODRIGUES, Públio Penna Firme; MONTARDO, Julio P.. A Influência da Adição de Fibras de Polipropileno nas Propriedades dos Concretos para Pisos e Pavimentos. In: IBRACON, 2002, Belo Horizonte - MG. Instituto Brasileiro do Concreto - 44° Congresso Brasileiro. Belo Horizonte – MG, 2002.

[7] MCCAIN, George N.; DEWOOLKAR, Mandar M. Porous Concrete Pavements: Mechanical and Hidraulic Properties. School of Engineering the University of Vermont. Burlington, USA, 2010.

[8] SHU, X.; HUANG, B.; WU, H,; DONG, Q.; BURDETTE, E.. Performance comparison of laboratory and field produced pervious concrete mixtures. Construction and Building Materials, v. 25, p.3187-3192, 2011.

[9] LYAN, C.; ZHUGE, Y.. Optimum mix design of enhanced permeable concrete – An experimental investigation. Construction and Building Materials, v. 24, p.2664-2671, 2010.

[10] NCPTC - NATIONAL CONCRETE PAVEMENT TECHNOLOGY CENTER. Mix Design Development for Pervious Concrete in Cold Weather Climates. Iowa Department of Transportation. Iowa Concrete Paving Association. 25. fev. 2006.

[11] ENVIROMENTAL PROTECTION AGENCY. Storm Water Technology Fact Sheet, Porous Pavement. EPA 832-F-99-023 Office of Water, Washington, D.C. 1999

[12] TEIXEIRA, B. C. S.; FORTES, R. M. Estudo da Dosagem de Concreto Poroso Aplicado a Pavimentação (Study of Pervious Concrete Dosage For Use In Pavements). In: CONINFRA – Anais do Congresso De Infraestrutura De Transportes, São Paulo. 2009: 12 p.

[13] IBRAHIM, A.; MAHMOUD, E; YAMIN, M; PATIBANDLA, V. C. Experimental study on Portland cement pervious concrete mechanical and hydrological properties. Construction and Building Materials, v. 50, p.524-529, 2014.

[14] BATEZINI, R.. Estudo preliminar de concreto permeáveis como revestimento de pavimento para áreas de veículos leves. 2013. 133 p. Dissertação (Mestrado) - Mestrado de Engenharia Civil, Escola Politécnica da Universidade de São Paulo, São Paulo, 2013.

[15] KAJIO, S.; TANAKA, S.; TOMITA, R.; NODA, E.; HASHIMOTO, S. Properties of Porous Concrete with High Strenght. Proceedings 8th International Symposium on Concrete Roads, Lisboa, p. 171-177, 1988.

[16] TENNIS, P. D.; LEMMING, M. L.; AKERS, D. J. Pervious Concrete Pavements, Skokie, Illinois: Portland Cement Association, 2004

[17] COSIC, K.; KORAT, L; DUCMAN, V.; NETINGER, I.. Influence of aggregate type and size on properties of pervious concrete. Construction and Building Materials, v. 78, p.69-76, 2015.

[18] BONICELLI, A.; GIUSTOZZI, F; CRISPINO, M.. Experimental study on the effects of fine sand addition on differentially compacted pervious concrete. Construction and Building Materials, v. 91, p.102-110, 2015.

[19] MAGUESVARI, M Uma; NARASIMHA, V.L.. Studies on Characterization of Pervious Concrete for Pavement Applications. Procedia - Social and Behavioral Sciences, ed.104, p. 198-207, 2013.

[20] SENISSE, Juliana; DAL MOLIN, D. C. C. A influência de microfibras de polipropileno e de aditivo superplastificante nas propriedades de concretos com níveis de resistência semelhantes. In: IBRACON, 2011, Florianópolis - SC. Anais do 53° Congresso Brasileiro do Concreto. Porto Alegre - RS, 2011.

[21] PERRONE, Vitor Cury et al. Estudo do comportamento à flexão de compósitos cimentícios reforçados com fibras de polipropileno de alta tenacidade. In: IBRACON, 2011, Florianópolis – SC. Anais do 53° Congresso Brasileiro do Concreto. Porto Alegre - RS, 2011.

[22] GESOGLU, M.; GÜNEYISI, E; KHOSHNAW, G.; IPEK, S.. Investigating properties of pervious concretes containing waste tire rubbers. Construction and Building Materials, v. 63, p.206-213, 2014.

[23] HESAMI, Saeid.; AHMADI, Saeed; NEMATZADEH, Mahdi. Effects of rice husk ash and fiber on mechanical properties of pervious concrete pavement. Construction and Building Materials, ed. 53, p. 680-691, 2014.

[24] AMARAL JUNIOR, Josué Coelho. Avaliação da influência da adição de fibras poliméricas nas propriedades térmicas e mecânicas do concreto. Dissertação (Mestrado) – Programa de Pós Graduação em Engenharia de Materiais, Centro Federal de Educação Tecnlógica de Minas Gerais, Belo Horizonte, 2016.

[25] LUCENA, Júlio César Tavares. Concreto reforçado com fibras de polipropileno: estudo de caso para aplicação em painel alveolar de parede fina. Dissertação (Mestrado) - Programa de Pós Graduação em Engenharia Civil. Escola de Engenharia de São Carlos, São Carlos, 2017.

[26] GUIMARÃES, Diego; SILVA FILHO, Luiz C. P. da; PACHECO, Alexandre R. Pisos industriais em concreto armado: determinação de teores ótimos de fibras de aço e polipropileno em ensaios mecânicos. In: IBRACON, 2011, Florianópolis - SC. Anais do 53° Congresso Brasileiro do Concreto. Porto Alegre - RS, 2011.

[27] REHDER, Benjamin.; BANH, Kingsten; NEITHALATH, Narayanan. Fracture behavior of pervious concretes: The effects of pore structure and fibers. Engineering Fracture Mechanics, ed. 118, p. 1-16, 2014.

[28] POLASTRE, B.; SANTOS, L. D. Concreto Permeável. Faculdade de Arquitetura e Urbanismo-USP. São Paulo: 2° Semestre de 2006. Disponível em: <http://www.usp.br> Acesso em: 04 de maio de 2013.
[29] SALES, T. L. Pavimento Permeável com Superfície em Blocos de Concreto de Alta Porosidade. 2008. 188 p. Dissertação (Mestrado) - Mestrado de Engenharia Civil, Departamento de Programa de Pós-graduação em Engenharia, Universidade Federal de Santa Catarina, Florianópolis, 2008.
[30] REYES, Fredy; TORRES, Andrés. Efecto de las fibras plasticas en la flexion de estructuras de pavimentos drenantes. Ingeniería de Construcción, Chile, v. 17, n. 2, p.93-102, 2002.
[31] NEITHALATH, Narayanan.; SUMANASOORIYA, Milani S; DEO, Omkar. Characterizing pore volume, sizes, and connectivity in pervious concretes for permeability prediction. Materials Characterization, ed. 61, p. 802-813, 2010.

Volume 12, Number 1 (February 2019) p. 122 – 138 • ISSN 1983-4195
http://dx.doi.org/10.1590/S1983-41952019000100010

REVISTA IBRACON DE ESTRUTURAS E MATERIAIS
IBRACON STRUCTURES AND MATERIALS JOURNAL

A numerical analysis of a concrete slab breaching using high explosives

Perfuração de placa de concreto por alto explosivo: uma análise numérica

M. L. COSTA NETO [a]
eng_murilolimeira@hotmail.com
https://orcid.org/0000-0001-8146-4883

G. N. DOZ [a]
graciela@unb.br
https://orcid.org/0000-0001-6428-4012

Abstract

Explosive breaching of walls, demolition of buildings with high structural robustness and non-programmed explosions may be extremely dangerous, the high risk of these events demands continuous researches to support the development of optimized constructive techniques and design. In this context, this work presents a numerical study of the explosive breaching of concrete wall using an optimized contact explosive charge with cilindrical shape, the CFD software Autodyn ® Ansys was used. The results were evaluated in terms of damage pattern of the concrete slab, where was considered the cratering dimensions, the breakthrough hole and concrete spalling. A significant gain of the destructive potential of the explosive was observed by the simple rearrangement of its dimensions when compared to the base model, also the robustness of software to model and simulate a complex experiment that involves the detonation of a contact explosive charge was verified.

Keywords: explosion, concrete, computational fluid dynamics.

Resumo

Invasão de perímetros com explosivos, demolições de estruturas robustas e incidentes envolvendo explosões não-programadas podem ser extremamente perigosos. A gravidade destes eventos demanda estudos que possam levar a um conhecimento mais profundo do fenômeno explosão e de sua interação com elementos estruturais. Este trabalho apresenta uma análise numérica da otimização geométrica de um explosivo cilíndrico a base de TNT na perfuração de uma placa de concreto, utilizando o software Autodyn ® Ansys. Os resultados foram avaliados em termos do padrão de dano produzido na placa, sendo estudadas a profundidade e as dimensões da região da cratera e de lascamento. Quanto à proposta de otimização, observou-se um ganho importante no potencial destrutivo do explosivo pelo simples rearranjo de suas dimensões, também se constatou a aplicabilidade do software em se replicar numericamente um experimento envolvendo explosões por contato.

Palavras-chave: explosão, concreto, fluidodinâmica computacional.

[a] *Universidade de Brasília, Departamento de Engenharia Civil e Ambiental, Brasília, DF, Brasil.*

Received: 10 Mar 2018 • Accepted: 17 May 2018 • Available Online: 05 Feb 2019

1. Introduction

The detonation of contact charges is commonly used to breach concrete elements, demolition of old structures and military operations in urban terrain. Due the risks involved and high applicability of this phenomena it became target of new researches, such as those developed by [1], [2], [3], [4], [5], [6], [7] and [8].
In these researches was observed a search for more knowledge of the close blast effects. This kind of event is more dangerous to structural elements than regular far-field explosions.
Considering close explosions, the applicability of breaching technique show itself as a powerful tool when the detonation has proximity to key structural elements or other urban structures that significantly restricts the use of large demolition charges. The suitable positioning of the explosive along the element to be breached and the determination of its mass are important factors considering an optimized application of the detonation energy and the safeness of nearby structural elements.
It is important to mention the contributions of Akers et al. [2] who developed numerical procedures and experiments to evaluate the damage to a reinforced concrete wall by the detonation of a C4 explosive device positioned on its surface. Remennikov et al. [9] analyzed the theoretical aspects of the contact explosions, presenting a formulation to predict the damage of this kind of event. Yue et al. [10] developed an analytical analysis to evaluate the damage on a concrete slab, considering a spherical-shaped explosive of TNT.
Considering the risks and costs involved in experimental approaches to study this kind of phenomenon, the numerical simulations emerge as efficient and safe alternative. The use of computational fluid dynamics technology for modeling explosions, impacts and damage assessment is relatively recent, some works as presented by [8], [11], [12], [13] and [14], for example, show the applicability of this numerical tool.
In this context, this work presents a numerical study involving the detonation of cylindrical explosives on a simple concrete slab, aiming the evaluation of the explosion energy optimization for breaching proposal.
The optimization of explosive geometry proposed in this work was developed based on the prediction formulations proposed by Remennikov et al. [9]. From these, a formulation is adjusted in order to relate the diameter of the explosive and its thickness, considering these values to analyze the thickness of the slab to be breached.
Therefore, it is possible to relate the dimensions of the explosive charge with the thickness of the concrete slab, abling a way to aim the most optimized relation.
To verify the optimization proposal, the experiments developed by Beppu et al. [15] was used. These experiments consist in a detonation of C4 cylindrical charge on a concrete slab. It is important to note that Remennikov et al. [9] also used this same experimental work to verify the applicability of its proposition.
Therefore, in addition to the original work proposal, it is possible to compare the numerical results obtained with the experimental results from Beppu et al. [15] and the analytical results of Remennikov et al. [9]. This allows an important analysis of the numerical tool's versatility in performing a simulation of a high complexity real event.

2. Basic concepts of contact explosions

The mass of explosive charge and the standoff distance are useful parameters in a blast damage prediction analysis. The detonation of charges in medium and large distances of the target produces shock waves that tends to engulfs the entire building and results in a more uniform loading. But, contact or close-range explosions provides a more concentrated energy distribution that results in a local damage.
The high level of stress transmitted to a structural element due a contact detonation produces a localized crushing and shattering effect on the material know as brisance [16].
When a shock wave produced by an explosive interact with a solid material, part of the blast wave energy is reflected due the difference of the material mechanical impedance, another part of this energy propagates through the material as a stress wave. This wave propagates through the structural element until it reach the back face and be reflected again. In the reinforced concrete elements, this second

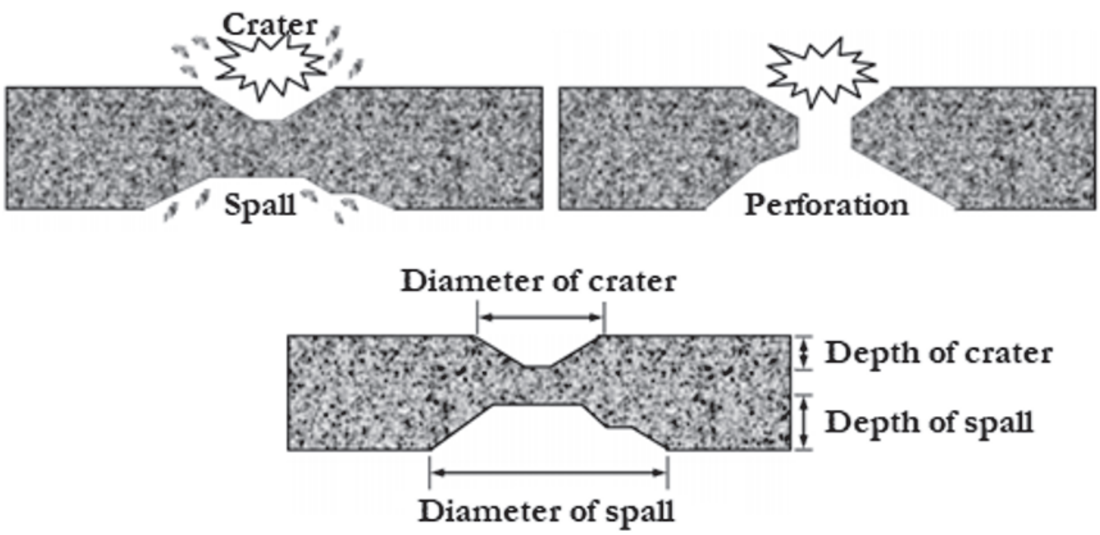

Figure 1
Damage pattern and important dimensions of a contact explosion, Beppu et al. [15]

reflection leads to a tension rebound from the back face that results in concrete spalling. The damaged concrete fails due tension stress and its particles are ejected from the back surface [17], as show in the Figure 1.

3. Experimental model

The numerical models were based on the experiment developed by Beppu et al. [15] where the test specimens were a 500 mm side and 80 mm thick square concrete slab, subjected to the detonation of 46 g of C4 positioned in the center of the plate.
The concrete used has a compressive strength of 28.9 MPa.
The authors reported that the explosive used in the experiments has a cylindrical shape, the diameter of which is approximately equal to the thickness.
However, the exact specific mass of the explosive used in the experiment was not given, so, for the calculation of C4 cylinder dimensions, a specific mass of approximately 1.6 g / cm³ [18] was considered, a value similar to that presented by Dobratz [19] and commonly shown in catalogs of demolition explosives.
In this work, the aspects of cratering damage (region in contact with the explosive) and spalling (posterior wall region) were evaluated.

4. Theoretical analysis

Considering that process of explosive charge detonation is instantaneous and it results in an impulsive loading, Remennikov et al. [9] proposed the formulation presented in Eq. 1.

$$C = \frac{K_0 n^2 h^3}{\mu} \quad (1)$$

where C is the mass of explosive in kg of TNT, h is the thickness of the slab or wall, μ is a shape factor related to the geometry of the explosive (cylindrical or prismatic), n is the spalling coefficient defined by Eq. 2 and K_0 relates the properties of the explosive and the target. K_0 can be defined as the specific mass of explosive necessary to destruction of 1 m³ of material.

$$n = \frac{X}{h} + tan\alpha \quad (2)$$

According to Remennikov et al. [9], in Eq. 2 that is suitable to cylindrical explosives, it is possible to consider α equal to 45° and X, which is the minimum radius of the pulse application area, as shown in the following Eq. 3.

$$\begin{cases} X = \dfrac{b-H}{2}, & when\ \dfrac{b}{H} \geq 2 \\ X = \dfrac{b}{4}, & when\ \dfrac{b}{H} \leq 2 \end{cases} \quad (3)$$

Where b and H are the diameter and thickness of the explosive, respectively.
Rearranging the terms of the formulae proposed by Remennikov et al. [9], it is possible to define a third degree polynomial as a function of h, as shown in Eq. 4. It is important to note that this expression is applicable only to cylindrical explosives.

$$h^3 + (b-H).h^2 + \left(\frac{b-H}{2}\right)^2.h - \frac{C}{K_0}\left(1 - 2\frac{H}{b} + \frac{4}{3}\frac{H^2}{b^2}\right) = 0 \quad (4)$$

In the previous equation, by fixing the mass of explosive C and changing the relations of b and H it is possible to find different values for h. This enabled a way to maximize the value of h (thickness of the wall to be breached) by optimizing the relation between the explosive dimensions.
Figure 2 shows a graphical representation of Eq. 4 for different geometrical relations, the horizontal axis is in logarithmic scale. In order to plot the results, firstly an explosive charge with 0,0575 kg was considered and K_0 was varied between 13 and 40 (plane and reinforced concrete), then the mass of the explosive was varied to 1 kg (mass value much higher than previously considered) with a K_0 value of 13.
The last graph showed a specific region in which the ratio between the diameter and the thickness of the explosive is optimized for breaching thicker concrete slabs, for a same mass of explosive. Thus, the diameter (b) and the thickness (H) ratio values (b/H) situated between 9 and 12 showed an optimal behavior for breaching. According to the previous graph, the terminology *optimized region for breaching* will be used in this work to refer to the explosive diameter and thickness ratio that presents a better performance for breaching concrete slabs.
Demolition manuals [20] suggest the use of explosive charges in which the cross-sectional dimensions of this are greater than the thickness, this indicates that the assumption made from the graph has a reliable applicability. The efficiency of a rearrangement of the explosive charge geometry for a better energetic use of the explosion for breaching slabs will be evaluated numerically in this work.

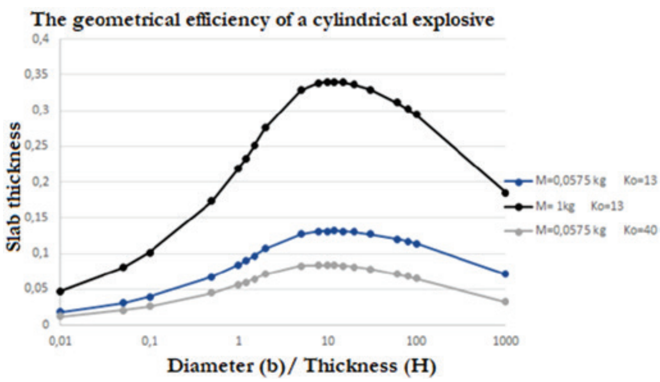

Figure 2
Geometric efficiency of cylindrical explosives based on the Remennikov et al. [9] formulation

5. Numerical modelling

The numerical simulations developed in this work were modeled in Ansys Autodyn software [18]. In this explicit analysis software, it is possible to model and simulate dynamic nonlinear problems involving impacts, penetration and explosions.
The software Autodyn [18] run simulations by the solution of conservation equations. During a simulation, the equations of mass, momentum and energy coupled with materials properties descriptions are solved simultaneously in each timestep [21]. In this context, for the model discretization an equation of state that relates the density and the internal energy with the pressure and a constitutive relation

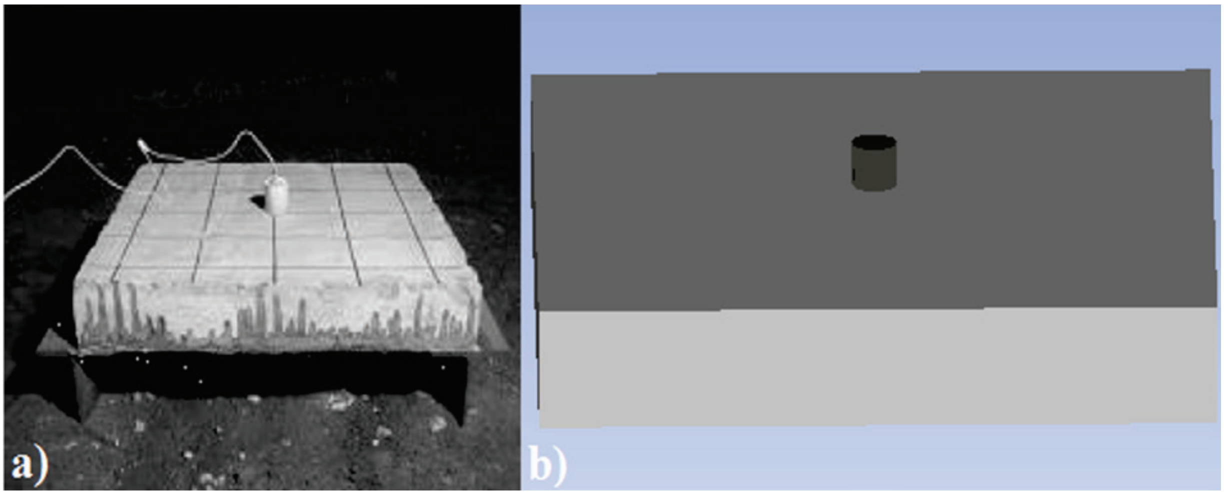

Figure 3
a) Experiment developed by Beppu et al. [15], b) numerical model from Autodyn [18]

that, basically, relates the tension in the material with the distortion of this one, [22] are used.
A set of numerical processors that can be applied to model different regions of the same problem is available [23] in Autodyn.
These processors have some differences between them, so that none of them alone can handle all the complexity of an entire explosion event and its interaction with a structure. Thus, a properly use of these processors are necessary to develop suitable models.
In the models, volume elements were used and two different processors were applied to define the solid and fluid regions. The Lagrangian processor was used in the calculations of solids (concrete) and the Eulerian in the fluids (air and combustion process of the explosive). It was enabled the interaction between these two distinct kinds of discretization, allowing a proper simulation of the interaction between the detonation products and the concrete slab.
The simulations performed in this work were modeled in a computer with a 3 GHz I5-7400 processor and 16 GB of RAM. To process 2 ms of each model with a mesh refinement of 1 mm was necessary approximately 3 weeks of computational work.

5.1 Numerical models

The simulations developed consist in the modeling of a concrete slab subjected to a detonation of a C4 cylindrical charge on its surface. The concrete slab is positioned on steel supports as the basis experiment [15].
Five simulations were performed in this work, the first and second simulations are similar to the experiments developed by Beppu et al. [15]. These were modeled to verify the influence of the mesh refinement in results accuracy, damage pattern and the computational reproducibility of the experiment, using meshes of 5 mm and 1 mm, respectively.
The Figure 3 shows the experimental model next to the developed numerical model. It is important to remember that in these cases it was considered a cylindrical explosive charge with a diameter and thickness of 34 mm and 33 mm, respectively. The thickness of the concrete slab is 80 mm.

In the third simulation, the proposed *optimized region for breaching* was evaluated. The modeling was performed using a 1 mm mesh refinement and a cylindrical explosive C4 charge with a diameter and thickness of 74 mm and 7 mm, respectively. The concrete slab used in this model is the same as the previous simulations and it is identical to the one that was used in the experiment.
In the fourth simulation, a concrete slab identical to that was used in the previous models was modeled. However, the detonated explosive charge has the ratio between the diameter and the thickness completely outside of *optimized region for breaching*, it has diameter and thickness of 15.8 mm and 155 mm, respectively.
In the fifth simulation, a concrete slab similar to the previous models was considered, except for the thickness that is 122 mm (53% thicker than the slab used in previous cases). This slab was subjected to a detonation of the same explosive used in the third model (the optimized explosive).
The thickness of the concrete plate developed in the fifth simulation was estimated from the Remennikov et al. [9] proposal.

5.2 Constitutive modeling

The simulated models demanded a modelling of some materials, such as concrete, C4 and air. Computational fluid dynamics technology requires an equation of state for the definition of materials, in addition to the constitutive models.
The ideal gas state equation of state was used for air, Eq. 5.

$$P = (\gamma - 1)\rho e \quad (5)$$

Table 1
Properties of air

Air	
γ	1.40
Specific mass	0.001225 g/cm³
Temperature	288.2 K
Specific heat	717.599976 J/kgK

Table 2
Properties of C4

C4	
Specific mass	1,601 g/cm³
C_1	6,0977 10^8 kPa
C_2	1,295 10^7 kPa
R_1	4.5
R_2	1.4
ω_{co}	0.25
Detonation velocity	8,193001 10^3 m/s
Energy C-J	9,000001 10^6 kJ/m³
Pressure C-J	2,080000 10^7 kPa

In the previous equation, γ is the adiabatic exponent, ρ is the specific mass of the air and e is the internal energy. The boundary conditions employed to the air allowed the simulation of a continuous medium, so when the shock wave reaches the model boundary it was not reflected. The air properties are shown in Table 1.
The equation of state JWL was used to describe the combustion and expansion process of C4 detonation products, Eq. 6. The properties of C4 are shown in Table 2.

$$P_h = C_1.\left(1-\frac{\omega_{co}}{R_1 V_e}\right)e^{-R_1 V_e} + C_2.\left(1-\frac{\omega_{co}}{R_2 V_e}\right)e^{-R_2 V_e} + \frac{\omega_{co} E_i}{V_e} \quad (6)$$

Where, P_h is the hydrostatic pressure, C_1, C_2, R_1, R_2 and ω_{co} are empirically derived constants related to the type of explosive used, V_e is the ratio between the specific volume of detonation products and the specific volume of undetonated explosive. E_i is the specific internal energy.
The P-alpha equation of state [24] was used for the concrete modeling and the RHT model was used to define strength and failure.
Considering that when a porous material subjected to a certain level of hydrostatic pressure begins to deform plastically, its density changes and, during this process, a certain amount of energy is absorbed, an equation of state that involves this phenomenon is required [25].
Thus, the use of the P-alpha equation of state is useful because it allows a suitable representation of the behavior of porous materials subjected to high stress levels [26]. This equation of state for fully compacted materials for p≥0 and p <0 is presented in the formulations shown in Eq.7 and Eq.8, respectively. Eq.9 presents this equation of state considering a porous material (p ≥ 0):

$$\mathrm{p} = A_1\mu + A_2\mu^2 + A_3\mu^3 + (B_0 + B_1\mu)\rho_0 \mathrm{e} \quad (7)$$

$$\mathrm{p} = T_1\mu + T_2\mu^2 + B_0\rho_0 \mathrm{e} \quad (8)$$

$$\mathrm{p} = A_1\bar{\mu} + A_2\bar{\mu}^2 + A_3\bar{\mu}^3 + (B_0 + B_1\bar{\mu})\rho_0 \mathrm{e} \quad (9)$$

Table 3
Properties of concrete

Concreto	
Specific mass	2.50 g/cm³
Compressive strength	28.9 MPa
Specific heat	654 J/kgK

Table 4
Results of experimental, numerical and analytical analysis

Model	Crater diameter (mm)	Spall diameter (mm)	Crater depth (mm)
Beppu et al. [15]	130-160	210	20-28
1° Simulation (5 mm)	100	180	20
2° Simulation (1 mm)	106	200	20
Remennikov et al. [9]	204	195	21

Where, p is the pressure, ρ_o is the initial density, A_n, B_n and T_n are material constants, e is the internal energy, μ is the relative volume change for the cases of fully compacted and porous material. Table 3 presents the properties used for concrete.
A suitable modeling of solids subjected to high intensity loads such as those coming from a contact explosion need erosion models to handle the large distortions presented by the Lagrangian mesh [27], in this work, the effective instantaneous geometric strain model with strain limit of 0.5 was used.
The supports used in the experiment were applied in the numerical model as boundary conditions that restricted vertical movement.

6. Results and discussion

6.1 First and second simulation

The first two simulations were based on the work developed by Beppu et al. [15]. The numerical reproducibility of the experiment and the performance of the 5 mm and 1 mm mesh refinements are evaluated.
The Table 4 presents the results obtained numerically in comparison with those obtained by Beppu et al. [15] and those estimated through the Remennikov et al. [9].
The numerical results obtained for the crater depth showed a good accuracy with the experimental ones, the same can be observed for the diameters of the cratering region and spalling region as can be seen in Figure 3. In this figure, a damage color scale is used, where 0 (blue color) represents the undamaged material and 1 the complete failure (red color).
The Figure 4 shows the damage pattern presented by the numerical simulation with that presented by the experiment, being possible to observe many similarities.
Considering meshes refinement It is possible to affirm that a greater refinement resulted in a more precise definition of the damage region.
The small differences between the experimental and numerical results may be related to the conditions of the concrete *in situ* or with some specifications of the models, for example, a greater refinement would probably bring more accurate results.
The 2 ms simulated for each model were sufficient to evaluate the presented damage pattern, in this time of simulation no further increases were observed to the damage caused and the kinetic energy of the elements was already very reduced. However, more simulation time would be necessary to define the final dimensions of the produced whole, which can be computationally expensive in explicit analysis software.

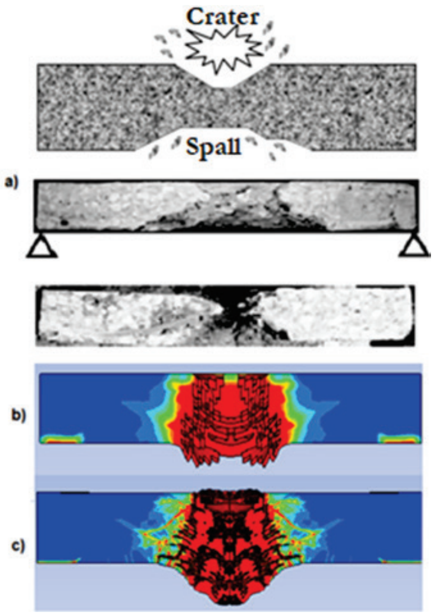

Figure 4
Experimental tests from Beppu et al. [15],
b) 1° Simulation at 2ms (5 mm mesh refinement)
and c) 2° simulation at 2ms (1 mm mesh refinement)

6.2 Third and fourth simulation

In these simulations the performance of the "*optimized region for breaching*" proposal was evaluated, using the base experimental model as parameter. In these simulations the third and fourth models presents an explosive with "optimized" dimensions and an explosive with dimensions outside the optimal relation, respectively. Table 5 presents the results found for these models in comparison to the experimental model considered as comparative parameter.
The results showed the influence of the explosive geometry on the level of damage in the concrete slab, it was verified that the rearrangement of the explosive dimensions was enough to significantly increase its destructive power.
In terms of breaching, the performance of the explosive with optimized geometry was superior than the standard situation, it has proved efficient by harnessing the explosive energy by channeling it for breaching. However, experiments and more simulations are necessary to verify the applicability of the proposal.
The fourth model has proven that only the contact with the mass of explosive is not sufficient for breaching a concrete slab, it is important to have a suitable arrangement between the surfaces of the explosive and the target to achieve the desired effect.
In the Figure 5 it is possible to see a comparison between the damage level of the models in 2 ms simulation here, the same damage color scale of Figure 4 is used. It's important to note that despite the same mass of explosive charge was used in both cases, the optimized geometry showed a much better performance.

Table 5
A comparison between different explosive charge geometries performance

Model	Crater diameter (mm)	Spall diameter (mm)	Crater depth (mm)
Beppu et al. [15]	130-160	210	20-28
2° Simulation (1 mm)	106	200	20
3° Simulation (1 mm)	166	236	35
4° Simulation (1 mm)	50	–	8

6.3 Fifth simulation

In this simulation, the optimized explosive geometry was used (same explosive that was used in the third simulation). However,

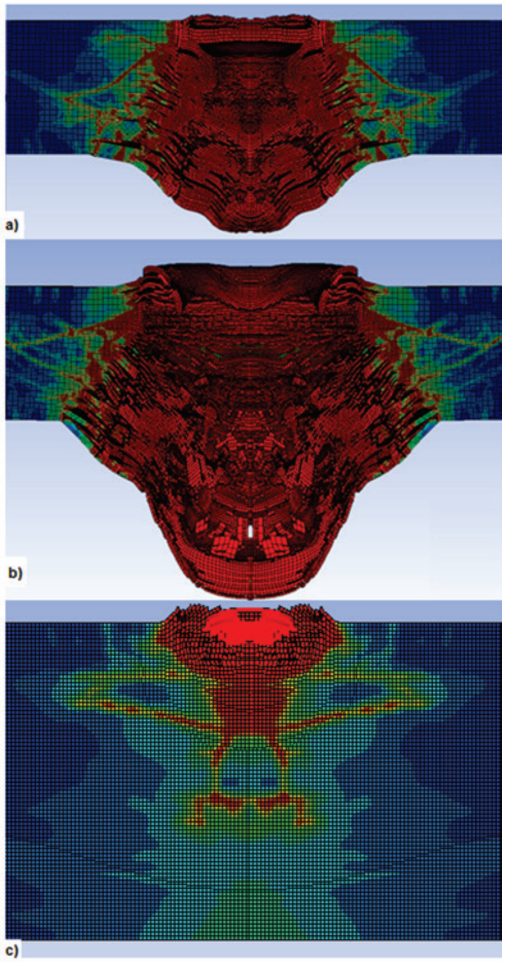

Figure 5
a) 2° simulation: explosive with regular dimensions,
b) 3° simulation: explosive with optimized dimensions and c) 4° simulation: explosive with poor dimensions ratio

Table 6
Results from the fifth simulation

Model	Crater diameter (mm)	Spall diameter (mm)	Crater depth (mm)
5° Simulation (1 mm)	160	300	34

the simulated concrete slab is thicker than previous cases, with a thickness of 122 mm.
Table 6 shows the obtained results.
It was observed that use of an explosive with optimized geometry resulted in an expressive breaching of the slab with thickness of 80 mm and the same explosive was capable of severely damages a thicker concrete slab (122 mm).
It is possible to clearly identify the cratering and spalling regions as shown in Figure 6. In this figure, it is also shown the results of the third simulation that enables a visual comparison between the performance of the same explosive in the perforation of a concrete slab with different thicknesses.
This simulation demonstrated that the explosive mass is not the main parameter to predict with high accuracy the damage in a concrete element. An optimized explosive geometry can be used to breaching or deal critical damage to slabs thicker than that predicted by formulations. However, it is clear that a larger mass of explosive would be required for a more effective breaching of this thicker concrete slab, maybe this points to a destructive potential threshold of the used explosive charge.

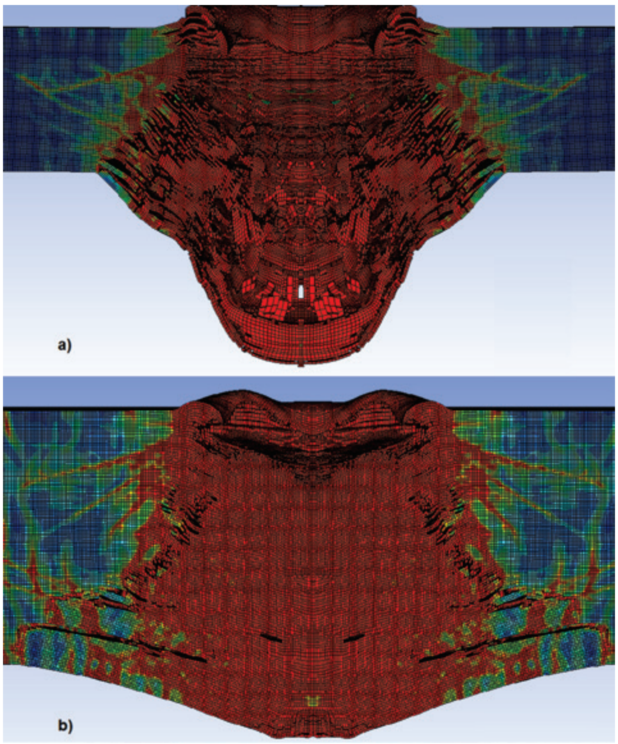

Figure 6
Damage level caused on a concrete slab by the detonation of an explosive with optimized geometry, 3° simulation (a); 5° simulation (b)

7. Conclusion

Numerical simulations were developed in this work in order to study the breaching of concrete slabs by an explosive charge.
The first two simulations developed were based on the work of Beppu et al. [15] and the results numerically obtained are very close to those found experimentally. Comparing the different meshes refinement sizes, it was observed that the finest mesh (1mm) presented the best results, with a more precise definition of the damage region. Due to the good precision presented, despite the high computational cost, this kind of mesh refinement may be indicated for similar computational modelings.
In the third and fourth simulation, the performance of the "*optimized region for breach*ing" proposal was evaluated. In those cases, the explosive mass was the same but the charge geometry was different.
It was verified in the third simulation, in which the explosive geometry was optimized, that the damage produced in the concrete slab was much higher than the simulated standard situation, which was based on the experiment of Beppu et al. [15] where the ratio of diameter to explosive thickness was 1.
This indicates that an explosive with suitable geometry show an optimized use of detonation energy that channeling a large portion of the detonation products to breaching the slab.
In the fourth simulation, in which was used an explosive with inappropriate dimensions (outside the optimized region for breaching), a significant loss of the energy of the explosion towards the medium was observed, in this way, only a little part of the detonation energy reached the concrete slab that resulted in a little crater (no breaching). It is important to point out that the explosive mass of third and fourth simulations were the same.
Therefore, besides the explosive mass, the explosive geometry showed a significant influence on the energy distribution along concrete surface, this points that explosive geometry is a very important parameter to develop damage prediction studies.
In the fifth simulation, the same explosive of the third simulation was applied, however the concrete slab to be perforated was about 53% thicker. It was observed that although the slab was much thicker, the explosive with optimized geometry managed to deal a significant level of damage in the concrete slab being possible to identify clearly the zones of cratering and spalling.
Nevertheless, a long simulation time would be necessary to clearly capture the final hole dimensions. Considering the same hardware used in previous simulations, its possible to estimate a time around two months to process the complete simulation in order to obtain the final hole dimensions for this case.
The results of this work showed that the proper design of the explosive geometry can guarantee a better use of its detonation energy to breaching. Therefore, the design of explosion-resistant concrete slabs and the development of damage prediction formulae need to take account, in addition to the explosive mass, the explosive geometry and its positioning along the surface of the slab.

8. Aknowledgments

The authors gratefully acknowledge the financial support of the CNPq.

9. References

[1] Akers, S. A., Weed, R., Rickman, D. D., Danielson, K. Numerical Simulations of Explosive Wall Breaching, Proceedings of the Users Group Conference, Computer Society, 2005, Denver, USA.

[2] Akers, S. A., Rickman, D. D., Ehrgott, J. Numerical Simulations of Blast Pressures During Wall Breaching, Proceedings of the Users Group Conference, Computer Society, 2006, Denver, USA.

[3] Wu, K. C., Li. B, T, K. C. The effects of explosive mass ratio on residual compressive capacity of contact blast damaged composite columns. Journal of Constructional Steel Research, vol. 67, 2011, pg 602-612.

[4] Li, B., Nair, A., Kai, Q. Residual Axial Capacity of Reinforced Concrete Columns with Simulated Blast Damage. Journal of Performance of Constructed Facilities, ASCE, vol. 26, 2012, 287-299.

[5] Y. Shi, W. Xiong, Z.-X. Li, Q. Xu. Experimental studies on the local damage and fragments of unreinforced masonry walls under close-in explosions. International Journal of Impact Engineering, vol. 90, 2016, 122–131.

[6] F. R. Zhang, C. Q. Wu, H. W. Wang. Y. Zhou. Numerical simulation of concrete filled steel tube columns against BLAST loads. Thin-Walled Structures, vol. 92, 2015, 82–92.

[7] Codina, R. H, Ambrosini, D. Borbón, F. M.. Columnas sometidas a explosiones de campo cercano. XXXVII Jornadas Sudamericanas de Ingenieria Estructural, 2016, Paraguai.

[8] Esteban, B., Gebbeken, N. A comparison of numerical modelling strategies in contact detonation scenarios with concrete targets. Int. J. of Comput. Methods Exp. Meas., vol. 4, nr. 3, 2016, pg 231–246.

[9] Remennikov, A. M., Mentus, I., Uy, B. Explosive breaching of walls with contact charges: theory and applications, Int. J. of Protective Structures, vol. 6, no. 4, 2015, pg 629–647.

[10] Yue, S., Qiu, Y, Zhang, N., Wang, M. Analytical study of local damage on concrete slab subjected to a contact explosion, Journal of Vibroengineering, vol. 19, nr. 2, 2017, pg 908-929.

[11] Quan X, Birnbaum N. Computer simulation of impact and collapse of New York World Trade Center north tower on September 11. In: Proceedings of the 20th international symposium on ballistics, 2002, Orlando.

[12] Kim, H., Ahn, J. and Ahn, H.Computational simulation of progressive collapse of reinforced concrete rigid frame with reinforcement contact model. Advances in Structural Engineering, vol. 19, nr. 6, 2016, pg 982-994.

[13] Li, J., Wu, C., Hao, H. and Su, Y. Experimental and numerical study on steel wire mesh reinforced concrete slab under contact explosion. Materials & Design, vol. 116, 2017, pg 77-91.

[14] Remennikov, A. M., Uy, B. Explosive testing and modelling of square tubular steel columns for near-field detonations, J. Constr. Steel Res., vol. 101, 2014, pg 290–303.

[15] Beppu, M., Ohno, T., Ohkubo, K., Li, B. and Satoh, K. Contact Explosion Resistance of Concrete Plates Externally Strengthened with FRP Laminates. International Journal of Protective Structures, vol. 1, nr. 2, 2010, pg.257-270.

[16] Mays, G. C., Smith, P. D. Blast effects on buildings, Thomas Telford, 1995, Londres.

[17] Millard, S. G., Molyneaux, T. C. K., Barnett,S. J., Gao, X. Dynamic enhancement of blast-resistant ultra high performance fibre-reinforced concrete under flexural and shear loading, Int. J. of Impact Eng., vol. 37, nr. 4, 2010, pg 405–413.

[18] ANSYS Autodyn Interactive Non-Linear Dynamic Analysis software version 15. User's Manual, SAS IP Inc, 2014, USA.

[19] Dobratz, B. M. Properties of Chemical Explosives ans Explosive Simulants, Universidade da Califórnia, UCRL-51319, Laboratório Lawrance Livermore, 1972, EUA .

[20] FM 3-34.214. Explosives and demolitions, Department of the Army, 2007, USA.

[21] Gebbeken, N., Ruppert, M. A new material model for concrete in high-dynamic hydrocode simulations, Arch. Appl. Mech., vol. 70, nr. 7, 2000, pg 463–478.

[22] Anderson Jr., J. D. Computational Fluid Dynamics. McGraw-Hill series, 1995, USA.

[23] Birnbaum, N. K., Clegg, R. A., Fairlie, G. E. Analysis of Blast Loads on Buildings, Century Dynamics Incorporated, ASME Pressure Vessels and Piping Conference, Structures Under Extreme Loading Conditions, 1996, USA.

[24] Herrmann,W. Constitutive equation for the dynamic compaction of ductile porous materials, J. Appl. Phys., vol. 40, nr. 6, 1969, pg 2490–2499.

[25] Hartmann, T., Pietzsch, A., Gebbeken, N. A Hydrocode Material Model for Concrete, International Journal of Protective Structures, vol. 1, nr 4, 2010, pg 443-468.

[26] Luccioni, B. M., Araoz, G. F., Labanda, N. A. Defining Erosion Limit for Concrete, Int. J. of Protective Structures, vol. 4, nr. 3, 2013, p. 315–340.

[27] Luccioni, B. M., Aráoz, G. Erosion Criteria for Frictional Materials Under Blast Load, Mecánica Computacional, vol. 30, 2011, p. 1809–1831.

Volume 12, Number 1 (February 2019) p. 122 – 138 • ISSN 1983-4195
http://dx.doi.org/10.1590/S1983-41952019000100010

REVISTA IBRACON DE ESTRUTURAS E MATERIAIS
IBRACON STRUCTURES AND MATERIALS JOURNAL

A numerical analysis of a concrete slab breaching using high explosives

Perfuração de placa de concreto por alto explosivo: uma análise numérica


M. L. COSTA NETO [a]
eng_murilolimeira@hotmail.com
https://orcid.org/0000-0001-8146-4883

G. N. DOZ [a]
graciela@unb.br
https://orcid.org/0000-0001-6428-4012

Abstract

Explosive breaching of walls, demolition of buildings with high structural robustness and non-programmed explosions may be extremely dangerous, the high risk of these events demands continuous researches to support the development of optimized constructive techniques and design. In this context, this work presents a numerical study of the explosive breaching of concrete wall using an optimized contact explosive charge with cilindrical shape, the CFD software Autodyn ® Ansys was used. The results were evaluated in terms of damage pattern of the concrete slab, where was considered the cratering dimensions, the breakthrough hole and concrete spalling. A significant gain of the destructive potential of the explosive was observed by the simple rearrangement of its dimensions when compared to the base model, also the robustness of software to model and simulate a complex experiment that involves the detonation of a contact explosive charge was verified.

Keywords: explosion, concrete, computational fluid dynamics.

Resumo

Invasão de perímetros com explosivos, demolições de estruturas robustas e incidentes envolvendo explosões não-programadas podem ser extremamente perigosos. A gravidade destes eventos demanda estudos que possam levar a um conhecimento mais profundo do fenômeno explosão e de sua interação com elementos estruturais. Este trabalho apresenta uma análise numérica da otimização geométrica de um explosivo cilíndrico a base de TNT na perfuração de uma placa de concreto, utilizando o software Autodyn ® Ansys. Os resultados foram avaliados em termos do padrão de dano produzido na placa, sendo estudadas a profundidade e as dimensões da região da cratera e de lascamento. Quanto à proposta de otimização, observou-se um ganho importante no potencial destrutivo do explosivo pelo simples rearranjo de suas dimensões, também se constatou a aplicabilidade do software em se replicar numericamente um experimento envolvendo explosões por contato.

Palavras-chave: explosão, concreto, fluidodinâmica computacional.

[a] *Universidade de Brasília, Departamento de Engenharia Civil e Ambiental, Brasília, DF, Brasil.*

Received: 10 Mar 2018 • Accepted: 17 May 2018 • Available Online: 05 Feb 2019

1. Introdução

A detonação de explosivos em contato com elementos de concreto é comumente utilizada para invasão de perímetros por forças especiais ou para demolição de edificações, tendo aplicações tanto civis como militares. O risco envolvido e a necessidade de maiores informações sobre este tipo de evento fizeram com que este tenha se tornado objeto de estudos recentes, como, por exemplo, os desenvolvidos por [1], [2], [3], [4], [5], [6], [7] e [8].
Em todos esses estudos, se observa uma busca por uma maior compreensão dos efeitos de uma explosão próxima ou em contato com o alvo. É importante lembrar que este tipo de explosão constitui o tipo mais agressivo às estruturas.
Neste contexto de explosões próximas, a utilização da técnica de perfuração ("*breaching*") costuma ser aplicada em variadas situações. O posicionamento adequado do explosivo ao longo do elemento a ser perfurado e a determinação de sua massa são fatores importantes quando se busca a aplicação otimizada da energia da detonação e a preservação da integridade dos elementos estruturais próximos a zona a ser perfurada.
Ainda com relação às explosões por contato, é importante citar as contribuições dos trabalhos de Akers et al. [2] que desenvolveram experimentos e procedimentos numéricos visando avaliar o dano causado em paredes de concreto armado pela detonação de dispositivos explosivos à base de C4 posicionados em sua superfície. Remennikov et al. [9] avaliaram os aspectos teóricos das explosões por contato, apresentando uma formulação para predição do dano deste tipo de evento. Yue et al. [10] desenvolveram um estudo analítico para avaliar os aspectos do dano em uma placa de concreto, considerando um explosivo a base de TNT e de formato esférico.
Considerando o risco e o custo envolvidos em abordagens experimentais para o estudo deste tipo de fenômeno, as simulações numéricas surgem como alternativas eficientes e seguras. A utilização da tecnologia da fluidodinâmica computacional para modelagem de explosões, impactos e avaliação de dano é relativamente recente, alguns trabalhos como os apresentados por [8], [11], [12], [13] e [14], por exemplo, demonstram a aplicabilidade deste tipo de recurso.
Nesse contexto, este trabalho apresenta um estudo numérico envolvendo a detonação de explosivos de geometria cilíndrica sobre uma placa de concreto simples, visando a avaliação de uma proposta de otimização energética da explosão para perfuração da placa.
A proposta apresentada foi desenvolvida com base nas formulações de predição de dano propostas por Remennikov et al. [9]. A partir delas, foi ajustada uma expressão para tornar possível relacionar o diâmetro do explosivo e sua espessura, considerando esta relação ao verificar a profundidade da placa a ser perfurada. Desse modo, consegue-se relacionar as dimensões da carga de explosivo com a espessura da placa a ser perfurada, podendo-se obter a relação mais eficiente.
Para verificar esta proposta, utilizaram-se os experimentos desenvolvidos por Beppu et al. [15] que consistem na detonação de uma carga cilíndrica de C4 sobre uma placa de concreto. É importante salientar que Remennikov et al. [9] também utilizou este mesmo trabalho experimental para verificar a aplicabilidade de sua proposição na predição de danos.
Por conta disso, em adição à proposta original do trabalho, é possível realizar uma comparação entre os resultados numéricos obtidos com os experimentais de Beppu et al. [15] e os analíticos de Remennikov et al. [9]. Isto permite uma análise importante da versatilidade da ferramenta numérica em realizar uma simulação de um evento real de elevada complexidade.

2. Fundamentos das explosões por contato

Assim como a massa do explosivo, a distância até o alvo, constitui um parâmetro importante na análise do evento e na predição dos danos a serem causados. Diferente de uma explosão a média ou longa distância, em que as pressões da onda de choque tendem a englobar o alvo por inteiro e carregá-lo mais uniformemente, as

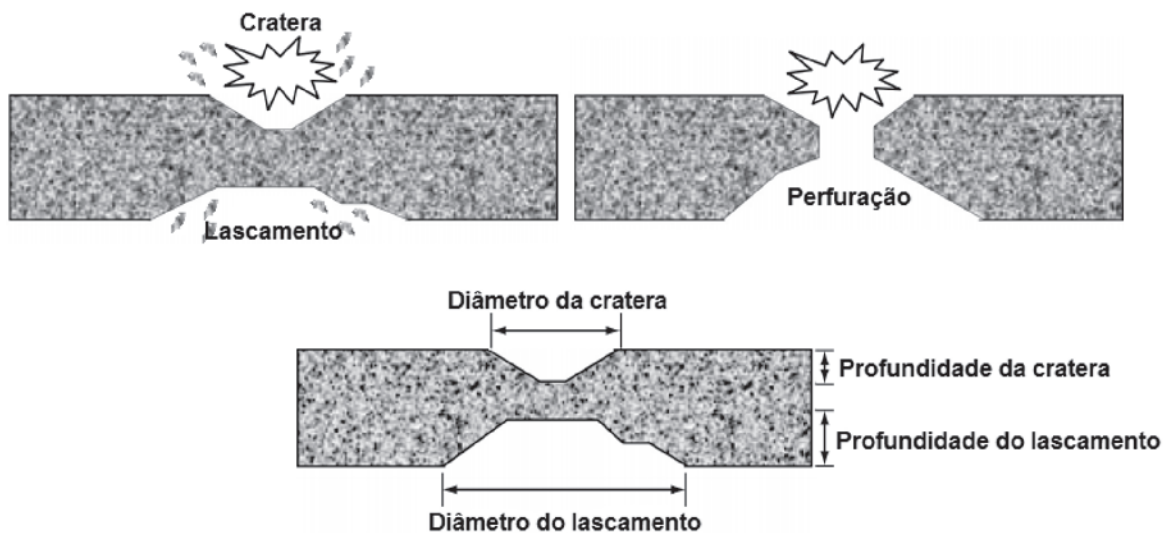

Figura 1
Padrão de dano e dimensões importantes para explosões por contato, Beppu et al. [15]

explosões muito próximas ou em contato são caracterizadas por produzirem dano mais localizado.
O elevado nível de tensão transmitido ao elemento em contato com o explosivo resulta em efeitos localizados de esmagamento e fragmentação. Este conjunto de efeitos relacionados com a capacidade destrutiva do explosivo aplicado pode ser sintetizado pela terminologia potência do explosivo (brisance) [16].
Basicamente, quando uma onda de choque produzida por uma explosão interage com a superfície de uma parede de concreto, por exemplo, parte da energia da onda é refletida devido à diferença entre as impedâncias mecânicas e a outra parte se propaga através do material como uma onda de tensão. A onda de tensão irá se propagar pela parede até atingir a face posterior e ser refletida, esta segunda reflexão resulta em tensões de tração na face posterior, provocando o lascamento do concreto. O concreto danificado irá falhar devido às tensões de tração e seus fragmentos serão projetados da parte de trás da parede [17]. O esquema do padrão de dano esperado por uma explosão por contato em um elemento de concreto pode ser observado na Figura 1.

3. Modelo experimental

Os modelos numéricos foram baseados no experimento desenvolvido por Beppu et al. [15] em que uma placa de concreto simples com 500 mm de lado e 80 mm de espessurafoi submetida à detonação de 46 g de C4 posicionado no centro da placa. O concreto possui resistência a compressão de 28,9 MPa .
O autores informaram que o explosivo utilizado nos experimentos possui um formato cilíndrico, sendo o diâmetro deste aproximadamente igual a espessura.
Entretanto, não foi fornecida a densidade exata do explosivo utilizado no experimento, desta forma, para o cálculo das dimensões do cilindro de C4, foi considerada uma densidade de aproximadamente 1,6 g/cm³ [18], um valor similar ao apresentado por Dobratz [19] e comumente considerado em catálogos de explosivos de demolição.
Neste trabalho, foram avaliados os aspectos de dano por crateramento (região em contato com o explosivo) e lascamento (região posterior da parede).

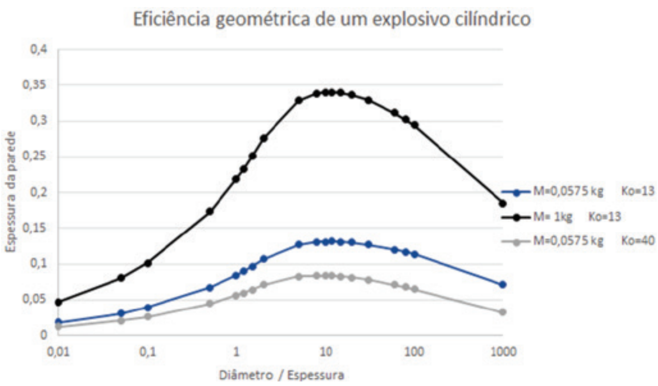

Figura 2
Eficiência geométrica de explosivos cilíndricos com base na proposta de Remennikov et al. [9]

4. Análise teórica

Considerando a hipótese da detonação instantânea e que a detonação de um explosivo em contato com a superfície de um sólido irá produzir um carregamento impulsivo sobre este, Remennikov et al. [9] propuseram a formulação apresentada na Eq. 1.

$$C = \frac{K_0 n^2 h^3}{\mu} \tag{1}$$

onde C é a massa de explosivo em kg de TNT, h é a espessura da placa ou parede, μ é um fator de forma relacionado com a geometria do explosivo (cilíndrico ou prismático), n é o coeficiente de lascamento definido pela Eq. 2 e K_0 relaciona as propriedades do explosivo e do alvo, sendo definido como a massa específica de explosivo necessária para a destruição de 1 m³ de material.

$$n = \frac{X}{h} + tan\alpha \tag{2}$$

De acordo com Remennikov et al. [9], na Eq. 2, aplicável para explosivos cilíndricos, é possível considerar α igual a 45º e X, que é o raio mínimo da área de aplicação de impulso, seguindo a Eq. 3.

$$\begin{cases} X = \dfrac{b-H}{2}, & para\ \dfrac{b}{H} \geq 2 \\ X = \dfrac{b}{4}, & para\ \dfrac{b}{H} \leq 2 \end{cases} \tag{3}$$

Onde b e H correspondem ao diâmetro e a espessura do explosivo, respectivamente.
A partir disso, rearranjando os termos da equação proposta por Remennikov et al. [9], é possível definir um polinômio de terceiro grau em função de h, conforme a Eq. 4. É importante ressaltar que esta expressão é aplicável apenas para explosivos cilíndricos.

$$h^3 + (b-H).h^2 + \left(\frac{b-H}{2}\right)^2.h - \frac{C}{K_0}\left(1 - 2\frac{H}{b} + \frac{4}{3}\frac{H^2}{b^2}\right) = 0 \tag{4}$$

Na equação anterior, fixando a massa de explosivo C e alterando as relações de b e H é possível se encontrar diferentes valores para h, deste modo, buscou-se encontrar uma relação otimizada das dimensões do explosivo de modo que se maximizasse o valor de h (espessura da parede a ser perfurada).
A Figura 2 mostra a representação gráfica da Eq. 4 para diferentes relações geométricas, o eixo horizontal está em escala logarítmica. Para plotagem, primeiro, considerou-se uma massa de explosivo de 0,0575 kg e variou-se o K_0 entre 13 e 40 (concreto simples e concreto reforçado), depois variou-se a massa de explosivo para 1 kg (valor em massa muito superior à considerada anteriormente) com um K_0 com valor de 13.
É possível observar nos gráficos uma região em que a relação entre o diâmetro e a espessura do explosivo é otimizada para perfuração placas de concreto mais espessas, apesar de mantida a mesma massa de explosivo. Desse modo, razões entre o diâmetro (b) e a espessura (H) de valores entre 9 e 12 apresentam-se como otimizadas, quanto ao parâmetro perfuração.
A terminologia *região de geometria otimizada para perfuração* será utilizada neste trabalho para se referir às relações entre diâmetro e espessura de explosivo que apresentam melhor desempenho para perfuração de placas segundo o gráfico anterior.
Manuais de demolição [20] sugerem a utilização de cargas de explosivo em que as dimensões da seção transversal deste sejam superio-

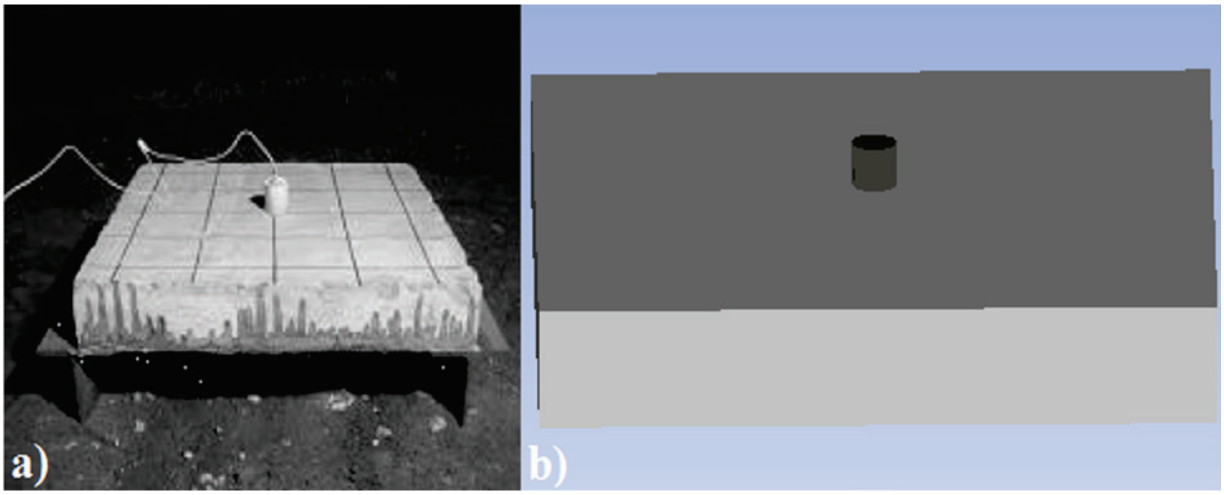

Figura 3
a) experimento desenvolvido por Beppu et al. [15], b) modelo numérico desenvolvido no Autodyn [18]

res à espessura, isto indica que as observações realizadas a partir do gráfico têm aplicabilidade. O quão eficiente é o rearranjo da geometria do explosivo para um melhor aproveitamento energético da explosão na perfuração da parede será avaliado numericamente neste trabalho.

5. Modelagem numérica

As simulações numéricas desenvolvidas neste trabalho foram modeladas no software Ansys Autodyn [18]. Neste software de análise explícita é possível o desenvolvimento de problemas dinâmicos não-lineares envolvendo impactos, penetração e explosão.
Nos hidrocódigos, como o Autodyn [18], a dinâmica do continuo é descrita a partir de um conjunto de equações diferenciais baseadas nos princípios de conservação de massa, movimento e energia que são solucionadas simultaneamente em cada passo de tempo (timestep) [21]. Nesse contexto, na discretização do problema são aplicadas uma equação de estado que relaciona a densidade e a energia interna com a pressão e uma relação constitutiva que, basicamente, relaciona a tensão no material com a distorção deste [22]. No programa, um conjunto de processadores numéricos que podem ser aplicados para modelar diferentes regiões de um mesmo problema está disponível [23].
Esses processadores possuem diferenças entre si, de modo que nenhum deles, isoladamente, pode lidar com toda a complexidade de um evento envolvendo a interação de uma explosão com uma estrutura de forma eficiente. Desse modo, para que a modelagem se dê de forma ideal cabe ao usuário a aplicação adequada desses processadores.
Nos modelos foram utilizados elementos de volume, sendo empregados dois diferentes processadores que contemplaram as zonas de sólido e fluido. O processador lagrangiano foi utilizado nos cálculos dos sólidos (concreto) e o euleriano nos fluidos (ar e processo de combustão do explosivo). Foi habilitada a interação entre estes dois tipos distintos de discretização, permitindo desta forma a simulação adequada da interação entre os produtos de detonação e a placa de concreto.
As simulações realizadas neste trabalho foram modeladas em um computador com processador I5-7400 3 GHz e 16 GB de RAM e o tempo médio para simulação de 2 ms de cada modelo com malha de refinamento 1 mm foi de, aproximadamente, 3 semanas.

5.1 Modelos numéricos

Os modelos desenvolvidos neste trabalho consistem na modelagem de uma placa de concreto simples submetida à detonação de um dispositivo cilíndrico de C4 sobre sua superfície. A placa de concreto é apoiada em suas extremidades conforme o experimento tomado como base [15].
Ao todo foram realizadas cinco simulações, a primeira e segunda simulações similares ao experimento de Beppu et al. [15]. Estas foram modeladas para verificar a influência do refinamento da malha na precisão dos resultados, padrão de dano e na reprodutibilidade computacional do experimento, sendo utilizadas malhas de 5 mm e 1 mm, respectivamente.
A Figura 3 ilustra o modelo experimental ao lado do modelo numérico desenvolvido. É importante lembrar que nesses casos foi considerado um explosivo cilíndrico com 34 mm de diâmetro e 33 mm de espessura, sendo a espessura da placa de concreto de 80 mm. Na terceira simulação foi avaliada a proposta de otimização geométrica da massa de explosivo. A modelagem foi realizada utilizando um refinamento de malha de 1 mm. de modo a situar-se na região ótima para perfuração, o explosivo a base de C4 foi modelado com 74 mm de diâmetro e 7 mm de espessura. Neste modelo, a placa de concreto utilizada é a mesma das simulações anteriores e idêntica à do experimento.

Tabela 1
Propriedades do ar

Ar	
γ	1,40
Densidade de referência	0,001225 g/cm^3
Temperatura de referência	288,2 K
Calor específico	717,599976 J/kgK

Tabela 2
Propriedades do C4

C4	
Densidade de referência	1,601 g/cm³
C_1	6,0977 10^8 kPa
C_2	1,295 10^7 kPa
R_1	4.5
R_2	1.4
ω_{co}	0.25
Velocidade de detonação	8,193001 10^3 m/s
Energia C-J	9,000001 10^6 kJ/m³
Pressão C-J	2,080000 10^7 kPa

Na quarta simulação foi desenvolvida uma placa de concreto idêntica à utilizada nos modelos anteriores, entretanto, o explosivo aplicado possui a relação entre o diâmetro e a espessura completamente fora de região otimizada, tendo 15,8 mm de diâmetro e 155 mm de espessura.

Na quinta e última simulação foi considerada uma placa de concreto similar aos modelos anteriores, exceto pela espessura que é de 122 mm (53% mais espessa que a placa empregada nos casos anteriores), esta placa foi submetida a detonação do mesmo explosivo com geometria otimizada utilizada no terceiro modelo.

A espessura da placa de concreto desenvolvida na quinta simulação foi estimada a partir da proposta de Remennikov et al. [9].

5.2 Modelos constitutivos

Para a elaboração dos modelos foi necessária a utilização de materiais como o concreto, o C4 e o ar. A tecnologia da fluidodinâmica computacional demanda uma equação de estado para definição dos materiais, em adição aos modelos constitutivos.

A equação de estado de gás ideal foi utilizada para o ar, Eq. 5.

$$P = (\gamma - 1)\rho e \tag{5}$$

Na equação anterior, γ é o expoente adiabático, ρ é a massa específica do ar e e é a energia interna. As condições de contorno empregadas no ar permitiam a simulação de um meio contínuo, dessa forma quando a onda de choque atingia a fronteira do modelo ela não era refletida. As propriedades do ar são apresentadas na Tabela 1.

Para descrever o processo de combustão e expansão dos produtos de detonação do C4, foi utilizada a equação de estado JWL, Eq. 6. As propriedades do C4 são apresentadas na Tabela 2.

$$P_h = C_1.\left(1 - \frac{\omega_{co}}{R_1 V_e}\right)e^{-R_1 V_e} + C_2.\left(1 - \frac{\omega_{co}}{R_2 V_e}\right)e^{-R_2 V_e} + \frac{\omega_{co} E_i}{V_e} \tag{6}$$

Tabela 3
Propriedades do concreto

Concreto	
Densidade de referência	2,50 g/cm³
Resistência à compressão	28,9 MPa
Calor específico	654 J/kgK

Tabela 4
Comparação entre os modelos experimental, o numérico e o teórico

Modelo	Diâmetro da cratera (mm)	Diâmetro do lascamento (mm)	Profundidade da cratera (mm)
Beppu et al. [15]	130-160	210	20-28
1° Simulation (5 mm)	100	180	20
2° Simulation (1 mm)	106	200	20
Remennikov et al. [9]	204	195	21

Em que, P_h é a pressão hidrostática, C_1, C_2, R_1, R_2 e ω_{co} são constantes obtidas empiricamente relacionadas com o tipo de explosivo utilizado, V_e é a razão entre o volume específico do produto de detonação e o volume específico do explosivo não detonado e E_i é a energia interna específica.

Para a modelagem do concreto foi utilizada a equação de estado P-alpha [24], sendo adotado o modelo RHT para definição da resistência e falha.

Considerando que quando um material poroso, submetido a um determinado nível de pressão hidrostática começa a se deformar plasticamente, sua densidade se modifica e, durante esse processo, uma certa quantidade de energia é absorvida, é necessária uma equação de estado que englobe este fenômeno [25].

Deste modo o uso da equação de estado P-alpha é interessante, pois permite uma boa representação do comportamento de materiais porosos submetidos a elevados níveis de tensão [26]. Esta equação de estado para materiais totalmente compactados para p≥0 e p<0 é apresentada nas formulações mostradas nas Eq.7 e Eq. 8, respectivamente. A Eq.9 apresenta esta equação de estado considerando um material poroso (p ≥ 0):

$$\mathrm{p} = A_1\mu + A_2\mu^2 + A_3\mu^3 + (B_0 + B_1\mu)\rho_0 \mathrm{e} \tag{7}$$

$$\mathrm{p} = T_1\mu + T_2\mu^2 + B_0\rho_0 \mathrm{e} \tag{8}$$

$$\mathrm{p} = A_1\bar{\mu} + A_2\bar{\mu}^2 + A_3\bar{\mu}^3 + (B_0 + B_1\bar{\mu})\rho_0 \mathrm{e} \tag{9}$$

Em que, p é a pressão, ρ_o é a densidade inicial, A_n, B_n e T_n são coeficientes definidos para o material analisado, e é a energia interna, μ é a alteração relativa de volume para os casos de material totalmente compactado e poroso. A Tabela 3 apresenta as propriedades empregadas para o concreto.

Para uma modelagem adequada de sólidos submetidos a carregamentos de alta intensidade como os advindos de uma explosão por contato, é necessária a utilização de modelos de erosão de modo regular as grandes distorções apresentadas pela malha Lagrangeana [27] (zona discretizada do sólido calculada pelo processador de Lagrange), neste trabalho foi utilizado o modelo de deformação geométrica instantânea efetiva com limite de deformação de 0.5.

Os apoios utilizados no experimento foram aplicados no modelo numérico como condições de contorno que restringiam o movimento vertical das extremidades.

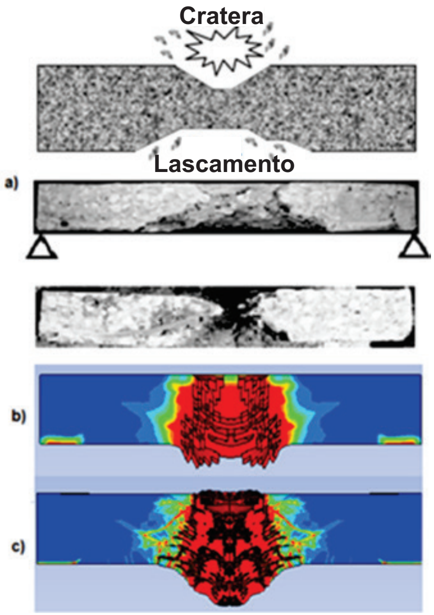

Figura 4
a) Esquema e experimento por Beppu et al. [15], b) 1° simulação em 2 ms (malha de 5 mm) e c) 2° simulação em 2ms (malha de 1 mm)

6. Resultados e discussão

6.1 Primeira e segunda simulação

As duas primeiras simulações realizadas foram baseadas no trabalho desenvolvido por Beppu et al. [15]. Buscou-se avaliar a reprodutibilidade numérica do experimento e o desempenho dos refinamentos de malha de 5 mm e de 1 mm.
A Tabela 4 apresenta os resultados obtidos numericamente em comparação com os obtidos por Beppu et al. [15] e os estimados através da formulação de Remennikov et al. [9].
Os resultados numéricos obtidos para a profundidade da cratera apresentam uma considerável precisão com os experimentais e uma boa representatividade, o mesmo pode ser observado para os diâmetros obtidos da região de crateramento (formada a partir da superfície de contato da placa com o explosivo) e região de lascamento (na parte posterior da placa de concreto), como pode ser visto na Figura 3. Nesta figura, é utilizada uma escala de dano (damage), em que 0 (cor azul) representa o material íntegro e 1 a falha completa (cor vermelha).
Ainda na Figura 4, é possível se comparar o padrão de dano apresentado pela simulação numérica com o apresentado pelo experimento, sendo possível observar muitas similaridades.
Com relação ao desempenho das malhas do modelo numérico é possível afirmar que um maior refinamento resultou numa definição mais precisa da região do dano.
As pequenas diferenças entre os resultados experimentais e os numéricos talvez estejam relacionadas às condições do concreto in loco ou com algumas especificações dos modelos, por exemplo, um refinamento maior, provavelmente, traria resultados mais precisos.
Os 2 ms simulados para cada modelo foram suficientes para determinação das grandezas apresentadas, neste tempo de simulação

Tabela 5
Resultados da proposta de geometria otimizada do explosivo

Modelo	Diâmetro da cratera (mm)	Diâmetro do lascamento (mm)	Profundidade da cratera (mm)
Beppu et al. [15]	130-160	210	20-28
2° Simulação (1 mm)	106	200	20
3° Simulação (1 mm)	166	236	35
4° Simulação (1 mm)	50	-	8

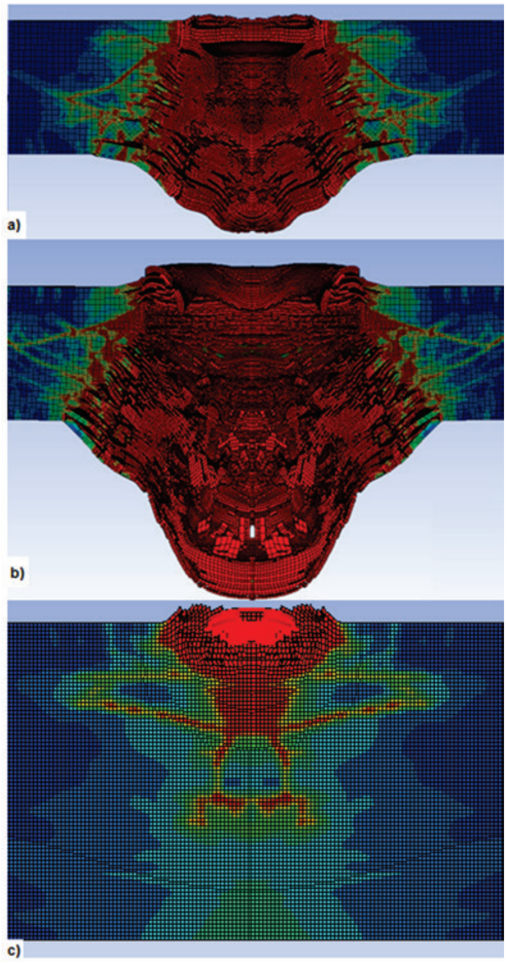

Figura 5
a) 2° Simulação em que foi utilizado um explosivo idêntico ao do experimento b) 3° simulação em que foi empregado um explosivo com geometria otimizada) e c) 4° simulação em que foi utilizado um explosivo com geometria inadequada

Tabela 6
Resultados da proposta de geometria otimizada do explosivo

Modelo	Diâmetro da cratera (mm)	Diâmetro do lascamento (mm)	Profundidade da cratera (mm)
5º Simulação (1 mm)	160	300	34

não se observava mais acréscimos ao dano causado e a energia cinética dos elementos já estava muito reduzida. Entretanto, para definição das dimensões exatas e finais do furo produzido seria necessário mais tempo de simulação, o que pode ser dispendioso em softwares de análise explícita.

6.2 Terceira e quarta simulação

Nestas simulações foi avaliado o desempenho da proposta de otimização geométrica do explosivo tendo como parâmetro para comparação o modelo experimental base. Nessas simulações o terceiro e quarto modelos apresentam um explosivo com geometria "otimizada" e um explosivo com geometria fora da relação ótima, respectivamente.
A Tabela 5 apresenta os resultados encontrados para esses modelos em comparação com o modelo experimental adotado como base.

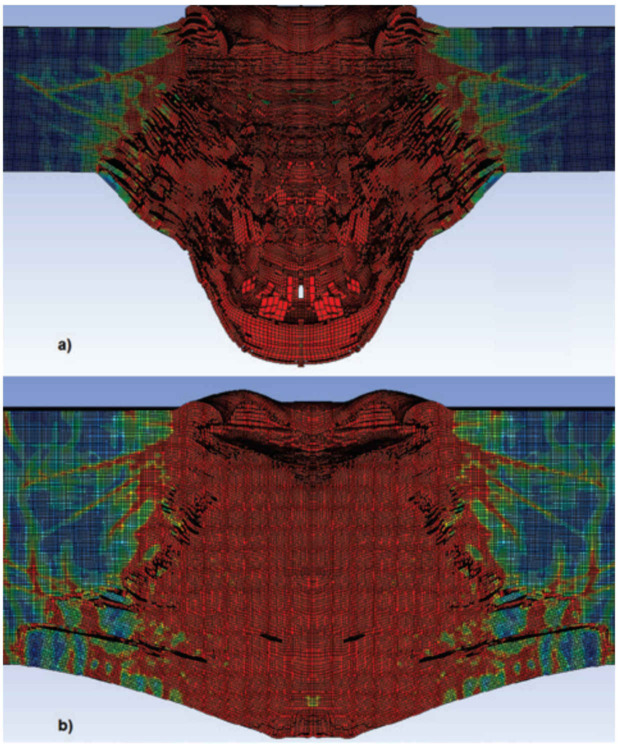

Figura 6
Nível de dano provocado numa placa de concreto pela detonação do explosivo com geometria otimizada, 3° simulação (a); 5° simulação (b)

Os resultados mostraram a influência da geometria do explosivo no nível de dano provocado na placa de concreto, verificou-se que o rearranjo das dimensões do explosivo foi suficiente para incrementar de forma relevante seu poder destrutivo. Em termos de perfuração, o desempenho do explosivo com geometria otimizada foi superior à situação padrão. Entretanto, são necessários experimentos e mais simulações para se constatar a aplicabilidade da proposta, a princípio, ela demonstrou-se eficiente no aproveitamento da energia do explosivo canalizando-a para perfuração da placa.
O quarto modelo comprovou que apenas o contato com a massa de explosivo não é suficiente para perfuração de uma placa, é importante uma disposição adequada entre as superfícies do explosivo e do alvo para que se obtenha o efeito desejado.
Na Figura 5 é possível observar uma comparação entre o nível de dano dos modelos em 2 ms de simulação, nas figuras é utilizada a mesma escala de dano da Figura 4. É importante salientar que a massa de explosivo em todos os modelos é a mesma e, que apesar de todos os explosivos utilizados serem cilíndricos, aplicou-se o conceito de geometria otimizada no explosivo da 3º simulação.

6.3 Quinta simulação

Nesta simulação foi utilizado o explosivo com geometria "otimizada" empregado na terceira simulação, mas a espessura da placa de concreto simulada foi 122 mm (53% mais espessa que nos casos anteriores).
A Tabela 6 apresenta os resultados obtidos.
Foi observado que a utilização de um explosivo com geometria otimizada resultou em uma perfuração expressiva da parede de 80 mm e que o mesmo explosivo foi capaz de danificar severamente uma placa de concreto bem mais espessa (122 mm), nela é possível identificar claramente a região de crateramento e de lascamento como mostra a Figura 6. Nesta figura, é mostrado também os resultados da 3º simulação de modo permitir uma visualização do desempenho do mesmo explosivo na perfuração de placas com diferentes espessuras.
Essa simulação demonstrou que não apenas a massa de explosivo é definitiva na predição do furo em um elemento de concreto, já que uma massa de explosivo inferior a necessária para perfuração conseguiu causar danos críticos na placa apenas por possuir uma geometria adequada para perfuração. Entretanto, fica claro que seria necessária uma maior massa de explosivo para uma perfuração mais efetiva desta placa de concreto mais espessa, o que aponta para o limiar do potencial destrutivo da massa de explosivo utilizada.

7. Conclusões

Neste trabalho foram desenvolvidos modelos numéricos em que se estudou a perfuração de placas de concreto por uma carga de explosivo em sua superfície.
As duas primeiras simulações desenvolvidas foram baseadas no trabalho de Beppu et al. [15] e os resultados apresentados por elas estão bem próximos dos encontrados experimentalmente. Comparando as diferentes malhas, observou-se que a malha com refinamento de 1 mm apresentou os melhores resultados, com uma definição mais precisa da região de dano. Devido a boa precisão apresentada, apesar do elevado custo computacional, este

tipo de refinamento de malha, aparentemente, pode ser indicado para estudos deste tipo.

Na terceira e quarta simulação foi analisada a proposta para otimização da geometria do explosivo, nela foi mantida a massa de C4 das simulações anteriores, mas se alterou as relações entre as dimensões do explosivo.

Verificou-se na terceira simulação, em que a razão entre o diâmetro e a espessura do explosivo estava na região de geometria otimizada para perfuração, que o dano produzido na placa de concreto foi bastante superior a situação padrão simulada, que foi baseada no experimento de Beppu et al. [15], em que a razão entre dimensões diâmetro e a espessura do explosivo eram iguais a 1.

Isto indica que em um explosivo com geometria adequada há um melhor aproveitamento da energia de detonação e uma canalização da energia produzida, sendo esta, direcionada para perfuração da placa.

Na quarta simulação, em que se utilizou um explosivo com dimensões muito fora da região de geometria otimizada, observou-se uma perda significativa da energia da explosão para o meio, desse modo, apenas uma parte da energia da detonação do explosivo atingiu a placa não conseguindo perfurá-la. É importante salientar que a massa de explosivo foi a mesma utilizada nos modelos anteriores e que o explosivo também estava em contato com a superfície da placa, com isso se pode concluir que, além da massa de explosivo, a disposição deste sobre a placa é de fundamental importância para definição da extensão do dano.

Por conta disso, conclui-se que não é possível se fazer uma predição adequada do dano de uma explosão conhecendo-se apenas a massa de explosivo e a distância até o alvo, a geometria do explosivo mostrou ter influência significativa no aproveitamento energético da explosão e, portanto, deve ser considerada ao se realizar estudos de predição de dano, principalmente em curtas distâncias.

Na quinta simulação, foi aplicado o mesmo explosivo da terceira simulação, entretanto a placa de concreto a ser perfurada era cerca de 53% maior. Constatou-se que apesar da placa ser bem mais espessa, o explosivo com geometria otimizada conseguiu causar danos significativos na placa sendo possível identificar as zonas de crateramento e lascamento.

Apesar disso seria necessário um tempo de simulação demasiadamente longo para se captar com clareza a região do furo dada a espessura do sólido. É estimado que, considerando o mesmo hardware utilizado, seria necessário um tempo de simulação em torno de dois meses para se obter a definição completa do furo neste caso. É importante observar que mesmo a carga de explosivo sendo inferior à necessária para a perfuração adequada desta placa espessa, ela foi suficiente para causar danos significativos.

Isto indica que o projeto adequado da geometria do explosivo pode garantir um melhor aproveitamento energético deste, ao passo que o desenvolvimento de placas de concreto resistentes a explosões deve também contemplar, além da massa, a geometria do explosivo e a disposição dele ao longo da superfície da placa.

8. Agradecimentos

Os autores agradecem ao CNPq pelo apoio fornecido à pesquisa realizada.

9. Referências bibliográficas

[1] Akers, S. A., Weed, R., Rickman, D. D., Danielson, K. Numerical Simulations of Explosive Wall Breaching, Proceedings of the Users Group Conference, Computer Society, 2005, Denver, USA.

[2] Akers, S. A., Rickman, D. D., Ehrgott, J. Numerical Simulations of Blast Pressures During Wall Breaching, Proceedings of the Users Group Conference, Computer Society, 2006, Denver, USA.

[3] Wu, K. C., Li. B, T, K. C. The effects of explosive mass ratio on residual compressive capacity of contact blast damaged composite columns. Journal of Constructional Steel Research, vol. 67, 2011, pg 602-612.

[4] Li, B., Nair, A., Kai, Q. Residual Axial Capacity of Reinforced Concrete Columns with Simulated Blast Damage. Journal of Performance of Constructed Facilities, ASCE, vol. 26, 2012, 287-299.

[5] Y. Shi, W. Xiong, Z.-X. Li, Q. Xu. Experimental studies on the local damage and fragments of unreinforced masonry walls under close-in explosions. International Journal of Impact Engineering, vol. 90, 2016, 122–131.

[6] F. R. Zhang, C. Q. Wu, H. W. Wang. Y. Zhou. Numerical simulation of concrete filled steel tube columns against BLAST loads. Thin-Walled Structures, vol. 92, 2015, 82–92.

[7] Codina, R. H, Ambrosini, D. Borbón, F. M.. Columnas sometidas a explosiones de campo cercano. XXXVII Jornadas Sudamericanas de Ingenieria Estructural, 2016, Paraguai.

[8] Esteban, B., Gebbeken, N. A comparison of numerical modelling strategies in contact detonation scenarios with concrete targets. Int. J. of Comput. Methods Exp. Meas., vol. 4, nr. 3, 2016, pg 231–246.

[9] Remennikov, A. M., Mentus, I., Uy, B. Explosive breaching of walls with contact charges: theory and applications, Int. J. of Protective Structures, vol. 6, no. 4, 2015, pg 629–647.

[10] Yue, S., Qiu, Y, Zhang, N., Wang, M. Analytical study of local damage on concrete slab subjected to a contact explosion, Journal of Vibroengineering, vol. 19, nr. 2, 2017, pg 908-929.

[11] Quan X, Birnbaum N. Computer simulation of impact and collapse of New York World Trade Center north tower on September 11. In: Proceedings of the 20th international symposium on ballistics, 2002, Orlando.

[12] Kim, H., Ahn, J. and Ahn, H.Computational simulation of progressive collapse of reinforced concrete rigid frame with reinforcement contact model. Advances in Structural Engineering, vol. 19, nr. 6, 2016, pg 982-994.

[13] Li, J., Wu, C., Hao, H. and Su, Y. Experimental and numerical study on steel wire mesh reinforced concrete slab under contact explosion. Materials & Design, vol. 116, 2017, pg 77-91.

[14] Remennikov, A. M., Uy, B. Explosive testing and modelling of square tubular steel columns for near-field detonations, J. Constr. Steel Res., vol. 101, 2014, pg 290–303.

[15] Beppu, M., Ohno, T., Ohkubo, K., Li, B. and Satoh, K. Contact Explosion Resistance of Concrete Plates Externally Strengthened with FRP Laminates. International Journal of Protective Structures, vol. 1, nr. 2, 2010, pg.257-270.

[16] Mays, G. C., Smith, P. D. Blast effects on buildings, Thomas Telford, 1995, Londres.
[17] Millard, S. G., Molyneaux, T. C. K., Barnett,S. J., Gao, X. Dynamic enhancement of blast-resistant ultra high performance fibre-reinforced concrete under flexural and shear loading, Int. J. of Impact Eng., vol. 37, nr. 4, 2010, pg 405–413.
[18] ANSYS Autodyn Interactive Non-Linear Dynamic Analysis software version 15. User's Manual, SAS IP Inc, 2014, USA.
[19] Dobratz, B. M. Properties of Chemical Explosives ans Explosive Simulants, Universidade da Califórnia, UCRL-51319, Laboratório Lawrance Livermore, 1972, EUA .
[20] FM 3-34.214. Explosives and demolitions, Department of the Army, 2007, USA.
[21] Gebbeken, N., Ruppert, M. A new material model for concrete in high-dynamic hydrocode simulations, Arch. Appl. Mech., vol. 70, nr. 7, 2000, pg 463–478.
[22] Anderson Jr., J. D. Computational Fluid Dynamics. McGraw-Hill series, 1995, USA.
[23] Birnbaum, N. K., Clegg, R. A., Fairlie, G. E. Analysis of Blast Loads on Buildings, Century Dynamics Incorporated, ASME Pressure Vessels and Piping Conference, Structures Under Extreme Loading Conditions, 1996, USA.
[24] Herrmann,W. Constitutive equation for the dynamic compaction of ductile porous materials, J. Appl. Phys., vol. 40, nr. 6, 1969, pg 2490–2499.
[25] Hartmann, T., Pietzsch, A., Gebbeken, N. A Hydrocode Material Model for Concrete, International Journal of Protective Structures, vol. 1, nr 4, 2010, pg 443-468.
[26] Luccioni, B. M., Araoz, G. F., Labanda, N. A. Defining Erosion Limit for Concrete, Int. J. of Protective Structures, vol. 4, nr. 3, 2013, p. 315–340.
[27] Luccioni, B. M., Aráoz, G. Erosion Criteria for Frictional Materials Under Blast Load, Mecánica Computacional, vol. 30, 2011, p. 1809–1831.

Volume 12, Number 1 (February 2019) p. 139 – 178 • ISSN 1983-4195
http://dx.doi.org/10.1590/S1983-41952019000100011

REVISTA IBRACON DE ESTRUTURAS E MATERIAIS
IBRACON STRUCTURES AND MATERIALS JOURNAL

Comparative analysis among standards of the area calculation of transversal reinforcement on reinforced concrete beams of high resistance subjected by shear force

Análise comparativa entre normas do cálculo da área da armadura transversal em vigas de concreto armado de resistência elevada submetidas à ação de força cortante

D. H. L. BRAZ [a]
danielhlbraz@gmail.com
https://orcid.org/0000-0003-2545-6058

R. BARROS [b]
rodrigobarros@ect.ufrn.br
https://orcid.org/0000-0002-7218-2646

J. N. DA SILVA FILHO [a,c]
jneres@ect.ufrn.br
https://orcid.org/0000-0002-9138-1771

Abstract

High strength concretes (HSC) correspond to a characteristic compression strength between 55 e 90 MPa. With the growing use of HSC, studies about the regular design standards of elements made of it, specifically standards about design on shear, become necessary. Hence, the main aspects of the NBR, Model Code 1990 e 2010, Portuguese Standard and German Standard related to the design on shear are presented. From the numerical simulations, with the addition of Cladera and Marí's experimental contributions, it is confirmed that the Brazilian design standard procedure produces lower transverse reinforcement areas in comparison to the ones predicted by the international codes; these, excepted by LoA III, do not consider the concrete contribution, in spite of being experimentally verified, leading to very conservative results.

Keywords: design, shear, high strength.

Resumo

Concretos de alta resistência (CAR) correspondem a uma resistência à compressão característica compreendida entre 55 e 90 MPa. Com a possibilidade crescente da utilização de CAR, faz-se necessária a realização de estudos que abordem os tratamentos normativos usuais acerca do dimensionamento de elementos por ele constituídos, especificamente, à ação de força cortante. Portanto, são apresentadas os principais aspectos da NBR, Model Code 1990 e 2010, Norma portuguesa e alemã acerca dos dimensionamento à cortante. Das simulações numéricas, acrescidas das contribuições experimentais de Cladera e Marí, constata-se que o procedimento de cálculo da NBR produz áreas de estribos inferiores às previstas pelos códigos internacionais; estes, com exceção do LoA III, não adotam a contribuição do concreto, apesar de esta ser verificada experimentalmente, levando a resultados muito conservadores.

Palavras-chave: dimensionamento, cortante, alta resistência.

[a] University of Brasília, Brasília, DF, Brasil;
[b] University of São Paulo, São Carlos, SP, Brasil;
[c] North Carolina State University, NC, USA.

Received: 28 Nov 2016 • Accepted: 27 Mar 2018 • Available Online: 05 Feb 2019

1. Introduction

High strength concretes (HSC) correspond to a characteristic compression strength (f_{ck}) between 55 e 90 MPa, according to ABNT NBR 6118:2014 [5]. Its use has been disseminated due to the demand for structures for which weight reduction is important and/or for when the architecture imposes the use of more slender pieces (Silva [1]). HSC are obtained by improving the compaction of the concrete mixtures, which improves the resistance of the paste and its interface with coarse aggregates (Cladera [2]).

From the analysis of the standard's procedures, the importance of the concrete class for the design of the elements is prominent. Thus, with the increased possibility of using concretes from group II, it is necessary to conduct studies that approach the usual codes' treatments regarding the design of high strength concrete elements, specifically the design on shear. According to Arslan [3], the

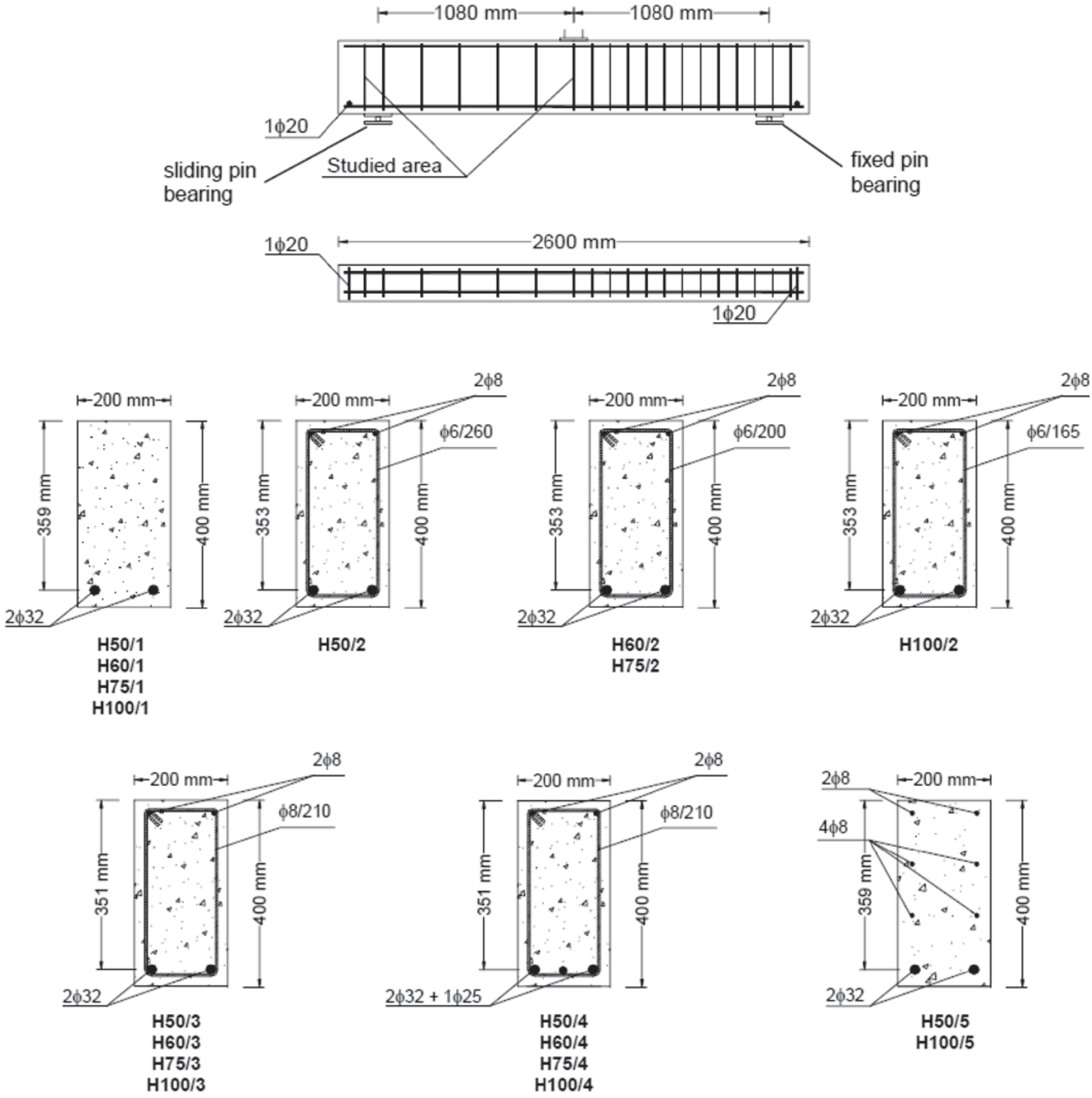

Figure 1
Test set-up and cross-section of the beam specimens. (Cladera [2])

Table 1
ANN for beams with web reinforcement.
Ranges of parameters in the database [4]

Parameter	Minimum	Maximum
d (mm)	198	925
d/b	0.792	4.5
ρ_l (%)	0.50	5.80
ρ_w (MPa)	0.33	3.57
f_c (MPa)	21	125.2
a/d	2.49	5.00
V (kN)	63.28	1172.19

concrete´s contribution is important in the design of beams where the factored shear force is close to the value of the shear force required to produce diagonal tension cracking, and also necessary for the economic design of beams and slabs with little or no shear reinforcement.

Among the experimental studies regarding the high strength concrete beams subjected to shear force, those of Cladera [2] and Cladera & Marí [4] are highlighted. In the first, 18 beams of reinforced concrete beams – which characteristics are illustrated in Figure 1 – with compressive strength between 50 and 87 MPa, were tested at the Structural Technology Laboratory of the Department of Construction Engineering at the School of Civil Engineering of Barcelona. The main objectives of the experimental program were to study the influence of concrete compressive strength in beams with and without shear reinforcement; to propose and verify a more adequate minimum amount of web reinforcement then the proposed by the Spanish code EHE Instrución de Hormigón Estructural of 1998; to evaluate the efficiency of the amount of shear and longitudinal reinforcement as a function of f_{ck}; and to study the influence of the longitudinally-distributed web reinforcement in beams without stirrups.

In the second [4], Eurocode 2, AASHTO LRFD and ACI 318-02 were evaluated with an Artificial Neural Network (ANN) based on 123 test-beams of high strength concrete. From the results of the ANN, the authors analyzed the influences of the amount of transverse web reinforcement, the effect of the beams' size and effective depth, of the concrete compressive strength, of the amount of longitudinal reinforcement and the ratio between shear span and the effective depth on the shear strength. Hence, an alternate design method was proposed. The ANN contemplated the test-beams with the characteristics indicated in Table 1.

1.1 Justification

The expansion of the use of high strength concretes indicates the need for better understanding the structural behavior of the elements made of it. This understanding comprehends the usual design standard's procedures. From the numerical analyses and simulations, comparisons are made to explain how each code approaches the issue, specifically about shear design. In addition, the experimental contributions of Cladera [2] and Cladera and Marí [4] will base the comparative analyses between the standard's predictions of shear reinforcement area and those demanded according to experimental results. The ultimate shear forces, the experimentally predicted and the obtained through normative calculation, are also contemplated in the analysis.

2. Analysed design standards

2.1 ABNT NBR 6118:2014 [5]

The Brazilian code presents two design models for linear elements subjected to shear force. For both, the minimum ratio of web reinforcement is given by:

$$\rho_{sw} = \frac{A_{sw}}{b_w \cdot s \cdot \text{sen}\alpha} \geq 0{,}2\frac{f_{ct,m}}{f_{ywk}} \quad (1)$$

where:
A_{sw} is the shear reinforcement area;
s is the longitudinal space between stirrups, along the longitudinal axis of the structural element;
α is the inclination of the transverse reinforcement related to the longitudinal axis of the structural element; it is contained in the interval 45° ≤ α ≤ 90°;
b_w is the effective web width;
f_{ywk} is the characteristic value of yield strength of the reinforcing steel;
$f_{ct,m}$ = 2,12 ln (1 + 0,11 f_{ck}) for concretes C55 até C90.
The resistance is considered satisfactory when simultaneously observes the following conditions:

$$V_{Sd} \leq V_{Rd2} \quad (2)$$

$$V_{Sd} \leq V_{Rd3} = V_c + V_{sw} \quad (3)$$

where:
V_{Sd} is the design value of applied shear force;
V_{Rd2} is the design shear strength related to the concrete failure by diagonal compression;
V_{Rd3} is the design shear force related to the diagonal tension failure, where V_c is the amount of shear force absorbed by the complementary mechanisms of the truss and V_{sw} the amount of shear force resisted by the transverse reinforcement.

2.1.1 Calculation Model I

This Model, conducted by the following expressions, admits struts' inclination of θ = 45° in relation to the longitudinal axis of the structural element and complementary portion V_c constant and independent from V_{Sd}.
a) Verification of the concrete failure by diagonal compression:

$$V_{Rd2} = 0{,}27 \propto_{v2} f_{cd}\, b_w\, d \quad (4)$$

where:
$\propto_{v2}$ = (1 - f_{ck}/250) and f_{ck} in MPa;
b) Calculation of the transverse reinforcement:

$$V_{Rd3} = V_c + V_{sw} \quad (5)$$

where:
$V_{sw} = (A_{sw} / s)\, 0{,}9 d f_{ywd}\, (\text{sen}\alpha + \cos\alpha)$
$V_c = V_{c0} = 0{,}6\, f_{ctd}\, b_w\, d$
$f_{ctd} = f_{ctk,inf} / \gamma_c = 0{,}7\, f_{ct,m} / \gamma_c$

where:
d is the distance between the compressed edge and the center of gravity of the reinforcement;
f_{ywd} is the stress on the passive transverse reinforcement not superior to 435 MPa.

2.1.2 Calculation Model II

This Model admits θ inclinations between 30º and 45º and the decrease of V_c with the increase of V_{Sd}.

a) Verification of the concrete failure by diagonal compression:

$$V_{Rd2} = 0{,}54 \propto_{v2} f_{cd}\, b_w\, d\, \mathrm{sen}^2\theta\,(\cot g\,\alpha + \cot g\,\theta) \quad (6)$$

b) Calculation of the transverse reinforcement, as shown on Equation 5, where:
$V_{sw} = (A_{sw} / s)\, 0{,}9df_{ywd}\, (\cot g\,\alpha + \cot g\,\theta)\, \mathrm{sen}\alpha$;
$V_{c1} = V_{c0}$ when $V_{Sd} \leq V_{c0}$;
$V_{c1} = 0$ when $V_{Sd} = V_{Rd2}$;
$V_{c1} = \left(\frac{V_{Rd2} - V_{Sd}}{V_{Rd2} - V_{c0}}\right) V_{c0}$ for intermediate values.

Table 2
Results of Model I of ABNT NBR 6118:2014

f_{ck} (MPa)	$f_{ct,m}$ (MPa)	f_{ctd} (MPa)	b_w (cm)	d (cm)	V_{Sd} (kN)	V_{Rd2} (kN)	V_{c0} (kN)	V_{sw} (kN)	A_{sw} (cm²/m)
55	4.14	2.07	12	40	100.00	397.13	59.62	40.38	2.58
55	4.14	2.07	12	40	125.00	397.13	59.62	65.38	4.17
55	4.14	2.07	12	40	150.00	397.13	59.62	90.38	5.77
55	4.14	2.07	12	40	175.00	397.13	59.62	115.38	7.37
60	4.30	2.15	12	40	100.00	422.13	61.92	38.08	2.43
60	4.30	2.15	12	40	125.00	422.13	61.92	63.08	4.03
60	4.30	2.15	12	40	150.00	422.13	61.92	88.08	5.62
60	4.30	2.15	12	40	175.00	422.13	61.92	113.08	7.22
70	4.59	2.29	12	40	100.00	466.56	66.04	33.96	2.20
70	4.59	2.29	12	40	125.00	466.56	66.04	58.96	3.76
70	4.59	2.29	12	40	150.00	466.56	66.04	83.96	5.36
70	4.59	2.29	12	40	175.00	466.56	66.04	108.96	6.96
80	4.84	2.42	12	40	100.00	503.59	69.68	30.32	2.32
80	4.84	2.42	12	40	125.00	503.59	69.68	55.32	3.53
80	4.84	2.42	12	40	150.00	503.59	69.68	80.32	5.13
80	4.84	2.42	12	40	175.00	503.59	69.68	105.32	6.73
90	5.06	2.53	12	40	100.00	533.21	72.92	27.08	2.43
90	5.06	2.53	12	40	125.00	533.21	72.92	52.08	3.33
90	5.06	2.53	12	40	150.00	533.21	72.92	77.08	4.92
90	5.06	2.53	12	40	175.00	533.21	72.92	102.08	6.52

Table 3
Results of Model II of ABNT NBR 6118:2014

f_{ck} (MPa)	$f_{ct,m}$ (MPa)	f_{ctd} (MPa)	θ°	b_w (cm)	d (cm)	V_{Sd} (kN)	V_{Rd2} (kN)	V_{c1} (kN)	V_{sw} (kN)	A_{sw} (cm²/m)
55	4.14	2.07	45	12	40	100.00	397.13	52.49	47.51	3.03
55	4.14	2.07	45	12	40	125.00	397.13	48.07	76.93	4.91
55	4.14	2.07	45	12	40	150.00	397.13	43.66	106.34	6.79
55	4.14	2.07	45	12	40	175.00	397.13	39.24	135.76	8.67
60	4.30	2.15	45	12	40	100.00	422.13	55.37	44.63	2.85
60	4.30	2.15	45	12	40	125.00	422.13	51.07	73.93	4.72
60	4.30	2.15	45	12	40	150.00	422.13	46.77	103.23	6.59
60	4.30	2.15	45	12	40	175.00	422.13	42.48	132.52	8.46
70	4.59	2.29	45	12	40	100.00	466.56	60.44	39.56	2.53
70	4.59	2.29	45	12	40	125.00	466.56	56.32	68.68	4.39
70	4.59	2.29	45	12	40	150.00	466.56	52.20	97.80	6.25
70	4.59	2.29	45	12	40	175.00	466.56	48.08	126.92	8.11
80	4.84	2.42	45	12	40	100.00	503.59	64.81	35.19	2.32
80	4.84	2.42	45	12	40	125.00	503.59	60.79	64.21	4.10
80	4.84	2.42	45	12	40	150.00	503.59	56.78	93.22	5.95
80	4.84	2.42	45	12	40	175.00	503.59	52.76	122.24	7.81
90	5.06	2.53	45	12	40	100.00	533.21	68.63	31.37	2.43
90	5.06	2.53	45	12	40	125.00	533.21	64.67	60.33	3.85
90	5.06	2.53	45	12	40	150.00	533.21	60.71	89.29	5.70
90	5.06	2.53	45	12	40	175.00	533.21	56.75	118.25	7.55

2.2 CEB-FIP Model Code 1990 [6]

The model code of 1990 brings in its section 6.3.3 *Shear and axial action effects* the considerations presented below. This standard establishes the θ inclination of the struts between 18.4º and 45º.

a) Minimum transverse reinforcement ratio:

$$\omega_{sw} = \frac{A_{sw} \cdot f_{yk}}{b_w \cdot s \cdot f_{ctm} \cdot \text{sen}\alpha} \geq 0{,}2 \tag{7}$$

where:

$$f_{ctm} = f_{ctko,m}\left(\frac{f_{ck}}{f_{cko}}\right)^{2/3}$$

f_{cko} = 10 MPa

$f_{ctko,m}$ = 1,40 MPa

b) Maximum shear resistance, with θ = 45°:

$$V_{Rd,max} = \frac{f_{cd2}}{2} b_w z(1 + \text{cotg } \alpha) \tag{8}$$

where:

$$f_{cd2} = 0{,}60\left[1 - \frac{f_{ck}}{250}\right] f_{cd}$$

Table 4
Results of MC 1990

f_{ck} (MPa)	$f_{ct,m}$ (MPa)	f_{cd2} (MPa)	b_w (cm)	d (cm)	θ°	$V_{Rd,max}$ (kN)	V_{Sd} (kN)	F_{Stw} (kN)	A_{sw} (cm²/m)
55	4.36	17.16	12	40	45	370.66	100.00	100.00	6.39
55	4.36	17.16	12	40	45	370.66	125.00	125.00	7.99
55	4.36	17.16	12	40	45	370.66	150.00	150.00	9.58
55	4.36	17.16	12	40	45	370.66	175.00	175.00	11.18
60	4.62	18.24	12	40	45	393.98	100.00	100.00	6.39
60	4.62	18.24	12	40	45	393.98	125.00	125.00	7.99
60	4.62	18.24	12	40	45	393.98	150.00	150.00	9.58
60	4.62	18.24	12	40	45	393.98	175.00	175.00	11.18
70	5.12	20.16	12	40	45	435.46	100.00	100.00	6.39
70	5.12	20.16	12	40	45	435.46	125.00	125.00	7.99
70	5.12	20.16	12	40	45	435.46	150.00	150.00	9.58
70	5.12	20.16	12	40	45	435.46	175.00	175.00	11.18
80	5.60	21.76	12	40	45	470.02	100.00	100.00	6.39
80	5.60	21.76	12	40	45	470.02	125.00	125.00	7.99
80	5.60	21.76	12	40	45	470.02	150.00	150.00	9.58
80	5.60	21.76	12	40	45	470.02	175.00	175.00	11.18
90	6.06	23.04	12	40	45	497.66	100.00	100.00	6.39
90	6.06	23.04	12	40	45	497.66	125.00	125.00	7.99
90	6.06	23.04	12	40	45	497.66	150.00	150.00	9.58
90	6.06	23.04	12	40	45	497.66	175.00	175.00	11.18

Table 5
Results of MC 2010 for LoA I

f_{ck} (MPa)	$f_{ct,m}$ (MPa)	b_w (cm)	d (cm)	θ°	k_ε	k_c	V_{Ed} (kN)	$V_{Rd,max}$ (kN)	$V_{Rd,s}$ (kN)	A_{sw} (cm²/m)
55	4.21	12	40	45	0.55	0.45	100.00	355.91	100.00	6.39
55	4.21	12	40	45			125.00	355.91	125.00	7.99
55	4.21	12	40	45			150.00	355.91	150.00	9.58
55	4.21	12	40	45			175.00	355.91	175.00	11.18
60	4.35	12	40	45	0.55	0.44	100.00	377.17	100.00	6.39
60	4.35	12	40	45			125.00	377.17	125.00	7.99
60	4.35	12	40	45			150.00	377.17	150.00	9.58
60	4.35	12	40	45			175.00	377.17	175.00	11.18
70	4.61	12	40	45	0.55	0.41	100.00	417.99	100.00	6.39
70	4.61	12	40	45			125.00	417.99	125.00	7.99
70	4.61	12	40	45			150.00	417.99	150.00	9.58
70	4.61	12	40	45			175.00	417.99	175.00	11.18
80	4.84	12	40	45	0.55	0.40	100.00	456.90	100.00	6.39
80	4.84	12	40	45			125.00	456.90	125.00	7.99
80	4.84	12	40	45			150.00	456.90	150.00	9.58
80	4.84	12	40	45			175.00	456.90	175.00	11.18
90	5.04	12	40	45	0.55	0.38	100.00	494.23	100.00	6.39
90	5.04	12	40	45			125.00	494.23	125.00	7.99
90	5.04	12	40	45			150.00	494.23	150.00	9.58
90	5.04	12	40	45			175.00	494.23	175.00	11.18

c) Tension of web steel:

$$F_{Stw} = \frac{V_{Sd}}{\text{sen } \propto} \quad (9)$$

$$F_{Rtw} = \left[\frac{A_{sw} \cdot f_{yd}}{s}\right] z(\text{cotg } \theta + \text{cotg } \alpha) \quad (10)$$

where:

F_{Stw} is the applied shear force on the transverse reinforcement;

F_{Rtw} is the resistant shear force of the reinforcement.

2.3 CEB-FIP Model Code 2010 [7]

Ahead, the considerations of the 2010 version of the model code are presented.

a) Minimum shear reinforcement area:

$$A_{sw,min} = 0{,}08 \cdot \sqrt{f_{ck}} \cdot \frac{b_w \cdot s_w}{f_{yk}} \quad (11)$$

b) Design shear resistance:

$$V_{Rd} = V_{Rd,c} + V_{Rd,s} \geq V_{Ed} \quad (12)$$

Table 6
Results of MC 2010 for LoA II

f_{ck} (MPa)	b_w (cm)	d (cm)	k_ε	k_c	V_{Ed} (kN)	$V_{Rd,max}$ (kN)	$V_{Rd,s}$ (kN)	A_{sw} (cm²/m)
55	12	40	0.65	0.53	100.00	420.62	100.00	6.39
55	12	40			125.00	420.62	125.00	7.99
55	12	40			150.00	420.62	150.00	9.58
55	12	40			175.00	420.62	175.00	11.18
60	12	40	0.65	0.52	100.00	445.74	100.00	6.39
60	12	40			125.00	445.74	125.00	7.99
60	12	40			150.00	445.74	150.00	9.58
60	12	40			175.00	445.74	175.00	11.18
70	12	40	0.65	0.49	100.00	493.99	100.00	6.39
70	12	40			125.00	493.99	125.00	7.99
70	12	40			150.00	493.99	150.00	9.58
70	12	40			175.00	493.99	175.00	11.18
80	12	40	0.65	0.47	100.00	539.98	100.00	6.39
80	12	40			125.00	539.98	125.00	7.99
80	12	40			150.00	539.98	150.00	9.58
80	12	40			175.00	539.98	175.00	11.18
90	12	40	0.65	0.38	100.00	584.09	100.00	6.39
90	12	40			125.00	584.09	125.00	7.99
90	12	40			150.00	584.09	150.00	9.58
90	12	40			175.00	584.09	175.00	11.18

Table 7
Results of MC 2010 for LoA III

f_{ck} (MPa)	b_w (cm)	d (cm)	θ_{min}	ε_x	k_ε	k_c	k_v	V_{Ed} (kN)	$V_{Rd,min}$ (kN)	$V_{Rd,c}$ (kN)	$V_{Rd,s}$ (kN)	A_{sw} (cm²/m)
55	12	40	30	0.001	0.65	0.53	0.116	100.00	364.27	24.79	75.21	4.80
55	12	40	30				0.105	125.00	364.27	22.45	102.55	6.55
55	12	40	30				0.094	150.00	364.27	20.10	129.90	8.30
55	12	40	30				0.083	175.00	364.27	17.76	157.24	10.05
60	12	40	30	0.001	0.65	0.52	0.119	100.00	386.02	26.45	73.55	4.70
60	12	40	30				0.108	125.00	386.02	24.14	100.86	6.44
60	12	40	30				0.098	150.00	386.02	21.82	128.18	8.19
60	12	40	30				0.087	175.00	386.02	19.51	155.49	9.93
70	12	40	30	0.001	0.65	0.49	0.123	100.00	427.80	28.25	71.75	4.58
70	12	40	30				0.113	125.00	427.80	26.09	98.91	6.32
70	12	40	30				0.104	150.00	427.80	23.94	126.06	8.05
70	12	40	30				0.095	175.00	427.80	21.78	153.22	9.79
80	12	40	30	0.001	0.65	0.47	0.126	100.00	467.63	28.98	71.02	4.54
80	12	40	30				0.117	125.00	467.63	27.01	97.99	6.26
80	12	40	30				0.109	150.00	467.63	25.04	124.96	7.98
80	12	40	30				0.100	175.00	467.63	23.07	151.93	9.71
90	12	40	45	0.001	0.65	0.45	0.128	100.00	505.83	29.58	70.42	4.50
90	12	40	45				0.120	125.00	505.83	27.75	97.25	6.21
90	12	40	45				0.113	150.00	505.83	25.93	124.07	7.93
90	12	40	45				0.105	175.00	505.83	24.11	150.89	9.64

where:
V_{Rd} is the design shear resistance;
$V_{Rd,c}$ is the design shear resistance attributed to the concrete;
$V_{Rd,s}$ is the design shear resistance provided by shear reinforcement;
V_{Ed} is the design shear force.
c) Maximum shear resistance for stirrups at 90°:

$$V_{Rd,max} = k_c \cdot \frac{f_{ck}}{\gamma_c} \cdot b_w \cdot z \cdot \text{sen}\,\theta \cdot \cos\theta \quad (13)$$

where:
$k_c = k_\varepsilon \cdot \eta_{fc}$ is the strength reduction factor;

$$\eta_{f_c} = \left(\frac{30}{f_{ck}}\right)^{1/3} \leq 1{,}0.$$

d) Design shear resistance provided by stirrups at 90°:

$$V_{Rd,s} = \frac{A_{sw}}{s_w} \cdot f_{ywd} \cdot z \cdot \text{cotg}\,\theta \quad (14)$$

e) Design shear resistance attributed to the concrete:

$$V_{Rd,c} = k_v \cdot \frac{\sqrt{f_{ck}}}{\gamma_c} \cdot b_w \cdot z \quad (15)$$

Table 8
Results of NP EN 1992-1-1, with υ

f_{ck} (MPa)	$f_{ct,m}$ (MPa)	υ	b_w (cm)	d (cm)	V_{Ed} (kN)	$V_{Rd,max}$ (kN)	$V_{Rd,s}$ (kN)	A_{sw} (cm²/m)
55	4.21	0.468	12	40	100.00	370.66	100.00	6.39
55	4.21	0.468	12	40	125.00	370.66	125.00	7.99
55	4.21	0.468	12	40	150.00	370.66	150.00	9.58
55	4.21	0.468	12	40	175.00	370.66	175.00	11.18
60	4.35	0.456	12	40	100.00	393.98	100.00	6.39
60	4.35	0.456	12	40	125.00	393.98	125.00	7.99
60	4.35	0.456	12	40	150.00	393.98	150.00	9.58
60	4.35	0.456	12	40	175.00	393.98	175.00	11.18
70	4.61	0.432	12	40	100.00	435.46	100.00	6.39
70	4.61	0.432	12	40	125.00	435.46	125.00	7.99
70	4.61	0.432	12	40	150.00	435.46	150.00	9.58
70	4.61	0.432	12	40	175.00	435.46	175.00	11.18
80	4.84	0.408	12	40	100.00	470.02	100.00	6.39
80	4.84	0.408	12	40	125.00	470.02	125.00	7.99
80	4.84	0.408	12	40	150.00	470.02	150.00	9.58
80	4.84	0.408	12	40	175.00	470.02	175.00	11.18
90	5.04	0.384	12	40	100.00	497.66	100.00	6.39
90	5.04	0.384	12	40	125.00	497.66	125.00	7.99
90	5.04	0.384	12	40	150.00	497.66	150.00	9.58
90	5.04	0.384	12	40	175.00	497.66	175.00	11.18

Table 9
Results of NP EN 1992-1-1, with υ

f_{ck} (MPa)	$υ_1$	b_w (cm)	d (cm)	V_{Ed} (kN)	$V_{Rd,max}$ (kN)	$V_{Rd,s}$ (kN)	A_{sw} (cm²/m)
55	0.60	12	40	100.00	475.20	100.00	6.94
55	0.60	12	40	125.00	475.20	125.00	8.68
55	0.60	12	40	150.00	475.20	150.00	10.42
55	0.60	12	40	175.00	475.20	175.00	12.15
60	0.60	12	40	100.00	518.40	100.00	6.94
60	0.60	12	40	125.00	518.40	125.00	8.68
60	0.60	12	40	150.00	518.40	150.00	10.42
60	0.60	12	40	175.00	518.40	175.00	12.15
70	0.55	12	40	100.00	554.40	100.00	6.94
70	0.55	12	40	125.00	554.40	125.00	8.68
70	0.55	12	40	150.00	554.40	150.00	10.42
70	0.55	12	40	175.00	554.40	175.00	12.15
80	0.50	12	40	100.00	576.00	100.00	6.94
80	0.50	12	40	125.00	576.00	125.00	8.68
80	0.50	12	40	150.00	576.00	150.00	10.42
80	0.50	12	40	175.00	576.00	175.00	12.15
90	0.50	12	40	100.00	648.00	100.00	6.94
90	0.50	12	40	125.00	648.00	125.00	8.68
90	0.50	12	40	150.00	648.00	150.00	10.42
90	0.50	12	40	175.00	648.00	175.00	12.15

where:

$\sqrt{f_{ck}} \leq 8\text{MPa}$.

f) Compressive stress field inclination:

$$\theta_{min} \leq \theta \leq 45° \quad (16)$$

The code also presents the levels-of-approximation approach. According to Muttoni and Ruiz [8], this approach is based on the use of theories based on physical parameters where the hypotheses for their applications can be refined according to the demand for accuracy. As Barros [9] highlights, the increase in the approximation level (I to IV) is followed by the increase of precision and of the time expended for the analyses.

2.3.1 Level I Approximation

In this level, the $V_{Rd,c}$ of Equation 12 is not considered. For reinforced concrete members, θ_{min} = 30°. In addition, to calculate $V_{Rd,max}$, $k_\varepsilon = 0,55$.

Table 10
Results of DIN 1045-1

f_{ck} (MPa)	$f_{ct,m}$ (MPa)	b_w (cm)	d (cm)	V_{Ed} (kN)	$V_{Rd,max}$ (kN)	$V_{Rd,s}$ (kN)	A_{sw} (cm²/m)
55	4.21	12	40	100.00	891.00	100.00	6.39
55	4.21	12	40	125.00	891.00	125.00	7.99
55	4.21	12	40	150.00	891.00	150.00	9.58
55	4.21	12	40	175.00	891.00	175.00	11.18
60	4.35	12	40	100.00	972.00	100.00	6.39
60	4.35	12	40	125.00	972.00	125.00	7.99
60	4.35	12	40	150.00	972.00	150.00	9.58
60	4.35	12	40	175.00	972.00	175.00	11.18
70	4.61	12	40	100.00	1134.00	100.00	6.39
70	4.61	12	40	125.00	1134.00	125.00	7.99
70	4.61	12	40	150.00	1134.00	150.00	9.58
70	4.61	12	40	175.00	1134.00	175.00	11.18
80	4.84	12	40	100.00	1296.00	100.00	6.39
80	4.84	12	40	125.00	1296.00	125.00	7.99
80	4.84	12	40	150.00	1296.00	150.00	9.58
80	4.84	12	40	175.00	1296.00	175.00	11.18
90	5.04	12	40	100.00	1458.00	100.00	6.39
90	5.04	12	40	125.00	1458.00	125.00	7.99
90	5.04	12	40	150.00	1458.00	150.00	9.58
90	5.04	12	40	175.00	1458.00	175.00	11.18

Table 11
Transverse reinforcement areas (cm²/m) for beams of 20 cm x 60 cm

f_{ck} (MPa)	V_{Sd} (kN)	NBR		MC 1990	MC 2010			NP EN 1992		DIN 1045
		M I	M II		LoA I	LoA II	LoA III	ν	ν_1	
55	200.00	3.31	3.31	8.52	8.52	8.52	5.68	8.52	9.26	8.52
55	250.00	4.30	5.06	10.65	10.65	10.65	8.01	10.65	11.57	10.65
55	300.00	6.43	7.56	12.78	12.78	12.78	10.34	12.78	13.89	12.78
55	375.00	9.62	11.32	15.97	15.97	15.97	13.83	15.97	17.36	15.97
60	200.00	3.44	3.44	8.52	8.52	8.52	5.51	8.52	9.26	8.52
60	250.00	4.05	4.75	10.65	10.65	10.65	7.83	10.65	11.57	10.65
60	300.00	6.18	7.24	12.78	12.78	12.78	10.16	12.78	13.89	12.78
60	375.00	9.37	10.99	15.97	15.97	15.97	13.65	15.97	17.36	15.97
70	200.00	3.67	3.67	8.52	8.52	8.52	5.33	8.52	9.26	8.52
70	250.00	3.67	4.21	10.65	10.65	10.65	7.64	10.65	11.57	10.65
70	300.00	5.74	6.69	12.78	12.78	12.78	9.95	12.78	13.89	12.78
70	375.00	8.94	10.41	15.97	15.97	15.97	13.42	15.97	17.36	15.97
80	200.00	3.87	3.87	8.52	8.52	8.52	5.26	8.52	9.26	8.52
80	250.00	3.87	3.87	10.65	10.65	10.65	7.56	10.65	11.57	10.65
80	300.00	5.36	6.22	12.78	12.78	12.78	9.86	12.78	13.89	12.78
80	375.00	8.55	9.92	15.97	15.97	15.97	13.31	15.97	17.36	15.97
90	200.00	4.05	4.05	8.52	8.52	8.52	5.21	8.52	9.26	8.52
90	250.00	4.05	4.05	10.65	10.65	10.65	7.50	10.65	11.57	10.65
90	300.00	5.01	5.80	12.78	12.78	12.78	9.78	12.78	13.89	12.78
90	375.00	8.20	9.50	15.97	15.97	15.97	13.21	15.97	17.36	15.97

2.3.2 Level II Approximation

As occurs in LoA I, the $V_{Rd,c}$ portion of Equation 12 is disregarded. The minimum inclination of the compressive stress field is given by Equation 17, but will be adopted as 30°. In addition, the parameter k_ε, given by Equation 18, will assume its maximum value of 0,65 on the further developed simulations.

$$\theta_{\min} = 20° + 10000\varepsilon_x \tag{17}$$

$$k_\varepsilon = \frac{1}{1{,}2 + 55\varepsilon_1} \leq 0{,}65 \tag{18}$$

2.3.3 Level III Approximation

In this level, the whole Equation 12 is valid. The maximum shear resistance is given by Equation 13 for $\theta = \theta_{min}$, given by Equation 17 and admitted as 30°. To determinate the $V_{Rd,c}$ attributed to the concrete (Equation 15), the parameter k_υ is calculated as shown on Equation 19. For the following examples, ε_x = 0,001.

$$k_v = \frac{0{,}4}{1 + 1500\varepsilon_x}\left(1 - \frac{V_{Ed}}{V_{Rd,max}(\theta_{\min})}\right) \geq 0 \tag{19}$$

2.3.4 Level IV approximation

The model code does not bring specific expressions for this level-of-approximation, but establishes that the resistance of members in shear or shear combined with torsion may be determined by satisfying the applicable conditions of equilibrium and compatibility of strains and by using appropriate stress-strain models for steel and for diagonally cracked concrete.

2.4 NP EN 1992-1-1:2010 [10]

Ahead, the Portuguese standard considerations on shear are shown.

a) Minimum shear reinforcement area: also given by Equation 11.

b) Design shear resistance:

$$V_{\mathrm{Rd}} = V_{\mathrm{Rd,s}} + V_{\mathrm{ccd}} + V_{\mathrm{td}} \tag{20}$$

where:

$V_{Rd,s}$ is the design value of the shear force which can be sustained by the yielding shear reinforcement;

V_{ccd} is the design value of the shear component of the force in the compression area (inclined compression chord);

V_{td} is the design value of the shear component of the force in the tensile reinforcement (inclined tensile chord).

c) Concrete compression strut inclination:

$$21{,}8° \leq \theta \leq 45° \tag{21}$$

d) Design value of the maximum shear force for stirrups at 90°:

$$V_{\mathrm{Rd,max}} = \propto_{\mathrm{cw}} \cdot b_{\mathrm{w}} \cdot z \cdot \nu_1 \cdot \frac{f_{\mathrm{ck}}}{\gamma_{\mathrm{c}}} / (\cot\theta + \mathrm{tg}\,\theta) \tag{22}$$

where:

v_1 is the strength reduction factor for concrete cracked in shear;

$\propto_{cw}$ is the coefficient taking account of the state of the stress in the compression chord. For reinforced concrete members, $\propto_{cw}$ = 1,0. The value of v_1 is given by Equation 23.

$$\nu = 0{,}6\left[1 - \frac{f_{\mathrm{ck}}}{250}\right] \tag{23}$$

If the design stress of the shear reinforcement is below 80% of the characteristic yield stress f_{yk}, v_1 may be taken as:

$v_1 = 0{,}6$ for $f_{ck} \leq 60$ MPa

$v_1 = 0{,}9 - f_{ck} / 200 > 0{,}5$ for $f_{ck} \geq 60$ MPa

e) Shear resistance of the stirrups at 90°:

$$V_{\mathrm{Rd},s} = \frac{A_{\mathrm{sw}}}{s} \cdot f_{\mathrm{ywd}} \cdot z \cdot \cot\theta \tag{24}$$

f) Maximum effective cross-sectional area of the shear reinforcement for $\theta = 45°$:

$$\frac{A_{\mathrm{sw,max}} \cdot f_{\mathrm{ywd}}}{b_{\mathrm{w}} \cdot s} \leq \frac{0{,}5 \cdot \propto_{\mathrm{cw}} \cdot \nu_1 \cdot f_{\mathrm{cd}}}{sen\,\alpha} \tag{25}$$

Table 12
Transverse reinforcement areas (cm²/m) for beams of 60 cm x 165 cm

f_{ck} (MPa)	V_{Sd} (kN)	NBR		MC 1990	MC 2010			NP EN 1992		DIN 1045
		M I	M II		LoA I	LoA II	LoA III	ν	ν_1	
55	3000	27.41	32.25	46.46	46.46	46.46	39.91	46.46	50.51	46.46
55	3200	30.50	35.89	49.56	49.56	49.56	43.30	49.56	53.87	49.56
55	3400	33.60	39.53	52.66	52.66	52.66	46.68	52.66	57.24	52.66
55	3600	36.69	43.18	55.76	55.76	55.76	50.07	55.76	60.61	55.76
60	3000	26.67	31.26	46.46	46.46	46.46	39.36	46.46	50.51	46.46
60	3200	29.77	34.89	49.56	49.56	49.56	42.74	49.56	53.87	49.56
60	3400	32.86	38.51	52.66	52.66	52.66	46.13	52.66	57.24	52.66
60	3600	35.96	42.14	55.76	55.76	55.76	49.51	55.76	60.61	55.76
70	3000	25.36	29.54	46.46	46.46	46.46	38.69	46.46	50.51	46.46
70	3200	28.45	33.14	49.56	49.56	49.56	42.06	49.56	53.87	49.56
70	3400	31.55	36.75	52.66	52.66	52.66	45.42	52.66	57.24	52.66
70	3600	34.64	40.36	55.76	55.76	55.76	48.79	55.76	60.61	55.76
80	3000	24.19	28.08	46.46	46.46	46.46	38.35	46.46	50.51	46.46
80	3200	27.29	31.67	49.56	49.56	49.56	41.69	49.56	53.87	49.56
80	3400	30.39	35.27	52.66	52.66	52.66	45.04	52.66	57.24	52.66
80	3600	33.48	38.86	55.76	55.76	55.76	48.38	55.76	60.61	55.76
90	3000	23.16	26.83	46.46	46.46	46.46	38.07	46.46	50.51	46.46
90	3200	26.25	30.41	49.56	49.56	49.56	41.40	49.56	53.87	49.56
90	3400	29.35	34.00	52.66	52.66	52.66	44.72	52.66	57.24	52.66
90	3600	32.45	37.59	55.76	55.76	55.76	48.05	55.76	60.61	55.76

2.5 DIN 1045-1:2001-07 [11]

The German standard establishes the following considerations on shear design.
a) Inclination of struts:

$$18{,}43° \leq \theta \leq 59{,}88° \quad (26)$$

b) Design shear resistance, limited by the strength of the struts:

$$V_{\mathrm{Rd,max}} = \frac{b_w \cdot z \cdot \alpha_c \cdot f_{ck}}{\operatorname{cotg}\theta + \operatorname{tg}\theta} \quad (27)$$

where:
α_c is a reduction factor equal to 0.75 η_1, that is, 0.75 for normal-weight concrete.
c) Design shear resistance, limited by the capacity of the shear reinforcement:

$$V_{\mathrm{Rd},sy} = \frac{A_{sw}}{s_w} \cdot f_{yd} \cdot z \cdot \operatorname{cotg}\theta \quad (28)$$

3. Numerical simulations of the reinforcement areas according to the design standards

With the objective of evaluating each analyzed procedure, three situations are proposed, each one with four intensities of shear force and considering the high strength classes of concrete. For comparison purposes, the inclinations of all struts will be taken as θ = 45°. The areas were calculated using the expressions presented in section 2.
After the proposed situations, the ultimate shear strengths obtained through the codes' expressions will be evaluated.

3.1 Exemple 01

The first example consists of a beam of 12 cm width by 40 cm, subjected to four shear force intensities: 100 kN, 125 kN, 150 kN and 175 kN. The transverse reinforcement areas obtained are presented in Tables 2 to 10.

Table 13
Ultimate shear strengths

Design standard	V/bd (MPa)				
	C55	C60	C70	C80	C90
NBR – I	8.27	8.79	9.72	10.49	11.11
NBR – II	8.27	8.79	9.72	10.49	11.11
MC 1990	7.72	8.21	9.07	9.79	10.37
MC 2010 LoA I	7.41	7.86	8.71	9.52	10.30
MC 2010 LoA II	8.76	9.29	10.29	11.25	12.17
MC 2010 LoA III	7.59	8.04	8.91	9.74	10.54
NP EN 1992 ν	7.72	8.21	9.07	9.79	10.37
NP EN 1992 ν_1	9.90	10.80	11.55	12.00	13.50
DIN 1045	18.56	20.25	23.63	27.00	30.38

Table 14
Comparative percentages of the areas of example 01

f_{ck} (MPa)	V_{Sd} (kN)	A_{sw} / $A_{sw\ (MC\ 1990)}$ %								
		NBR		MC 1990	MC 2010			NP EN 1992		DIN 1045
		M I	M II		LoA I	LoA II	LoA III	ν	ν_1	
55	100	40.36	47.49	100.00	100.00	100.00	75.21	100.00	108.70	100.00
55	125	52.28	61.51	100.00	100.00	100.00	82.04	100.00	108.70	100.00
55	150	60.22	70.86	100.00	100.00	100.00	86.60	100.00	108.70	100.00
55	175	65.90	77.54	100.00	100.00	100.00	89.85	100.00	108.70	100.00
60	100	38.07	44.61	100.00	100.00	100.00	73.55	100.00	108.70	100.00
60	125	50.44	59.11	100.00	100.00	100.00	80.69	100.00	108.70	100.00
60	150	58.69	68.78	100.00	100.00	100.00	85.45	100.00	108.70	100.00
60	175	64.59	75.69	100.00	100.00	100.00	88.85	100.00	108.70	100.00
70	100	34.46	39.54	100.00	100.00	100.00	71.75	100.00	108.70	100.00
70	125	47.14	54.92	100.00	100.00	100.00	79.13	100.00	108.70	100.00
70	150	55.94	65.17	100.00	100.00	100.00	84.04	100.00	108.70	100.00
70	175	62.23	72.49	100.00	100.00	100.00	87.55	100.00	108.70	100.00
80	100	36.35	36.35	100.00	100.00	100.00	71.02	100.00	108.70	100.00
80	125	44.24	51.34	100.00	100.00	100.00	78.39	100.00	108.70	100.00
80	150	53.52	62.12	100.00	100.00	100.00	83.31	100.00	108.70	100.00
80	175	60.15	69.81	100.00	100.00	100.00	86.82	100.00	108.70	100.00
90	100	38.05	38.05	100.00	100.00	100.00	70.42	100.00	108.70	100.00
90	125	41.64	48.24	100.00	100.00	100.00	77.80	100.00	108.70	100.00
90	150	51.36	59.49	100.00	100.00	100.00	82.71	100.00	108.70	100.00
90	175	58.30	67.54	100.00	100.00	100.00	86.22	100.00	108.70	100.00

3.2 Exemple 02

The second example consists of a beam of 20 cm width by 60 cm, subjected to four shear force intensities: 200 kN, 250 kN, 300 kN and 375 kN. Table 11 demonstrates the area values obtained from each normative treatment.

3.3 Exemple 03

The third example consists of a beam of 60 cm width by 165 cm, subjected to shear forces of 3000 kN, 3200 kN, 3400 kN and 3600 kN. The calculation areas obtained are presented in Table 12.

Table 15
Comparative percentages of the areas of example 02

f_{ck} (MPa)	V_{Sd} (kN)	A_{sw} / $A_{sw\ (MC\ 1990)}$ %								
		NBR		MC 1990	MC 2010			NP EN 1992		DIN 1045
		M I	M II		LoA I	LoA II	LoA III	ν	ν_1	
55	200	38.88	38.88	100.00	100.00	100.00	66.66	100.00	108.70	100.00
55	250	40.36	47.49	100.00	100.00	100.00	75.21	100.00	108.70	100.00
55	300	50.29	59.17	100.00	100.00	100.00	80.90	100.00	108.70	100.00
55	375	60.22	70.86	100.00	100.00	100.00	86.60	100.00	108.70	100.00
60	200	40.38	40.38	100.00	100.00	100.00	64.63	100.00	108.70	100.00
60	250	38.07	44.61	100.00	100.00	100.00	73.55	100.00	108.70	100.00
60	300	48.38	56.70	100.00	100.00	100.00	79.50	100.00	108.70	100.00
60	375	58.69	68.78	100.00	100.00	100.00	85.45	100.00	108.70	100.00
70	200	43.07	43.07	100.00	100.00	100.00	62.54	100.00	108.70	100.00
70	250	34.46	39.54	100.00	100.00	100.00	71.75	100.00	108.70	100.00
70	300	44.94	52.35	100.00	100.00	100.00	77.90	100.00	108.70	100.00
70	375	55.94	65.17	100.00	100.00	100.00	84.04	100.00	108.70	100.00
80	200	45.44	45.44	100.00	100.00	100.00	61.80	100.00	108.70	100.00
80	250	36.35	36.35	100.00	100.00	100.00	71.02	100.00	108.70	100.00
80	300	41.92	48.65	100.00	100.00	100.00	77.16	100.00	108.70	100.00
80	375	53.52	62.12	100.00	100.00	100.00	83.31	100.00	108.70	100.00
90	200	47.56	47.56	100.00	100.00	100.00	61.21	100.00	108.70	100.00
90	250	38.05	38.05	100.00	100.00	100.00	70.42	100.00	108.70	100.00
90	300	39.21	45.42	100.00	100.00	100.00	76.57	100.00	108.70	100.00
90	375	51.36	59.49	100.00	100.00	100.00	82.71	100.00	108.70	100.00

Table 16
Comparative percentages of the areas of example 03

f_{ck} (MPa)	V_{Sd} (kN)	A_{sw} / $A_{sw\ (MC\ 1990)}$ %								
		NBR		MC 1990	MC 2010			NP EN 1992		DIN 1045
		M I	M II		LoA I	LoA II	LoA III	ν	ν_1	
55	3000	58.98	69.40	100.00	100.00	100.00	85.89	100.00	108.70	100.00
55	3200	61.54	72.41	100.00	100.00	100.00	87.36	100.00	108.70	100.00
55	3400	63.80	75.07	100.00	100.00	100.00	88.65	100.00	108.70	100.00
55	3600	65.81	77.43	100.00	100.00	100.00	89.80	100.00	108.70	100.00
60	3000	57.40	67.27	100.00	100.00	100.00	84.71	100.00	108.70	100.00
60	3200	60.06	70.39	100.00	100.00	100.00	86.24	100.00	108.70	100.00
60	3400	62.41	73.14	100.00	100.00	100.00	87.59	100.00	108.70	100.00
60	3600	64.50	75.58	100.00	100.00	100.00	88.80	100.00	108.70	100.00
70	3000	54.57	63.57	100.00	100.00	100.00	83.27	100.00	108.70	100.00
70	3200	57.41	66.87	100.00	100.00	100.00	84.86	100.00	108.70	100.00
70	3400	59.91	69.79	100.00	100.00	100.00	86.25	100.00	108.70	100.00
70	3600	62.13	72.38	100.00	100.00	100.00	87.50	100.00	108.70	100.00
80	3000	52.07	60.43	100.00	100.00	100.00	82.54	100.00	108.70	100.00
80	3200	55.06	63.91	100.00	100.00	100.00	84.12	100.00	108.70	100.00
80	3400	57.70	66.97	100.00	100.00	100.00	85.52	100.00	108.70	100.00
80	3600	60.05	69.69	100.00	100.00	100.00	86.76	100.00	108.70	100.00
90	3000	49.84	57.74	100.00	100.00	100.00	81.94	100.00	108.70	100.00
90	3200	52.97	61.36	100.00	100.00	100.00	83.53	100.00	108.70	100.00
90	3400	55.74	64.57	100.00	100.00	100.00	84.93	100.00	108.70	100.00
90	3600	58.19	67.41	100.00	100.00	100.00	86.17	100.00	108.70	100.00

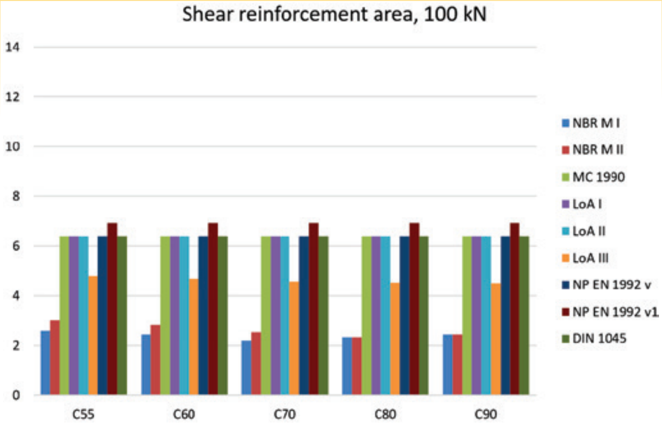

Figure 2
Comparative graph of the transverse reinforcement areas (cm^2/m) of example 01 (beams of 12 cm by 40 cm), for applied shear force of 100 kN

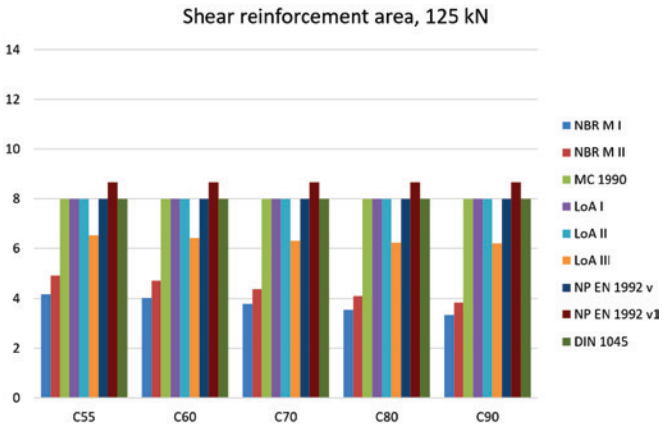

Figure 3
Comparative graph of the transverse reinforcement areas (cm^2/m) of example 01 (beams of 12 cm by 40 cm), for applied shear force of 125 kN

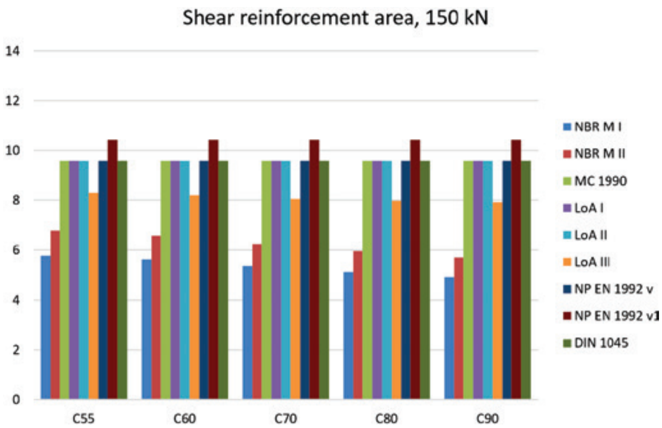

Figure 4
Comparative graph of the transverse reinforcement areas (cm^2/m) of example 01 (beams of 12 cm by 40 cm), for applied shear force of 150 kN

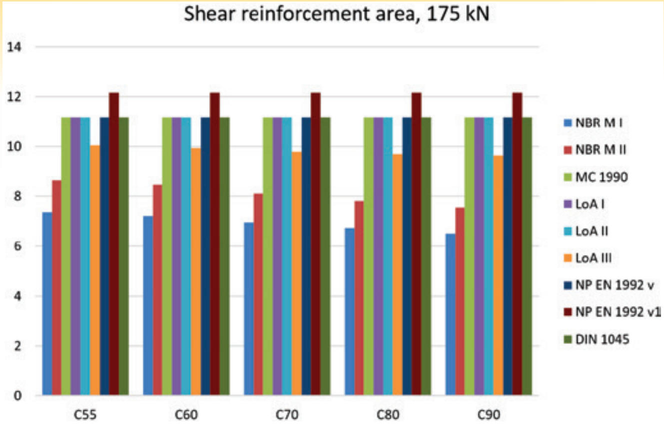

Figure 5
Comparative graph of the transverse reinforcement areas (cm^2/m) of example 01 (beams of 12 cm by 40 cm), for applied shear force of 175 kN

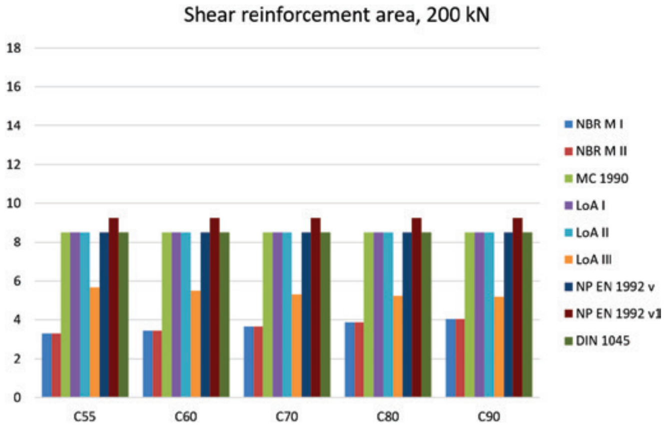

Figure 6
Comparative graph of the transverse reinforcement areas (cm^2/m) of example 02 (beams of 20 cm by 60 cm), for applied shear force of 200 kN

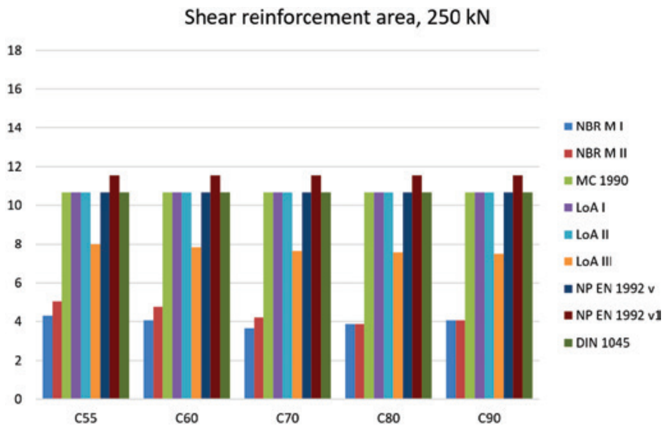

Figure 7
Comparative graph of the transverse reinforcement areas (cm^2/m) of example 02 (beams of 20 cm by 60 cm), for applied shear force of 250 kN

3.4 Ultimate shear strength

Table 13 shows the ultimate shear strengths, as stresses (MPa), for each concrete class, obtained through the studied normative procedures' expressions.

3.5 Comparison of results

Based on the obtained results, the comparative Tables 14, 15 and 16, respectively related to examples 01, 02 and 03, are presented. Comparative graphs are presented in Figures 2, 3, 4, 5 (example 01); 6, 7, 8, 9 (example 02) and 10, 11, 12, 13 (example 03), for each shear force intensity and cross section situation. In the Tables, the resulting areas were considered as a percentage of the calculated areas by the Model Code 1990.

In Tables 14, 15 and 16 it can be verified that the international methodologies – apart from *LoA* III of MC 2010 [7] and the calculation procedure of the Portuguese code [10] which uses the parameter v_1 in the calculation (destined for situations in which the design stress of the shear reinforcement are below 80% of the characteristic yield stress) – generate the same transverse reinforcement

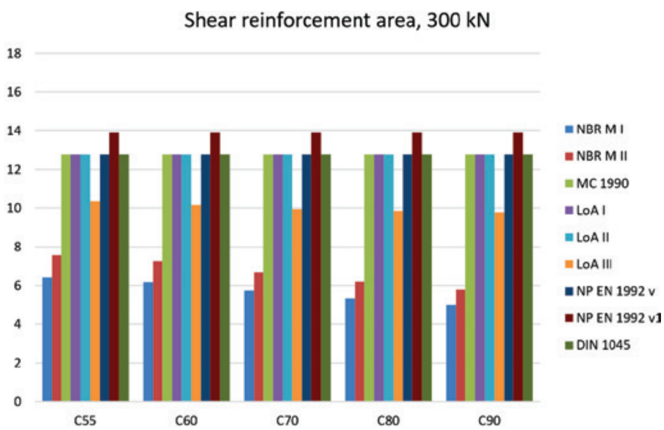

Figure 8
Comparative graph of the transverse reinforcement areas (cm²/m) of example 02 (beams of 20 cm by 60 cm), for applied shear force of 300 kN

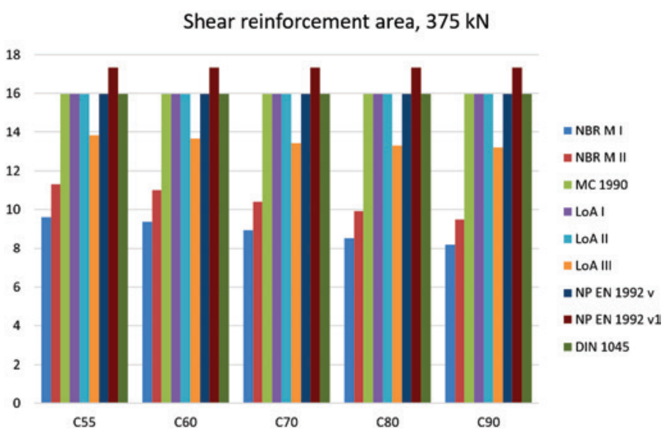

Figure 9
Comparative graph of the transverse reinforcement areas (cm²/m) of example 02 (beams of 20 cm by 60 cm), for applied shear force of 375 kN

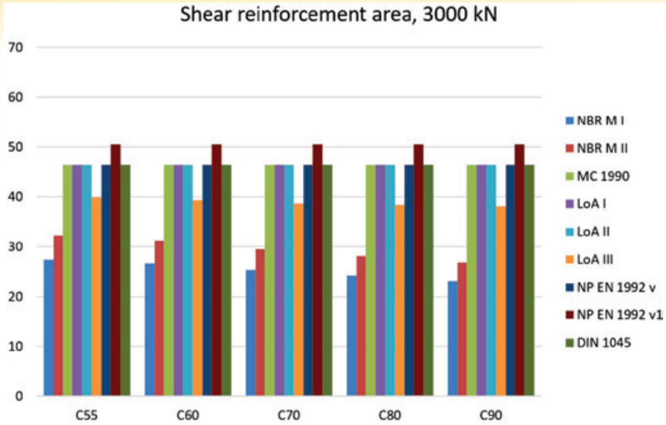

Figure 10
Comparative graph of the transverse reinforcement areas (cm²/m) of example 03 (beams of 60 cm por 165 cm), for applied shear force of 3000 kN

Figure 11
Comparative graph of the transverse reinforcement areas (cm²/m) of example 03 (beams of 60 cm por 165 cm), for applied shear force of 3200 kN

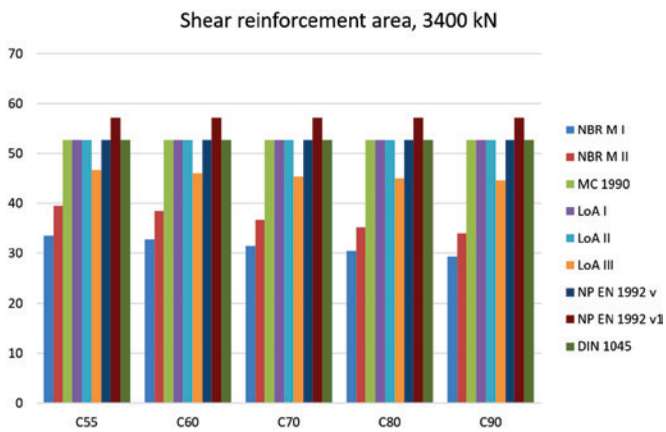

Figure 12
Comparative graph of the transverse reinforcement areas (cm²/m) of example 03 (beams of 60 cm por 165 cm), for applied shear force of 3400 kN

Table 17
Results of DIN 1045-1

Beam	f_c (MPa)	b (mm)	d (mm)	Shear reinforcement		Longitudinal reinforcement		$V_{failure}$ (kN)
				ϕ/s (mm)	ρ_w (MPa)	n ϕ	ρ_l	
H60/2	60.8	200	353	ϕ6/200	0.747	2ϕ32	2.28	179.74
H60/3	60.8	200	351	ϕ8/210	1.267	2ϕ32	2.29	258.78
H60/4	60.8	200	351	ϕ8/210	1.267	2ϕ32 + 1ϕ25	2.99	308.71
H75/2	68.9	200	353	ϕ6/200	0.747	2ϕ32	2.28	203.94
H75/3	68.9	200	351	ϕ8/210	1.267	2ϕ32	2.29	269.35
H75/4	68.9	200	351	ϕ8/210	1.267	2ϕ32 + 1ϕ25	2.99	255.23
H100/2	87.0	200	353	ϕ6/165	0.906	2ϕ32	2.28	225.55
H100/3	87.0	200	351	ϕ8/210	1.291	2ϕ32	2.29	253.64
H100/4	87.0	200	351	ϕ8/210	1.291	2ϕ32 + 1ϕ25	2.99	266.53

areas, for the same shear intensities, beam's cross sections and inclination of the struts of 45º.
Same as Models I and II of the NBR [5], Level III Approximation presents decreases on the required reinforcement areas for considering the concrete contribution in the design. The portions correspondent to these contributions increase while the concrete class escalates, and reduce with the rise of the applied shear forces. For all proposed situations, Models I and II of the Brazilian code generated the smallest areas.

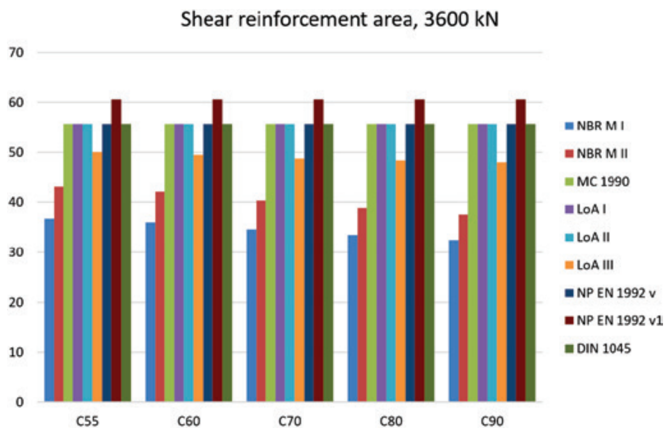

Figure 13
Comparative graph of the transverse reinforcement areas (cm_2/m) of example 03 (beams of 60 cm por 165 cm), for applied shear force of 3600 kN

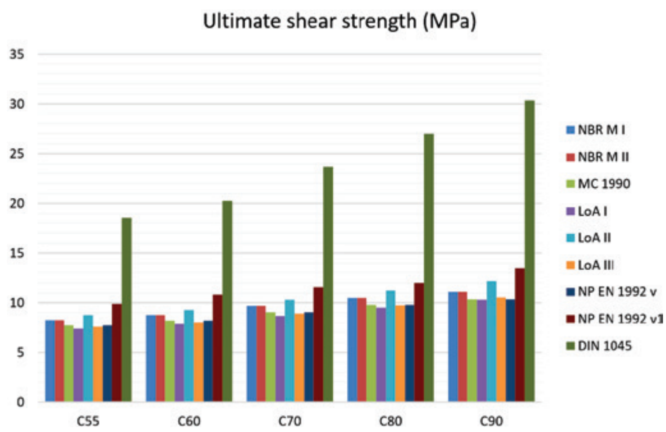

Figure 14
Comparative graph of the ultimate shear strengths (MPa)

Table 18
Properties of the transverse reinforcement bars

Diameter – Series	Area (mm²)	f_y (MPa)	f_u (MPa)
ϕ6 – H60 and H75	28.27	530	680
ϕ8 – H60 and H75	50.27	530	685
ϕ6 – H100	28.27	530	680
ϕ8 – H100	50.27	540	672

It is possible to verify that the German standard predicts shear resistances superior to the others, as presented in Figure 14. The other codes, including the Brazilian, comprehend higher values of reduction factors over the resistance, which is significantly penalized. It must be questioned whether this higher admissible resistance of the German code is justifiable by the higher rigor demanded in executing the concrete or by other factors unrelated to the calculation procedure, which are not contemplated in the design standard.

4. Experimental analysis

From the previous simulations, it is observed that the NBR calculation procedure produces smaller areas than the analyzed international procedures. Among them, only *LoA* III of the Model Code 2010 [7] adopts the complementary mechanisms of the concrete (pin effect, aggregate gearing and arch effect) contributions. The remaining international codes presented the inconsistency of generating equal shear reinforcement areas for the same cross section and applied force, even with increase of the compression

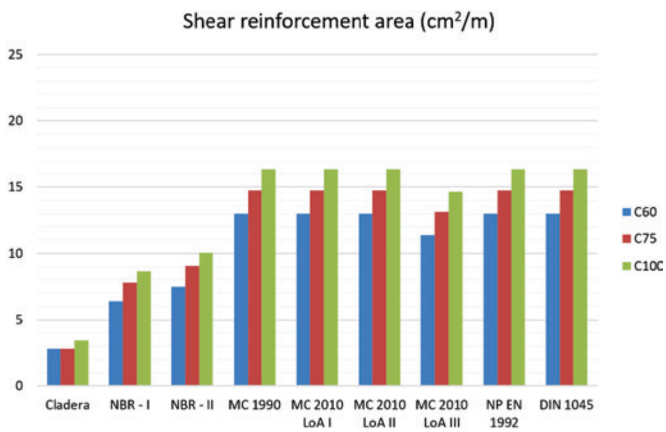

Figure 15
Comparative graph of the transverse reinforcement areas (cm²/m) of the beams of series 2

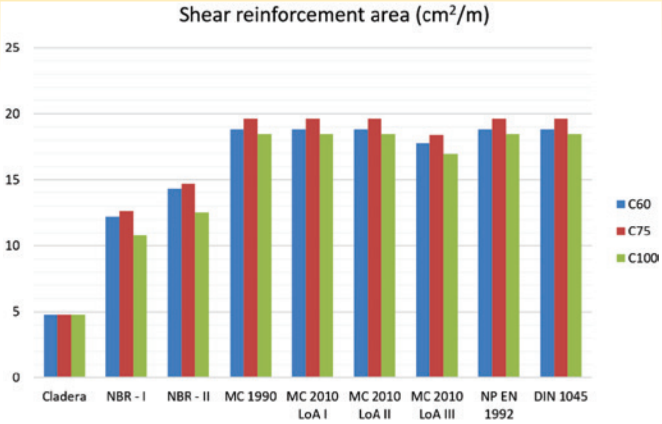

Figure 16
Comparative graph of the transverse reinforcement areas (cm²/m) of the beams of series 3

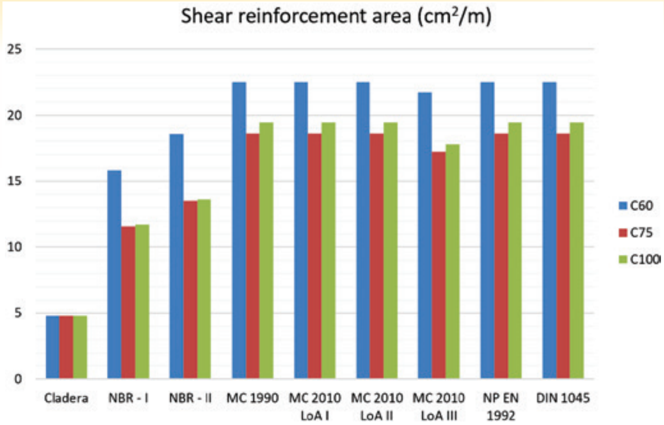

Figure 17
Comparative graph of the transverse reinforcement areas (cm²/m) of the beams of series 4

strength. Because of this, and with the intent to enrich the discussion, a comparison between the experimental results [2, 4] and the normative predictions will be performed.
Considering the results obtained by Cladera [2], the test-beams of series 2 (H60/2, H75/2 and H100/2), 3 (H60/3, H75/3 and H100/3) and 4 (H60/4, H75/4 and H100/4), which characteristics are expressed in Table 17 and illustrated in Figure 1, will be contemplated. These were selected by meeting the f_{ck} range of group II (between 55 MPa and 90 MPa), and for being transversely reinforced, allowing the desired comparisons.
Tables 19, 20 and 21 present the areas required by the studied codes for the experimental situations [2]. These were cal-

Table 19
Transverse reinforcement areas (cm²/m) for beams of series 2

Beam	f_{ck} (MPa)	b_w (cm)	d (cm)	V_{sd} (kN)	A_{sw} (cm²/m)
H60/2	60.8	20	35.3	179.74	2.82
NBR - I	60.8	20	35.3	179.74	6.38
NBR - II	60.8	20	35.3	179.74	7.47
MC 1990	60.8	20	35.3	179.74	13.01
MC 2010 LoA I	60.8	20	35.3	179.74	13.01
MC 2010 LoA II	60.8	20	35.3	179.74	13.01
MC 2010 LoA III	60.8	20	35.3	179.74	11.38
NP EN 1992	60.8	20	35.3	179.74	13.01
DIN 1045	60.8	20	35.3	179.74	13.01
Beam	**f_{ck} (MPa)**	**b_w (cm)**	**d (cm)**	**V_{sd} (kN)**	**A_{sw} (cm²/m)**
H75/2	68.9	20	35.3	203.94	2.82
NBR - I	68.9	20	35.3	203.94	7.77
NBR - II	68.9	20	35.3	203.94	9.06
MC 1990	68.9	20	35.3	203.94	14.76
MC 2010 LoA I	68.9	20	35.3	203.94	14.76
MC 2010 LoA II	68.9	20	35.3	203.94	14.76
MC 2010 LoA III	68.9	20	35.3	203.94	13.14
NP EN 1992	68.9	20	35.3	203.94	14.76
DIN 1045	68.9	20	35.3	203.94	14.76
Beam	**f_{ck} (MPa)**	**b_w (cm)**	**d (cm)**	**V_{sd} (kN)**	**A_{sw} (cm²/m)**
H100/2	87.0	20	35.3	225.55	3.42
NBR - I	87.0	20	35.3	225.55	8.66
NBR - II	87.0	20	35.3	225.55	10.03
MC 1990	87.0	20	35.3	225.55	16.33
MC 2010 LoA I	87.0	20	35.3	225.55	16.33
MC 2010 LoA II	87.0	20	35.3	225.55	16.33
MC 2010 LoA III	87.0	20	35.3	225.55	14.64
NP EN 1992	87.0	20	35.3	225.55	16.33
DIN 1045	87.0	20	35.3	225.55	16.33

culated considering the failure shear $V_{failure}$ (Table 17), experimentally achieved, as an applied shear force and by using the effectively observed compression strength of the concrete (60.8 MPa, 68.9 MPa and 87 MPa). It must be noted that on the standard's

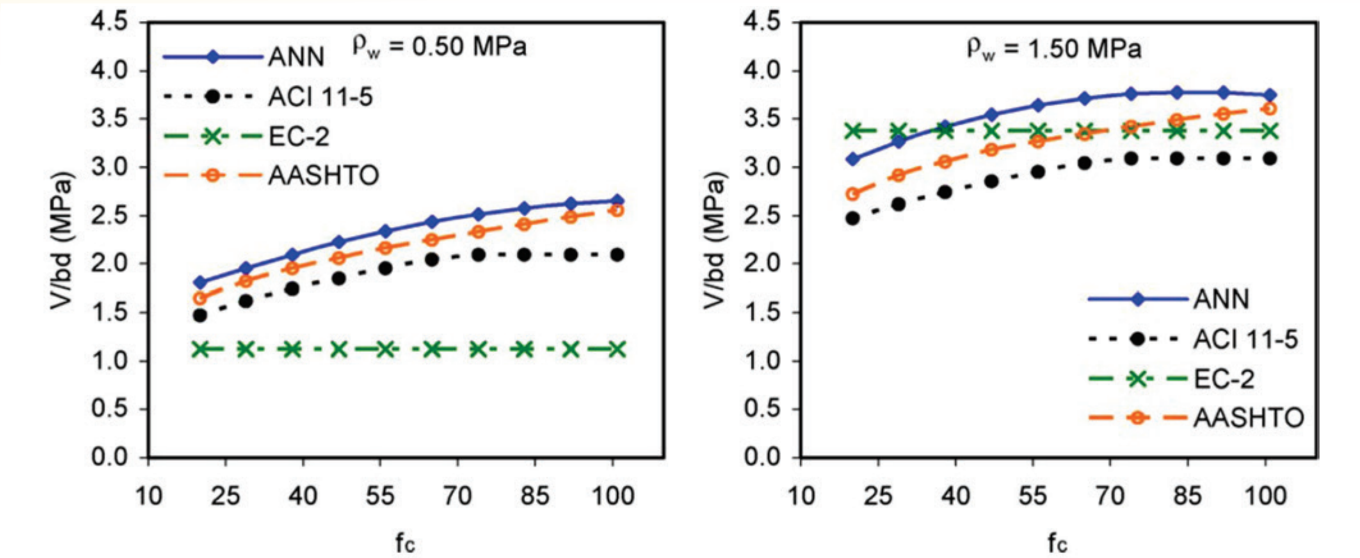

Figure 18
ANN results as compared to the ACI 11-5, EC-2 and AASHTO predictions for beams with web reinforcement. Influence of the concrete compressive strength in relation to the amount of transverse reinforcement. (Cladera & Marí [4])

Table 20
Transverse reinforcement areas (cm^2/m) for beams of series 3

Beam	f_{ck} (MPa)	b_w (cm)	d (cm)	V_{Sd} (kN)	A_{sw} (cm^2/m)
H60/3	60.8	20	35.1	258.78	4.78
NBR - I	60.8	20	35.1	258.78	12.20
NBR - II	60.8	20	35.1	258.78	14.29
MC 1990	60.8	20	35.1	258.78	18.84
MC 2010 LoA I	60.8	20	35.1	258.78	18.84
MC 2010 LoA II	60.8	20	35.1	258.78	18.84
MC 2010 LoA III	60.8	20	35.1	258.78	17.75
NP EN 1992	60.8	20	35.1	258.78	18.84
DIN 1045	60.8	20	35.1	258.78	18.84
Beam	**f_{ck} (MPa)**	**b_w (cm)**	**d (cm)**	**V_{Sd} (kN)**	**A_{sw} (cm^2/m)**
H75/3	68.9	20	35.1	269.35	4.78
NBR - I	68.9	20	35.1	269.35	12.62
NBR - II	68.9	20	35.1	269.35	14.71
MC 1990	68.9	20	35.1	269.35	19.61
MC 2010 LoA I	68.9	20	35.1	269.35	19.61
MC 2010 LoA II	68.9	20	35.1	269.35	19.61
MC 2010 LoA III	68.9	20	35.1	269.35	18.41
NP EN 1992	68.9	20	35.1	269.35	19.61
DIN 1045	68.9	20	35.1	269.35	19.61
Beam	**f_{ck} (MPa)**	**b_w (cm)**	**d (cm)**	**V_{Sd} (kN)**	**A_{sw} (cm^2/m)**
H100/3	87.0	20	35.1	253.64	4.78
NBR - I	87.0	20	35.1	253.64	10.80
NBR - II	87.0	20	35.1	253.64	12.51
MC 1990	87.0	20	35.1	253.64	18.47
MC 2010 LoA I	87.0	20	35.1	253.64	18.47
MC 2010 LoA II	87.0	20	35.1	253.64	18.47
MC 2010 LoA III	87.0	20	35.1	253.64	16.94
NP EN 1992	87.0	20	35.1	253.64	18.47
DIN 1045	87.0	20	35.1	253.64	18.47

predictions CA-50 steel was used. On the other hand, Cladera [2] adopted the experimentally obtained yield stress, presented in Table 18, for determining the area of the transverse reinforcement. Furthermore, to make the comparison viable, like the author, no majoring factors on the applied forces or reduction coefficients on resistances were used. The areas predicted by the codes and the experimental ones correspondent to the failure shear forces are shown in Figures 15, 16 and 17. It is noticed that the predicted areas by the codes are superior to the experimentally required, indicating a "reserve" of resistance. According to the aforementioned by the numerical simulations of section 3, the international standards generate greater transverse reinforcement areas then the national. The expected decrease via *LoA* III procedure of the Model Code 2010 [7] is highlighted, differing from the predictions of the other European codes. These last do not consider the concrete contribution, which in fact observed, as identified by Cladera & Marí [4] (Figure 18).

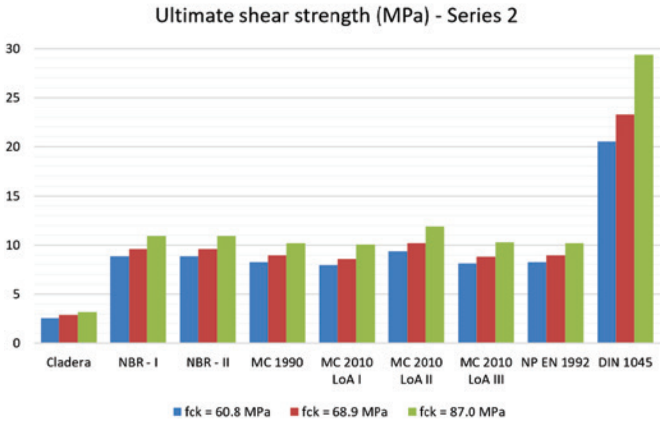

Figure 19
Comparative graph of the ultimate shear strengths (MPa) of series 2

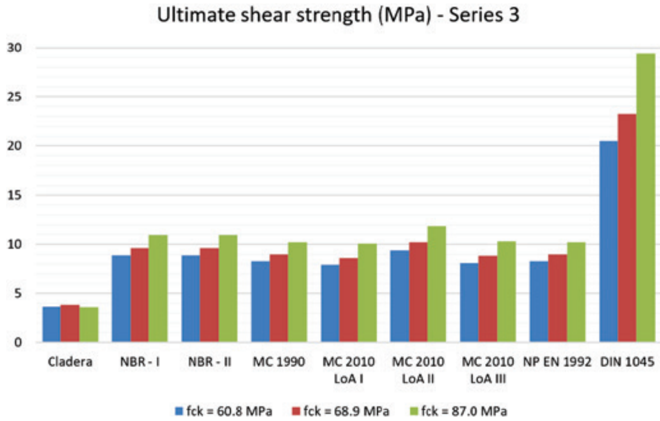

Figure 20
Comparative graph of the ultimate shear strengths (MPa) of series 3

Table 21
Transverse reinforcement areas (cm²/m) for beams of series 4

Beam	f_{ck} (MPa)	b_w (cm)	d (cm)	V_{Sd} (kN)	A_{sw} (cm²/m)
H60/4	60.8	20	35.1	308.71	4.78
NBR - I	60.8	20	35.1	308.71	15.84
NBR - II	60.8	20	35.1	308.71	18.55
MC 1990	60.8	20	35.1	308.71	22.48
MC 2010 LoA I	60.8	20	35.1	308.71	22.48
MC 2010 LoA II	60.8	20	35.1	308.71	22.48
MC 2010 LoA III	60.8	20	35.1	308.71	21.72
NP EN 1992	60.8	20	35.1	308.71	22.48
DIN 1045	60.8	20	35.1	308.71	22.48

Beam	f_{ck} (MPa)	b_w (cm)	d (cm)	V_{Sd} (kN)	A_{sw} (cm²/m)
H75/4	68.9	20	35.1	255.23	4.78
NBR - I	68.9	20	35.1	255.23	11.59
NBR - II	68.9	20	35.1	255.23	13.51
MC 1990	68.9	20	35.1	255.23	18.58
MC 2010 LoA I	68.9	20	35.1	255.23	18.58
MC 2010 LoA II	68.9	20	35.1	255.23	18.58
MC 2010 LoA III	68.9	20	35.1	255.23	17.29
NP EN 1992	68.9	20	35.1	255.23	18.58
DIN 1045	68.9	20	35.1	255.23	18.58

Beam	f_{ck} (MPa)	b_w (cm)	d (cm)	V_{Sd} (kN)	A_{sw} (cm²/m)
H100/4	87.0	20	35.1	266.53	4.78
NBR - I	87.0	20	35.1	266.53	11.73
NBR - II	87.0	20	35.1	266.53	13.60
MC 1990	87.0	20	35.1	266.53	19.41
MC 2010 LoA I	87.0	20	35.1	266.53	19.41
MC 2010 LoA II	87.0	20	35.1	266.53	19.41
MC 2010 LoA III	87.0	20	35.1	266.53	17.94
NP EN 1992	87.0	20	35.1	266.53	19.41
DIN 1045	87.0	20	35.1	266.53	19.41

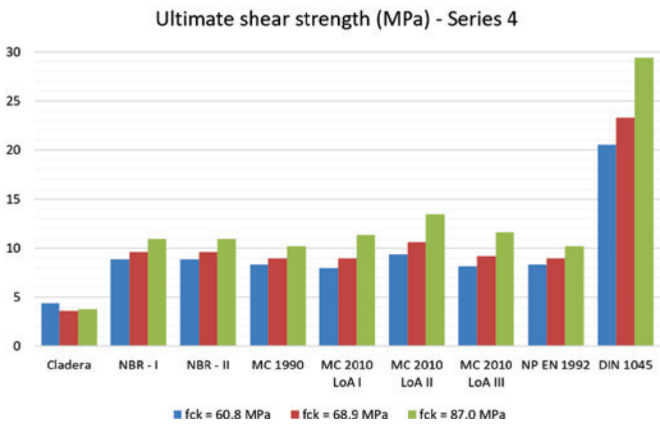

Figure 21
Comparative graph of the ultimate shear strengths (MPa) of series 4

The ANN curve – relative to the experimental results of beams of 350 mm of effective depth, 330 mm width, relation a/d = 3, and longitudinal reinforcement ratio of ρ_l = 3% - indicates the growth of shear strength with the increase of the concrete class. Despite contemplated by the American codes ACI 318-02 and AASHTO LRDF – not studied in the present work – in a conservative manner, this behavior is not considered by the Eurocode 2 [10], which admits that variations on shear resistance are due only to the transverse reinforcement, indicated by the translation of the EC-2 curve, with the increase in the transverse reinforcement rate from ρ_w = 0.50 MPa to ρ_w = 1.50 MPa.
If on one hand, most normative predictions do not consider the concrete contribution in the transverse reinforcement design, on the other, all predict ultimate shear strengths superior to those experimentally observed by Cladera [2], as presented in Table 22, which data are illustrated in Figures 19, 20 and 21. As verified in section 3.5, the German procedure predicted the highest resistances.
With the analysis of the ultimate shear strength, it is again noticeable

Table 22
Ultimate shear strengths (MPa)

Beam	f_{ck} (MPa)	V_{Ru} (MPa)		
		Série 2	Série 3	Série 4
Cladera	60.8	2.55	3.69	4.40
NBR - I	60.8	8.87	8.87	8.87
NBR - II	60.8	8.87	8.87	8.87
MC 1990	60.8	8.28	8.28	8.28
MC 2010 LoA I	60.8	7.93	7.93	7.93
MC 2010 LoA II	60.8	9.37	9.37	9.37
MC 2010 LoA III	60.8	8.11	8.11	8.11
NP EN 1992	60.8	8.28	8.28	8.28
DIN 1045	60.8	20.52	20.52	20.52

Beam	f_{ck} (MPa)	V_{Ru} (MPa)		
		Série 2	Série 3	Série 4
Cladera	68.9	2.89	3.84	3.64
NBR - I	68.9	9.63	9.63	9.63
NBR - II	68.9	9.63	9.63	9.63
MC 1990	68.9	8.98	8.98	8.98
MC 2010 LoA I	68.9	8.62	8.62	8.98
MC 2010 LoA II	68.9	10.18	10.18	10.62
MC 2010 LoA III	68.9	8.82	8.82	9.19
NP EN 1992	68.9	8.98	8.98	8.98
DIN 1045	68.9	23.25	23.25	23.25

Beam	f_{ck} (MPa)	V_{Ru} (MPa)		
		Série 2	Série 3	Série 4
Cladera	87.0	3.19	3.61	3.80
NBR - I	87.0	10.94	10.94	10.94
NBR - II	87.0	10.94	10.94	10.94
MC 1990	87.0	10.21	10.21	10.21
MC 2010 LoA I	87.0	10.07	10.07	11.34
MC 2010 LoA II	87.0	11.90	11.90	13.41
MC 2010 LoA III	87.0	10.30	10.30	11.61
NP EN 1992	87.0	10.21	10.21	10.21
DIN 1045	87.0	29.36	29.36	29.36

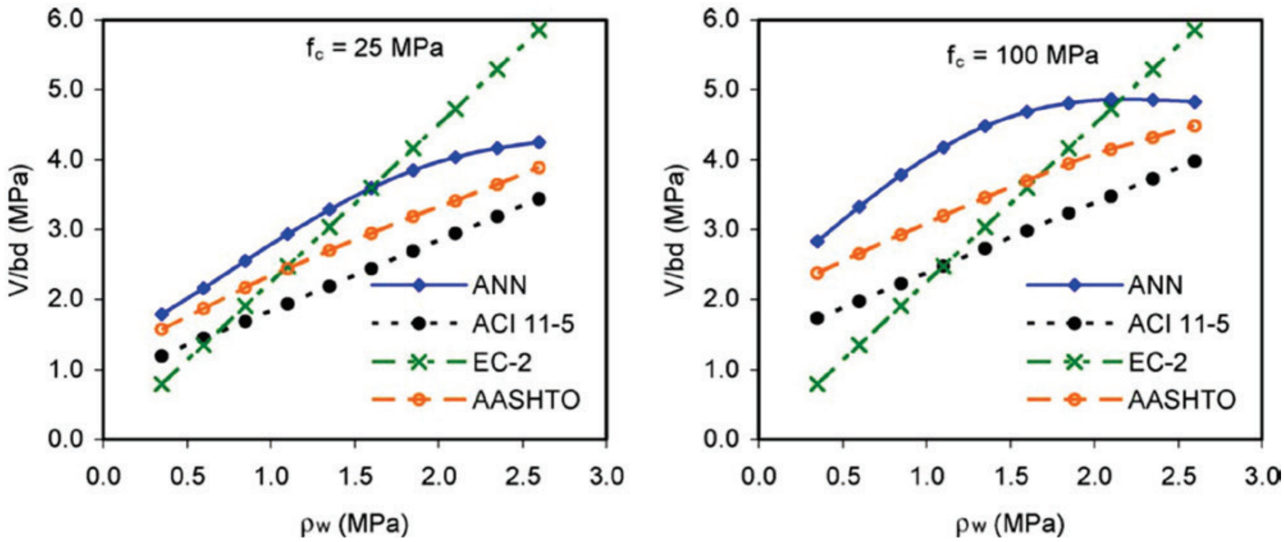

Figure 22
ANN results compared to the ACI 11-5, EC-2 and AASHTO predictions for beams with web reinforcement. Influence of the amount of shear reinforcement in relation to the concrete compressive strength (Cladera & Marí [4])

that, despite the growth of the shear resistance with the increase of the concrete class, in accordance to the normative procedures and experimental results, this behavior is not translated into advantage in design by the European procedures (apart from *LoA* III).

5. Conclusions

Due to the diffusion of high strength concretes, it is necessary to study the normative design procedures – specifically on shear design – which encompass concretes of classes C55 to C90. This work, therefore, aimed to analytically compare the usual normative methodologies in light of experimental results [2, 4].
From the analyses, one concludes that the NBR procedure produces areas inferior to the studied international codes. Unlike the Brazilian standard [5], they do not consider (apart from *LoA* III) the complementary concrete mechanisms contribution (pin effect, aggregate gearing and arch effect), despite experimentally observed.
According to the data shown in Tables 14, 15 and 16, one verifies that the MC 1990 [6] and MC 2010 [7] (*LoA* I and *LoA* II) calculation procedures and the Portuguese [10] (considering parameter v) and German codes [11] give the same areas for the same cross sections, shear intensities and inclination of the struts.
As verified at the 50th Brazilian Congress on Concrete [12] for concretes of group I, the use of Model II of NBR [5] in concretes of group II for given shear force, cross section and compressed diagonal inclination of 45º, results in areas superior to those obtained by Model I, when these are greater than the normative minimum.
The procedures that adopt a concrete contribution present reductions in the transverse reinforcement areas with the increase of the concrete class for a same applied shear force and cross section. In general, for the same class the areas increase with the loads.
Despite of not incorporating the concrete contribution in the design, the analyzed international procedures – as well as the national – predicted an increase in the ultimate shear force with the growth of the concrete class. In the performed comparisons it was detected that this same increase is superior to that experimentally obtained by Cladera [2], which reinforces the inconsistency and conservatism of these codes.
The lack of consideration of the concrete portion by part of the analyzed international codes leads to very conservative results, given that, regardless of class, for a same applied force, the areas are equal. Cladera & Marí [4] confirm this behavior when comparing the results of the ANN with the areas predicted by the Eurocode 2, as demonstrates Figure 22.

6. Acknowledgments

The autors thank CAPES - Coordination for the Improvement of Higher Education Personnel, CNPq - National Council for Scientific and Technological Development and the PROPESQ of UFRN.

7. References

[1] SILVA, Inês Santana da. Concreto de Alta Resistência: Composição, Propriedades e Dimensionamento. 1995. 149 f. Dissertação (Mestrado) - Curso de Engenharia de Estruturas, Escola de Engenharia de São Carlos, São Carlos, 1995.
[2] CLADERA, Antoni. Shear Design of Reinforced High-Strength Concrete Beams. 2002. 159 f. Tese (Doutorado) - Curso de Enginyeria Civil, Departament D'enginyeria de La Construcció, Universitat Politècnica de Catalunya, Barcelona, 2002.
[3] ARSLAN, Güray. Shear strength of reinforced concrete beams with stirrups. Materials And Structures, [s.l.], v. 41, n. 1, p.113-122, 28 fev. 2007. Springer Nature. http://dx.doi.org/10.1617/s11527-007-9223-3.

[4] CLADERA, A.; MARÍ, A. R.. Shear design procedure for reinforced normal and high-strength concrete beams using artificial neural networks. Part II: beams with stirrups. Engineering Structures, Elsevier, Amsterdam, v. 26, n. 7, p.927-936, 23 fev. 2004.

[5] ASSOCIAÇÃO BRASILEIRA DE NORMAS TÉCNICAS. NBR 6118: Projeto de estruturas de concreto - Procedimento. 3 ed. Rio de Janeiro, 2014.

[6] COMITE EURO-INTERNACIONAL DU BETON. MC 1990: Design Code. Lausanne, 1990.

[7] COMITE EURO-INTERNACIONAL DU BETON. MC 2010: Model Code 2010. Lausanne, 2010.

[8] MUTTONI, Aurelio; RUIZ, Miguel Fernández. The levels-of-approximation approach in MC 2010: application to punching shear provisions. Structural Concrete,[s.l.], v. 13, n. 1, p.32-41, mar. 2012. Wiley-Blackwell. http://dx.doi.org/10.1002/suco.201100032.

[9] BARROS, Rodrigo. Como as normas brasileiras e europeias tratam o problema da força cortante em elementos lineares de concreto. TQS News, [s.i.], v. , n. 36, p.44-45, 36 mar. 2013.

[10] COMITÉ EUROPEU DE NORMALIZAÇÃO. NP EN 1992-1-1: Projecto de estruturas de betão. Parte 1-1: Regras gerais e regras para edifícios. Bruxelas, 2010.

[11] DEUTSCHES INSTITUT FÜR NORMUNG. DIN 1045-1:2001-07: Plain, reinforced and prestress concrete structures. Part 1: Design and construction. Berlin, 2001.

[12] CONGRESSO BRASILEIRO DE CONCRETO, 50., 2008, Salvador. Cálculo da área da armadura transversal em elementos lineares de concreto armado submetidas à ação de força cortante: análise comparativa entre os Modelos I e II da NBR 6118:2003. Salvador: Ibracon, 2008. 16 p.

Volume 12, Number 1 (February 2019) p. 139 – 178 • ISSN 1983-4195
http://dx.doi.org/10.1590/S1983-41952019000100011

IBRACON

REVISTA IBRACON DE ESTRUTURAS E MATERIAIS
IBRACON STRUCTURES AND MATERIALS JOURNAL

Comparative analysis among standards of the area calculation of transversal reinforcement on reinforced concrete beams of high resistance subjected by shear force

Análise comparativa entre normas do cálculo da área da armadura transversal em vigas de concreto armado de resistência elevada submetidas à ação de força cortante

D. H. L. BRAZ [a]
danielhlbraz@gmail.com
https://orcid.org/0000-0003-2545-6058

R. BARROS [b]
rodrigobarros@ect.ufrn.br
https://orcid.org/0000-0002-7218-2646

J. N. DA SILVA FILHO [a,c]
jneres@ect.ufrn.br
https://orcid.org/0000-0002-9138-1771

Abstract

High strength concretes (HSC) correspond to a characteristic compression strength between 55 e 90 MPa. With the growing use of HSC, studies about the regular design standards of elements made of it, specifically standards about design on shear, become necessary. Hence, the main aspects of the NBR, Model Code 1990 e 2010, Portuguese Standard and German Standard related to the design on shear are presented. From the numerical simulations, with the addition of Cladera and Marí's experimental contributions, it is confirmed that the Brazilian design standard procedure produces lower transverse reinforcement areas in comparison to the ones predicted by the international codes; these, excepted by LoA III, do not consider the concrete contribution, in spite of being experimentally verified, leading to very conservative results.

Keywords: design, shear, high strength.

Resumo

Concretos de alta resistência (CAR) correspondem a uma resistência à compressão característica compreendida entre 55 e 90 MPa. Com a possibilidade crescente da utilização de CAR, faz-se necessária a realização de estudos que abordem os tratamentos normativos usuais acerca do dimensionamento de elementos por ele constituídos, especificamente, à ação de força cortante. Portanto, são apresentadas os principais aspectos da NBR, Model Code 1990 e 2010, Norma portuguesa e alemã acerca dos dimensionamento à cortante. Das simulações numéricas, acrescidas das contribuições experimentais de Cladera e Marí, constata-se que o procedimento de cálculo da NBR produz áreas de estribos inferiores às previstas pelos códigos internacionais; estes, com exceção do LoA III, não adotam a contribuição do concreto, apesar de esta ser verificada experimentalmente, levando a resultados muito conservadores.

Palavras-chave: dimensionamento, cortante, alta resistência.

[a] *University of Brasília, Brasília, DF, Brasil;*
[b] *University of São Paulo, São Carlos, SP, Brasil;*
[c] *North Carolina State University, NC, USA.*

Received: 28 Nov 2016 • Accepted: 27 Mar 2018 • Available Online: 05 Feb 2019

1. Introdução

Concretos de alta resistência (CAR) correspondem a uma resistência à compressão característica, f_{ck}, compreendida entre 55 e 90 MPa, de acordo com a NBR 6118:2014 [5]. A sua utilização tem sido difundida devido à demanda por estruturas nas quais são importantes a redução do peso e/ou quando a arquitetura impõe o uso de peças mais esbeltas (Silva [1]). CAR são obtidos através de melhorias na compactação da mistura de concreto, o que melhora a resistência da pasta e da interface da pasta com os agregados graúdos (Cladera [2]).

Da análise dos procedimentos normativos, destaca-se a importância da classe do concreto no dimensionamento dos elementos. Deste modo, com a possibilidade crescente de utilização de concretos do grupo II, faz-se necessária a realização de estudos que abordem os tratamentos normativos usuais acerca do dimensionamento

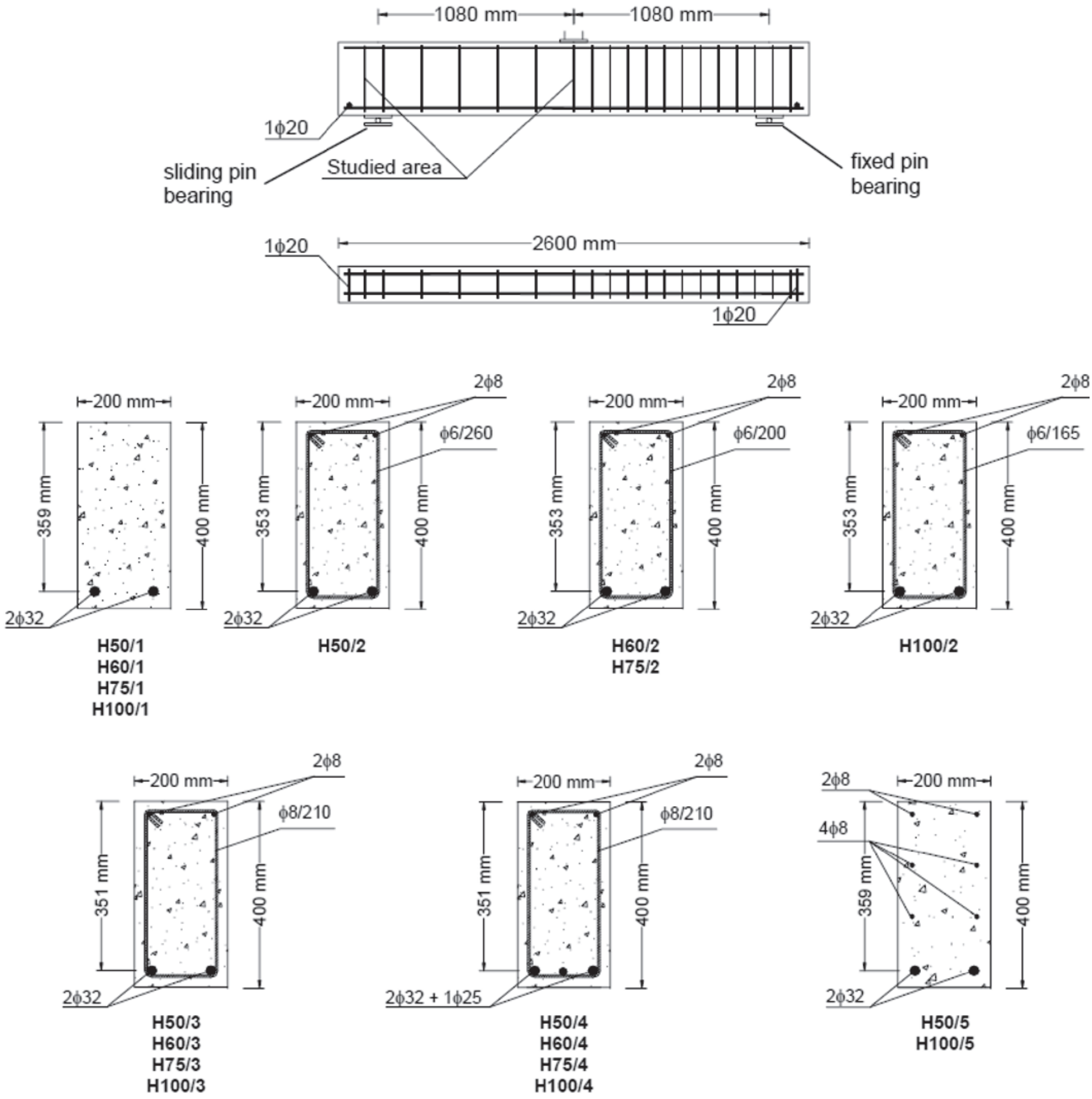

Figura 1
Esquema de ensaio e seções transversais das vigas ensaiadas. (Cladera [2])

Tabela 1
ANN para vigas com armadura transversal. Amplitude de parâmetros da base de dados [4]

Parâmetro	Mínimo	Máximo
d (mm)	198	925
d/b	0,792	4,5
ρ_l (%)	0,50	5,80
ρ_w (MPa)	0,33	3,57
f_c (MPa)	21	125,2
a/d	2,49	5,00
V (kN)	63,28	1172,19

de elementos de concreto de alta resistência, especificamente, à ação de força cortante. Conforme destaca Arslan [3], a contribuição do concreto é importante no dimensionamento de vigas em que a força cortante solicitante é próxima do valor de esforço requerido para produzir ruptura da diagonal tracionada, além de ser necessária para dimensionamentos econômicos de vigas e lajes com pouca ou nenhuma armadura transversal.

Dentre os estudos experimentais acerca de vigas de concreto de alta resistência solicitadas à cortante, destacam-se o de Cladera [2] e o de Cladera & Marí [4]. No primeiro, foram ensaiadas 18 vigas de concreto armado - cujas características são ilustradas na Figura 1 - com resistências à compressão entre 50 a 87 MPa, no Laboratório de Tecnologia Estrutural do Departamento de Engenharia da Construção na Escola de Engenharia Civil de Barcelona. Os principais objetivos do programa experimental eram estudar a influência da resistência à compressão em vigas com e sem armadura transversal; propor e verificar uma quantidade de armadura mínima mais adequada que a proposta pelo código espanhol EHE *Instrución de Hormigón Estructural* de 1998; avaliar a eficiência da quantidade de estribos e de armadura longitudinal em função do f_{ck} e estudar a influência da distribuição longitudinal de armadura em vigas sem estribos.

No segundo [4], foram avaliados o Eurocode 2, AASHTO LRFD e o ACI 318-02 a partir de uma rede artificial neural (ANN - Artificial Neural Network) baseada em 123 vigas-teste de concreto de alta resistência. A partir dos resultados da ANN, os autores analisaram as influências da quantidade de estribos, dos efeitos das dimensões da viga e profundidade útil, da resistência à compressão do concreto, da quantidade de armadura longitudinal e da razão entre vão de cortante e altura útil na resistência ao cisalhamento. Dos resultados, propuseram um método alternativo de dimensionamento. A ANN contemplou vigas-teste com as características indicadas na Tabela 1.

1.1 Justificativa

A expansão do uso de concretos de alta resistência aponta para a necessidade da melhor compreensão do comportamento estrutural dos elementos por eles constituídos. Este entendimento passa pela análise dos tratamentos normativos usuais. Das análises e simulações numéricas, fazem-se comparações para explicitar como cada norma aborda a questão, especificamente, do dimensionamento à força cortante. Em acréscimo a estes, as contribuições experimentais de Cladera [2] e Cladera & Marí [4] fundamentarão as análises comparativas entre as previsões normativas de área de armadura transversal e as que seriam exigidas segundo os resultados experimentais. Serão também englobados na análise os esforços cortantes resistentes últimos, tanto os previstos experimentalmente quanto os obtidos via cálculo normativo.

2. Tratamentos normativos analisados

2.1 NBR 6118:2014 [5]

A norma brasileira possui dois modelos de cálculo de elementos lineares submetidos à força cortante. Para ambos, é válida a taxa geométrica mínima de armadura dada por:

$$\rho_{sw} = \frac{A_{sw}}{b_w \cdot s \cdot \text{sen}\alpha} \geq 0{,}2\frac{f_{ct,m}}{f_{ywk}} \quad (1)$$

onde:
A_{sw} é a área da seção transversal dos estribos;
s é o espaçamento dos estribos, medido segundo o eixo longitudinal do elemento estrutural;
α é a inclinação dos estribos em relação ao eixo longitudinal do elemento estrutural, situado no intervalo 45° ≤ α ≤ 90°;
b_w é a largura média da alma, medida ao longo da altura útil da seção;
f_{ywk} é a resistência característica ao escoamento do aço da armadura transversal;
$f_{ct,m}$ = 2,12 ln (1 + 0,11 f_{ck}) para concretos de classes C55 até C90.
A resistência é considerada satisfatória quando verificadas simultaneamente as seguintes condições:

$$V_{Sd} \leq V_{Rd2} \quad (2)$$

$$V_{Sd} \leq V_{Rd3} = V_c + V_{sw} \quad (3)$$

onde:
V_{Sd} é a força cortante solicitante de cálculo, na seção;
V_{Rd2} é a força cortante resistente de cálculo, relativa à ruína das diagonais comprimidas;
V_{Rd3} é a força cortante resistente de cálculo, relativa à ruína por tração diagonal, onde V_c é a parcela de força cortante absorvida por mecanismos complementares ao da treliça e V_{sw} a parcela resistida pela armadura transversal.

2.1.1 Modelo de cálculo I

Este, regido pelas expressões a seguir, admite diagonais comprimidas inclinadas de θ = 45° em relação ao eixo longitudinal do elemento estrutural e parcela complementar V_c constante e independente de V_{Sd}.
a) Verificação da compressão diagonal do concreto:

$$V_{Rd2} = 0{,}27 \propto_{v2} f_{cd}\, b_w\, d \quad (4)$$

onde:
$\propto_{v2}$ = (1 - f_{ck}/250) e f_{ck} em MPa;
b) Cálculo da armadura transversal:

$$V_{Rd3} = V_c + V_{sw} \quad (5)$$

onde:
V_{sw} = (A_{sw} / s) 0,9df_{ywd} (senα + cosα)
V_c = V_{c0} = 0,6 f_{ctd} b_w d

$f_{ctd} = f_{ctk,inf} / \gamma_c = 0,7\ f_{ct,m} / \gamma_c$
onde:
d é a distância entre a borda comprimida ao centro de gravidade da armadura de tração;
f_{ywd} é a tensão na armadura transversal passiva não superior a 435 MPa.

2.1.2 Modelo de cálculo II

Este, por sua vez, admite inclinações θ entre 30° e 45° e redução de V_c com o aumento de V_{Sd}.
a) Verificação da compressão diagonal do concreto:

$$V_{Rd2} = 0{,}54 \propto_{v2} f_{cd}\, b_w\, d\, \text{sen}^2\theta\, (\text{cotg}\,\alpha + \text{cotg}\,\theta) \quad (6)$$

b) Cálculo da armadura transversal: conforme a Equação 5, sendo:
$V_{sw} = (A_{sw} / s)\ 0{,}9df_{ywd}\ (\text{cotg}\ \alpha + \text{cotg}\ \theta)\ \text{sen}\alpha$;
$V_{c1} = V_{c0}$ quando $V_{Sd} \leq V_{c0}$;
$V_{c1} = 0$ quando $V_{Sd} = V_{Rd2}$;

$$V_{c1} = \left(\frac{V_{Rd2} - V_{Sd}}{V_{Rd2} - V_{c0}}\right) V_{c0} \text{ para valores intermediários.}$$

2.2 CEB-FIP Model Code 1990 [6]

O código modelo de 1990 traz em sua seção 6.3.3 *Shear and axial action effects* as considerações de cálculo apresentadas adiante. Esta norma estabelece inclinação da diagonal comprimida θ entre 18,4° e 45°.

Tabela 2
Resultados do Modelo I da NBR 6118

f_{ck} (MPa)	$f_{ct,m}$ (MPa)	f_{ctd} (MPa)	b_w (cm)	d (cm)	V_{Sd} (kN)	V_{Rd2} (kN)	V_{c0} (kN)	V_{sw} (kN)	A_{sw} (cm²/m)
55	4,14	2,07	12	40	100,00	397,13	59,62	40,38	2,58
55	4,14	2,07	12	40	125,00	397,13	59,62	65,38	4,17
55	4,14	2,07	12	40	150,00	397,13	59,62	90,38	5,77
55	4,14	2,07	12	40	175,00	397,13	59,62	115,38	7,37
60	4,30	2,15	12	40	100,00	422,13	61,92	38,08	2,43
60	4,30	2,15	12	40	125,00	422,13	61,92	63,08	4,03
60	4,30	2,15	12	40	150,00	422,13	61,92	88,08	5,62
60	4,30	2,15	12	40	175,00	422,13	61,92	113,08	7,22
70	4,59	2,29	12	40	100,00	466,56	66,04	33,96	2,20
70	4,59	2,29	12	40	125,00	466,56	66,04	58,96	3,76
70	4,59	2,29	12	40	150,00	466,56	66,04	83,96	5,36
70	4,59	2,29	12	40	175,00	466,56	66,04	108,96	6,96
80	4,84	2,42	12	40	100,00	503,59	69,68	30,32	2,32
80	4,84	2,42	12	40	125,00	503,59	69,68	55,32	3,53
80	4,84	2,42	12	40	150,00	503,59	69,68	80,32	5,13
80	4,84	2,42	12	40	175,00	503,59	69,68	105,32	6,73
90	5,06	2,53	12	40	100,00	533,21	72,92	27,08	2,43
90	5,06	2,53	12	40	125,00	533,21	72,92	52,08	3,33
90	5,06	2,53	12	40	150,00	533,21	72,92	77,08	4,92
90	5,06	2,53	12	40	175,00	533,21	72,92	102,08	6,52

Tabela 3
Resultados do Modelo II da NBR 6118

f_{ck} (MPa)	$f_{ct,m}$ (MPa)	f_{ctd} (MPa)	θ°	b_w (cm)	d (cm)	V_{Sd} (kN)	V_{Rd2} (kN)	V_{c1} (kN)	V_{sw} (kN)	A_{sw} (cm²/m)
55	4,14	2,07	45	12	40	100,00	397,13	52,49	47,51	3,03
55	4,14	2,07	45	12	40	125,00	397,13	48,07	76,93	4,91
55	4,14	2,07	45	12	40	150,00	397,13	43,66	106,34	6,79
55	4,14	2,07	45	12	40	175,00	397,13	39,24	135,76	8,67
60	4,30	2,15	45	12	40	100,00	422,13	55,37	44,63	2,85
60	4,30	2,15	45	12	40	125,00	422,13	51,07	73,93	4,72
60	4,30	2,15	45	12	40	150,00	422,13	46,77	103,23	6,59
60	4,30	2,15	45	12	40	175,00	422,13	42,48	132,52	8,46
70	4,59	2,29	45	12	40	100,00	466,56	60,44	39,56	2,53
70	4,59	2,29	45	12	40	125,00	466,56	56,32	68,68	4,39
70	4,59	2,29	45	12	40	150,00	466,56	52,20	97,80	6,25
70	4,59	2,29	45	12	40	175,00	466,56	48,08	126,92	8,11
80	4,84	2,42	45	12	40	100,00	503,59	64,81	35,19	2,32
80	4,84	2,42	45	12	40	125,00	503,59	60,79	64,21	4,10
80	4,84	2,42	45	12	40	150,00	503,59	56,78	93,22	5,95
80	4,84	2,42	45	12	40	175,00	503,59	52,76	122,24	7,81
90	5,06	2,53	45	12	40	100,00	533,21	68,63	31,37	2,43
90	5,06	2,53	45	12	40	125,00	533,21	64,67	60,33	3,85
90	5,06	2,53	45	12	40	150,00	533,21	60,71	89,29	5,70
90	5,06	2,53	45	12	40	175,00	533,21	56,75	118,25	7,55

a) Taxa de armadura transversal mínima:

$$\omega_{sw} = \frac{A_{sw} \cdot f_{yk}}{b_w \cdot s \cdot f_{ctm} \cdot \text{sen}\alpha} \geq 0{,}2 \qquad (7)$$

onde:

$$f_{ctm} = f_{ctko,m} \left(\frac{f_{ck}}{f_{cko}} \right)^{2/3}$$

f_{cko} = 10 MPa

$f_{ctko,m}$ = 1,40 MPa

b) Esforço cortante resistente máximo, para θ = 45°:

$$V_{Rd,max} = \frac{f_{cd2}}{2} b_w z(1 + \text{cotg } \propto) \qquad (8)$$

onde:

c) Esforço resistente dos estribos:

$$F_{Stw} = \frac{V_{Sd}}{\text{sen } \propto} \qquad (9)$$

$$F_{Rtw} = \left[\frac{A_{sw} \cdot f_{yd}}{s} \right] z(\text{cotg } \theta + \text{cotg } \alpha) \qquad (10)$$

onde:

F_{Stw} é a força solicitante da armadura transversal;

F_{Rtw} é a força resistente da armadura transversal.

Tabela 4
Resultados do MC 1990

f_{ck} (MPa)	$f_{ct,m}$ (MPa)	f_{cd2} (MPa)	b_w (cm)	d (cm)	θ°	$V_{Rd,max}$ (kN)	V_{Sd} (kN)	F_{Stw} (kN)	A_{sw} (cm²/m)
55	4,36	17,16	12	40	45	370,66	100,00	100,00	6,39
55	4,36	17,16	12	40	45	370,66	125,00	125,00	7,99
55	4,36	17,16	12	40	45	370,66	150,00	150,00	9,58
55	4,36	17,16	12	40	45	370,66	175,00	175,00	11,18
60	4,62	18,24	12	40	45	393,98	100,00	100,00	6,39
60	4,62	18,24	12	40	45	393,98	125,00	125,00	7,99
60	4,62	18,24	12	40	45	393,98	150,00	150,00	9,58
60	4,62	18,24	12	40	45	393,98	175,00	175,00	11,18
70	5,12	20,16	12	40	45	435,46	100,00	100,00	6,39
70	5,12	20,16	12	40	45	435,46	125,00	125,00	7,99
70	5,12	20,16	12	40	45	435,46	150,00	150,00	9,58
70	5,12	20,16	12	40	45	435,46	175,00	175,00	11,18
80	5,60	21,76	12	40	45	470,02	100,00	100,00	6,39
80	5,60	21,76	12	40	45	470,02	125,00	125,00	7,99
80	5,60	21,76	12	40	45	470,02	150,00	150,00	9,58
80	5,60	21,76	12	40	45	470,02	175,00	175,00	11,18
90	6,06	23,04	12	40	45	497,66	100,00	100,00	6,39
90	6,06	23,04	12	40	45	497,66	125,00	125,00	7,99
90	6,06	23,04	12	40	45	497,66	150,00	150,00	9,58
90	6,06	23,04	12	40	45	497,66	175,00	175,00	11,18

Tabela 5
Resultados do MC 2010 para LoA I

f_{ck} (MPa)	$f_{ct,m}$ (MPa)	b_w (cm)	d (cm)	θ°	k_ε	k_c	V_{Ed} (kN)	$V_{Rd,max}$ (kN)	$V_{Rd,s}$ (kN)	A_{sw} (cm²/m)
55	4,21	12	40	45	0,55	0,45	100,00	355,91	100,00	6,39
55	4,21	12	40	45			125,00	355,91	125,00	7,99
55	4,21	12	40	45			150,00	355,91	150,00	9,58
55	4,21	12	40	45			175,00	355,91	175,00	11,18
60	4,35	12	40	45	0,55	0,44	100,00	377,17	100,00	6,39
60	4,35	12	40	45			125,00	377,17	125,00	7,99
60	4,35	12	40	45			150,00	377,17	150,00	9,58
60	4,35	12	40	45			175,00	377,17	175,00	11,18
70	4,61	12	40	45	0,55	0,41	100,00	417,99	100,00	6,39
70	4,61	12	40	45			125,00	417,99	125,00	7,99
70	4,61	12	40	45			150,00	417,99	150,00	9,58
70	4,61	12	40	45			175,00	417,99	175,00	11,18
80	4,84	12	40	45	0,55	0,40	100,00	456,90	100,00	6,39
80	4,84	12	40	45			125,00	456,90	125,00	7,99
80	4,84	12	40	45			150,00	456,90	150,00	9,58
80	4,84	12	40	45			175,00	456,90	175,00	11,18
90	5,04	12	40	45	0,55	0,38	100,00	494,23	100,00	6,39
90	5,04	12	40	45			125,00	494,23	125,00	7,99
90	5,04	12	40	45			150,00	494,23	150,00	9,58
90	5,04	12	40	45			175,00	494,23	175,00	11,18

2.3 CEB-FIP Model Code 2010 [7]

Adiante, apresentam-se as considerações de cálculo da versão 2010 do código modelo.

a) Área de armadura transversal mínima:

$$A_{sw,min} = 0{,}08 \cdot \sqrt{f_{ck}} \cdot \frac{b_w \cdot s_w}{f_{yk}} \quad (11)$$

b) Esforço cortante resistente de projeto:

$$V_{Rd} = V_{Rd,c} + V_{Rd,s} \geq V_{Ed} \quad (12)$$

onde:

V_{Rd} é a resistência à cortante de projeto;

$V_{Rd,c}$ é a resistência à cortante atribuída ao concreto;

$V_{Rd,s}$ é a resistência à cortante provida pela armadura transversal;

V_{Ed} é a força cortante de projeto.

c) Esforço cortante resistente máximo, para estribos a 90°:

$$V_{Rd,max} = k_c \cdot \frac{f_{ck}}{\gamma_c} \cdot b_w \cdot z \cdot \text{sen}\,\theta \cdot \cos\theta \quad (13)$$

onde:

$k_c = k_\varepsilon \cdot \eta_{fc}$ é o fator de redução da resistência;

Tabela 6

Resultados do MC 2010 para LoA II

f_{ck} (MPa)	b_w (cm)	d (cm)	k_ε	k_c	V_{Ed} (kN)	$V_{Rd,max}$ (kN)	$V_{Rd,s}$ (kN)	A_{sw} (cm²/m)
55	12	40	0,65	0,53	100,00	420,62	100,00	6,39
55	12	40			125,00	420,62	125,00	7,99
55	12	40			150,00	420,62	150,00	9,58
55	12	40			175,00	420,62	175,00	11,18
60	12	40	0,65	0,52	100,00	445,74	100,00	6,39
60	12	40			125,00	445,74	125,00	7,99
60	12	40			150,00	445,74	150,00	9,58
60	12	40			175,00	445,74	175,00	11,18
70	12	40	0,65	0,49	100,00	493,99	100,00	6,39
70	12	40			125,00	493,99	125,00	7,99
70	12	40			150,00	493,99	150,00	9,58
70	12	40			175,00	493,99	175,00	11,18
80	12	40	0,65	0,47	100,00	539,98	100,00	6,39
80	12	40			125,00	539,98	125,00	7,99
80	12	40			150,00	539,98	150,00	9,58
80	12	40			175,00	539,98	175,00	11,18
90	12	40	0,65	0,38	100,00	584,09	100,00	6,39
90	12	40			125,00	584,09	125,00	7,99
90	12	40			150,00	584,09	150,00	9,58
90	12	40			175,00	584,09	175,00	11,18

Tabela 7

Resultados do MC 2010 para LoA III

f_{ck} (MPa)	b_w (cm)	d (cm)	θ_{min}	ε_x	k_ε	k_c	k_v	V_{Ed} (kN)	$V_{Rd,min}$ (kN)	$V_{Rd,c}$ (kN)	$V_{Rd,s}$ (kN)	A_{sw} (cm²/m)
55	12	40	30	0,001	0,65	0,53	0,116	100,00	364,27	24,79	75,21	4,80
55	12	40	30				0,105	125,00	364,27	22,45	102,55	6,55
55	12	40	30				0,094	150,00	364,27	20,10	129,90	8,30
55	12	40	30				0,083	175,00	364,27	17,76	157,24	10,05
60	12	40	30	0,001	0,65	0,52	0,119	100,00	386,02	26,45	73,55	4,70
60	12	40	30				0,108	125,00	386,02	24,14	100,86	6,44
60	12	40	30				0,098	150,00	386,02	21,82	128,18	8,19
60	12	40	30				0,087	175,00	386,02	19,51	155,49	9,93
70	12	40	30	0,001	0,65	0,49	0,123	100,00	427,80	28,25	71,75	4,58
70	12	40	30				0,113	125,00	427,80	26,09	98,91	6,32
70	12	40	30				0,104	150,00	427,80	23,94	126,06	8,05
70	12	40	30				0,095	175,00	427,80	21,78	153,22	9,79
80	12	40	30	0,001	0,65	0,47	0,126	100,00	467,63	28,98	71,02	4,54
80	12	40	30				0,117	125,00	467,63	27,01	97,99	6,26
80	12	40	30				0,109	150,00	467,63	25,04	124,96	7,98
80	12	40	30				0,100	175,00	467,63	23,07	151,93	9,71
90	12	40	45	0,001	0,65	0,45	0,128	100,00	505,83	29,58	70,42	4,50
90	12	40	45				0,120	125,00	505,83	27,75	97,25	6,21
90	12	40	45				0,113	150,00	505,83	25,93	124,07	7,93
90	12	40	45				0,105	175,00	505,83	24,11	150,89	9,64

$$\eta_{f_c} = \left(\frac{30}{f_{ck}}\right)^{1/3} \leq 1{,}0 .$$

d) Esforço resistente dos estribos a 90°:
(Equação 14)
e) Esforço resistente atribuído ao concreto:

$$V_{Rd,c} = k_v \cdot \frac{\sqrt{f_{ck}}}{\gamma_c} \cdot b_w \cdot z \tag{15}$$

onde:

$$\sqrt{f_{ck}} \leq 8\text{MPa}.$$

f) Inclinação da diagonal comprimida:

$$\theta_{\min} \leq \theta \leq 45° \tag{16}$$

O código apresenta ainda a metodologia dos níveis de aproximação (*Levels of approximation*). Segundo Muttoni e Ruiz [8], esta abordagem é baseada no uso de teorias embasadas em parâmetros físicos em que as hipóteses para as suas aplicações podem ser refinadas conforme a demanda por acurácia. Conforme destaca Barros [9], o aumento do nível de aproximação (I ao IV) é acompanhado pelo aumento da precisão e do tempo depreendido para as análises.

Tabela 8
Resultados da NP EN 1992-1-1, com υ

f_{ck} (MPa)	$f_{ct,m}$ (MPa)	υ	b_w (cm)	d (cm)	V_{Ed} (kN)	$V_{Rd,max}$ (kN)	$V_{Rd,s}$ (kN)	A_{sw} (cm²/m)
55	4,21	0,468	12	40	100,00	370,66	100,00	6,39
55	4,21	0,468	12	40	125,00	370,66	125,00	7,99
55	4,21	0,468	12	40	150,00	370,66	150,00	9,58
55	4,21	0,468	12	40	175,00	370,66	175,00	11,18
60	4,35	0,456	12	40	100,00	393,98	100,00	6,39
60	4,35	0,456	12	40	125,00	393,98	125,00	7,99
60	4,35	0,456	12	40	150,00	393,98	150,00	9,58
60	4,35	0,456	12	40	175,00	393,98	175,00	11,18
70	4,61	0,432	12	40	100,00	435,46	100,00	6,39
70	4,61	0,432	12	40	125,00	435,46	125,00	7,99
70	4,61	0,432	12	40	150,00	435,46	150,00	9,58
70	4,61	0,432	12	40	175,00	435,46	175,00	11,18
80	4,84	0,408	12	40	100,00	470,02	100,00	6,39
80	4,84	0,408	12	40	125,00	470,02	125,00	7,99
80	4,84	0,408	12	40	150,00	470,02	150,00	9,58
80	4,84	0,408	12	40	175,00	470,02	175,00	11,18
90	5,04	0,384	12	40	100,00	497,66	100,00	6,39
90	5,04	0,384	12	40	125,00	497,66	125,00	7,99
90	5,04	0,384	12	40	150,00	497,66	150,00	9,58
90	5,04	0,384	12	40	175,00	497,66	175,00	11,18

Tabela 9
Resultados da NP EN 1992-1-1, com υ_1

f_{ck} (MPa)	υ_1	b_w (cm)	d (cm)	V_{Ed} (kN)	$V_{Rd,max}$ (kN)	$V_{Rd,s}$ (kN)	A_{sw} (cm²/m)
55	0,60	12	40	100,00	475,20	100,00	6,94
55	0,60	12	40	125,00	475,20	125,00	8,68
55	0,60	12	40	150,00	475,20	150,00	10,42
55	0,60	12	40	175,00	475,20	175,00	12,15
60	0,60	12	40	100,00	518,40	100,00	6,94
60	0,60	12	40	125,00	518,40	125,00	8,68
60	0,60	12	40	150,00	518,40	150,00	10,42
60	0,60	12	40	175,00	518,40	175,00	12,15
70	0,55	12	40	100,00	554,40	100,00	6,94
70	0,55	12	40	125,00	554,40	125,00	8,68
70	0,55	12	40	150,00	554,40	150,00	10,42
70	0,55	12	40	175,00	554,40	175,00	12,15
80	0,50	12	40	100,00	576,00	100,00	6,94
80	0,50	12	40	125,00	576,00	125,00	8,68
80	0,50	12	40	150,00	576,00	150,00	10,42
80	0,50	12	40	175,00	576,00	175,00	12,15
90	0,50	12	40	100,00	648,00	100,00	6,94
90	0,50	12	40	125,00	648,00	125,00	8,68
90	0,50	12	40	150,00	648,00	150,00	10,42
90	0,50	12	40	175,00	648,00	175,00	12,15

2.3.1 Level I of approximation

Para este nível, desconsidera-se a parcela $V_{Rd,c}$ da Equação 12. Para membros de concreto armado, toma-se θ_{min} = 30°. Além disso, para o cálculo de $V_{Rd,max}$, 0,55.

2.3.2 Level II of approximation

Assim como no *LoA I*, desconsidera-se a parcela $V_{Rd,c}$ da Equação 12. A inclinação mínima da biela é dada pela Equação 17, mas será adotada em 30°. Além disso, o parâmetro k_{ε}, dado pela Equação 18, assumirá o seu valor máximo de 0,65 nas simulações desenvolvidas adiante.

$$\theta_{\min} = 20° + 10000\varepsilon_x \quad (17)$$

$$k_{\varepsilon} = \frac{1}{1,2 + 55\varepsilon_1} \leq 0,65 \quad (18)$$

2.3.3 Level III of approximation

Para este nível, é válida a Equação 12. O esforço cortante resistente

Tabela 10
Resultados da DIN 1045-1

f_{ck} (MPa)	$f_{ct,m}$ (MPa)	b_w (cm)	d (cm)	V_{Ed} (kN)	$V_{Rd,max}$ (kN)	$V_{Rd,s}$ (kN)	A_{sw} (cm²/m)
55	4,21	12	40	100,00	891,00	100,00	6,39
55	4,21	12	40	125,00	891,00	125,00	7,99
55	4,21	12	40	150,00	891,00	150,00	9,58
55	4,21	12	40	175,00	891,00	175,00	11,18
60	4,35	12	40	100,00	972,00	100,00	6,39
60	4,35	12	40	125,00	972,00	125,00	7,99
60	4,35	12	40	150,00	972,00	150,00	9,58
60	4,35	12	40	175,00	972,00	175,00	11,18
70	4,61	12	40	100,00	1134,00	100,00	6,39
70	4,61	12	40	125,00	1134,00	125,00	7,99
70	4,61	12	40	150,00	1134,00	150,00	9,58
70	4,61	12	40	175,00	1134,00	175,00	11,18
80	4,84	12	40	100,00	1296,00	100,00	6,39
80	4,84	12	40	125,00	1296,00	125,00	7,99
80	4,84	12	40	150,00	1296,00	150,00	9,58
80	4,84	12	40	175,00	1296,00	175,00	11,18
90	5,04	12	40	100,00	1458,00	100,00	6,39
90	5,04	12	40	125,00	1458,00	125,00	7,99
90	5,04	12	40	150,00	1458,00	150,00	9,58
90	5,04	12	40	175,00	1458,00	175,00	11,18

Tabela 11
Áreas de armadura transversal (cm²/m) para vigas de 20 cm x 60 cm

f_{ck} (MPa)	V_{Sd} (kN)	NBR		MC 1990	MC 2010			NP EN 1992		DIN 1045
		M I	M II		LoA I	LoA II	LoA III	ν	ν_1	
55	200,00	3,31	3,31	8,52	8,52	8,52	5,68	8,52	9,26	8,52
55	250,00	4,30	5,06	10,65	10,65	10,65	8,01	10,65	11,57	10,65
55	300,00	6,43	7,56	12,78	12,78	12,78	10,34	12,78	13,89	12,78
55	375,00	9,62	11,32	15,97	15,97	15,97	13,83	15,97	17,36	15,97
60	200,00	3,44	3,44	8,52	8,52	8,52	5,51	8,52	9,26	8,52
60	250,00	4,05	4,75	10,65	10,65	10,65	7,83	10,65	11,57	10,65
60	300,00	6,18	7,24	12,78	12,78	12,78	10,16	12,78	13,89	12,78
60	375,00	9,37	10,99	15,97	15,97	15,97	13,65	15,97	17,36	15,97
70	200,00	3,67	3,67	8,52	8,52	8,52	5,33	8,52	9,26	8,52
70	250,00	3,67	4,21	10,65	10,65	10,65	7,64	10,65	11,57	10,65
70	300,00	5,74	6,69	12,78	12,78	12,78	9,95	12,78	13,89	12,78
70	375,00	8,94	10,41	15,97	15,97	15,97	13,42	15,97	17,36	15,97
80	200,00	3,87	3,87	8,52	8,52	8,52	5,26	8,52	9,26	8,52
80	250,00	3,87	3,87	10,65	10,65	10,65	7,56	10,65	11,57	10,65
80	300,00	5,36	6,22	12,78	12,78	12,78	9,86	12,78	13,89	12,78
80	375,00	8,55	9,92	15,97	15,97	15,97	13,31	15,97	17,36	15,97
90	200,00	4,05	4,05	8,52	8,52	8,52	5,21	8,52	9,26	8,52
90	250,00	4,05	4,05	10,65	10,65	10,65	7,50	10,65	11,57	10,65
90	300,00	5,01	5,80	12,78	12,78	12,78	9,78	12,78	13,89	12,78
90	375,00	8,20	9,50	15,97	15,97	15,97	13,21	15,97	17,36	15,97

máximo é dado pela Equação 13 para $\theta = \theta_{min}$, dado pela Equação 17 e aqui admitido igual a 30°. Para determinação da parcela $V_{Rd,c}$ atribuída ao concreto pela Equação 15, o parâmetro k_v é calculado pela Equação 19. Para os exemplos de cálculo adiante, admite-se $\varepsilon_x = 0{,}001$.

$$k_v = \frac{0{,}4}{1+1500\varepsilon_x}\left(1-\frac{V_{Ed}}{V_{Rd,max}(\theta_{min})}\right) \geq 0 \quad (19)$$

2.3.4 Level IV of approximation

O código modelo não traz expressões específicas para este nível de aproximação, mas estabelece que a resistência de membros em cisalhamento ou cisalhamento combinado com torção pode ser determinada pela satisfação de condições aplicáveis de equilíbrio e compatibilidade de deformações e ao se utilizar modelos de tensão-deformação apropriados para o aço e para concretos com fissuras diagonais.

2.4 NP EN 1992-1-1:2010 [10]

As considerações de cálculo da norma portuguesa são expostas adiante.

a) Taxa de armadura transversal mínima: também dada pela Equação 11;

b) Esforço cortante resistente de projeto:

$$V_{Rd} = V_{Rd,s} + V_{ccd} + V_{td} \quad (20)$$

onde:

$V_{Rd,s}$ é o valor de cálculo do esforço cortante equilibrado pela armadura transversal na tensão de escoamento;

V_{ccd} é a componente do esforço cortante da força de compressão (banzo comprimido inclinado);

V_{td} é a componente do esforço cortante na armadura de tração (banzo tracionado inclinado).

c) Inclinação da diagonal comprimida:

$$21{,}8° \leq \theta \leq 45° \quad (21)$$

d) Esforço cortante resistente máximo, para estribos a 90°:

$$V_{Rd,max} = \alpha_{cw} \cdot b_w \cdot z \cdot \nu_1 \cdot \frac{f_{ck}}{\gamma_c} / (\cot\theta + \operatorname{tg}\theta) \quad (22)$$

onde:

ν_1 é o coeficiente de redução da resistência do concreto fissurado por cortante;

α_{cw} é o coeficiente que tem em conta o estado de tensão no banzo comprimido. Para elementos em concreto armado, $\alpha_{cw} = 1{,}0$. O valor de ν_1 é dado pela Equação 23.

$$\nu = 0{,}6\left[1-\frac{f_{ck}}{250}\right] \quad (23)$$

Se o valor de cálculo da tensão da armadura transversal for inferior a 80% do valor característico de escoamento f_{yk}, poderá adotar-se para ν_1:

$\nu_1 = 0{,}6$ para $f_{ck} \leq 60$ MPa

$\nu_1 = 0{,}9 - f_{ck} / 200 > 0{,}5$ para $f_{ck} \geq 60$ MPa

e) Esforço resistente dos estribos a 90°:

$$V_{Rd,s} = \frac{A_{sw}}{s} \cdot f_{ywd} \cdot z \cdot \cot\theta \quad (24)$$

f) Área efetiva máxima de armadura transversal, para $\theta = 45°$:

$$\frac{A_{sw,max} \cdot f_{ywd}}{b_w \cdot s} \leq \frac{0{,}5 \cdot \alpha_{cw} \cdot \nu_1 \cdot f_{cd}}{sen\,\alpha} \quad (25)$$

2.5 DIN 1045-1:2001-07 [11]

A norma alemã estabelece as considerações de cálculo que se seguem.

a) Inclinação das bielas:

$$18{,}43° \leq \theta \leq 59{,}88° \quad (26)$$

b) Esforço cortante resistente máximo, para estribos a 90°:

$$V_{Rd,max} = \frac{b_w \cdot z \cdot \alpha_c \cdot f_{ck}}{\cot\theta + \operatorname{tg}\theta} \quad (27)$$

onde:

α_c é um fator de redução dado por $0{,}75\,\eta_1$, isto é, 0,75 para concretos normais.

Tabela 12
Áreas de armadura transversal (cm²/m) para vigas de 60 cm x 165 cm

f_{ck} (MPa)	V_{Sd} (kN)	NBR		MC 1990	MC 2010			NP EN 1992		DIN 1045
		M I	M II		LoA I	LoA II	LoA III	ν	ν_1	
55	3000	27,41	32,25	46,46	46,46	46,46	39,91	46,46	50,51	46,46
55	3200	30,50	35,89	49,56	49,56	49,56	43,30	49,56	53,87	49,56
55	3400	33,60	39,53	52,66	52,66	52,66	46,68	52,66	57,24	52,66
55	3600	36,69	43,18	55,76	55,76	55,76	50,07	55,76	60,61	55,76
60	3000	26,67	31,26	46,46	46,46	46,46	39,36	46,46	50,51	46,46
60	3200	29,77	34,89	49,56	49,56	49,56	42,74	49,56	53,87	49,56
60	3400	32,86	38,51	52,66	52,66	52,66	46,13	52,66	57,24	52,66
60	3600	35,96	42,14	55,76	55,76	55,76	49,51	55,76	60,61	55,76
70	3000	25,36	29,54	46,46	46,46	46,46	38,69	46,46	50,51	46,46
70	3200	28,45	33,14	49,56	49,56	49,56	42,06	49,56	53,87	49,56
70	3400	31,55	36,75	52,66	52,66	52,66	45,42	52,66	57,24	52,66
70	3600	34,64	40,36	55,76	55,76	55,76	48,79	55,76	60,61	55,76
80	3000	24,19	28,08	46,46	46,46	46,46	38,35	46,46	50,51	46,46
80	3200	27,29	31,67	49,56	49,56	49,56	41,69	49,56	53,87	49,56
80	3400	30,39	35,27	52,66	52,66	52,66	45,04	52,66	57,24	52,66
80	3600	33,48	38,86	55,76	55,76	55,76	48,38	55,76	60,61	55,76
90	3000	23,16	26,83	46,46	46,46	46,46	38,07	46,46	50,51	46,46
90	3200	26,25	30,41	49,56	49,56	49,56	41,40	49,56	53,87	49,56
90	3400	29,35	34,00	52,66	52,66	52,66	44,72	52,66	57,24	52,66
90	3600	32,45	37,59	55,76	55,76	55,76	48,05	55,76	60,61	55,76

c) Esforço resistente dos estribos a 90°:

$$V_{Rd,sy} = \frac{A_{sw}}{s_w} \cdot f_{yd} \cdot z \cdot \text{cotg}\,\theta \quad (28)$$

3. Simulações numéricas das áreas de armadura transversal pelas normas

Com o intuito de avaliar cada tratamento analisado, são propostas três situações de cálculo, cada qual com quatro intensidades de força cortante e considerando as classes de alta resistência do concreto. Para fins comparativos, foram adotadas inclinações de biela de θ = 45° em todos. As áreas foram calculadas a partir das expressões apresentadas na seção 2.

Após as situações de cálculo propostas, serão avaliados os esforços cortantes resistentes últimos obtidos a partir das metodologias de cálculo dos procedimentos normativos estudados.

3.1 Exemplo 01

O primeiro exemplo é de uma viga de 12 cm de largura por 40 cm, solicitada por quatro intensidades de força cortante: 100 kN, 125 kN, 150 kN e 175 kN. As áreas de armadura transversal obtidas são apresentadas nas tabelas 2 a 10.

3.2 Exemplo 02

O segundo exemplo é de uma viga de 20 cm de largura por 60 cm, solicitada por forças cortantes de 200 kN, 250 kN, 300 kN e 375 kN. Na tabela 11, são dispostos os valores de áreas obtidas a partir de cada tratamento normativo.

3.3 Exemplo 03

O exemplo 03 corresponde a uma viga de 60 cm de largura por 165 cm, submetida a esforços cortantes de 3000 kN, 3200 kN, 3400 kN e 3600 kN. As áreas de cálculo obtidas são apresentadas na tabela 12.

3.4 Esforços cortantes resistentes últimos

Na Tabela 13, são apresentados os esforços cortantes resistentes

Tabela 13
Esforços cortantes resistentes últimos

Norma	V/bd (MPa)				
	C55	C60	C70	C80	C90
NBR – I	8,27	8,79	9,72	10,49	11,11
NBR – II	8,27	8,79	9,72	10,49	11,11
MC 1990	7,72	8,21	9,07	9,79	10,37
MC 2010 LoA I	7,41	7,86	8,71	9,52	10,30
MC 2010 LoA II	8,76	9,29	10,29	11,25	12,17
MC 2010 LoA III	7,59	8,04	8,91	9,74	10,54
NP EN 1992 ν	7,72	8,21	9,07	9,79	10,37
NP EN 1992 ν_1	9,90	10,80	11,55	12,00	13,50
DIN 1045	18,56	20,25	23,63	27,00	30,38

Tabela 14
Percentuais comparativos das áreas obtidas no exemplo 01

f_{ck} (MPa)	V_{Sd} (kN)	A_{sw} / $A_{sw\,(MC\,1990)}$ %								
		NBR		MC 1990	MC 2010			NP EN 1992		DIN 1045
		M I	M II		LoA I	LoA II	LoA III	ν	ν_1	
55	100	40,36	47,49	100,00	100,00	100,00	75,21	100,00	108,70	100,00
55	125	52,28	61,51	100,00	100,00	100,00	82,04	100,00	108,70	100,00
55	150	60,22	70,86	100,00	100,00	100,00	86,60	100,00	108,70	100,00
55	175	65,90	77,54	100,00	100,00	100,00	89,85	100,00	108,70	100,00
60	100	38,07	44,61	100,00	100,00	100,00	73,55	100,00	108,70	100,00
60	125	50,44	59,11	100,00	100,00	100,00	80,69	100,00	108,70	100,00
60	150	58,69	68,78	100,00	100,00	100,00	85,45	100,00	108,70	100,00
60	175	64,59	75,69	100,00	100,00	100,00	88,85	100,00	108,70	100,00
70	100	34,46	39,54	100,00	100,00	100,00	71,75	100,00	108,70	100,00
70	125	47,14	54,92	100,00	100,00	100,00	79,13	100,00	108,70	100,00
70	150	55,94	65,17	100,00	100,00	100,00	84,04	100,00	108,70	100,00
70	175	62,23	72,49	100,00	100,00	100,00	87,55	100,00	108,70	100,00
80	100	36,35	36,35	100,00	100,00	100,00	71,02	100,00	108,70	100,00
80	125	44,24	51,34	100,00	100,00	100,00	78,39	100,00	108,70	100,00
80	150	53,52	62,12	100,00	100,00	100,00	83,31	100,00	108,70	100,00
80	175	60,15	69,81	100,00	100,00	100,00	86,82	100,00	108,70	100,00
90	100	38,05	38,05	100,00	100,00	100,00	70,42	100,00	108,70	100,00
90	125	41,64	48,24	100,00	100,00	100,00	77,80	100,00	108,70	100,00
90	150	51,36	59,49	100,00	100,00	100,00	82,71	100,00	108,70	100,00
90	175	58,30	67,54	100,00	100,00	100,00	86,22	100,00	108,70	100,00

últimos, na forma de tensão (MPa), para cada classe de concreto, obtidos a partir das metodologias de cálculo dos procedimentos normativos estudados.

3.5 Comparação dos resultados

A partir dos resultados obtidos, apresentam-se as tabelas comparativas 14, 15 e 16 referentes, respectivamente, aos exemplos 01, 02 e 03. Para cada situação de intensidade de força cortante e seção transversal, apresentam-se os gráficos comparativos nas figuras 2, 3, 4, 5 (exemplo 01); 6, 7, 8, e 9 (exemplo 02); 10, 11, 12 e 13 (exemplo 03). Nas tabelas, as áreas resultantes foram tomadas percentualmente em relação às respectivas áreas calculadas pelo Model Code 1990.

Das tabelas 14, 15 e 16 constata-se que os tratamentos internacionais utilizados - com exceção do LoA III do MC 2010 [7] e do

Tabela 15
Percentuais comparativos das áreas obtidas no exemplo 02

f_{ck} (MPa)	V_{Sd} (kN)	$A_{sw} / A_{sw\,(MC\,1990)}$ %								
		NBR		MC 1990	MC 2010			NP EN 1992		DIN 1045
		M I	M II		LoA I	LoA II	LoA III	ν	ν_1	
55	200	38,88	38,88	100,00	100,00	100,00	66,66	100,00	108,70	100,00
55	250	40,36	47,49	100,00	100,00	100,00	75,21	100,00	108,70	100,00
55	300	50,29	59,17	100,00	100,00	100,00	80,90	100,00	108,70	100,00
55	375	60,22	70,86	100,00	100,00	100,00	86,60	100,00	108,70	100,00
60	200	40,38	40,38	100,00	100,00	100,00	64,63	100,00	108,70	100,00
60	250	38,07	44,61	100,00	100,00	100,00	73,55	100,00	108,70	100,00
60	300	48,38	56,70	100,00	100,00	100,00	79,50	100,00	108,70	100,00
60	375	58,69	68,78	100,00	100,00	100,00	85,45	100,00	108,70	100,00
70	200	43,07	43,07	100,00	100,00	100,00	62,54	100,00	108,70	100,00
70	250	34,46	39,54	100,00	100,00	100,00	71,75	100,00	108,70	100,00
70	300	44,94	52,35	100,00	100,00	100,00	77,90	100,00	108,70	100,00
70	375	55,94	65,17	100,00	100,00	100,00	84,04	100,00	108,70	100,00
80	200	45,44	45,44	100,00	100,00	100,00	61,80	100,00	108,70	100,00
80	250	36,35	36,35	100,00	100,00	100,00	71,02	100,00	108,70	100,00
80	300	41,92	48,65	100,00	100,00	100,00	77,16	100,00	108,70	100,00
80	375	53,52	62,12	100,00	100,00	100,00	83,31	100,00	108,70	100,00
90	200	47,56	47,56	100,00	100,00	100,00	61,21	100,00	108,70	100,00
90	250	38,05	38,05	100,00	100,00	100,00	70,42	100,00	108,70	100,00
90	300	39,21	45,42	100,00	100,00	100,00	76,57	100,00	108,70	100,00
90	375	51,36	59,49	100,00	100,00	100,00	82,71	100,00	108,70	100,00

Tabela 16
Percentuais comparativos das áreas obtidas no exemplo 03

f_{ck} (MPa)	V_{Sd} (kN)	$A_{sw} / A_{sw\,(MC\,1990)}$ %								
		NBR		MC 1990	MC 2010			NP EN 1992		DIN 1045
		M I	M II		LoA I	LoA II	LoA III	ν	ν_1	
55	3000	58,98	69,40	100,00	100,00	100,00	85,89	100,00	108,70	100,00
55	3200	61,54	72,41	100,00	100,00	100,00	87,36	100,00	108,70	100,00
55	3400	63,80	75,07	100,00	100,00	100,00	88,65	100,00	108,70	100,00
55	3600	65,81	77,43	100,00	100,00	100,00	89,80	100,00	108,70	100,00
60	3000	57,40	67,27	100,00	100,00	100,00	84,71	100,00	108,70	100,00
60	3200	60,06	70,39	100,00	100,00	100,00	86,24	100,00	108,70	100,00
60	3400	62,41	73,14	100,00	100,00	100,00	87,59	100,00	108,70	100,00
60	3600	64,50	75,58	100,00	100,00	100,00	88,80	100,00	108,70	100,00
70	3000	54,57	63,57	100,00	100,00	100,00	83,27	100,00	108,70	100,00
70	3200	57,41	66,87	100,00	100,00	100,00	84,86	100,00	108,70	100,00
70	3400	59,91	69,79	100,00	100,00	100,00	86,25	100,00	108,70	100,00
70	3600	62,13	72,38	100,00	100,00	100,00	87,50	100,00	108,70	100,00
80	3000	52,07	60,43	100,00	100,00	100,00	82,54	100,00	108,70	100,00
80	3200	55,06	63,91	100,00	100,00	100,00	84,12	100,00	108,70	100,00
80	3400	57,70	66,97	100,00	100,00	100,00	85,52	100,00	108,70	100,00
80	3600	60,05	69,69	100,00	100,00	100,00	86,76	100,00	108,70	100,00
90	3000	49,84	57,74	100,00	100,00	100,00	81,94	100,00	108,70	100,00
90	3200	52,97	61,36	100,00	100,00	100,00	83,53	100,00	108,70	100,00
90	3400	55,74	64,57	100,00	100,00	100,00	84,93	100,00	108,70	100,00
90	3600	58,19	67,41	100,00	100,00	100,00	86,17	100,00	108,70	100,00

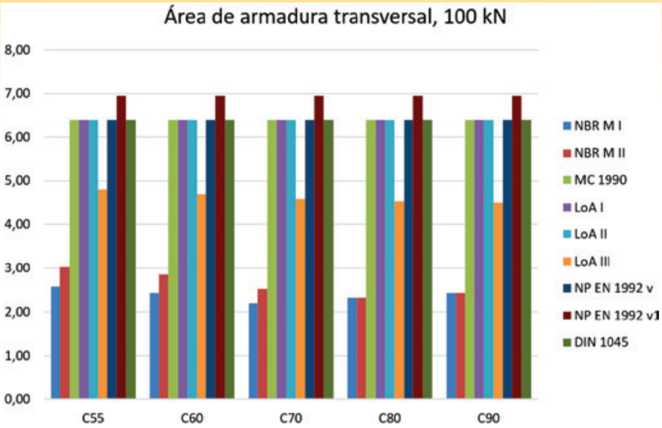

Figura 2
Gráfico comparativo das áreas de armadura transversal (cm²/m) do exemplo 01 (vigas de 12 cm por 40 cm), para força cortante de 100 kN

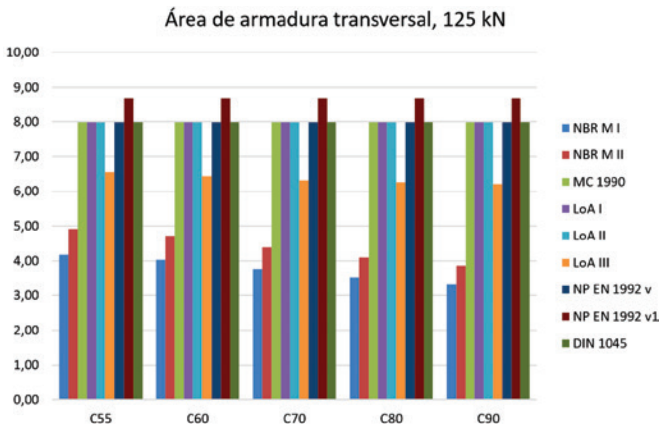

Figura 3
Gráfico comparativo das áreas de armadura transversal (cm²/m) do exemplo 01 (vigas de 12 cm por 40 cm), para força cortante de 125 kN

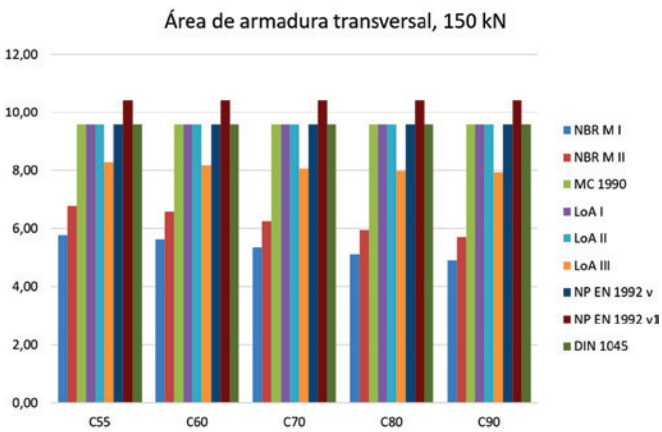

Figura 4
Gráfico comparativo das áreas de armadura transversal (cm²/m) do exemplo 01 (vigas de 12 cm por 40 cm), para força cortante de 150 kN

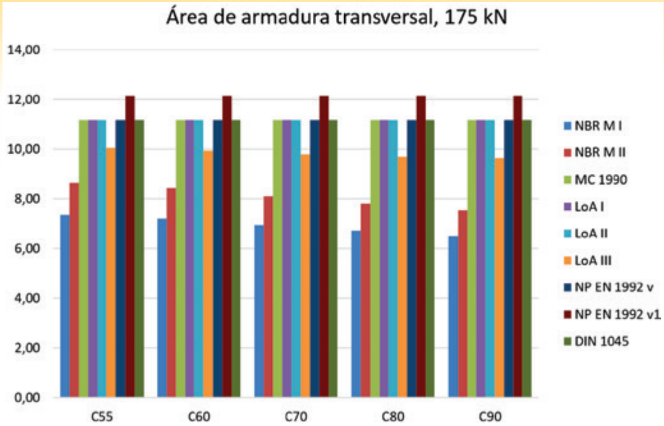

Figura 5
Gráfico comparativo das áreas de armadura transversal (cm²/m) do exemplo 01 (vigas de 12 cm por 40 cm), para força cortante de 175 kN

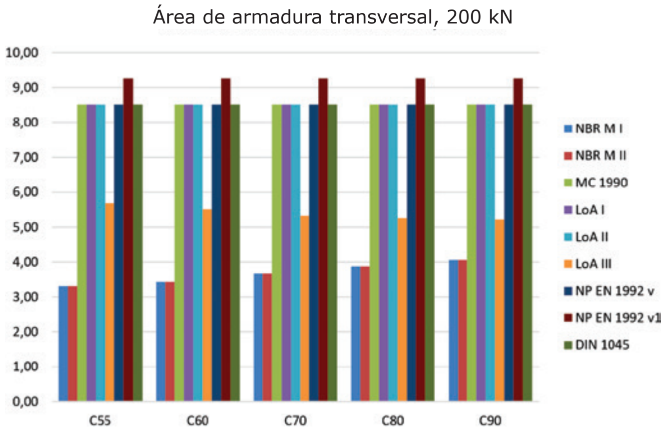

Figura 6
Gráfico comparativo das áreas de armadura transversal (cm²/m) do exemplo 02 (vigas de 20 cm por 60 cm), para força cortante de 200 kN

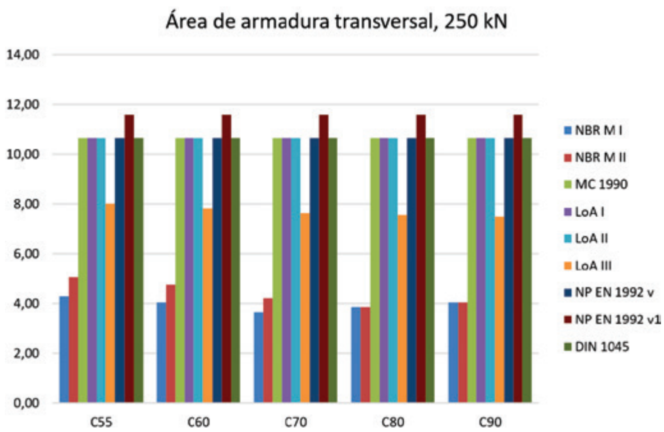

Figura 7
Gráfico comparativo das áreas de armadura transversal (cm²/m) do exemplo 02 (vigas de 20 cm por 60 cm), para força cortante de 250 kN

procedimento de cálculo da norma portuguesa [10] que utiliza o parâmetro ν_1 no cálculo (destinado para situações em que as tensões nas armaduras são inferiores a 80% da tensão característica de escoamento) - geraram as mesmas áreas de armadura transversal, para as mesmas intensidades de cortante, seção transversal de viga e inclinação de biela de 45°.

Assim como os Modelos I e II da NBR [5], o *Level of approximation* III apresenta uma redução por considerar a contribuição do concreto no dimensionamento. As parcelas correspondentes a esta contribuição aumentam com o aumento da classe do concreto, e diminuem com o aumento das solicitações. Em todas as situações propostas, os Modelos I e II da norma nacional geraram as menores áreas.

É possível constatar que a norma alemã prevê uma resistência bem superior às demais, conforme exposto na Figura 14. As demais normas, incluindo a nacional, compreendem fatores redutores de maior intensidade sobre a resistência, que a penalizam de forma mais significativa. Há de se questionar se essa maior resistência admissível pela norma alemã é justificada pelo maior rigor exigido na execução do concreto ou por outros fatores alheios ao procedimento de cálculo que não estão contemplados na norma de projeto.

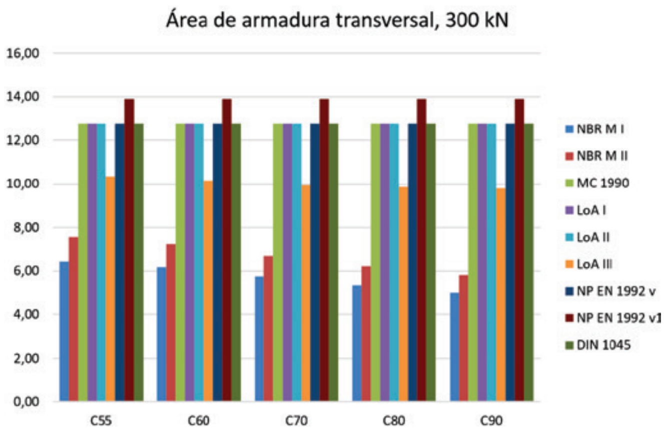

Figura 8
Gráfico comparativo das áreas de armadura transversal (cm²/m) do exemplo 02 (vigas de 20 cm por 60 cm), para força cortante de 300 kN

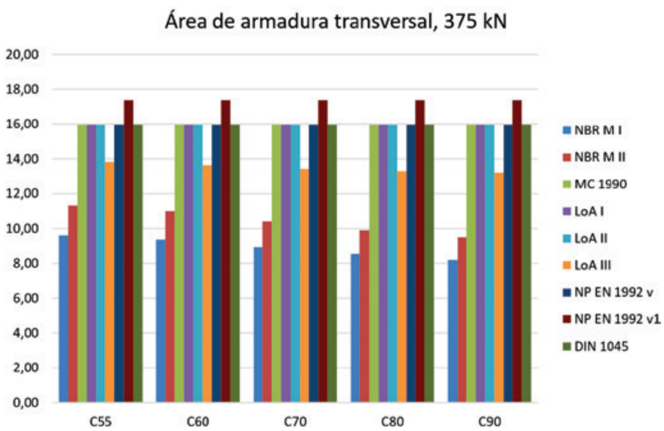

Figura 9
Gráfico comparativo das áreas de armadura transversal (cm²/m) do exemplo 02 (vigas de 20 cm por 60 cm), para força cortante de 375 kN

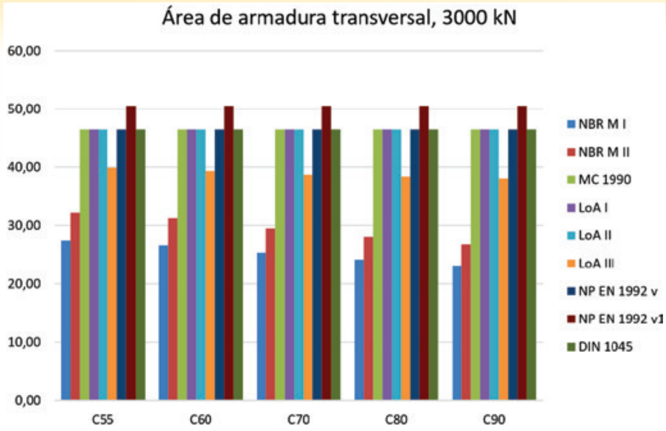

Figura 10
Gráfico comparativo das áreas de armadura transversal (cm²/m) do exemplo 03 (vigas de 60 cm por 165 cm), para força cortante de 3000 kN

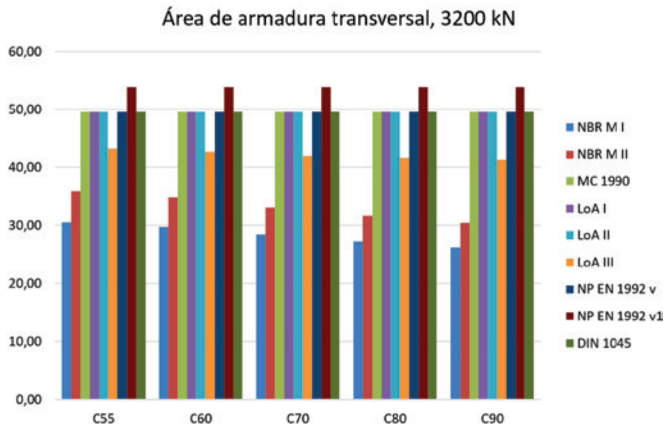

Figura 11
Gráfico comparativo das áreas de armadura transversal (cm²/m) do exemplo 03 (vigas de 60 cm por 165 cm), para força cortante de 3200 kN

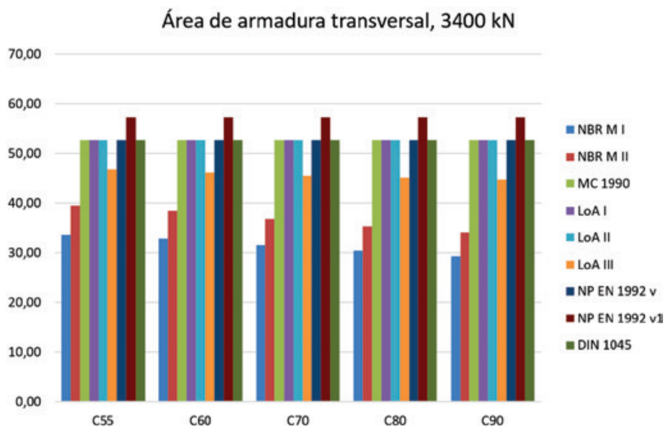

Figura 12
Gráfico comparativo das áreas de armadura transversal (cm²/m) do exemplo 03 (vigas de 60 cm por 165 cm), para força cortante de 3400 kN

Tabela 17
Detalhes das vigas de CAR ensaiadas

Viga	f_c (MPa)	b (mm)	d (mm)	Armadura transversal		Armadura longitudinal		V_{falha} (kN)
				ϕ/s (mm)	ρ_w (MPa)	n ϕ	ρ_l	
H60/2	60,8	200	353	ϕ6/200	0,747	2ϕ32	2,28	179,74
H60/3	60,8	200	351	ϕ8/210	1,267	2ϕ32	2,29	258,78
H60/4	60,8	200	351	ϕ8/210	1,267	2ϕ32 + 1ϕ25	2,99	308,71
H75/2	68,9	200	353	ϕ6/200	0,747	2ϕ32	2,28	203,94
H75/3	68,9	200	351	ϕ8/210	1,267	2ϕ32	2,29	269,35
H75/4	68,9	200	351	ϕ8/210	1,267	2ϕ32 + 1ϕ25	2,99	255,23
H100/2	87,0	200	353	ϕ6/165	0,906	2ϕ32	2,28	225,55
H100/3	87,0	200	351	ϕ8/210	1,291	2ϕ32	2,29	253,64
H100/4	87,0	200	351	ϕ8/210	1,291	2ϕ32 + 1ϕ25	2,99	266,53

4. Análise experimental

Das simulações anteriores, observa-se que o procedimento de cálculo da NBR produz áreas inferiores aos procedimentos internacionais analisados. Dentre estes, apenas o *LoA* III do Model Code 2010 [7] adota a parcela de contribuição dos mecanismos complementares do concreto (efeito pino, engrenamento de agregado e efeito arco). Os demais códigos internacionais apresentam a incoerência de, para uma mesma seção transversal e solicitação, mesmo com o aumento da resistência à compressão do concreto, as áreas previstas de estribos serem iguais. Em face destas constatações e com o intuito de enriquecer a discussão, procederar-se-á a comparação entre os resultados experimentais [2, 4] e as previsões normativas de área.

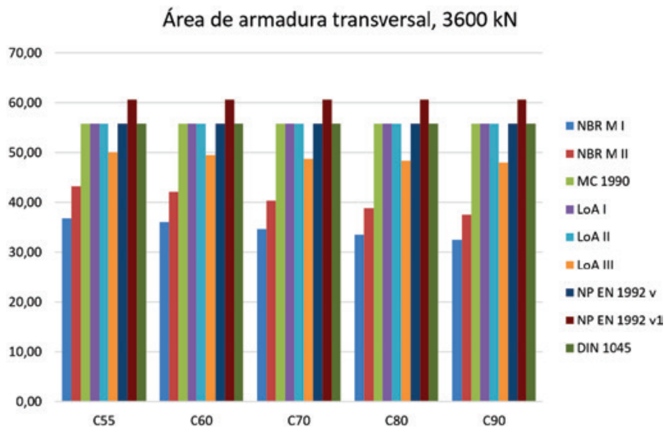

Figura 13
Gráfico comparativo das áreas de armadura transversal (cm^2/m) do exemplo 03 (vigas de 60 cm por 165 cm), para força cortante de 3600 kN

Tabela 18
Propriedades das barras de reforço transversal

Bitola – Série	Área (mm^2)	f_y (MPa)	f_u (MPa)
ϕ6 – H60 e H75	28,27	530	680
ϕ8 – H60 e H75	50,27	530	685
ϕ6 – H100	28,27	530	680
ϕ8 – H100	50,27	540	672

Considerando os resultados de Cladera [2], serão consideradas as vigas ensaiadas das séries 2 (H60/2, H75/2 e H100/2), 3 (H60/3, H75/3 e H100/3) e 4 (H60/4, H75/4 e H100/4) cujas características são expressas na Tabela 17, já ilustradas na Figura 1. Estas foram selecionadas por atenderem a amplitude de f_{ck} do grupo II (entre 55 MPa e 90 MPa) e por serem armadas com estribos, permitindo as comparações desejadas.

Nas tabelas 19, 20 e 21 a seguir, apresentam-se as áreas previstas pelos códigos estudados para as situações adotadas experimentalmente [2]. Estas áreas foram calculadas considerando o cortante de falha (Tabela 17), obtido experimentalmente, como solicitação e a resistência à compressão do concreto efetivamente observada nos experimentos (60,8 MPa, 68,9 MPa e 87 MPa). Ressalta-se que nos cálculos via normas foram adotados aço CA-50; experimentalmente,

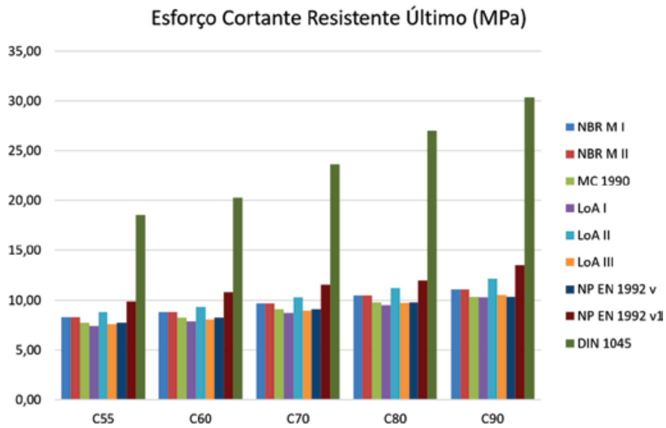

Figura 14
Gráfico comparativo dos esforços cortantes resistentes últimos (MPa)

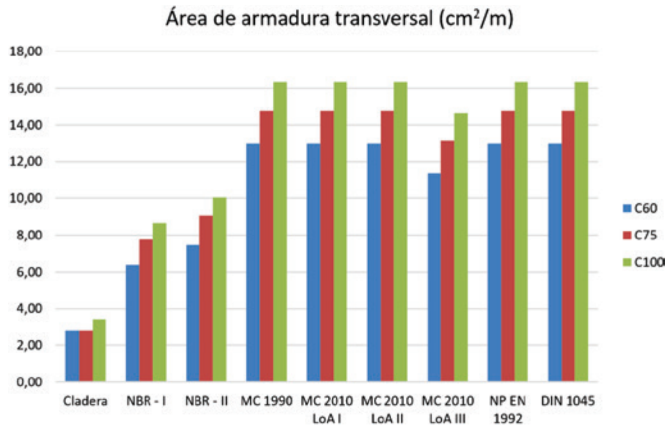

Figura 15
Gráfico comparativo das áreas de armadura transversal (cm^2/m) das vigas da série 2

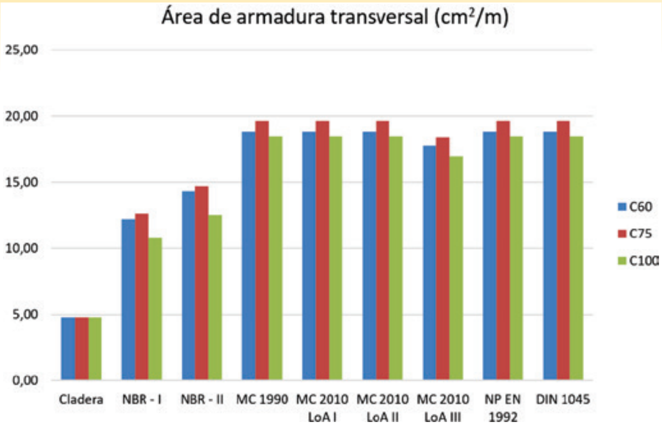

Figura 16
Gráfico comparativo das áreas de armadura transversal (cm²/m) das vigas da série 3

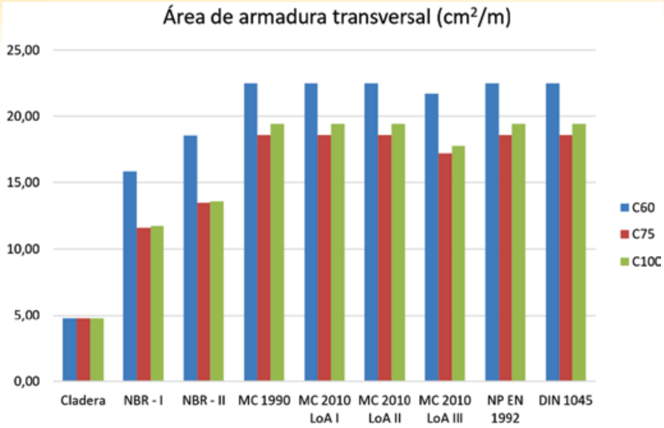

Figura 17
Gráfico comparativo das áreas de armadura transversal (cm²/m) das vigas da série 4

Cladera [2] adotou a tensão de escoamento real obtida via experimentos, conforme a Tabela 18, na determinação da área de armadura transversal. Além disso, para viabilizar a comparação, assim como o fez o autor, não foram utilizados coeficientes majoradores de solicitações e minoradores de resistência.
As áreas previstas pelos códigos e as experimentais correspondentes aos esforços cortante de falha são expostas nas Figuras 15, 16 e 17.

Nota-se que as áreas previstas pelos códigos são superiores às efetivamente requeridas experimentalmente, indicando uma “reserva” de resistência. Conforme já indicado pelas simulações numéricas da seção 3, as normas internacionais geram áreas de estribos maiores que as nacionais. Ressalta-se a diminuição esperada via rotina de cálculo do *LoA* III do Model Code 2010 [7], que difere das previsões dos demais códigos europeus. Estas últimas consideram a contribuição do concreto, que é de fato

Tabela 19
Áreas de armadura transversal (cm²/m) para as vigas da série 2

Viga	f_{ck} (MPa)	b_w (cm)	d (cm)	V_{Sd} (kN)	A_{sw} (cm²/m)
H60/2	60,8	20	35,3	179,74	2,82
NBR - I	60,8	20	35,3	179,74	6,38
NBR - II	60,8	20	35,3	179,74	7,47
MC 1990	60,8	20	35,3	179,74	13,01
MC 2010 LoA I	60,8	20	35,3	179,74	13,01
MC 2010 LoA II	60,8	20	35,3	179,74	13,01
MC 2010 LoA III	60,8	20	35,3	179,74	11,38
NP EN 1992	60,8	20	35,3	179,74	13,01
DIN 1045	60,8	20	35,3	179,74	13,01
Viga	**f_{ck} (MPa)**	**b_w (cm)**	**d (cm)**	**V_{Sd} (kN)**	**A_{sw} (cm²/m)**
H75/2	68,9	20	35,3	203,94	2,82
NBR - I	68,9	20	35,3	203,94	7,77
NBR - II	68,9	20	35,3	203,94	9,06
MC 1990	68,9	20	35,3	203,94	14,76
MC 2010 LoA I	68,9	20	35,3	203,94	14,76
MC 2010 LoA II	68,9	20	35,3	203,94	14,76
MC 2010 LoA III	68,9	20	35,3	203,94	13,14
NP EN 1992	68,9	20	35,3	203,94	14,76
DIN 1045	68,9	20	35,3	203,94	14,76
v	**f_{ck} (MPa)**	**b_w (cm)**	**d (cm)**	**V_{Sd} (kN)**	**A_{sw} (cm²/m)**
H100/2	87,0	20	35,3	225,55	3,42
NBR - I	87,0	20	35,3	225,55	8,66
NBR - II	87,0	20	35,3	225,55	10,03
MC 1990	87,0	20	35,3	225,55	16,33
MC 2010 LoA I	87,0	20	35,3	225,55	16,33
MC 2010 LoA II	87,0	20	35,3	225,55	16,33
MC 2010 LoA III	87,0	20	35,3	225,55	14,64
NP EN 1992	87,0	20	35,3	225,55	16,33
DIN 1045	87,0	20	35,3	225,55	16,33

observada, conforme identificado por Cladera & Marí [4] (Figura 18).

A curva ANN - relativa a resultados experimentais de vigas de altura útil de 350 mm, largura de 300 mm, relação entre vão e

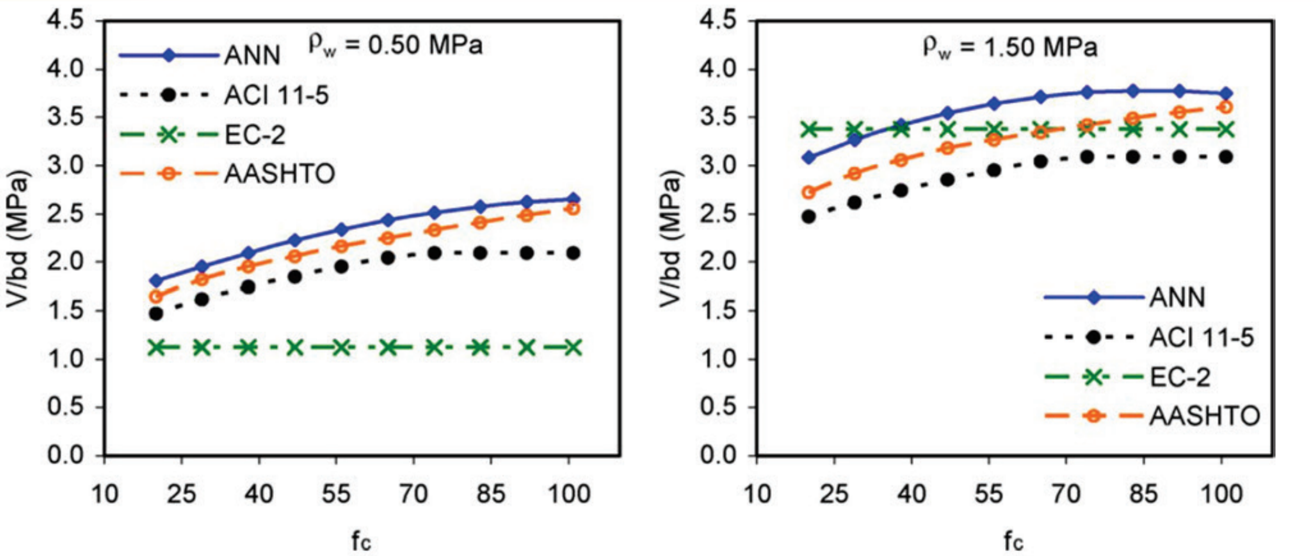

Figura 18
Resultados da ANN comparados com as previsões do ACI, Eurocode 2 e AASHTO para vigas com armadura transversal. Influência da resistência à compressão do concreto em relação à quantidade de armadura transversal (Cladera & Marí [4])

Tabela 20
TÁreas de armadura transversal (cm²/m) para as vigas da série 3

Viga	f_{ck} (MPa)	b_w (cm)	d (cm)	V_{Sd} (kN)	A_{sw} (cm²/m)
H60/3	60,8	20	35,1	258,78	4,78
NBR - I	60,8	20	35,1	258,78	12,20
NBR - II	60,8	20	35,1	258,78	14,29
MC 1990	60,8	20	35,1	258,78	18,84
MC 2010 LoA I	60,8	20	35,1	258,78	18,84
MC 2010 LoA II	60,8	20	35,1	258,78	18,84
MC 2010 LoA III	60,8	20	35,1	258,78	17,75
NP EN 1992	60,8	20	35,1	258,78	18,84
DIN 1045	60,8	20	35,1	258,78	18,84

Viga	f_{ck} (MPa)	b_w (cm)	d (cm)	V_{Sd} (kN)	A_{sw} (cm²/m)
H75/3	68,9	20	35,1	269,35	4,78
NBR - I	68,9	20	35,1	269,35	12,62
NBR - II	68,9	20	35,1	269,35	14,71
MC 1990	68,9	20	35,1	269,35	19,61
MC 2010 LoA I	68,9	20	35,1	269,35	19,61
MC 2010 LoA II	68,9	20	35,1	269,35	19,61
MC 2010 LoA III	68,9	20	35,1	269,35	18,41
NP EN 1992	68,9	20	35,1	269,35	19,61
DIN 1045	68,9	20	35,1	269,35	19,61

Viga	f_{ck} (MPa)	b_w (cm)	d (cm)	V_{Sd} (kN)	A_{sw} (cm²/m)
H100/3	87,0	20	35,1	253,64	4,78
NBR - I	87,0	20	35,1	253,64	10,80
NBR - II	87,0	20	35,1	253,64	12,51
MC 1990	87,0	20	35,1	253,64	18,47
MC 2010 LoA I	87,0	20	35,1	253,64	18,47
MC 2010 LoA II	87,0	20	35,1	253,64	18,47
MC 2010 LoA III	87,0	20	35,1	253,64	16,94
NP EN 1992	87,0	20	35,1	253,64	18,47
DIN 1045	87,0	20	35,1	253,64	18,47

altura útil a/d = 3 e taxa de armadura longitudinal de ρ_l = 3% - aponta para o crescimento da cortante resistente de cálculo com o aumento da classe do concreto. Observa-se que este comportamento, apesar de contemplado pelas normas americanas ACI 318-02 e AASHTO LRDF – não compreendidas no presente trabalho – de modo conservador, não é considerado pelo Eurocode 2 [10], que admite que a cortante resistente varia devido apenas à armadura transversal, indicado pela translação da curva EC-2 com o aumento da taxa de armadura transversal de ρ_w = 0,50 MPa para ρ_w = 1,50 MPa.

Se por um lado a maior parte dos procedimentos normativos não considera a contribuição do concreto no dimensionamento da armadura transversal, todos eles preveem esforços cortantes resistentes últimos superiores aos efetivamente observados experimentalmente por Cladera [2], conforme apresentado na Tabela 22, cujos dados estão ilustrados nas Figuras 19, 20 e 21. Assim como

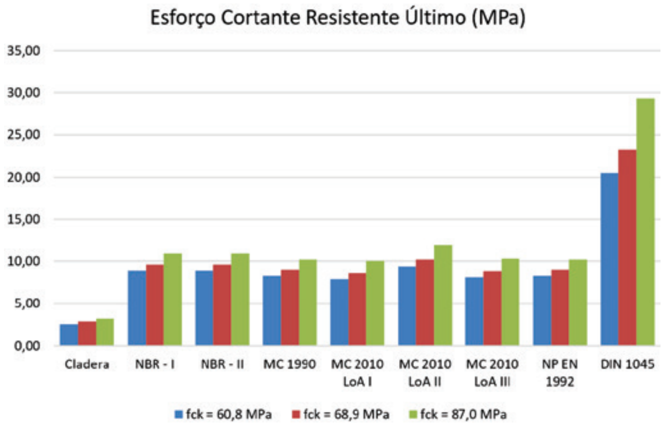

Figura 19
Gráfico comparativo dos esforços cortantes resistentes últimos (MPa) da série 2

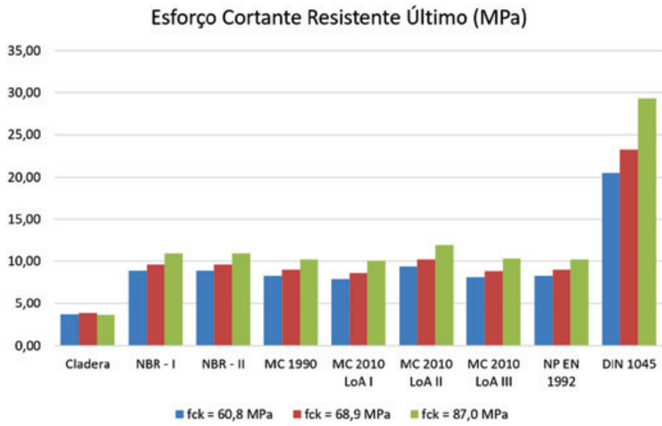

Figura 20
Gráfico comparativo dos esforços cortantes resistentes últimos (MPa) da série 3

Tabela 21
Áreas de armadura transversal (cm²/m) para as vigas da série 4

Viga	f_{ck} (MPa)	b_w (cm)	d (cm)	V_{Sd} (kN)	A_{sw} (cm²/m)
H60/4	60,8	20	35,1	308,71	4,78
NBR - I	60,8	20	35,1	308,71	15,84
NBR - II	60,8	20	35,1	308,71	18,55
MC 1990	60,8	20	35,1	308,71	22,48
MC 2010 LoA I	60,8	20	35,1	308,71	22,48
MC 2010 LoA II	60,8	20	35,1	308,71	22,48
MC 2010 LoA III	60,8	20	35,1	308,71	21,72
NP EN 1992	60,8	20	35,1	308,71	22,48
DIN 1045	60,8	20	35,1	308,71	22,48
Viga	**f_{ck} (MPa)**	**b_w (cm)**	**d (cm)**	**V_{Sd} (kN)**	**A_{sw} (cm²/m)**
H75/4	68,9	20	35,1	255,23	4,78
NBR - I	68,9	20	35,1	255,23	11,59
NBR - II	68,9	20	35,1	255,23	13,51
MC 1990	68,9	20	35,1	255,23	18,58
MC 2010 LoA I	68,9	20	35,1	255,23	18,58
MC 2010 LoA II	68,9	20	35,1	255,23	18,58
MC 2010 LoA III	68,9	20	35,1	255,23	17,29
NP EN 1992	68,9	20	35,1	255,23	18,58
DIN 1045	68,9	20	35,1	255,23	18,58
Viga	**f_{ck} (MPa)**	**b_w (cm)**	**d (cm)**	**V_{Sd} (kN)**	**A_{sw} (cm²/m)**
H100/4	87,0	20	35,1	266,53	4,78
NBR - I	87,0	20	35,1	266,53	11,73
NBR - II	87,0	20	35,1	266,53	13,60
MC 1990	87,0	20	35,1	266,53	19,41
MC 2010 LoA I	87,0	20	35,1	266,53	19,41
MC 2010 LoA II	87,0	20	35,1	266,53	19,41
MC 2010 LoA III	87,0	20	35,1	266,53	17,94
NP EN 1992	87,0	20	35,1	266,53	19,41
DIN 1045	87,0	20	35,1	266,53	19,41

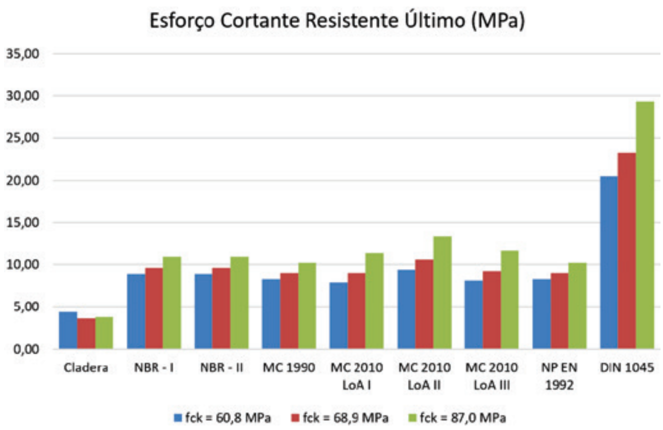

Figura 21
Gráfico comparativo dos esforços cortantes resistentes últimos (MPa) da série 4

constatado na seção 3.5 do presente trabalho, o procedimento alemão previu as maiores resistências.

Da análise dos cortantes resistentes últimos, depreende-se mais uma vez que, apesar de a resistência ao cortante crescer com o aumento da classe do concreto, em consonância com os procedimentos normativos e com os resultados experimentais, este comportamento não é traduzido em vantagem no dimensionamento pelos procedimentos europeus (com exceção do *LoA* III).

5. Conclusões

Devido à difusão de concretos de alta resistência, é necessário o estudo dos procedimentos normativos de dimensionamento - especificamente do dimensionamento à cortante - que compreendem concretos das classes C55 a C90. Este trabalho, portanto, objetivou comparar analiticamente os tratamentos normativos usuais, à luz de resultados experimentais [2, 4].

Tabela 22
Esforços cortantes resistentes últimos (MPa)

Viga	f_{ck} (MPa)	V_{Ru} (MPa)		
		Série 2	Série 3	Série 4
Cladera	60,8	2,55	3,69	4,40
NBR - I	60,8	8,87	8,87	8,87
NBR - II	60,8	8,87	8,87	8,87
MC 1990	60,8	8,28	8,28	8,28
MC 2010 LoA I	60,8	7,93	7,93	7,93
MC 2010 LoA II	60,8	9,37	9,37	9,37
MC 2010 LoA III	60,8	8,11	8,11	8,11
NP EN 1992	60,8	8,28	8,28	8,28
DIN 1045	60,8	20,52	20,52	20,52

Viga	f_{ck} (MPa)	V_{Ru} (MPa)		
		Série 2	Série 3	Série 4
Cladera	68,9	2,89	3,84	3,64
NBR - I	68,9	9,63	9,63	9,63
NBR - II	68,9	9,63	9,63	9,63
MC 1990	68,9	8,98	8,98	8,98
MC 2010 LoA I	68,9	8,62	8,62	8,98
MC 2010 LoA II	68,9	10,18	10,18	10,62
MC 2010 LoA III	68,9	8,82	8,82	9,19
NP EN 1992	68,9	8,98	8,98	8,98
DIN 1045	68,9	23,25	23,25	23,25

Viga	f_{ck} (MPa)	V_{Ru} (MPa)		
		Série 2	Série 3	Série 4
Cladera	87,0	3,19	3,61	3,80
NBR - I	87,0	10,94	10,94	10,94
NBR - II	87,0	10,94	10,94	10,94
MC 1990	87,0	10,21	10,21	10,21
MC 2010 LoA I	87,0	10,07	10,07	11,34
MC 2010 LoA II	87,0	11,90	11,90	13,41
MC 2010 LoA III	87,0	10,30	10,30	11,61
NP EN 1992	87,0	10,21	10,21	10,21
DIN 1045	87,0	29,36	29,36	29,36

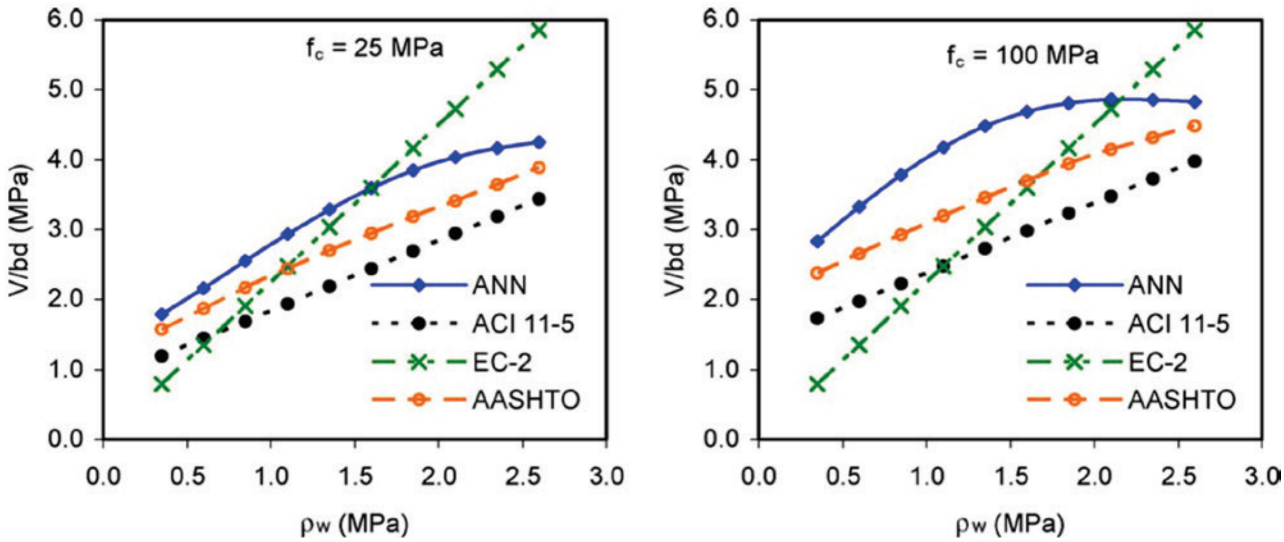

Figura 22
Resultados da ANN comparados com as previsões do ACI, Eurocode 2 e AASHTO para vigas com armadura transversal. Influência da quantidade de armadura de cisalhamento em relação à resistência de compressão do concreto (Cladera & Marí [4])

Das análises feitas, conclui-se que o procedimento de cálculo da NBR produz áreas inferiores aos procedimentos internacionais analisados. Diferente da norma brasileira [5], estes não consideram (com exceção do *LoA* III) a parcela de contribuição dos mecanismos complementares do concreto (efeito pino, engrenamento de agregado e efeito arco), apesar de esta ser observada experimentalmente.
De acordo com os dados das tabelas 14, 15 e 16, constata-se que os procedimentos de cálculo do MC 1990 [6], MC 2010 [7] (*LoA* I e *LoA* II) e das normas portuguesa [10] (considerando o parâmetro v) e alemã [11] fornecem as mesmas áreas, fixadas as seções, intensidades de cortante e inclinação da diagonal comprimida.
Assim como constatado no 50° Congresso Brasileiro de Concreto [12] para concretos do grupo I, a utilização do Modelo II de cálculo da NBR [5] em concretos do grupo II, para determinada força cortante, seção transversal e inclinação de diagonal comprimida de 45°, resulta em áreas superiores às obtidas pelo Modelo I, quando estas são superiores às mínimas de norma.
Os procedimentos que adotam a contribuição do concreto apresentam reduções nas áreas de estribos com o aumento da classe, para uma mesma solicitação e seção transversal. No geral, para uma mesma classe de resistência, as áreas aumentam com as solicitações.
Apesar de não compreenderem no cálculo a contribuição do concreto, os procedimentos internacionais analisados - assim como o nacional - preveem um aumento do esforço cortante resistente último com o aumento da classe do concreto. Das comparações feitas, detectou-se que este mesmo aumento é inclusive superior ao obtido experimentalmente por Cladera [2], o que reforça a incoerência e o conservadorismo destes códigos.
A não consideração da parcela do concreto por parte das normas internacionais analisadas leva a resultados muito conservadores, visto que independente da classe, para uma mesma solicitação, as áreas são iguais. Cladera & Marí [4] confirmam este comportamento ao comparar os resultados da ANN com as áreas previstas pelo Eurocode 2, conforme aponta a Figura 22.

6. Agradecimentos

Os autores agradecem à CAPES - Coordenação de Aperfeiçoamento de Pessoal de Nível Superior, ao CNPq - Conselho Nacional de Desenvolvimento Científico e Tecnológico e ao Departamento de Engenharia Civil da UFRN.

7. Referências bibliográficas

[1] SILVA, Inês Santana da. Concreto de Alta Resistência: Composição, Propriedades e Dimensionamento. 1995. 149 f. Dissertação (Mestrado) - Curso de Engenharia de Estruturas, Escola de Engenharia de São Carlos, São Carlos, 1995.
[2] CLADERA, Antoni. Shear Design of Reinforced High-Strength Concrete Beams. 2002. 159 f. Tese (Doutorado) - Curso de Enginyeria Civil, Departament D'enginyeria de La Construcció, Universitat Politècnica de Catalunya, Barcelona, 2002.
[3] ARSLAN, Güray. Shear strength of reinforced concrete beams with stirrups. Materials And Structures, [s.l.], v. 41, n. 1, p.113-122, 28 fev. 2007. Springer Nature. http://dx.doi.org/10.1617/s11527-007-9223-3.
[4] CLADERA, A.; MARÍ, A. R.. Shear design procedure for reinforced normal and high-strength concrete beams using artificial neural networks. Part II: beams with stirrups. Engineering Structures, Elsevier, Amsterdam, v. 26, n. 7, p.927-936, 23 fev. 2004.
[5] ASSOCIAÇÃO BRASILEIRA DE NORMAS TÉCNICAS. NBR 6118: Projeto de estruturas de concreto - Procedimento. 3 ed. Rio de Janeiro, 2014.

[6] COMITE EURO-INTERNACIONAL DU BETON. MC 1990: Design Code. Lausanne, 1990.
[7] COMITE EURO-INTERNACIONAL DU BETON. MC 2010: Model Code 2010. Lausanne, 2010.
[8] MUTTONI, Aurelio; RUIZ, Miguel Fernández. The levels-of-approximation approach in MC 2010: application to punching shear provisions**.** Structural Concrete,[s.l.], v. 13, n. 1, p.32-41, mar. 2012. Wiley-Blackwell. http://dx.doi.org/10.1002/suco.201100032.
[9] BARROS, Rodrigo. Como as normas brasileiras e europeias tratam o problema da força cortante em elementos lineares de concreto. TQS News, [s.i.], v. , n. 36, p.44-45, 36 mar. 2013.
[10] COMITÉ EUROPEU DE NORMALIZAÇÃO. NP EN 1992-1-1: Projecto de estruturas de betão. Parte 1-1: Regras gerais e regras para edifícios. Bruxelas, 2010.
[11] DEUTSCHES INSTITUT FÜR NORMUNG. DIN 1045-1:2001-07: Plain, reinforced and prestress concrete structures. Part 1: Design and construction. Berlin, 2001.
[12] CONGRESSO BRASILEIRO DE CONCRETO, 50., 2008, Salvador. Cálculo da área da armadura transversal em elementos lineares de concreto armado submetidas à ação de força cortante: análise comparativa entre os Modelos I e II da NBR 6118:2003. Salvador: Ibracon, 2008. 16 p.

Volume 12, Number 1 (February 2019) p. 179 – 198 • ISSN 1983-4195
http://dx.doi.org/10.1590/S1983-41952019000100012

REVISTA IBRACON DE ESTRUTURAS E MATERIAIS
IBRACON STRUCTURES AND MATERIALS JOURNAL

Behavior of the self-compacting mortar with sugarcane bagasse ash in the fresh and hardened state

Estudo do comportamento da argamassa autoadensável com cinza do bagaço de cana-de-açúcar no estado fresco e endurecido

V. C. SANTOS [a]
viniciuscarrijodossantos@gmail.com
https://orcid.org/0000-0002-7501-4998

R. D. VANDERLEI [a]
rdvanderlei@uem.br
https://orcid.org/0000-0001-5676-6951

K. K. MORAES [a]
katherinekaneda@hotmail.com
https://orcid.org/0000-0003-4461-850X

E. T. D. F. ROSINA [a]
eti_tayna@hotmail.com
https://orcid.org/0000-0003-4796-9284

G. M. BALBINO [a]
guilhermebalbino1@live.com
https://orcid.org/0000-0001-6394-3805

Abstract

Self-compacting concrete (SCC) is a material with high workability and moderate viscosity when compared to conventional concrete. Due to its advantages, the SCC has been investigated in the last decades and the research studies the use of new components in its structure and the search for the improvement of its performance, both in the fluid and in the hardened state. The goal of this study was to evaluate the behavior of self-compacting mortars with limestone filler and with the addition of sugarcane bagasse ash (SBA) partially replacing the small aggregate. To reach this goal, initially, a rate of replacement of natural sand by SBA was set. Afterwards, slump-flow and funnel-V tests were carried out in order to check the behavior of the mortars in the fresh state. After checking the behavior of the mortars in their fresh state, the different mix proportions that achieved the best aspects of fluidity and viscosity was selected, and, for self-compacting mortars, specimens were molded to determine tensile strength at 28 days, and compressive strength at 7 and 28 days. The experimental analyses demonstrated an increase in viscosity and reduction in fluidity with increasing content of limestone filler, facilitating the obtaining of self-compacting mortars. Regarding the performance of the material in the hardened state, the mortars showed a slight increase in tensile and compressive strength due to the filler effect of fines. It was possible to replace 40% of the small aggregate with SBA.

Keywords: self-compacting mortar, sugarcane bagasse ash, limestone.

Resumo

O concreto autoadensável (CAA) é um material que apresenta alta trabalhabilidade e moderada viscosidade quando comparado ao concreto convencional. Em função de suas vantagens, nas últimas décadas, o CAA vem sendo investigado e as pesquisas abordam a utilização de novos componentes em sua estrutura e a busca pela melhoria de seu desempenho, tanto no estado fluido quanto no endurecido. Este estudo teve como objetivo avaliar o comportamento de argamassas autoadensáveis com fíler calcário e com a adição de cinza do bagaço de cana-de-açúcar (CBCA) em substituição parcial ao agregado miúdo. Para atingir este objetivo, inicialmente, uma taxa de substituição de areia natural por CBCA foi definida. Na sequência, foram realizados ensaios de espalhamento e funil-V com o intuito de verificar o comportamento das argamassas no estado fresco. Após a verificação do comportamento das argamassas em seu estado fresco, a série de traços que obteve os melhores aspectos de fluidez e viscosidade foi selecionada, e, para as argamassas autoadensáveis foram moldados corpos-de-prova para determinação da resistência à tração aos 28 dias, e resistência à compressão aos 7 e 28 dias. As análises experimentais demonstraram um aumento de viscosidade e redução da fluidez à medida em que se aumentava o teor de fíler calcário, facilitando a obtenção de argamassas autoadensáveis. Com relação ao desempenho do material no estado endurecido, as argamassas apresentaram leve incremento de resistência à tração e à compressão, devido ao efeito fíler dos finos. Foi possível substituir 40% do agregado miúdo por CBCA.

Palavras-chave: argamassa autoadensável, cinza do bagaço de cana-de-açúcar, fíler calcário.

[a] *State University of Maringá, Civil Engineering Department, Maringá, PR, Brazil.*

Received: 07 Dec 2016 • Accepted: 21 Aug 2018 • Available Online: 05 Feb 2019

1. Introduction

Concrete is the most widely used construction material in the world, but with all the dynamics and innovations in engineering projects, it was necessary to carry out in-depth studies on this component of civil construction, developing new types of concrete that go beyond conventional concrete such as high-performance concrete, fiber reinforced concrete, concrete with high content of pozzolanic additives, apparent concrete, white, colored, sustainable and self-supporting concretes, among others [1].

The emergence of the material that would later be called self-compacting concrete was justified by [2], due to the low ability that the workers had to perform a satisfactory concreting. The demand for ever more durable concrete structures also encouraged the development of a material that was spread by the action of its own weight, material that would reduce the need for human intervention, resulting in better concreted parts.

Self-compacting concrete (SCC) is a material that does not require vibration during the launching and densification phases; however, in order to be considered self-compacting, it must meet certain requirements: workable, no segregation, no exudation, or blockages in densely reinforced structural elements [3].

In order to effectively determine the proportion of constituent materials of self-compacting concrete, it is important to pay special attention to the mortar dosing, since the SCC is composed primarily of mortar and large aggregate. For this reason, it is more convenient to make the adjustments and tests in the mortar phase, which will later compose the SCC.

When the concrete is deformable, the cement paste with high viscosity prevents the increase of internal stress on the large aggregate particles. The high deformability of the self-compacting concrete can be obtained only by the use of superplasticizer additive, without the need to change the water/cement ratio of the mortar [2].

The achievement of good results in self-compacting concretes is possible through studies on the dosing of mortar. By studying the mortar, it is possible to determine if the material has too much fluidity, low viscosity, segregation and exudation. The mortar dosing step is very important, considering that in this phase the proportions of materials must be constituted in such a way that the SCC does not lose workability.

Another important factor in the production of concrete is the high consumption of aggregates, among them, sand, a natural resource very exploited and used by civil construction as a small aggregate. The extraction of alluvial materials from rivers has been strongly condemned by several sectors of society, this is mainly due to the potential imbalance that this activity can cause in fluvial dynamics, as an immediate consequence of this activity occurs the redefinition of the limits of the channel, either by removal or addition of materials, which in turn can promote changes in sediment flow and sediment transport patterns [4].

In the sugar and alcohol industry, one of the by-products generated from the production of sugar, alcohol and other products is sugarcane bagasse (SB). From the energy cogeneration in the sugar-alcohol plants, where the SB is used as fuel for the boilers in the generation of energy, a residue called Sugarcane Bagasse Ash (SBA) is originated, which until now has no economic value for the industry.

Given the environmental imbalances that sand extraction can cause, the use of renewable and alternative materials may be a solution. Therefore, one of the proposals of this study is the use of SBA, material from renewable sources, replacing partially the small aggregate (sand), in the dosage of self-compacting mortars.

In Brazil, the sugar and alcohol industry consists of a very well-structured segment, in terms of its production chain. The country is the world's largest producer of sugarcane, followed by India and China. For the 2016/2017 growing season, the country expects to produce and to destine to the industry 684.77 million tons of sugarcane (3.27% more than the previous harvest), distributed in an area of about 8.97 million hectares in all producing states. The largest Brazilian State in sugarcane production is São Paulo (52.30% of the planted area), and Paraná ranks 4th in the ranking of producing states, with 7.00% of the Brazilian area planted [5].

According to FIESP/CIESP [6] data, 260 kilograms SB are generated for each ton of processed sugarcane, of these 260 kilograms of BCA destined for burning, 6.20 kilograms of SBA are generated. Therefore, when applying these values to the projection of the 2016/2017 sugarcane harvest in Brazil, considering that all the expected production is destined to the industry, approximately 178 million tons of BCA would be generated, if all this bagasse was destined for burning approximately 4.24 million tons of SBA would be generated in the crop in question.

The goal of this study is to develop mortar with self-compacting characteristics, partially replacing the small aggregate with sugarcane bagasse ash (SBA) and using the limestone filler as fine to control the viscosity. In this way, it was evaluated the behavior of its mechanical properties (compressive and tensile strength).

Table 1
Characterization of CP V ARI Ultra cement [8]

Control item	Unit	Average
Initial setting time	hours	1.50
Final setting time	hours	8.90
Specific gravity	g/cm³	3.20
Compressive strength at the end of day 1	MPa	11.10
Compressive strength at 3 days	MPa	23.90
Compressive strength at 7 days	MPa	32.80
Compressive strength at 28 days	MPa	36.70

Table 2
Sand characterization

Characteristics	Unit	Values
Specific mass (γ_s)	kg/dm³	2.65
Aggregate absorption (ABS)	%	–
Loose unit weight	kg/dm³	1.52
Compacted unit weight	kg/dm³	1.63
Maximum characteristic diameter ($\phi_{max.}$)	mm	1.20
Fineness module	%	2.84

2. Material and experimental program

The experimental program was divided into 4 phases and was developed at the Construction Materials Laboratory, State University of Maringá (UEM). The steps performed in the experimental program are presented below:
In sections 2.1 to 2.5, each step of the experimental program is presented in detail.
I Characterization of materials - Phase 1;
II Study of the composition of the small aggregate - Phase 2;
III Determination of the optimal proportion of the small aggregate – Phase 3;
IV Self-compacting mortar dosage - Phase 4;
V Evaluation of the mortar in the hardened state - Phase 5.

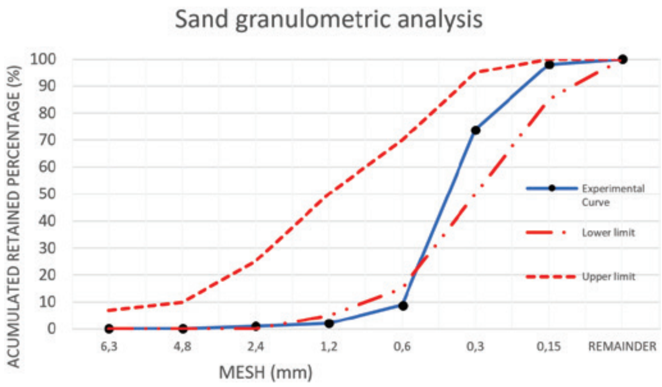

Figure 1
Particle size distribution of the sand used according to NBR 7211:2009

2.1 Material

The constituent materials in the self-compacting mortar were: Cement; water; sand (medium and fine particle size); Sugarcane bagasse ash (SBA); Calcitic Limestone Filler, and; superplasticizer additive.
The cement used for dosing the mortar was the CPV ARI RS, called Portland cement of high initial strength and resistant to sulfates provided by Votorantim Cimento LTDA. For the determination of the characteristics of the material, the cement characterization was carried out according to NBR 5733: 1991 [7]. The results of the characterization provided by the manufacturer are listed in table 1.
According to NBR 5733: 1991 [7], which deals with Portland cement of high initial strength, the binder used in the research meets the requirements of high initial strength obtained by milling Portland clinker, and consists mainly of hydraulic calcium silicates to which the amount of one or more forms of calcium sulfate is added during the operation.
The sand used is of quartz origin from the region of Maringá, State of Paraná. The particle size composition of the sand was based on the NBR NM 248: 2003 [9], and for the classification of this aggregate, it was used NBR 7211: 2009 [10]. NBR NM 30: 2001 [11] was also used to determine the water absorption of the small aggregate. NBR NM 52: 2002 [12] was applied to determine the specific gravity and apparent specific gravity of the small aggregate. The NBR NM 45: 2006 was used to determine the unit weight and void volume of the small aggregate [13]. Table 2 presents the results for the sand characterization.
From the results obtained by the particle size classification, the limits of the particle size distribution were plotted, as can be seen in figure 1. The additive used in the research was GLENIUM 51, which is classified as third generation for concrete, the product is liquid and free of chlorides, is generally applied to high performance concretes, where it is aimed to minimize the water/cement ratio and increase the durability of the material. The additive is based on a modified polycarboxylic ether chain, which acts as a dispersant of the cementitious material, providing a high reduction in water consumption and superplastification of the material, increasing the workability of the concrete without changing the bonding time. GLENIUM 51 information can be seen in table 3.

Table 3
Information on the superplasticizer additive used [14]

Manufacturer	Name	Function	Chemical basis	Solid content (%)	pH	Viscosity (cps)	Density (g/cm³)	Aspect	Solubility	Color
BASF S/A	Glenium 51	Third generation superplasticizer additive	Polycarboxylic ether	28.50 31.50	5–7	<150	1.07 1.11	Liquid	Total in water	Cloudy white

Table 4
Information on the calcitic limestone used [15]

Manufacturer	Name	Function	Chemical basis	Particle size	Color
Cazanga	Calcitic Limestone	Applications in the construction and animal feed industry	CaO: minimum of 51.80% MgO: maximum of 1% Ca: minimum of 37% Mg: minimum of 0.63%	94% passing through 325 mesh sieve, 94% smaller than 45 µm (0.045mm)	White

The limestone filler used was of calcitic origin and its characteristics, provided by the manufacturer, are listed in table 4. The sugarcane bagasse ash, used in this study, was collected at the Santa Terezinha Plant in the district of Iguatemi, near the municipality of Maringá, Northwest region of the State of Paraná. To perform the research, the ash was used in natural condition, having as sole processing the sieving through the 0.595mm mesh (# 30), in order to remove the coarse material and impurities.

As the sugarcane bagasse ash used in this research is the same lot as that used in the researches of Nunes [16], Souto [17] and Nagano [18], the chemical and physical characteristics were taken from the researches of the authors mentioned above. Therefore, this information can be seen in table 5.

The water used in the experiments came from the supply network of the municipality of Maringá, State of Paraná, which according to the requirements of NBR 15900-1: 2009 [19], is entitled Water for kneading concrete-requirements.

2.2 Composition of the small aggregate

In order to determine an optimal composition between the small aggregates and the SBA, a study was performed to optimize the compactness between them. For this study, the NBR norm NM 45: 2006 [13] was used to determine the unit weight in the hardened state, where the test was performed for each of the compositions analyzed and the unit weight in the dry compacted state was determined, in this way, the greater unit mass would represent the best composition among the aggregates.

The assay was performed by varying the percentage of the sand composition and SBA 10 by 10% until reaching a composition with

Table 5
Characterization of sugarcane bagasse ash from the Iguatemi Plant [16, 17, 18]

Characteristics	Unit	Values
* Degree of uniformity (U)	–	1.62
*D_{10}	mm	0.13
*D_{30}	mm	0.18
*D_{80}	mm	0.21
* Uniformity	–	U<5 (very uniform)
*Coefficient of curvature (CC)	–	1.19
* Particle size distribution	–	Well graduated
* Particle size classification	–	Similar to sand
* Specific mass	g/cm³	2.64
* Moisture content	%	0.27
** Specific area	m²/kg	5,356
** Mineralogical composition – X diffraction	Quartz (SiO_2)	Highly crystalline, no amorphous phase
** Total organic matter	%	3.55
** Organic carbon	%	1.97
** Pozzolanic activity	Mg CaO/g	23
** SiO_2	–	High silica content in the form of quartz attributed to low pozzolanic activity
*** C	mg/kg	486
*** MO		8.85
*** CaO		1.02
*** MgO		0.15
*** K_2O		0.37
*** P_2O_5		0.01
*** Fe		1,375.65
*** Cu		29.73
*** Mn		70.96
*** Zn		16.82

equal amounts of the two materials (50% sand and 50% SBA). The composition with the highest unit mass in the hardened state was the one used in the mortar dosages.

2.3 Determining the optimal proportion of small aggregate

In order to define the optimal proportion of small aggregate, three series of mix proportions were developed with a cement/small aggregate ratio of 1: 1, 1: 2 and 1: 3, in mass, respectively. After the mortars were made, the slump-flow and V-funnel tests were performed for mortars and the self-compacting parameters (Gm and Rm) were obtained in order to determine the best aggregate ratio (sand + SBA) per cement (ar/c) for the production of mortars with the materials used.

2.4 Dosage of the self-compacting mortar

For the development and evaluation of the mortar, the methodology proposed by Okamura and Ouchi [2] was used, in which the properties of the mortar in the fresh state (fluidity and viscosity) were analyzed. Mortars already dosed with the optimal proportion of small aggregate were produced with six proportions of limestone filler in relation to the cement mass (f/c of 0, 0.10, 0.20, 0.30, 0.40 and 0.50), and for each of the six proportions were varied six dosages of superplasticizer additive (sp/c in % of 0, 0.20, 0.40, 0.60, 0.80, 1.00).
After preparation of the mortar, the mini-cone slump-flow and V-funnel tests were performed for mortars in order to obtain the G_m and R_m indices, according to equations 1 and 2.

$$G_m = \frac{(d_1 \times d_2 - d_0^2)}{{d_0}^2} \quad (1)$$

Where: Gm: Relative slump-flow for mortars. d_1: first slump-flow diameter obtained with the mini-cone for mortars. d_2: second slump-flow diameter obtained with the mini-cone for mortars. d_0^2: diameter of the base of the mini-cone for mortars.

$$R_m = \frac{10}{Tempo\ de\ escoamento\ (seg)} \quad (2)$$

Where: R_m is the relative flow velocity for mortars.
Determining the values of Gm and Rm of the mortar test and carrying out the tests, the fluidity and viscosity properties of the mortar were evaluated for self-compacting mortars.
High value of Gm indicates greater deformability of the mortar, and lower value of Rm indicates higher viscosity. Domone and Jin [20] suggest a value of Gm ≥ 8, corresponding to slump-flow diameters ≥ 300 mm; and Rm from 1 to 5, corresponding to flow times from 2 s to 10 s. Takada and tangtemsirikul [21] argue that mortars with Gm = 5 and Rm = 1 are considered very acceptable for obtaining concretes with self-compacting properties. On the other hand, Edmatsu *et al*. [22] consider that Gm values between 3 and 7, corresponding to slump-flow diameters of mortar between 200 mm and 283 mm, and Rm between 1 and 2, corresponding to flow times of 5 to 10 seconds, are considered satisfactory for mortars to be used in the production of SCC. For Nepomuceno and Oliveira [23], the Gm should vary from 5.30 to 5.90 and the Rm should be between 1.14 and 1.30, which represents a flow time between 7.70 and 8.80 seconds and a slump-flow between 251 mm and 262 mm.

2.5 Evaluation of the mortar in the hardened state

Compressive strength tests were performed at ages of 7 and 28 days and flexural tensile strength at 28 days. For the mortar mix proportions considered to be self-compacting, 3 specimens were prepared for each age, considering the minimum requirement according to the standard and the limitations of the raw material (SBA) of the same lot for all dosages. For the execution of the test of flexural tensile strength, prismatic molds of size 40 mm X 40 mm X 160 mm were used. The determination of axial compression strength was performed using cylindrical specimens molded with 50 mm in diameter and 100 mm in height. The specimens were kept in a moist curing process until the test age, in which the bases of the specimens were prepared.
The tests of flexural tensile strength were performed from the procedure specified by NBR 13279 [24]. For the axial compressive strength determination, NBR 5739 [25] was used.

3. Results and discussions

3.1 Properties in the fresh state

The compositions used to determine the compactness between sand and SBA and the results of the unit mass obtained are shown in figure 2. The highest unit mass found among all the compositions was 1.69, however, the same value is observed in two proportions, with 70% medium sand and 30% SBA and with 60% medium sand and 40% SBA. In this way, it was decided to use a higher amount of SBA increasing the use of this residue, so that all the mix proportions of mortar were generated by a proportion of small aggregate composed of 60% sand and 40% SBA.
In order to define the optimal aggregate content used in the tests, three small aggregate dosages were analyzed in relation to the cement mass (1: 1, 2: 1 and 3: 1). Table 6 lists the results of the self-compacting properties for the three proportions.

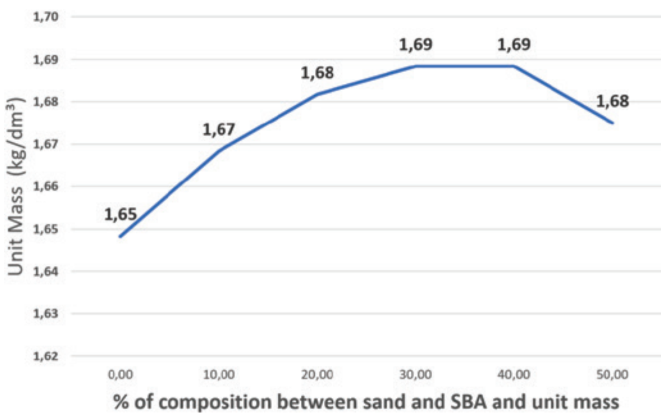

Figure 2
Composition between sand and SBA and unit mass in the hardened state

Table 6
Results for the fresh state test in the determination of the optimal content of small aggregate

SP/cement (%)	D1 slump-flow (mm)	D2 slump-flow (mm)	Flow time (s)	Gm	Rm
		Sand : Cement (s/c) mix 1:1			
0.00	165	160	3.00	1.64	3.34
0.20	280	284	1.66	6.95	6.02
0.40	370	365	1.84	12.50	5.43
A partir de 0.60	Segregação	Segregação	Segregação	Segregação	Segregação

SP/cement (%)	D1 slump-flow (mm)	D2 slump-flow (mm)	Flow time (s)	Gm	Rm
		Sand : Cement (s/c) mix 2:1			
0.00	100	100	–	–	–
0.20	140	149	5.00	1.09	2.00
0.40	255	258	3.25	5.58	3.08
0.60	360	375	2.32	12.50	4.31
0.80	330	345	1.64	10.38	6.10
1.00	–	–	–	–	–

SP/cement (%)	D1 slump-flow (mm)	D2 slump-flow (mm)	Flow time (s)	Gm	Rm
		Sand : Cement (s/c) mix 3:1			
0.00	–	–	–	–	–
0.20	100	100	–	–	–
0.40	100	100	–	–	–
0.60	100	100	–	–	–
0.80	100	100	–	–	–
1.00	100	100	–	–	–

As can be seen in table 6, the tests carried out with ar/c ratio of 3: 1 showed no fluidity signal, thus the flow time values were zero as the material remained cohesive in the V-funnel, the same occurred with the Rm. The mortars produced with a small aggregate ratio of 2: 1 presented adequate fluidity, however, when observing the relative flow index, a high Rm value was observed due to the low viscosity. The best behavior of the mortars was obtained with ar/c ratio of 2: 1, in this way, the mortars produced in the study have this dosage.

After determining the proportion of aggregate to be used in the mortar dosages, the mortar tests were performed by varying the fines content, in order to identify the behavior of the material and obtain

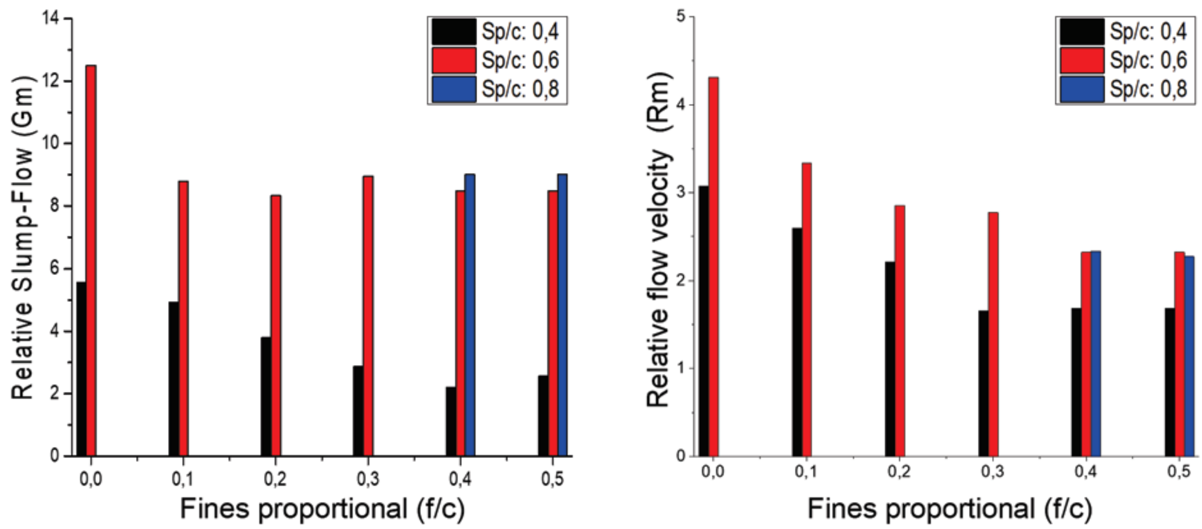

Figure 3
Relative slump-flow area (G_m) and Relative flow velocity (R_m) for self-compacting mortars

the best relationship between very high fluidity and moderate viscosity required for the mortar be considered self-compacting.

In order to obtain higher viscosity of the mortar with SBA, the addition of fines at six proportions was done, being: 0.00; 0.10; 0.20; 0.30; 0.40 and 0.50 of filler/cement ratio, in addition, for each of the dosages of f/c the sp/c ratio was varied in: 0.00; 0.20; 0.40; 0.60; 0.80; and, 1.00%.

For an initial evaluation of its behavior, cone tests were carried out to determine the slump-flow of mortars and v-funnel tests were performed to determine the viscosity of mortars, thus obtaining the indices Gm and Rm. From the determination of the relative slump-flow index (Gm) and the relative flow index (Rm), it was possible to evaluate the high fluidity and moderate viscosity required by the mortar to be considered self-compacting. The results obtained with the tests for all the mortars are presented in table 7. For the proportions of fines of 0, 0.10, 0.20, and 0.30, the mortars with 0.40 and 0.60% sp/c ratio presented high fluidity and moderate viscosity, however, mortars produced with more than 0.80% of sp/c showed signs of segregation. With the insertion of a higher content of fines (0.40 and 0.50 f/c), it was possible to produce Self-Compating Mortars (SCM) with up to 0.80% sp/c. All mortars produced with 1.00% superplasticizer additive, relative to the cement mass (sp/c), presented signs of segregation, with material concentration at the center of the slump-flow and exudation of the mixture at the edges.

The relative slump-flow (G_m) and relative flow velocity (R_m) indices of the self-compacting mortars are shown in figure 3. The slump-

Table 7

Results of mini-cone slump-flow (Gm) and mini-V-funnel (Rm) for the traces dosed

Characteristics of the test: small aggregate/cement = 2 water/cement = 0.50						
Fines/cement	**Sp/cement (%)**	**Slump-flow D1 (mm)**	**Slump-flow D2 (mm)**	**Flow time (s)**	**Gm**	**Rm**
0.00	0.00	100	100	–	0.00	0.00
	0.20	140	149	5.00	1.08	2.00
	0.40	255	258	3.25	5.57	3.07
	0.60	360	375	2.32	12.50	4.31
	0.80	330	345	1.65	10.38	6.09
	1.00	–	–	–	–	–
0.1	0.00	102	102	–	0.04	–
	0.20	110	108	13.00	0.18	0.76
	0.40	243	244	3.85	4.93	2.59
	0.60	314	312	3.00	8.79	3.33
	0.80	333	360	2.80	10.98	3.57
	1.00	346	340	3.20	10.76	3.12
0.2	0.00	100	100	–	–	–
	0.20	110	110	17.00	0.21	0.58
	0.40	224	214	4.53	3.79	2.21
	0.60	302	309	3.50	8.33	2.85
	0.80	318	310	3.40	8.85	2.94
	1.00	–	–	–	–	–
0.3	0.00	100	100	–	–	–
	0.20	106	100	35.00	0.06	0.28
	0.40	198	196	6.00	2.88	1.66
	0.60	317	314	3.60	8.95	2.77
	0.80	315	313	3.20	8.86	3.12
	1.00	–	–	–	–	–
0.4	0.00	100	100	–	–	–
	0.20	103	104	–	0.07	–
	0.40	177	181	5.90	2.20	1.69
	0.60	310	306	4.30	8.48	2.32
	0.80	317	316	4.30	9.01	2.32
	1.00	348	337	4.20	10.72	2.38
0.5	0.00	100	100	–	–	–
	0.20	103	104	–	0.07	–
	0.40	197	181	5.90	2.56	1.69
	0.60	310	306	4.30	8.48	2.32
	0.80	317	316	4.40	9.01	2.27
	1.00	348	337	4.40	10.72	2.27

Figure 4
Slump-flow of mortar with 0.30 for f/c and 0.40% for sp/c

flow (G_m) obtained in mortars considered as self-compacting demonstrate that the higher the use of superplasticizer additive, the greater the relative slump-flow. The impact of the changes in the fines proportions is more evident when using 0.40% sp/c ratio, for the other superplasticizer additive contents, the slump-flow change is smaller.
The relative viscosity (Rm) obtained by means of the v-funnel test for mortars aims to demonstrate mainly the viscosity of the analyzed material, in this way, the smaller the value of Rm the more viscous the mortar. Mortars with 0.40% sp/c ratio showed the highest viscosity, while mortars with 0.60 and 0.80% sp/c ratio did not present major changes. For all the mortars analyzed, the increase in the content of fines gave rise to more viscous mortars, this phenomenon occurs because the limestone filler composes the mortar, filling the voids and consequently increasing the cohesion due to the large surface area of the material. Nevertheless, the maximum effect of the increment in fine material occurs in the ratios of 0.40 and 0.50 of f/c, where the viscosity variation is almost null.
Finally, the mortar with the best relationship between fluidity and viscosity and the most capable of producing mix proportions of self-compacting concrete, with the required characteristics, was with 0.40% sp/c ratio and 30% fine content, relative to the mass of cement. This mix proportions presented average slump-flow of 197.00 millimeters and flow time of 6 seconds, the values for slump-flow and relative flow were respectively 2.88 and 1.66. Figure 4 illustrates the slump-flow obtained by this mortar. This mortar presented the fluidity necessary to be considered self-compacting and presented very high viscosity, the latter being a vital property when inserting large aggregate in the mortar for the production of self-compacting concrete.

3.2 Properties in the hardened state

The results obtained with tensile strength tests from mean values and standard deviations can be visualized in figure 5.
The self-compacting mortars presented a slight gain of tensile strength by increasing the content of limestone filler. The mortars with higher fines contents presented greater tensile strength, this is because the limestone filler filled empty spaces of the mortar.
The results of the compressive strength tests at 7 days, with their mean values and standard deviations, can be visualized in figure 6. The mortars showed an increase in the compressive strength as they increased the indices of sp/c evaluated, this result was already expected because the a/c ratios used were maintained. On the other hand, the increase in the content of fines resulted in an increase in the compressive strength of the mortars, even though the mortars with 0.50 f/c presented the best results for the fracture performed at 7 days.
The results obtained with the compressive strength tests at 28 days with their mean values and standard deviations can be visualized in figure 7. At 28 days, it is possible to notice a general

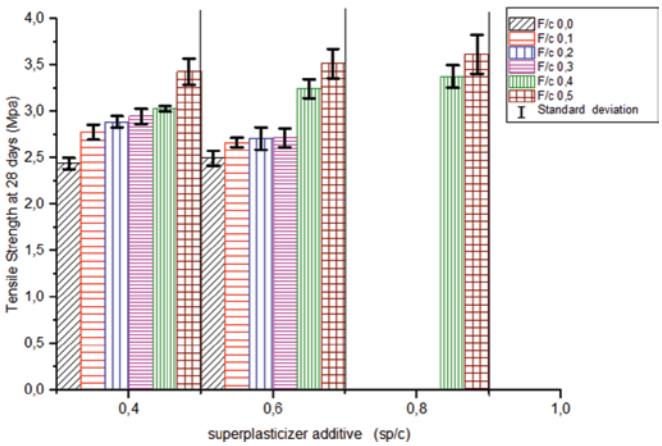

Figure 5
Tensile strength at 28 days for self-compacting mortars

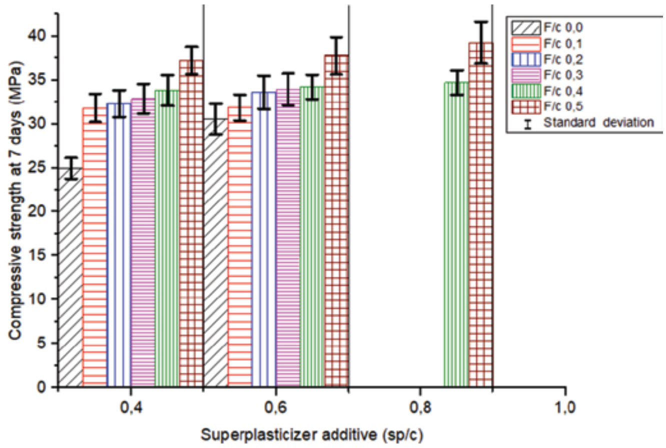

Figure 6
Compressive strength at 7 days for self-compacting mortars

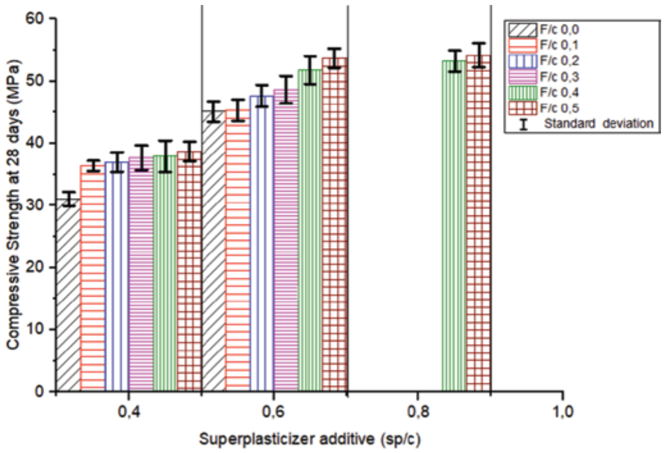

Figure 7
Compressive strength at 28 days for self-compacting mortars

increase in the compressive strength in the mortars by means of the increase in the content of superplasticizer additive comparing the mix proportions with 0.40 and 0.60% sp/c ratio, this effect is justified by the maintenance of the a/c ratio of materials and increase in the use of additive, which when combined, lead to increased hydration of the cement. It is also possible to verify that the increment of calcitic limestone produces an increase in the compressive strength of the mortar because of the greater cohesion and compactness of the materials.

Macedo [26] added sugarcane bagasse ash in mortars and obtained average results of compressive strength at 28 days of 44.70 MPa with ash content of 3%, with 5% addition of ash, the strength was 48.30 MPa, with 8% addition, the strength was of 46.80% and of 51.00 MPa with 10% addition. In the present study, the result of compressive strength obtained from self-compacting mortar with 0.30 of f/c and 0.40% of sp/c was 35.40 MPa, a result similar to those obtained by Nagano [18], in which self-compacting concrete produced with substitution of 10% sand by sugarcane bagasse ash presented compressive strength at 28 days of 30.85 MPa.

Mollin Filho [27] produced self-compacting concretes with replacement of 10% sand with sugarcane bagasse ash and reported a tensile strength of 2.56 MPa. For the mortar considered self-compacting, in the present study, tensile strength was 2.80 MPa close to that obtained by Mollin Filho [27], considering a greater use of SBA.

4. Conclusions

In the fresh state, from the variation in the fine content, it was possible to identify a relationship between increment of calcitic limestone filler and viscosity, while the increase in the dosage of this material provided a reduction in the fluidity. In this way, it can be concluded that the calcitic limestone filler can be used in order to increase the viscosity and to obtain self-compacting mortars. On the other hand, there was a stagnation of this behavior (fluidity and viscosity) in mortars with 0.40 and 0.50 of f/c ratio.

The analyzed variations in the superplasticizer additive proved the expected behavior, as the superplasticizer additive dosage increases, there is a higher fluidity and lower viscosity in the mortars. Another behavior verified, along with the use of fines, is that using very high fines to obtain high viscosity, requires a proportional increase in the superplasticizer additive used.

In the hardened state, the variations analyzed showed little change in the results. The tensile and compressive strength increases slightly as the use of fines and superplasticizer additive increases. The increased use of fines provides an increase in strength due to the filler effect of the material. The increase in strength, obtained by the increase of the sp/c ratio, is provided by the fact that the same water ratio is used in different superplasticizer additive rates.

Another important point to be highlighted is the definition of optimal ranges for obtaining self-compacting mortars with the materials dosed. The mortars that obtained the best aspects of fluidity and viscosity were those produced with a f/c ratio of 0.30, while the optimum superplasticizer additive dosage range was 0.40 - 0.60%, in relation to the cement mass.

In this way, it is possible to produce mortars with self-compacting properties with high rate of sugarcane bagasse ash and to obtain increase in viscosity by increasing the dosage of fines. With the results obtained, it is possible to define mix proportions of mortars that will serve as a basis for the production of concretes with self-compacting properties, from the definition of the viscosity and fluidity to be obtained, being possible to define the content of fines more suitable for the SCC production.

Thus, it is feasible to produce concretes with the partial replacement of the small aggregate by sugarcane bagasse ash (SBA), taking into account the conditions under which the experiments of this study were subjected to. Thus, from the results obtained through this study, it was possible to replace 40% of the small aggregate with CBCA obtaining a larger unit mass of the composition made between sand and SBA.

5. Acknowledgements

To the Graduate Program in Urban Engineering (PEU) and to the Department of Civil Engineering (DEC-UEM), for contributions and assistance during the research.

To the Construction Materials Laboratory for the provision of resources used during the research.

To the Santa Terezinha Plant for donating the SBA.

To BASF do Brasil, which through the engineer Vitor M. Marconi granted the sponsorship of the superplasticizer additive Glenium 51.

6. References

[1] ALCOFORADO, L. F. M. Viabilidade econômica do concreto auto-adensável na construção de prédios em Goiânia – GO. Journal on-line Especialize, Goiânia, v. 3, n. 1, p. 1-13, 2013.

[2] OKAMURA, H.; OUCHI, M. Self-compacting concrete. Journal of Advanced Concrete Technology, Tokyo, vol. 1, n. 1, p. 5-15, abr. 2003.

[3] ALCANTARA, M. A. M.; SANTOS, B. V. Concreto auto-adensável com cinzas de bagaço de cana como finos: Reologia do concreto fresco e comportamento no estado endurecido. Eletronic Journal of Civil Engineering, V. 5, N. 1, p. 17-35, 2012.

[4] OLIVEIRA, F. L; MELLO, E. F. A mineração de areia e os impactos ambientais na bacia do rio São João, RJ. Brazilian Journal of Geosciences, Rio de Janeiro, V. 37, 2º ed., p 374-389, 2007.

[5] CONAB - COMPANHIA NACIONAL DE ABASTECIMENTO. Acompanhamento de safra brasileira: cana-de-açúcar, segundo levantamento, agosto/2016 - Companhia Nacional de Abastecimento. – Brasília: CONAB 2016.

[6] FIESP/CIESP – FEDERAÇÃO DA INDÚSTRIAS DO ESTADO DE SÃO PAULO/ CENTRO DAS INDÚSTRIAS DO ESTADO DE SÃO PAULO Ampliação da oferta de energia através da biomassa. São Paulo: 2001.

[7] ASSOCIAÇÃO BRASILEIRA DE NORMAS TÉCNICAS. ABNT NBR 5733. Cimento Portland de alta resistência inicial. Rio de Janeiro, 1991

[8] OKAMURA, H.; OUCHI, M. Self-compacting concrete. Journal of Advanced Concrete Technology, Tokyo, vol. 1, n. 1, p. 5-15, abr. 2003.

[9] VOTORANTIM. Catálogo de cimentos 2016. Available in: <http://www.mapadaobra.com.br/produtos/cimento/linha>. Access in: November 13, 2015.

[10] ASSOCIAÇÃO BRASILEIRA DE NORMAS TÉCNICAS. ABNT NBR NM 248. Agregados - Determinação da composição granulométrica. Rio de Janeiro, 2003.

[11] ASSOCIAÇÃO BRASILEIRA DE NORMAS TÉCNICAS. ABNT NBR NM 30. Agregado miúdo - Determinação da absorção de água. Rio de Janeiro, 2001.

[12] ASSOCIAÇÃO BRASILEIRA DE NORMAS TÉCNICAS. ABNT NBR NM 52. Agregado miúdo - Determinação de massa específica e massa específica aparente. Rio de Janeiro, 2002.

[13] ASSOCIAÇÃO BRASILEIRA DE NORMAS TÉCNICAS. ABNT NBR NM 45. Agregados - Determinação da massa unitária e do volume de vazios. Rio de Janeiro. 2006.

[14] BASF. Ficha técnica de produto: GLENIUM 51 - Aditivo Superplastificante de terceira geração. Available in: < https://www.ntcbrasil.com.br/wp-content/uploads/2014/12/glenium-51--especificacoes-completas.pdf >. Access in: July 12, 2015.

[15] CAZANGA. Calcário Agrícola: características do produto. Available in: < http://www.cazanga.com.br/index.asp?c=paginas&modulo=conteudo&url=80 >. Access in: August 26, 2015.

[16] NUNES, I. H. S. Estudo das características físicas e químicas da cinza do bagaço de cana-de-açúcar para uso na construção. Masters dissertation. State University of Maringá, UEM, Technology Center, Maringá, 2009.

[17] SOUTO, J. M. F. Avaliação do desempenho da cinza do bagaço de cana-de-açúcar na produção de concretos. 2009, 118f. Master dissertation. State University of Maringá, UEM, Technology Center, Maringá, 2010.

[18] NAGANO, M. F. Dosagem do concreto autoadensável utilizando a cinza do bagaço de cana-de-açúcar. 2014, 142f. Master dissertation. State University of Maringá, UEM, Techonolgy Center, Maringá, 2014.

[19] ASSOCIAÇÃO BRASILEIRA DE NORMAS TÉCNICAS. ABNT NBR 15900-1. Água para amassamento do concreto. Rio de Janeiro, 2009.

[20] DOMONE, P. L; JIN, J. Properties of mortar for self-compacting concrete. In: FIRST INTERNATIONAL RILEM SYMPOSIUM ON SELF-COMPACTING CONCRETE, p. 109-120, 1999.

[21] TAKADA, K; TANGTEMSIRIKUL, S. Testing of fresh concrete. In: SELF-COMPACTING CONCRETE: STATE-OF--THE-ART REPORT OF RILEM TECHNICAL COMMITTEE 174-SCC. Cachan: RILEM Publications, S.A.R.L., 2000, p. 20-34.

[22] EDMATSU, H; NISHIDA, N; OUCHI, M. A rational mix-design method for self-compacting concrete considering interaction between coarse aggregate and mortar particles. In: FIRST INTERNATIONAL RILEM SYMPOSIUM ON SELF-COMPACTING CONCRETE, 1999, p. 309-320.

[23] NEPOMUCENO, M; OLIVEIRA, L.; LOPES, S. Methodology for mix design of the mortar phase of self-compacting concrete using different mineral additions in binary blends of powders. Construction and Building Materials. v. 26, n.1, p. 317-326, 2012.

[24] ASSOCIAÇÃO BRASILEIRA DE NORMAS TÉCNICAS. ABNT NBR 13279. Argamassa para assentamento e revestimento de paredes e tetos – Determinação da resistência à tração na flexão e à compressão. Rio de Janeiro, 2005.

[25] ASSOCIAÇÃO BRASILEIRA DE NORMAS TÉCNICAS. ABNT NBR 5739. Concreto – Ensaio de compressão de corpos-de prova cilíndricos. Rio de Janeiro, 2007.

[26] MACEDO, P. C. Avaliação do desempenho de argamassas com adição de cinza do bagaço de cana-de-açúcar. 2009. 116 f. Master dissertation. Paulista State University, Ilha Solteira Engineering College, 2009.

Volume 12, Number 1 (February 2019) p. 179 – 198 • ISSN 1983-4195
http://dx.doi.org/10.1590/S1983-41952019000100012

REVISTA IBRACON DE ESTRUTURAS E MATERIAIS
IBRACON STRUCTURES AND MATERIALS JOURNAL

Behavior of the self-compacting mortar with sugarcane bagasse ash in the fresh and hardened state

Estudo do comportamento da argamassa autoadensável com cinza do bagaço de cana-de-açúcar no estado fresco e endurecido

V. C. SANTOS [a]
viniciuscarrijodossantos@gmail.com
https://orcid.org/0000-0002-7501-4998

R. D. VANDERLEI [a]
rdvanderlei@uem.br
https://orcid.org/0000-0001-5676-6951

K. K. MORAES [a]
katherinekaneda@hotmail.com
https://orcid.org/0000-0003-4461-850X

E. T. D. F. ROSINA [a]
eti_tayna@hotmail.com
https://orcid.org/0000-0003-4796-9284

G. M. BALBINO [a]
guilhermebalbino1@live.com
https://orcid.org/0000-0001-6394-3805

Abstract

Self-compacting concrete (SCC) is a material with high workability and moderate viscosity when compared to conventional concrete. Due to its advantages, the SCC has been investigated in the last decades and the research studies the use of new components in its structure and the search for the improvement of its performance, both in the fluid and in the hardened state. The goal of this study was to evaluate the behavior of self-compacting mortars with limestone filler and with the addition of sugarcane bagasse ash (SBA) partially replacing the small aggregate. To reach this goal, initially, a rate of replacement of natural sand by SBA was set. Afterwards, slump-flow and funnel-V tests were carried out in order to check the behavior of the mortars in the fresh state. After checking the behavior of the mortars in their fresh state, the different mix proportions that achieved the best aspects of fluidity and viscosity was selected, and, for self-compacting mortars, specimens were molded to determine tensile strength at 28 days, and compressive strength at 7 and 28 days. The experimental analyses demonstrated an increase in viscosity and reduction in fluidity with increasing content of limestone filler, facilitating the obtaining of self-compacting mortars. Regarding the performance of the material in the hardened state, the mortars showed a slight increase in tensile and compressive strength due to the filler effect of fines. It was possible to replace 40% of the small aggregate with SBA.

Keywords: self-compacting mortar, sugarcane bagasse ash, limestone.

Resumo

O concreto autoadensável (CAA) é um material que apresenta alta trabalhabilidade e moderada viscosidade quando comparado ao concreto convencional. Em função de suas vantagens, nas últimas décadas, o CAA vem sendo investigado e as pesquisas abordam a utilização de novos componentes em sua estrutura e a busca pela melhoria de seu desempenho, tanto no estado fluido quanto no endurecido. Este estudo teve como objetivo avaliar o comportamento de argamassas autoadensáveis com fíler calcário e com a adição de cinza do bagaço de cana-de-açúcar (CBCA) em substituição parcial ao agregado miúdo. Para atingir este objetivo, inicialmente, uma taxa de substituição de areia natural por CBCA foi definida. Na sequência, foram realizados ensaios de espalhamento e funil-V com o intuito de verificar o comportamento das argamassas no estado fresco. Após a verificação do comportamento das argamassas em seu estado fresco, a série de traços que obteve os melhores aspectos de fluidez e viscosidade foi selecionada, e, para as argamassas autoadensáveis foram moldados corpos-de-prova para determinação da resistência à tração aos 28 dias, e resistência à compressão aos 7 e 28 dias. As análises experimentais demonstraram um aumento de viscosidade e redução da fluidez à medida em que se aumentava o teor de fíler calcário, facilitando a obtenção de argamassas autoadensáveis. Com relação ao desempenho do material no estado endurecido, as argamassas apresentaram leve incremento de resistência à tração e à compressão, devido ao efeito fíler dos finos. Foi possível substituir 40% do agregado miúdo por CBCA.

Palavras-chave: argamassa autoadensável, cinza do bagaço de cana-de-açúcar, fíler calcário.

[a] *State University of Maringá, Civil Engineering Department, Maringá, PR, Brazil.*

Received: 07 Dec 2016 • Accepted: 21 Aug 2018 • Available Online: 05 Feb 2019

1. Introdução

O concreto é o material de construção mais utilizado no mundo, porém, com toda dinâmica e inovações nos projetos de engenharia, exigiu-se estudos aprofundados a respeito desse componente da construção civil, desenvolvendo-se novos tipos de concreto que vão além do concreto convencional, como o concreto de alto desempenho, concreto reforçado com fibras, concretos com altos teores de adições pozolânicas, concretos aparentes, brancos, coloridos, sustentáveis e autoadensáveis, entre outros [1].

O surgimento do material que posteriormente seria chamado de concreto autoadensável foi justificado por [2], em função da baixa habilidade que os trabalhadores possuíam para realizar uma concretagem satisfatória. A demanda por estruturas de concreto cada vez mais duráveis também incentivou o desenvolvimento de um material que se espalhasse pela ação de seu peso próprio, material este que reduziria a necessidade de intervenção humana, tendo como resultado peças melhor concretadas.

O concreto autoadensável (CAA) é um material que não necessita de vibração durante as fases de lançamento e de adensamento, no entanto, para que seja considerado autoadensável ele deve atender a alguns requisitos: apresentar-se fluido, não apresentar segregação, exsudação, ou surgimento de bloqueios em peças densamente armadas [3].

Para determinar a proporção de materiais constituintes do concreto autoadensável de maneira eficaz, é importante dispensar uma atenção especial no estudo a respeito da dosagem da argamassa, tendo em vista que o CAA é composto basicamente por argamassa e agregado graúdo. Por este motivo, torna-se mais conveniente realizar os ajustes e testes na fase da argamassa, que posteriormente irá compor o CAA. Quando o concreto é deformável, a pasta com alta viscosidade impede o aumento da tensão interna sobre as partículas de agregado graúdo. A alta deformabilidade do concreto autoadensável pode ser obtida apenas pelo emprego de aditivo superplastificante, sem a necessidade de alteração da relação água/cimento da argamassa [2].

A obtenção de bons resultados em concretos autoadensáveis é possível por meio da realização de estudos referentes à dosagem de argamassa. Por meio do estudo da argamassa é possível determinar se o material apresenta fluidez demasiada, baixa viscosidade, segregação e exsudação. A etapa de dosagem da argamassa é muito importante, tendo em vista que nesta fase as proporções de materiais devem ser constituídas de maneira que o CAA não perca trabalhabilidade.

Outro fator preponderante na produção de concretos é o elevado consumo de agregados, dentre eles, a areia, um recurso natural muito explorado e utilizado pela construção civil como agregado miúdo. A extração de materiais aluvionares em rios vem sendo fortemente condenada por diversos setores da sociedade, isto se deve principalmente em função do potencial desequilíbrio que esta atividade pode causar na dinâmica fluvial, em consequência imediata a esta atividade ocorre a redefinição dos limites do canal, seja pela retirada ou adição de materiais, que por sua vez pode promover mudanças no padrão de fluxo e transporte de sedimentos [4].

Na indústria sucroalcooleira, um dos subprodutos gerados a partir da produção de açúcar, álcool e outros produtos, é o bagaço da cana-de-açúcar (BCA). A partir da cogeração de energia nas usinas sucroalcooleiras, processo em que o BCA é utilizado como combustível para as caldeiras na geração de energia, origina-se um resíduo denominado Cinza do Bagaço de Cana-de-açúcar (CBCA), que até o momento não possui valor econômico para a indústria.

Tendo em vista os desequilíbrios ambientais que a extração da areia pode causar, a utilização de materiais renováveis e alternativos pode ser uma solução. Assim sendo, uma das propostas deste estudo consiste na utilização da CBCA, material proveniente de fontes renováveis, em substituição parcial ao agregado miúdo (areia), na dosagem de argamassas autoadensáveis.

No Brasil, o setor sucroalcooleiro consiste em um segmento muito bem estruturado, em termos de sua cadeia produtiva. O país é o maior produtor mundial de cana-de-açúcar, seguido pela Índia e China. Para a safra 2016/2017, espera-se produzir no país e destinar à indústria 684,77 milhões de toneladas de cana-de-açúcar (3,27% a mais do que a safra anterior), distribuídos em uma área de cerca de 8,97 milhões de hectares em todos os estados produtores. O maior estado brasileiro produtor de cana-de-açúcar é São Paulo (52,30 % da área plantada), sendo que o Paraná ocupa a 4º posição no *ranking* dos estados produtores, com 7,00 % de toda a área brasileira plantada [5].

Conforme dados da FIESP/CIESP [6], a cada tonelada de cana-de-açúcar processada são gerados 260 quilogramas de BCA, destes 260 quilogramas de BCA destinados à queima, gera-se 6,20 quilogramas de CBCA. Sendo assim, ao aplicar estes valores à projeção da safra 2016/2017 de cana-de-açúcar no Brasil, considerando que toda a produção esperada seja destinada à indústria, seriam geradas aproximadamente 178 milhões de toneladas de BCA, caso todo este bagaço fosse destinado à queima, seriam geradas aproximadamente 4,24 milhões de toneladas de CBCA na safra em questão.

O objetivo deste estudo é desenvolver argamassa com características autoadensáveis, substituindo parcialmente o agregado miúdo por cinza do bagaço de cana-de-açúcar (CBCA) e utilizando como finos o fíler calcário para controlar a viscosidade. Avaliando assim, o comportamento de suas propriedades mecânicas (compressão e tração).

Tabela 1
Caracterização do cimento CP V ARI Ultra [8]

Item de controle	Unidade	Média
Início da pega	horas	1,50
Término de pega	horas	8,90
Massa específica	g/cm^3	3,20
Resistência a compressão ao término do 1° dia	MPa	11,10
Resistência a compressão aos 3 dias	MPa	23,90
Resistência a compressão aos 7 dias	MPa	32,80
Resistência a compressão aos 28 dias	MPa	36,70

Tabela 2
Caracterização da areia

Características	Unidade	Valores
Massa específica (γ_s)	kg/dm³	2,65
Absorção do agregado (ABS)	%	–
Massa unitária solta (MU)	kg/dm³	1,52
Massa unitária compactada (MUC)	kg/dm³	1,63
Diâmetro máximo característico ($\phi_{max.}$)	mm	1,20
Módulo de finura	%	2,84

2. Materiais e programa experimental

O programa experimental foi dividido em 4 fases e foi desenvolvido no laboratório de materiais de construção da Universidade Estadual de Maringá (UEM). As etapas realizadas no programa experimental são apresentadas a seguir:
I Caracterização dos materiais - Fase 1;
II Estudo da composição do agregado miúdo - Fase 2;
III Determinação da proporção ótima de agregado miúdo – Fase 3;
IV Dosagem da argamassa autoadensável - Fase 4;
V Avaliação da argamassa no estado endurecido – Fase 5.
Nos tópicos 2.1 a 2.5 apresentam-se, detalhadas, cada uma das etapas do programa experimental.

2.1 Materiais

Os materiais constituintes na argamassa autoadensável foram: Cimento; água; areia (granulometria média e fina); Cinza do bagaço de cana-de-açúcar (CBCA); Fíler Calcário Calcítico, e; aditivo superplastificante.
O cimento utilizado para dosagem da argamassa foi o CPV ARI RS, denominado Cimento Portland de alta resistência inicial e resistente a sulfatos fornecido pela Votorantim Cimento LTDA. Para a determinação das características do material realizou-se a caracterização do cimento segundo a NBR 5733:1991 [7]. Os resultados da caracterização fornecida pelo fabricante são apresentados na tabela 1.
De acordo com a NBR 5733:1991 [7], que trata dos cimentos Portland de alta resistência inicial, o aglomerante utilizado na pesquisa atende às exigências de alta resistência inicial, obtido pela moagem do clínquer Portland, e é constituído principalmente por silicatos de cálcio hidráulicos, ao qual se adiciona durante a operação a quantidade de uma ou mais formas de sulfato de cálcio.
A areia utilizada é de origem quartzosa da região de Maringá – PR. A composição granulométrica da areia foi baseada na NBR NM 248: 2003 [9], e para a classificação deste agregado foi utilizada a NBR 7211: 2009 [10]. Utilizou-se, ainda, a NBR NM 30:2001 [11] para a determinação da absorção de água do agregado miúdo. A NBR NM 52:2002 [12] foi aplicada a fim de determinar a massa específica e a massa específica aparente do agregado miúdo. Para a determinação da massa unitária e do volume de vazios do agregado miúdo foi utilizada a NBR NM 45: 2006 [13]. Na tabela 2 apresentam-se os resultados para a caracterização da areia.

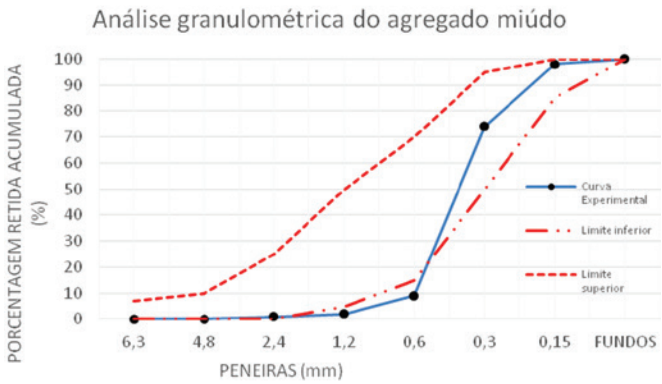

Figura 1
Distribuição granulométrica da areia utilizada segundo a NBR 7211:2009 [10]

O aditivo utilizado na pesquisa foi o GLENIUM 51, sendo este classificado como de terceira geração para concreto, o produto é liquido e livre de cloretos, é aplicado geralmente em concretos de alto desempenho, onde se objetiva minimizar a relação água/cimento e aumentar a durabilidade do material. O aditivo é baseado em uma cadeia de éter policarboxílico modificado que age como dispersante do material cimentício, proporcionando alta redução no consumo de água e a superplastificação do material, aumentando a trabalhabilidade do concreto sem alterar o tempo de pega. As informações do GLENIUM 51 podem serem visualizadas na tabela 3.

Tabela 3
Informações sobre o aditivo superplastificante utilizado [14]

Fabricante	Nome	Função	Base química	Teor de sólido (%)	pH	Viscosidade (cps)	Densidade (g/cm³)	Aspecto	Solubilidade	Cor
BASF S/A	Glenium 51	Aditivo superplastificante de terceira geração	Éter policarboxílico	28,50 31,50	5-7	<150	1,07 1,11	Líquido	Total na água	Branco turvo

Tabela 4
Informações sobre o fíler calcário calcítico utilizado [15]

Fabricante	Nome	Função	Base química	Base granulométrica	Cor
Cazanga	Calcário calcítico	Aplicações na indústria de construção e de alimentação animal	CaO: mínimo de 51,80% MgO: máximo de 1% Ca: mínimo de 37% Mg: máximo de 0,63%	94% passante em peneira 325 *mesh* 94% menores que 45 µm (0,045mm)	Branca

O fíler calcário utilizado foi o de origem calcítica e as suas características, fornecidas pelo fabricante, apresentam-se na tabela 4.
A cinza do bagaço de cana-de-açúcar, utilizada neste estudo, foi coletada na Usina Santa Terezinha no distrito de Iguatemi, nas proximidades de Maringá, região Noroeste do Paraná. Para realização da pesquisa, utilizou-se a cinza em condição natural, tendo como único beneficiamento o peneiramento na malha 0,595mm (#30), com o objetivo de retirar o material grosseiro e impurezas.
Como a cinza do bagaço de cana-de-açúcar utilizada nesta pesquisa é do mesmo lote da utilizada nas pesquisas de Nunes [16], Souto [17] e Nagano [18] as características químicas e físicas foram retiradas das pesquisas dos autores supracitados. Assim sendo, estas informações podem ser visualizadas na tabela 5.
A água utilizada nos experimentos é proveniente da rede de abastecimento da cidade de Maringá -PR, que de acordo com os requisitos da NBR 15900-1:2009 [19] intitulada Água para amassamento do concreto-requisitos.

2.2 Estudo da composição do agregado miúdo

A fim de determinar uma composição ótima entre o agregados miúdo e a CBCA foi realizado um estudo para otimizar a compacidade entre eles. Para realização do estudo utilizou-se a norma NBR NM 45:2006 [13] para determinação da massa unitária no estado compactado, em que, o ensaio era executado para cada uma das composições analisadas e a massa unitária no estado compactado seco era determinada, desta maneira, a maior massa unitária representaria a melhor composição entre os agregados.
O ensaio foi realizado variando o percentual da composição da areia e CBCA de 10 em 10% até atingir uma composição com

Tabela 5
Caracterização da cinza do bagaço de cana-de-açúcar utilizada oriunda da Usina de Iguatemi [16, 17, 18]

Características	Unidade	Valores
*Grau de uniformidade (U)	–	1,62
*D_{10}	mm	0,13
*D_{30}	mm	0,18
*D_{80}	mm	0,21
*Uniformidade	–	U<5 (Muito uniforme)
*Coeficiente de curvatura (CC)	–	1,19
*Distribuição granulométrica	–	Bem graduado
*Classificação granulométrica	–	Semelhança a areia
* Massa específica	g/cm³	2,64
* Teor de umidade	%	0,27
** Área específica	m²/kg	5356
** Composição mineralógica – Difração X	Quartzo (SiO_2)	Altamente cristalino ausência de fase amorfa
** Matéria orgânica total	%	3,55
** Carbono orgânico	%	1,97
** Atividade pozolânica	Mg CaO/g	23
** SiO_2	–	Alto teor de sílica sob a forma de quartzo atribuído a baixa atividade pozolânicas
*** C	mg/kg	486
*** MO		8,85
*** CaO		1,02
*** MgO		0,15
*** K_2O		0,37
*** P_2O_5		0,01
*** Fe		1.375,65
*** Cu		29,73
*** Mn		70,96
*** Zn		16,82

quantidades iguais dos dois materiais (50% areia e 50% de CBCA). A composição com maior massa unitária no estado compactado foi a utilizada nas dosagens de argamassa.

2.3 Determinação da proporção ótima de agregado miúdo

Para definir a proporção ótima de agregado miúdo foram desenvolvidas três séries de traços com relação cimento/agregado miúdo em massa de 1:1, 1:2 e 1:3 respectivamente. Após a confecção das argamassas foram realizados os ensaios de espalhamento e funil-V para argamassas e obtidos os parâmetros de autoadensabilidade (Gm e Rm) a fim de determinar a melhor relação de agregado miúdo (areia + CBCA) por cimento (ar/c) para a produção de argamassas com os materiais utilizados.

2.4 Dosagem da argamassa autoadensável

Para desenvolvimento e avaliação da argamassa foi utilizada a metodologia proposta por Okamura e Ouchi [2], em que foram analisadas as propriedades da argamassa no estado fresco (fluidez e viscosidade). As argamassas dosadas já com a proporção ótima de agregado miúdo foram produzidas em seis proporções de fíler calcário em relação a massa de cimento (f/c de 0; 0,10; 0,20; 0,30; 0,40 e 0,50), e, para cada uma das seis proporções foram variadas seis dosagens de aditivo superplastificante (sp/c em % de 0; 0,20; 0,40; 0,60; 0,80; 1,00).
Após confecção da argamassa foram realizados os ensaios de espalhamento e funil-V para argamassas com o intuito de obter os índices G_m e R_m, conforme a equação 1 e 2.

$$G_m = \frac{(d_1 \times d_2 - d_0^2)}{d_0{}^2} \quad (1)$$

Em que: Gm: Índice de espalhamento relativo para argamassas. d_1: primeiro diâmetro do espalhamento obtido com o mini cone para argamassas. d_2: segundo diâmetro do espalhamento obtido com o mini cone para argamassas. d_0^2: diâmetro da base do mini cone para argamassas.

$$R_m = \frac{10}{Tempo\ de\ escoamento\ (seg)} \quad (2)$$

Em que: R_m é o escoamento relativo para argamassas.
Determinados os valores de Gm e Rm do ensaio da argamassa e realizados os ensaios, foram avaliadas as propriedades de fluidez e viscosidade da argamassa para determinação das argamassas autoadensáveis.
Alto valor de Gm indica maior deformabilidade da argamassa, e menor valor de Rm indica maior viscosidade. Domone e Jin [20] sugerem um valor de Gm ≥ 8, correspondente a diâmetros de espalhamento ≥ 300 mm; e Rm de 1 a 5, correspondentes a tempos de escoamento de 2 s a 10 s. Takada e tangtemsirikul [21] defendem que argamassas com Gm = 5 e Rm = 1 são consideradas bem aceitáveis para obter concretos com propriedades autoadensáveis. Por outro lado, Edmatsu *et al*. [22] consideram que valores de Gm entre 3 e 7, correspondentes a diâmetros de espalhamento de argamassa entre 200 mm a 283 mm, e de Rm entre 1 e 2, correspondendo a tempos de escoamento de 5 a 10 segundos, são considerados satisfatórios para as argamassas serem utilizadas na produção de CAA. Para Nepomuceno e Oliveira [23], o Gm deve variar de 5,30 à 5,90 e o Rm deve ficar entre 1,14 e 1,30 o que representa um tempo de escoamento entre 7,70 e 8,80 segundos e um espalhamento entre 251 mm e 262 mm.

2.5 Avaliação da argamassa no estado endurecido

Foram realizados ensaios de resistência à compressão nas idades de 7 e 28 dias e de resistência à tração na flexão aos 28 dias. Para os traços de argamassa considerados autoadensáveis foram confeccionados 3 corpos de prova para cada idade, considerando a necessidade mínima segundo a norma e as limitações de matéria-prima (CBCA) do mesmo lote para realização de todas as dosagens. Para a execução do ensaio de resistência à tração na flexão foram utilizados moldes prismáticos de dimensão 40 mm X 40 mm X 160 mm. A determinação da resistência à compressão axial foi realizada utilizando corpos de prova cilíndricos moldados com 50 mm de diâmetro e 100 mm de altura. Os corpos de prova foram mantidos em processo de cura úmida até a idade do ensaio, no qual foram preparadas as bases dos corpos de prova.
Os ensaios de resistência à tração na flexão foram realizados a partir do procedimento especificado pela NBR 13279 [24]. Para a determinação da resistência à compressão axial foi utilizada a NBR 5739 [25].

3. Resultados e discussões

3.1 Propriedades no estado fresco

As composições utilizadas para a determinação da compacidade entre areia e CBCA e os resultados das massas unitárias obtidas apresentam-se na figura 2. A maior massa unitária observada entre todas as composições foi de 1,69, entretanto, o mesmo valor é observado em duas proporções, com 70% de areia média e 30% de CBCA e com 60% de areia média e 40% de CBCA. Desta forma, optou-se pela proporção que utilizasse maior quantidade de CBCA aumentando o aproveitamento deste resíduo, de modo que todos os traços de argamassa foram gerados por uma proporção

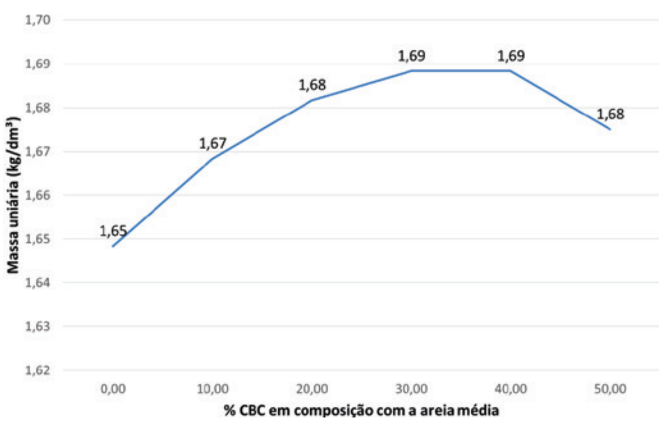

Figura 2
Composição entre areia e CBCA e massa unitária no estado compactado

Tabela 6
Resultados para o ensaio no estado fresco na definição do teor ótimo de agregado miúdo

SP/cimento (%)	Espalhamento D1 (mm)	Espalhamento D2 (mm)	Tempo de escoamento (s)	G_m	R_m
		Areia: Cimento (ar/c) de 1:1			
0,00	165	160	3,00	1,64	3,34
0,20	280	284	1,66	6,95	6,02
0,40	370	365	1,84	12,50	5,43
A partir de 0,60	Segregação	Segregação	Segregação	Segregação	Segregação
SP/cimento (%)	**Espalhamento D1 (mm)**	**Espalhamento D2 (mm)**	**Tempo de escoamento (s)**	**G_m**	**R_m**
		Areia: Cimento de 2:1			
0,00	100	100	–	–	–
0,20	140	149	5,00	1,09	2,00
0,40	255	258	3,25	5,58	3,08
0,60	360	375	2,32	12,50	4,31
0,80	330	345	1,64	10,38	6,10
1,00	–	–	–	–	–
SP/cimento (%)	**Espalhamento D1 (mm)**	**Espalhamento D2 (mm)**	**Tempo de escoamento (s)**	**G_m**	**R_m**
		Areia: Cimento de 3:1			
0,00	-	-	-	-	-
0,20	100	100	-	-	-
0,40	100	100	-	-	-
0,60	100	100	-	-	-
0,80	100	100	-	-	-
1,00	100	100	-	-	-

de agregado miúdo composta por 60% de areia e 40% de CBCA. Para definir o teor ótimo de agregado utilizado nos ensaios foram analisadas três dosagens de agregado miúdo em relação a massa de cimento (1:1; 2:1; e, 3:1). A tabela 6 demonstra os resultados das propriedades autoadensáveis para as três proporções.

Como pode ser observado na tabela 6, os ensaios realizados com relação ar/c de 3:1 não apresentaram nenhum sinal de fluidez, desta maneira os valores de tempo de escoamento foram nulos já que o material permaneceu coeso no funil-V, o mesmo ocorreu com o Rm. As argamassas produzidas com proporção de

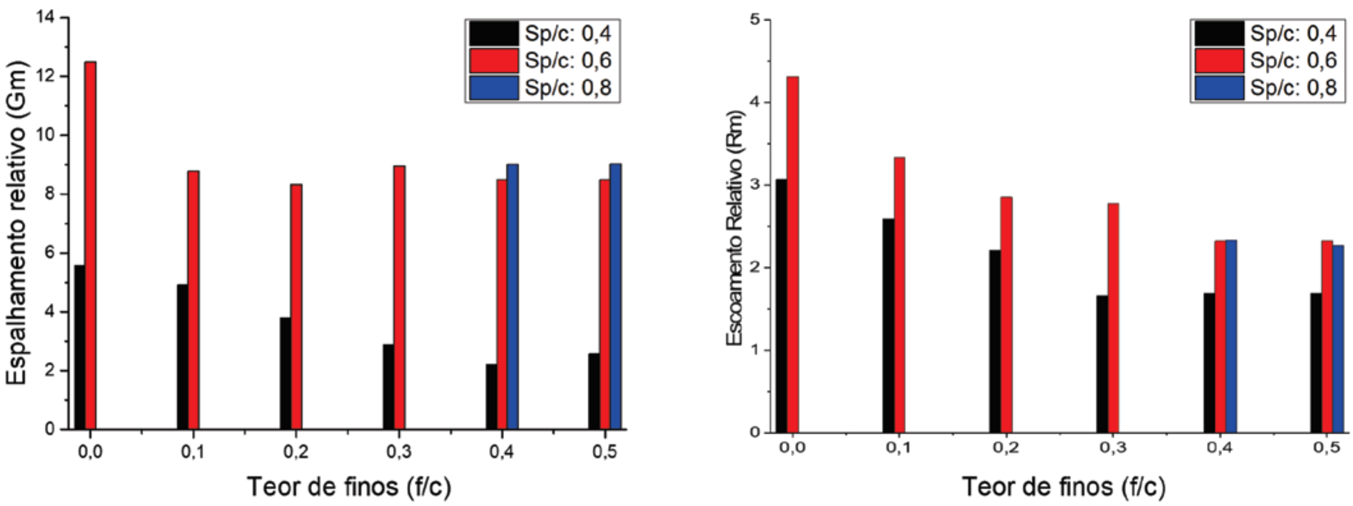

Figura 3
Índice de espalhamento relativo (G_m) e Índice de escoamento relativo (R_m) para as argamassas autoadensáveis

agregado miúdo de 2:1 apresentaram fluidez adequada, porém, ao observar o índice de escoamento relativo nota-se um alto valor de Rm resultante da baixa viscosidade. O melhor comportamento das argamassas foi obtido com relação ar/c de 2:1, desta maneira, as argamassas produzidas na sequência do estudo possuem essa dosagem.

Após a definição da proporção de agregado a ser utilizado nas dosagens de argamassa foram realizados os ensaios com as argamassas variando o teor de finos, a fim de identificar o comportamento do material e obter a melhor relação entre altíssima fluidez e moderada viscosidade necessárias para a argamassa ser considerada autoadensável.

Para se obter maior viscosidade da argamassa com CBCA foi realizada a adição de finos em seis proporções, sendo elas: 0,00; 0,10; 0,20; 0,30; 0,40 e 0,50 de relação fíler/cimento, além disso, para cada uma das dosagens de f/c foi variada a relação de sp/c em: 0,00; 0,20; 0,40; 0;60; 0,80; e, 1,00 %.

Para uma avaliação inicial do seu comportamento, foram realizados os ensaios por meio do cone para determinação de espalhamento de argamassas e o funil-v para determinação da viscosidade de argamassas e obtido os índices Gm e Rm. A partir da determinação do índice de espalhamento relativo (Gm) e do índice de escoamento relativo (Rm) foi possível avaliar a alta fluidez e moderada viscosidade requisitada pela argamassa para ser considerada autoadensável. Os resultados obtidos com os ensaios para todas as argamassas dosadas são apresentados na tabela 7.

Tabela 7

Resultados de espalhamento (G_m) e viscosidade (R_m) para os traços dosados

Características do ensaio: agregado miúdo/cimento = 2 água/cimento = 0,50						
Finos/cimento	**SP/cimento (%)**	**Espalhamento D1 (mm)**	**Espalhamento D2 (mm)**	**Tempo de escoamento (s)**	**G_m**	**R_m**
0,00	0,00	100	100	–	0,00	0,00
	0,20	140	149	5,00	1,08	2,00
	0,40	255	258	3,25	5,57	3,07
	0,60	360	375	2,32	12,50	4,31
	0,80	330	345	1,65	10,38	6,09
	1,00	–	–	–	–	–
0,1	0,00	102	102	–	0,04	–
	0,20	110	108	13,00	0,18	0,76
	0,40	243	244	3,85	4,93	2,59
	0,60	314	312	3,00	8,79	3,33
	0,80	333	360	2,80	10,98	3,57
	1,00	346	340	3,20	10,76	3,12
0,2	0,00	100	100	–	–	–
	0,20	110	110	17,00	0,21	0,58
	0,40	224	214	4,53	3,79	2,21
	0,60	302	309	3,50	8,33	2,85
	0,80	318	310	3,40	8,85	2,94
	1,00	–	–	–	–	–
0,3	0,00	100	100	–	–	–
	0,20	106	100	35,00	0,06	0,28
	0,40	198	196	6,00	2,88	1,66
	0,60	317	314	3,60	8,95	2,77
	0,80	315	313	3,20	8,86	3,12
	1,00	–	–	–	–	–
0,4	0,00	100	100	–	–	–
	0,20	103	104	–	0,07	–
	0,40	177	181	5,90	2,20	1,69
	0,60	310	306	4,30	8,48	2,32
	0,80	317	316	4,30	9,01	2,32
	1,00	348	337	4,20	10,72	2,38
0,5	0,00	100	100	–	–	–
	0,20	103	104	–	0,07	–
	0,40	197	181	5,90	2,56	1,69
	0,60	310	306	4,30	8,48	2,32
	0,80	317	316	4,40	9,01	2,27
	1,00	348	337	4,40	10,72	2,27

Figura 4
Espalhamento da argamassa com 0,30 de f/c e 0,40% de sp/c

Para as proporções de finos de 0, 0,10, 0,20, e 0,30 as argamassas com 0,40 e 0,60% de relação sp/c apresentaram elevada fluidez e moderada viscosidade, porém, as argamassas produzidas com mais que 0,80% de sp/c apresentaram sinais de segregação. Com a inserção de um maior teor de finos (0,40 e 0,50 de f/c) foi possível produzir argamassas autoadensáveis com até 0,80% de sp/c. Todas as argamassas produzidas com 1,00% de teor de aditivo superplastificante, em relação a massa de cimento (sp/c), apresentaram sinais de segregação, com concentração de material no centro do espalhamento e exsudação da mistura nas bordas.
Os índices de espalhamento relativo (G_m) e escoamento relativa (R_m) das argamassas autoadensáveis apresentam-se na figura 3. Os espalhamentos (G_m) obtidos nas argamassas consideradas autoadensáveis demonstram que quanto maior a utilização de aditivo superplastificante maior será o espalhamento relativo. O impacto das alterações das proporções de finos é mais evidente ao se utilizar 0,40% de relação sp/c, para os outros teores de aditivo superplastificante a alteração dos espalhamentos é menor.
A viscosidade relativa (Rm) obtida por meio do ensaio do funil-v para argamassas tem por objetivo demonstrar principalmente a viscosidade do material analisado, desta maneira, quanto menor o valor de Rm mais viscosa é a argamassa. As argamassas com 0,40% de relação sp/c apresentaram a maior viscosidade, já as argamassas com 0,60 e 0,80% de relação sp/c não apresentaram grandes alterações. Para todas as argamassas analisadas o aumento do teor de finos originava argamassas mais viscosas, este fenômeno ocorre, pois, o fíler calcário calcítico compõe a argamassa preenchendo os espaços vazios e consequentemente aumentando a coesão devido à grande área superficial do material. Porém, o ponto máximo de efeito do incremento de material fino ocorre nas relações de 0,40 e 0,50 de f/c, onde a variação de viscosidade é quase nula.
Por fim, a argamassa com melhor relação entre fluidez e viscosidade e mais apta a produzir traços de concreto autoadensável, com as características necessárias, foi a com 0,40% de relação sp/c e teor de finos de 30%, em relação a massa de cimento. Este traço apresentou espalhamento médio de 197,00 milímetros e tempo de escoamento de 6 segundos, os valores para espalhamento e escoamento relativo foram respectivamente de 2,88 e 1,66. A figura 4 demonstra o espalhamento obtido por esta argamassa. Esta argamassa apresentou a fluidez necessária para ser considerada autoadensável e apresentou altíssima viscosidade, sendo esta última uma propriedade vital ao inserir agregado graúdo na argamassa para a produção de concreto autoadensável.

3.2 Propriedades no estado endurecido

Os resultados obtidos com os ensaios de resistência à tração a partir dos valores médios e desvios padrões podem ser visualizados na figura 5.
As argamassas autoadensáveis apresentaram leve ganho de resistência à tração por meio do incremento do fíler calcário calcítico. As argamassas com maiores teores de finos apresentaram

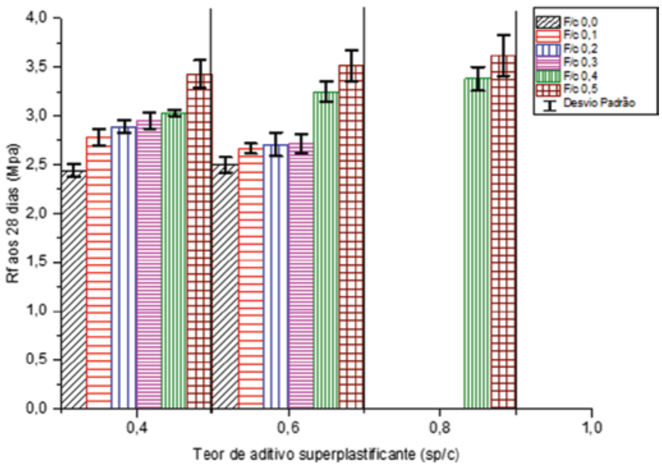

Figura 5
Resistência à tração aos 28 dias para as argamassas autoadensáveis

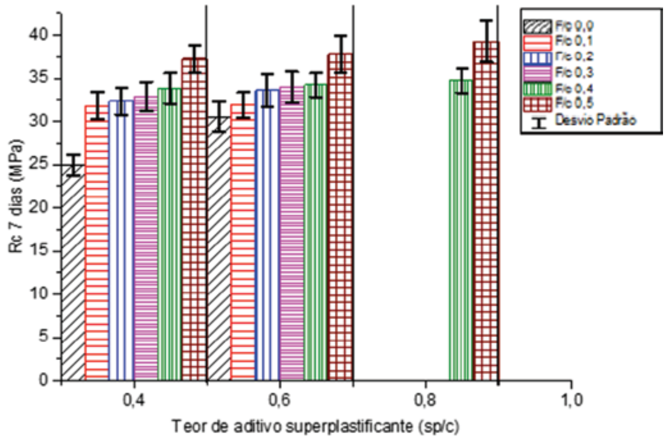

Figura 6
Resistência à compressão aos 7 dias para as argamassas autoadensáveis

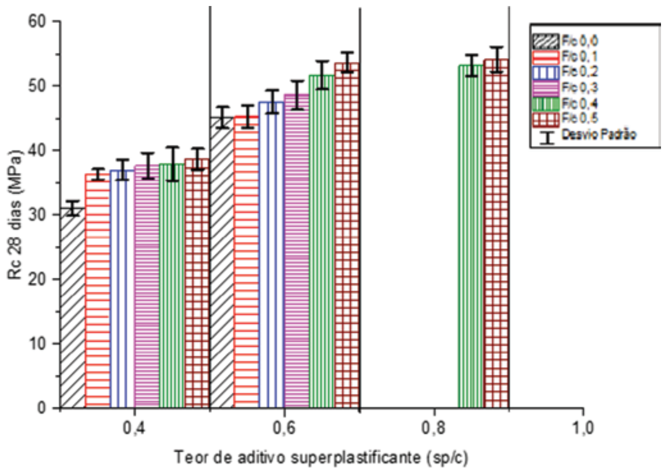

Figura 7
Resistência à compressão aos 28 dias para as argamassas autoadensáveis

maior resistência à tração, isto ocorre porque o fíler calcário calcítico preencheu espaços vazios da argamassa.
Os resultados obtidos com os ensaios de resistência à compressão aos 7 dias, com seus valores médios e desvios padrões, podem ser visualizados na figura 6. As argamassas aparesentaram aumento na resistência à compressão conforme aumentavam-se os índices de sp/c avaliados, este resultado já era esperado pois foram mantidos as relações a/c utilizadas. Por outro lado, o aumento no teor de finos resultou em um acréscimo da resistência à compressão das argamassas mesmo que pequeno, as argamassas com f/c de 0,50 apresentaram os melhores resultados para os rompimentos realizados aos 7 dias.
Os resultados obtidos com os ensaios de resistência à compressão aos 28 dias com seus valores médios e desvios padrões podem ser visualizados na figura 7. Aos 28 dias, é possivel notar um incremento geral da resistência à compressão nas argamassas por meio do aumento do teor de aditivo superplastificante comparando os traços com 0,40 e 0,60% de relação sp/c, este efeito justifica-se a partir da manutenção da relação a/c dos materiais e aumento da utilização de aditivo, fatores estes que, quando combinados, levam a um aumento de hidratação do cimento. Também é possível verificar que o incremento de fíler calcário calcítico produz um aumento da resistência à compressão das argamassas devido a maior coesão e compacidade dos materiais.
Macedo [26] realizou adição da cinza do bagaço de cana-de-açúcar em argamassas e obteve resultados médios de resistência à compressão aos 28 dias de 44,70 MPa com teor de adição de cinza de 3%, já com 5% de adição de cinza a resistência foi de 48,30 MPa, com 8% de adição a resistência foi de 46,80% e de 51,00 MPa com 10% de adição. No presente estudo, o resultado de resistência à compressão obtido da argamassa considerada autoadensável com 0,30 de relação f/c e 0,40% de sp/c foi de 35,40 MPa, resultado semelhante aos obtidos por Nagano [18] no qual concretos autoadensáveis produzidos com substituição de 10% da areia por cinza do bagaço de cana-de-açúcar apresentaram resistência à compressão aos 28 dias de 30,85 MPa.
Mollin Filho [27] produziu concretos autoadensáveis com substituição de 10% da areia por cinza do bagaço de cana-de-açúcar e obteve resultado de resistência à tração de 2,56 MPa. Para a argamassa considerada autoadensável, no presente estudo, a resistência à tração foi de 2,80 MPa próxima ao obtido por Mollin Filho [27], considerando uma maior utilização de CBCA.

4. Conclusões

No estado fresco, a partir da variação do teor de finos, foi possível identificar uma relação entre incremento de fíler calcário calcítico e viscosidade, ao mesmo tempo que o aumento na dosagem desse material proporcionava uma redução da fluidez. Desta maneira, conclui-se que o filer calcário calcítico pode ser utilizado a fim de aumentar a viscosidade e obter argamassas autoadensáveis. Por outro lado, observou-se uma estagnação deste comportamento (fluidez e viscosidade) nas argamassas com 0,40 e 0,50 de relação f/c.
As variações analisadas de aditivo superplastificante comprovaram o comportamento esperado, conforme se aumenta a dosagem de aditivo superplastificante obtém-se uma maior fluidez e menor viscosidade nas argamassas. Outro comportamento verificado, conjuntamente com a utilização de finos, é que ao se utilizar altíssimos teores de finos para a obtenção de alta viscosidade é necessário um aumento proporcional na relação de aditivo superplastificante utilizado.
No estado endurecido, as variações analisadas apresentaram pouca alteração nos resultados. A resistência à tração e à compressão aumenta sutilmente à medida em que se aumenta a utilização de finos e de aditivo superplastificante. O aumento da utilização de finos proporciona um aumento da resistência devido ao efeito fíler do material. Já o aumento da resistência, obtido pelo aumento da relação sp/c, é proporcionado pelo fato de se utilizar a mesma relação de água em diferentes taxas de aditivo superplastificante.
Outro ponto importante a ser destacado é a definição de faixas ótimas para a obtenção de argamassas autoadensáveis com os materiais dosados. As argamassas que obtiveram melhores aspectos de fluidez e viscosidade foram as produzidas com relação f/c de 0,30, já a taxa ótima de dosagem de aditivo superplastificante é de 0,40 a 0,60%, em relação à massa de cimento.
Desta maneira, constata-se que é possível produzir argamassas com propriedades autoadensáveis com alta taxa de utilização de cinza de bagaço de cana-de-açúcar e obter incremento de viscosidade por meio de aumento na dosagem de finos. Com os resultados obtidos é possível definir traços de argamassas que servirão de base para produção de concretos com propriedades autoadensáveis, a partir da definição da viscosidade e fluidez a serem obtidos, podendo ser definido o teor de finos mais adequado para a produção do CAA.
Assim sendo, se torna viável produzir concretos com a substituição parcial do agregado miúdo por cinza do bagaço de cana-de-açúcar (CBCA), levando em consideração as condições as quais os experimentos deste estudo foram submetidos. De modo que, a partir dos resultados obtidos por meio deste estudo, foi possível substituir 40% do agregado miúdo por CBCA obtendo maior massa unitária da composição feita entre areia e CBCA.

5. Agradecimentos

Ao Programa de Pós-Graduação em Engenharia Urbana (PEU) e ao Departamento de Engenharia Civil (DEC-UEM), pelas contribuições e auxílio durante a pesquisa.
Ao Laboratório de Materiais de Construção pela disposição de recursos utilizados durante a pesquisa.
À Usina Santa Terezinha pela doação da CBCA.
À BASF do Brasil, que por meio do engenheiro Vitor M. Marconi concedeu o patrocínio do aditivo superplastificante Glenium 51.

6. Referências bibliográficas

[1] ALCOFORADO, L. F. M. Viabilidade econômica do concreto auto-adensável na construção de prédios em Goiânia – GO. Journal on-line Especialize, Goiânia, v. 3, n. 1, p. 1-13, 2013.
[2] OKAMURA, H.; OUCHI, M. Self-compacting concrete. Journal of Advanced Concrete Technology, Tokyo, vol. 1, n. 1, p. 5-15, abr. 2003.
[3] ALCANTARA, M. A. M.; SANTOS, B. V. Concreto auto--adensável com cinzas de bagaço de cana como finos: Reologia do concreto fresco e comportamento no estado endurecido. Eletronic Journal of Civil Engineering, V. 5, N. 1, p. 17-35, 2012.
[4] OLIVEIRA, F. L; MELLO, E. F. A mineração de areia e os impactos ambientais na bacia do rio São João, RJ. Brazilian Journal of Geosciences, Rio de Janeiro, V. 37, 2º ed., p 374-389, 2007.
[5] CONAB - COMPANHIA NACIONAL DE ABASTECIMENTO. Acompanhamento de safra brasileira: cana-de-açúcar, segundo levantamento, agosto/2016 - Companhia Nacional de Abastecimento. – Brasília: CONAB 2016.
[6] FIESP/CIESP – FEDERAÇÃO DA INDÚSTRIAS DO ESTADO DE SÃO PAULO/ CENTRO DAS INDÚSTRIAS DO ESTADO DE SÃO PAULO Ampliação da oferta de energia através da biomassa. São Paulo: 2001.
[7] ASSOCIAÇÃO BRASILEIRA DE NORMAS TÉCNICAS. ABNT NBR 5733. Cimento Portland de alta resistência inicial. Rio de Janeiro, 1991
[8] OKAMURA, H.; OUCHI, M. Self-compacting concrete. Journal of Advanced Concrete Technology, Tokyo, vol. 1, n. 1, p. 5-15, abr. 2003.
[9] VOTORANTIM. Catálogo de cimentos 2016. Available in: <http://www.mapadaobra.com.br/produtos/cimento/linha>. Access in: November 13, 2015.
[10] ASSOCIAÇÃO BRASILEIRA DE NORMAS TÉCNICAS. ABNT NBR NM 248. Agregados - Determinação da composição granulométrica. Rio de Janeiro, 2003.
[11] ASSOCIAÇÃO BRASILEIRA DE NORMAS TÉCNICAS. ABNT NBR NM 30. Agregado miúdo - Determinação da absorção de água. Rio de Janeiro, 2001.
[12] ASSOCIAÇÃO BRASILEIRA DE NORMAS TÉCNICAS. ABNT NBR NM 52. Agregado miúdo - Determinação de massa específica e massa específica aparente. Rio de Janeiro, 2002.
[13] ASSOCIAÇÃO BRASILEIRA DE NORMAS TÉCNICAS. ABNT NBR NM 45. Agregados - Determinação da massa unitária e do volume de vazios. Rio de Janeiro. 2006.
[14] BASF. Ficha técnica de produto: GLENIUM 51 - Aditivo Superplastificante de terceira geração. Available in: < https://www.ntcbrasil.com.br/wp-content/uploads/2014/12/glenium-51--especificacoes-completas.pdf >. Access in: July 12, 2015.
[15] CAZANGA. Calcário Agrícola: características do produto. Available in: < http://www.cazanga.com.br/index.asp?c=paginas&modulo=conteudo&url=80 >. Access in: August 26, 2015.
[16] NUNES, I. H. S. Estudo das características físicas e químicas da cinza do bagaço de cana-de-açúcar para uso na construção. Masters dissertation. State University of Maringá, UEM, Technology Center, Maringá, 2009.
[17] SOUTO, J. M. F. Avaliação do desempenho da cinza do bagaço de cana-de-açúcar na produção de concretos. 2009, 118f. Master dissertation. State University of Maringá, UEM, Technology Center, Maringá, 2010.
[18] NAGANO, M. F. Dosagem do concreto autoadensável utilizando a cinza do bagaço de cana-de-açúcar. 2014, 142f. Master dissertation. State University of Maringá, UEM, Techonolgy Center, Maringá, 2014.
[19] ASSOCIAÇÃO BRASILEIRA DE NORMAS TÉCNICAS. ABNT NBR 15900-1. Água para amassamento do concreto. Rio de Janeiro, 2009.
[20] DOMONE, P. L; JIN, J. Properties of mortar for self-compacting concrete. In: FIRST INTERNATIONAL RILEM SYMPOSIUM ON SELF-COMPACTING CONCRETE, p. 109-120, 1999.
[21] TAKADA, K; TANGTEMSIRIKUL, S. Testing of fresh concrete. In: SELF-COMPACTING CONCRETE: STATE-OF--THE-ART REPORT OF RILEM TECHNICAL COMMITTEE 174-SCC. Cachan: RILEM Publications, S.A.R.L., 2000, p. 20-34.
[22] EDMATSU, H; NISHIDA, N; OUCHI, M. A rational mix-design method for self-compacting concrete considering interaction between coarse aggregate and mortar particles. In: FIRST INTERNATIONAL RILEM SYMPOSIUM ON SELF-COMPACTING CONCRETE, 1999, p. 309-320.
[23] NEPOMUCENO, M; OLIVEIRA, L.; LOPES, S. Methodology for mix design of the mortar phase of self-compacting concrete using different mineral additions in binary blends of powders. Construction and Building Materials. v. 26, n.1, p. 317-326, 2012.
[24] ASSOCIAÇÃO BRASILEIRA DE NORMAS TÉCNICAS. ABNT NBR 13279. Argamassa para assentamento e revestimento de paredes e tetos – Determinação da resistência à tração na flexão e à compressão. Rio de Janeiro, 2005.
[25] ASSOCIAÇÃO BRASILEIRA DE NORMAS TÉCNICAS. ABNT NBR 5739. Concreto – Ensaio de compressão de corpos-de prova cilíndricos. Rio de Janeiro, 2007.
[26] MACEDO, P. C. Avaliação do desempenho de argamassas com adição de cinza do bagaço de cana-de-açúcar. 2009. 116 f. Master dissertation. Paulista State University, Ilha Solteira Engineering College, 2009.

Volume 12, Number 1 (February 2019) p. 199 – 209 • ISSN 1983-4195
http://dx.doi.org/10.1590/S1983-41952019000100012

REVISTA IBRACON DE ESTRUTURAS E MATERIAIS
IBRACON STRUCTURES AND MATERIALS JOURNAL

Analysis of strengthening procedures of reinforced concrete highway bridges: a brazilian case study

Análise de procedimentos de reforço de pontes rodoviárias: um estudo de caso brasileiro

D. M. CARVALHO [a]
davidsonmatosdnit@gmail.com
https://orcid.org/0000-0003-3412-6552

J. M. F. CALIXTO [a]
calixto@dees.ufmg.br
https://orcid.org/0000-0003-2828-0967

Abstract

The Brazilian federal highway system is largely made up of reinforced concrete (RC) bridges built prior to 1984. Thus, these bridges have incompatible geometry and loading carrying capacity with nowadays traffic. In this scenario, the goal of this investigation was the evaluation of the widening and strengthening procedures used in these RC bridges. The study also includes comparing their performance with the respective new bridges built next to them, which received new highway lanes. This comparison is adequate, considering that, both bridges are inserted in the same environment, are subjected to the same traffic characteristics and have similar spans and structural systems. The results obtained allow us to know the effectiveness of the widening and strengthening interventions carried out, from the point of view of durability, contributing to the improvement of future rehabilitation design for reinforced concrete highway bridges.

Keywords: reinforced concrete highway bridges, strengthening procedures, performance.

Resumo

O sistema rodoviário federal brasileiro é constituído em grande parte por pontes construídas antes de 1984. Assim, essas pontes possuem geometria e capacidade de carga incompatíveis com o tráfego atual. Nesse cenário, o objetivo deste estudo foi a avaliação dos procedimentos de alargamento e reforço empregados em uma ponte de concreto armado que foi reabilitada, visando atender às novas exigências de uma rodovia que foi duplicada. O estudo também inclui a comparação do seu desempenho com a ponte nova, também em concreto armado, que foi construída ao lado para receber a pista nova. Esta comparação se mostra adequada, considerando que ambas as pontes são inseridas no mesmo microclima, estão sujeitas às mesmas características de tráfego e têm vãos e sistemas estruturais semelhantes.Os resultados obtidos permitem conhecer a eficácia das intervenções de alargamento e reforço realizadas, sob o ponto de vista da durabilidade, contribuindo para a melhoria de projetos futuros de reabilitação de pontes rodoviárias de concreto armado.

Palavras-chave: pontes rodoviárias em concreto armado, procedimentos de reforço, desempenho.

[a] *Federal University of Minas Gerais, MG, Brazil.*

Received: 24 Jan 2018 • Accepted: 07 May 2018 • Available Online: 05 Feb 2019

1. Introduction

The reinforced concrete (RC) bridges that make up the Brazilian highway system were built from the 1940s, along with the edition of the first Brazilian standards (DNIT [4]). Since then, there has been an evolution of the calculation tools, the materials used in the works, the construction techniques and the vehicles that use the highways, resulting in several updates of standards over time and consequently a very heterogeneous profile of bridges, with different characteristics such as class, geometry, mobile design loads, types of safety barriers and guardrails, which vary according to the construction date.

Considering that the growth of the Brazilian highway system had its apex in the 1960s and 1970s, it is verified that most of the reinforced concrete bridges were built before 1984, that is, they are prior to the validity of the norm NBR-7188 [2] and therefore need strengthening to suit nowadays load carrying capacity.

Currently there is a growing demand for widening and strengthening of reinforced concrete highway bridges. In addition of presenting structural problems (either due to the deterioration of the structure as well as the obsolescence in terms of live loads required by the current design codes), these bridges have also insufficient cross sections for the current traffic demand (Vitório and Barros [12]).

According to a report of the Brazilian Federal Accounting Office (TCU [10]), of a total of 5,612 bridges belonging to the federal road network, 4,105 have lane narrowing problems. In addition, of the 4,739 bridges registered in the Bridges Management System of the National Department of Transport Infrastructure, 261 are in a poor state of conservation and seven in a precarious state of conservation, that is, they require short-term and immediate interventions, respectively (DNIT [6]).

According to Vitório [11], the activities of widening and strengthening of highway bridges began to draw the attention of the Brazilian technical community from the mid-90s, when several works of duplication and / or enlargement of relevant federal and state highways started. These works have shown the need for further studies on structural interventions in bridges and overpasses. Records of technical and managerial information regarding the performance of interventions that have already been performed do not address properly the aspects of durability. In an investigation by Oliveira [9], some aspects were pointed out in the structural strengthening interventions carried out on RC bridges, which inevitably compromised the durability of the structure and new placed reinforcement. This information is essential to identify problems which should be avoided in strengthening procedures to be carried out in the future. In this scenario, the goal of this investigation was the evaluation of the widening and strengthening procedures used in RC bridges that were rehabilitated, aiming to meet the new requirements of a highway that underwent duplication. The study also includes comparing their performance with the respective new bridges built next to them, which received new highway lanes. This comparison is adequate, considering that, both bridges are inserted in the same environment, are subjected to the same traffic characteristics and have similar spans and structural systems. Surveys in both bridges were executed after the intervention in accordance with the Brazilian current standards. Detailed study of both bridges were conducted including their original design and blueprints, survey reports throughout their service life, strengthening design and procedures as well as a recent evaluation of their performance. The chosen bridges are located over the Pará River on Brazilian highway BR 262 in Nova Serrana, Minas Gerais. Figure 1 shows an overview of these evaluated bridges.

Figure 1
Overview of the evaluated bridges. To the left is the rehabilitated bridge and to the right the new bridge

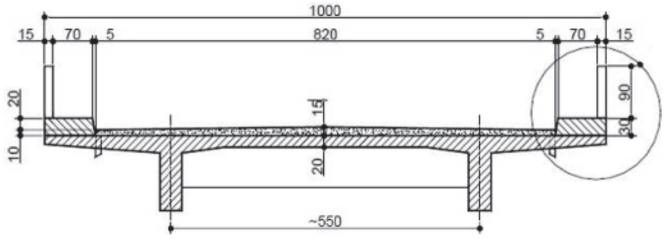

Figure 2
Cross section of the original bridge (dimensions are in centimeters)

2. Rehabilited bridge

2.1 Description of the original bridge

The original bridge (class 360 kN) was designed in 1965 by the Brazilian Federal Highway Department - DNER. It was designed according to Brazilian codes: NB-1/1960, NB-2/1960 and NB-6/1960. These codes determined the bridge class, their geometrical characteristics and the live loads to be adopted in bridge design.

This bridge had a length of 230 meters, divided into ten spans of 22 meters and two 5 meters cantilevers at both ends. It had a total width of 10.0 meters (8.20 m roller tracks, with two bearing ranges, wheel guard and body guard). The superstructure is formed by a RC slab over two main beams (Figure 2), simply supported on eleven pairs of columns, and twenty-two transversal beams. The supports have bracing beams at the top and also in the middle and their infrastructure consisted of 22 caissons. The structure of the

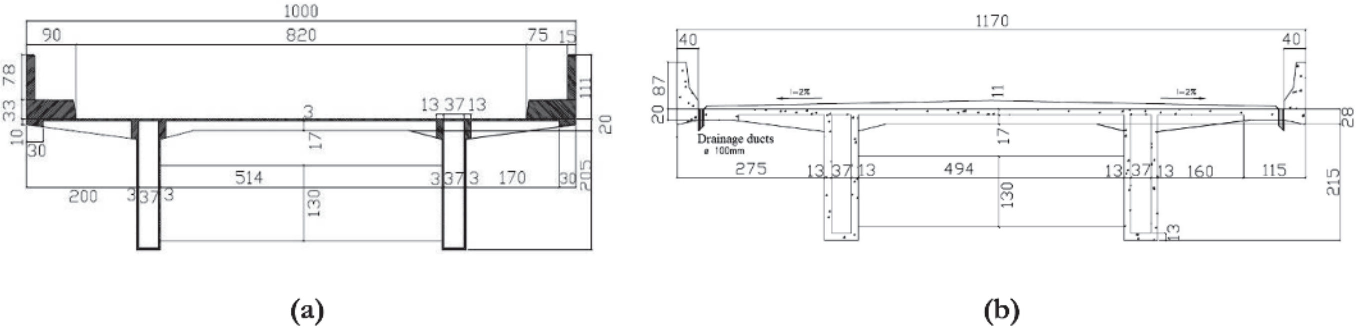

Figure 3
Details of the strengthening procedure. (a) Demolition parts, (b) Formwork and concrete replacement (dimensions are in centimeters)

bridge is further composed of bearing walls at both ends and three expansion joints: two at both ends and one at the middle span. Rubber pads were used on three column lines (1st, 6th and 11th) and lead plates on the other supports.

2.2 Strengthening procedures

The rehabilitation interventions of the bridge were carried out from July 2010 to July 2011 and were aimed at meeting the new requirements of the BR-262 highway that was being duplicated. The design increased the bridge total width from 10.0 to 11.70 meters, which corresponded to two track lanes and shoulder. The bridge was also designed for a live load class of 450 kN. The strengthening procedures also include replacement of support devices, of the pavement, of expansion joints and exchange of wheel guards and guardrails by New Jersey barriers, as well as repairing the concrete where necessary.

The method used for increasing the bridge width consisted of extending the existing slabs at both sides without the addition of new supports and new beams; conventional reinforced concrete was employed. The strengthening of the superstructure was based on the increase of the cross section of the structural elements with addition of new reinforcement (increase in the dimensions of the main beams and addition of new overlay on the slab). Details of these procedures are shown schematically in Figure 3.

The initially design plan included the demolition of the guardrails, of wheel guards and of 30 cm at the ends of the slabs on the sides of the bridge. In addition a 3 cm concrete layer was removed from top surface of the slab and from the faces of the two main beams, aiming to prepare these surfaces for the new repairing concrete. Then, a new 11 cm top slab was cast, along with the new slab with a width of 1.15 m on each side of the bridge (30 cm demolished + 85 cm for the widening). New Jersey barriers and a new 13 cm concrete layer on the faces of the main beams were also cast. The concrete characteristic compressive strength was equal to 30 MPa. Drainage ducts with a diameter of 100 mm were installed on both sides of the bridge.

The column sizes were also increased. The procedure consisted first of the removal of a 3 cm concrete layer of all column sides followed by the placement of additional reinforcement and the casting of a new 13 cm concrete layer. The concrete characteristic compressive strength was equal to 25 MPa. Corbels were also built at the tops of the columns with the objective of supporting the hydraulic jacks that were used for the replacement of the support devices. Mobile 39 mm thick neoprene type pads were installed in all supports: their horizontal dimensions were 35 x 45 cm on the columns at the ends of the bridge and of 45 x 60 cm on the others. Twenty-two new pile caps around each column were built as shown in Figure 4. The concrete characteristic compressive strength was equal to 25 MPa. A deep foundation system consisted of four root-type piles (200 mm diameter) for each pile cap.

In addition to the widening and strengthening interventions, the rehabilitation design consisted of sealing existing cracks at the bottom surface of the slab and repairing the transversal beams and bearing walls where corrosion of the reinforcement was detected. These procedures were intended to treat those locations that did not receive strengthening interventions, but only where they were needed.

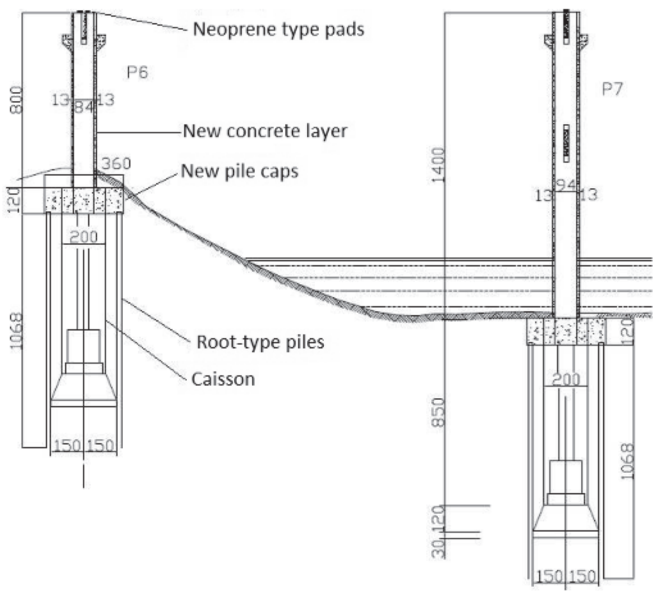

Figure 4
Details of the strengthening of the foundations (dimensions are in centimeters)

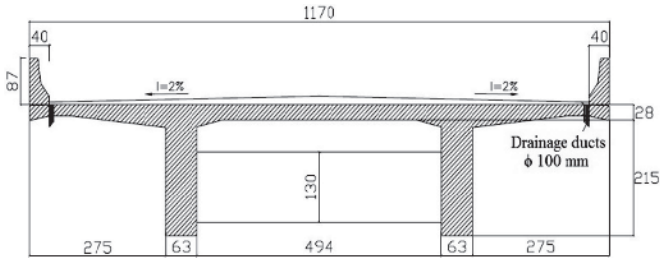

Figure 5
Cross section of the new bridge (dimensions are in centimeters)

3. New bridge

A 450 kN class new bridge was designed in 2006 by DNIT for the duplication of interstate BR-262 highway. Construction of the bridge took place from May 2009 to September 2010. It was then used as a traffic diversion during the rehabilitation of the old bridge and from July 2011, it began to integrate the duplicate interstate highway.

This bridge is also 230 meters in length, and has the same structural system and the same spans of the old bridge. The RC members have the same cross sections of the old bridge elements after the rehabilitation interventions. The concrete characteristic compressive strength was equal to 25 MPa for the foundation elements and 30 MPa for the rest; the specified cover to reinforcement was 3 cm. The bridge foundations in this case consisted of only caissons. Figure 5 shows the cross section with the geometric characteristics of the new bridge.

4. Previous inspections

The first inspections were carried out by the concessionaire Triunfo-Concebra, responsible for this segment of the interstate highway since of March 2014. An initial inspection was carried out on April 11, 2014 and since then routine inspections are per-formed annually. The main damages identified in these inspections are presented in Table 1.

5. Results of the 2017 inspection

The rehabilitated and the new bridge were inspected on June 7, 2017, following the criteria established by NBR 9452 (ABNT [3]) and DNIT 010/2004 - PRO (DNIT [6]). These inspections had the objective of evaluating the current state of the two bridges. The following equipment was employed: tools for cleaning activities and inspection, goggles for improving the vision and measurement devices. In addition to the visual inspection, a pacometer, made by Bosch model D-tect 150 Professional, was used to verify the cover to the reinforcement. The main damages and anomalies identified in each constituent element of the evaluated bridges are presented next.

5.1 Inspection of the rehabilitated bridge

5.1.1 Roller track

According to what had been reported in previous inspections, there is a lane narrowing on the bridge due to the existence of a pedestrian walkway on the place in which, according to the design, there should be the continuity of the shoulder. The pavement on the both bridge accesses shows only minor irregularities and a patch on the expansion joint was executed to correct a small step caused by a settlement. This settlement also caused a vertical misalignment of the safety barrier and sinking of the wings. This in turn led to crushing of the concrete and the exposition of the reinforcement on the left side of the bearing wall. On the right side, although the vertical displacement of the bearing wall had not occurred, it did not resist the weight of the wing, which caused cracking, the disintegration of the concrete and reinforcement exposure. The bearing walls also showed water infiltration points, most likely associated with drainage problems on the both sides of the bridge accesses. Several pathologies were identified in the safety barriers and guardrail, such as cracks, disintegration of the concrete, displacements, stains, and exposed and/or corroded reinforcements. The tests made with the pacometer indicated values of reinforcement covers on the barriers different from the design; this fact that can justify the early emergence of damages related to reinforcement corrosion. The expansion joints were obstructed by the asphalt coating, blocking the free

Table 1
Results of previous inspections of both bridges

Bridge	Year	Identified damages
Rehabilitated	2014	Decreased cross-section of the road; vegetation without maintenance; walkway with debris.
Rehabilitated	2015	Lack of vegetation protection on slopes; infiltrations and problems in the drainage system at the bridge both ends; cracks on wings; deteriorated concrete in safety barriers; maintenance problems in dripping pan and drainage ducts.
Rehabilitated	2016	Deteriorated expansion joints.
New	2014	Decreased cross-section of the road; vegetation without maintenance; walkway with debris.
New	2015	Lack of vegetation protection on slopes; infiltrations and problems in the drainage system at the bridge both ends; cracks on wings; deteriorated concrete in safety barriers; maintenance problems in dripping pan and drainage ducts.
New	2016	Deteriorated expansion joints.

movement of the superstructure and consequently leading the accumulation of moisture and the deterioration of the sealing material. Moreover, there was accumulation of debris on the roller track close to the expansion joint. Figure 6 shows the conditions of the roller track, including the retaining structure, the drainage system and guardrails.

5.1.2 Superstructure

The main damage that was identified in the super-structure was the concrete crushing of cantilever slab due to the settlement of the land fill which was not resisted by the bearing wall. There were also damages on the under surface of the slab related to failure in the drainage ducts and dripping pans that were poorly functioning, allowing water percolation through the slab on both cantilever sides. Infiltration stains in places that did not receive repair or strengthening interventions were also found. The presence of water on the under surface of the slab and the infiltrations may lead to leaching, concrete porosity increase and strength reduction which can make it more

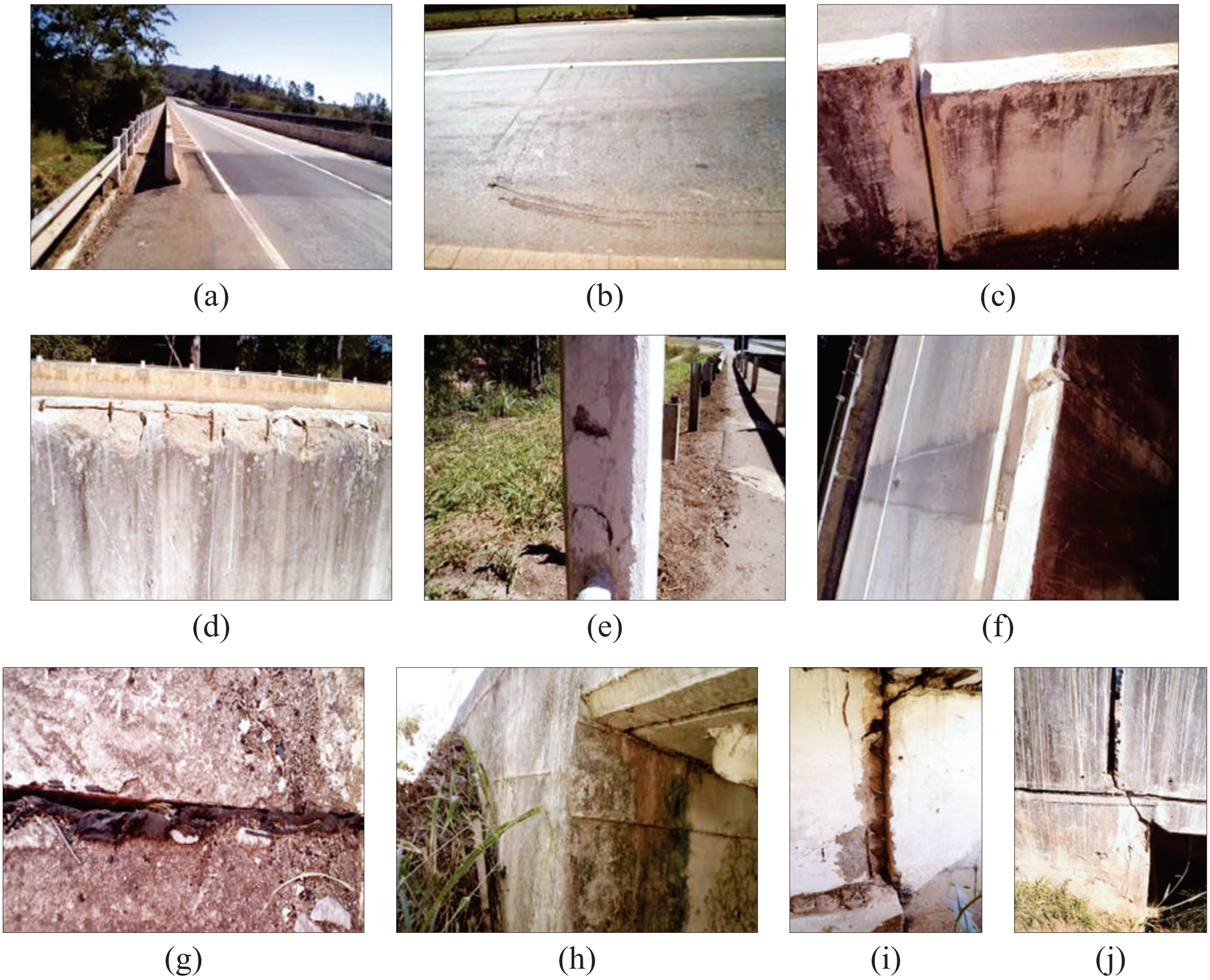

Figure 6
Conditions of the roller track. (a) Lane narrowing on the bridge and patch on the expansion joint, (b) Irregularities in the pavement on the access road, (c) Vertical misalignment of the New Jersey barrier, (d) Disintegration of the concrete and exposed reinforcement on the New Jersey barrier, (e) Reinforcement corrosion on the guardrail, (f) Expansion joint obstructed by the asphalt coating, (g) Deteriorated sealing material at the walkway, (h) Water infiltration points at the bearing wall; (i) Sinking of part of the bearing wall (left side), with crushing of the concrete and the exposition of the reinforcement, (j) Cracking, disintegration of the concrete and reinforcement exposure on the right side of the bearing wall

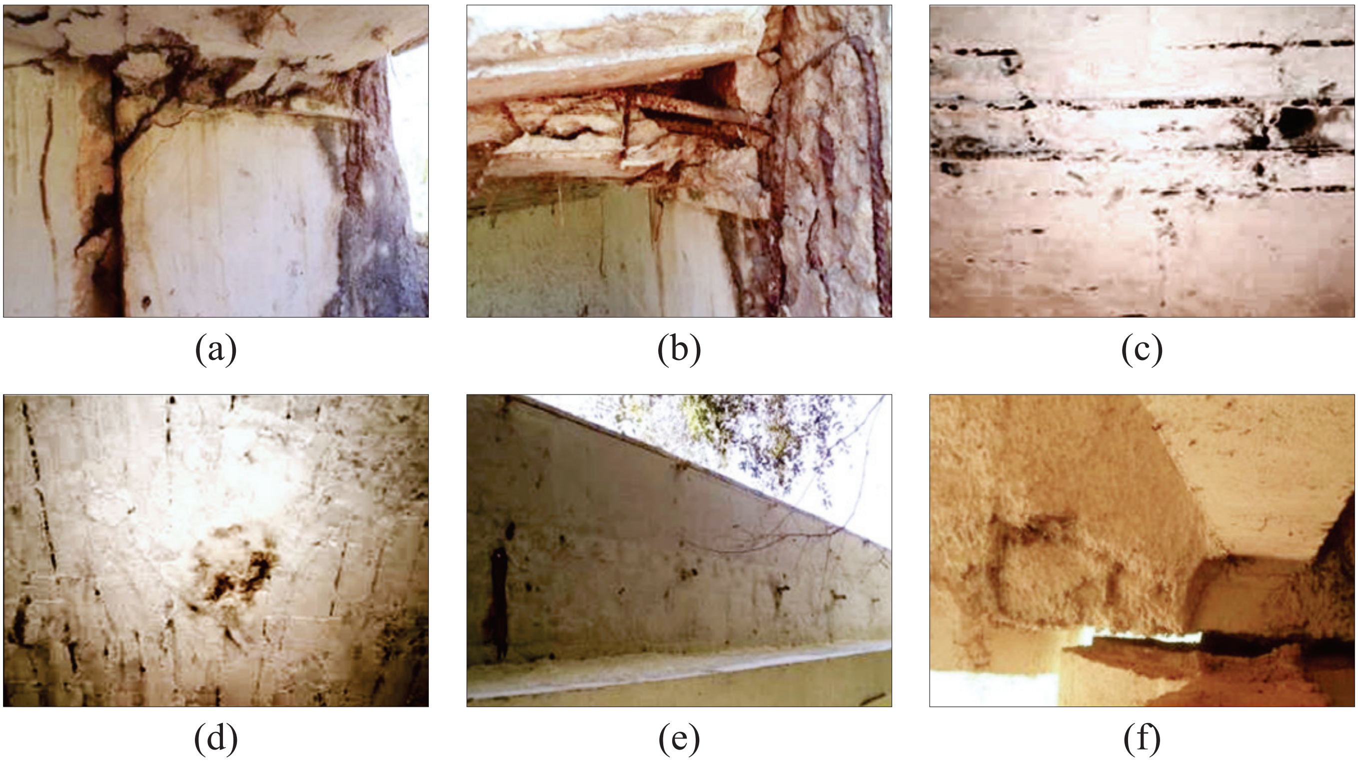

Figure 7
Main damages identified in the superstructure. (a) Concrete rupture of the cantilever slab, (b) Detail of the bended slab with crushing of the concrete and reinforcement exposure, (c) Exposed reinforcement on the under surface of the slab, (d) Infiltration stains at the bottom surface of the slab (e) Damaged drainage ducts, allowing water percolation through the slab, (f) Localized concrete casting voids were noticed on the under surface of retrofitted main beams with exposed reinforcement

vulnerable (HELENE [7]). Localized concrete casting voids were noticed on the under surface of retrofitted main beams next to the support columns. The measurements made with the pacometer showed insufficient concrete cover on the transversal beams and the slab, including the retrofitted parts of these elements. These aspects are shown in Figure 7.

5.1.3 Mesostructure

The mesostructure is in good condition of preservation. Only a few localized concrete casting voids in retrofitted columns have been identified; but they did not cause any type of structural deficiency. Signs of water infiltration in the sixth line of columns were noticed

Figure 8
Damages identified in the mesostructure. (a) Signs of water infiltration in the columns and transversal beam, due to failures in the sealing of the expansion joint (b) Exposed reinforcement in the column strengthening

due to failures in the sealing of the expansion joint. These damages are shown in Figure 8.

5.1.4 Infrastructure

The most relevant identified anomalies in this bridge are in the new and strengthened elements of the foundation. The pile caps and part of the root-type piles were executed above water level, different from the design, which prescribed buried piles. This pile position compromises their durability and also reduces the contribution of lateral friction in increasing the load carrying capacity of the foundation. Major execution problems were visible at the top of the root type piles: significant reduction of their cross section dimensions due to the presence of concreting honeycombs or due to disintegration of concrete associated with the poor quality of the material. Failures in the bonding of the pile caps with the root-type piles prevent the strengthened elements to resist additional load and effectively contribute to the increase in the load carrying capacity of the foundation. Only the old caissons are bearing the bridge's increased load. There was no vegetation protection on the slopes which led to signs of erosion that needed correction to avoid the future occurrence of any kind of instability in the foundation or retaining structures of the roller track. Figure 9 illustrates these aspects.

5.2 Inspection of the new bridge

5.2.1 Roller track

The new bridge presents lane narrowing for the same reasons as the old bridge. The pavement was in good conditions, having presented only a few deviations on the road accesses to the bridge. Settlement of the land fill of both accesses could also be observed, resulting in vertical misalignment of the safety barrier. Safety barriers and guardrail showed several pathologies most likely associated with the insufficient thickness of reinforcement cover. The expansion joints located at the ends of the bridge were completely obstructed by the asphalt coating. The joint located in the middle of the bridge, although unobstructed, also showed problems in the sealing due to deterioration of its filling material. There was a hole on the floor of the walkway caused by the settlement of the land fill at the exit of the bridge, which crushed the concrete on that part. The bearing walls presented water infiltration points most likely associated with malfunctioning of the drainage system. Figure 10 shows these conditions.

5.2.2 Superstructure

The main pathological problems identified in the structure were

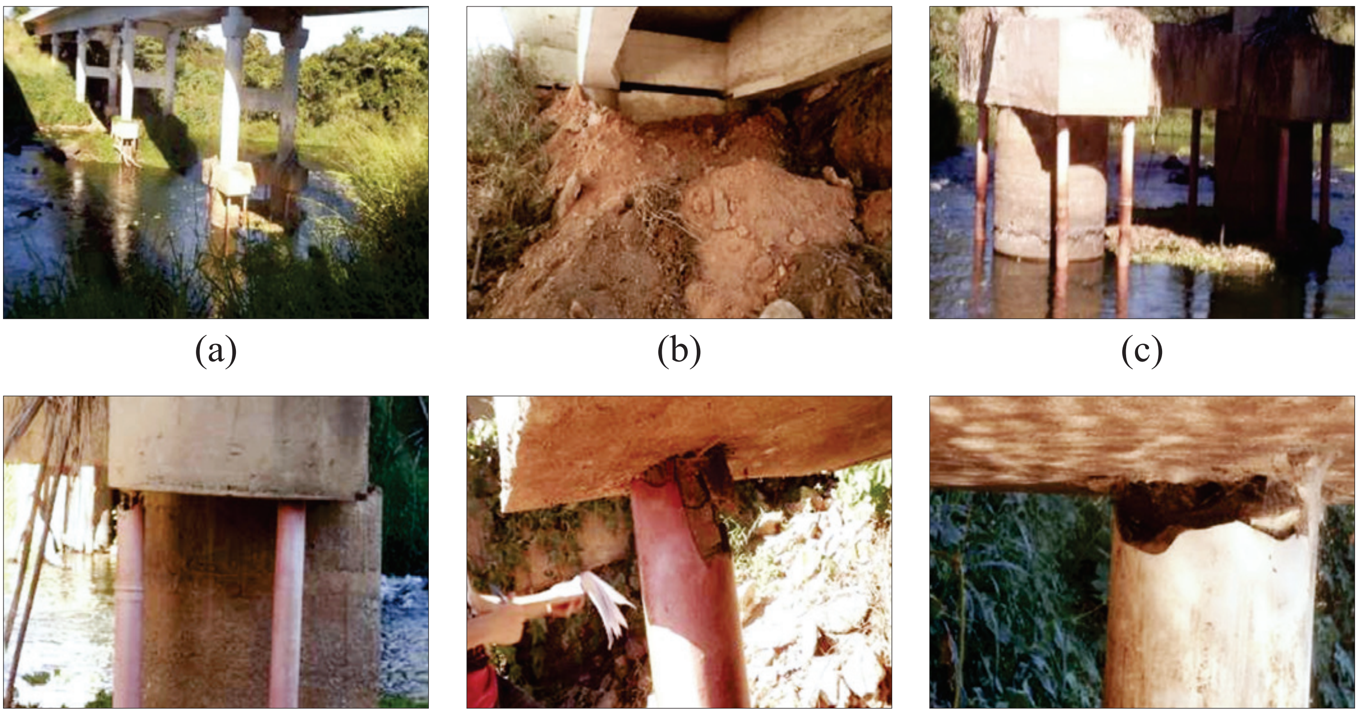

(a) (b) (c)

(d) (e) (f)

Figure 9
Main problems related to infrastructure. (a) Exposed pile caps and part of the root-type piles, (b) Signs of erosion and lack of vegetation protection on the slope, (c) Damages at the top of the root-type piles, (d) Lack of concrete at the top of the pile in which the cap rests, (e) Disintegration of concrete at the top of the pile, (f) Concreting voids at the top of the pile

related to the drainage system, which was not efficient. There were some infiltration stains in the gaps of the slab and in one transversal beam caused by rupture of the sealing material in one of the expansion joints. Reinforcement was exposed on the top surface of the slab of the walkway. The main beams showed cracks on their lateral faces due to bending, but the openings were within acceptable levels according to norm NBR 6118 (ABNT [1]). The results of the pacometer tests showed insufficient concrete in the slab and in main and transversal beams. These aspects are illustrated in Figure 11.

5.2.3 Mesostructure

In general, the elements of the mesostructure were in good conditions. Some signs of infiltration caused by rupture of the sealing material were identified in the bracing beam that connects the columns located below the expansion joint (Figure 12 a). The supporting devices were obstructed by styrofoam and mortar residues compromising their optimal performance (Figure 12 b). Reinforcement cover was smaller than prescribed by design.

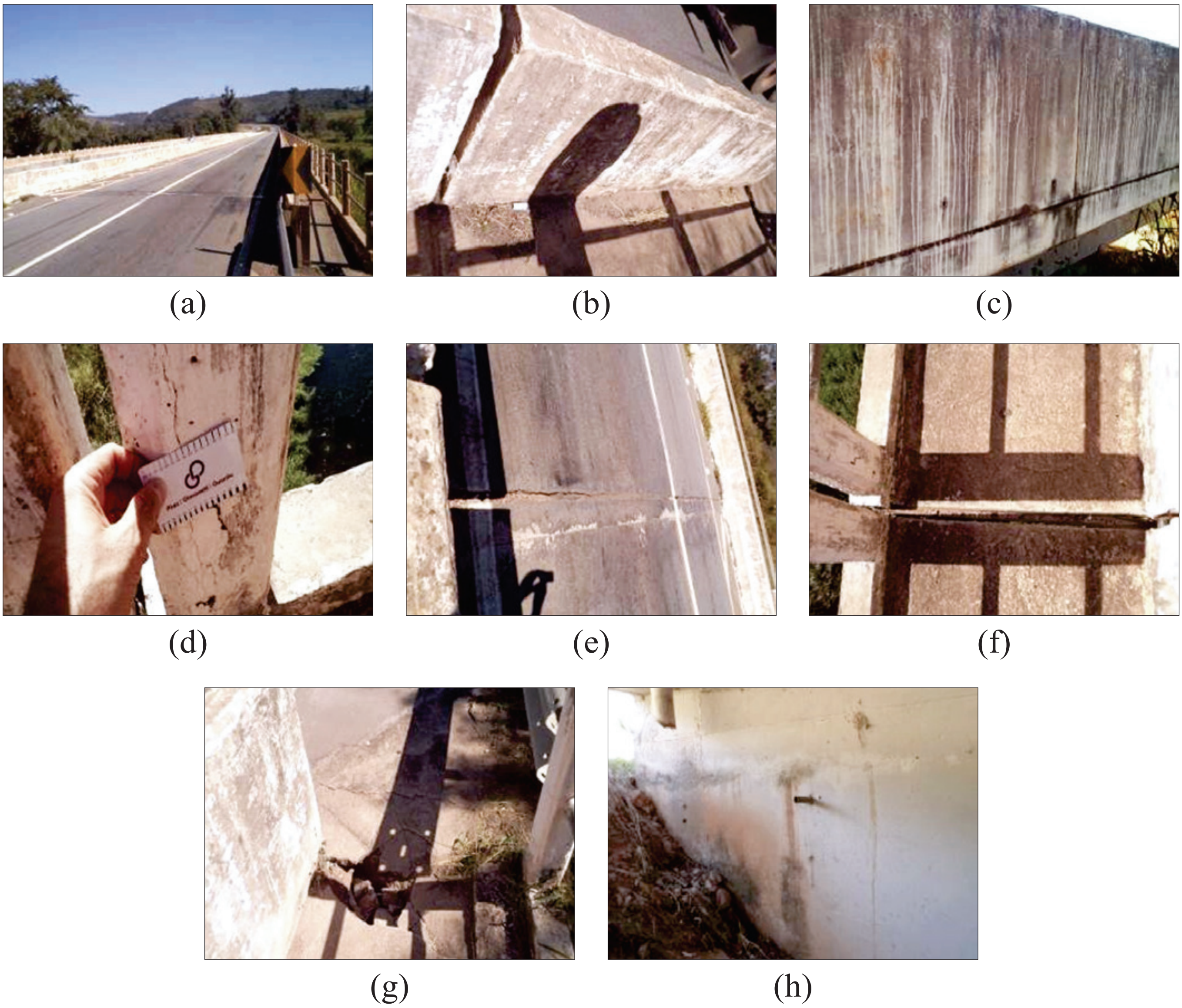

Figure 10
Conditions of the roller track. (a) Lane narrowing on the bridge, (b) Vertical misalignment of the New Jersey barrier, (c) Infiltration stains on the New Jersey barrier, (d) Cracking with opening of 0.4 mm in the guardrail due to reinforcement corrosion, (e) Expansion joint obstructed by the asphalt coating, (f) Deteriorated sealing material at the walkway, (g) Hole on the floor of the walkway, caused by the settlement of the land fill, (h) Water infiltration points on the bearing wall

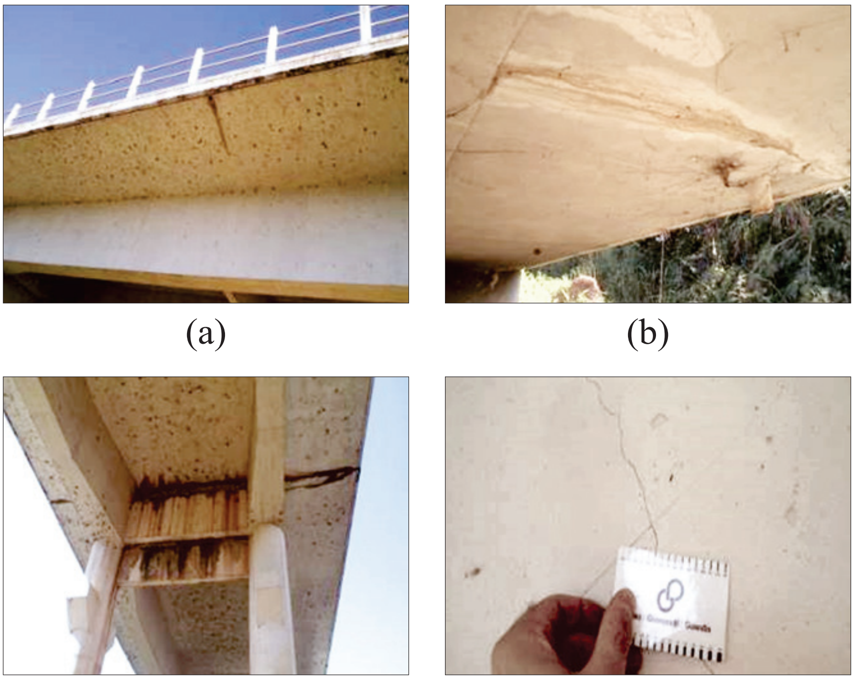

(a) (b)

(c) (d)

Figure 11
Main damages identified in the superstructure. (a) Malfunctioning of the dripping pan, (b) Malfunctioning of drainage ducts and of the dripping pan, (c) Infiltration stains in the slab and in one transversal beam, caused by rupture in the sealing material in one of the expansion joints, (d) Cracking with a maximum opening of 0.3 mm at the lateral side of the main beams

5.2.4 Infrastructure

Despite its largest part not being visible, it is assumed that the infrastructure is in good state of preservation since there was no sign of consolidation or displacement of the foundation. Only the absence of vegetation protection on the slopes and some minor erosions caused by bad positioning of some drainage ducts that direct rain water to the exit of the land fill were observed (Figure 13).

5.3 Comparative analysis of the inspection evaluation

In general, the new bridge had a satisfactory performance: no significant damage that may affect the stability of the construction was detected. As for the rehabilitated bridge, its performance was subpar, with several damages or anomalies that may compromise not only its structural safety but also its long-term durability. Figure 14 shows a chart with the technical grades attributed to

(a) (b)

Figure 12
Main damages found in the mesostructure. (a) Infiltration stains on the bracing beam of the columns located be-low the expansion joint, (b) Presence of mortar residues around the support device

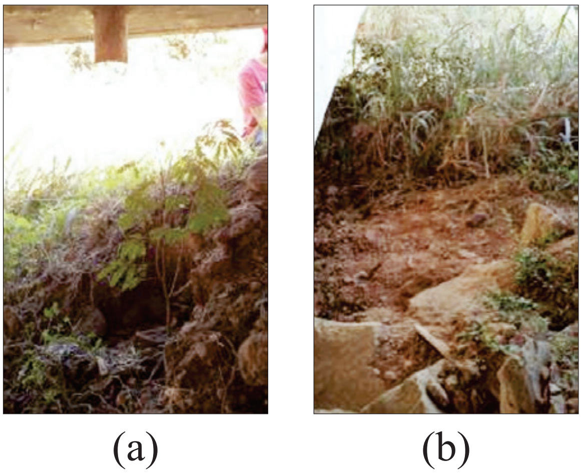

Figure 13
Main damages identified in the infrastructure.
(a) Minor erosion on the slope caused by bad positioning of drainage duct, (c) Another erosion on the slope

each bridge, in accordance to the criteria established by Brazilian standard NBR 9452 (ABNT [3]).

The smaller technical grades of the rehabilitated bridge, related to structural and durability aspects, are due to deficient performance of the new and retrofitted concrete elements. The poor conditions of the rehabilitated bridge's safety barriers interfered on its technical grade according to the functionality behavior. The existence of cracks in the main beams and erosions located on the slopes of both bridge accesses were the most influential aspects in the evaluation of the new bridge. According to the results, correction of the anomalies that cause structural insufficiency and affect the long-term durability of the rehabilitated bridge should be the short term actions to be taken. The medium term actions correspond to the correction of problems that affect its functionality. For the new bridge, monitoring the cracks in the main beams of the new is recommended as a medium term measure; correction of the erosions on the slope may also be necessary.

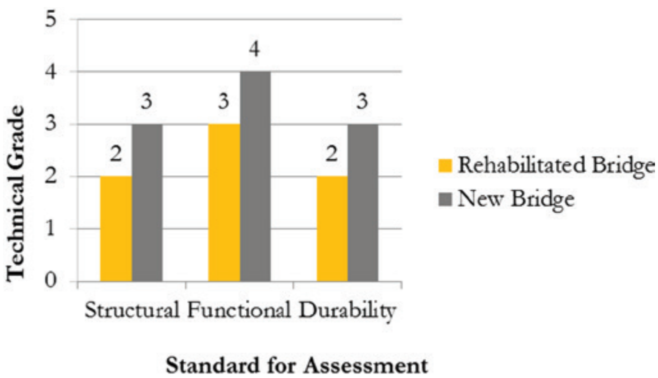

Figure 14
Technical grades attributed to each bridge

6. Conclusions

The main damages identified in the rehabilitated bridge are located in the strengthened foundation elements and in both bridge access (with consequences on the performance of the wings, bearing wall and slab). These problems are related to deficient retrofitting execution procedures and to the absence of a repair design for the structural elements that did not need strengthening.

Considering the problems identified in the widening and strengthening interventions, and the narrow scope of the repair design, it can be concluded that the rehabilitation of the bridge was not effective in this case. Besides ensuring the geometrical and load carrying capacity readjustment, the rehabilitation procedures should have provided an increase on the service life performance of all elements that compose the bridge. These aspects make the early emergence of aforementioned problems unacceptable.

The occurrence of common damages in both bridges was also verified. The drainage system proved to be inefficient, not being able to collect rainwater from the road and protect the superstructure of the bridges. According to Mehta and Monteiro [8], water is a key factor when it comes to durability issues with the concrete structures since it may cause its degradation by physical and/or chemical processes, besides corrosion of the embed reinforcement. The new concrete elements, such as New Jersey barriers and guardrails do not present adequate performance due to insufficient reinforcement cover, in disagreement with the design. The expansion joints are obstructed by the asphalt coating, compromising its optimal performance and the durability of the structure as a whole. The absence of the design for pedestrian walkways resulted in the narrowing of both bridges, compromising the safety of the road's users.

Maintenance activities have a fundamental role in the long-term durability of reinforced concrete bridges (DNIT [5]). This study indicates that the maintenance on both inspected bridges deserves more attention since they will ensure safety and comfort the users through the execution of cleaning activities on the road as well as minor correction procedures such as rehabilitation of the drainage system devices. They have low cost and big impact on the long-term durability of the structure.

The analysis of the data collected during the inspections and the level of deterioration of each evaluated bridge show that the rehabilitated bridge had a much inferior performance when compared to the new bridge that was built next to it. However, the main anomalies that were identified are related to major retrofitting execution problems that could have been avoided with a more rigorous quality control during that the rehabilitation construction phase of the old bridge. So, in spite of the result found in this particularly bridge when compared to a new one, repairing and strengthening procedures of old reinforced concrete bridges to meet nowadays traffic demands is still a viable solution.

7. References

[1] ASSOCIAÇÃO BRASILEIRA DE NORMAS TÉCNICAS – ABNT, 2014. NBR 6118: Projeto de estruturas de concreto - Procedimento. Rio de Janeiro.

[2] ___, 1984. NBR 7188: Carga móvel em ponte rodoviária e passarela de pedestre. Rio de Janeiro.

[3] ___, 2016. NBR 9452: Inspeção de pontes, viadutos e passarelas de concreto. Rio de Janeiro.

[4] DEPARTAMENTO NACIONAL DE INFRAESTRUTURA DE TRANSPORTES – DNIT, 2004a. Manual de Inspeção de Pontes rodoviárias. Rio de Janeiro.

[5] ___, 2010. Manual de Recuperação de Pontes e Viadutos Rodoviários. Rio de Janeiro.

[6] ___, 2004b. Norma DNIT 010/2004 – PRO – Inspeções em pontes e viadutos de concreto armado e protendido - Procedimento. Rio de Janeiro.

[7] HELENE, Paulo (ed.), 2003. Manual de Reabilitação de Estruturas de Concreto: Reparo, Reforço e Proteção. Red Rehabilitar, São Paulo.

[8] MEHTA, P. Kumar; MONTEIRO, Paulo J. M., 1994. Concreto, microestrutura, propriedades e materiais. Tradução: Antônio Carmona Filho et al. São Paulo: PINI.

[9] OLIVEIRA, C.B.L., 2013. Análise da eficácia de métodos de reforço de pontes rodoviárias de concreto armado. Dissertação – Curso de Pós-Graduação em Construção Civil, Universidade Federal de Minas Gerais, Belo Horizonte, MG.

[10] TRIBUNAL DE CONTAS DA UNIÃO – TCU, 2012. Acordão 725/2012– Plenário. Brasília.

[11] VITÓRIO, J.A.P., 2013. Um estudo comparativo sobre métodos de alargamento de pontes rodoviárias de concreto armado, com a utilização das normas brasileiras e eurocódigos. Tese de doutorado na Universidade do Porto, Portugal.

[12] VITÓRIO, J.A.P.; BARROS, R.M.M.C., 2014. A utilização do Eurocódigo em Projetos de Alargamento e Reforço de Pontes Rodoviárias de Concreto. VII Congresso Brasileiro de Pontes e Estruturas. Rio de Janeiro, RJ.

IBRACON

REVISTA IBRACON DE ESTRUTURAS E MATERIAIS

IBRACON STRUCTURES AND MATERIALS JOURNAL

Volume 12, Number 1
February, 2019
ISSN: 1983-4195

Contents

Analysis of the brazilian federal bridge inventory
C. B. L. OLIVEIRA, M. GRECO and T. N. BITTENCOURT
1

Analytical study of cylindrical tanks including soil-structure interaction
R. L. C. SILVA, G. B. MARQUES, E. N. LAGES and S. P. C. MARQUES
14

Geometric optimization associated with the use of high-strength concrete in viaducts
E. V. W. TRENTINI and C. H. MARTINS
23

Effects of* Bacillus subtilis *biocementation on the mechanical properties of mortars
N. SCHWANTES-CEZARIO, M. F. PORTO, G. F. B. SANDOVAL, G. F. N. NOGUEIRA, A. F. COUTO and B. M. TORALLES
31

Numerical study of the behaviour of loop bar splicing in joints of reinforced concrete structures
T. D. L. VASCONCELOS and V. G. HAACH
39

Experimental analysis of load capacity in beams with steel fiber reinforcement on the compression face
C. C. DEGHENHARD, B. V. SILVA and F. PELISSER
69

Strut-and-tie models for linear and nonlinear behavior of concrete based on topological evolutionary structure optimization (ESO)
R. M. LANES, M. GRECO and M. B. B. F. GUERRA
87

Pervious concrete: study of dosage and polypropylene fibers addiction
S. E. PILZ, P. OLIVEIRA, F. REGOSO, V. A. PAULON and M. F. COSTELLA
101

A numerical analysis of a concrete slab breaching using high explosives
M. L. COSTA NETO and G. N. DOZ
122

Comparative analysis among standards of the area calculation of transversal reinforcement on reinforced concrete beams of high resistance subjected by shear force
D. H. L. BRAZ, R. BARROS and J. N. DA SILVA FILHO
139

Behavior of the self-compacting mortar with sugarcane bagasse ash in the fresh and hardened state
V. C. SANTOS, R. D. VANDERLEI, K. K. MORAES, E. T. D. F. ROSINA and G. M. BALBINO
179

Analysis of strengthening procedures of reinforced concrete highway bridges: a brazilian case study
D. M. CARVALHO and J. M. F. CALIXTO
199